Integrated strato-tectonic, U-Pb geochronology and metallogenic studies of the Oudalan-Gorouol volcano-sedimentary Belt (OGB) and the Gorom-Gorom granitoid terrane (GGGT), Burkina Faso and Niger, West Africa

Asinne Tshibubudze

A dissertation submitted to the Faculty of Science, University of the Witwatersrand, Johannesburg, in fulfilment of the requirements of the degree of Doctor of Philosophy in Science

2015

FRONTISPIECE

"Scientists still do not appear to understand sufficiently that all earth sciences must contribute evidence toward unveiling the state of our planet in earlier times, and that the truth of the matter can only be reached by combing all this evidence. It is only by combing the information furnished by all the earth sciences that we can hope to determine 'truth' here, that is to say, to find the picture that sets out all the known facts in the best arrangement and that therefore has the highest degree of probability. Further, we have to be prepared always for the possibility that each new discovery, no matter what science furnishes it, may modify the conclusions we draw." (Wegener, 1964).

DECLARATION

I declare that this dissertation is my own work. It is being submitted for the Degree of Doctor of Philosophy in Science in the University of the Witwatersrand, Johannesburg. It has not been submitted before for any degree or examination in any other University.

Asinne Tshibubudze

13th day of January 2015.

ACKNOWLEDGMENTS

I would like to extend my gratitude to the following people who have motivated, guided and helped me when I was completing this work: -

My supervisor, Prof. Kim A.A. Hein is thanked for her patience, thorough and constructive comments.

Thanks are due to the staff of the EarthLab at the University of Witwatersrand Johannesburg, the John de Laetre Centre at the Curtin University of Technology, the University of Western Australia Centre for Exploration and Targeting (CET), Orezone Resources (now known as Orezone Gold Corporation), IAMGOLD's Ouagadougou and Essakane Mine offices, and the University of Ouagadougou, especially P. Marquis, A. Zongo, O. Derra, E. Maes, M. Pratas, J. Aphane, A. Kennedy, R. Taylor, H. Gao, C. Isaac, B. Li, C. Schindler, L. Parra Avila, and my trusted drivers M. Sadiwidi, A. Traore, and R. Garba. I acknowledge M. Lompo and S. Naba of the University of Ouagadougou for assisting with transport logistics during field visits. Not forgetting the University of the Witwatersrand, Johannesburg, School of Geosciences staff members who encouraged and guided me while considering doing this work.

This research was sponsored by a BHP Billiton scholarship through the University of the Witwatersrand Johannesburg, the AMIRA WAXI P934 Phase II sponsors, Orezone Resources (Burkina Faso), IAMGOLD Essakane S.A. and AngloGold Ashanti. I am greatly indebted to Orezone Resources and IAMGOLD for providing support when conducting fieldwork on their permits in Burkina Faso and Niger.

I wish to gratefully acknowledge AMIRA International and the industry sponsors, including AusAid and the ARC Linkage Project LP110100667, for their support of the WAXI project (P934A). I am also appreciative of the contribution of the various Geological Surveys/Department of Mines in West Africa as sponsors in-kind of WAXI. Finally, I wish to recognize our WAXI research colleagues from the various institutions from around the world.

I will lastly like to thank my wife (P.P. Tshibubudze) for taking the time to proof read my work, and for her patience and encouragement.

TABLE OF CONTENTS

CHAPTER 5: Structural setting of gold deposits in the Oudalan-Gorouol volcano-sedimentary belt east of the Markoye Shear Zone, West African Craton

CHAPTER 6: Geology and structure of the Gorom-Gorom Granitoid Terrane

LIST OF FIGURES

the overlap is not significance. MapInfo® 9 was used in plotting the data and automatically converted the data on 30P to 31P grid with the right settings.

Figure 4.1: Reduced to Pole Airborne Magnetic Analytical signal data for the OGB in Burkina Faso and Niger. The data was acquired along east-west flight lines in 1998 by Gold Fields Exploration. The north-northeast trending Markoye Shear Zone is localized at the western side of the image.

Figure 4.2: Airborne magnetic TMI Reduced to Pole (RTP) 1st vertical derivative of the north-eastern Burkina Faso, afters Mayes (1997).

Figure 4.3: Magnetic reduced to pole image of the Essakane-Falagountou area in the OGB, acquired along north-south flight line. The white lines and the red dots are related to the exploration drill holes and samples (not part of this work). A broad magnetic high is observed over the region southwest of the Essakane gold mine, indicating the presence of a magmatic intrusion in the area.

Figure 4.4: A 1:500 000 scale LANDSAT, Bands 741 RGB image of the OGB, GGGT and surrounding areas. The drainage pattern is modified parallel-dendritic, indicating a structural control to the drainage in the area.

Figure 4.5: A 1:250 000 scale ASTER image of the north-eastern area of the Oudalan province. The geology and geomorphology could be identified and targeted through the data extracted from this image including position of outcrops.

Figure 4.6: A 1:500,000 Topographic map covering portions of the Oudalan, Seno and Tillabéri provinces in Burkina Faso and Niger. The map was used to locate most of the geographic features in the study area.

Figure 4.7: The overlay of Reduced to Pole (RTP) Airborne Magnetic Analytical signal data of the OGB in Burkina Faso and Niger (50% translucency) and the Airborne magnetic TMI Reduced to Pole (RTP) 1st vertical derivative of the north-eastern Burkina Faso. The overlay provides the coverage of the area of study with very good data correspondence.

Figure 4.8: An overlay of Reduced to The Pole (RTP) Airborne Magnetic Analytical signal data of the OGB in Burkina Faso and Niger, and the Airborne magnetic TMI Reduced to The Pole (RTP) 1st vertical derivative of the north-eastern Burkina Faso for the study area. (b) Combined worm map of lineaments extracted from the airborne magnetic data. The lineaments are defined by magnetic lows or highs. The attribute are interpreted to indicate the dominant trends of shear, faults and to a certain degree lithological boundaries. (c) Combined worm map of lineaments extracted from the magnetic data. The study area is dominated by northwest trending lineaments that are crosscut by second-order northeast trending lineaments interpreted as dolerite or gabbro dykes and sills. (d) Combined magnetic lows interpreted as linear and folded dykes/sills. (e) Ultra-mafic units of the OGB and GGGT.

Figure 4.9: (a) Magnetic reduced to pole image of the Essakane-Falagountou area in the OGB. (b) The worm map of the magnetic reduced to pole image. A broad magnetic high is observed in the region southwest of the Essakane gold mine and has the same magnetic intensity as the YMC.

Figure 4.10: (a) Reduced to the pole Airborne Magnetic Analytical signal data of the OGB in Burkina Faso and Niger. (b) Worm map of folded magnetic high dykes/sills as extracted from Figure 4.7a. (c) Location of magnetic lows that are interpreted as the Dori and Tera batholiths. (d) General area covered by the supracrustal rocks (grey) and the contact aureole (pink) of plutons and batholiths.

Figure 4.11: (a) Airborne magnetic TMI reduced to the pole (RTP) 1st vertical derivative of the Oudalan province. (b) Regions of high magnetic intensity signature (red) and low magnetic intensity signature (light yellow) extracted for the OGB and GGGT.

Figure 4.12: (a) The LANDSAT image of the OGB, GGGT. (b) The attributes extracted for drainage patterns and dune sands. The drainage pattern represents a modified parallel-dendritic pattern, indicating a possible structural control to the drainage in the area. (c) Lineaments extracted from the LANDSAT and ASTER images. The lineaments correspond with drainage system in the region. (d) Outcrop attribute layer of competent units that are folded indicating a polyphase deformation may have taken place. (e) Attribute layer of the lithological trend in the study area. (f) Attribute layer indicating the location of batholiths and plutons. Continued overleaf.

Figure 4.12 (continued): (g) Outcrops of crosscutting dykes interpreted to be the gabbro-dolerite dykes. (h) General location of the supracrustal units. (i) Attribute layer with location of the laterite cap and the MgO deposits. (j) Geographic attributes including roads, villages, and mine sites of artisanal workings.

Figure 4.13: A map of the combined information extracted from geophysical and remotely sensed data of the OGB and the GGGT area.

Figure 4.14: A map of the combined information extracted only from the geophysical and remotely sensed data excluding the sand dunes, drainages, towns and villages, roads, artisanal mine sites and dams. This map served as the hypothesis on which field studies were focused in Chapter 5-7.

Figure 5.1: Location map of the Oudalan Gorouol belt of Burkina Faso and Niger, together with the Bouroum, Yalago and Goren greenstone belts. Modified after Hein et al. (2004).

Figure 5.2: Schematic geology map of the OGB indicating the location of the Essakane Mine and Gosséy, Falagountou, Sokadie, Tin Zoubratan and Takabangou deposits. The boundaries of the OGB are defined by (1) the Markoye Shear Zone (MSZ), (2) the Tin Takanet-Bellekcire Shear Zone, and (3) the Dori Marginal Shear Zone (DMSZ). Research studies by Tshibubudze et al. (2009) of the Markoye Shear Zone are indicated by the insert box.

Figure 5.3: Lithologies of the OGB.

(a). Tuffaceous beds of the meta-volcanic sequence (UTM 31P, 0188468, 1573703).

(b). Silicified agglomerate unit of the meta-volcanic sequence near the contact with the Dori Batholith (UTM 31P, 0187383, 1574283).

(c). Pillowed basalt of the meta-volcanic sequence near the contact with the Dori Batholith (UTM 31P, 0187383, 1574283).

(d). Matrix to clast-supported polymictic conglomerate beds near the Tin Zoubratan artisanal (UTM 31P, 0183827, 1602472). Clasts are composed of angular clasts, pebbles and boulders of granite, granodiorite, gabbro, fuchsitic chert, and chert.

(e). Matrix-supported polymictic conglomerate in coarse greywacke, clasts are composed of angular clasts of quartz and quartz-carbonate vein clasts, andesite, basalt, volcaniclastic sedimentary rocks and schist (UTM 31P, 0177800, 1596649).

(f). Stromatoforms in sandy dolomite (~5m) south of the Essakane gold mine (UTM: 31P 0187303, 1588249).

Figure 5.4: Plutonic igneous rocks of the Oudalan-Gorouol area.

(a). The Dori Batholith is a medium-grained hornblende-plagioclase-quartz ± biotite ± K-feldspar granodiorite. It is phenocrystic in plagioclase (1-2cm) and hosts mafic xenoliths (UTM 30P, 0821592, 1559159).

(b). The Tera Batholith is situated in the southeast of the study area. It is composed of plagioclase feldspar, quartz, hornblende and biotite and is foliated and sheared along the Tin Takanet-Bellekcire Shear Zone (UTM 31P, 0235492, 1586086).

(c). The Dolbel batholith. The batholith is composed of 5 mm phenocrysts of plagioclase (30 % of the total volume) in a medium-grained (0.5-1.0 mm in size) groundmass of quartz and K-feldspar, with accessory biotite and chlorite (UTM 31P, 0213792, 1614382).

(d). Porphyritic monzonite dykes of the OGB. They are composed of phenocrysts of zoned plagioclase in a fine to medium groundmass of quartz, plagioclase, muscovite, biotite, chlorite and sulphides (UTM 31P, 0188829, 1588399).

(e). Porphyritic monzonite dykes of the OGB exhibiting randomly orientated plagioclase phenocrysts that are euhedral to anhedral (UTM 31P, 0184195, 1602936).

Figure 5.5: (a) The mylonitic shear bands with a dextral (reverse) displacement along the Saoga branch. (b) The Fe-manganese rich meta-sedimentary rocks are folded at all scales. The closed folds plunge steeply to the northeast.

Figure 5.6: (a). Schematic map of the Dori Marginal Shear Zone (DMSZ) and Sokadie Shear Zone. (b). The DMSZ hosts numerous quartz-ankerite extension veins (V_{1-x}) and is intensely lineated and rodded as manifested by L_{1-x}. (c). Cross section through the DMSZ along section line A-B. The DMSZ and Sokadie Shear Zone dip steeply to moderately south and exhibited reverse displacement with south block up.

Figure 5.7: Equal area stereographic projections of poles to S_{1-x}, L_{1-x} and S_2 in subdomains A-C. S_2 is disjunctive and crosscuts the DMSZ and Dori Batholith.

Figure 5.8: Schematic map of the Kargouna Shear Zone Complex. The Afu Branch is moderately west-dipping, while the Waho Branch dips moderately to steeply east. The Afu Branch crosscuts the Dori Batholith, DMSZ, Sokadie Shear Zone, gneissic rocks northeast of the Dori Batholith, and metasedimentary and metavolcanic rocks in the contact aureole of the Dori Batholith.

Figure 5.9: The gneissic unit that outcrops along the KSZC is crosscut by discontinuous outcrop scale parallel faults that help in determining the overall displacement of the Waho branch. The faults crosscut quartz-carbonate veins. The sense of displacement along the faults is sinistral strike-slip to oblique (east block up).

Figure 5.10: Schematic map of the Bom Kodjelé Trend (Domain G). It is an approximately 3km wide thrust zone that trends north-northwest and dips moderately northeast. It is dominated by quartz-chlorite-muscovite schist that hosts brecciated and boudinaged buck-quartz-carbonate ± tourmaline veins and iron-rich cataclasites.

Figure 5.11: Schematic chart of the strato-tectonic relationships established for the OGB.

Figure 6.1: The simplified geological and geographic map of the GGGT, including the extracted data from the regional geophysical images.

Figure 6.2: (a) Granodiorite dyke crosscutting the Lilengo Gneiss Complex (UTM 30P, 0805407, 1585491). (b) Granite dyke crosscut the Lilengo Gneiss Complex (UTM 30P, 0804617, 1584659). (c) The Lilengo Gneiss Complex (UTM 30P, 0811742, 1608135) and the (d) Lilengo Gneiss Complex migmatite (UTM 30P, 0807828, 1594675). (e) Northwest-trending foliation in the Lilengo Gneiss Complex is crosscut and crenulated by a disjunctive northeast trending foliation and faults (UTM 30P, 0765125, 1556780). The north-northeast trending faults (S_2) have sinistral displacement, and displace S_1 foliation and V_1 veins.

Figure 6.3: (a) Photograph of Amphibolite unit which is dark in colour. It host a penetrative and pervasive cleavage and exhibit fine compositional banding (UTM 30P, 0806590, 1593286). (b) Amphibolite with plagioclase porphyroblasts (UTM 30P, 0794957, 1594647). (c) Banded iron formation with fine laminations of light grey chert and dark brown fine grained ironstone (UTM 30P, 0807971, 1593763). (d) Quartzite unit of the GGGT composed of fine to coarse interlocking quartz granules, amphibole, carbonate, muscovite and sericite (UTM 30P, 0808076, 1583557).

Figure 6.4: (a) The name of Mrs Pink is associated with the pink colour of the granite (UTM 30P, 0819922, 1616778). (b) The Mrs Pink granite outcrop with rounded mafic xenoliths, where Mrs Pink and the xenoliths are crosscut by a weak foliation (UTM 30P, 0785692, 1610204), (c) The contact between Mrs Pink granite and the granodiorite-tonalite (UTM 30P, 0781517, 1617563). The granodiorite-tonalite is phenocrystic in plagioclase and amphibole, while Mrs

Pink granite is recrystallised at the contact. (d) A granodiorite-tonalite dyke crosscutting the Mrs Pink granite (UTM 30 P, 0799963, 1585180) indicating that the granodiorite-tonalite is younger than the Mrs Pink granite.

Figure 6.5: (a) The granodiorite-tonalite hosts elongated and stretched mafic and angular xenoliths and have potassic alteration in places (UTM 30P, 0803958, 1585126). The granodiorite-tonalite is also intruded by aplite-granite dykes (b). The mafic xenoliths are dominantly stretched and elongated along the orientation of the foliation (UTM 30P, 0797401, 1564022). (c) The Lilengo gneiss xenoliths within the granodiorite-tonalite, indicating that the Lilengo gneiss is older than the granodiorite-tonalite (UTM 30P, 0800724, 1585124). (d) Mrs Pink granite xenoliths in the granodiorite-tonalite (UTM 30P, 0799704, 1608584). The contact is crosscut and displaced by northeast trending faults with a dextral oblique-slip displacement. (e) Amphibolite xenoliths within the granodiorite-tonalite (UTM 30P, 0818525, 1618707). Continue overleaf.

Figure 6.5 (continued): (f) Metasedimentary xenoliths with compositional layering within the granodiorite-tonalite indicating that the metasedimentary sequences are older than the granodiorite-tonalite (UTM 30P, 0809052, 1580334). (g) Fine grained potash feldspar-rich aplite-granite dykes that crosscut both the granodiorite-tonalite and the gneiss xenolith (UTM 30P, 0803958, 1585126).

Figure 6.6: The map of an outcrop showing different phases of magmatic intrusions that dominate the GGGT (UTM 30P, 0801190, 1585594). The granodiorite-tonalite with mafic xenoliths is in contact with the granodiorite. The relationship indicates that granodiorite intruded the granodiorite-tonalite. The granodiorite is crosscut by north-northeast trending, steeply dipping to the southeast shear zones that have a dextral displacement. The granodiorite-tonalite is crosscut by pegmatite veins that do not crosscut the granodiorite. Both the granodiorite with mafic xenoliths and the granodiorite and the pegmatite veins are later crosscut by aplite dyke. (Insert) The image taken of the contact of the granodiorite and the granodiorite-tonalite, indicated by a box in the outcrop map, showing some of the mafic xenoliths that have folded quartz veins.

Figure 6.7: A photograph of a phenocrystic pyroxenite that have crystals that are greater than 2 cm long in a pyroxene, hornblende, biotite and plagioclase groundmass, giving the pyroxenite a spotted texture (UTM 30P 0800213, 1562317).

Figure 6.8: The migmatitic gneiss outcrop with garnet porphyroblast. The presence of garnet porhyroblasts suggests that the metamorphic grade could have or attained granulite facies (UTM 30P 0805407, 1585491) within the Lilengo gneiss complex.

Figure 6.9 Equal area stereographic projection of poles and contour plot of mylonitic foliation and lineation data measured along the D1 mylonite zones. (a) D1 mylonite zones in the GGGT

have a calculated mean principal orientation of 320°/64° E with calculated β axis of 63°→036°. (b) L_{1my} has a mean principal direction of 60°→039°.

Figure 6.10: A photograph and sketch of the outcrop along the Billiata West mylonite zone, showing a well developed mylonitic S_1-C_{my} fabric that indicates a dextral displacement.

Figure 6.11: Equal area stereographic projection of poles and contour plot of mylonitic foliation and lineation data measured along D1 mylonite zones. (a) East-northeast trending mylonite zones in the GGGT have a calculated mean principal orientation of 065°/71° N. (b) The mineral lineation data has a mean principal direction of L_{1my} of 29°→051°. The calculated beta axis has an orientation of 1°→064°.

Figure 6.12: Equal area stereographic projection of poles and contour plot of mylonitic foliation and lineation data measured along the mylonite zones. (a) North-northeast trending mylonite zones in the GGGT have a calculated mean principal orientation of 021°/76° E, with a calculated beta axis of 41°→033°. (b) The mineral lineation data has a mean principal direction of L_{1my} of 50°→053°.

Figure 6.13: Outside the mylonite zones, D1 is associated with, (a) a northwest trending foliation, which dips moderately to the northeast. (b) Mesoscopic quartz-albite veins that are folded and transposed, the veins are isoclinal and asymmetrically folded along northwest trending fold axes. (c) Dilational jogs that are right stepping and are composed of breccia of host rocks and quartz-carbonate-sulphides veins. (d) North-northeast trending left stepping en-echelon tension gashes.

Figure 6.14: The schematic summary of the overall tectonics during D1 deformation, depicting the structures that are associated with D1 deformation along the mylonite zones (yellow) and outside the mylonite zones. The tectonic transport direction in D1 is towards the southwest.

Figure 6.15: Equal area stereographic projection of poles and contour plot of D2 mylonitic foliation and lineation data measured along the mylonite zones. (a) North-northeast trending mylonite zones in the GGGT have a calculated mean principal orientation of 031°/81° E. (b) The mineral lineation data has a mean principal direction of L_{2my} of 76°→106°.

Figure 6.16: Equal area stereographic projection of poles and contour plot of D2 mylonitic foliation and lineation data measured along the mylonite zones. (a) East-northeast L_{2my} adjacent to the MSZ with a calculated average of 9°→056°. (b) Mean calculated stretching lineation L_{2my} with a mean principal direction of 59°→316° distal to the MSZ. (c) S_2-C_{my} of east-northeast trending mylonite zones has a calculated mean principal orientation of 060°/64° N.

Figure 6.17: Distal to the mylonite zones in the GGGT, D2 is associated with the formation of, (a) Northeast to east-northeast trending crenulating and disjunctive regional S_2-C cleavage. (b) North-northeast trending faults with fault planes that are chloritized. (c) Northeast trending boudinaged mafic xenoliths in granodiorite. (d) Sigmoidal en-echelon (V_2) quartz-carbonate

veins which step right and crosscut S_1-C. (e) Isoclinally folded V_1 quartz-carbonate veins with north-northeast trending fold axes (F_2).

Figure 6.18: The schematic summary of the overall tectonics during D2 deformation, depicting the structures that were reactivated or formed during D2 deformation. The tectonic transport direction in D2 was towards the southwest. Yellow lines are indicating the mylonite zone.

Figure 6.19: Photographs of the well exposed boudinage along the Sabce ultra-mylonite Zone. (a and b) The plan view of a boudin enclosed by S_1 and S_2 along the Sabce ultra-mylonite Zone that is later crosscut by S_3 foliation UTM 30P 0794388, 1593212). (c) A photomicrograph the ultra-mylonite under crossed polarized light. The potash feldspar sigma clast exhibits dextral displacement in polished thin section scale during D2.

Figure 6.20: A photomicrograph of the andalusite (And) and sillimanite (Sil) porphyroblasts from manganese rich shale at Billiata under crossed polarized light. (a) The core of the andalusite is made up of sillimanite crystals and the marginal rims are andalusite with minor clusters of inclusions of sillimanite. (b) The inclusions of sillimanite crystals occur within the andalusite porphyroblast indicating that the P-T conditions reached sillimanite and andalusite stability field.

Figure 6.21: Schematic strato-tectonic summary of the GGGT.

Figure 7.1: Geology map of the study area with sample location for the analysed samples (yellow dots and age boxes). Several other yellow dots are locations points of the several samples collected during the study.

Figure 7.2: (a) Granodiorite gneiss with folded leucocratic layers that are dominated by plagioclase and quartz minerals (UTM, 30P 1608135, 0811742). (b) Photomicrograph of the sample BF-1144, (Hbl = hornblende, Qtz = quartz, Plag = plagioclase crystals). (c) Cathodoluminesence images of zircon crystals that were analysed, they have well defined cores and rims, the cores were targeted. Numbers refers to the grain number in Table 7.1. Ellipses mark the location of the analysed spots. (d) The U-Pb Concordia diagram of the data points of the granodiorite gneiss.

Figure 7.3: Tectono-magmatic discrimination diagrams for granitoids (a) Nb-Y granite discrimination diagram showing the fields of volcanic arc (VAG), syn-collisional (syn-COLG), within-plate (WPG), and ocean ridge (ORG) granites, red line is the boundary for ORG from anomalous ridges after Pearce et al. (1984). The diagram does not discriminate between syn-collisional and volcanic-arc granites and hence diagram (b) was also plotted. (b) Rb-(Y+Nb) tectono-magmatic discrimination diagram for granitoids sampled and aliased for geochemical composition and geochronology. The Rb-(Y+Nb) tectono-magmatic discrimination diagram discriminates between syn-collisional and volcanic-arc granites.

Figure 7.4: Mrs Pink granite sampled proximal to the MSZ (UTM, 30P 1618845, 0822069). (a) Field image of the Mrs Pink granite sample. (b) Photomicrograph of the sample BF_1146, (Hbl =

hornblende, Qtz = quartz, Micr = Microcline, B = Biotite, Plag = plagioclase crystals) (c) Cathodoluminesence images of zircon crystals that were analysed, they have well defined cores and oscillatory rims, the cores were targeted. Ellipses mark the location of the analysed spots. (d) The U-Pb Concordia diagram of the strongly concordant data points of the Mrs Pink granite. (e) Age distribution bars of the calculated mean age of coherent group on 13 spots analysis.

Figure 7.5: (a) Outcrop image of Mrs Pink granite (UTM, 30P 1612261, 0800455), it was given the name due to its outstanding pink colour. (b) Microstructural composition of the Mrs Pink granite, minerals include biotite (B), hornblende (hbl), microcline (Micr), Quartz (Qtz), and Plagioclase (plag). (c) Cathodoluminesence image of the zircon crystals that were analysed. The Ellipses indicate the analysed spot. Where the rims could be analysed, both the core and the rim were targeted with the beam for analysis. (d) The U-Pb Concordia age diagram of the data points from the Mrs Pink granite. The data points are discordant along a single discordia.

Figure 7.6: (a) The Dembam Member polymictic conglomerate east of the village of Markoye (UTM, 31P 1619591, 0182783). (b) Photomicrograph of the sample BF_1147, the Plag (plagioclase), Ortho (orthoclase) and Micr (microcline) crystals are altered, and the Chl (chlorite) is growing over the re-crystallised Qtz (quartz). (c) Zircon crystals that were analysed, they lack well defined rims, the cores were targeted. Numbers refers to the grain number in Table 7.3. Ellipses mark the location of the analysed spots. (d) U-Pb Concordia diagram for the granite clast.

Figure 7.7: (a) The Gorom-Gorom granodiorite (UTM, 30P 1596251, 0800771). (b) Photomicrograph of the sample BF_1149, the Plag (plagioclase), Ortho (orthoclase) and Micr (microcline) crystals are altered, and the Chl (chlorite), Mus (muscovite) and Hbl (hornblende) are growing interstitial to the recrystallised Qtz (quartz). (c) Zircon crystals that were analysed, the cores were targeted. Ellipses mark the location of the analysed spots. (d) U-Pb Concordia diagram for the Gorom-Gorom granodiorite.

Figure 7.8: (a) The porphyritic monzodiorite (UTM, 31P 1601807, 0185023) from the OGB with euhedral and sub-rounded plagioclase crystals. (b) The microstructure of the porphyritic monzonite is dominated by dusty plagioclase (plag), Albite (alb), Pyroxene (pyr) and interstitial chlorite. (c) Cathodoluminesence image of one of the zircon crystal that was analysed with two spots. (d) The U-Pb Concordia-discordant diagram with the calculated age data plot from the five analysed spots.

Figure 7.9: Dori granodiorite gneiss (UTM, 31P 1564900, 0177188). (a) Field image of the Dori granodiorite gneiss showing a development of leucocratic and melanocratic layers. (b) Photomicrograph showing alignment of hornblende (Hbl), and the Plag (plagioclase), Qtz (quartz) and Micr (microcline) crystals that dominate the leucocratic bands. (c) Zircon crystals that were analysed, they have well defined oscillatory zoning, the cores and rims of the zircon

crystals were targeted. Ellipses mark the location of the analysed spots. (d) The U-Pb Concordia diagram of the Dori granodiorite gneiss. The data plot show a strong concordant age at 2148 Ma. (e) Mean coherent age of 12 spots grains with 2σ error bars. The mean coherent age of 12 grains (2137.9 ± 6.6 Ma) is younger than the Concordia age of 2148 ± 9.3 Ma on 16 grain spots.

Figure 7.10: Dori granodiorite gneiss (UTM, 31P 1565561, 0182376). (a) Outcrop field image of the Dori granodiorite gneiss showing a development of leucocratic and melanocratic layers. (b) Photomicrograph showing the microstructural composition that consist of chlorite (Chl), hornblende (Hbl), Plag (plagioclase), Qtz (quartz) and Micr (microcline) crystals that dominate the leucocratic bands. (c) Zircon crystals that were analysed, they have well defined oscillatory zoning, the cores and rims of the zircon crystals were targeted. Ellipses mark the location of the analysed spots. (d) The U-Pb Concordia diagram of the data from the Dori granodiorite.

Figure 7.11: (a) The Kel Enguef migmatite unit showing flow texture that developed during re-crystallization (UTM, 30P 1594675, 0808119). (b) Photomicrograph of the sample BF_1299, showing alignment of hornblende (Hbl), and the Plag (plagioclase), Qtz (quartz) and Micr (microcline) crystals that dominate the leucocratic bands. (c) Zircon crystals that were analysed, they lack well defined rims, the cores of the zircon crystals were targeted. Numbers refers to the grain number in Table 7.2. Ellipses mark the location of the analysed spots. (d) The U-Pb Concordia diagram of the migmatite.

Figure 7.12: (a) The porphyritic granodiorite (UTM, 31P 1617054, 0181894) outcrops at the fold east of Markoye village. (b) The minerals are altered and include muscovite (Mus), plagioclase (plag), orthoclase (Ortho), and quartz. (c) Cathodoluminesence image of the zircon crystals that were analysed. The Ellipses indicate the analysed spot. (d) The U-Pb Concordia age diagram on 16 grain spots. (e) U-Pb Concordia age diagram on 13 grain spots after eliminating the 3 spots with high percentage of discordance.

Figure 7.13: (a) Tin-Taradat granodiorite has banding in places (UTM, 31P 1618574, 0179168). (b) The photomicrograph showing the interlocking crystals of microcline (Micr), quartz (qtz), plagioclase (plag) and hornblende (hbl) with overprinting chlorite (Chl). (c) Cathodoluminesence image of the euhedral zircon crystals that were analysed. (d) U-Pb Concordia age diagram calculated on 16 grain spots.

Figure 7.14: The U-Pb ages summary plot, indicating the distribution of crystallisation, inherited, new growth, core and rim ages from the analyzed samples in Table 7.11.

Figure 7.15: (a) Whole rock REE patterns for samples collected for geochronology, normalised to condrite meteorite. The majority of samples (felsic granitoids) exhibit a REE pattern with near flat HREE. (b) Multi-elements diagram for the samples collected for geochronology analysis. All the samples have a significant depletion in phosphorus.

Figure 8.1: The schematic strato-tectonic summary for the OGB and GGGT established from crosscutting relationships and U-Pb ages.

Figure 8.2: Combined strato-tectono-magmatic summary of the OGB and GGGT, showing similarity and differences across the MSZ between the two terranes.

Figure 8.3: Summary of geochronology results in a flow chat format, from oldest to youngest, and their possible implications for the region and the WAC.

Figure 8.4: Summary plot for the crystallisation U-Pb ages established from the OGB and GGGT, as reported and plotted in Figure 8.3. The ages obtained from intrusive rocks of the OGB and GGGT correspond with the magmatic cycles reported in the WAC.

Figure 8.5: Tectonic evolution of the OGB and GGGT. (a) Formation of the Oudalan basin and the deposition of the Birimian type sequence within the back arc basin. (b) Deformation in D1 associated with plutonic emplacement and basin inversion. (c) Deformation in D2 during the Eburnean Orogeny with syn-tectonic emplacement of TTG. (d) The present day west to east cross-section from the GGGT to the OGB across the MSZ.

LIST OF TABLES

ABSTRACT

The Palaeoproterozoic Baoulé-Mossi domain of the West African Craton in northeastern Burkina Faso hosts numerous gold deposits such as Essakane and Tarpako. Integrated strato-tectonic, geophysical, geochemical, geochronological, regional stratigraphic framework and metallogenic studies of the Oudalan-Gorouol volcano-sedimentary Belt and the Gorom-Gorom Granitoid Terrane have provided new insight into the geotectonic evolution of the northeastern part of Burkina Faso. This work outlines the structural context and architecture necessary for forming these deposits. In this work, a new strato-tectonic model is proposed for the area by integrating field data and geophysical, geochemical, and geochronological data.

The integrated data highlights and characterizes the setting of the Essakane gold mine and gold camp relative to the location of other regional gold deposits, metamorphosed Birimian Supergroup, intrusive rocks and shear zones. Structural, geochemical and geochronological analyses have helped to clarify the geological evolution of the Oudalan-Gorouol volcano-sedimentary Belt and the Gorom-Gorom Granitoid Terrane during the Tangaean (D1) and Eburnean (D2) orogenies through to the Wabo Tampelse Event (D3). Further to these, zircon U-Pb geochronology data have demonstrated that the Oudalan-Gorouol volcano-sedimentary Belt and the Gorom-Gorom Granitoid Terrane represent some of the oldest outcropping geology in the Palaeoproterozoic Baoulé-Mossi domain recognised to date. The geochronology and geology suggest that the basement or a pre-Birimian crust to the Birimian Supergroup may be found in the northeast of Burkina Faso.

The Eburnean Orogeny in northeastern Burkina Faso is preceded by two phases of deformation ($D_{1\text{-}x}$ and D1), and two phases of magmatism. The first, $D_{1\text{-}x}$, is associated with the emplacement of the Dori Batholith at the onset of D1 (2164 – 2141 Ma). D1 ductile-brittle deformation formed F_1 folds and discrete high-strain mylonite zones that deformed the Oudalan-Gorouol volcano-sedimentary Belt and the Gorom-Gorom Granitoid Terrane during a southwest-directed palaeo-principal compressive stress. The pre-Birimian to Birimian supracrustal rocks and intrusions were regionally metamorphosed during D1 to greenschist to amphibolite facies with development of mineral assemblage of quartz-chlorite-muscovite ± chloritoid to biotite-potash feldspar ± hornblende. D1 is also associated with volcanic arc type calc-alkaline magmatism, producing TTGs enriched in heavy rare earth elements.

The Eburnean Orogeny (2130 – 1980 Ma) is characterised by northwest-southeast shortening; it was followed by north-northwest - south-southeast shortening with development of northeast trending sinistral strike-slip faults and shears. D2 brittle-(ductile) deformation is manifested by refolding of F_1 by northeast-trending F_2, and development of a pervasive northeast-trending S_2 to S_2-C foliation. Metamorphic grade attained greenschist facies during D2, with development of mineral assemblage of quartz-chlorite-muscovite ± actinolite.

The Wabo Tampelse (D3) deformation event is brittle in character and does not significantly affect the regional geological architecture in the study area.

CHAPTER 1
INTRODUCTION

1.1. Preamble

The Oudalan-Gorouol (volcano-sedimentary) belt (OGB) and the Gorom-Gorom granitoid terrane (GGGT) in the northeast of Burkina Faso forms part of the Palaeoproterozoic Baoulé-Mossi domain of the West African Craton (WAC) (Figure 1.1). The OGB and GGGT are situated in the Oudalan province of Burkina Faso, 320 km northeast of the city of Ouagadougou, with the Gorouol region being located in the Tillabéri province in the Republic of Niger, 300 km northwest of the city of Niamey.

The geology, structure and metallogenesis of the OGB and GGGT has been studied by Jeambrun et al. (1970), Nikiéma (1992), Pons et al. (1995), Rogers and Dong (2000), Rogers (2001), Delisle (2003), Kerr (2004a-e) and Tshibubudze et al. (2009). Studies by Rogers (2001), Rogers and Dong (2000), Delisle (2003) and Kerr (2004a-e) are limited to the numerous gold deposits and their immediate host rocks, or selective petrographic work of samples collected from these deposits (cf. Taner, 2004). Nikiéma (1992) and Tshibubudze et al. (2009) studied the Markoye Shear Zone and its tectonic evolution in the region east of the town of Markoye, but did not attempt to understand its relationship to local gold occurrences. Geology studies by Jeambrun et al. (1970), Nikiéma (1992) and Tshibubudze et al. (2009) were restricted to the Oudalan province in Burkina Faso and did not include studies of the Tillabéri province of Niger, which hosts the immediate extension of the OGB in that country. Pons et al. (1995) studied pluton emplacement and the structural evolution in the Gorouol region and further south in Niger. However, until 2007 integrated strato-tectonic, geophysical, geochemical, geochronological and metallogenic studies of the OGB and the GGGT had not been undertaken and the regional stratigraphic framework of the OGB and GGGT had not been established making correlations with other provinces across the WAC difficult. This became particularly important in 2007 (a time of intense exploration in the OGB) because evaluation of gold occurrences in the Oudalan province at the historic Essakane and Falagountou artisanal mine sites by BHP, Gold Fields in Joint Venture with Orezone Resources, and finally Orezone Resources Inc had shown that a considerable gold reserve was located in the region. Detailed and integrated studies were warranted to establish the spatial and temporal relationships of gold mineralisation, and place them in a strato-tectonic framework.

Furthermore, the OGB and GGGT presented numerous complexities in terms of their structural architectures that strongly suggested the accepted tectonic models for the West African craton needed re-evaluation. Rather than a single deformation model for gold formation constrained to the Eburnean orogeny (c.f., Milési et al., 1991, 1992; Boher et al., 1992; Allibone et al., 2002;

Feybesse et al., 2006; Vidal et al., 2009, De Kock et al., 2009; 2011), LANDSAT and ASTER imagery, and structural mapping of key locations by Tshibubudze et al. (2009) in the OGB fuelled debates (unpublished) that the region had been deformed during at least two discrete tectonic events. Structural and kinematic studies of the 5km wide north-northeast trending Markoye Shear Zone, and a mylonite zone on the northern margin of the Dori Batholith also showed them to be complex tectonic zones in contrast to the simple fault zones presented by Jeambrun et al. (1970) and Nikiéma (1992).

A detailed investigation of the regional structural and stratigraphic character of the OGB and GGGT was therefore warranted in order to develop a robust strato-tectonic-metallogenic model that could be used to focus cost-effective exploration for gold and base metals (Ni, PGE, Pb-Zn-Cu), and to positively contribute to a fuller understanding of the tectonic evolution of the WAC. The new model would also make possible comparisons with other gold rich domains possible, such as those in Ghana and Mali.

Importantly, the OGB hosts several deposits and deposit styles including gold mineralization at Essakane, Gosséy, Korizéna, Falagountou and Kossa (Milési et al., 1992; Castaing et al., 2003; Tshibubudze et al., 2009). According to Foster and Piper (1993) and Lompo (2001) several deposits are associated with sulphidised brittle-ductile shear zones, including gold in sheeted and stockwork quartz veins. Of significance is that the northwest-trending folds and faults that host Essakane, Falagountou, Tin Zoubratan, Bom Kodjelé and Kossa are crosscut by faults that are north-northeast trending; the intersections between the two are clearly prospective for gold and are peppered by artisanal gold mine workings (Tshibubudze and Hein., 2013; this research). The OGB thus provided an excellent natural laboratory to establish the temporal and spatial relationships between structure and gold metallogenesis, to test existing models of gold metallogenesis, and establish a strato-tectonic framework to gold mineralisation in the WAC.

Finally, geochemical and geochronological studies of key rock units uniquely constrained relative chronologies to absolute time making correlation with greenstone belts elsewhere in the WAC possible. The data suggested that the OGB and GGGT represents some of the oldest outcropping geology in the Palaeoproterozoic Baoulé-Mossi domain (Tshibubudze et al., 2013) with strong correlations with the geology of Ghana (WAXI, 2013).

1.2. Thesis organization

This thesis is divided into 10 chapters including the Introduction. The Introduction chapter introduces the main problems in the study area and the rationale of the study.

Chapter 2 provides an overview of the geological background as published in relation to the study area. It also identifies the key problems that are related to the stratigraphy, mineralisation and tectonics of the WAC.

Chapter 3 provides details of the scientific methods used in addressing the problems identified in the study area. The methods used for data collection and analysis are explained in detail.

Chapter 4 explains how the geophysical, and remotely sensed data, such as LANDSAT and ASTER was used to extract geographical and geological data necessary to understand the regional geographic and geological setting. The extracted data was used in field mapping to create a base strato-structural-metallogenic hypothesis map.

Chapter 5 presents research published by Tshibubudze and Hein (2010) entitled "*Tectonic evolution of the Oudalan-Gorouol greenstone belt in NE Burkina Faso and Niger, West African craton*" (Appendix A), and Tshibubudze and Hein (2013) entitled "*Structural setting of gold deposits in the Oudalan-Gorouol volcano-sedimentary belt east of the Markoye Shear Zone, West African Craton*" (Appendix B). It also presents research submitted for publication by Tshibubudze et al., entitled "*Gold mineralization in the Essakane goldfield, Burkina Faso*" (Appendix C). Chapter 5 presents the structural geology of Oudalan-Gorouol belt in Burkina Faso and Niger and characterizes the setting of the Essakane gold mine and gold camp. The chapter reports the lithologies that ultimately define a volcano-sedimentary belt rather than a greenstone belt (*sensu stricto*), and which host gold mineralisation in the region. It summarizes and describes the character of intrusive rocks of the greater Oudalan region and establishes a relative chronology of crosscutting relationships that broadly constrains the structural evolution of the OGB. A tectonic model for the formation of the OGB is proposed. The chapter contextualises the geology of the hanging-wall to the MSZ and the tectonic relationship of major shear zones and gold mineralisation. It gives a structural layout of first, second and third order structures. The chapter also clarifies the crosscutting relationships of structural events in the hanging-wall of the MSZ.

Chapter 6 contextualises the geology of the western (footwall block) of the MSZ herein termed the GGGT, and its tectonic evolution. The plutonic rocks of the GGGT are described and the spatial and temporal relationships of geological and structural elements are described. The chapter also creates a strato-tectonic model of the GGGT based on the tectonic evolution of the major crosscutting shear zone (the Sabce Shear Zone), so the footwall and the hanging-wall blocks (i.e. the OGB) can be compared and contrasted.

Chapter 7 geochemically classifies the key intrusive rocks and establishes their absolute chronology. This chapter incorporates the published research of Tshibubudze et al. (2013) entitled "*Oldest U-Pb crystallisation ages from the Oudalan-Gorouol belt of Burkina Faso*" (Appendix D), which reports the oldest zircon U-Pb crystallisation ages yet measured in the WAC on three unique samples of supracrustal rocks from the Oudalan province. The geochronology and geology suggests

that the basement to the Birimian Supergroup may be found in the northeast of Burkina Faso, or alternatively, that a >2200 Ma syn-Birimian granite-granodiorite suite can be found in that region, the 2200 Ma age being regarded as the 1st magmatic event in the WAC (WAXI, 2013).

Chapter 8 synthesises the data and interpretations of the study by combining and comparing the findings with data and interpretations of other researchers of the WAC. The evolution of the OGB and GGGT is compared with other belts in the WAC, and the implications of this study for the Palaeoproterozoic tectonic evolution are discussed.

Chapter 9 summarises the main findings of the study and Chapter 10 makes suggestions and recommendations for future work.

1.3. Authorship statement

Professor Kim A.A. Hein was responsible for setting the project objectives and its concepts. The overview of the candidate's contribution to published works is summarized below.

Chapter 5: *Tshibubudze, A., Hein, K.A.A., 2013. Structural setting of gold deposits in the Oudalan-Gorouol volcano-sedimentary belt east of the Markoye Shear Zone, West African craton. Journal of African Earth Sciences 80, 31-47.*

Tshibubudze, A., Hein, K.A.A., Pratas, M., Rogers, J., submitted. Gold mineralization in the Essakane goldfield, Burkina Faso. In (Markwitz, V, Hein, K.A.A., Robb, L. (Editors), Minerals Atlas Monograph of West Africa. Published by the Geological Society of South Africa.

The candidate was the primary researcher, and collected and interpreted field data, and developed the model for the tectonic evolution of the belt. Hein supervised field work, the development of the tectonic model and edited versions of the manuscript. Pratas and Rogers assisted with logistic support and discussions during field work.

Chapter 7: *Tshibubudze, A. Hein, K.A.A., Peters, L.F.H., Woolfe, A.J., McCuaig, T.C., 2013. Oldest U-Pb crystallisation ages from the Oudalan-Gorouol belt of Burkina Faso. South African Journal of Geology 116, 169-181.*

The candidate was the primary researcher, and collected and interpreted field data, and undertook geochronological studies at Curtin University of Technology and University of Western Australia. Hein supervised the work and edited versions of the manuscript. Peters and Woolfe were

supervised by Tshibubudze and Hein in their Honours research in 2011 and contributed limited data from their respective field areas in the Kel Engeuf and East Markoye regions, respectively. McCuaig assisted with logistic support and discussions during geochronological studies at Curtin University of Technology in Western Australia.

Supplementary Peer Reviewed Abstract:

Tshibubudze, A., Hein, K.A.A., 2010. Tectonic evolution of the Oudalan-Gorouol greenstone belt in NE Burkina Faso and Niger, West African craton. Geophysical Research Abstracts. Volume 12, EGU2010-708, 2010 EGU General Assembly 2010, ISSN of eISSN: 1607-7962. (Appendix A).

Aspects of this research are incorporated in Chapter 5. The candidate was the primary researcher, and collected and interpreted field data, and developed the model for the tectonic evolution of the belt. The oral presentation at the European Geosciences Union General Assembly was delivered by the candidate. Hein supervised field work, the development of the tectonic model and edited versions of the manuscript.

Supplementary manuscript:

Tshibubudze, A., Hein, K.A.A., Marquis, P., 2009. The Markoye Shear Zone in NE Burkina Faso. Journal of African Earth Sciences 55, 245-256 (Appendix E).

Field data collected during the course of the PhD research was added to the 2009 data set and is presented in Chapters 5 and 7. The candidate was the primary researcher as an honours candidate in 2007, and collected and interpreted field data, and developed the model for the tectonic evolution of the belt. Hein conceptualized the research, supervised field work, assisted with structural modeling and edited versions of the manuscript. Marquis supported the research through sponsorship from Orezone Resources Inc.

1.4. Exploration and Mining History

Mining activities in the OGB have been traced to the early 1960s, where mining was carried out by artisanal miners who, according to Gleeson and Poulin (1989) used quartz vein debris as indicators of gold prospectivity. Formalised small-scale mining at Essakane was conducted by Compagnie d'Exploitation des Mines d'Or du Burkina (CEMOB), which was owned by the government of Burkina Faso. However modern artisanal gold mining began around 1980 (Jaques et al., 2006; Luning, 2008; Werthmann, 2009). The principal operations conducted by CEMOB were the treatment of the mine tailings that were collected from artisans working for gold. BHP, Coronation International Mining Corporation and Ranger Minerals NL undertook further exploration, but in 2003

the permits were transferred to the Joint Venture partners of Gold Fields Mining International (Pty) Ltd and Orezone Resources Inc.

Orezone Resources Inc acquired the full rights over the Essakane permits, and after intensive mapping, trenching, diamond, and reverse circulation drilling programs the company reported approximately 4 million ounces of Measured and Indicated Resources and 1.3 million ounces of Inferred Resource using a 0.5 g/tonne cut-off grade (Gignac et al., 2009).

During 2008 the Essakane deposit and permits were sold to IAMGOLD Corporation who is now the operator and owner. IAMGOLD has developed the Essakane mine site with construction of a treatment plant and crushers, and an opencast mine on the site of the Essakane deposit, with an estimated 5 million ounces of Measured and Indicated Resource calculated at 0.9 g/t gold reported on the 31 December 2012 (IAMGOLD Corporation, 2012).

Similar to the Essakane goldfields, the artisanal mining in the Kossa region in Niger preceded commercial mine exploration in the last two decades. Exploration in the Kossa region was undertaken by Etruscan Gold Mining from 1997 until 2005 (Mobbs, 1997) when Orezone Resources Inc purchased the permit for further exploration. Currently the Kossa goldfields are the focus of gold exploration by Taruga Gold Limited.

1.5. Aims of the research

The principal aims and objectives of this project were:

- To complete a geophysical and GIS evaluation of the existing data from LANDSAT, ASTER, and Google Earth imagery, and geophysical data including radiometric, gravity and 1st and 2nd derivative reduced to the pole magnetic data.
- To investigate the regional structural and stratigraphic character of the OGB and the GGGT in order to develop a strato-tectonic-metallogenic model of the Essakane goldfield, and the Kossa goldfield.
- To establish the tectonic history of the OGB and GGGT with particular reference to first and second order structures and to establish their temporal and spatial relationships.
- To understand the tectonic controls to gold mineralization through systematic mapping of key deposits such as Essakane and Falagountou.
- To establish the relative (or absolute) chronology of structural events and finger-print the timing of gold metallogenesis in the Essakane, Falagountou, Sokadie and Kossa goldfields.
- To evaluate the relationship of the western block (GGGT) and the eastern block (OGB) to the MSZ within the tectonic model.
- To evaluate the geochemical signature and absolute geochronological ages of igneous rocks in the study area to establish a tectono-magmatic environment of emplacement, and establish the absolute chronology of emplacement events within the tectonic framework.

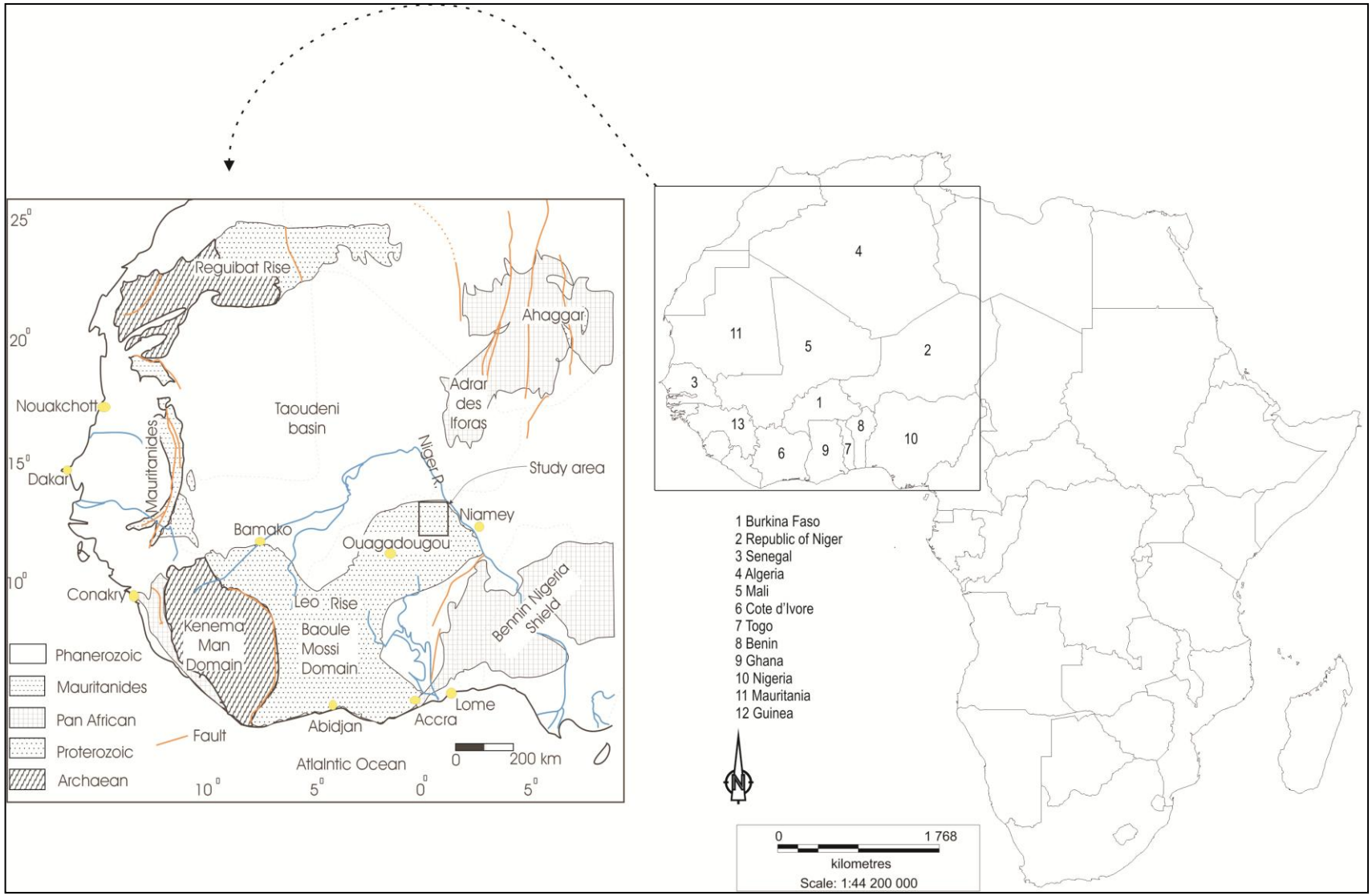

Figure 1.1: Geological overview of the West African Craton with major geological domains, and the area of study located west of the Niger River on the border of Burkina Faso and the Republic of Niger, within the Baoulé Mossi Domain.

1.6. Location and Physiography

The study area is located in the Oudalan province in the northeast of Burkina Faso and a portion of the adjoining Tillabéri Province in the west of the Republic of Niger (Figure 1.2). These provinces are located in the semi-arid sub-Saharan region known as the Sahel of Africa (Herrmann et al., 2005). The provinces are situated approximately 320 km from Ouagadougou (Burkina Faso) and 300 km from Niamey (Republic of Niger). Both Burkina Faso and Niger are landlocked countries and are rated as some of the poorest countries in the world according to the United Nations Multi-dimensional Poverty Index ratings (Alkire and Aguilar, 2012). The neighbouring countries to Burkina Faso and Niger include Mali, Benin, Togo, Ghana, and Côte d'lvoire, Nigeria, Algeria, Libya and Chad (Figure 1.1).

Climatically they have two distinct seasons; the wet/rainy season and the dry season (Herrmann et al., 2005; Kandji et al., 2006). The rainy season lasts for about four months from late May to September each year, while the rest of the year forms a dry season. Over 80% of Niger's territory is formed by the Sahara Desert, whereas about 50% of Burkina Faso (northern territory) forms part of the Sahel (Sub-Sahara) region. The vegetation in the region of study is open savannah to semi-arid desert (Herrmann et al., 2005; Kandji et al., 2006).

The multi-ethnic society of Niger is dominated by the Hausa, but other groups include the Tuareg, Fulani, Kanuri, Arab, Toubou, Djerma-Songhani and Gourmantche. The official languages of Niger are French, Hausa, Fulfude, Kanuri, Gulmancema, Zarma and Tamasheq. The vast majority (more than 90%) of the people practice Islam (Muslim), with a minority who practice Christianity or traditional indigenous religious beliefs (animism).

For the most part, Niger is topographically flat with isolated hills of laterite and erg sand dunes of the Sahara Desert. Niger has been a significant producer of uranium ore since the early 1960s from the northern region in the town of Arlit, and hosts some of the world's largest uranium deposits (Capus et al., 2004). There are also substantial deposits of oil, gold, coal, iron, limestone and gypsum (Capus et al., 2004; Soto-Viruet, 2010).

In contrast, the multi-ethnic society in Burkina Faso is dominated by two ethnic groups, the Mossi and the Bobo but minority groups include the Fulani (Peul) and Tuareg to the north (Jaques et al., 2006). The official languages of Burkina Faso include French, Moré and Dioula. About 60% of the population practice Islam, with approximately 24% who practice traditional indigenous beliefs, and about 16% who are Christian.

The country is topographically flat with isolated hills and sand dunes that dominate the northern region. The climate is tropical Savannah-Sahel with daytime temperatures ranging from 5° to 47°C.

The natural resources of Burkina Faso include manganese, copper, iron, limestone, marble, phosphate, pumice, salt, and most importantly, gold (Seymour et al., 2012).

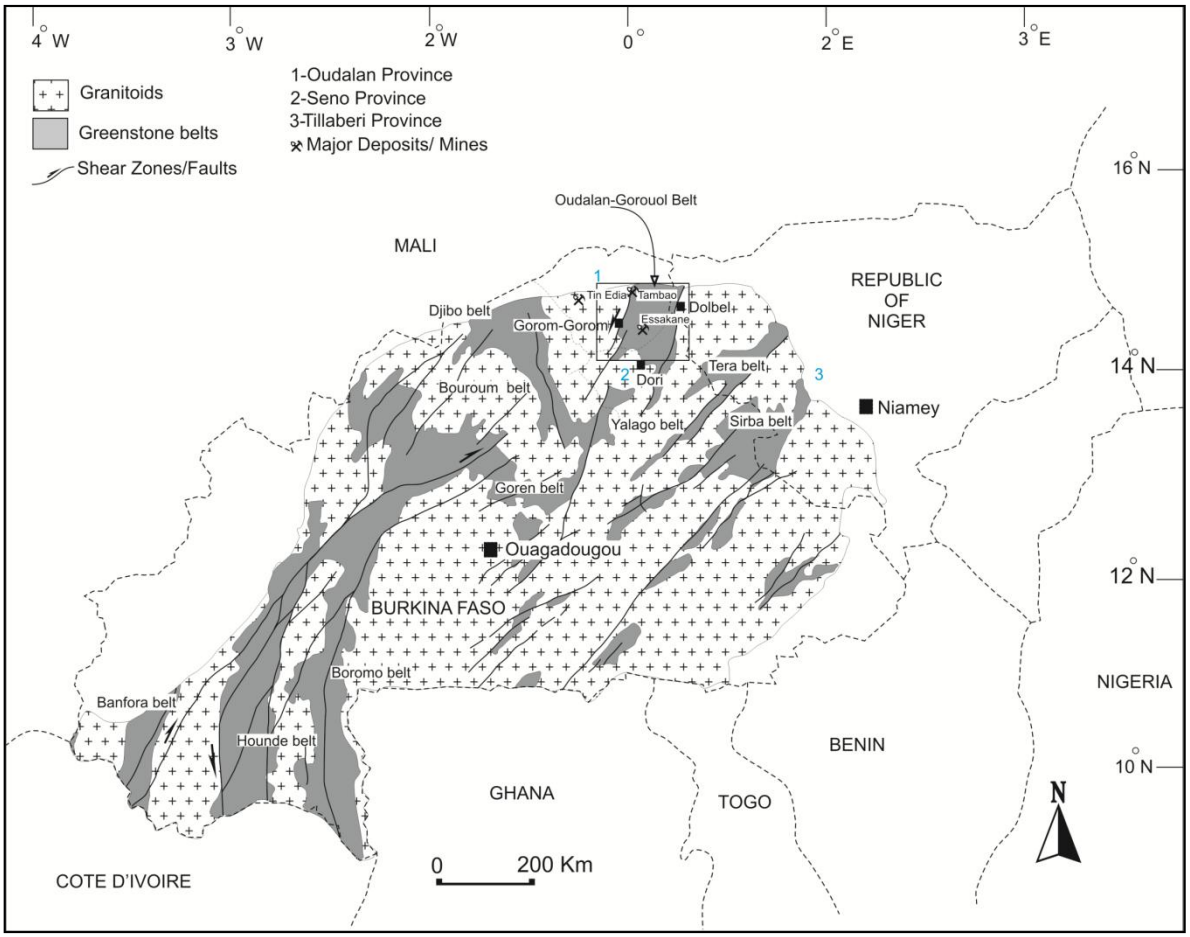

Figure 1.2: A map of Burkina Faso and the Republic of Niger, with provincial boundaries. The map shows the geographic location and orientation of the Oudalan-Gorouol belt including the surrounding granitoid terranes and other major Birimian belts in Burkina Faso and the Republic of Niger.

1.7 Conventions and Acronyms

Throughout this thesis several formats and terms have been adopted in order to avoid confusion and to aid in readability. These include:-

1. The term '*Essakane goldfields'* has been adopted to include the Essakane mine, exploration prospects within the bounders of Burkina Faso along the Essakane trend, and artisanal workings. The main exploration prospects include Essakane North, Essakane Main Zone, and Essakane South.
2. The '*Kossa goldfields'* refer to all the artisanal workings along the Kossa trend in Niger. These include, Kossa South, KBF, and Kossa North.
3. All the other deposits will be referred by their specific names when necessary, for example, Tin Zoubratan.

4. The term '*artisanal mine'* is used to refer to all informal mining operations by local people '*Artisans, locally called the Orpailleurs in the French language*' at a sub-industrial scale using traditional methods (Jaques et al., 2006).
5. A *gold prospect* is defined as an area assessed to be a geological or geophysical anomaly with respect to gold.
6. The acronym '*Dx*' refers to the deformation event or phase, in which *x* indicates the order, first, second or third event. All the elements related to such an event will be indicated with the same acronym, i.e. *Lx* for lineation, *Sx* for foliation, *Fx* for folds, *Vx* for veins, etc.
7. All structural readings are quoted with respect to Magnetic North. True North lies 2° west of Magnetic North. Stereographic projections are always lower hemisphere equal area plots, unless otherwise stated.
8. The term '*gneiss*' is used for rocks which show compositional banding (Geller et al., 2003), thus foliated granite is not considered to be a gneiss under this definition.
9. The term '*migmatitic gneiss'* is used for compositionally banded felsic igneous rocks that show macroscopic evidence of partial melting (Wimmenauer and Bryhni, 2007).
10. The term '*granitoid*' is used as a general term for a range of compositions, inclusive of all felsic and intermediate intrusive igneous rocks.
11. The term '*cleavage*' is used to define closely positioned parallel planes in a rock.
12. The term '*schistosity*' is used to define a penetrative or non-penetrative foliation with visible phyllosilicates/platy minerals parallel with the foliation (McClay, 1991; Geller et al., 2003).

The following abbreviations are used:

AFM	Al, Fe, Mg diagram
ASTER	Advanced Space-borne Thermal Emission and Reflection Radiometer
BRGM	Bureau de Recherches Géologues et Minières
BUMIGEB	Bureau des Mines et de la Géologie du Burkina
CD	Compact disc
CEMOB	Compagnie d'Exploitation des Mines d'Or du Burkina
°C	Degree Celsius/Centigrade
DMSZ	Dori Marginal Shear Zone
Ga	Giga-annum, billions of years
GGGT	Gorom-Gorom granitoid terrane
GIS	Geographic Information Systems
GMT	Greenwich Mean Time
GPS	Global Positioning System
HREE	Heavy Rare Earth Elements
ICP-MS	Inductively Coupled Plasma Mass Spectrometry

KSZC	Kargouna Shear Zone Complex
LANDSAT	Land Remote-Sensing Satellite
LREE	Light Rare Earth Elements
Ma	Mega-annum, millions of years
MSZ	Markoye Shear Zone
OGB	Oudalan-Gorouol (Volcano-Sedimentary) Belt
PPM	Parts Per Million
PTS	Polished Thin Section
REE	Rare Earth Elements
RTP	Reduction to the Pole
SHRIMP	Sensitive High-Resolution Ion Microprobe
SPOT	Système Pour l'Observation de la Terre
TAS	Total Alkali Silica diagram
TMI	Total Magnetic Intensity
TTG	Tonalite-Trondhjemite-Granodiorite
UTM	Universal Transverse Mercator
WAC	West African Craton
WAXI	West African Exploration Initiative
WGS 84	World Geodetic System 1984
XRF	X-ray Fluorescence

CHAPTER 2
REGIONAL GEOLOGY

2.1. Introduction

The West African Craton (WAC) consists of an Archaean and Palaeoproterozoic basement that is divided into the Reguibat Rise in the north and the Leo-Man Rise in the south (Figure 1.1) (Thiéblemont et al., 2004). They are separated by the Taoudeni Basin, which is Neoproterozoic to Devonian in age. Two Palaeoproterozoic inliers crop out within the central west of the Taoudeni basin; the Kedougou-Kéniéba (KKI) and the Kayes inliers (Gueye et al., 2007; 2008).

The Leo-Man Rise is composed of two domains, the Archaean Kénéma-Man domain in the southwest which is dated at 3542-3535 Ma (U-Pb zircon, Thiéblemont et al., 2001; 2004) and the Palaeoproterozoic (2.3-1.8 Ga) Baoulé-Mossi domain in the east (Feybesse et al., 2006) in which the study area in the Oudalan-Gorouol volcano-sedimentary belt (OGB) is situated. The Kénéma-Man domain consists of a granite-gneiss complex and granulitic metagabbro (Thiéblemont et al., 2001). The Baoulé-Mossi domain consists of metamorphosed Birimian sequences (herein referred to as the Birimian Supergroup) including clastic, volcaniclastic and volcanic rocks, that were deposited at approximately 2.3-2.1 Ga (Castaing et al., 2003; Feybesse et al., 2006; Pawlig et al., 2006) and were accreted at approximately 2.1 Ga during the Eburnean Orogeny (Milési et al., 1991, 1992; Boher et al., 1992). Syn-tectonic granitoids were emplaced during three magmatic cycles at 2200, 2160-2130 and 2100-2070 Ma (Hirdes and Davis, 2002; Pawlig et al., 2006; Gueye et al., 2007, 2008; Vidal et al., 2009; Lompo, 2009, 2010).

The metasedimentary rocks of the Tarkwa Group unconformably overlie the Birimian Supergroup (Hastings, 1982; Leube et al., 1990; Milési et al., 1992). The Tarkwa Group is dated at 2150-2130 Ma or 2107-2097 Ma (U-Pb and Pb-Pb single detrital zircon ages; Davis et al., 1994; Perrouty et al., 2012).

2.2. Regional stratigraphy

Junner (1935; 1940) in Leube et al. (1990) divided the stratigraphy of the Birimian Supergroup into two distinct series, B1 and B2 for which Feybesse et al. (1990), Leube et al. (1990), Hirdes et al. (1996), and Milési et al. (1991, 1992) contended that the lower Birimian series (B1) was predominantly sedimentary in origin and included dacitic/rhyodacitic metavolcanoclastic sediments, metagreywacke with intercalated black metasiltstone and manganiferous chert, argillite, shale and chemical metasedimentary rocks. The upper Birimian series (B2) consisted of metamorphosed basic (tholeiites; pillow lavas and basalts) and intermediate lavas and pyroclastic rocks (Leube et al., 1990; Milési et al., 1991, 1992; Hirdes et al., 1996; Davis et al., 1994; Naba et al., 2004).

In-contrast, Baratoux et al. (2011), established that in the Banfora, Houndé, and Boromo belts in southwest Burkina Faso, B2 underlies B1 and is dominated by metavolcanic sequences (Vidal and Alric 1994). These are unconformably overlain by younger Tarkwa Group metasedimentary rocks.

Further to this, stratigraphic sections have been established for several greenstone belts in the WAC (Figure 2.1), and vary from one greenstone belt to the other (Davies et al., submitted). The stratigraphic sections established by Roddaz et al. (2007) from the Djibo belt and by Hein et al. (2004), Hein (2010) and Peters, (2014) from the Goren belt, established that the metavolcanic and metasedimentary units are intercalated. Similarly, the stratigraphy of the Yalago volcano-sedimentary belt from the Taparko region, as compiled in a local map by Vanin et al. (2004), indicates that the metamorphosed volcanoclastic and sedimentary rocks are intercalated with the tholeiitic basalts that are overlain by a series of tholeiitic pillow basalts and a sequence of rhyolite tuffs (WAXI, 2013; Davies at al., submitted). Additionally, the southern Bouroum belt consists of a volcanic sequence of mafic lavas, tuffs, and pyroclastites that are overlain by volcano-sedimentary sequence (Zonou et al., 1985; Vanin et al., 2004; WAXI, 2013). These are intercalated with shale, siltstone, and black grey silty shale. Peters (2014) concluded that the mafic volcanics of the Goren belt are intercalated with siltstone, chemical sedimentary exhalite deposits, epiclastic greywacke units, basalt-derived volcanoclastic units and a pyroclastic interbed layer.

Moreover, the stratigraphic sections established by Sylvester and Attoh (1992) from the Nangodi belt in southern Ghana (Figure 2.1), conform with the B1 and B2 classification of Junner (1935; 1940); the Dixcove and Winneba belts in southern Ghana are dominated by metavolcanic units that are unconformably overlain by the Tarkwa Group of sedimentary rocks. Leube et al. (1990) concluded that the relationship between metavolcanic and metasedimentary units is time equivalent with granitoid emplacement. Consequently, the order of the stratigraphy has been the subject of debate between a number of researchers (c.f., Hein et al., 2004; Naba et al., 2004; Baratoux et al., 2011; Peters, 2011). However, a recent summation of the stratigraphy across the WAC by WAXI (2013; Davies et al., submitted) has resolved that each belt is unique; intercalated ocean island arc to back-arc volcanic and volcano-sedimentary sequences are unconformably overlain by arc accretion (predominately) sedimentary sequences. These are unconformably overlain by Tarkwa-like sequences.

Numerous calc-alkaline plutons intruded the Palaeoproterozoic sequences including tonalite-trondjhemite-granodiorite (TTG), diorite, meta-diorite and leucogranites (Pons et al., 1995; Naba et al., 2004; Pawlig et al., 2006; Vidal et al., 2009; Tshibubudze and Hein, 2013; WAXI, 2013). In Burkina Faso, two emplacement events are recognised (Castaing et al., 2003; Naba et al., 2004); (1) a TTG suite which is composed of granodiorite, tonalite and quartz-diorite that intruded metasedimentary and metavolcanic rocks of the Birimian Supergroup between 2210 and 2100 Ma (Castaing et al., 2003), and (2) A granite suite that is localized along shear zones. Castaing et al. (op. cit.) summarized that the granite suite intruded metamorphosed sedimentary and volcanic sequences of the Birimian Supergroup and TTG suite granitoids between 2150 and 2130 Ma. However, adamellite

granites are older than the TTG Eburnean granitoids in the OGB because they are crosscut by the TTG suite granitoids (Tshibubudze et al., 2009).

The emplacement of TTG suite granitoids in Burkina Faso accords with magmatic cycles 1 and 2 of Pawlig et al. (2006) and Gueye et al. (2007; 2008) at 2200 and 2160-2130 Ma. McCuaig (2006), McCuaig et al. (2009) and Tapsoba et al. (2013a) concluded that the TTG suite plutons of northeast Burkina Faso were emplaced between 2181 ± 7 Ma and 2132 ± 4 Ma and granite suites at 2151 ± 10 Ma. From this, Tapsoba et al. (2013a) restricted emplacement of granitoids in northeast Burkina Faso to 2190-2150 Ma. However, a suite of granodiorite and granites dated at 2255-2253 Ma (U-Pb zircon) from the northern and western extensions of the OGB may represent basement to the Birimian Supergroup in the WAC (Tshibubudze et al., 2013, Chapter 7; Appendix D).

Gabbro, metagabbro, diorite and trondhjemite intrusions have been interpreted as syn-tectonic with emplacement of Birimian metavolcanic sequences (Béziat et al., 2000; Hein et al., 2004; Peters, 2014) and co-magmatic (Béziat et al., 2000). Northwest and northeast trending gabbro/dolerite dykes and sills crosscut the Birimian Supergroup and intrusive complexes in the northeast of Burkina Faso. The youngest crosscutting dyke swarm is dated at 250 ± 13 Ma (K-Ar whole rock method) (Hottin and Ouedraogo, 1992).

Furthermore, (layered) ultramafic-mafic complexes crop out in several regions of Burkina Faso including the Djibo belt (Debat et al., 2003), the Goren belt (Hein et al., 2004) and the OGB (Tshibubudze et al., 2009). Mickus (2008) modelled mafic complexes from regional gravity data and concluded that in the Oudalan-Gorouol region they extend to a maximum depth of 1.5 to 5.5 km. The base metal and gold deposits of Goko and Perkoa in the Boromo-Goren belt and Diouga, Gangoal, Boure, Bayildiaga in the Bouroum-Yalago belt (Castaing et al., 2003) are situated along the margins of some of these ultramafic-mafic complexes (Mickus, 2008) and may be related.

The Tarkwa Group, which unconformably overlies the Birimian Supergroup, is defined from southeast Ghana as a series of clastic metasedimentary rocks that are derived from erosion of the Birimian Supergroup (Leube et al., 1990; Milési et al., 1991; Turner et al., 1993). The Tarkwa Group was deformed and metamorphosed to greenschist facies by gravity tectonics and during the Eburnean Orogeny (Milési et al., 1989, 1991; Leube et al., 1990). The maximum age of deposition of the Tarkwa Group is accepted as 2132 ± 2.8 Ma (Davis et al., 1994; Pigois et al., 2003), but this age has been reinterpreted by Perrouty et al. (2012) using the detrital zircon data of Pigois et al. (2003) to represent the rocks that were exposed during deposition of the Tarkwa Group. Perrouty et al. (2012) argued that the age of the Tarkwa Group is younger than expected at 2107-2097 Ma, as constrained by U/Pb ages of metamorphic titanite and zircon from a metagabbro sill within the Tarkwa Group and crosscutting granitoids dated at 2097 ± 2 Ma (Oberthür et al., 1998).

Metasedimentary rocks classified as Tarkwa Group by Jeambrun et al. (1970), Milési et al. (1989) and Bossière et al. (1996) in the OGB were reclassified as Birimian flysch-type metasedimentary rocks by Tshibubudze et al. (2009) and Peters (2011) because their clasts component

was unlike the Tarkwa type-section rocks in southeast Ghana, i.e., the Tarkwa Group does not crop out in the OGB. Sub-angular to sub-rounded clasts and boulders in the flysch-type metasedimentary rocks include basalt, andesite, granodiorite, granite, volcanoclastic metasediments, chert, and lithic fragments in a greenish-grey greywacke-lithic matrix.

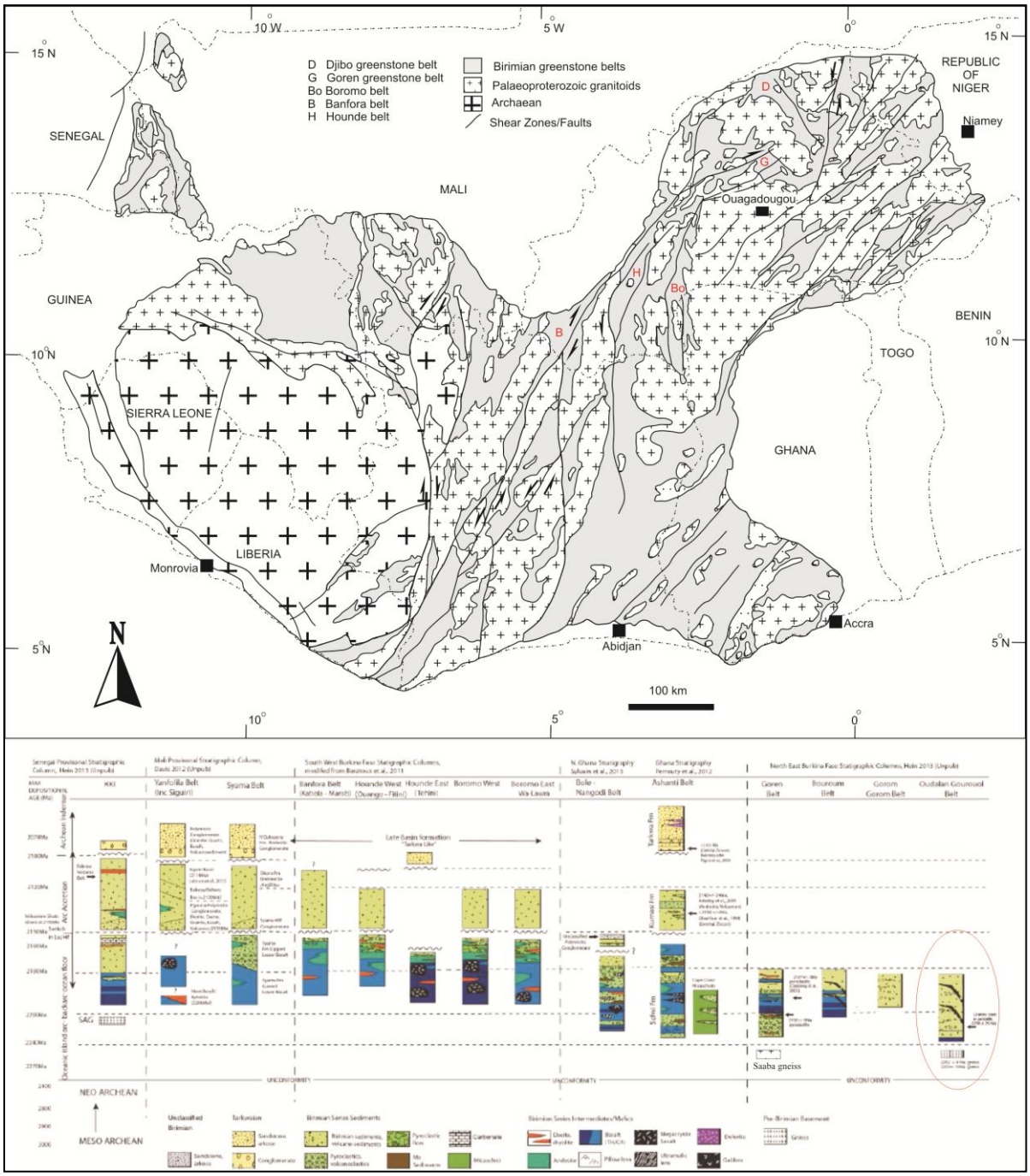

Figure 2.1: The Baoulé-Mossi domain of the West African Craton, re-drawn after Metelka et al. (2011) showing distribution of greenstone belts with reference to those that have stratigraphic sections established and published. The stratigraphic sections established from different greenstone belts within the WAC by WAXI (2013) and Davies et al. (submitted), indicates that each greenstone belt has its own stratigraphic section that differs from the next greenstone belt.

2.3. Regional structure and metamorphism

It has been generally accepted that the metamorphosed clastic, volcaniclastic and volcanic rocks of the Birimian Supergroup were metamorphosed during the progressive Eburnean Orogeny (Feybesse et al., 2006) with further metamorphism related to the intrusion of granitoids. Metamorphic grade attained greenschist facies (Milési et al., 1989, 1991; Bossière et al., 1996; Hirdes et al., 1996) with formation of chlorite-muscovite dominant mineral assemblages, and low to medium grade amphibolite facies with hornblende-andalusite dominant mineral assemblages (Bossière et al., 1996; Béziat et al., 2000; Debat et al., 2003; Naba et al., 2004). Low to medium grade amphibolite facies is important in the contact aureole of granitoids (Pons et al., 1995; Debat et al., 2003; Pawlig et al., 2006; Vidal et al., 2009). Studies by Ganne et al. (2012) of samples that contain chlorite and phengite have shown that blueschist metamorphic facies could have been attained in some areas of the craton. The Tarkwa Group is metamorphosed to greenschist facies with development of chlorite and sericite (Milési et al., 1989, 1991; Leube et al., 1990).

Several deformation events are recognized in parts of the Palaeoproterozoic WAC; they have historically been assigned as phases or events of the Eburnean Orogeny (Allibone et al., 2002; Feybesse et al., 2006; Vidal et al., 2009, De Kock et al., 2009, 2011; Perrouty et al., 2012). This interpretation lead Allibone et al. (2002) and Feybesse et al. (2006) to divide the Eburnean Orogeny into Eburnean I and II, and De Kock et al. (2011, 2012) and Perrouty et al. (2012) into the Eoeburnean and Eburnean.

Allibone et al. (2002) reported that the Eburnean I (2200-2150 Ma) cycle was dominated by eruption of volcanic rocks and emplacement of granitoids accompanied by regional metamorphism. The Eburnean II (2116-2088 Ma) cycle involved northwest-southeast compression, during formation of northeast-trending structures, upright folds with east-striking axial planes and moderate northeast plunging axes. This was later followed by a north-northeast to south-southwest horizontal compression that formed sinistral strike-slip faults.

In contrast, the Eoeburnean (>2150 Ma) as defined by De Kock et al. (2011, 2012) is associated with formation of amphibolite with migmatization. Perrouty et al. (2012) associated the Eoeburnean (2187-2158 Ma) with volcanism and emplacement of granitoids, the development of regional scale folds and bedding parallel foliation, and the development of east-west trending structures during a regional north-south shortening.

Additionally, the Tangaean Event (2170-2130 Ma) of Tshibubudze et al. (2009), and Hein (2010) is defined by northwest to north-northwest trending dextral-reverse shear zones, and fold-thrust belts that developed during a period of northeast-southwest crustal shortening. It is recognised across the Goren, Bouroum-Yalago and Oudalan-Gorouol belts of northeast Burkina Faso, and also crosscuts the Pissila Batholith in the Saaba gneiss complex (Simoko, 2012).

Thus the Eburnean I of Allibone et al. (2002), Eoeburnean of De Kock et al. (2011, 2012) and Perrouty et al. (2012), and the Tangaean Event of Tshibubudze et al. (2009), and Hein, (2010) are subsets that bear similar tectonic characteristics and geochronological constrains. They are herein interpreted as the same tectonic event that took place at approximately 2.20-2.15 Ma (Figure 2.2).

Moreover, comprehensive and integrated research studies by WAXI (2013) have convincingly demonstrated that the deposition of the lower Birimian Supergroup in an oceanic arc to back arc setting was followed by local micro-plate accretion during the Tangaean/ Eoeburnean/ Eburnean I at approximately 2.20-2.15 Ga (Tshibubudze et al., 2009; Hein, 2010; Baratoux et al., 2011; Metelka et al., 2011; Tshibubudze and Hein, 2013, Chapter 5). This was followed by polycyclic deformation in the Eburnean Orogeny (Eburnean II) at approximately 2.14-2.08 Ga (Milési et al., 1991, 1992; Boher et al., 1992; Taylor et al., 1992). The Eburnean Orogeny is thereby restricted to northwest-southeast shortening with local development of crenulation cleavages, isoclinal folds, shear zones, and thrust faults (Allibone et al., 2002; Hein et al., 2004; Feybesse et al., 2006; Tshibubudze et al., 2009; Vidal et al., 2009; De Kock et al., 2009; 2011; Perrouty et al., 2012). Northwest-southeast shortening in the Eburnean Orogeny (herein termed EO_A) was followed by north-northwest to south-southeast shortening in EO_B with development of sinistral strike-slip faults and shears. The regional D1 classification is thus defined by the Tangaean/ Eoeburnean/ Eburnean I event. The regional D2 classification is defined by the Eburnean Orogeny where EO_A and EO_B form discrete tectonic events within the Eburnean orogenic cycle, as established by Feybesse et al. (2006).

Regional D3 in the WAC is characterized by west-northwest trending shears and folds that developed during north-south compression in the Wabo-Tampelse Event (Hein et al., 2004; Hein, 2010; Baratoux et al., 2011).

In the northeast of Burkina Faso the structural architecture is dominated by the Markoye Shear Zone (MSZ). The MSZ is defined by an approximately 5 km wide zone of steeply dipping quartz-muscovite schist that is transitional with, and encloses mylonite zones, including the Mukosi Mylonite Zone of Tshibubudze et al. (2009). The MSZ hosts zones of L-tectonite and pseudotachylite vein complexes (c.f., Tshibubudze et al., 2009, Appendix E). It also hosts en echelon buck quartz and quartz-carbonate vein arrays, and is crosscut by discontinuous quartz-chlorite-(muscovite) shears. The MSZ trends north-northeast to northeast and is clearly visible on LANDSAT imagery, in RTP magnetic data and gravity data (Mickus, 2008). It forms the interpreted western boundary of the OGB and eastern boundary of the GGGT block. According to Tshibubudze et al. (2009) the MSZ is steeply east-dipping.

In Niger on the eastern margin of the OGB, Pons et al. (1995) interpreted that interference from emplacement of plutons during transcurrent deformation resulted in the development of sinistral north to north-northeast trending strike-slip faults such as the Tin-Takanet-Bellekcire Fault and a regional northeast trending schistosity. The Tin-Takanet-Bellekcire Fault can be interpreted as the eastern boundary of the OGB. This fault traverses the Tin-Takanet village in the south of the OGB and

the Bellekcire village in the north, which is due east of Dolbel village (Milési et al., 1989; Pons et al., 1995).

In summary, Tshibubudze et al. (2009, Appendix E), Hein (2010), De Kock et al. (2011, 2012), Perrouty et al. (2012), Tshibubudze and Hein (2013, Chapter 5, Appendix B), and Tapsoba et al. (2013b) concur that a tectonic event at 2.20-2.15 Ma, predates the polycyclic Eburnean Orogeny at 2.13-1.98 Ga as recognised by Leube et al. (1990), Milési et al. (1991; 1992), Ledru et al. (1991), and Feybesse et al. (2006). These were followed by the Wabo-Tampelse Event (undated).

2.4. Regional Geochronology

The results of geochronological studies of the WAC have been reported by Hirdes et al. (1987; Rb/Sr; 1992, 1996), Milési et al. (1989; Rb/Sr), Leube et al. (1990), Léger et al. (1992; Rb-Sr isochron), Davis et al. (1994; U-Pb single detrital zircon), Pons et al. (1995), Bossière et al. (1996; Pb-evaporation), Hirdes and Davis (1998, 2002; U-Pb zircon), Oberthür et al. (1998; U-Pb zircon), Egal et al. (2002; Pb-evaporation), Castaing et al. (2003; Pb-Pb and K-Ar), Dioh et al. (2006), Feybesse et al. (2006; Pb-evaporation; Sm-Nd; K-Ar; and Ar^{39}/Ar^{40}), De Kock et al. (2011; U-Pb zircon), Tapsoba et al. (2013a; U-Pb zircon, 2013b; Ar^{40}/Ar^{39}) and Tshibubudze et al. (2013; U-Pb zircon). A summary plot of reported ages is presented in Figure 2.2. Temporal relationships between the reported ages for the Birimian Supergroup, TTG granitoids intrusion phases and Tarkwa Group are also presented.

The ocean island arc to backarc sequences of the Birimian Supergroup were deposited approximately at 2238-2150 Ma (WAXI, 2013). The oldest age for Birimian Supergroup has been obtained for a rhyolitic tuff from the Goren greenstone belt (using Pb-Pb and U-Pb zircon) at 2238 ± 5 Ma (Sample MD1264) and 2171 ± 7 Ma for rhyolite (Sample MD0207) from the Houndé greenstone belt (Castaing et al., 2003). Arc accretion sequences were deposited unconformably at 2150-2100 Ma, while the Tarkwa Group was deposited at 2107-1980 Ma (WAXI, 2013).

However, for the majority of geochronological studies completed in the WAC, the oldest U-Pb and Pb-Pb ages are for plutonic rocks and reported as inherited zircon ages. They included reports by (1) Gasquet et al. (2003) from the Dabakala tonalite (Côte d'Ivoire) at 2312 ± 17 Ma, (2) Thomas et al. (2009) from the Gondo granite gneiss in Ghana at 2876 Ma, (3) Siegfried et al. (2009) from the Ifantayire granite gneiss in Ghana at 2386 and 2258 Ma, and (4) De Kock et al. (2009) from the Bomburi granodiorite in Ghana at 2227 Ma. The oldest U-Pb crystallisation ages reported are derived from Ghana from a gabbro unit in the Sefwi belt at 2222 ± 32 Ma (K-Ar age) (Feybesse et al., 2006), and studies from the northeast Burkina Faso for granodiorite gneiss and granite at 2255-2253 Ma (Tshibubudze et al., 2013, Chapter 7; Appendix D).

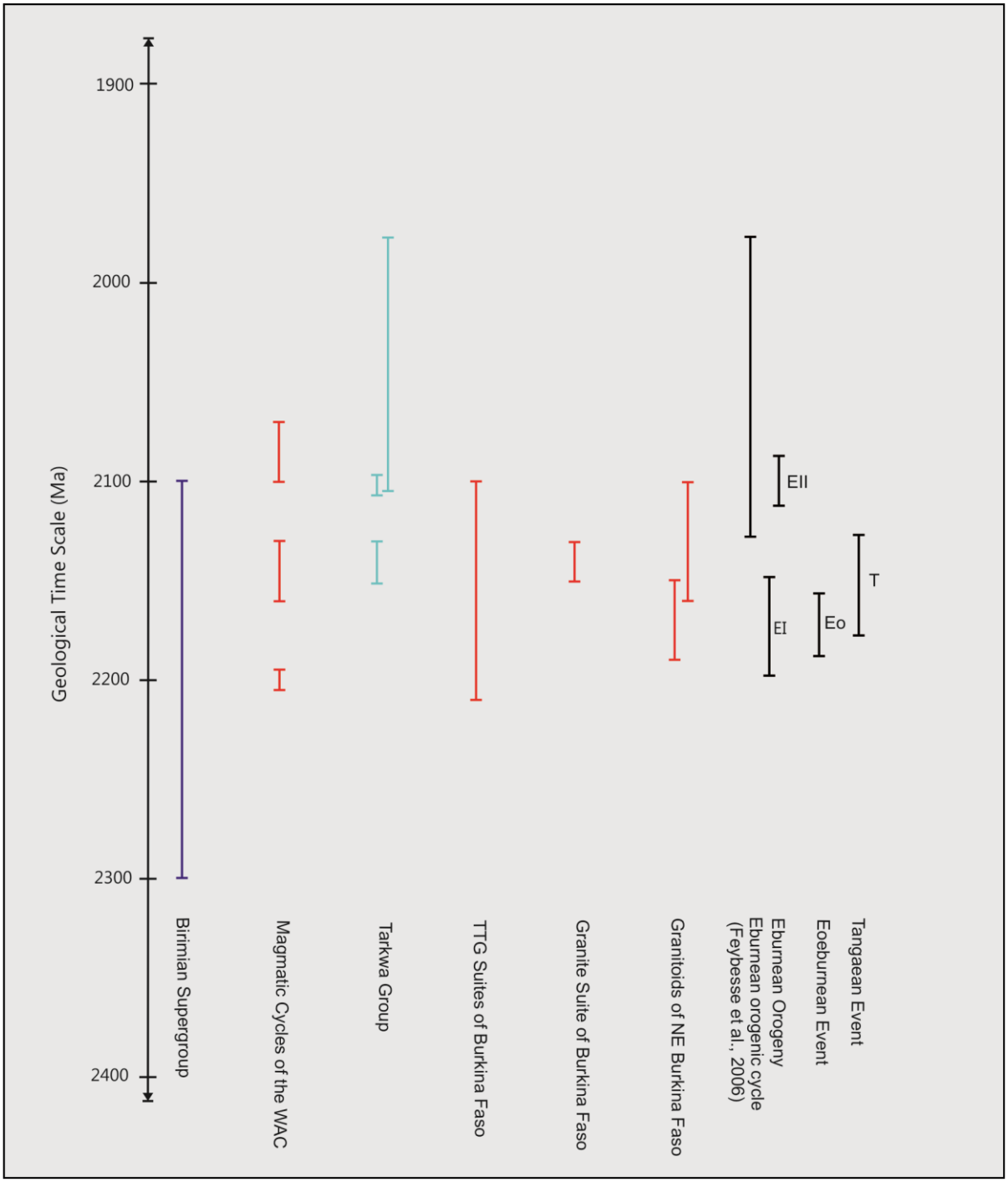

Figure 2.2: The summary plot of geochronological age constrains reported by Hirdes et al. (1987; Rb/Sr; 1992, 1996), Milési et al. (1989; Rb/Sr), Leube et al.(1990), Léger et al. (1992; Rb-Sr isochron), Davis et al. (1994; U-Pb single detrital zircon), Pons et al. (1995), Bossière et al. (1996; Pb-evaporation), Hirdes and Davis (1998, 2002; U-Pb zircon), Oberthür et al. (1998; U-Pb zircon), Egal et al. (2002; Pb-evaporation), Castaing et al. (2003; Pb-Pb and K-Ar), Dioh et al. (2006), Feybesse et al. (2006; Pb-evaporation; Sm-Nd; K-Ar; and Ar^{39}/Ar^{40}), De Kock et al. (2011; U-Pb zircon), and Tapsoba et al. (2013a; U-Pb zircon, 2013b; Ar^{40}/Ar^{39}) illustrating the age range distribution relationship between the reported age of the Birimian Supergroup, Tarkwa Group, TTG suite granitoids including the specific age constrains from Burkina Faso. The age constrains of the polycyclic Eburnean orogeny, Eburnean I and II (EI and EII), Eoeburnean event (Eo), and the Tangaean Event (T) are also presented. The Eburnean I, Eoeburnean event and the Tangaean Event are constrained to within the same time range and are probably the same event.

2.5. Regional Geophysics

Regional geophysical data and images for Burkina Faso have been published by Mickus (2008), who analysed and interpreted the regional gravity data covering the entire of Burkina Faso. However, the majority of the geophysical data and images currently available has not been published and is owned by exploration and mining companies. The base regional airborne magnetic data is owned by BUMIGEB. The data and imagery include, the Airborne Magnetic Analytical Signal, Airborne magnetic TMI Reduced to the pole (RTP) and RTP 1st vertical derivative of the eastern Burkina Faso (A315 E45) at 1:600 000 scale and they cover the area of study.

2.6. Regional metallogeny

The WAC hosts metallogenic deposits of gold, diamond, iron, manganese, silver, lead, molybdenum, antimony, copper and zinc in Birimian Supergroup and intrusive rocks, and the Tarkwa Group (Hastings, 1982; Milési et al., 1989, 1992; Hein et al., 2004; Mickus, 2008; WAXI, 2013), and nickel, chromium, and Platinum Group Elements (PGE) in (layered) ultramafic-mafic complexes (Mabidi et al., 2007; Mickus, 2008). Several deposits and deposit styles occur in the study area including;

(1) Manganese deposits at Tambão close to border with Niger, and at Billiata (Figure 1.2).

(2) Gold mineralization at Essakane, Gosséy, Korizéna, Falagountou, Takabangou, Tassiri, Bom Kodjelé, Sokadié, and Kossa artisanal mines (Milési et al., 1992; Nikiéma, 1992; Tshibubudze et al., 2009).

(3) Pegmatites veins near Tambão that host tourmaline, plagioclase and topaz crystals.

(4) Pb-Zn-Mo in the Kuorki area (Niger) (Milési et al., 1989)

(5) Fe-Ti-V mineralization occurs in the Tin Edia deposit (Figure 1.2) located at the north-western margin of the GGGT (Neyberg et al., 1980).

Several deposits are associated with the sulphidised brittle-ductile shear zones including gold in sheeted and stockwork quartz veins, copper as malachite in buck quartz veins, and tourmaline and topaz in pegmatite and buck quartz veins (Foster and Piper, 1993; Lompo, 2001; Feybesse et al., 2006; Tshibubudze, 2007).

Foster and Piper (1993), Groves et al. (1998), Feybesse et al. (2006), Béziat et al. (2008) and WAXI (2013) have restricted the main phase of gold mineralization in the WAC to the Eburnean Orogeny due to many common characteristics the deposits share. However, this does not include gold hosted by the Tarkwa Group meta-sedimentary units in Ghana (Milési et al., 1991; Feybesse et al., 2006) and placer gold in palaeochannels in western Mali (Hein and Tshibubudze, 2007; Matabane, 2008; Hein et al., submitted (a)). Gold mineralization at Morila (Mali), Kiaka (southwest Burkina Faso), and Wassa (Ghana) formed prior to the Eburnean orogeny (WAXI, 2013).

There is a strong structural control to gold mineralization at all levels (first to third-order structures) within the craton. Nikiéma (1992) concluded that gold mineralization in the OGB was distributed along shear zones (structurally-hosted lode-gold) and is epigenic in origin (c.f., Groves et al., 1998; Béziat et al., 2008). These deposits are commonly cited in second- or third-order structures that splay-off first-order crustal-scale structures (Groves et al., 1998), or are sited along the trend of the first-order crustal-scale structures (Tshibubudze et al., 2009, Appendix E).

Feybesse et al. (2006) described two styles of gold mineralization that are either associated with arsenopyrite with disseminated pyrite or are associated with pyrite only from Ghana. Béziat et al. (2008) concluded that almost all gold deposits in the north-eastern part of the WAC (Burkina Faso and Niger) occurs within or adjacent to quartz vein systems that are not related to intrusion of granitoids. They accounted for two major styles of gold mineralization:

(1) Gold mineralization hosted in deformed quartz-veins, where gold occurs within the veins and is associated with sulphides or tourmaline. However sulphides and tourmaline rarely occurs in the same vein, thus this can be further separated into sulphide veins and tourmaline veins. Groves et al. (1998) stated that the tourmaline phase associated with orogenic gold deposits is considered to be barren since it is associated with high temperature.

(2) Gold mineralization is disseminated in the selvage of undeformed quartz-albite-carbonate veins.

CHAPTER 3
METHODOLOGY

3.1. Introduction

The basic procedures of field work, data collection, data interpretation and analysis were used in this research project, and are outlined in this chapter. Geological mapping, geometric, kinematic and analytical structural geology, sampling for petrology and geochronology studies, and core logging was undertaken during 2008-2011. The research approach incorporated the use and interpretation of geophysical data, including aeromagnetic data (RTP 1st and 2nd vertical derivative), airborne magnetic TMI reduced to pole data, gravity data, ASTER, SPOT and LANDSAT imagery that covered the study area (Figure 3.1).

As detailed in Chapter 4, geology and topographic maps (1:250 000) and airborne magnetic data (1:250 000 and 1:600 000) were used to delineate structures of interest in the belt. LANDSAT (1:250 000) and ASTER (1:250 000) imagery were used to help in interpretation of the data, and in locating geological and geographical features. The extracted data was validated with surface mapping, highlighting the value of combined interpretation of geophysical and remotely sensed data in regional mapping in Burkina Faso and Niger.

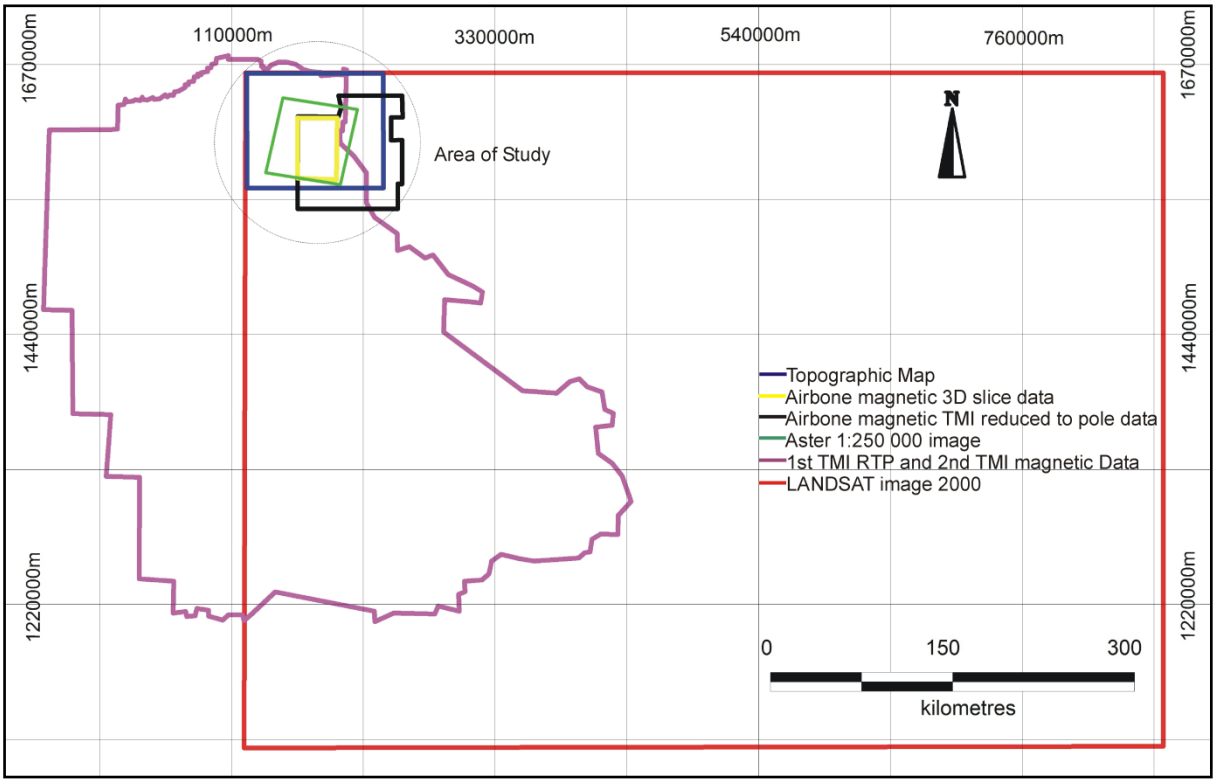

Figure 3.1: The coverage of data sets for the area of study. The area of study is covered by a number of geophysical data sets, including aeromagnetic data (RTP 1st and 2nd vertical derivative), airborne magnetic TMI reduced to pole (1:500 000) imagery, ASTER, SPOT and LANDSAT (1:500 000 and 1:3000 000) imagery.

3.2. Data collection and field studies

The field work component of this project was divided into three seasons; the seasons were allocated early and later in the year to coincide with favourable climatic conditions in West Africa. The areas of principal investigation in the OGB (deposit scale) were the Essakane, Falagountou, Gosséy, Sokadie, Tassiri, Takabangou, Bom Kodjelé and Bom Kodjelé east, Gaigou and Tin Zoubratan gold deposits in NE Burkina Faso, and the Kossa goldfield including Kossa, Kossa South, KBF, Fanchio, and Fatatako deposits in the Republic of Niger (Appendix F).

Field seasons focussed on:-

- Geographic and geologic reconnaissance study of the OGB and GGGT.
- Detailed mapping of deposits and major shear zones, and establishing the structural architecture of the OGB and GGGT. A summary map of the geology is presented in Figure 3.2. In February – April, June – August, and November - December of 2008 a detailed geological and structural mapping project was conducted across the OGB, and at some key deposits. The second season in 2009 focused on detailed mapping of deposits and major shear zones, and establishing the structural architecture of the belt. The third season focused on problematic areas that were identified during the first two field seasons, with selected previous station points revisited.
- Detailed structural mapping of the MSZ was completed in January of 2007 as part of the Honours degree and is reported in Appendix E. Detailed mapping of the southern part of the MSZ was completed in June 2008 as part of the PhD.
- Detailed mapping of the GGGT was completed between November 2010 and January 2011, and is presented in Chapter 6 which details the geology and structure of the GGGT.
- During deposit scale mapping, the crosscutting relationships of mineralized veins were used to distinguish several phases/events of mineralization.
- The relative chronology of lithological units and granitoids, and structural elements, were established first, and this helped in targeting key samples that could be strategically collected for geochemical and absolute geochronological study.
- A short field season was completed in March 2010 and focused on the sampling for geochemical and geochronology studies.

For each mapped station point, lithological and structural and kinematic data were recorded, a photographic record was made, and GPS (Geographic Positioning System) controlled station points were established using Universal Transverse Mercator grid coordinates (UTM, WGS 84). The station point data is reported in Appendix G (CD).

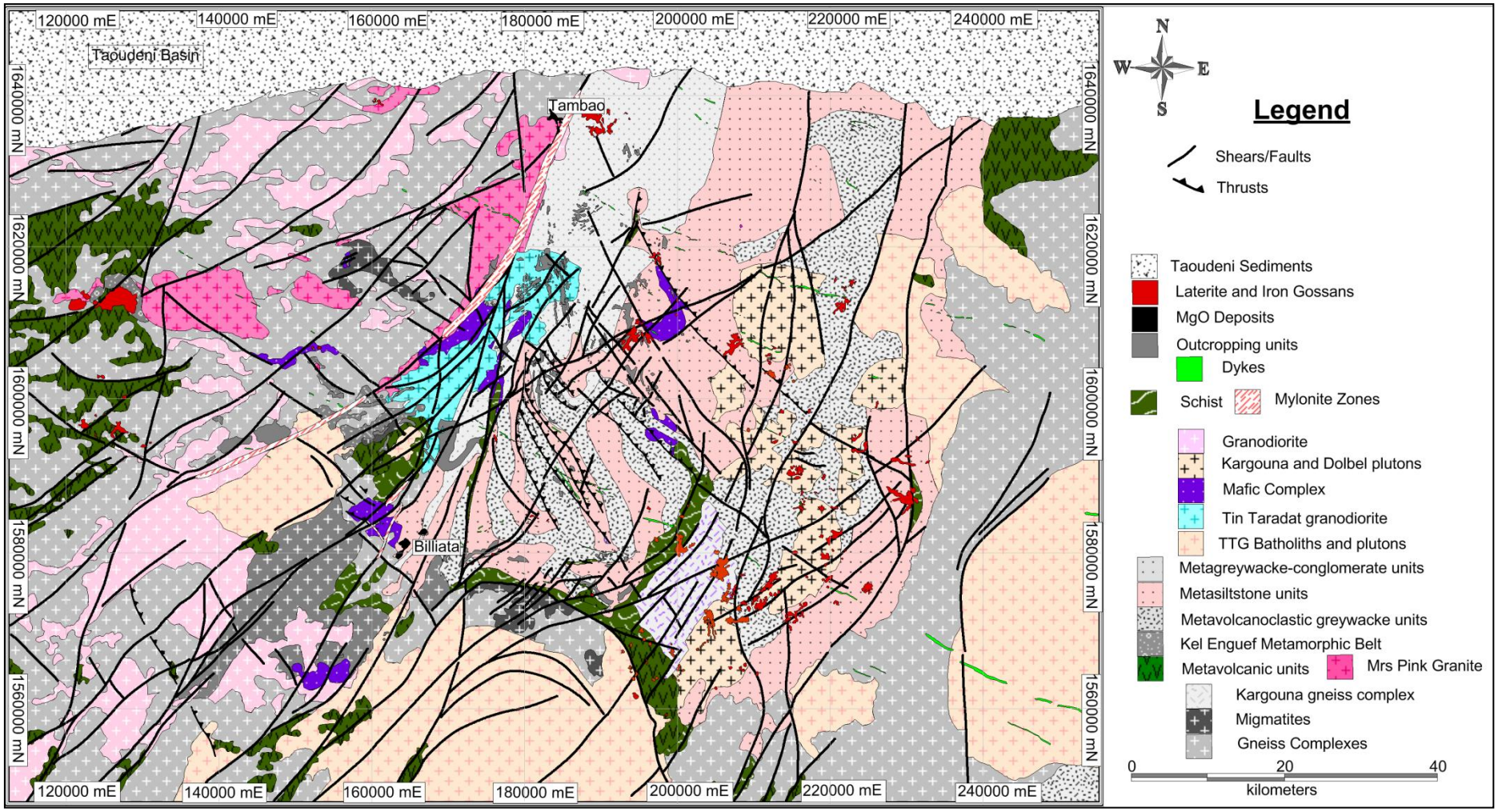

Figure 3.2: A geological summary map of mapped and extracted data for the OGB and GGGT.

3.2.1. Petrographic and mineralogical studies

Selected samples of the lithologies were collected for geochemical and petrographic studies. A total number of 149 samples were collected for this study. Both oriented and non-oriented samples were collected to assist with lithological descriptions and micro-structural analysis. Oriented samples were referenced to magnetic north and marked with horizontal and vertical orientation lines in the field. Samples were labelled, described and carefully bagged. All samples were transported to Orezone Resources Inc in Ouagadougou after the 2008 and 2009 field seasons. In 2010 and 2011 they were transported to IAMGOLD Essakane S.A. main office in Ouagadougou, and then transported to Johannesburg by Air France and SDV International Couriers. Clearance for samples transport was obtained from the Bureau des Mines et de la Géologie du Burkina (BUMIGEB) in Burkina Faso.

In Johannesburg, samples were catalogued and submitted to SGS laboratories in Booysens to make 23 polished thin sections (PTS). Another 15 non-oriented and 17 oriented samples were prepared at the School of Geosciences Thin Section Laboratory at the University of the Witwatersrand, Johannesburg. An extra 32 polished thin sections were prepared for mineral identification and to establish the presence of zircons for geochronological studies. Zeiss and Olympus TH4-200 refracted and reflected microscopes with Cannon cameras were used to study the polished thin sections at the University of Witwatersrand, Johannesburg. Core logging was completed during the second field season in 2008 at Essakane core yard. Diamond drill holes from Essakane, Sokadie, Kossa, and Gosséy deposits were logged to get a better understanding of the geology and host to mineralisation.

3.3. Data processing and interpretation

The UTM zones in the area are 30P and 31P, and the field area straddles the 0° longitude GMT (Greenwich Mean Time). The GPS coordinates are thus reported in zones 30P and 31P. The overlap error between UTM 30P and 31P grids (Figure 3.3) at the regional scale has little significance and can be considered to be negligible. However at the deposit scale it can be problematic for borehole and other target focused tasks because the grids diverge towards the south of the field area. However, a larger portion (95%) of the field area of the OGB was in the 31P zone, and the GGGT is within the 30P zone. Grid conversion between 30P and 31P zone used the Discover 3.2® data utilities option.

An Excel (Microsoft) spreadsheet was created to catalogue structural elements and lithological descriptions. The spreadsheet is presented in Appendix G in the enclosed CD. The data is presented in the file: *field data 2008-2011* and comprises 3 worksheets that include, combined data, 30P and 31P.

Corel DRAW® 9.0 was used for maps and diagrams. GEOrient® 9.4.0 (Holcombe, 2008) was used to analyse structural data. MapInfo Professional 8.5® and Discover 3.2® were used for map-

making, plotting station points and structural data. While in the field, base maps were created using the N31-30-2000 LANDSAT image for station point reference, and structural architecture. Blank maps for field mapping were created using MapInfo Professional 8.5® and Discover 3.2® softwares, and then digitized using Corel DRAW® 9.0.

The conversion of data from historical Adindan datum to UTM grid WGS 84 datum was completed at the Orezone Resources (Inc.) office in Ouagadougou to achieve one universal mapping space. This was necessary because historical data for Burkina Faso is reported in UTM grid and Adindan datum, while data from the Republic of Niger is reported on UTM grid WGS 84 datum.

3.4. Geochemistry and geochronology

Thirty-two samples for geochemical and geochronological analyses were collected from strategic locations across the study area where their stratigraphic position was well understood and the crosscutting relationship well established. The samples were trimmed in the field using a rock pick to remove any weathered surface, then afterwards, further trimmed and cleaned using a rock saw at the University of the Witwatersrand, Johannesburg. The cleaned pieces were washed and crushed to centimetre-sized fragments using a carbon steel jaw crusher. Sample crushing was done at the University of the Witwatersrand EarthLab. The crushing laboratory was cleaned before use to avoid contamination and the jaw crusher was thoroughly cleaned before and after each sample was crushed; the chip tray was cleaned with water and then dried with acetone. The jaw crusher was cleaned with a steel brush and then with acetone. A vacuum cleaner was used to clean chips and remove dust from the crusher.

After crushing, a representative sample for ICP-MS and XRF was collected by splitting the sample into halves until ~50g was left over for milling into powder using a Dickie and Stockler TS 250 MILL tungsten-carbide ring-mill. The milling pot was washed with water, and afterwards cleaned and dried using acetone. It was then cleaned using silica chips by milling. After this a portion of the sample was milled to sterilise the pot, and then sample milled.

The standard method and calibration standards used at the laboratory for ICP-MS and XRF analysis are presented in Appendix H.

The samples selected for geochronology of zircon and baddeleyite were put back into the milling pot to mill them to 500 μm for mineral separation. After ~30 seconds of milling the samples were sieved. The fine grinds that pass through the 500 μm sieve and a 250 μm sieve were collected.

Mineral separation was completed at the University of the Witwatersrand EarthLab using gravity separation in water (Wilfley percussion table) under controlled flow conditions. The heavy separates were dried overnight in an oven at 80 °C. The samples were then separated into batches and a hand magnet was used to remove magnetite and iron fillings from each batch. The remaining separates were then mixed and treated in a glass separating funnel using Bromoform ($CHBr_3$:

2.89g/cm^3) to separate the sample. The solution in the funnel was constantly stirred to facilitate density separation.

The heavy mineral separates were then drained into a filter paper and washed with distilled water and acetone and dried in the oven at 80 °C. The heavy mineral concentrates were then processed on the basis of magnetic susceptibility using the Frantz magnetic separator. The longitudinal tilt angle of 5° and a magnetic current from 0.15–1.5 A was used. The remaining non-magnetic separates were purified using methylene iodine (CH_2I_2: 3.3g/cm^3) to obtain a concentrate of mineral with density greater than 3.3g/cm^3. Finally, the zircon and baddeleyite crystal population (to be analysed) was handpicked and sorted on the basis of colour, size and shape of individual grains, or the other minerals were handpicked to leave behind a pure zircon concentrate. All size fractions were retained for storage and future reference. Particular care was taken during the mineral separation procedure to avoid cross-contamination of samples.

3.4.1. Mount preparation and polishing

A population of zircon and baddeleyite crystals were immersed in ethanol liquid in a Petri dish to enhance the optical properties so a population of about 80-100 crystals was selected. The samples were left to dry in the laboratory but covered by another Petri dish of a larger diameter to avoid contamination. The ethanol takes about 10-20 minutes to completely evaporate. After all the ethanol had evaporated, the zircon crystals were hand-picked under a binocular microscope and mounted on a 25 mm diameter mount with 3 standards. The standards described by Wingate and Kirkland (2011) were used and included:-,

1. NBS610 (Glass) calibration for common (^{204}Pb);
2. BR266 with a standardized age of 559 Ma and has 903 ppm U (calibration standard for zircon after Stern, 2001); and
3. OGC 1 (Owens Gully Diorite: 3465 Ma), which is a standard used to monitor the ^{207}Pb/^{206}Pb ratio.

Each mount included a maximum of three samples.

The samples were stuck to a double-sided tape which had been stuck to a clean glass plate. A Teflon ring was used to mark a circle on the tape from the inner part of the Teflon ring. Then the backing paper was removed and rows were cut according to the number of samples including the standard squares at the centre. The samples holes were cut within a 1.2 cm diameter area in the centre of the mount because that is the only area that can be analysed. The backing paper was then placed back on the tape, and all the other holes were covered; when only the one that is in use is left open, to avoid contamination. Using tweezers, the population of zircons was hand-picked using a binocular microscope and placed on the adhesive. A map was created for the mounts to mark were each sample

and standard was located. At the end of these processes the adhesive had a 1.2 cm diameter area covered by three groups of unknown samples and three known groups of standard samples.

The backing paper was removed from the zircon mount face. A Teflon ring smeared with petroleum jelly was placed over the zircons, with the zircons at the centre of the Teflon ring. Using a Teflon cup, a 5.00g epoxy resin was weighed and a 1.00g hardener was added to the epoxy resin in the cup. The hardener and the resin were mixed together until the mixture was smooth and uniform. The mixture was placed in the sonic bath for 5 minutes, to eliminate gas bubbles. The epoxy was poured down the side of the Teflon ring in such as way as to cover the zircons and the entire bottom of the mount. The mould was placed under a binocular microscope to check for air bubbles in the face and around zircons. The rest of the epoxy was added to the mould. A weight was placed on top of the Teflon ring to allow the epoxy to harden over night.

After removing the mount from the Teflon ring, the back of the mount was ground to a thickness of ~5mm using a grinding wheel at Curtin University of Technology geology department. The mount face was then ground with a wet sandpaper P2000 (14-15 μm) grit. After grinding, the face was polished using fine grained diamond powder starting from 3-1/4 μm grit final polish.

3.4.2. Mount cleaning and gold coating

All the steps were completed while wearing gloves as this is a requirement at the John de Laeter Centre, for both cleaning and gold coating, to avoid grease from fingers. The mounts were cleaned thoroughly with propanol, and cleaned thoroughly again with petroleum spirit using Kim Wipes. They were placed face-up in the beaker with petroleum spirit and placed in the ultrasonic bath for 5 minutes. The process was repeated using a soap solution (Decon) and Kim Wipes. The mounts and the beaker were rinsed with de-ionized water several times and placed in the ultrasonic bath twice for 5 minutes using de-ionized water. The mounts were dried in the oven at 50 °C for more than an hour before gold coating.

The thickness monitor of the gold sputter coater was reset to zero, and gold coating thickness was set at 40 nm. The inside of the vacuum chamber was cleaned with Kim Wipes. After cleaning, the mounts were placed in the centre of the chamber with dish face-up, and high purity gold was added to the wire basket. With the lid and shutter closed and high vacuum reached, the gold was melted at 5-6A current; the current was increased slowly from zero to the range between 5-6A so to evaporate any impurities. Then the shutter was opened to allow gold deposition, and the current was increased again to melt the gold. The deposition automatically stopped when the thickness of the gold reached 40 nm. Then an edge-to-edge resistance was checked to establish that it was higher than 15 ohms.

3.4.3. Reflected and scanning electron microscope (SEM) imaging

Each mount was photographed in reflected light. Cathodoluminescence (CL) imaging was undertaken to reveal the internal structure of the sample zircons and baddeleyite. Backscattered-electron (BSE) imaging was used to reveal imperfections in the zircons and baddeleyite, using the JEOL JSM 6400 scanning electron microscope at the Centre for Microscopy, Characterisation and Analysis at the University of Western Australia. The crystals selected for analysis, and target areas for spot analysis, depended on their reflected-light, CL, and BSE characteristics.

3.4.4. SHRIMP U-Pb and data reduction

The ion microprobe analysis of the samples was completed in four 48 hours sessions using the SHRIMP II at Curtin University of Technology in Perth, Western Australia. The analysis of ~15-20 grains per sample was completed with a primary beam at 10 keV, and a spot diameter of ~20 μm. The net primary ion current was 2.0-3.0 nA during a 6 cycle/scan through the required isotopic mass ranges for each spot. The standard BR266, was analysed 10-20 times minimum for all SHRIMP sessions to monitor and compensate for instrumental drift. The standard OGC1, was analysed ~3-4 times for each session.

The SHRIMP U-Pb zircon data were reduced using the SQUID 2.50® (Ludwig, 2009) and Isoplot 3.00®, Microsoft Excel® macro add-ins (Ludwig, 2003). The data was corrected for common Pb using measured ^{204}Pb. The uncertainties for all individual isotopic ratios and dates analysed for each session were taken at 1σ level. The weighted mean dates are reported with 95% confidence level. The plotted U-Pb data are plotted using a normal Wetherill Concordia diagram option in Isoplot 3.00®.

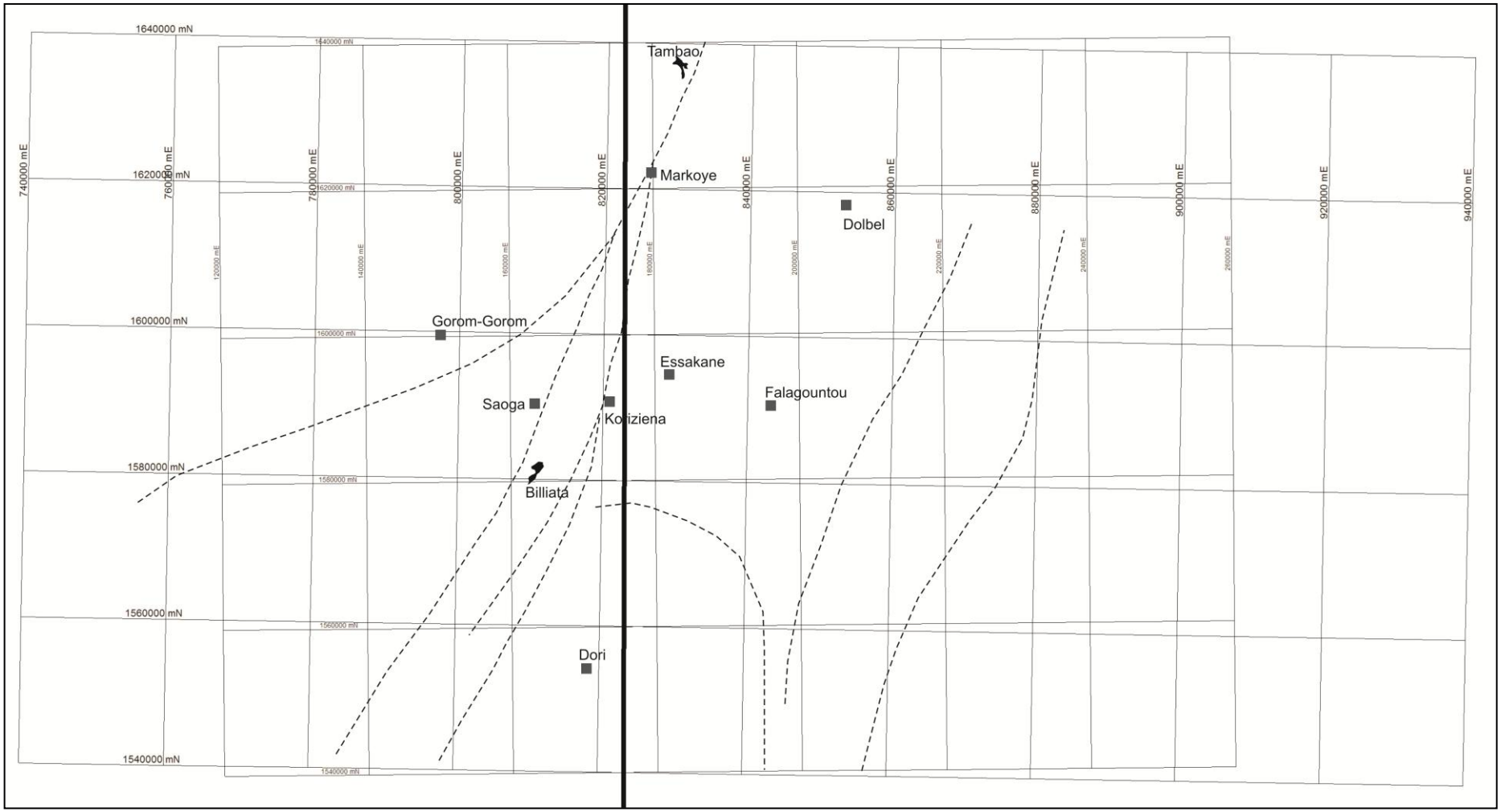

Figure 3.3: The overlap and distortion that exist between the 30P and 31P grids. The solid black line is the GMT (Greenwich Mean Time) line. The two grids overlap well close to the GMT on both side of the grid system, and distort far from the GMT, however at the scale of this work, the overlap is not significance. MapInfo® 9 was used in plotting the data and automatically converted the data on 30P to 31P grid with the right settings.

CHAPTER 4
GIS AND IMAGE DATA EXTRACTION

4.1. Introduction

The OGB and the GGGT are extensively covered by dune sands and laterite in places, saprolite and alluvium profile with limited exposure of the Birimian Supergroup and magmatic rocks. The challenge of outcrop availability in the region required a desktop study to focus fieldwork and help strategically target areas of good outcrop exposure. Thus, a desktop study was undertaken to extract geographical, geological and geomorphological attributes, and from magnetic data, magnetic domains and geologic attributes such as batholiths, plutons, dykes and structural lineaments. The extracted data presented was qualitative and is highly dependent on the quality, scale and resolution of the primary data used. Attributes were extracted from;

(1) A regional Airborne Magnetic Analytical Signal image (1:500,000) of the OGB and a portion of the GGGT (e.g., Figure 4.1) as produced in 1998 by Goldfields Exploration using east-west flight lines data.

(2) 1:600,000 scale airborne magnetic TMI Reduced to The Pole (RTP) 1st vertical derivative image of Eastern Burkina Faso (e.g., Figure 4.2), A315 E45, Adindan datum, NUTM30 Projection, North-South flight lines as produced by Mayes (1997).

(3) Magnetic reduced to pole image (1:250,000) of the Essakane area, provided by Orezone Resources Inc. (e.g., Figure 4.3).

(4) 1:500,000 scale LANDSAT image, p194r050_741, ETM, Bands 741 in RGB, (NASA) (e.g., Figure 4.4).

(5) 1:250,000 ASTER image, composite RGB bands 123N (e.g., Figure 4.5).

(6) 1:500,000 Topographic map covering portions of the Oudalan, Seno and Tillabéri provinces (e.g., Figure 4.6)

The area covered by these datasets is presented in Figure 3.1 and includes the study area. The processes and procedures of extracting attributes from LANDSAT, Google SPOT image and ASTER images were based on their basic characteristics including tone, texture, pattern and shape of attributes as described by Allum (1966) and Drury (2001) as key basic characteristics for extracting geologic data from images. The process of geophysical data extraction by tracing the trends of magnetic highs after Isles et al. (1990) was used to produce worm maps. Airborne magnetic analytical signal data of the OGB in Burkina Faso and Niger, Magnetic reduced to pole image of the Essakane area, Airborne magnetic TMI Reduced to Pole (RTP) 1st vertical derivative of Eastern Burkina Faso, and Airborne

magnetic TMI Reduced to Pole (RTP) of Eastern Burkina Faso were overlain and/or merged in MapInfo® to enhance attributes (e.g., Figure 4.7).

The extraction process was computer based using MapInfo®, CorelDraw®, and Discover®. The attributes were extracted in MapInfo®. The attributes layers included; Artisanal Mine Workings/Orpaillage sites, Roads, Dune Sands, MgO Deposits, Laterite Caps and Fe Gossan, Rivers/ Drainage Pattern, Outcrops of greywacke-conglomerate units (competent units), Outcrops of Gabbro-Dolerite dykes, Lineaments Analysis, Dykes and Sills, Ultra-mafic Complexes (YMC), Plutons and Batholiths, Regions of magnetic high and low, Regions of Supracrustals, Contact Aureole, Trends of Lithologies and structures, Regions of Vegetation, Dams, Towns and Villages, and Simplified River Pattern. Attributes file names are listed in Table 4.1. Several attributes were extracted from the different data sets increasing the confidence level of those attributes. An attribute versus dataset table is presented as Table 4.2 and summarizes the confidence of the extracted attributes. The regional geological map which combines this data is presented in Figure 4.13 and represents a hypothesis map which formed the base for ground-truthing and data validation studies. An interpreted geological map based on Figure 4.13 is presented in Figure 4.14; there is little difference demonstrating that a significant amount of geological data can be extracted through careful and considered desktop evaluation that combines geography, geology, and geophysics.

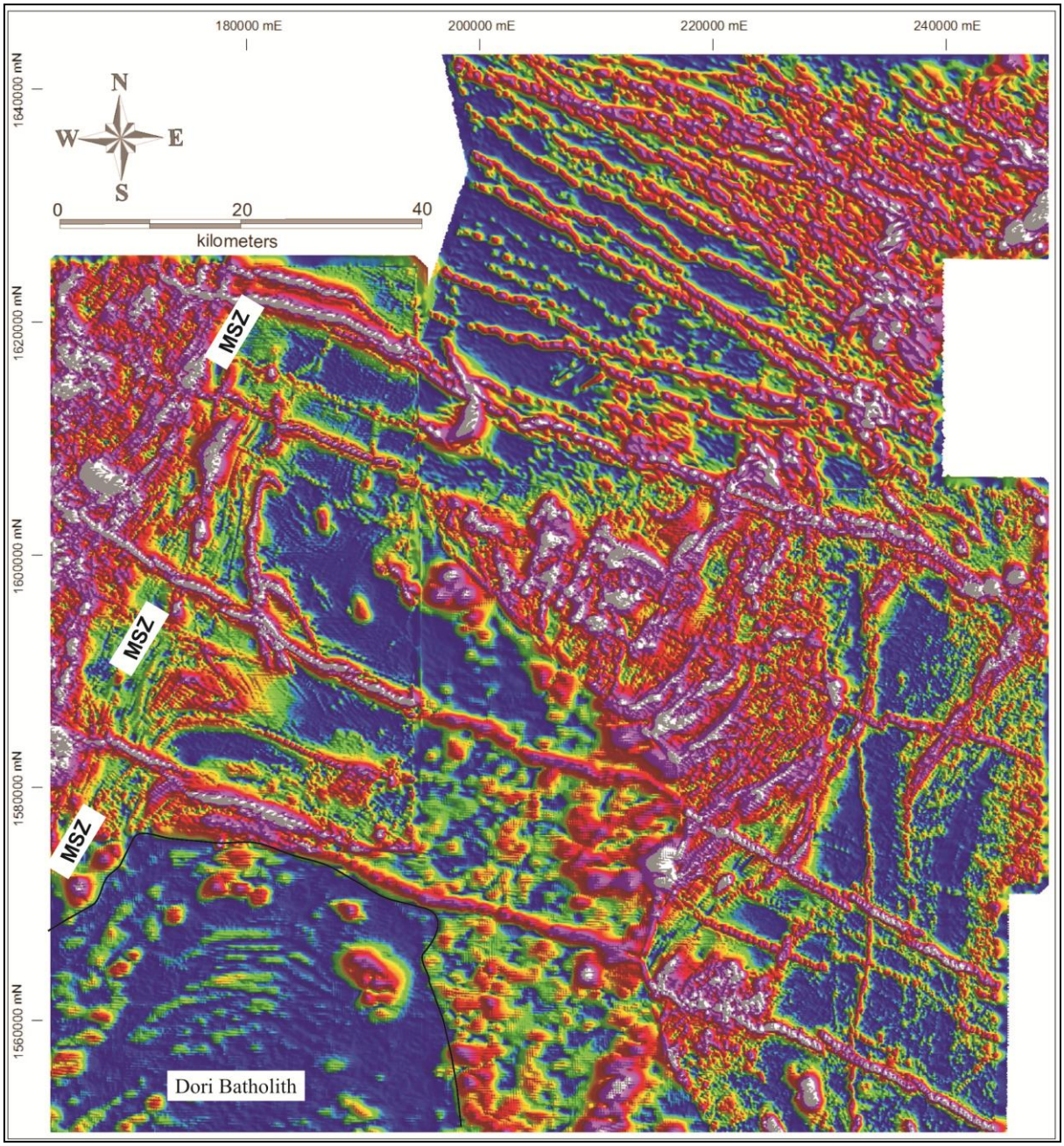

Figure 4.1: Reduced to Pole Airborne Magnetic Analytical signal data for the OGB in Burkina Faso and Niger. The data was acquired along east-west flight lines in 1998 by Gold Fields Exploration. The north-northeast trending Markoye Shear Zone is localized at the western side of the image.

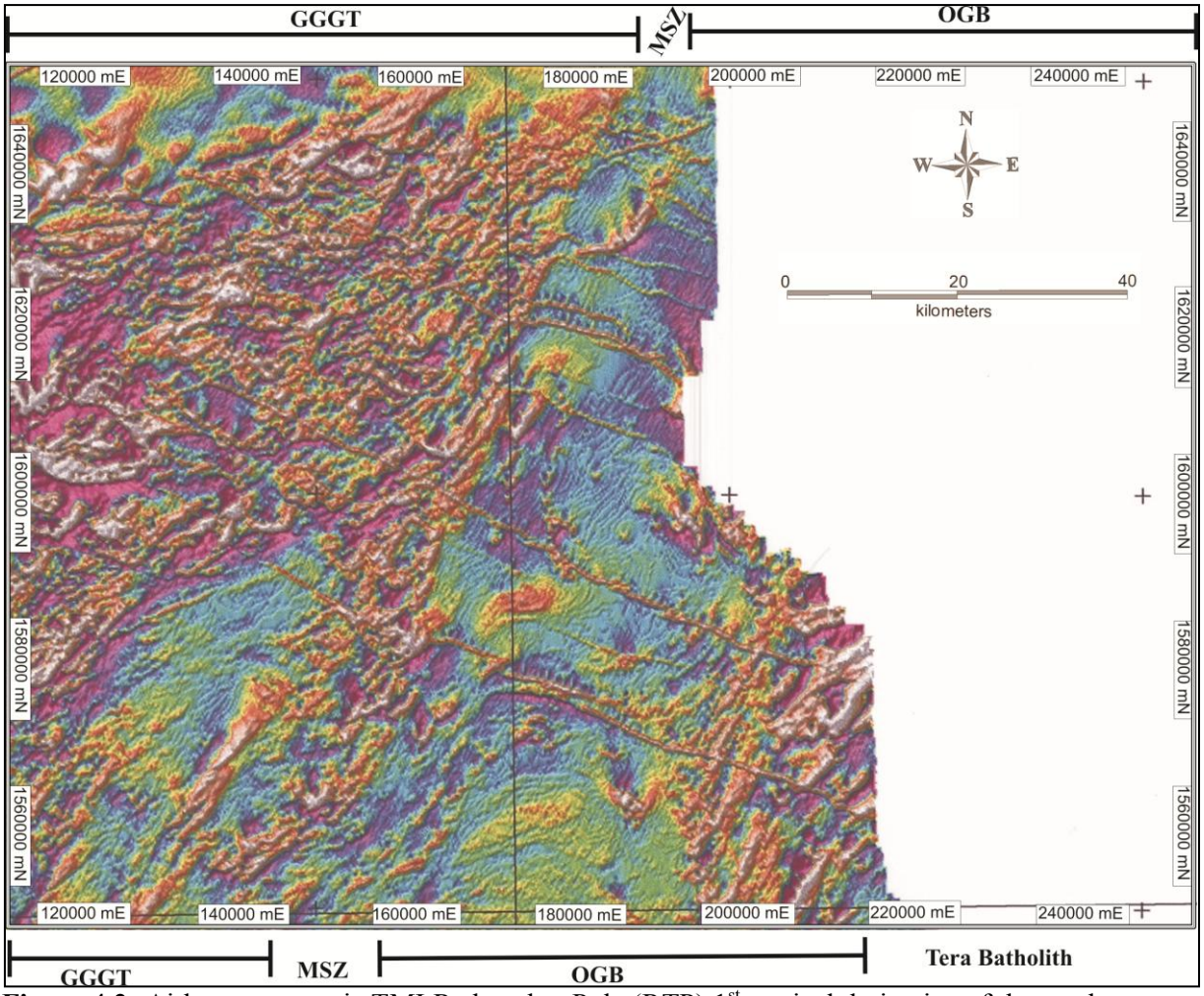

Figure 4.2: Airborne magnetic TMI Reduced to Pole (RTP) 1st vertical derivative of the north-eastern Burkina Faso, afters Mayes (1997).

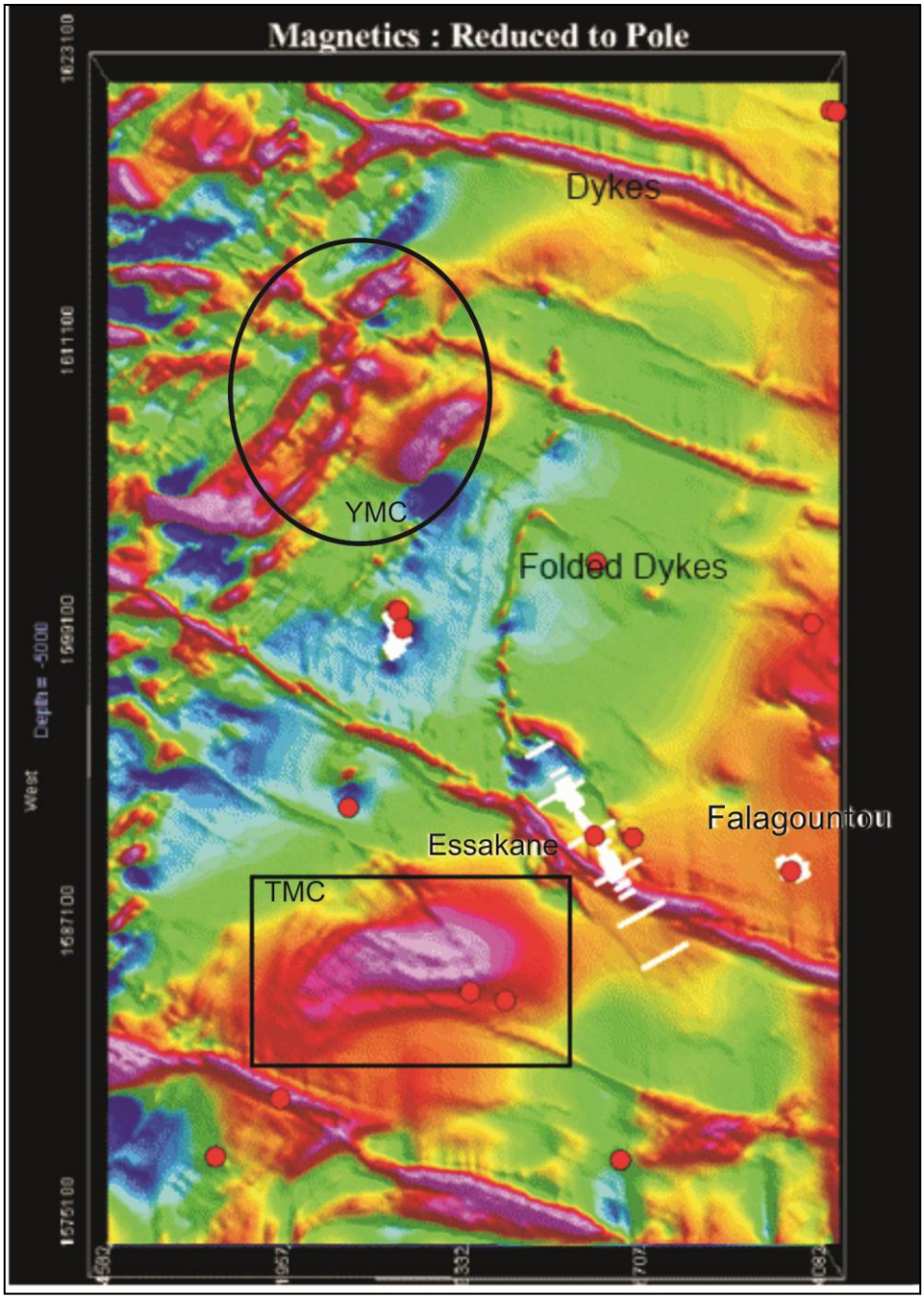

Figure 4.3: Magnetic reduced to pole image of the Essakane-Falagountou area in the OGB, acquired along north-south flight line. The white lines and the red dots are related to the exploration drill holes and samples (not part of this work). A broad magnetic high is observed over the region southwest of the Essakane gold mine, indicating the presence of a magmatic intrusion in the area.

Figure 4.4: A 1:500 000 scale LANDSAT, Bands 741 RGB image of the OGB, GGGT and surrounding areas. The drainage pattern is modified parallel-dendritic, indicating a structural control to the drainage in the area.

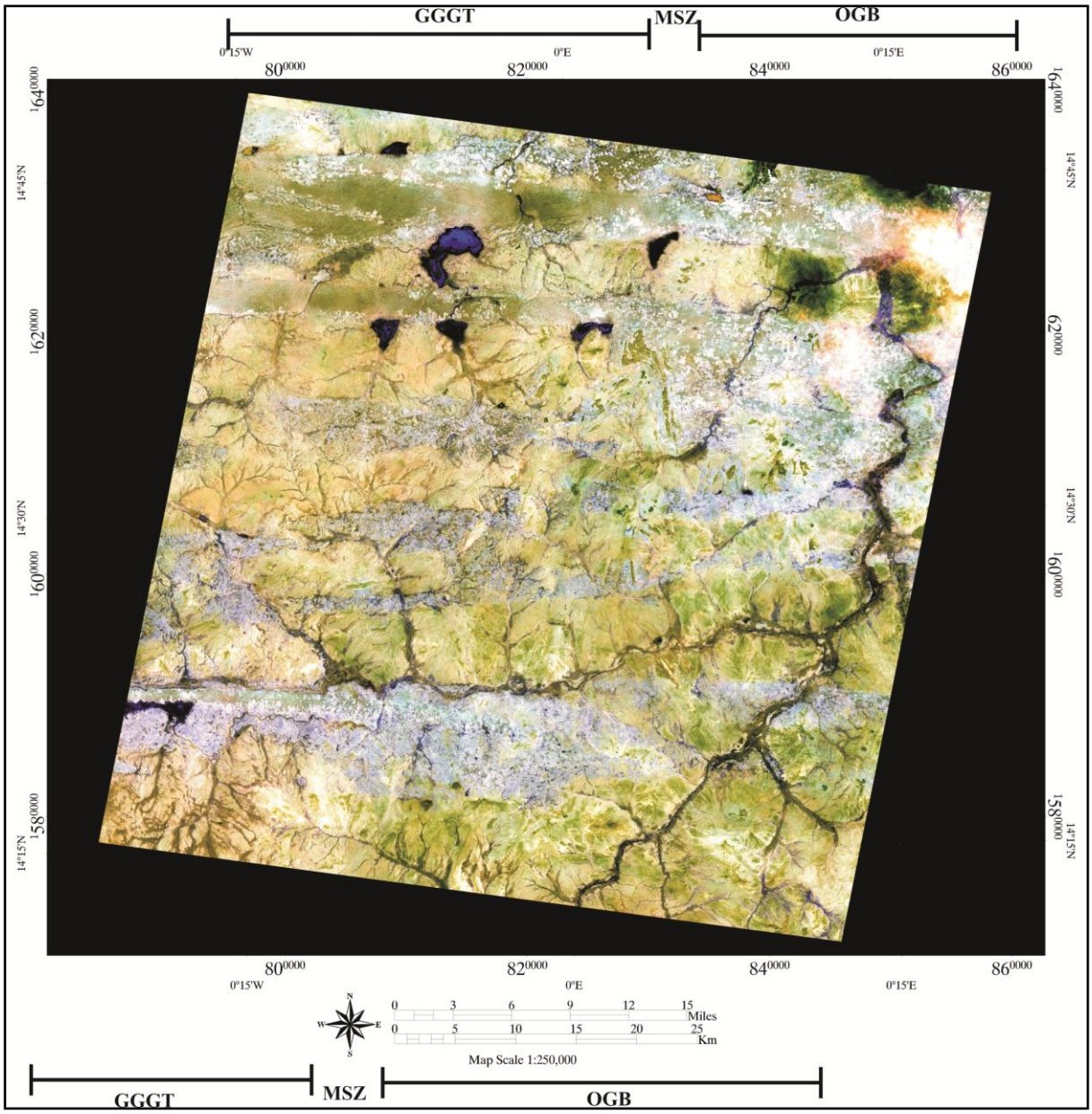

Figure 4.5: A 1:250 000 scale ASTER image of the north-eastern area of the Oudalan province. The geology and geomorphology could be identified and targeted through the data extracted from this image including position of outcrops.

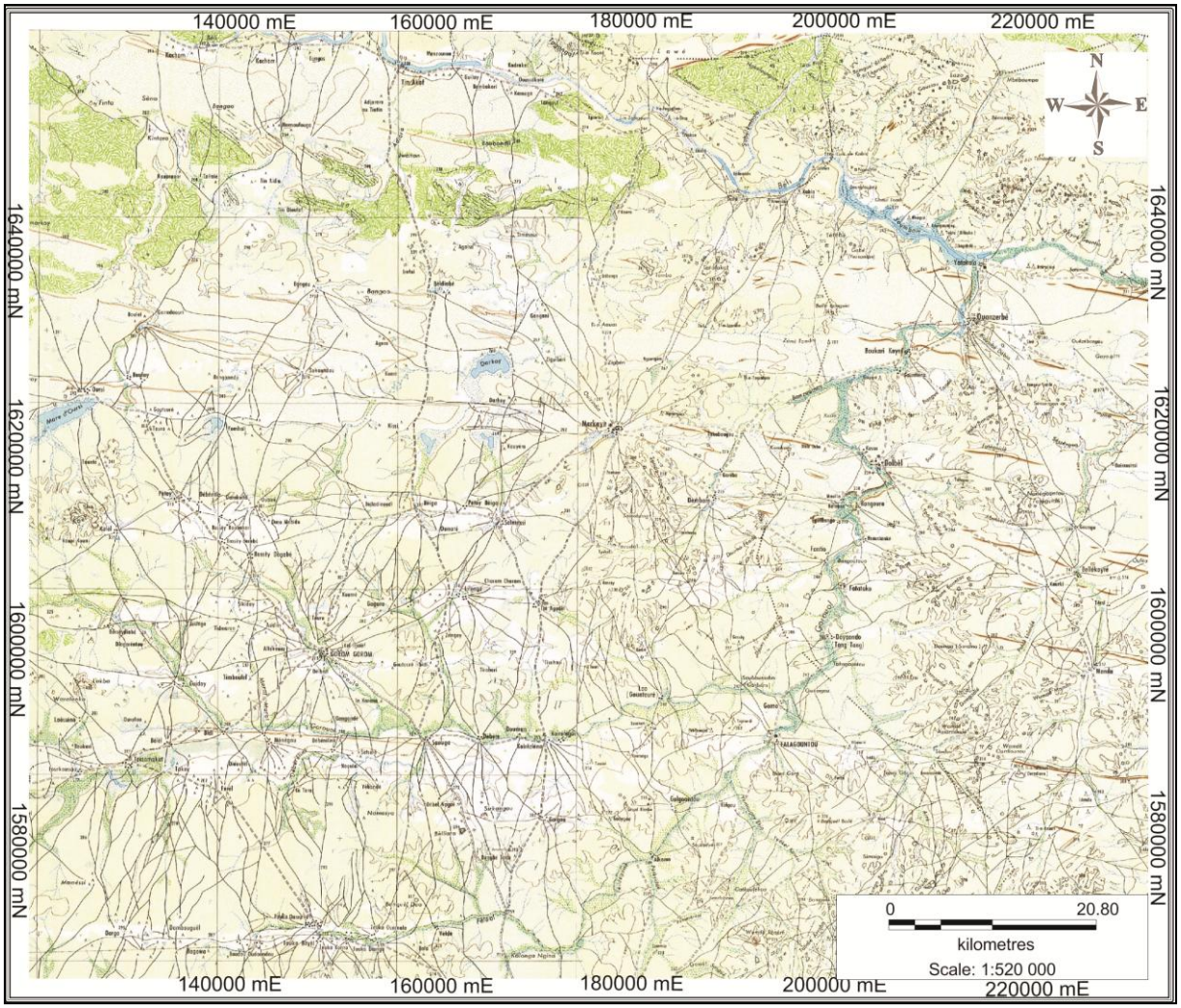

Figure 4.6: A 1:500,000 Topographic map covering portions of the Oudalan, Seno and Tillabéri provinces in Burkina Faso and Niger. The map was used to locate most of the geographic features in the study area.

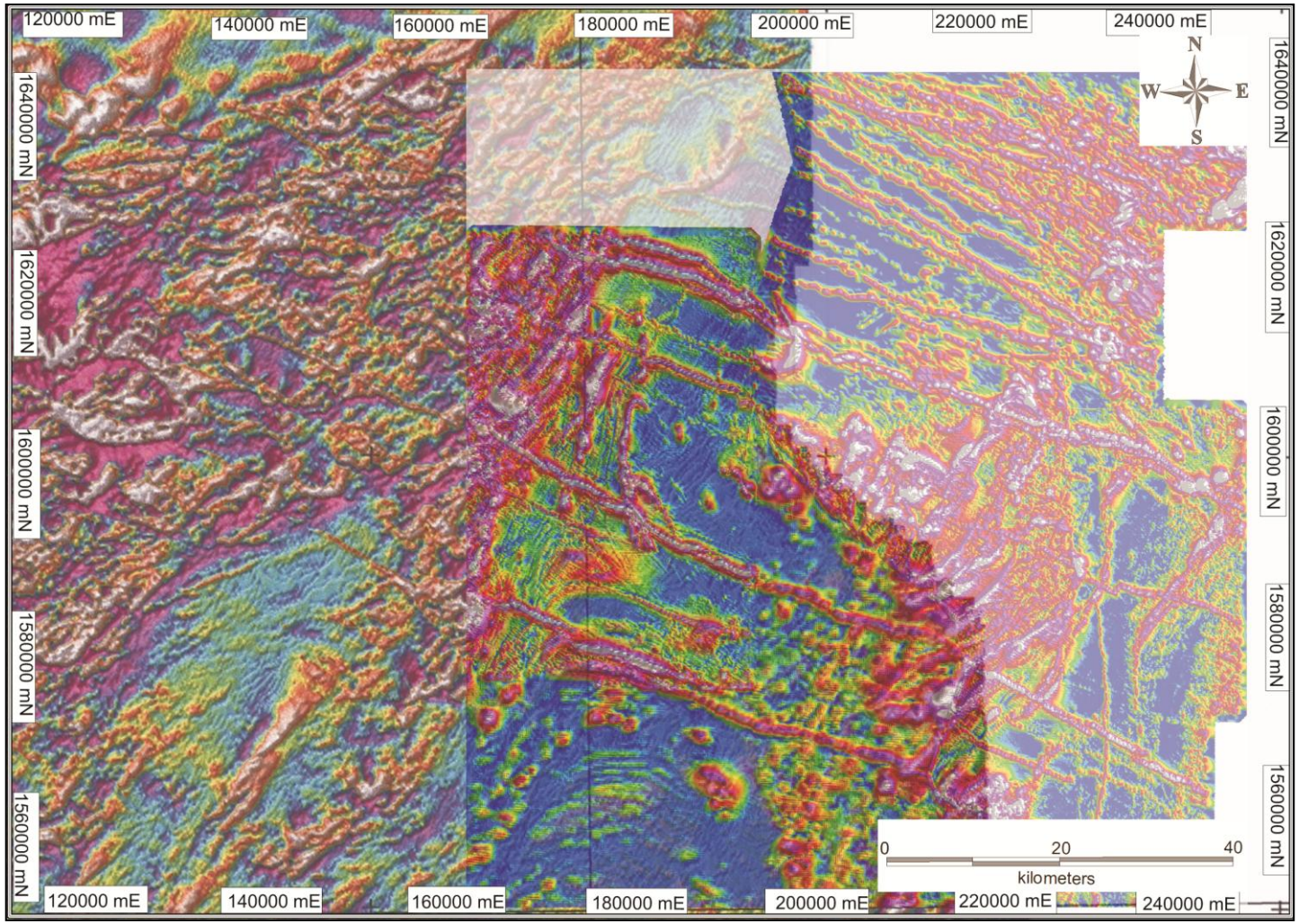

Figure 4.7: The overlay of Reduced to Pole (RTP) Airborne Magnetic Analytical signal data of the OGB in Burkina Faso and Niger (50% translucency) and the Airborne magnetic TMI Reduced to Pole (RTP) 1st vertical derivative of the north-eastern Burkina Faso. The overlay provides the coverage of the area of study with very good data correspondence.

	Attributes Layer	File Name	Data Used for extraction
1	Artisanal Mine Workings/Orpaillage sites	Artisanal Mine Working Sites_28_01_2014.TAB	LANDSAT and ASTER
2	Roads	OGB and GGGT Roads_28_01_2014	LANDSAT and ASTER
3	Dune Sands	Dune Sands_28_01_2014.TAB	LANDSAT and ASTER
4	MgO Deposits	MgO Deposits_28_01_2014.TAB	LANDSAT and ASTER
5	Laterite and Fe Gossan	Laterite Caps and Fe Gossan_28_01_2014.TAB	LANDSAT and ASTER
6	Rivers/ Drainage Pattern	Rivers/Drainage Pattern_28_01_2014	LANDSAT and ASTER
7	Outcrops of Greywacke-Conglomerate	Outcrops of Greywacke-Conglomerate Units_28_01_2014.TAB	LANDSAT and ASTER
8	Outcrops of Gabbro-Dolerite dykes	Outcrops of Gabbro-dolerite dykes_28_01_2014.TAB	LANDSAT and ASTER
9	Lineaments	Lineaments Analysis_LANDSAT & ASTER_29_01_2014.TAB	LANDSAT and ASTER
10	Dykes and Sills	Dykes and Sills_Mag Inter_28_01_2014.TAB	Airborne Magnetic Analytical Signal data; Airborne magnetic TMI Reduced to pole (RTP) 1st vertical derivative of Eastern Burkina Faso; and Airborne magnetic TMI Reduced to pole (RTP) of Eastern Burkina Faso
11	Ultra-mafic units (YMC)	Pyroxenite-Hornblendite Intrusions (YMC)_28_01_2014.TAB	Airborne Magnetic Analytical Signal data; Airborne magnetic TMI Reduced to pole (RTP) 1st vertical derivative of Eastern Burkina Faso; and Airborne magnetic TMI Reduced to pole (RTP) of Eastern Burkina Faso
12	Lineament Analysis	Lineaments Analysis_Geophys_29_01_2014.TAB	Airborne Magnetic Analytical Signal data; Airborne magnetic TMI Reduced to pole (RTP) 1st vertical derivative of Eastern Burkina Faso; and Airborne magnetic TMI Reduced to pole (RTP) of Eastern Burkina Faso
13	Towns and Villages	Towns and Villages_29_01_2014.TAB	Fieldwork, LANDSAT, ASTER, and Google Earth
14	Simplified River Pattern	River Pattern_29_01_2014.TAB	LANDSAT and ASTER

Table 4.1: Table of attribute layers and the file names used in the CD in Appendix G.

	Attributes	Trends of Lithologies	Dams	Outcrop positions and shape and form of competent units	Artisanal workings	Roads	Dune sands and Vegetation	General area of Supracrustal Rocks	Drainage system and alluvium and vegetation	Dykes outcrops	Plutons	Folded dykes/Sills	linear dykes-Magnetic highs	linear dykes-Magnetic lows	Contact Aoureole	Mafic Complex	Domain of low magnetic intensity	Domains of high magnetic intensity	NW trending lineaments	NE-trending lineaments	N-S trending Lineaments	E-W-trending lineaments
Datasets	LANDSAT	X	X	X	X	X	X	X	X	X	X								X	X	X	X
	ASTER	X	X	X	X	X	X	X	X	X	X								X	X	X	X
	Google Earth	X	X	X	X	X	X	X	X	X	X								X	X	X	X
	Airborne Magnetic Analytical Signal Data							X			X	X	X	X	X	X			X	X	X	X
	Airborne Magnetic reduced to pole image of the Essakane-Falagountou area											X	X	X		X			X	X	X	X
	Airborne magnetic TMI Reduced to the pole (RTP) 1st Vertical derivative							X			X	X	X	X	X	X	X	X	X	X	X	X
	Airborne magnetic TMI Reduced to the pole (RTP)							X			X	X	X						X	X	X	X
	Airborne Magnetic Total Field							X			X	X	X						X	X	X	X
	Airborne Vertical Gradient							X			X	X	X						X	X	X	

Table 4.2: Attribute confidence table of extracted datasets.

4.2. Airborne Magnetic Analytical Signal, Airborne magnetic TMI Reduced to The Pole (RTP) and RTP 1st vertical derivative and Magnetic 3D slice data interpretation

4.2.1. Lineaments

These data sets were used to trace lineaments in the domains that are dominated by metasedimentary units and magmatic rocks across the study area. Northeast to north-northeast, northwest, and north-south trending lineaments dominate the study area, and curvilinear lineaments dominate the southern domain of the study area (Figures 4.8b). The northwest trending lineaments are crosscut by northeast to north-northeast trending lineaments. The northwest and north-northeast trending lineaments are crosscut by north-south trending lineaments. This crosscutting relationship may suggest three separate periods of lineament development, with northwest trending preceding the northeast to north-northeast, and north-south trending lineaments. The northwest trending lineaments are curvilinear east of Gossey in the MSZ and near Falagountou; they are restricted to the region bounded by the domains of northeast to north-northeast trending lineaments (Figure 4.8b). Northwest sigmoidal lineaments occur in the GGGT.

The Markoye Shear Zone, the Takabangou Shear Zone (Tshibubudze et al., 2009), and Kargouna Shear Zone are clearly defined as northeast to north-northeast trending complex sets of parallel lineaments (Figure 4.8b; Chapter 5) and are zones of intense deformation. The Sabce Shear Zone (Chapter 6) is defined by a set of northeast trending structural lineaments that crosscut the GGGT (Figure 4.8b).

4.2.2. Magnetic Dykes and Sills

The area of study is crosscut by northwest trending linear magnetic high-low couplets (Figure 4.1, 4.2, 4.3), with minor northeast trending magnetic highs and lows, and minor north-south trending magnetic highs. These are interpreted to be suites of dykes. The dykes are strongly magnetic for the most part in the north of the study area (Figure 4.1) and are interpreted to be dolerite and/or gabbro dykes of high magnetic intensity (Figures 4.8c, d, 4.9b, and 4.10b).

Linear magnetic highs that are concordant to sedimentary layering/bedding north of the Essakane village are interpreted as sills (Figure 4.13, 4.14). They are folded with sedimentary units (Chapter 5), and are crosscut by the northwest trending dykes.

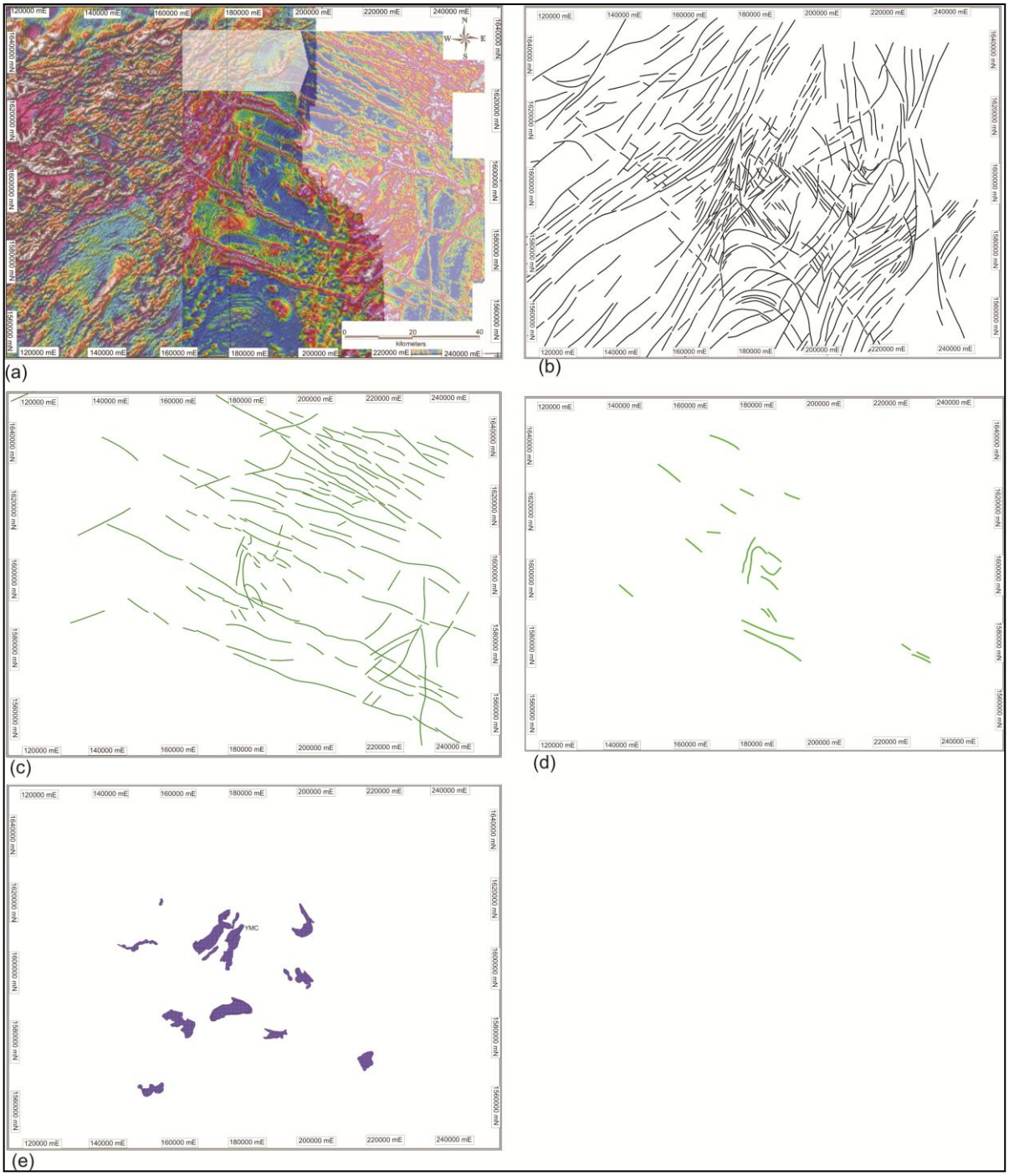

Figure 4.8: An overlay of Reduced to The Pole (RTP) Airborne Magnetic Analytical signal data of the OGB in Burkina Faso and Niger, and the Airborne magnetic TMI Reduced to The Pole (RTP) 1st vertical derivative of the north-eastern Burkina Faso for the study area. (b) Combined worm map of lineaments extracted from the airborne magnetic data. The lineaments are defined by magnetic lows or highs. The attribute are interpreted to indicate the dominant trends of shear, faults and to a certain degree lithological boundaries. (c) Combined worm map of lineaments extracted from the magnetic data. The study area is dominated by northwest trending lineaments that are crosscut by second-order northeast trending lineaments interpreted as dolerite or gabbro dykes and sills. (d) Combined magnetic lows interpreted as linear and folded dykes/sills. (e) Ultra-mafic units of the OGB and GGGT.

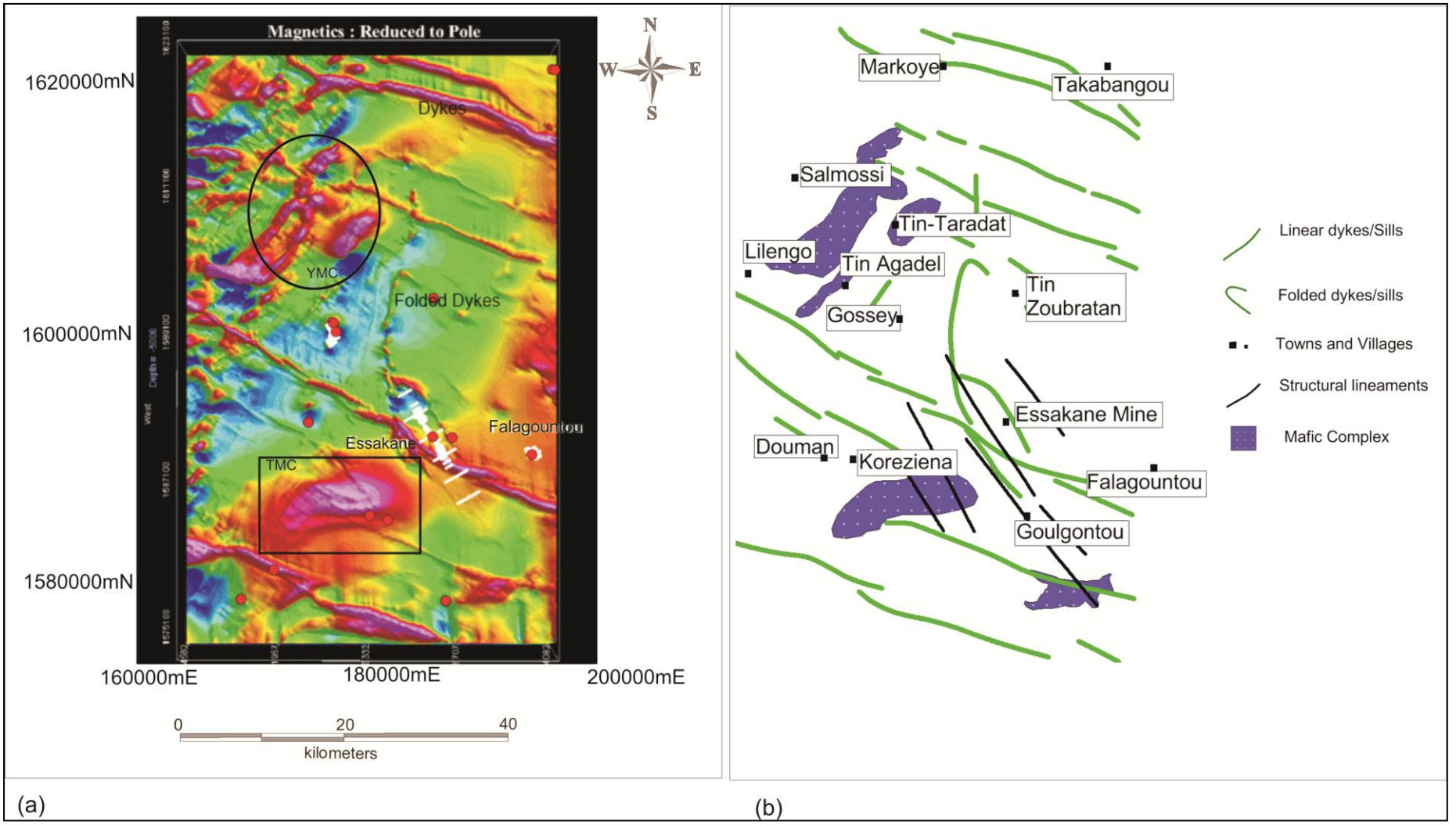

Figure 4.9: (a) Magnetic reduced to pole image of the Essakane-Falagountou area in the OGB. (b) The worm map of the magnetic reduced to pole image. A broad magnetic high is observed in the region southwest of the Essakane gold mine and has the same magnetic intensity as the YMC.

4.2.3. Batholiths and Plutons

Batholiths and plutons are represented in Figures 4.1, 4.2, 4.3, 4.10 and 4.11 by regions of magnetic low, which are homogenous in terms of magnetic intensity and texture. A magnetic low covers most of the area in the OGB and GGGT (Figure 4.10, 4.11). The margins of batholiths and plutons are relatively well defined by magnetic highs or spotted magnetic highs around and above the interpreted locations of batholiths and plutons, and their contact aureole (Figure 4.10a, d). Most of the OGB is defined by a regional magnetic low. Tshibubudze et al. (2009), and Tshibubudze and Hein (2013) demonstrated that outcrops in the Tin-Taradat and Dori Batholith are correlated with this magnetic low and are granodiorite-tonalite in composition. The Dori Batholith and the Tin-Taradat pluton are thereby interpreted as a single intrusive mass (Figure 4.11). They are crosscut by the major lineaments that represent the MSZ.

An intense linear magnetic high (15km long x 5km wide) north of the village of Tin Taradat was defined by Tshibubudze et al. (2009) as a pyroxenite-norite body and termed the Yacouba Mafic Complex (YMC) (Figure 4.9). Tshibubudze (2007) described the presence of nickel-sulphides and suggested that the YMC might present a nickel copper sulphide exploration target. It is clear from the magnetic data (Figures 4.1, 4.2, 4.3) that several similar magnetic, highs occur across the study area (Figure 4.8e). These are also interpreted as pyroxenite-norite plutons and dykes. The broad magnetic high (10 km long x 5 km wide) west-southwest of the Essakane gold mine (Figure 4.3, 4.9) might also have potential for nickel-sulphide mineralization and is herein termed the Tassiri Mafic Complex (TMC).

The YMC is also evident in this magnetic reduced to pole image, as are northwest trending dykes and northerly trending folded dykes north of Essakane. The magnetic reduced to pole image presents evidence for northwest trending linear magnetic lows at Essakane that may correspond with northwest trending thrusts and reverse faults (Chapter 5) (Figure 4.9).

4.3. LANDSAT and ASTER image interpretation

LANDSAT and ASTER images for the study area present a broad view of the surface geology and geographic features including surface lineaments, drainage patterns, sand dunes, lithologies and man-made elements. To some degree, drainage patterns conform to underlying geological features, because streams always follow the line of least resistant, and the interpretation may therefore reflect the gross structural architecture of the crust. However, Metelka et al. (2011) have indicated that this is not always the case as variations do occur with respect to the interpretation of LANDSAT and ASTER, and the field data. Thus ground truthing was essential to validate extracted attributes.

The river patterns interpreted from the LANDSAT image are representative of a modified parallel-dendritic pattern as defined by Drury (2001) (Figure 4.4, 4.12b). The parallel pattern is

superimposed on an underlying structural architecture in the area (Allum, 1966). The overall lineaments interpreted from river drainages and tributaries are represented in Figure 4.12c. The dominant drainages trend either northwest or northeast with a subordinate north-south trend. The northwest and northeast trending lineaments corresponds with northwest and northeast trending magnetic lineaments (Section 4.2) and reflect shear zones and faults (Chapter 5 and 6). However, in the Dori Batholith the lineament grain is radial and /or concentric with edges of the batholith (Figure 4.12c). The lineaments in the Dori Batholith may be related to cooling processes subsequent to emplacement, or more likely unloading joints (Twidale, 1982; Gerrard, 1990) formed during erosion of the batholith. Some lineaments may possibly represent shears that are concentric to the batholiths (e.g. the Dori Marginal Shear Zone, Chapter 5). These concentric lineaments are crosscut by northeast trending lineaments (Figure 4.12c).

4.3.1. Metasedimentary units

Different rock types respond to weathering and erosion in different ways (Gibbs et al., 1999). In the OGB, uplands are represented by competent rock units, while low lands are represented by relatively incompetent rock units. In the GGGT near Gorom-Gorom, uplands trend northeast to easterly. Competent rock units are clearly multiply folded (Figures 4.4; 4.5, 4.12a, d, e) suggesting polyphase deformation took place in the OGB with at least two folding events; this interpretation agrees well with the interpretation of Hein and Tshibubudze (2007) and Tshibubudze et al. (2009). For example, northwest trending tight folds to the west of Tin Zoubratan (Figure 4.4; 4.5, 4.12d) are clearly refolded along northeast trending axes to form open folds.

4.3.2. Plutons and dykes

Across the study area, plutons are relatively easy to identify using LANDSAT ETM Bands 741 (Figure 4.4) as equal tonal areas which are pink, such as the Tera and Dori batholiths and perhaps the Dolbel region (Figure 4.12f). Several crosscutting dykes can be traced across the OGB and GGGT and most of these are northwest trending (Figure 4.12g).

4.3.3. Dune Sands

The study area as interpreted from the LANDSAT image and ASTER is covered by east-west trending longitudinal sand dunes (Figure 4.4; 4.5, 4.12b). They present as green to light yellow false colour in the LANDSAT image (Band 741). They have a light blue to white false colour in the ASTER image. They represent the migratory sands of the Sahara Desert which is located north of the study area, but in Burkina Faso, the dunes are largely stabilized by sparse vegetation (c.f., Jeambrun et al., 1970).

4.3.4. Artisanal workings

In the study area artisanal workings appear as bleached zones in LANDSAT and ASTER images particularly around the Essakane mine. The interpreted artisanal sites overlap with known locations of gold deposits and prospects (Figure 4.12j, 4.13). They are located proximal to plutons or crosscutting dykes or sills. They are hosted along the northwest trending lineaments, with a few hosted along the northeast to north-northeast trending lineaments. This strongly suggests that northwest and northeast to north-northeast trending lineaments are prospective for gold, and that a spatial relationship may exist between structures and intrusions.

4.4. Interpretation and tentative chronology of crosscutting relationship

Based on the extracted attributes outlined above, their trend, form and character and crosscutting relationship, a tentative geological history of the study area suggests that, from oldest to youngest;

Airborne Magnetic Analytical Signal, Airborne Magnetic TMI Reduced to Pole (RTP) and RTP 1st vertical derivative and Magnetic reduced to pole image, LANDSAT, and ASTER images demonstrate that the intrusion of north-northwest to north trending gabbro and pyroxenite sills/dykes predates the formation of northwest trending lineaments that are crosscut by northeast trending lineaments. The northwest trending gabbro and pyroxenite sills/dykes are crosscut by northwest trending lineaments and are folded to produce a northwest trending fold axial trace. The intrusion of granitoids, including the Tin-Taradat pluton and the Dori granodiorite-tonalite batholiths, predates the formation of northeast to north-northeast trending lineaments. The northeast to north-northeast trending lineaments that crosscut the entire study area have been interpreted to be shear and faults and joints (c.f., Tshibubudze et al., 2009; Tshibubudze and Hein, 2013). These were followed by a formation of north-south trending lineaments that crosscut the northwest and northeast trending lineaments.

LANDSAT, ASTER and magnetic data demonstrate that the emplacement of northwest trending dolerite/gabbro dykes postdate formation of northwest and northeast trending lineaments in the study area. This was post-dated by formation of east-northeast trending faults that crosscut and displaces northwest and northeast trending lineaments. The deposition of dune sands and laterite accumulation postdates the intrusion of northwest trending dykes.

The geophysical datasets and remotely sensed data provide a useful and simple interpretive strato-tectonic framework that formed the basis for geological studies.

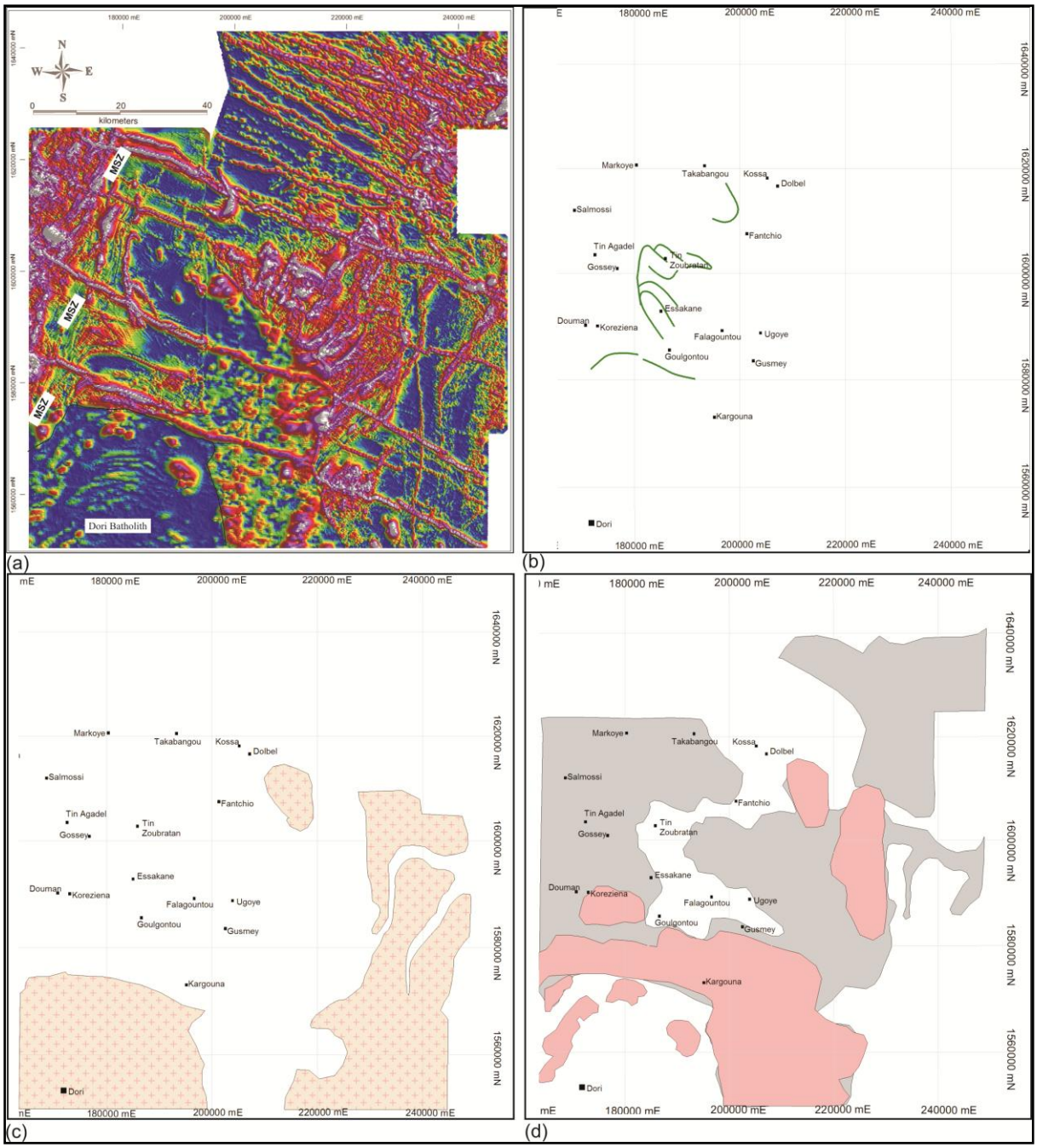

Figure 4.10: (a) Reduced to the pole Airborne Magnetic Analytical signal data of the OGB in Burkina Faso and Niger. (b) Worm map of folded magnetic high dykes/sills as extracted from Figure 4.7a. (c) Location of magnetic lows that are interpreted as the Dori and Tera batholiths. (d) General area covered by the supracrustal rocks (grey) and the contact aureole (pink) of plutons and batholiths.

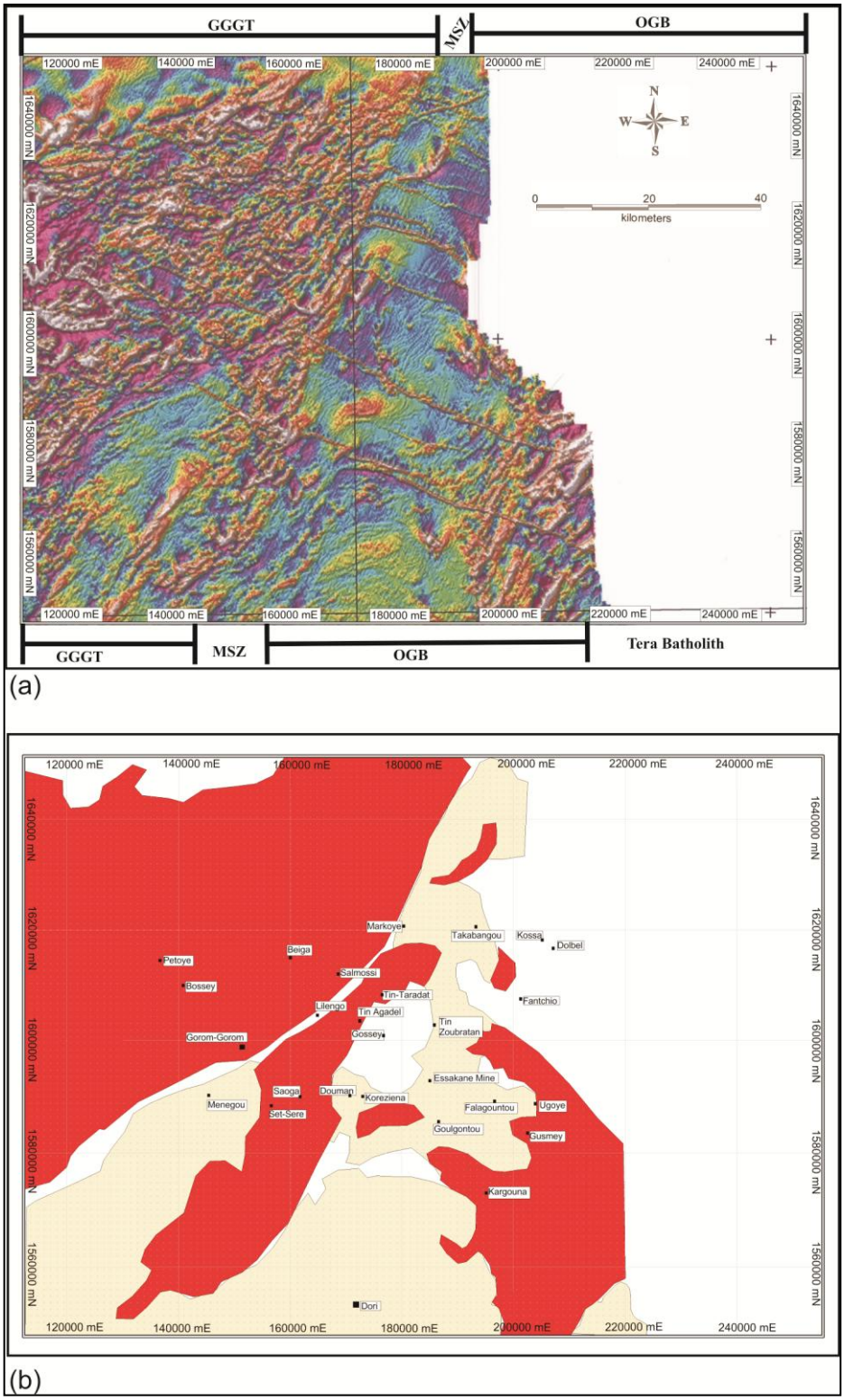

Figure 4.11: (a) Airborne magnetic TMI reduced to the pole (RTP) 1st vertical derivative of the Oudalan province. (b) Regions of high magnetic intensity signature (red) and low magnetic intensity signature (light yellow) extracted for the OGB and GGGT.

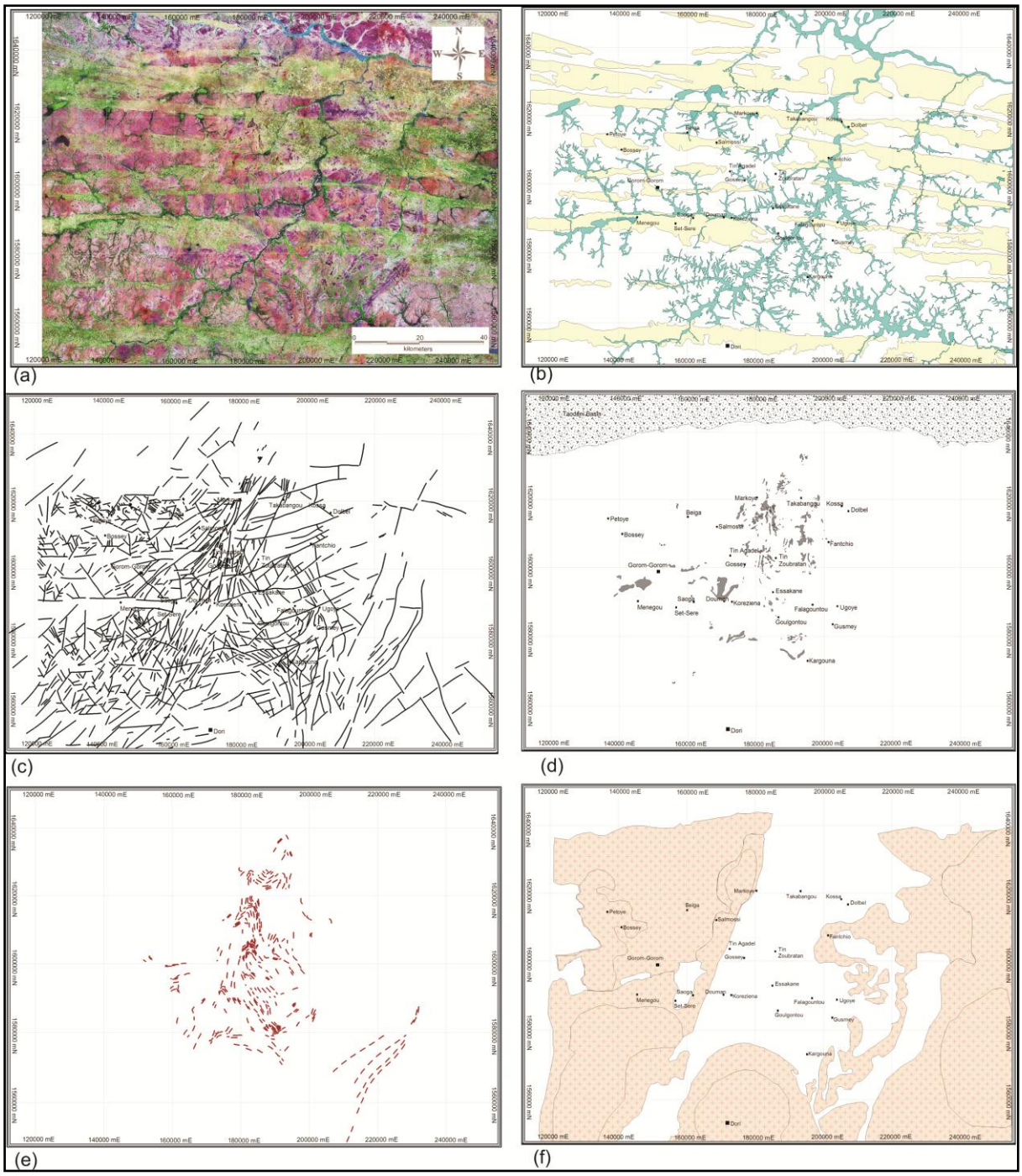

Figure 4.12: (a) The LANDSAT image of the OGB, GGGT. (b) The attributes extracted for drainage patterns and dune sands. The drainage pattern represents a modified parallel-dendritic pattern, indicating a possible structural control to the drainage in the area. (c) Lineaments extracted from the LANDSAT and ASTER images. The lineaments correspond with drainage system in the region. (d) Outcrop attribute layer of competent units that are folded indicating a polyphase deformation may have taken place. (e) Attribute layer of the lithological trend in the study area. (f) Attribute layer indicating the location of batholiths and plutons. Continued overleaf.

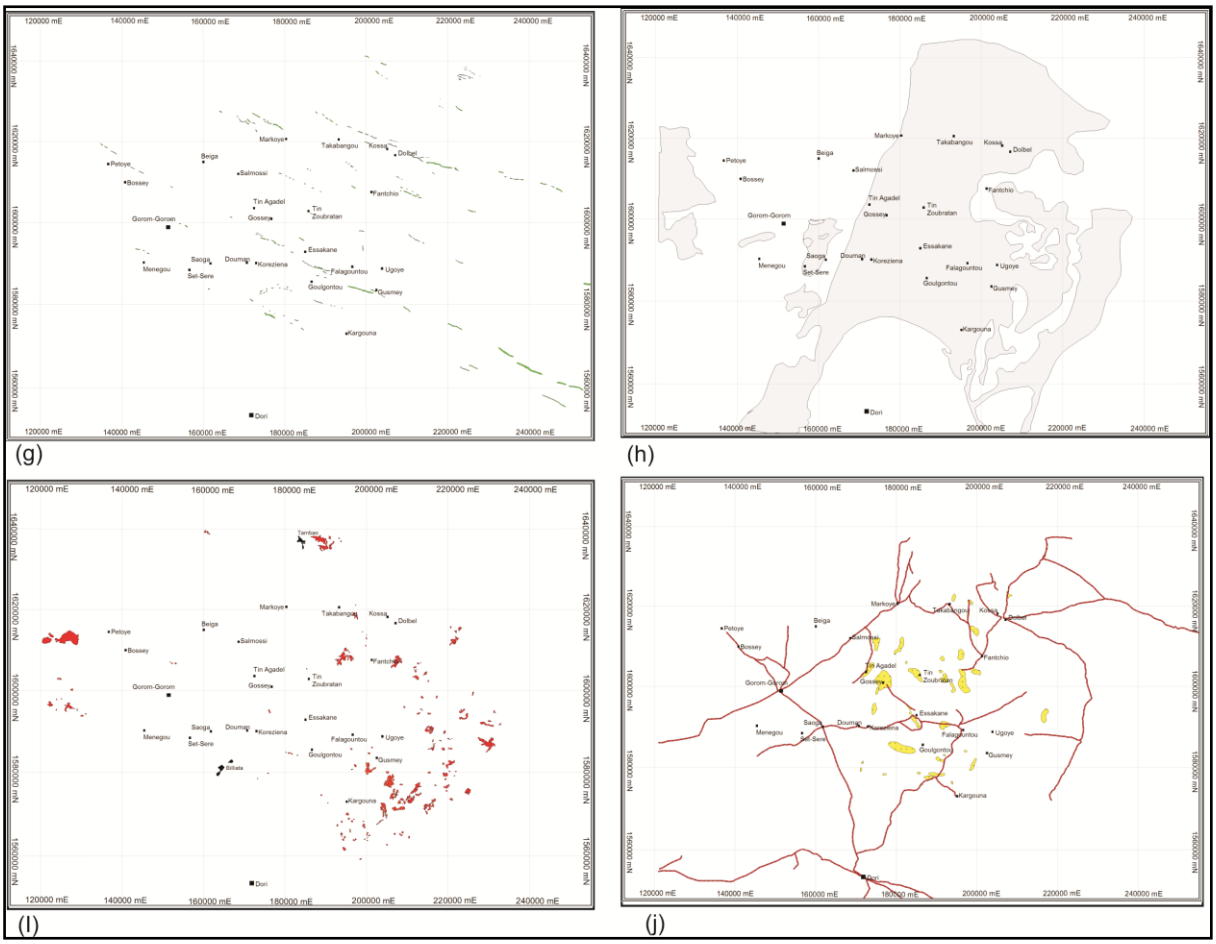

Figure 4.12 (continued): (g) Outcrops of crosscutting dykes interpreted to be the gabbro-dolerite dykes. (h) General location of the supracrustal units. (i) Attribute layer with location of the laterite cap and the MgO deposits. (j) Geographic attributes including roads, villages, and mine sites of artisanal workings.

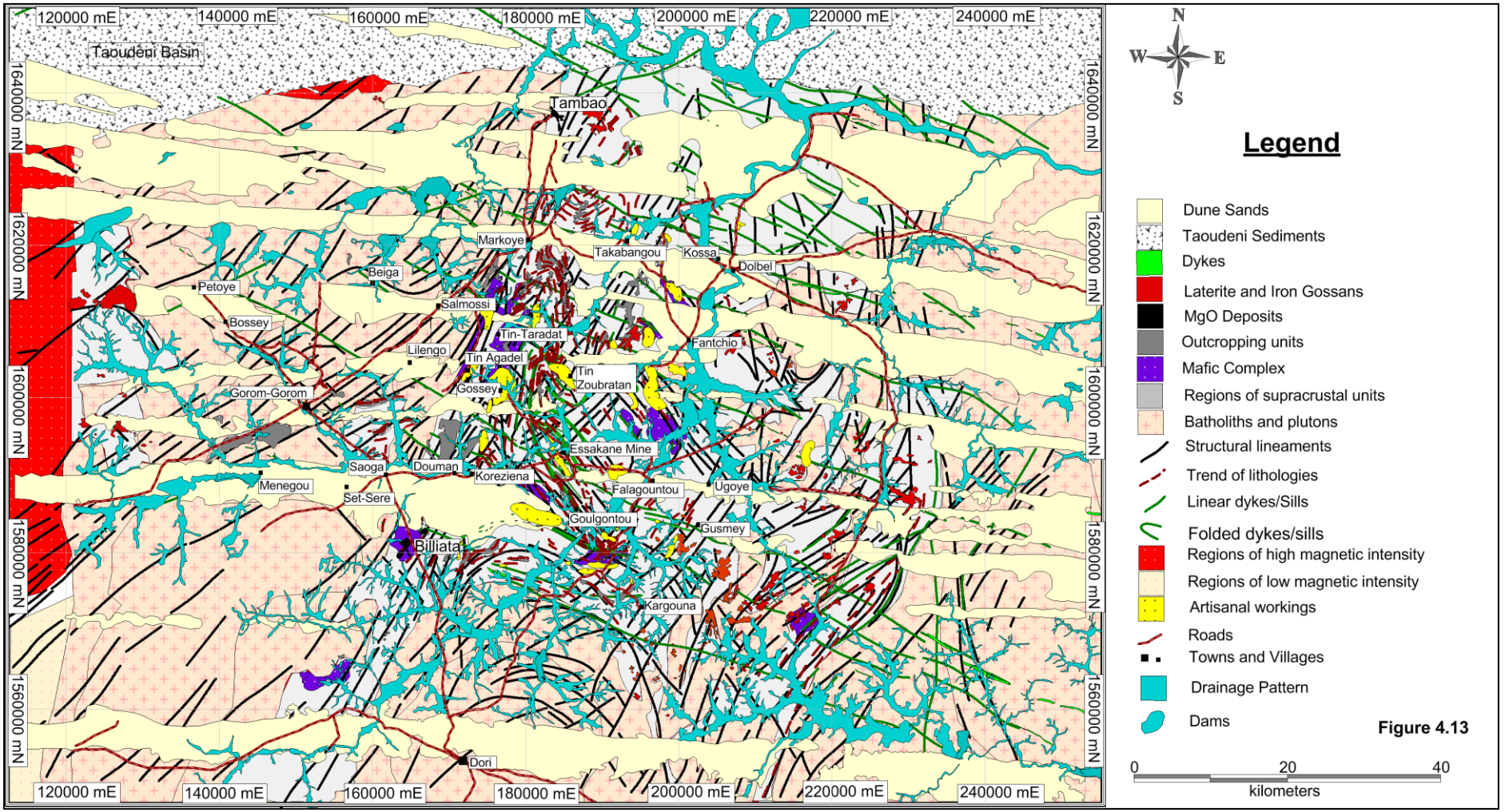

Figure 4.13: A map of the combined information extracted from geophysical and remotely sensed data of the OGB and the GGGT area.

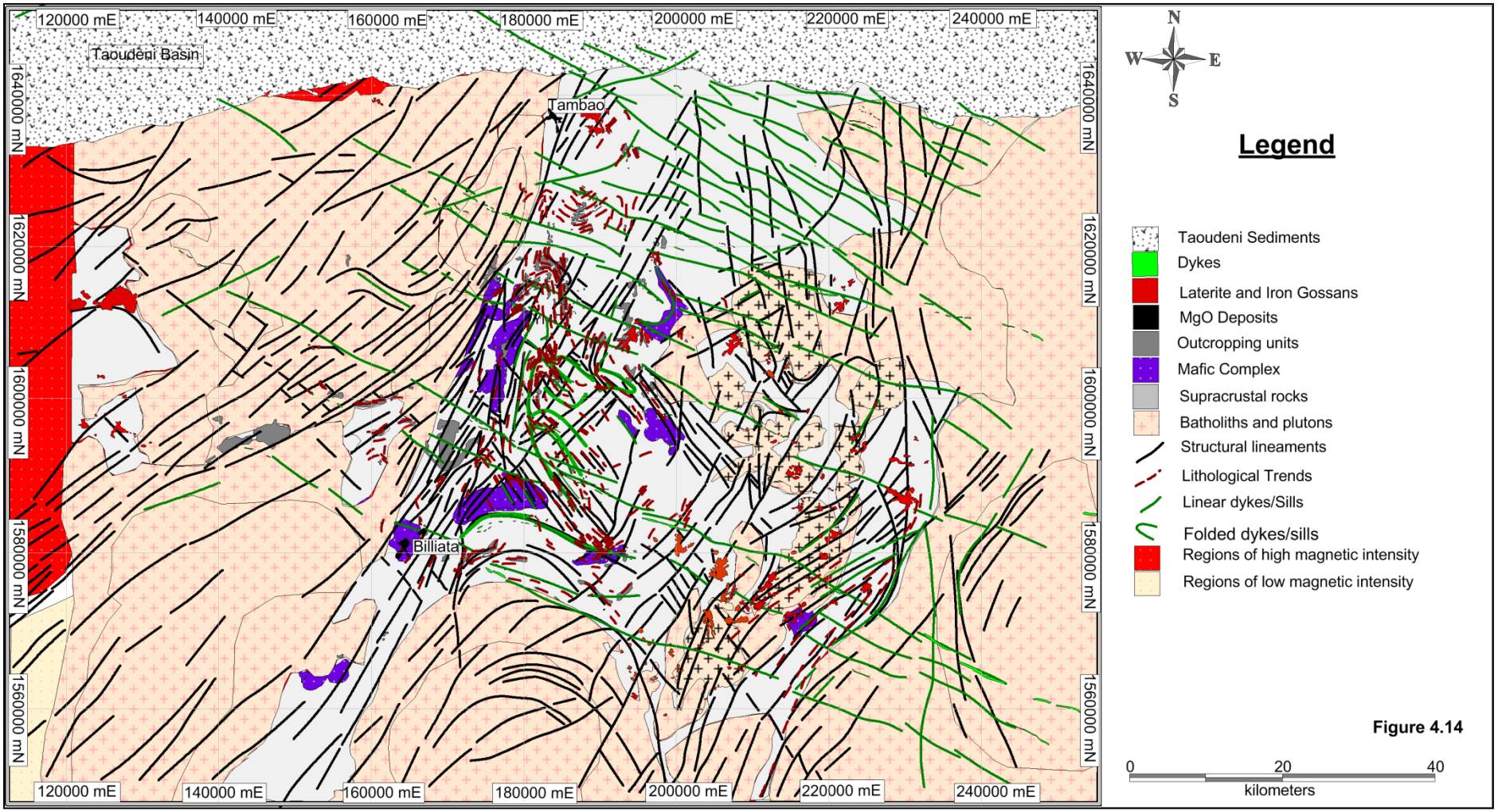

Figure 4.14: A map of the combined information extracted only from the geophysical and remotely sensed data excluding the sand dunes, drainages, towns and villages, roads, artisanal mine sites and dams. This map served as the hypothesis on which field studies were focused in Chapter 5-7.

CHAPTER 5
STRUCTURAL SETTING OF GOLD DEPOSITS IN THE OUDALAN-GOROUOL VOLCANO-SEDIMENTARY BELT EAST OF THE MARKOYE SHEAR ZONE, WEST AFRICAN CRATON

5.1. Preamble

Chapter 5 has been published under the reference: "*Tshibubudze, A., Hein, K.A.A., 2013 'Structural setting of gold deposits in the Oudalan-Gorouol volcano-sedimentary belt east of the Markoye Shear Zone, West African craton' Journal of African Earth Sciences 80, 31-47"* which is presented in Appendix B. Aspects of this chapter are reported as the submitted manuscript: "*Tshibubudze, A., Hein, K.A.A., Pratas, M., Rogers, J., submitted. Gold mineralization in the Essakane goldfield, Burkina Faso. In (Markwitz, V, Hein, K.A.A., Robb, L. (Editors), Minerals Atlas Monograph of West Africa. Published by the Geological Society of South Africa"* this is presented in Appendix C.

Additional sections or edits to the published text are enclosed in square brackets for clarity. References and Acknowledgements from the original published work are compiled in the Acknowledgements and References sections of this thesis.

5.2. Abstract

The Oudalan-Gorouol volcano-sedimentary belt (OGB) of Burkina Faso and Niger hosts meta-volcanic and metasedimentary sequences of the Birimian Supergroup that were folded and deformed during emplacement of the Dori Batholith (D_{1-x}), the Tangaean Event (D1) and the Eburnean Orogeny (D2).

The emplacement of the Dori Batholith accompanied aureole deformation (D_{1-x}) and the development of proto-mylonite, migmatite, gneiss and schist on the northern margin of the batholith. Contact metamorphic grade reached granulite facies with partial melting of the supracrustal sequences. Emplacement of the Dori Batholith was succeeded by emplacement of monzonite dykes and sills through the OGB.

The Tangaean Event (D1) accompanied formation of (a) the Saoga Branch of the Markoye Shear Zone (MSZ), (b) the Mukosi and Billiata mylonite zones that are hosted in the MSZ, (c) the Afu Branch of the Kargouna Shear Zone Complex (KSZC), and (d) northwest-trending thrust-folds (F_1) that crosscut the OGB and coalesce with the MSZ. Metamorphic grade attained amphibolite facies in mylonite or proto-mylonite zones in the Saoga and Afu branches. D1 was succeeded by emplacement of alkali-granite plutons of the Dolbel Batholith.

The Eburnean Orogeny, D2, accompanied formation of (a) the Korizéna Branch of the MSZ, (b) the Waho Branch of the KSZC, and (c) northeast–trending shear-faults which crosscut the OGB. D2 is manifested by refolding of F_1 by northeast-trending F_2, and development of a pervasive northeast-trending S_2 to S_2-C. Metamorphic grade attained greenschist facies during D2 with development of the mineral assemblage quartz-chlorite-muscovite ± actinolite. D2 was succeeded by emplacement of northwest-trending gabbro and dolerite dykes.

The OGB hosts structurally-controlled gold deposits that are sited along 5 metallogenic corridors and include the Essakane, Tin-Fal, Bom Kodjelé, Kossa and Tassiri trends. Gold mineralisation is preferentially located where northeast-trending faults and shears crosscut northwest-trending thrust-folds, or where northwest-trending thrust-folds coalesce with north-northeast trending shears. An intimate relationship thus exists between D1 and D2 structures and gold mineralisation in the OGB. Gold in sheeted-stockwork veins is hosted in competent rocks units including conglomerate beds, greywacke, quartzite, monzonite dykes, pyroxenite-gabbro sills and D1 buck quartz veins. Gold in fine veinlets may also be hosted in massive shale units.

5.3. Introduction

The Oudalan-Gorouol volcano-sedimentary belt (OGB) in northeast Burkina Faso and Niger [Figure 5.1] is known for its remotely situated structurally-hosted gold deposits (Tshibubudze and Hein 2010) including Essakane, Gosséy, Falagountou, Sokadie, Tin Zoubratan and Takabangou [Figure 5.2]. The Essakane gold deposit reached production in late 2010 and will become one of the largest gold producers in West Africa and the African continent.

Structural and tectonic studies by Tshibubudze et al. (2009) argued that two deformation events could be recognized without ambiguity in the OGB. Those studies linked tectonic activity on the steeply east-dipping Markoye Shear Zone (MSZ) to regional deformation in the belt. Formation of a northwest-trending fold-thrust belt during D1 was linked to dextral-reverse displacement on the MSZ during the Tangaean Event, (ca. 2170-2130 Ma, Hein, 2010). Progressive development of north-northeast to northeast-trending mylonite and shears, L-tectonites, and vein arrays of pseudotachylite, quartz-carbonate, buck quartz, and quartz cataclasite was linked to sinistral-reverse reactivation of the MSZ during the Eburnean Orogeny (ca. 2130-1980 Ma, Feybesse et al., 2006).

Although Tshibubudze et al. (2009) did not establish a detailed tectonic framework for gold metallogenesis throughout the OGB, vein-stockwork gold mineralization at the Essakane artisanal gold site was interpreted to have formed late in D2. However, additional research indicates that an intimate relationship exists between the tectonic development of the OGB in D1 and D2, and formation of gold deposits. Second and third-order splay faults and shears of the Tangaean Event matured as sites of gold deposition during the Eburnean Orogeny. The deposits are thus structurally hosted.

In this paper, we present research on the structural geology of Oudalan-Gorouol belt, Burkina Faso and Niger where we characterize the setting of the Essakane gold mine and gold camp in the northeast of Burkina Faso. We report on the lithologies that ultimately define a volcano-sedimentary belt rather than a greenstone belt (*sensu stricto*) and which host gold mineralisation in the region. We summarise the character of intrusive rocks of the greater Oudalan region and establish a relative chronology of crosscutting relationship which broadly constrains the structural evolution of the OGB; and tectonic model for its formation of the OGB is proposed.

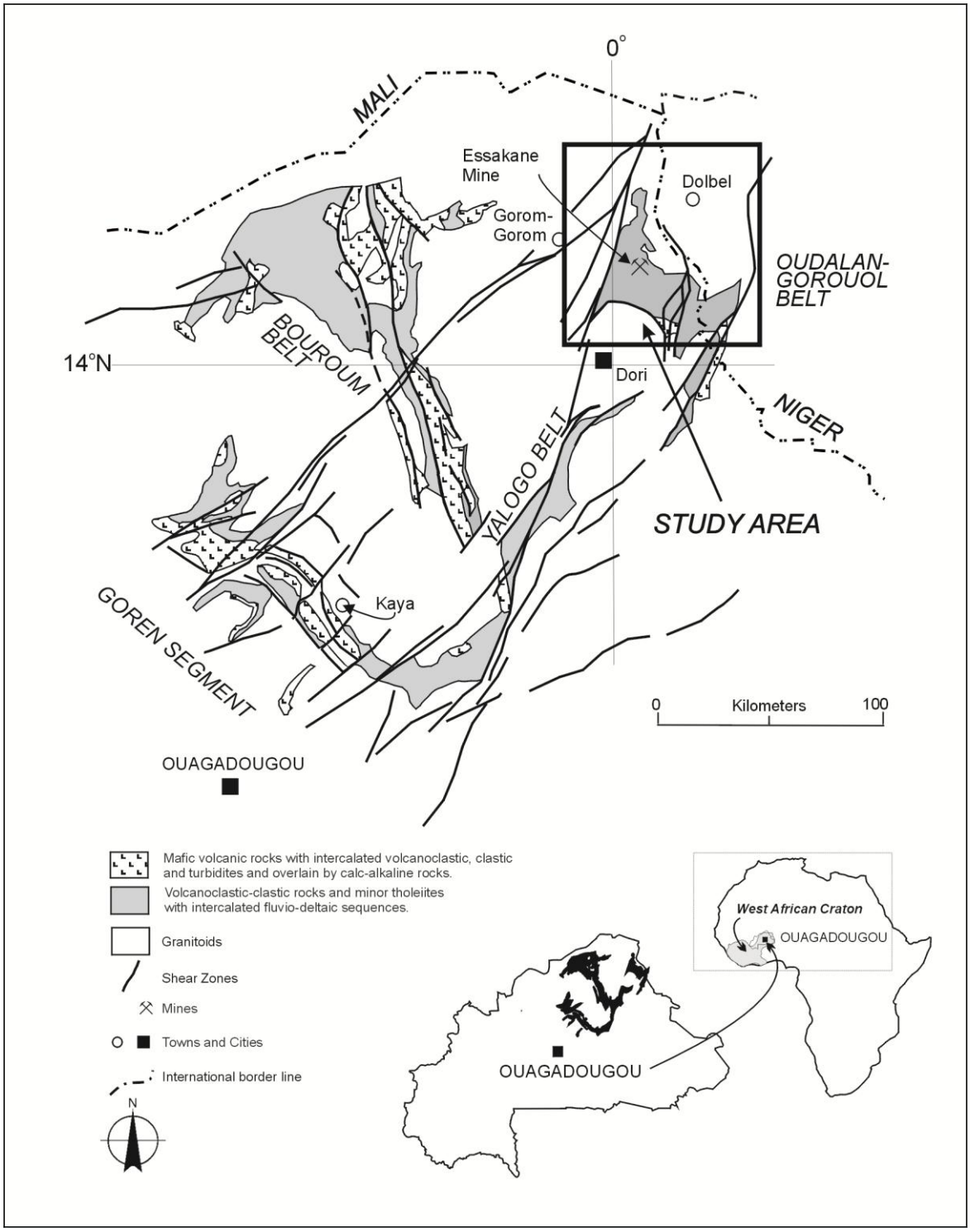

Figure 5.1: Location map of the Oudalan Gorouol belt of Burkina Faso and Niger, together with the Bouroum, Yalago and Goren greenstone belts. Modified after Hein et al. (2004).

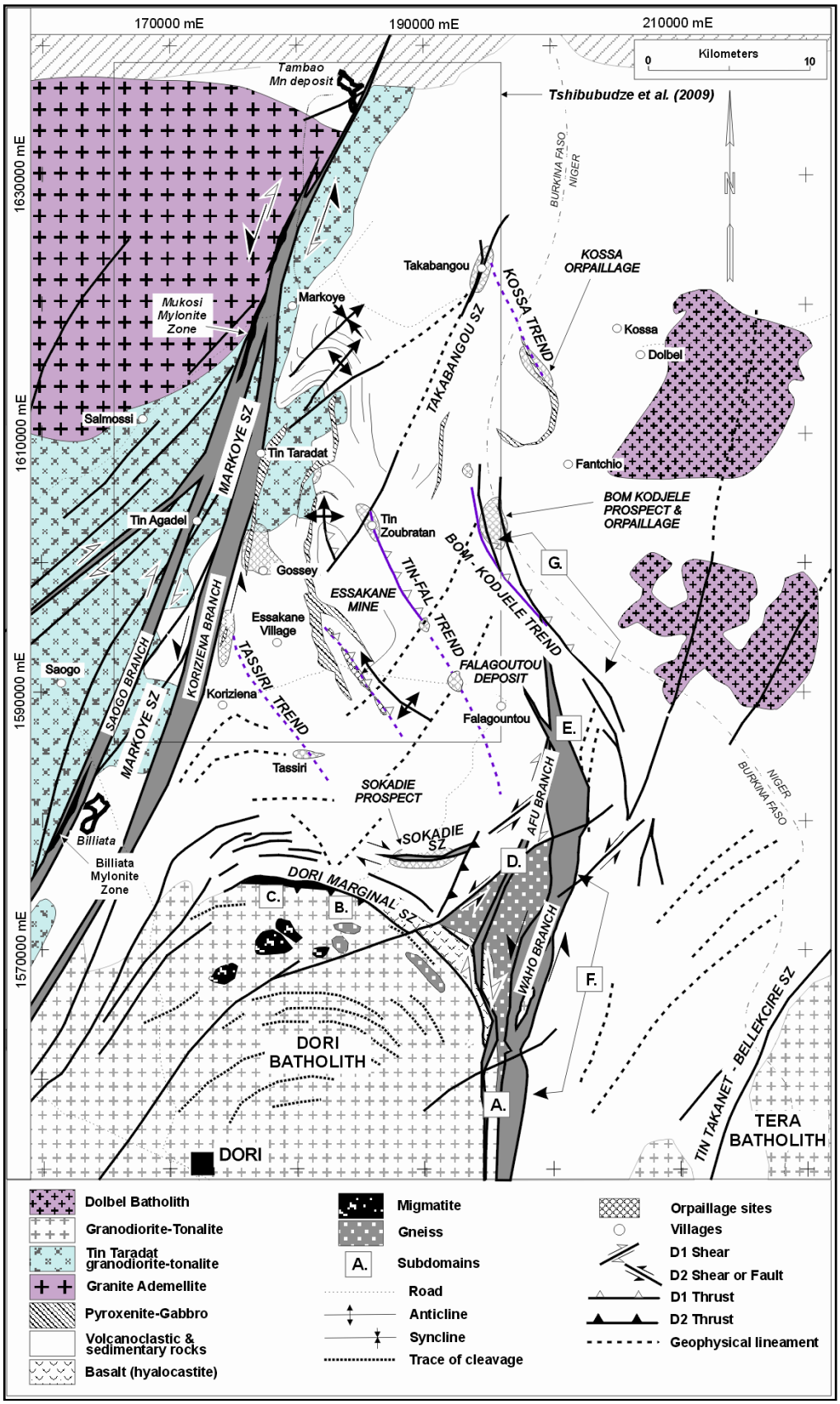

Figure 5.2: Schematic geology map of the OGB indicating the location of the Essakane Mine and Gosséy, Falagountou, Sokadie, Tin Zoubratan and Takabangou deposits. The boundaries of the OGB are defined by (1) the Markoye Shear Zone (MSZ), (2) the Tin Takanet-Bellekcire Shear Zone, and (3) the Dori Marginal Shear Zone (DMSZ). Research studies by Tshibubudze et al. (2009) of the Markoye Shear Zone are indicated by the insert box.

5.4. Geological setting

The West African Craton (WAC) is composed of an Archaean-Palaeoproterozoic basement that is divided into the Reguibat Rise and the Leo-Man Rise. They are unconformably overlain by Neoproterozoic to Holocene sedimentary sequences. The Leo-Man Rise is further subdivided into the Archaean Kénéma-Man domain (ca. 3.5 Ga) and the Palaeoproterozoic (2.3-1.8 Ga) Baoulé-Mossi domain (Feybesse et al., 2006). The Kénéma-Man domain consists of a granite-gneiss complex and granulitic meta-gabbro (Thiéblemont et al., 2001). The Baoulé-Mossi domain consists of Birimian meta-sedimentary and meta-volcanic sequences that were deposited at ca. 2.3 Ga (Feybesse et al., 2006; Pawlig et al., 2006). Emplacement of TTG suite granitoids occurred at 2200, 2160-2130 and 2100-2070 Ma, concomitant to greenstone belt deformation (c.f., Hirdes and Davis, 2002; Pawlig et al., 2006; Gueye et al.,2007, 2008; Lompo, 2009, 2010) during the Tangaean Event (2170-2130 Ma, c.f. Tshibubudze et al., 2009; Hein 2010), the polycyclic Eburnean Orogeny (2130-1980 Ma, Feybesse et al., 2006) and the Wabo-Tampelse Event (c.f., Hein et al., 2004; Hein, 2010). The Tarkwa Group unconformably overlies the Birimian [Supergroup] (Hastings, 1982; Leube et al., 1990; Milési et al., 1992), but does not crop out in the Oudalan-Gorouol belt (Tshibubudze et al., 2009). It is dated at 2194-2132 Ma (single detrital U-Pb zircon, Davis et al., 1994) or 2133 ± 4 Ma (maximum date from detrital zircon, Pigois et al., 2003) in its type locality in Ghana.

During the Eburnean Orogeny numerous calc-alkaline plutons intruded the Palaeoproterozoic sequences (Pawlig et al., 2006) including tonalite-trondjhemite-granodiorite (TTG), diorite, meta-diorite and leucogranite, and these are collectively termed Eburnean granitoids (c.f., Pons et al., 1995; Naba et al., 2004; Pawlig et al., 2006; Lompo, 2009; Vidal et al., 2009). Two emplacement events are currently recognised in Burkina Faso (Castaing et al., 2003; Naba et al., 2004), (1) TTG Suite (amphibole-bearing) which is composed of granodiorite, tonalite and quartz-diorite that intruded Birimian supracrustal sequences between 2210 and 2160 Ma (c.f., Castaing et al., 2003; Lompo, 2009, 2010). (2) A granite suite (biotite ± muscovite) that is localized along shear zones and which intruded Birimian supracrustal sequences and TTG suite granitoids between 2150 and 1950 Ma (Castaing et al., 2003; Lompo, 2009, 2010). In the Oudalan Gorouol belt potassic-rich granite (*sensu stricto*) and pyroxenite-gabbro dykes/sills are intruded by granitoids and thus pre-date their emplacement (c.f., Tshibubudze, et al., 2009). Northwest and northeast-trending dolerite dykes crosscut the WAC and were probably emplaced during the final breakup of supercontinents at 1.4-1.2 Ga (Zhao et al., 2002).

Several deposits and deposit styles occur in the OGB including; (1) Manganese deposits at Tambão (Beauvais et al., 2008), Billiata and south of the Kel Enguef metamorphic belt (Woolfe, 2011) (2) gold mineralization at Essakane, Gosséy, Koreziéna, Falagountou, Takabangou, Tassiri, Bom Kodjelé, Sokadie, and Kossa orpaillage (artisanal mining) sites (Milési et al., 1992; Nikiéma, 1992; Castaing et al., 2003; Nkuna, 2009; Tshibubudze, et al., 2009), (3) pegmatite veins bearing tourmaline, plagioclase and topaz crystals near the village of Tambão, and (4) Pb-Zn-Mo mineralisation in the

Kuorki area of Niger (Milési et al., 1989). Several deposits are associated with the sulphidised brittle-ductile shear zones including gold in sheeted and stockwork quartz veins, copper as malachite in buck quartz veins, and tourmaline and topaz in pegmatite and buck quartz veins (Foster and Piper, 1993; Castaing et al., 2003; Feybesse et al., 2006; Tshibubudze, 2007).

There is a strong structural control to gold mineralization at all levels within the WAC (Milési et al., 1989; Castaing et al., 2003). Gold deposits are commonly situated in second or third-order structures adjacent to first-order crustal-scale structures (Groves et al., 1998) and are thus interpreted as epigenic in origin (c.f., Groves et al., 1998; Béziat et al., 2008). Gold mineralization in the OGB is distributed along shear zones as structurally-hosted lode-gold (Nikiéma, 1992; Tshibubudze et al., 2009).

5.5. Methods and procedures

Field studies were undertaken during 2009-2010 and focussed on mapping of lithologies, igneous rocks and major structures in the hangingwall of the Markoye Shear Zone (MSZ), which trends north-northeast and dips steeply east, i.e., map work took place in the region east of the MSZ and included the Essakane and Falagountou goldfields. Samples for petrographic studies were collected from outcrops across the region and from diamond drill core at the Essakane, Falagountou and Sokadie deposits [Figure 5.2]. Limited petrographic study of the Essakane and Falagountou gold deposits was reported by Nkuna (2009) and are not repeated herein.

Prior to field mapping, ASTER (1:250 000) and LANDSAT (1:250 000) imagery was interpreted to extract major lineaments and sparse outcrop. The land surface in the northeast of Burkina Faso and Niger is denudated and desertified yet supports fields of maize and cotton. It was important to use remotely sensed data in regional mapping because of the sparse outcrop, but interpretation demanded considerable ground-truthing. The interpretation of geophysical datasets included aeromagnetic (RTP 1st and 2nd vertical derivative aeromagnetic, and TMI RTP) and kilometre-scale gravity, and these supplemented field and remotely sensed datasets. Geographic and geologic reconnaissance studies were conducted before field work commenced. Even though outcrop was limited in the area, several east-west and north-south traverses were completed across the region, from Burkina Faso into the western portion of the Republic of Niger [Figure 5.2]. Sub-crop mapping proved useful and effective in areas of limited outcrop, or thin sand cover.

GPS co-ordinates were reported in UTM zones 30P and 31P zones using Discover 3.2® MapInfo Professional V8.5®; the field area is bisected by the Prime Meridian (0° longitude). Structural analysis, calculated means and contour plots used GEOrient 9.2® (Holcombe, 2008).

5.6. Lithologies of the OGB

The lithologies of the OGB in the area around Essakane were reported by Tshibubudze et al. (2009), but are updated herein to include the entire OGB. The sequences consist of folded, sheared and/or mylonitized volcanic, volcano-sedimentary and sedimentary sequences that were metamorphosed to upper greenschist facies and locally, to amphibolite facies. They were contact metamorphosed to hornblende-hornfels facies adjacent to intruding granitoids, dykes and sills. Five volcano-sedimentary sequences are defined for the OGB:

(1) A meta-volcanic sequence (~150m thick) that consists of pyroclastic and tuff beds, hyaloclastic and pillow basalt, and agglomerate [Figures 5.3a-c] crops out between the Sokadie orpaillage and the Dori Batholith [Figure 5.2]. The pyroclastic facies hosts angular and sub-rounded basalt clasts in a lithified volcanic dust or ash matrix.

(2) A greywacke-siltstone-shale sequence interbedded with rare chert beds and banded iron formation. This sequence disconformably overlies the meta-volcanic sequences.

(3) A sandy dolomite (~5m thick) crops out south of the Essakane gold mine and hosts stromatoforms [Figure 5.3f]. It is variably ferriginized, chloritized and epidotized.

(4) A sequence of interbedded conglomerate-greywacke-siltstone-shale units that conformably overlays the greywacke-siltstone-shale sequence. Conglomerate beds are polymictic and matrix-supported or rarely, clast-supported [Figures 5.3d, e]. They are composed of sub-rounded to angular clasts, pebbles and boulders (up to 30cm in diameter) of granite, granodiorite, gabbro, fuchsitic chert, chert, quartz and quartz-carbonate vein clasts, andesite, basalt, volcaniclastic sedimentary rocks and schist. The matrix is generally composed of fine to coarse-grained, poorly-sorted greywacke or gritstone which is sometimes volcaniclastic. The size and variable composition of clasts, pebbles and boulders suggests a provenance that is metamorphic-volcanic-plutonic in character.

(5) A greywacke sequence conformably overlies the conglomerate-greywacke-siltstone-shale sequence. It is composed of bedded, cross-bedded, slump-folded and scoured, medium-grained, quartz and feldspar-rich sandstone. Cross-bedded greywacke beds predominate. Fuchsite layers, thin chert beds, shale with mud-cracks and fine laminations, siltstone, pebble beds and mud balls are intercalated with greywacke units. An interbedded conglomerate member up to 10 metres thick is similar in composition to the polymictic, matrix-supported conglomerates in the underlying conglomerate-greywacke-siltstone-shale sequence. Based on stratigraphic studies east of the township of Markoye by Peters (2011), the greywacke sequence exceeds 4.2 kilometres in true stratigraphic thickness.

Laterite is randomly distributed throughout the OGB. In-situ laterite was deposited during the Cretaceous-Tertiary (c.f., Brown et al., 1994; Burke and Gunnell, 2008) and was deeply eroded during the Eocene to Miocene epochs (Brown et al., 1994; Beauvais et al., 2008) to form several discrete transported laterite profiles.

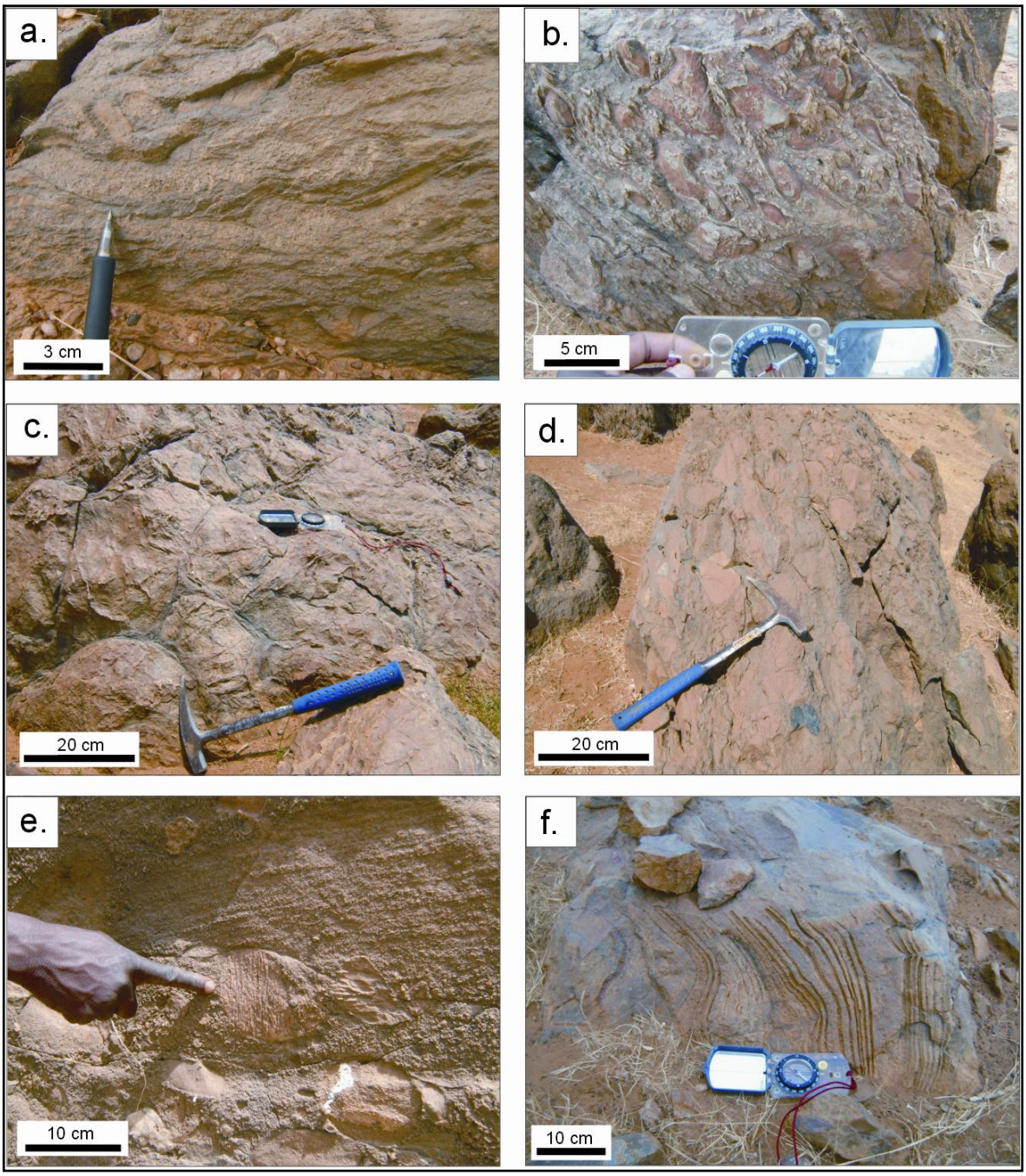

Figure 5.3: Lithologies of the OGB.
(a). Tuffaceous beds of the meta-volcanic sequence (UTM 31P, 0188468, 1573703).
(b). Silicified agglomerate unit of the meta-volcanic sequence near the contact with the Dori Batholith (UTM 31P, 0187383, 1574283).
(c). Pillowed basalt of the meta-volcanic sequence near the contact with the Dori Batholith (UTM 31P, 0187383, 1574283).
(d). Matrix to clast-supported polymictic conglomerate beds near the Tin Zoubratan artisanal (UTM 31P, 0183827, 1602472). Clasts are composed of angular clasts, pebbles and boulders of granite, granodiorite, gabbro, fuchsitic chert, and chert.
(e). Matrix-supported polymictic conglomerate in coarse greywacke, clasts are composed of angular clasts of quartz and quartz-carbonate vein clasts, andesite, basalt, volcaniclastic sedimentary rocks and schist (UTM 31P, 0177800, 1596649).
(f). Stromatoforms in sandy dolomite (~5m) south of the Essakane gold mine (UTM: 31P 0187303, 1588249).

5.7. Intrusive rocks of the Oudalan-Gorouol area

A significant proportion of the Oudalan-Gorouol area is composed of magmatic rocks [Figure 5.2]. They include the Dori, Tin Taradat, Dolbel and Terra batholiths, the Yacouba Mafic Complex (Tshibubudze et al., 2009), porphyry dykes and sills, a series of north-trending gabbro sills, and northwest-tending gabbro and dolerite dykes that are dated at 250 ± 13 Ma (K-Ar whole rock dating) (Hottin and Ouedraogo, 1992).

The Dori Batholith crops out at the southern margin of the study area [Figure 5.2] as a medium-grained hornblende-plagioclase-quartz ± biotite ± K-feldspar granodiorite. It crosscuts and intrudes the metavolcanic and greywacke-siltstone-shale sequences on its northern margin. The granodiorite contains plagioclase phenocrysts (1-2cm) and hosts mafic xenoliths [Figure 5.4a]. The batholith has an internal foliation that parallels the intrusive contact on the northern margin of the batholith. The foliation is transitional with, and grades into migmatite and then gneiss at the contact margin; the contact margin is deformed with development of proto-mylonite, LS-tectonite and schist that is herein termed the Dori Marginal Shear Zone (DMSZ). The internal foliation, migmatite, gneiss and DMSZ are interpreted as syn-genetic and syn-emplacement in age. A northwest-trending cleavage (S_1), faults and folds crosscut the batholith and the DMSZ indicating a late formation. They are crosscut by a northeast-trending cleavage (S_2), faults and buck quartz veins (V_2), and by west-northwest trending gabbro dykes.

The Tera Batholith is composed of plagioclase feldspar, quartz, hornblende and biotite and is foliated and sheared [Figure 5.4b] along the Tin Takanet-Bellekcire Shear Zone, which coalesces with the Kargouna Shear Zone south of the study area [Figure 5.2].

The Tin Taradat granodiorite-tonalite crops out south of the town of Markoye and intrudes volcano-sedimentary and sedimentary sequences east of the Markoye Shear Zone (MSZ). The granodiorite-tonalite is coarse to medium-grained and composed of plagioclase, quartz, hornblende and biotite. It hosts elongate-ovoid mafic xenoliths that trend northwest and plunge to the west. Between the Gosséy orpaillage and Tambão manganese deposit the pluton is foliated and/or sheared in the MSZ (Tshibubudze et al., 2009).

The Dolbel batholith crops out along the eastern margin of the OGB in Niger and consists of several small alkali-granite plutons (Pons et al., 1995) that are dated at 2137 ± 126 Ma (Léger et al., 1992; Rb-Sr isochron). The plutons host mafic xenoliths and lithic xenoliths of greywacke-sandstone [Figure 5.4c]. The plutons are composed of 5 mm phenocrysts of plagioclase (30 % of the total volume) in a medium-grained (0.5-1.0 mm in size) groundmass of quartz and K-feldspar, with accessory biotite and chlorite. They are crosscut by northeast-trending buck quartz-carbonate veins.

The Yacouba Mafic Complex (YMC) as defined by Tshibubudze et al. (2009) crops out northeast of Tin Taradat and near the village of Gosséy adjacent to the MSZ [Figure 5.2], and is

readily identified from geophysical data in which it presents as a 12 km long, 3 km wide linear north-trending magnetic high. The YMC is a layered pyroxenite-gabbro that hosts lithic xenoliths of meta-greywacke and quartzite. Pyroxenite layers consist of >1cm pyroxene and olivine phenocrysts in a pyroxene-olivine-nepheline groundmass. The YMC crosscuts the Tin Taradat granodiorite-tonalite. An equal intensity magnetic high near the Kossa orpaillage in Niger may be similar in composition to the YMC however, it does not crop out. The magnetic trace forms a crescent-shaped magnetic high.

Furthermore, dolerite-gabbro sills (and dykes) occur throughout the OGB and are bedding parallel in the metasedimentary units, which they contact metamorphosed to hornblende-hornfels facies. The sills (and dykes) are typically composed of medium to coarse crystals of pyroxene, amphibole, plagioclase and magnetite. They are crosscut by a northeast-trending regional cleavage. Several exploration diamond drill holes at the Essakane Mine deposit have intersected the sills; they exhibit sharp contacts with the metasedimentary rocks but have locally folded and veined the rocks in the inner contact aureole. Thin quartz-carbonate veins (less than 2 cms thick) are orientated approximately perpendicular to the contact and are auriferous in disseminated gold.

A series of porphyritic monzonite dykes also occur throughout the OGB and parallel bedding in metasedimentary units. They are porphyritic with phenocrysts of zoned plagioclase in a fine to medium groundmass of quartz, plagioclase, muscovite, biotite, chlorite and sulphides (including chalcopyrite, pyrite and arsenopyrite). Plagioclase phenocrysts are randomly orientated and euhedral to anhedral [Figures 5.4d, e]. They are folded along northwest-trending fold axes and crosscut by a northeast-trending regional cleavage. Immediately north of the Essakane Mine the dykes host gold mineralisation. They are crosscut by west-northwest trending dolerite-gabbro dykes south of the Falagountou orpaillage.

A series of northwest-trending dolerite-gabbro dykes crosscut the OGB and intrusive complexes in the northeast of Burkina Faso, and are dated at 250 ± 13 Ma (K-Ar whole rock dating) (Hottin and Ouedraogo, 1992).

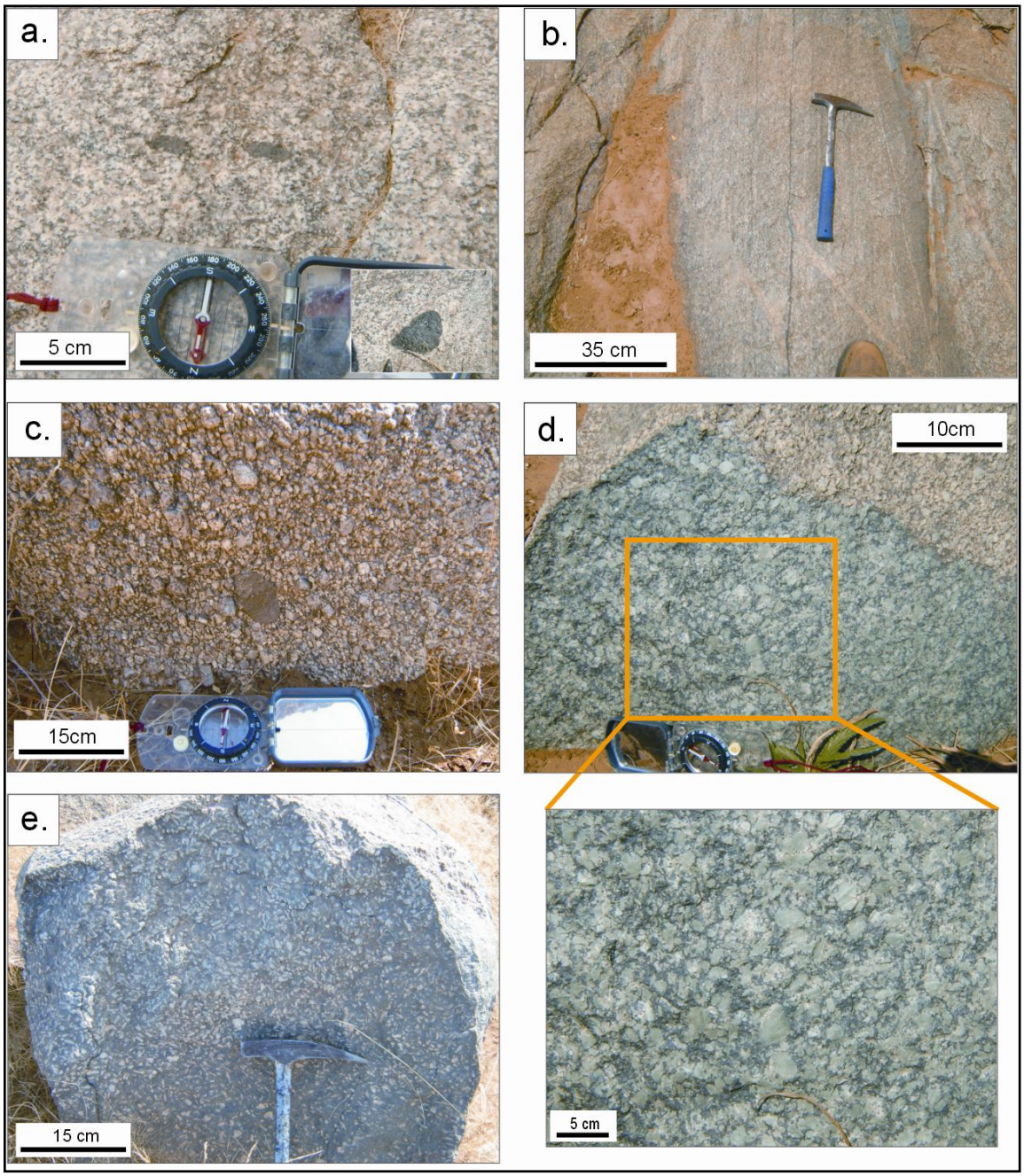

Figure 5.4: Plutonic igneous rocks of the Oudalan-Gorouol area.
(a). The Dori Batholith is a medium-grained hornblende-plagioclase-quartz ± biotite ± K-feldspar granodiorite. It is phenocrystic in plagioclase (1-2cm) and hosts mafic xenoliths (UTM 30P, 0821592, 1559159).
(b). The Tera Batholith is situated in the southeast of the study area. It is composed of plagioclase feldspar, quartz, hornblende and biotite and is foliated and sheared along the Tin Takanet-Bellekcire Shear Zone (UTM 31P, 0235492, 1586086).
(c). The Dolbel batholith. The batholith is composed of 5 mm phenocrysts of plagioclase (30 % of the total volume) in a medium-grained (0.5-1.0 mm in size) groundmass of quartz and K-feldspar, with accessory biotite and chlorite (UTM 31P, 0213792, 1614382).
(d). Porphyritic monzonite dykes of the OGB. They are composed of phenocrysts of zoned plagioclase in a fine to medium groundmass of quartz, plagioclase, muscovite, biotite, chlorite and sulphides (UTM 31P, 0188829, 1588399).
(e). Porphyritic monzonite dykes of the OGB exhibiting randomly orientated plagioclase phenocrysts that are euhedral to anhedral (UTM 31P, 0184195, 1602936).

5.8. Shear zones

The margins of the OGB are defined by (1) the Markoye Shear Zone (MSZ) on the western margin which hosts the Koreziéna, Gosséy and Tin Taradat gold prospects, (2) the Tin Takanet-Bellekcire Shear Zone on the eastern margin in Niger, and (3) the Dori Marginal Shear Zone (DMSZ) on the southern margin. The northern margin of the OGB is bounded by sediments of the Meso to NeoProterozoic Taoudeni Basin [Figure 5.2]. The Tin Takanet-Bellekcire Shear Zone, which hosts gold orpaillages sites along its length was not extensively studied due to limited access and is not discussed further. The Kargouna Shear Zone Complex (KSZC) lies central to the OGB and crosscuts the Dori Batholith and the DMSZ on the eastern margin of the batholith; it therefore formed during or after emplacement of the batholith and the DMSZ. The KSZC hosts gold deposits approximately 6 kms east of the town of Falagountou.

Between the MSZ and the KSZC, the OGB is crosscut by several northwest and northeast-trending splay shears including the Takabangou Shear Zone, which hosts the Takabangou prospect and orpaillage. The belt is also crosscut by northwest-trending, southwest-verging thrust-folds. Northwest-trending shears and thrust folds are crosscut by northeast-trending shears.

The thrust-folds are significant because they host gold mineralization in sheeted veins in the folded hangingwall of thrusts. They include gold mineralisation in the Essakane Mine, the Tassiri prospect, and the Kossa deposit [Figure 5.2]. Gold mineralisation at the Bom Kodjelé orpaillage is hosted in the Bom Kodjelé Shear Zone (thrust), while gold mineralisation at the Falagountou deposit is hosted in an anticline, but the fold is not well exposed.

5.8.1. Markoye Shear Zone (MSZ)

The Markoye Shear Zone trends north-northeast between the towns of Markoye and Saoga where it hosts gold deposits and orpaillage sites at Gosséy and Tin Taradat, and a gold prospect at Koreziéna [Figure 5.2]. The MSZ is defined by a wide zone of quartz-muscovite schist that is transitional with, and encloses mylonite zones, including the Mukosi Mylonite Zone (Tshibubudze et al., 2009). The Mukosi Mylonite Zone is situated in the northeast of the study area in a flexure in the MSZ where the Tin Taradat granodiorite abuts a granite-adamellite in the western block. Macroscopic boudins of the Tin Taradat granodiorite and granite-adamellite are enclosed by siliceous ultramylonite and mylonite. Numerous metre to centimetre-scale pseudotachylite veins splay southwest into the western block of the MSZ, and northeast into the eastern block of the MSZ away from the mylonite zone. Buck quartz-carbonate and quartz cataclasite veins are hosted in quartz-muscovite schist throughout the MSZ. This schist is crosscut by narrow, discontinuous quartz-chlorite (± muscovite) shears.

The studies between the Tambão and Billiata manganese deposits [Figure 5.2] showed that the MSZ has two main branches. These coalesce near the town of Markoye. The western branch (herein

termed the Saogo branch) trends north-northeast. It is characterised by dextral-reverse displacement (with east block up) as indicated by shear bands and sigma clasts in mylonite in the Billiata and Mukosi Mylonite zones [Figure 5.5a]. Southwest and northwest-trending anastomosing mylonite zones splay-off the Saogo branch into the western block of the MSZ.

The eastern branch of the MSZ (herein termed the Koreziéna branch) trends northerly and is characterised by sinistral-reverse displacement (east block up) as evidenced by S_2-C foliation in quartz-muscovite schist and massive macroscopic sigmoidal buck-quartz-carbonate veins (V_2) and iron-rich cataclasites that are right-stepping. The buck quartz-carbonate veins are crosscut by narrow (mm-scale), discontinuous quartz-chlorite (± muscovite) shears. Mylonite does not occur in the Koreziéna branch in the study area.

The region between the Saogo and Koreziéna branches of the MSZ is poorly exposed and covered by sand dunes, but subcrop and outcrop mapping on the limited exposures indicated that the region consists of Fe-manganese rich metasedimentary rocks (at Billiata), polymictic meta-conglomerate, siltstone, meta-volcaniclastic greywacke and quartzite. The meta-sedimentary rocks are tightly folded (F_2) at all scales and boudinaged. The folds plunge steeply to the northeast. The folded rocks are crosscut by narrow shear zones (~1 m wide) that trend north-northeasterly [Figure. 5.5b].

The region north of the town of Markoye where the Saogo and Koreziéna branches coalesce is poorly exposed because of sand dune cover. However, mylonite crops out on the western margin of the MSZ, and schistosed granodiorite crops out on the eastern margin of the MSZ. Immediately east of the Tambão manganese deposit, an anastomosing foliation in granodiorite marks the north-northeast strike extent of the Koreziéna branch. Thereby it is interpreted that the Saogo branch terminates between Markoye and Tambão, and that the Koreziéna branch weakens.

Furthermore, structural and kinematic studies in the region between the towns of Markoye and Koreziéna by Tshibubudze (2007), Tshibubudze et al. (2009), and Tshibubudze and Hein (2010) have demonstrated that the OGB underwent at least two phases of deformation, with dextral-reverse displacement (east block up) in D1 on the MSZ being followed by sinistral-reverse displacement (east block up) in D2. It is now evident from the extended studies of 2008-2010 that the Saogo branch formed during dextral reverse displacement in D1 with development of mylonite, ultramylonite and pseudotachylite veins, while the Koreziéna branch formed during sinistral reverse displacement in D2 with development of buck quartz and quartz cataclasite veins in a quartz-chlorite-muscovite schist. It is important to note that the Koreziéna branch and not the Saogo branch, is an important host to auriferous buck quartz veins and orpaillages sites.

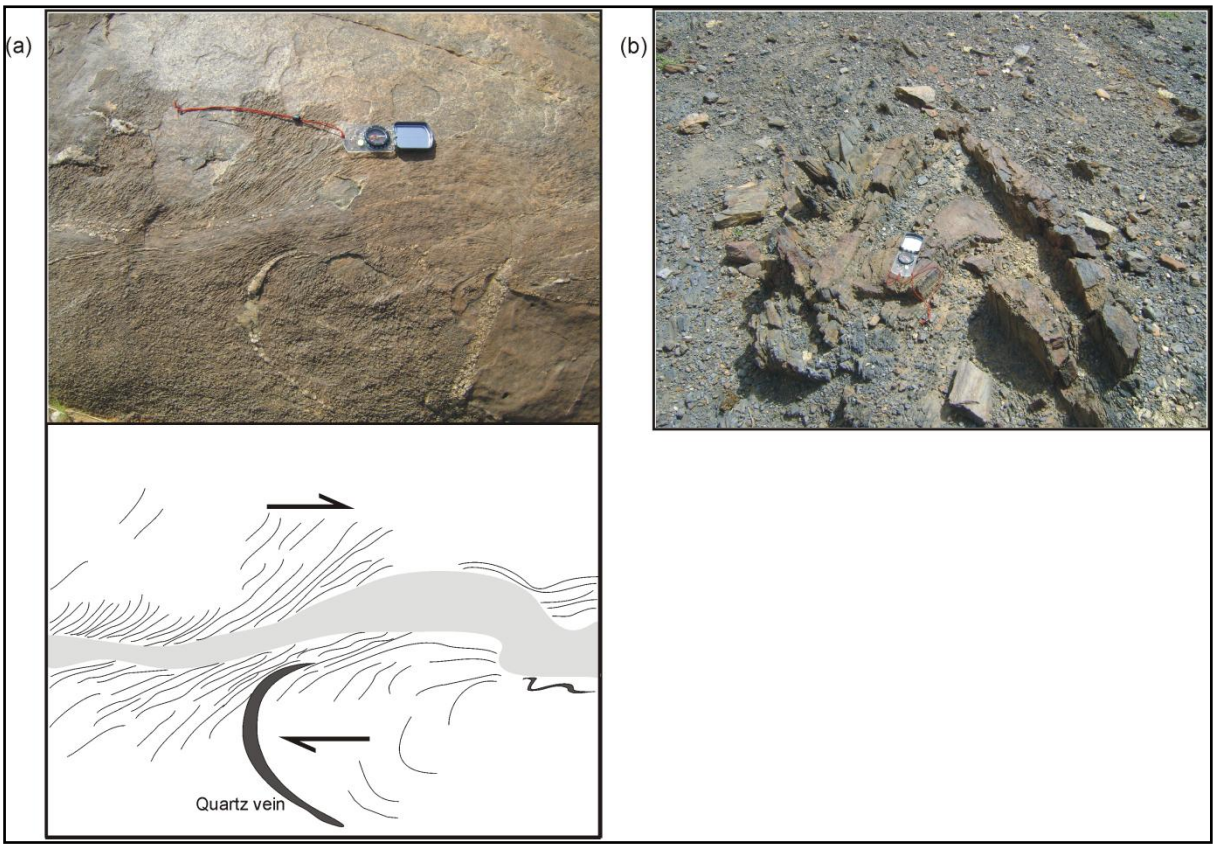

Figure 5.5: (a) The mylonitic shear bands with a dextral (reverse) displacement along the Saoga branch. (b) The Fe-manganese rich meta-sedimentary rocks are folded at all scales. The closed folds plunge steeply to the northeast.

5.8.2. Dori Marginal Shear Zone (DMSZ)

The Dori Marginal Shear Zone (DMSZ) bounds the southern margin of the OGB [Figures 5.2, 5.6]. The DMSZ is not known to host gold deposits but small artisanal pits suggest that gold may have been found historically. The DMSZ is crosscut by the KSZC, D1 and D2 structures (including faults, folds, foliations and veins) and west-northwest trending dolerite-gabbro dykes.

The DMSZ parallels the outcrop margin of the Dori Batholith; it is thus arcuate in outcrop form [Figure 5.6a]. It consists of proto-mylonite, LS tectonite ($LS_{1\text{-}x}$) and schist at the contact with the Dori Batholith and these are crosscut by a northwest-trending disjunctive cleavage (S_1) which in turn, is crosscut by a weak, non-penetrative northeast-trending foliation (S_2). The proto-mylonite is glassy and intensely lineated or rodded ($L_{1\text{-}x}$). It hosts numerous intrafolial and isoclinal folds ($F_{1\text{-}x}$) that plunge steeply to the south. Horizontal quartz-ankerite veins ($V_{1\text{-}x}$) are developed perpendicular to $L_{1\text{-}x}$ and are interpreted to have formed during vertical stretch on the DMSZ [Figure 5.6b].

Three subdomains (A, B and C) have been defined along the DMSZ [Figure 5.2]; equal area stereographic projections of poles to foliation are presented in [Figures 5.7a-f]. Sub-domain A is north-northwest trending and steeply west-dipping with a calculated mean strike and dip for $S_{1\text{-}x}$ of 333°/70°W. Subdomains B and C trend west-northwesterly with calculated mean strikes and dips for $S_{1\text{-}x}$ of 291°/77°N and 275°/81°S, respectively. The mean calculated dip and dip direction for $L_{1\text{-}x}$ in

Subdomain C is 70° towards 214° [Figure 5.7d] with southwest block up (as indicated from accretion steps), which is consistent with reverse-(sinistral) displacement in that location, i.e., block transport was towards the northeast [Figure 5.6c].

$S_{1\text{-}x}$ and $V_{1\text{-}x}$ are crosscut by S_2 and folded by F_2. The calculated mean strike and dip for S_2 in Subdomains A and B are 048°/75°N and 011°/81°E [Figures 5.7e-f], respectively; S_2 in Subdomain C trends northeast (based on limited data). S_2 is disjunctive to crenulating and refracts across the Dori Batholith, or where rock units are competent.

In summary, proto-mylonite, LS tectonite ($LS_{1\text{-}x}$ and $L_{1\text{-}x}$), horizontal extension veins ($V_{1\text{-}x}$), and schist ($S_{1\text{-}x}$) of the DMSZ, together with the (1) marginal gneiss in the chilled margin of the Dori Batholith, (2) the migmatite, and (3) the foliation in the batholith, comprise a broad zone of deformation that formed synchronous to pluton emplacement. These were subsequently deformed and overprinted in D1 by S_1 (northwest-trending discontinuous disjunctive cleavage), drag folded against F_2 faults and overprinted by S_2 (northeast-trending penetrative continuous disjunctive cleavage).

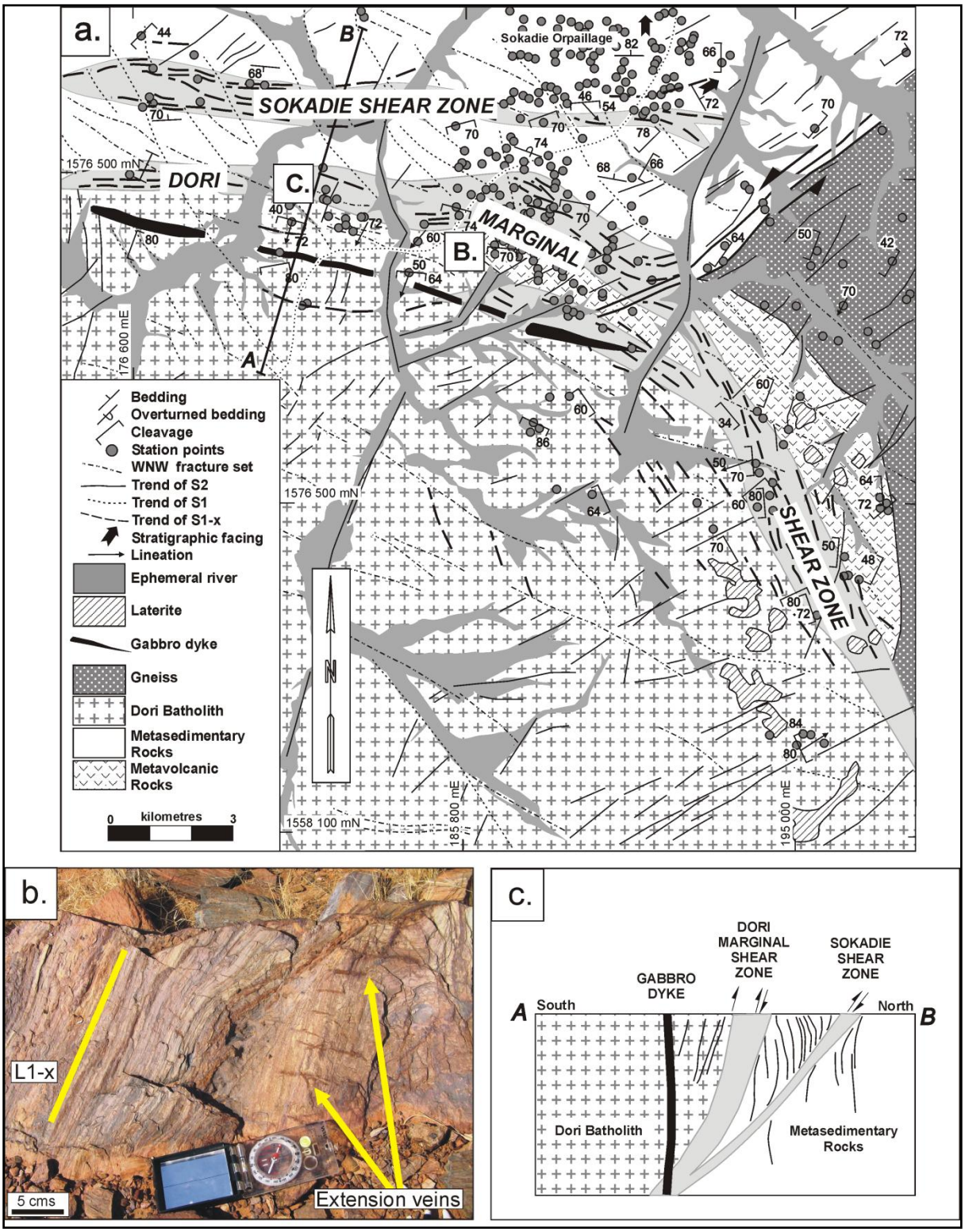

Figure 5.6: (a). Schematic map of the Dori Marginal Shear Zone (DMSZ) and Sokadie Shear Zone. (b). The DMSZ hosts numerous quartz-ankerite extension veins ($V_{1\text{-}x}$) and is intensely lineated and rodded as manifested by $L_{1\text{-}x}$. (c). Cross section through the DMSZ along section line A-B. The DMSZ and Sokadie Shear Zone dip steeply to moderately south and exhibited reverse displacement with south block up.

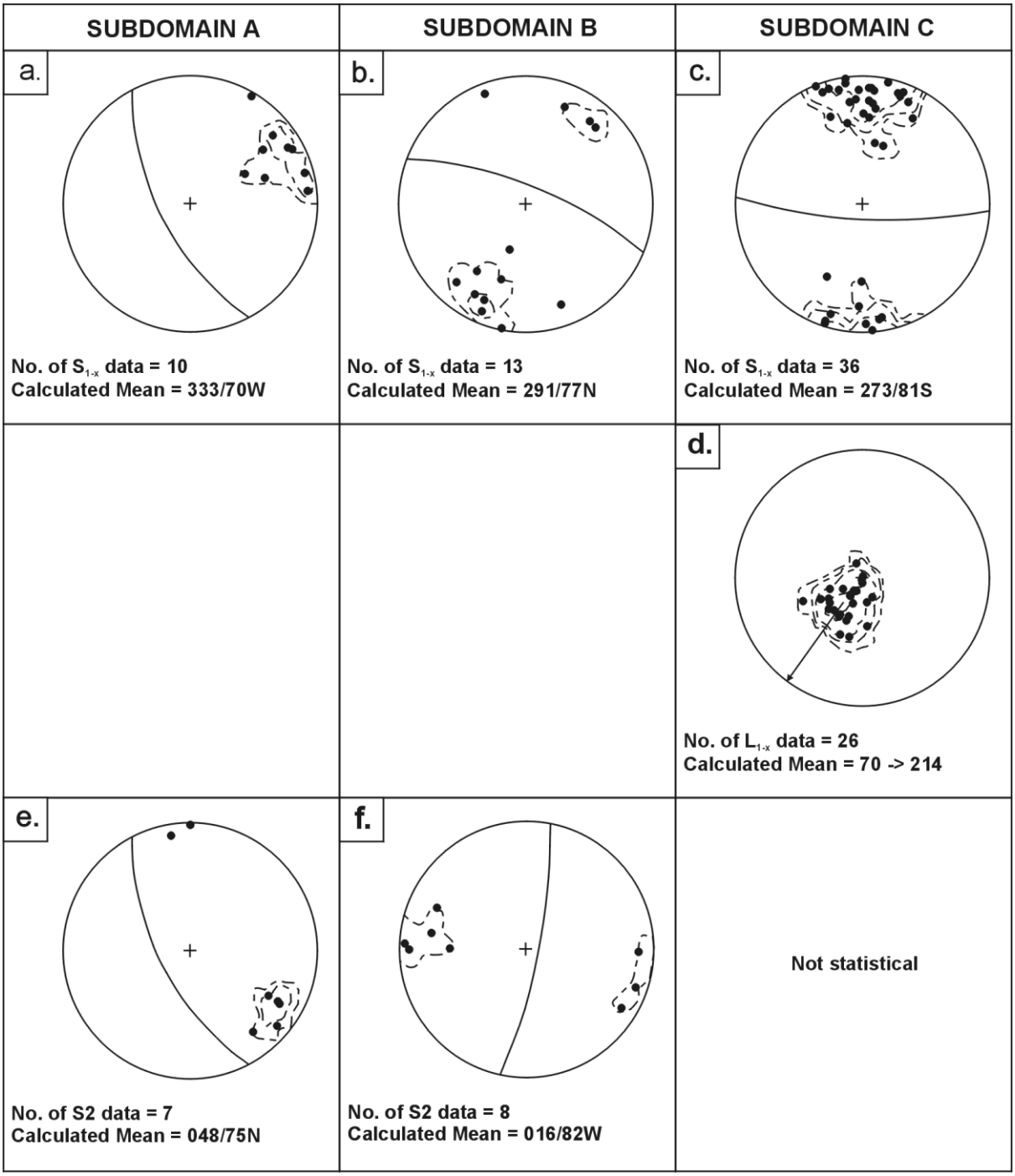

Figure 5.7: Equal area stereographic projections of poles to $S_{1\text{-}x}$, $L_{1\text{-}x}$ and S_2 in subdomains A-C. S_2 is disjunctive and crosscuts the DMSZ and Dori Batholith.

5.8.3. The Kargouna Shear Zone Complex (KSZC)

The Kargouna Shear Zone Complex consists of the Afu and Waho branches [Figures 5.2, 5.8]. The Afu Branch is moderately west-dipping, while the Waho Branch is moderately to steeply east-dipping. They are characterised by quartz-chlorite-muscovite schist that hosts brecciated, sigmoidal buck quartz-carbonate veins, and iron-rich cataclasite veins. The buck quartz-carbonate veins are tourmaline-rich near the contact margin of the Dori Batholith. The region between the branches is composed of biotite-amphibole-potassium feldspar gneiss that is sericitised [Figure 5.9a].

The Afu Branch crosscuts the Dori Batholith, DMSZ, Sokadie Shear Zone, gneissic rocks northeast of the Dori Batholith, and metasedimentary and metavolcanic rocks in the contact aureole of the Dori Batholith. The Afu branch thus formed after $D_{1\text{-}x}$. In Subdomains D and E [Figure 5.2] the Afu Branch dips moderately west with a mean calculated dip and strike of S_1 of 024°/60°W and 024°/53°W, respectively. Displacement in the Afu Branch is dextral strike-slip as indicated from the asymmetry of boudins, mesoscopic mica fish, limited S_1-C schistosity, and a near horizontal L_1 (stretching lineation). S_1 and S_1-C schistosity are crosscut by a northeast-trending, steeply south-dipping foliation (S_2) and northeast-trending sigmoidal buck quartz veins (V_2) that measure approximately 40-50 m in length. V_2 veins are right-stepping indicating sinistral displacement in the plane of V_2.

The Waho Branch Subdomain F in [Figure 5.2] crosscuts the Dori Batholith, gneissic rocks northeast of the Dori Batholith, metasedimentary and metavolcanic rocks in the contact aureole of the Dori Batholith, and S_1 and F_1. The Waho Branch therefore formed after $D_{1\text{-}x}$ and D1. The Waho Branch dips moderately to steeply east with a mean calculated strike and dip of S_2 of 021°/69°E. Displacement in the Waho branch is sinistral strike-slip as indicated from the asymmetry of boudins, numerous sigma clasts (of dominantly quartz), shear bands, limited S_2-C foliation, and a near horizontal stretching lineation (L_2) [Figure 5.8]. In this branch, north-trending asymmetric buck quartz vein (10-20 metres in length) step right indicating sinistral displacement along the length of the branch. [Further to this, the Waho branch has northeast trending faults that have a sinistral strike-slip displacement and they displace the quartz-carbonate veins [Figure 5.9b].]The Waho Branch is crosscut by porphyritic granodiorite and a west-northwest trending foliation (S_3) that is non-penetrative and non-pervasive.

5.8.4. Takabangou Shear Zone

The Takabangou Shear Zone crosscuts F_1 thrust-folds, folded monzonite dykes, gabbro-pyroxenite dykes and sills, and S_1 and V_1 north of Essakane and at Tin Zoubratan prospect [Figure 5.2]. The shear therefore formed after D1. It trends north-northeast and dips moderately southeast with a mean calculated strike and dip of S_2 of 042°/55°E. It consists of quartz-chlorite-muscovite schist that grades into mylonite; it exhibits numerous delta and sigma clasts that indicate sinistral-reverse displacement (southeast block up) was dominant during formation of the shear zone. A stretching lineation generally plunges southeast with a mean calculated dip-dip direction of 43° towards 171°.

The northwestern block of the Takabangou Shear Zone is composed of re-crystallized volcaniclastic greywacke (of the greywacke sequence), while the southeastern block is composed of conglomerate-greywacke-siltstone-shale units that are crosscut by quartz-carbonate veins.

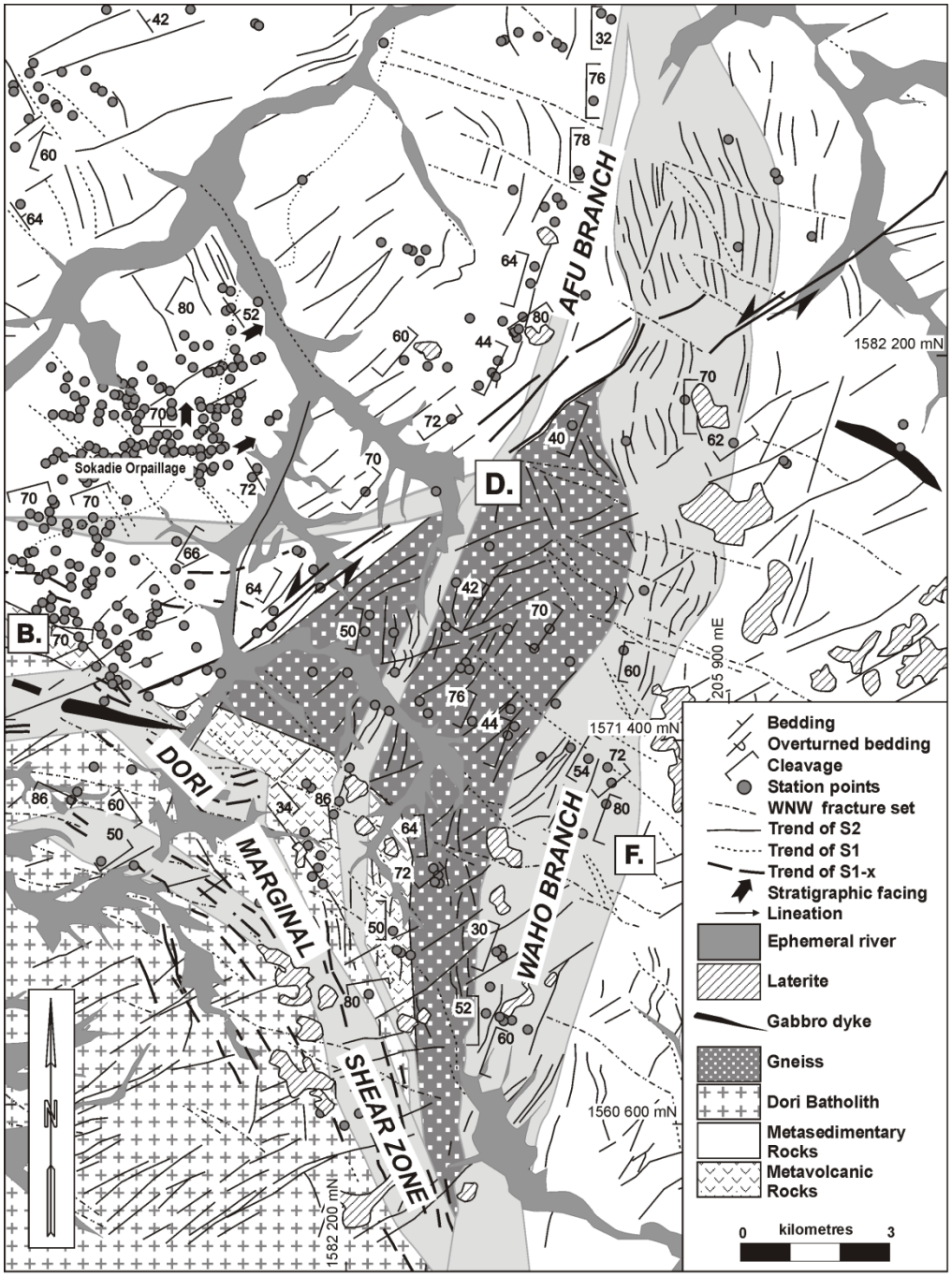

Figure 5.8: Schematic map of the Kargouna Shear Zone Complex. The Afu Branch is moderately west-dipping, while the Waho Branch dips moderately to steeply east. The Afu Branch crosscuts the Dori Batholith, DMSZ, Sokadie Shear Zone, gneissic rocks northeast of the Dori Batholith, and metasedimentary and metavolcanic rocks in the contact aureole of the Dori Batholith.

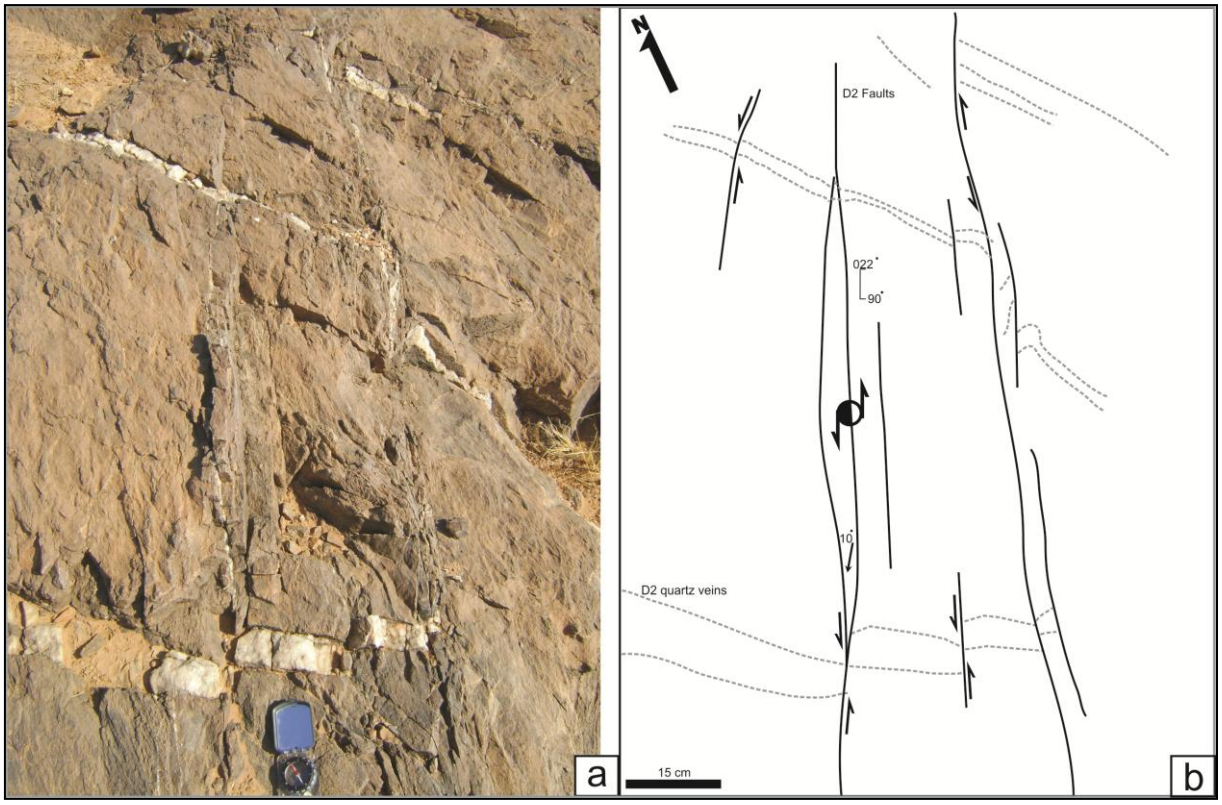

Figure 5.9: The gneissic unit that outcrops along the KSZC is crosscut by discontinuous outcrop scale parallel faults that help in determining the overall displacement of the Waho branch. The faults crosscut quartz-carbonate veins. The sense of displacement along the faults is sinistral strike-slip to oblique (east block up).

5.8.5. Sokadie Shear Zone

The triangular region between the DMSZ and the KSZC is structurally complex [Figure 5.2]. The region hosts deformed pillow and hyaloclastite basalt, and meta-sedimentary rocks of the overlying (unconformably) greywacke-siltstone-shale sequence. The Sokadie Shear Zone bounds the northern margin of the region, while the Waho Branch (of the KSZC) and the DMSZ bound the eastern and south-western margins, respectively. A northeast-trending sinistral shear-fault crosscuts and displaces the metavolcanic and metasedimentary units in the Sokadie region, and the Dori Batholith.

The Sokadie Shear Zone hosts the Sokadie orpaillage-prospect and is the site of several discontinuous buck quartz veins (20-30 m long), and numerous mesoscopic folded and boudinaged quartz-carbonate veins (Nkuna, 2009). It is crosscut by the northerly-trending thrust, a non-pervasive, northwest-trending foliation (interpreted as S_1), a northeast trending penetrative disjunctive cleavage (interpreted to be S_2) and west-northwest trending gabbro dykes. The Sokadie Shear Zone thus predates those structures; it is consequently interpreted as being a co-shear to the DMSZ, which it sub-parallels.

At the Sokadie orpaillage S_{1-x}-C schistosity in the Sokadie Shear Zone indicates that displacement was dextral strike-slip. At the Sokadie orpaillage the shear zone comprises a steeply

south-dipping quartz-chlorite-ankerite ± sulphide ± cordierite schist (interpreted as S_{1-x} to S_{1-x}-C) with a mean calculated strike and dip of 070°/68°S. The shear hosts a complex array of tight to isoclinally-folded quartz-carbonate veins, massive buck quartz veins, and a moderately to steeply plunging lineation (L_{1-x}) with a calculated mean of 68° towards 159°. At the Sokadie orpaillage it exhibits evidence of progressive deformation (in outcrop and diamond core) with several stages of quartz-carbonate vein development in which older veins are sequentially deformed, folded and boudinaged before being overprinted by a second, third or even a fourth set of veins. The Sokadie deposit/orpaillage has been interpreted by Kerr (2004c) as a mineralised system in an east-west trending synform that plunges toward the southeast.

5.9. Gold trends

Gold trends in the OGB occur where northeast-trending geophysical lineaments that are interpreted to be faults or shear zones, crosscut northwest-trending geophysical lineaments or thrust-folds. They may also occur where northwest-trending geophysical lineaments or thrust-folds coalesce with north-northeast trending shear zones such as the Koreziéna branch of the MSZ. The trends include the Essakane Mine Trend, Tin Zoubratan – Falagountou Trend (herein termed the Tin-Fal Trend), Bom Kodjelé Trend, Tassiri Trend and Kossa Trend.

5.9.1. Essakane Mine Trend

The Essakane Mine Trend is characterised by an open asymmetric anticline (F_1) whose fold axial plane dips moderately northeast. The fold closes and plunges gently to the northwest. Fold vergence is southwest indicating that tectonic transport was towards the southwest during fold formation.

The dominant rock types of the Essakane orpaillage are a deeply weathered sequence of interbedded conglomerate-greywacke-siltstone-shale; a dolomite unit subcrops southeast of the Essakane Mine. Several generations of auriferous veins are recognised in trenches which crosscut the Essakane Main Zone including arsenopyrite-pyrite-gold mineralisation in quartz veins that are crosscut by vein-stockwork gold mineralization (Tshibubudze et al., 2009).

The Essakane Mine Trend is crosscut by the northeast-trending Takabangou Shear Zone [Figure 5.2]. Northeast-trending geophysical lineaments that are parallel to the Takabangou Shear Zone, and are interpreted to be faults or shear zones, crosscut the Essakane Trend at Essakane South, and between Essakane South and the Sokadie orpaillage [Figure 5.2].

5.9.2. Tin Zoubratan – Falagountou Trend (Tin-Fal Trend)

The northwest-trending Tin-Fal Trend is defined by an upright, shallowly southeast to northwest-plunging anticline-syncline pair that is tight to isoclinal in form. The calculated mean of the

fold plunge is 7° towards 151°, but the fold axis is refolded along northeast-trending F_2 fold axes. The syncline near the Tin Zoubratan orpaillage is tight to isoclinal and closes to the northwest with a calculated fold plunge of 32° towards 173°.

The Tin-Fal Trend hosts several orpaillage sites including the Tin Zoubratan and Falagountou orpaillages-deposits. They are hosted in the conglomerate-greywacke-siltstone-shale sequence. The orpaillage sites are located where the Tin-Fal Trend is crosscut by northeast-trending shears and/or northeast-trending geophysical lineaments that are interpreted to be faults or shear zones. In these sites of intersection, the metasedimentary rocks are hosted by auriferous buck and stockwork quartz veins. Malachite staining indicates the presence of copper sulphides (Nkuna, 2009).

5.9.3. Bom Kodjelé Trend

The Bom Kodjelé Trend is an approximately 3km wide thrust zone that trends north-northwest and dips moderately northeast [Figures 5.2, 5.10a-d]. It is dominated by quartz-chlorite-muscovite schist that hosts brecciated and boudinaged buck-quartz-carbonate ± tourmaline veins and iron-rich cataclasites (V_1). The dominantly S_1 to S_1-C foliation has a mean calculated strike and dip of 354°/53°E [Figure 5.10b], but the northerly trend of calculated data expresses refolding of S_1 and S_1-C by F_2 folds, and drag folding of S_1 and S_1-C near the margin of northeast-trending faults. Symmetrical boudins of quartz vein generally plunge 48° towards 053°; they are scarred by a strong stretching lineation and slickensides (L_1). Displacement on the Bom Kodjelé Trend is thereby dominantly reverse with northeast block up.

The Bom Kodjelé Trend is crosscut by a disjunctive to crenulating S_2 foliation that trends northeast, with a mean calculated strike and dip of 061°/79°N [Figure 5.10c]. It parallels northeast-trending faults that host rare northeast-trending buck quartz veins. The mean calculated dip and dip direction of F_2 folds is 20° towards 053° [Figure 5.10d].

The Bom Kodjelé Trend hosts gold mineralisation at the Bom Kodjelé orpaillage, and 6 kms east of the town of Falagountou where the Bom Kodjelé Shear Zone coalesces with the KSZC. The orpaillage sites are located where northeast-trending geophysical lineaments (that are interpreted to be faults or shear zones) intersect the trend. In these sites of intersection, the metasedimentary rocks host auriferous buck and stockwork quartz veins.

5.9.4. Tassiri Trend

The Tassiri Trend hosts gold mineralisation at the Tassiri orpaillage and north of the town of Koreziéna where the Tassiri Trend coalesces with the Koreziéna branch of the MSZ. The Tassiri orpaillage is the site of a 100 x 60m artisan opencast that is peppered with orpaillage shafts. These may exceed 10m in depth. It is hosted in folded, but deeply weathered (kaolinized) metasedimentary rocks of the conglomerate-greywacke-siltstone-shale sequence that are folded about a northwest-trending F_1 fold (anticline) axis. The units are crosscut by sheeted northwest-trending stockwork

quartz-carbonate veins with a mean calculated strike and dip of 348°/44°E. The sheeted veins form an open antiform within F_1.

The Tassiri orpaillage is crosscut by a weathered mafic dyke. The dyke is crosscut by S_1 that is predominately defined by chlorite; the mean calculated strike and dip of S_1 is 342°/46°E.

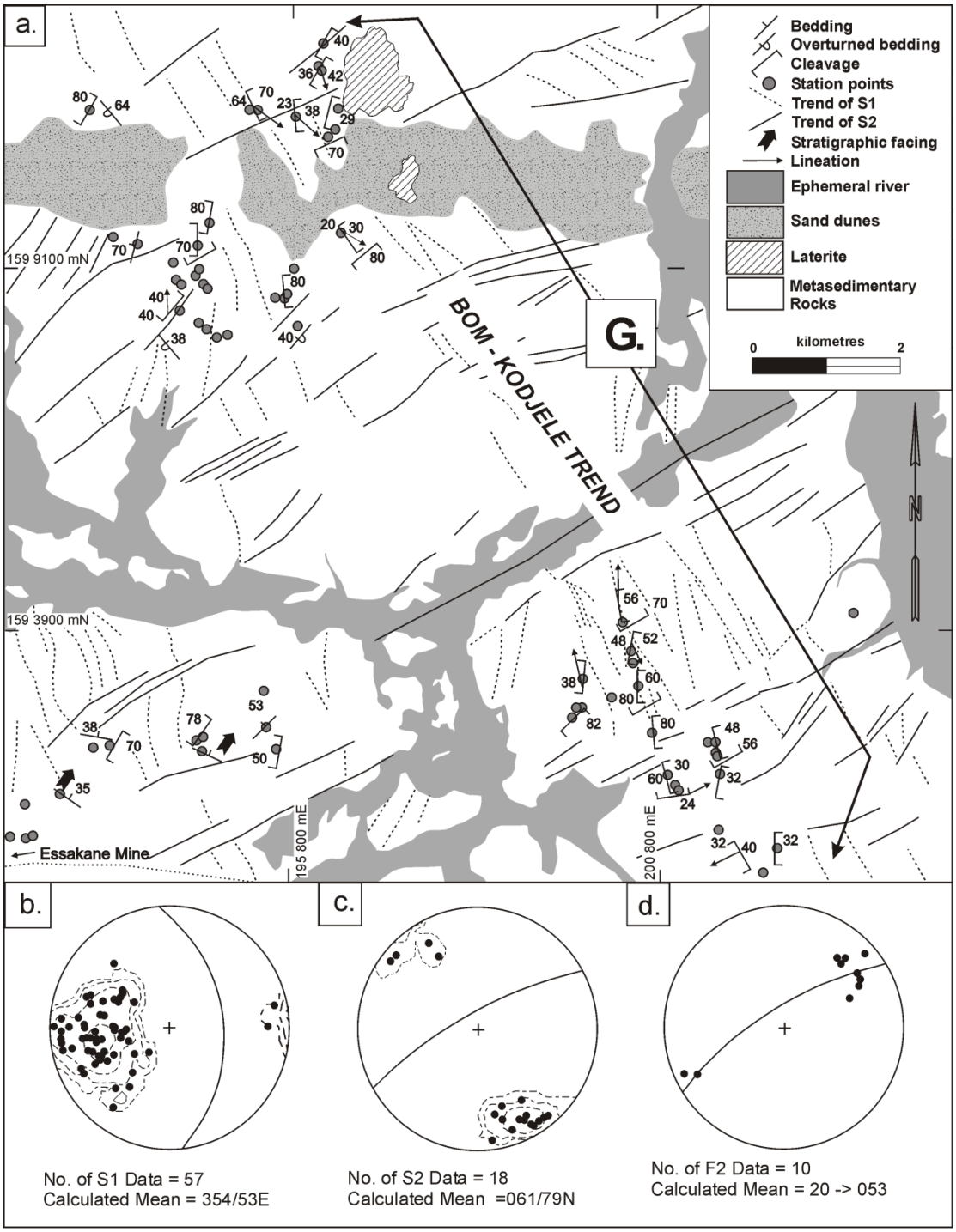

Figure 5.10: Schematic map of the Bom Kodjelé Trend (Domain G). It is an approximately 3km wide thrust zone that trends north-northwest and dips moderately northeast. It is dominated by quartz-chlorite-muscovite schist that hosts brecciated and boudinaged buck-quartz-carbonate ± tourmaline veins and iron-rich cataclasites.

5.9.5. Kossa Trend

The northwest-trending Kossa Trend hosts the Kossa, Kossa South and KBF prospects and the Kossa orpaillage, and is coincident with a northwest-trending geophysical lineament. The prospects are hosted in a corridor of tightly folded metasedimentary rocks in which northwest-trending fold axes (F_1) are refolded about northeast-trending fold axis (F_2). The Kossa orpaillage is situated adjacent to a crescent-shaped magnetic high that is interpreted to be a layered pyroxenite-gabbro because of its equal magnetic signature to the Yacouba Mafic Complex.

5.10. Discussion

5.10.1. Tectonic history

The tectonic history of the OGB records a complex interrelationship between pluton emplacement, structure and gold metallogenesis in which at least 2 unique regional deformation events took place, i.e., D1 and D2. The meta-volcanic sequence, greywacke-siltstone-shale sequence, sandy dolomite unit, interbedded conglomerate-greywacke-siltstone-shale sequence and greywacke sequence were folded, sheared and/or mylonitized during these events. D1 and D2 were preceded by emplacement of the Dori Batholith with development of proto-mylonite to schist in the country rock, and migmatite and gneiss at the pluton margin.

Regional metamorphic grade across the OGB is thereby complex. Background metamorphic grade is greenschist facies. Low grade greenschist facies assemblages in the north of the OGB (east of the town of Markoye) grade into greenschist (Tshibubudze et al., 2009; Peters, 2011) or lower amphibolite facies in the south of the OGB (at Sokadie orpaillage). Metamorphic grade attained amphibolite facies in mylonite or proto-mylonite zones in the Saoga and Afu branches, and attains granulite facies in migmatites in the Dori Batholith (i.e., banded coarse grained assemblage of plagioclase, hornblende and quartz). D1 shear zones generally attain upper greenschist to amphibolite facies with development of the mineral assemblage of quartz-chlorite-muscovite ± chloritoid to biotite-potash feldspar ± hornblende. D2 shear zones generally attain greenschist facies with development of the mineral assemblage of quartz-chlorite-muscovite ± actinolite. In the contact aureole of dykes and sills, metamorphic grade attains hornblende-hornfels facies with development of the mineral assemblage hornblende-biotite ± cordierite ± sulphides in the proximal contact aureole and epidote-chlorite ± albite ± sulphides in the medial contact aureole. Granulite facies metamorphism accompanied partial melting of metavolcanic and metasedimentary rocks and development of migmatite in the chilled margin of the Dori Batholith.

The relative tectonic history of the OGB is summarized in [Figure 5.11] as established from crosscutting relationships and published geochronology for the northeast of Burkina Faso:-

1. The inferred basement rocks of the OGB include the granite-adamellite and the Tin-Taradat granodiorite-tonalite (the age of the intrusions is the focus of current geochronology studies).

The Tin-Taradat granodiorite-tonalite intruded the granite-adamellite and hosts its enclaves (Tshibubudze et al., 2009), which indicates that the granite-adamellite is the oldest rock unit in the OGB.

2. Mafic volcanic and metasedimentary sequences were deposited above the basement units during basin formation. The units include (1) the meta-volcanic sequence (basaltic hyaloclastite), (2) a greywacke-siltstone-shale sequence, (3) a sandy dolomite unit, (4) a conglomerate-greywacke-siltstone-shale sequence and (5) a greywacke sequence. The supracrustal sequences are herein assigned to the Birimian Supergroup based on correlation with studies by Feybesse et al. (1990), Leube et al. (1990), Hirdes et al. (1996), Milési et al. (1991, 1992), Hein et al. (2004) and Lompo (2009). The environment of deposition has been interpreted as a shallow marine continental shelf or delta-front setting (c.f., Tshibubudze et al., 2009), and is the focus of current research by Peters (2011).
3. The mafic volcanic and metasedimentary sequences were subsequently intruded by gabbro-diorite-pyroxenite sills/dykes, or gabbro-diorite-pyroxenite sills/dykes were emplaced synchronous to deposition. Béziat et al. (2000) interpreted that gabbro, diorite and trondhjemite intrusions were syn-tectonic with emplacement of meta-volcanic sequences in the West African craton and co-magmatic. In concurrence, the gabbro-diorite-pyroxenite sills/dykes in the OGB (including the YMC) are tentatively assigned as co-magmatic with the metavolcanic sequences of the OGB.
4. The supracrustal sequences were subsequently intruded by the Dori Batholith with contact metamorphism of the country rock. Metamorphism to granulite facies accompanied formation of the DMSZ, marginal gneiss, an internal foliation and migmatite in $D_{1\text{-}x}$. The emplacement direction was towards the northeast along the northern margin of the Dori Batholith, as indicated by the stretching lineation ($L_{1\text{-}x}$) that plunges steeply southwest.
5. The supracrustal sequences were intruded by monzonite sills/dykes. They sills/dykes crosscut the granite-adamellite and Tin-Taradat granodiorite-tonalite. They are folded by F_1 and crosscut by S_1. They were therefore emplacement pre-D1. The relative timing with respect to the Dori Batholith is not known.
6. The supracrustal sequences, gabbro-diorite-pyroxenite sills/dykes, Dori Batholith and monzonite sills/dykes were deformed in D1. D1 is associated with the formation of (a) the Saoga Branch of the MSZ, (b) the Mukosi and Billiata mylonite zones, (c) the Afu Branch of the KSZC, and (d) northwest-trending thrust-folds (F_1) that crosscut the OGB and coalesce with the MSZ. The sense of displacement on the Saoga Branch of MSZ and Afu Branch of the KSZC in D1 was dextral (reverse) as manifested by development of S_1 to S_1-C foliations, macroscopic to mesoscopic asymmetric boudins, *en echelon* pseudotachylite veins, shear bands, sigma clasts, mesoscopic mica fish and a strong stretching lineation (L_1) The palaeo-compressive stress direction in D1 is interpreted to be southwest-directed. This event has been

defined as the Tangaean Event by Tshibubudze et al. (2009), Tshibubudze and Hein (2010) and Hein (2010) and is tentatively dated at 2170-2130 Ma.

7. The Dolbel Batholith was emplaced post-D1 and crosscuts D1 structures including F_1 folds. It is crosscut by D2 buck quartz veins and S_2.
8. The second deformation, D2, is associated with the formation of the Korizéna Branch of the MSZ, the Waho Branch of the KSZC, and northeast–trending faults that transect the OGB. D2 is manifested by refolding of F_1 by northeast-trending F_2, and development of a pervasive northeast-trending cleavage (S_2 to S_2-C). The sense of displacement along the Korizéna Branch of the MSZ and Waho Branch of the KSZC was sinistral (reverse). D2 was accompanied by dilation of northwest-trending D1 thrust-folds to form (a) auriferous quartz and quartz-carbonate sheeted and stockwork veins, (b) quartz-chlorite ± muscovite shears (sinistral brittle-ductile shear zones), (c) quartz-chlorite-ankerite ± sulphide ± cordierite schist, (d) massive macroscopic sigmoidal buck-quartz-carbonate veins, (e) iron-rich cataclasites, and (f) auriferous buck quartz veins. S_1 was folded and/or crenulated. Discontinuous quartz-chlorite (± muscovite) shears, boudins, sigma clasts, shear bands, and a stretching lineation (L_2) also formed during D2. The palaeo-compressive stress in D2 is interpreted to be northwest-directed. The event is herein correlated with the deformation during the Eburnean Orogeny of Feybesse et al. (2006) that is dated at 2130-1980 Ma.
9. D2 was succeeded by the intrusion of west-northwest trending dolerite-gabbro dykes that crosscut the granite-adamellite, Tin-Taradat granodiorite-tonalite, supracrustal sequences, the Dori Batholith, and D1 and D2 structures. They are dated at 250 Ma (Hottin and Ouedraogo, 1992).

5.10.2. *Emplacement of the Dori Batholith*

The emplacement of the Dori Batholith was accompanied by aureole deformation and the development of proto-mylonite, migmatite, gneiss and schist. The deformation is assigned to $D_{1\text{-}x}$ because it is restricted to the margin of the batholith. $D_{1\text{-}x}$ is crosscut by D1 and D2 structures.

Vidal et al. (2009) and Lompo (2009, 2010) contended that the tectonic evolution of the Eburnean Orogeny was initiated by a "weak-type" vertical tectonic event involving the diapiric ascent of magma and deformation of the country rock synchronous to cooling and crystallisation (Vidal et al., 2009; Lompo, 2010). They proposed a vertical tectonic (diapiric) model for the emplacement of early Eburnean granitoids of the West African Craton that intruded at 2200-2198 Ma during a regional scale northwest-southeast orientated horizontal shortening event (Gueye et al., 2007, 2008; Lompo, 2009; De Kock et al., 2009). Vidal et al. (2009) and Lompo (2009) added that during the ascent of granitoids, the country rocks were transported downwards along the margins of the intrusions, and folded to produce upright narrow synclines (Miller and Paterson, 1999; Vidal et al., 2009; Lompo,

2009). Marginal shear zones formed during horizontal flow of magma at a high angle to the regional-scale horizontal shortening.

The suggestion that an early "weak-type" deformation may have affected the WAC is consistent with crosscutting relationships in the OGB that indicate the Dori Batholith was emplaced early in the tectonic evolution of the belt. However, the manner of emplacement is not *sensu stricto* diapiric in character and the relative timing of emplacement does not correspond with emplacement during the Eburnean Orogeny.

[Diapirism of magma involves aureole deformation with pluton-up kinematic indicators and downward return flow of the country rock. Diapirism involves complex internal folding, development of concentric foliations, constrictional strain along the margins to form outward-dipping marginal shear zones (that dip away from the intrusion), the formation of rim synclines and down-dip stretching lineations. Displacement in country rocks is normal relative to the diapiric mass. Paterson and Fowler (1993) and Miller and Paterson (1999) suggested that marginal shear zones act as host rock transfer zones during ascent. Steeply-dipping foliations with down-dip stretching lineations are a common feature (Paterson et al., 1991; Paterson and Fowler, 1993; Miller and Paterson, 1999). The country rock may also suffer partial melting during diapiric ascent. Migmatites may occur around the intrusion margins (Paterson et al., 1991; Paterson and Fowler, 1993).]

In comparison with the diapiric model (c.f., Paterson et al., 1991; Paterson and Fowler, 1993; Miller and Paterson, 1999), the proto-mylonite and schist along the northern margin of the Dori Batholith dips towards the batholith (not outward) and records a reverse sense of displacement (not normal), with pluton block up (i.e., southwest block up). Displacement on the DMSZ on the northern margin is towards the northeast with development of an east-west trending synform in the Sokadie region (Kerr, 2004c), but displacement on the eastern margin of the batholith along KSZC is characteristically strike-slip (whether in the Afu or Waho branches). Thus apparent diapirism may be restricted to a small section of the northern margin.

Alternatively, the structural relationships observed for the DMSZ and the Dori Batholith accords with experimental models for pluton/batholith emplacement that takes place at the onset of compressive regimes (c.f., Montanari et al., 2010). In these models pluton/batholith emplacement is facilitated by development of inward-dipping reverse faults (such as the DMSZ and Sokadie Shear Zone) and fault-related drag folds at the margins of the pluton/batholith (such as the synform in the Sokadie region), and a macroscopic anticline (dome) above the pluton/batholith.

We therefore interpret that the Dori Batholith was emplaced during onset of a compressive regime that is described by the Tangaean Event of Tshibubudze et al. (2009), Tshibubudze and Hein (2010) and Hein (2010) based on the crosscutting features that indicate that the Dori Batholith was emplaced pre-D1, D1 being the Tangaean Event. Furthermore emplacement of the Dori Batholith probably included wall rock stoping, roof uplift as evidenced from angular wall rock enclaves along

the margins between Subdomains A and B, formation of marginal shear zones, and migmatite (c.f., Paterson and Fowler, 1993; Brown, 2001; Montanari et al., 2010).

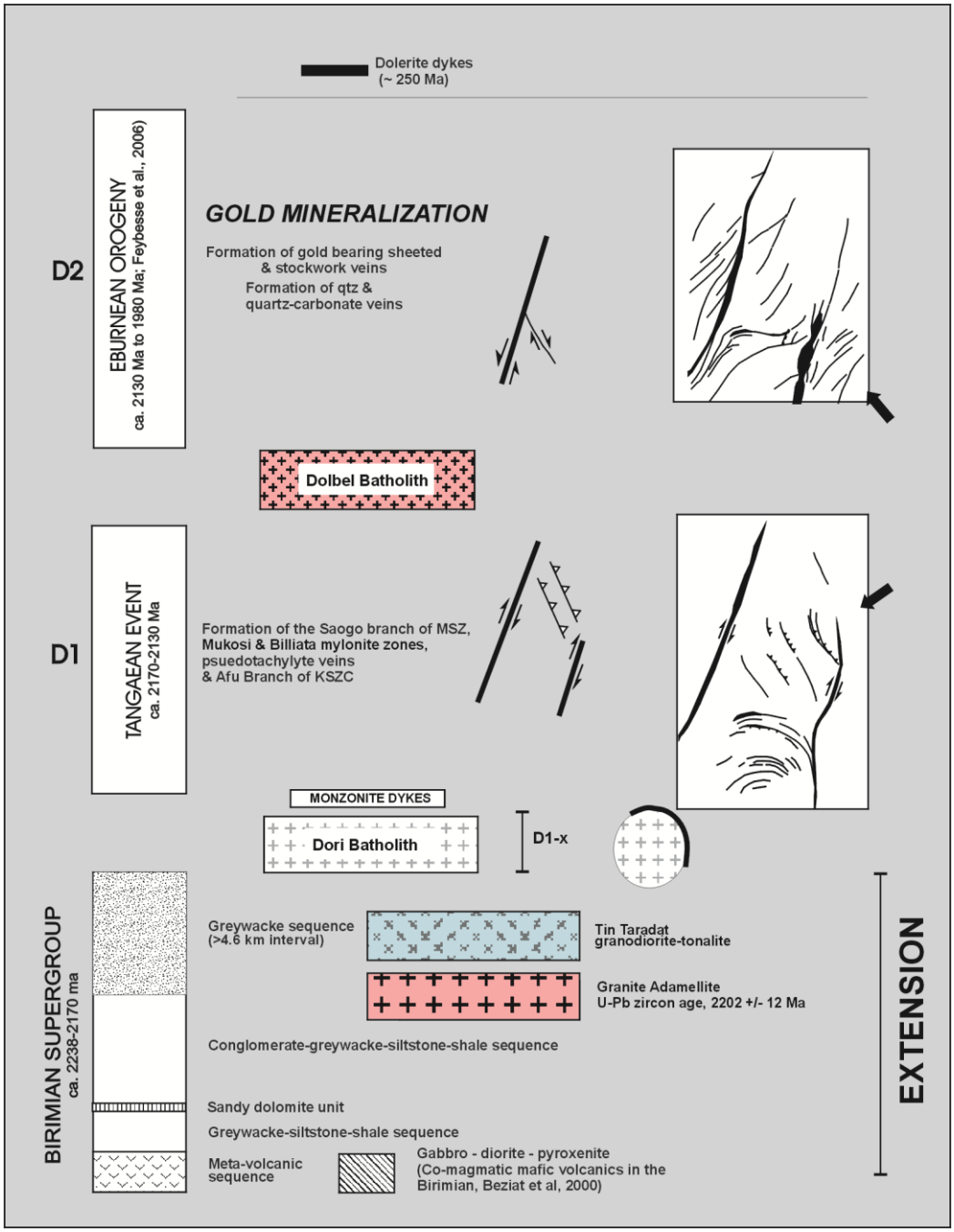

Figure 5.11: Schematic chart of the strato-tectonic relationships established for the OGB.

5.10.3. Gold metallogenesis

Several styles of gold deposit are now recognised in the West African craton including gold hosted by disseminated pyrite in tourmalinized stratabound mineralization (Dommanget et al., 1993; Fouillac et al., 1993), in northwest-trending structural jogs in sodically altered shear zones (Quick, 2011), sheeted vein type gold (Béziat et al., 2008), intrusion-related gold (Hein and Matabane,

accepted), Eocene-Miocene placer gold above a fault (Matsheka and Hein, 2011), and numerous placer deposits.

From the data presented we concur with Foster and Piper (1993), Groves et al. (1998), Feybesse et al. (2006) and Béziat et al. (2008) that gold mineralisation in the OGB formed during deformation associated with the Eburnean Orogeny. Gold mineralisation has a spatial and temporal relationship with both D1 and D2 structures. Gold mineralisation is sited along 5 northwest-trending metallogenic corridors, and specifically, where northeast-trending faults and shears crosscut northwest-trending thrust-folds. D1 structures where dilated in D2 (during the Eburnean Orogeny) with development of sheeted and stockwork vein systems. The sites of intersection effectively became fluid conduits. The source of gold is interpreted to be the metasedimentary rock sequences. However, the source of fluid is not known and is the subject of on-going ore genesis studies in the OGB. Gold mineralisation in sheeted and stockwork veins preferentially occurs in massive competent rocks units including conglomerate beds, greywacke, quartzite, monzonite dykes, pyroxenite-gabbro sills and D1 buck quartz veins. Gold in fine veinlets may also be hosted in massive shale units. Gold is also hosted in veins in the Tin Taradat granodiorite-diorite and in gold-molybdenite-copper veins in the Dolbel Batholith.

5.11. Conclusions

An intimate relationship exists between the tectonic development of the OGB and deposition of gold metallogenesis. Mafic volcanic and metasedimentary sequences of the (1) the meta-volcanic sequence (basaltic hyaloclastite), (2) a greywacke-siltstone-shale sequence, (3) a sandy dolomite unit, (4) a conglomerate-greywacke-siltstone-shale sequence and (5) a greywacke sequence were deformed and metamorphosed during 2 regional deformation events and emplacement of plutons.

The emplacement of the Dori Batholith in $D_{1\text{-}x}$ was accompanied by aureole deformation and the development of proto-mylonite, migmatite, gneiss and schist, with contact metamorphism to granulite facies. The inward-dipping DMSZ and Sokadie Shear Zone (reverse sense of displacement with pluton up), and fault-related drag folds at the margins of the pluton/batholith suggest that the batholith may have been emplaced at the onset of the Tangaean Event.

The magmatic-tectonic event, as manifested by the emplacement of the Dori Batholith ($D_{1\text{-}x}$), was succeeded by deformation during the Tangaean Event (D1) and the Eburnean Orogeny (D2). Metamorphic grade during regional deformation attained lower greenschist to lower amphibolite facies. Second and third-order northwest-trending splay faults and shears of the Tangaean Event matured as sites of gold deposition during the Eburnean Orogeny. The deposits are structurally thereby hosted.

Gold mineralisation is sited along 5 northwest-trending metallogenic corridors, specifically, where northeast-trending faults and shears crosscut or coalesce with northwest-trending thrust-folds

(or geophysical lineaments), or where north-west trending faults coalesce with north-northeast trending shear zones. D1 structures where dilated in D2 (during the Eburnean Orogeny) with development of sheeted and stockwork vein systems.

CHAPTER 6
GEOLOGY AND STRUCTURE OF THE GOROM-GOROM GRANITOID TERRANE

6.1. Introduction

The western footwall block to the Markoye Shear Zone (MSZ) is termed the Gorom-Gorom Granitoid Terrane (GGGT) and covers most of the surface area of the Oudalan province, and a portion of the Seno province (Figure 1.2). Interpretation of LANDSAT and Google Earth Spot images, and RTP magnetic images (Chapter 4) were used to delineate areas of outcrop, and east-west and north-south mapping traverses. The GGGT is generally made up of pre-Birimian granodiorite gneiss, metamorphosed and tectonised Birimian sedimentary and volcanic units, and these are intruded by suites of TTG to granite plutons and dykes. Samples of these were collected for geochemical analysis and geochronology study to establish the absolute geochronology of emplacement events (Chapter 7). Plutons and dykes included adamellite granite (hereafter termed Mrs Pink granite), hornblende granodiorite-tonalite, gabbro-pyroxenite and dolerite.

The region is dominated by E-W trending sand dunes of the Sahara Desert (Figure 6.1; Figure 4.13), and with rare outcrops of laterite and ferricrete in places.

6.2. Pre-Birimian - Lilengo gneiss complex

A granodiorite gneiss (termed the Lilengo gneiss complex, after the village of Lilengo near Gorom-Gorom) is overlain by Birimian sedimentary and volcanic units on an interpreted angular unconformity that separates highly deformed, high grade metamorphic gneiss-migmatite from moderately deformed, greenschist-amphibolite facies rocks. An unconformity is interpreted from several outcrop exposures in the GGGT, and report (1) a substantial change across a few metres in metamorphic grade, (2) change in character and orientation of fabric in the rock, (3) change in the intensity of deformation. Gneiss-migmatite and volcano-sedimentary rocks are thus juxtaposed. The Lilengo gneiss complex is intruded by suites of TTG and granite plutons, mafic dykes (Figure 6.2a, b) and pegmatite veins.

The Lilengo gneiss complex exhibits a banded gneissic foliation defined by alignment of quartz, plagioclase, potash feldspar, amphibole (hornblende) and biotite. It has well-defined leucocratic and melanocratic layers (Figure 6.2c, d). The layers range in thickness from 0.1 to 5 cm. The melanocratic layers are dominated by hornblende, biotite (with a preferred orientation) and magnetite, while the leucocratic layers are dominated by plagioclase, potassium feldspar and quartz. The Lilengo gneiss complex is crosscut by a northwest trending parallel (S_1) foliation and a north-northeast trending crenulating to disjunctive (C-S_2) foliation (Figure 6.2e).

The Lilengo gneiss complex is migmatitic in places (Figure 6.2d). The migmatite is granodioritic in composition with leucocratic and melanocratic layers with magmatic intrafolial folds (Figure 6.2d). The melanocratic layers are dominated by hornblende and quartz with accessory biotite, hornblende and plagioclase, while the leucocratic layers are dominated by plagioclase and quartz (up to 2 mm in size), with accessory potash feldspar, muscovite, biotite and garnet.

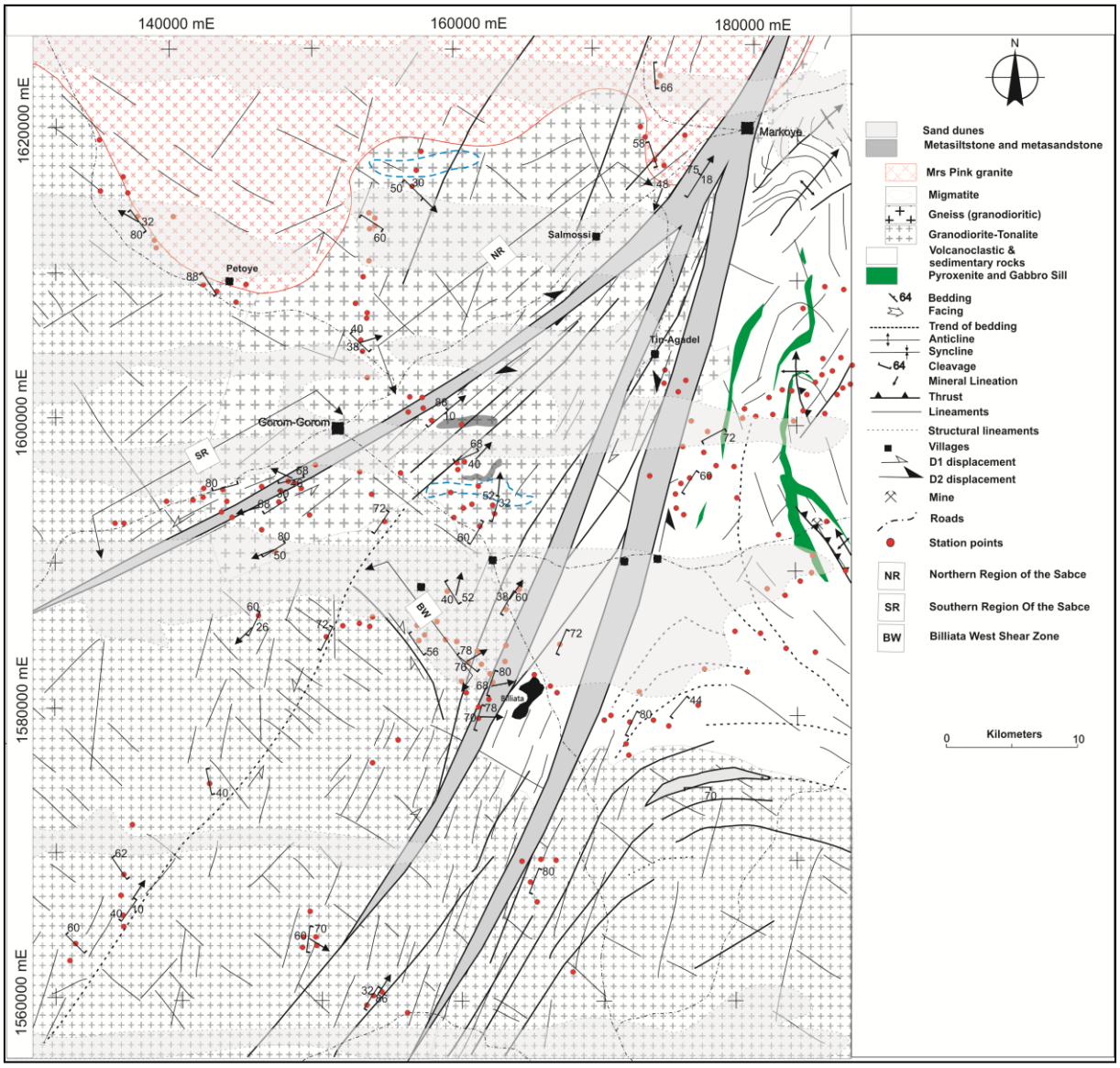

Figure 6.1: The simplified geological and geographic map of the GGGT, including the extracted data from the regional geophysical images.

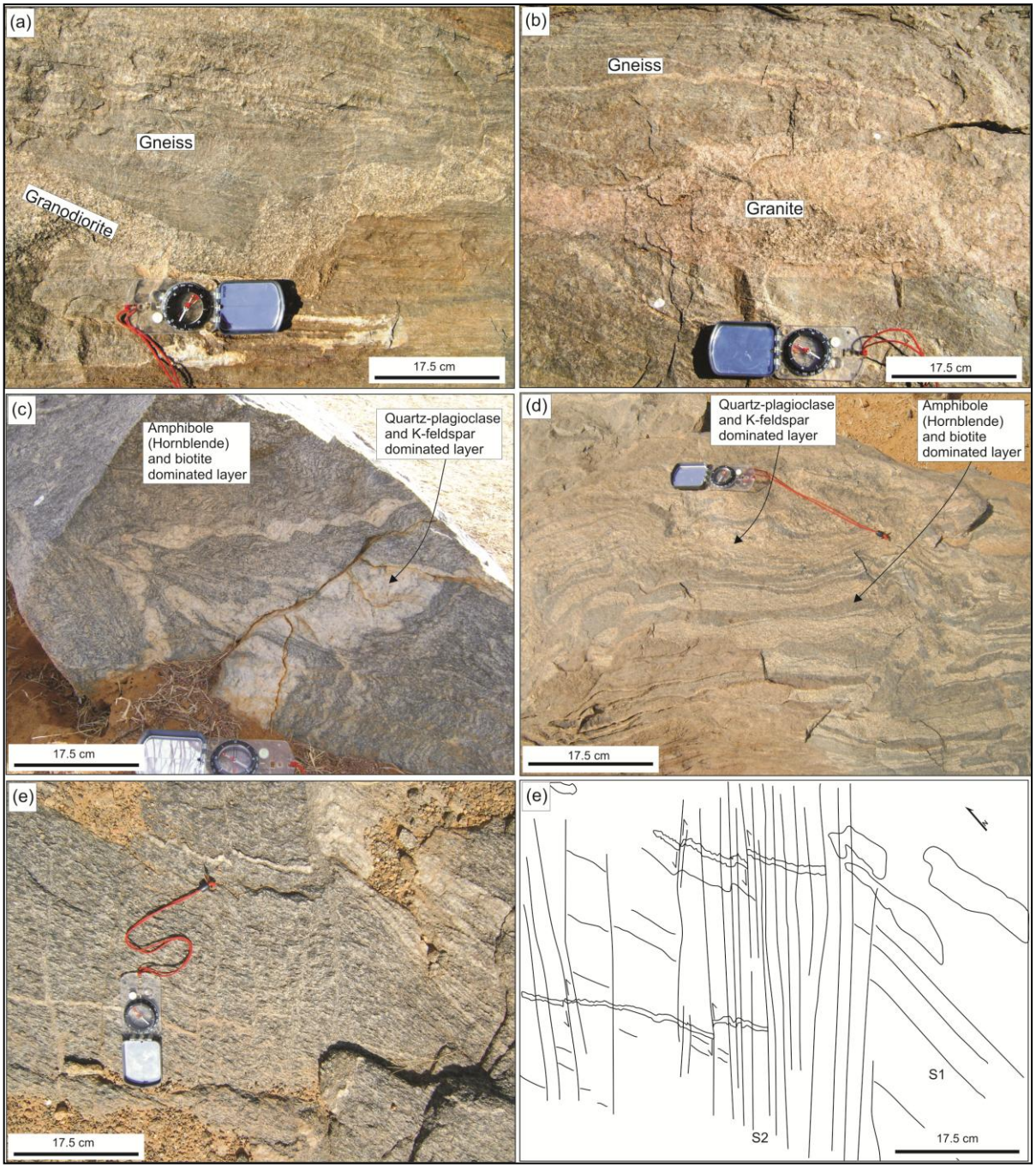

Figure 6.2: (a) Granodiorite dyke crosscutting the Lilengo Gneiss Complex (UTM 30P, 0805407, 1585491). (b) Granite dyke crosscut the Lilengo Gneiss Complex (UTM 30P, 0804617, 1584659). (c) The Lilengo Gneiss Complex (UTM 30P, 0811742, 1608135) and the (d) Lilengo Gneiss Complex migmatite (UTM 30P, 0807828, 1594675). (e) Northwest-trending foliation in the Lilengo Gneiss Complex is crosscut and crenulated by a disjunctive northeast trending foliation and faults (UTM 30P, 0765125, 1556780). The north-northeast trending faults (S_2) have sinistral displacement, and displace S_1 foliation and V_1 veins.

6.3. Birimian sedimentary and volcanic units

6.3.1. Amphibolite unit

The amphibolite unit is dark in colour with a strong pervasive cleavage. It exhibits fine compositional banding dominated by carbonate and plagioclase that alternate with layers dominated by hornblende, carbonate and quartz. These are chloritized (Figure 6.3a). The amphibolite hosts porphyroblasts of plagioclase in a dark green amphibole (hornblende) matrix (Figure 6.3b). The amphibolite is interpreted to have originally been mafic volcanic unit.

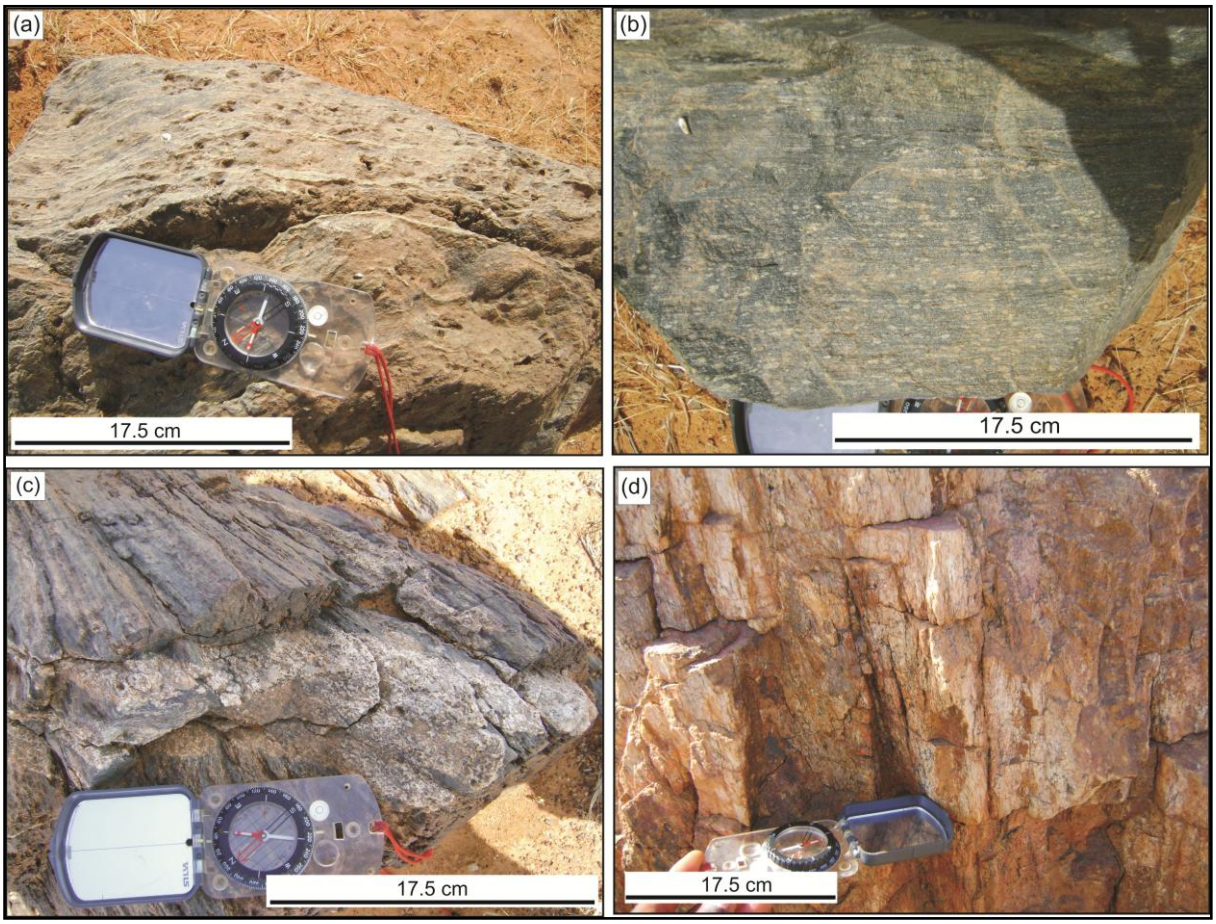

Figure 6.3: (a) Photograph of Amphibolite unit which is dark in colour. It host a penetrative and pervasive cleavage and exhibit fine compositional banding (UTM 30P, 0806590, 1593286). (b) Amphibolite with plagioclase porphyroblasts (UTM 30P, 0794957, 1594647). (c) Banded iron formation with fine laminations of light grey chert and dark brown fine grained ironstone (UTM 30P, 0807971, 1593763). (d) Quartzite unit of the GGGT composed of fine to coarse interlocking quartz granules, amphibole, carbonate, muscovite and sericite (UTM 30P, 0808076, 1583557).

6.3.2. Banded Iron Formation (BIF), quartzite, metagritstone and metasiltstone

The GGGT hosts narrow belts of sedimentary rocks that are metamorphosed to upper greenschist-amphibolite facies (Castaing et al., 2003, Woolfe, 2011) (Figures 4.14 and 6.1) and tectonised. These rocks crop out in the Kel Enguef metamorphic belt (Woolfe, 2011), and west of Billiata (Figures 4.14 and 6.1). They unconformably overlay the Lilengo gneiss complex.

The sedimentary and volcanic rocks are schistosed (in part), folded and crosscut by shear zones and faults. The quartzite, metagritstone, metasiltstone and BIF form dominant hills in the GGGT that were readily identified from LANDSAT and Google Earth Spot images (Figure 4.4).

A carbonaceous BIF unit (1-2 m thick) overlies amphibolite in the southern Kel Enguef metamorphic belt. The BIF is characterised by fine laminations of light grey chert and dark brown fine grained ironstone (Figure 6.3c). It is overlain by a sequence of intercalated quartzite, metagritstone, and metasiltstone units. The quartzite and metagritstone units are dominantly composed of fine to coarse interlocking quartz granules, amphibole (hornblende), carbonate, albite, epidote, muscovite and sericite (Figure 6.3d). There is compositional variation within the quartzite that resolves a compositional layering after bedding, with layers that are dominated by iron oxide with variable amounts of muscovite and epidote. The compositional layering trends east-west and dips 20-30°N.

6.4. Magmatic rocks of the GGGT and their crosscutting relationships

The GGGT is intruded by the Mrs Pink granite, and hornblende granodiorite-tonalite, and these are crosscut by gabbro-pyroxenite, aplite-granite, and dolerite dykes. The Mrs Pink granite intrudes the Lilengo gneiss complex. The Mrs Pink granite is intruded by a hornblende bearing granodiorite-tonalite pluton (Tshibubudze et al., 2009). The age of the Lilengo gneiss complex and the Mrs Pink granite was established from geochronological study (Chapter 7) to confirm that the Mrs Pink is younger than the Lilengo gneiss complex.

6.4.1. Mrs Pink granite

The Mrs Pink granite, as the name implies, is dominantly pink in colour reflecting potassic alteration in the chilled margin and throughout the pluton (Figure 6.4a). The Mrs Pink granite is medium to coarse crystalline and composed of millimetre-sized crystals of potassium feldspar (microcline), quartz, plagioclase, biotite and aggregates of hornblende in a quartz-feldspar rich groundmass. The pluton is deuterically altered, and silicified in places, and biotite is chloritized. The Mrs Pink granite has granophyric and myrmekitic intergrowths of quartz and potash feldspar, or plagioclase. It hosts ovoid mafic xenoliths (Figure 6.4b). It is foliated and lineated adjacent to the MSZ (Tshibubudze et al., 2009) and the Sabce Shear Zone (Section 6.5). The aureole of Mrs Pink granite in the Lilengo gneiss complex is dominated by quartz-potash feldspar alteration as disseminated vein sets.

The Mrs Pink granite is crosscut by granodiorite-tonalite, gabbro and aplite-granite dykes, indicating that it is older than these rocks in the GGGT (Figure 6.4c, d). It is also crosscut by northwest and north to north-northeast trending discrete shear-mylonite zones indicating that it is older.

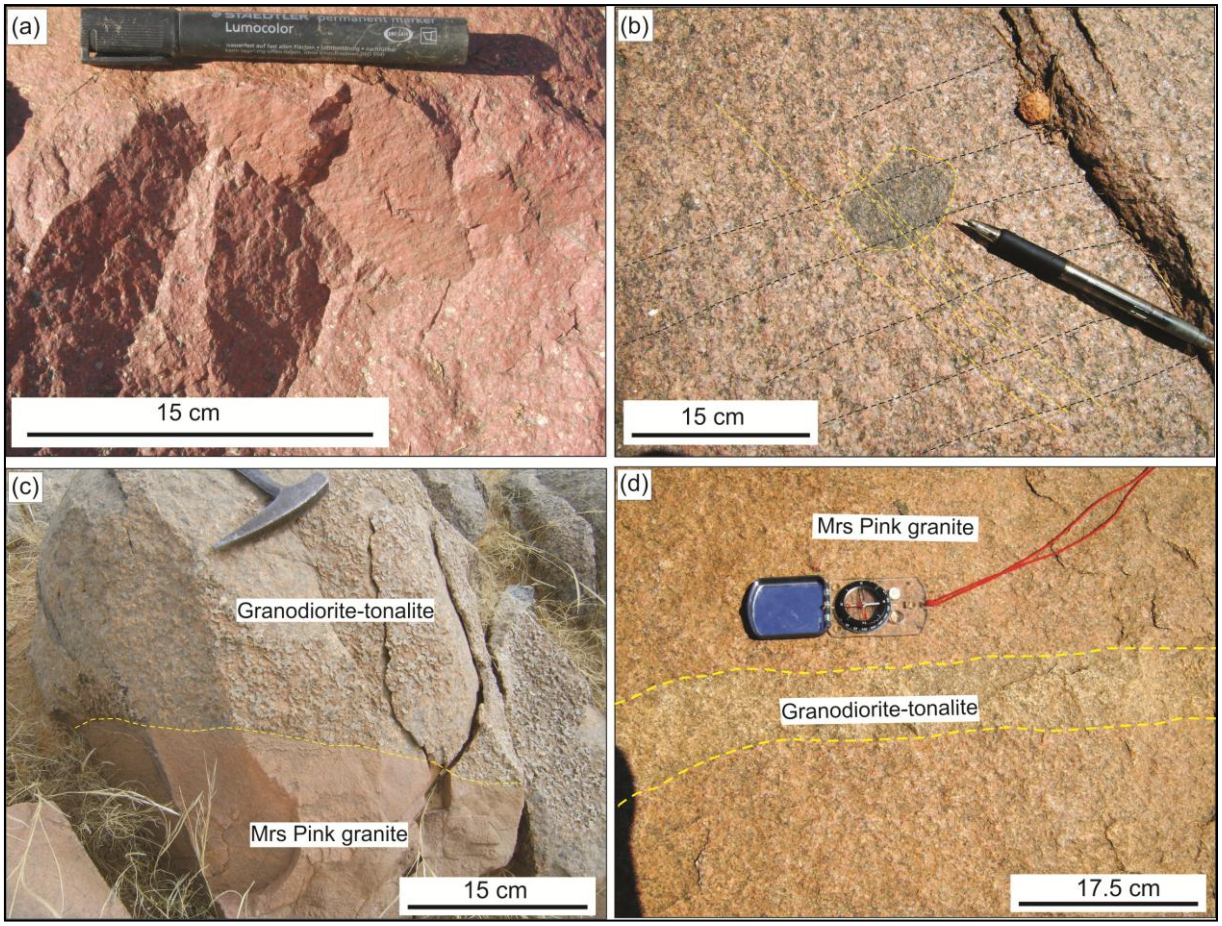

Figure 6.4: (a) The name of Mrs Pink is associated with the pink colour of the granite (UTM 30P, 0819922, 1616778). (b) The Mrs Pink granite outcrop with rounded mafic xenoliths, where Mrs Pink and the xenoliths are crosscut by a weak foliation (UTM 30P, 0785692, 1610204), (c) The contact between Mrs Pink granite and the granodiorite-tonalite (UTM 30P, 0781517, 1617563). The granodiorite-tonalite is phenocrystic in plagioclase and amphibole, while Mrs Pink granite is recrystallised at the contact. (d) A granodiorite-tonalite dyke crosscutting the Mrs Pink granite (UTM 30 P, 0799963, 1585180) indicating that the granodiorite-tonalite is younger than the Mrs Pink granite.

6.4.2. Hornblende-bearing granodiorite-tonalite

The hornblende-bearing granodiorite-tonalite is composed of hornblende phenocrysts in a ground mass of plagioclase and quartz, with variable proportions of potash feldspar. In some places it is tonalitic and is composed of plagioclase, hornblende, and minor quartz, with equigranular crystals. It hosts mafic xenoliths whose long axes predominantly trend northwest (Figure 6.5a, b). The granodiorite-tonalite also host xenoliths of the Lilengo gneiss complex (Figure 6.5c), the Mrs Pink granite (Figure 6.5d), amphibolite (Figure 6.5e) and layered sedimentary rocks (Figure 6.5f). This indicates that the emplacement of the granodiorite-tonalite postdates these rocks. The granodiorite-tonalite is chloritised and kaolinised in places.

Moreover, the granodiorite-tonalite crosscuts east-west trending proto-mylonite and mylonite zones, as discussed in Section 6.5. It is sequentially crosscut by;

(1) Granite dykes (Figure 6.5a, g).

(2) Medium grained granodiorite dykes which trend north-northeast (Figure 6.6 insert).

(3) North-northeast trending shear-faults (Figure 6.6).

(4) Pegmatite veins (Figure 6.6).

(5) Aplite-granite dykes (Figure 6.5g; 6.6).

These relationships are presented in a schematic diagram in Figure 6.6.

6.4.3. Pegmatite veins

The pegmatite veins in the GGGT are composed of 1-2 cm sized quartz and plagioclase crystals, and potash feldspar. Crystal growth is generally syntaxial. Some veins are zoned with coarse crystals central to the vein and fine to medium sized crystals at the margins of the veins. Two phases of pegmatite veining were established; pegmatite veins that are deformed (folded and schistosed) and crosscut by northwest trending shears and faults, and pegmatite veins that are not deformed and composed of quartz and plagioclase crystals.

6.4.4. Gabbro-pyroxenite dykes

The gabbro and pyroxenite dykes in the GGGT are phenocrystic in pyroxene with a ground mass of clino-pyroxene, plagioclase, and hornblende. The phenocrysts of pyroxene are 2 cm in size, giving the pyroxenite a spotted texture (Figure 6.7).

Several pyroxenite dykes are oriented parallel to the north-northeast trending shear zones and these are sometimes dominated by hornblende, biotite, pyroxene, tremolite and plagioclase (thus hornblendite), with well-defined mineral lineation (defined by hornblende). Gabbro dykes are composed of hornblende, plagioclase, quartz, biotite and potash feldspar.

6.4.5. Aplite-granite dykes

Aplite dykes in the GGGT consist of fine equigranular crystals of potash feldspar (microcline) and quartz, and are gradational in composition with granite dykes. The granite dykes are composed of potash feldspar (microcline), quartz, and plagioclase, with accessory muscovite, and biotite. The size of the aplite-granite dykes ranges from 10 cm to ~1m wide (Figure 6.5a, g, 6.6). They are similar in composition to aplite dykes mapped in the Goren and Sabba region by Hein et al. (2004) and Simoko (2011) and across northeast Burkina Faso.

6.4.6. Dolerite dykes

Northwest trending dolerite dykes crosscut all units in the GGGT. They are composed of pyroxene, amphibole, and plagioclase. They are readily identified using the LANDSAT, ASTER and RTP magnetic data of the region. They are abundant to the north of the study area and are dated at 250 ± 13 Ma (K-Ar whole rock method) (Hottin and Ouedraogo, 1992).

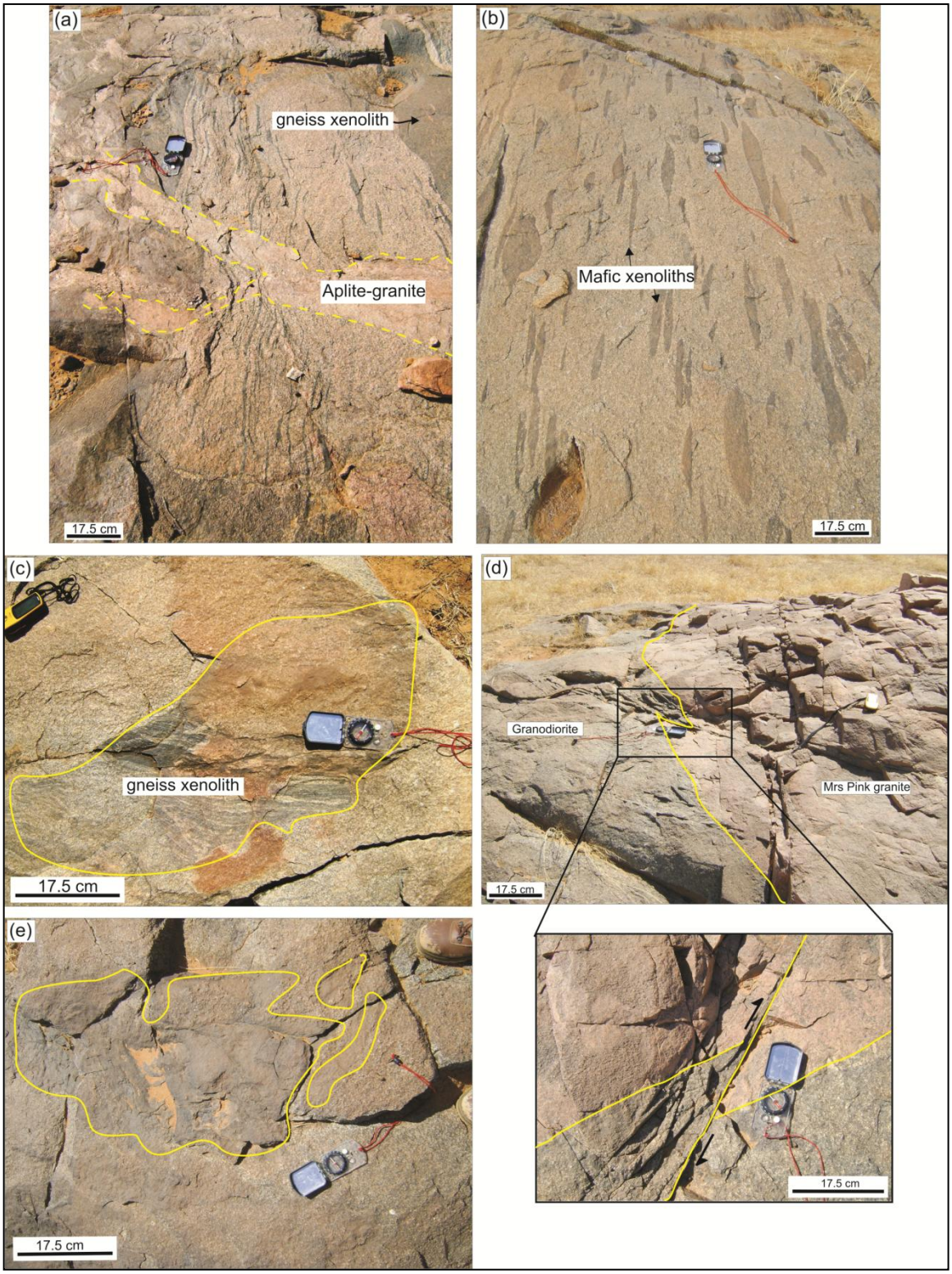

Figure 6.5: (a) The granodiorite-tonalite hosts elongated and stretched mafic and angular xenoliths and have potassic alteration in places (UTM 30P, 0803958, 1585126). The granodiorite-tonalite is also intruded by aplite-granite dykes (b). The mafic xenoliths are dominantly stretched and elongated along the orientation of the foliation (UTM 30P, 0797401, 1564022). (c) The Lilengo gneiss xenoliths within the granodiorite-tonalite, indicating that the Lilengo gneiss is older than the granodiorite-tonalite (UTM 30P, 0800724, 1585124). (d) Mrs Pink granite xenoliths in the granodiorite-tonalite (UTM 30P, 0799704, 1608584). The contact is crosscut and displaced by northeast trending faults with a dextral oblique-slip displacement. (e) Amphibolite xenoliths within the granodiorite-tonalite (UTM 30P, 0818525, 1618707). Continue overleaf.

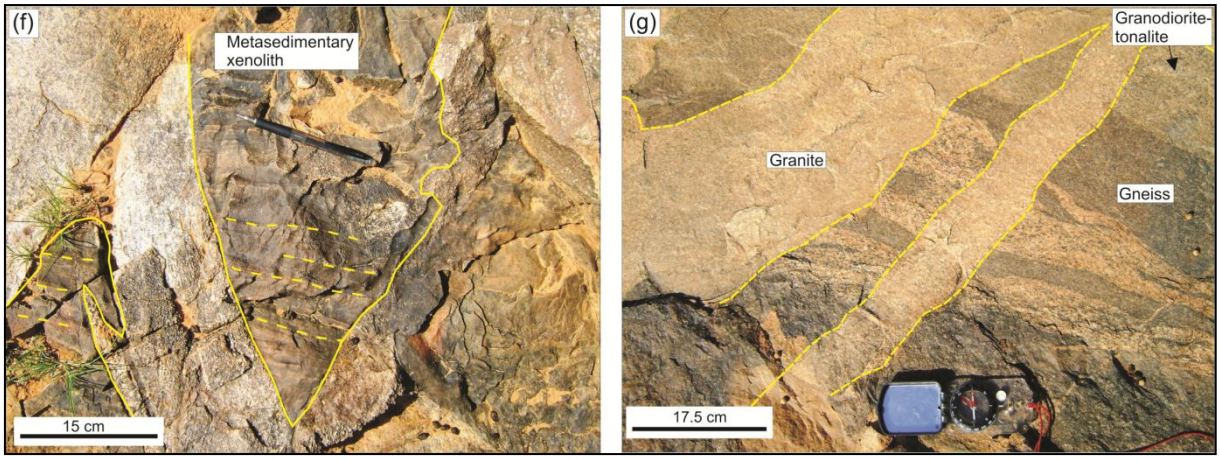

Figure 6.5 (continued): (f) Metasedimentary xenoliths with compositional layering within the granodiorite-tonalite indicating that the metasedimentary sequences are older than the granodiorite-tonalite (UTM 30P, 0809052, 1580334). (g) Fine grained potash feldspar-rich aplite-granite dykes that crosscut both the granodiorite-tonalite and the gneiss xenolith (UTM 30P, 0803958, 1585126).

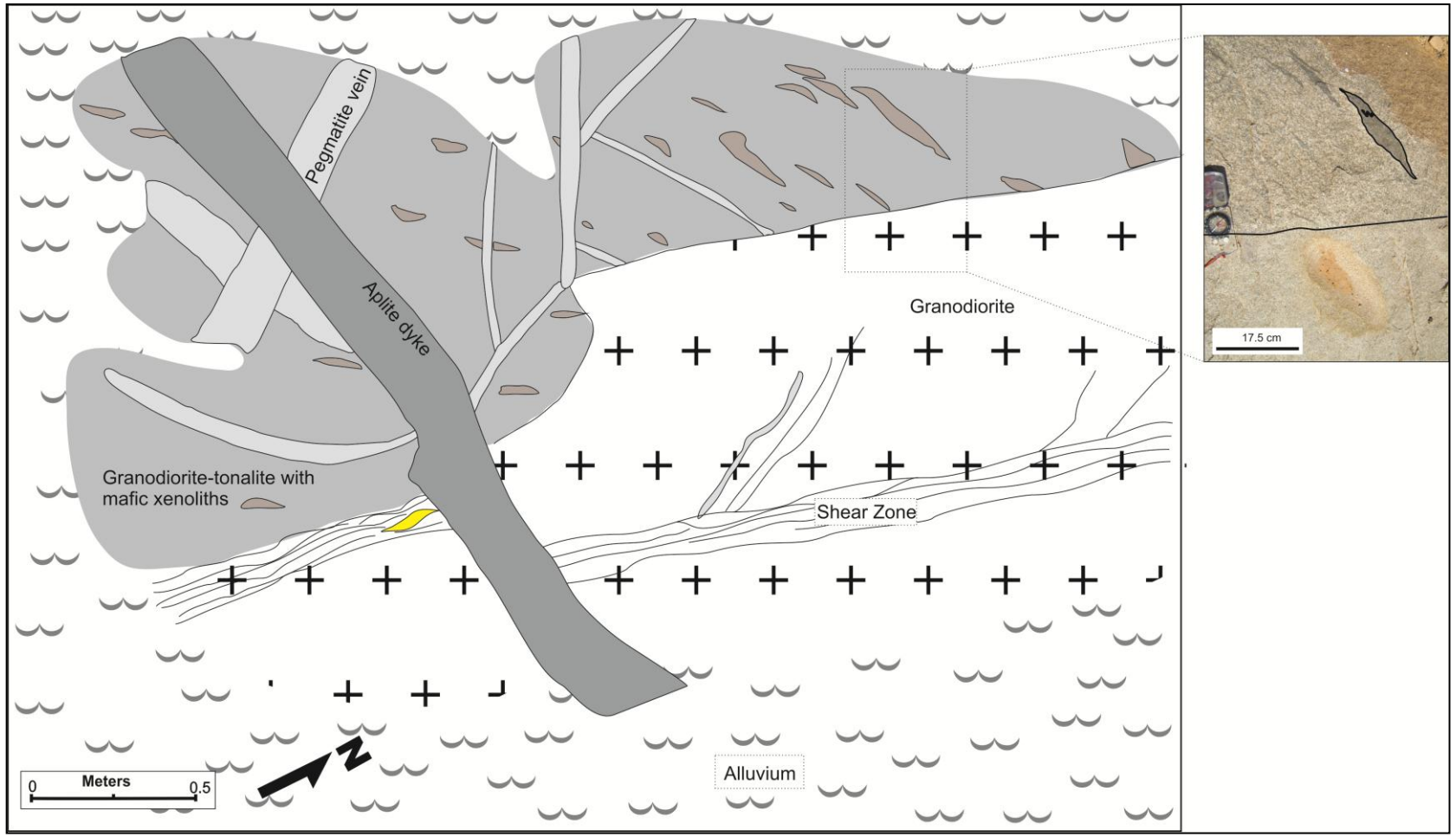

Figure 6.6: The map of an outcrop showing different phases of magmatic intrusions that dominate the GGGT (UTM 30P, 0801190, 1585594). The granodiorite-tonalite with mafic xenoliths is in contact with the granodiorite. The relationship indicates that granodiorite intruded the granodiorite-tonalite. The granodiorite is crosscut by north-northeast trending, steeply dipping to the southeast shear zones that have a dextral displacement. The granodiorite-tonalite is crosscut by pegmatite veins that do not crosscut the granodiorite. Both the granodiorite with mafic xenoliths and the granodiorite and the pegmatite veins are later crosscut by aplite dyke. (Insert) The image taken of the contact of the granodiorite and the granodiorite-tonalite, indicated by a box in the outcrop map, showing some of the mafic xenoliths that have folded quartz veins.

Figure 6.7: A photograph of a phenocrystic pyroxenite that have crystals that are greater than 2 cm long in a pyroxene, hornblende, biotite and plagioclase groundmass, giving the pyroxenite a spotted texture (UTM 30P 0800213, 1562317).

6.5. Structure and the tectonic overview

In general, the GGGT is a pre-Birimian gneissic-migmatite terrane that is unconformably overlain by Birimian supracrustal sequences and intruded by pre to syn tectonic plutons. The terrane is crosscut by northwest-trending mylonite zones, quartz-carbonate buck quartz veins, folds, and associated mylonitic foliation which formed in D1 (e.g. Billiata West Mylonite Zone). These were crosscut by north-northeast trending shears to mylonite zones (e.g. Sabce Shear Zone), L-tectonites, conjugate sets of shear fractures, and buck quartz-carbonate veins, which formed in D2. In turn these are crosscut by a west-northwest trending shear faults and cleavage that formed in D3.

6.5.1. Lilengo gneiss complex

An early deformation in the GGGT is recorded by the presence of the Lilengo gneiss complex. Intrafolial folds in the gneiss and migmatite are generally east-northeast trending, and gently to steeply dipping to the north. Formation of gneiss was accompanied by recrystallisation and partial melting to form migmatite and is gradational from gneiss to proto-migmatite to migmatite. The leucocratic zones in the host garnet, plagioclase, quartz and potash feldspar porphyroblasts indicating that metamorphism attained granulite facies (Figure 6.8). This suggests that the Lilengo gneiss was subjected to high pressure and temperature with a possible residence at depths in the lower continental crust as suggested by Ganne et al. (2014) who studied the metamorphic facies variation across eastern Burkina Faso. The Lilengo gneiss complex is interpreted as basement to the Birimian Supergroup.

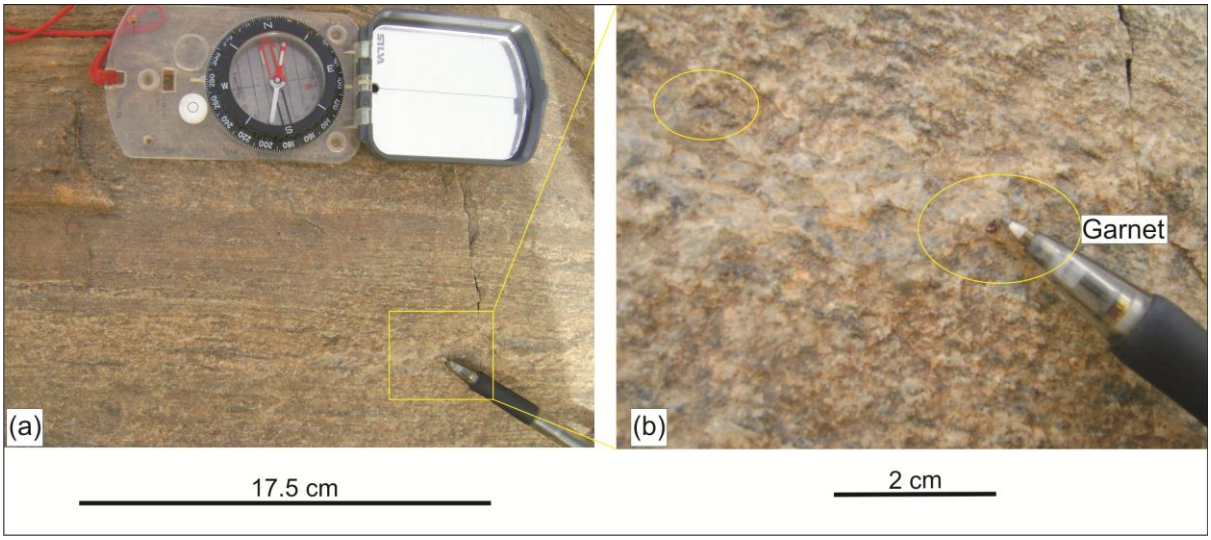

Figure 6.8: The migmatitic gneiss outcrop with garnet porphyroblast. The presence of garnet porhyroblasts suggests that the metamorphic grade could have or attained granulite facies (UTM 30P 0805407, 1585491) within the Lilengo gneiss complex.

6.5.2. D1 Deformation

The D1 ductile-brittle deformation is generally characterized by (1) northwest and north-northeast trending discrete high-strained mylonite zones, (2) conjugate east-northeast trending discrete high-strain mylonite zones, (3) numerous mesoscopic quartz-albite veins that are folded and transposed with the mylonite zones, (4) a northwest trending S_1-C shear bands, and (5) L-tectonites. A schematic summary of the tectonic elements and structural architecture in the GGGT during D1 is presented in Figure 6.14.

D1 deformation is defined by a 25-30 km wide 1st order scale north-northeast trending shear domain that is bounded by the Gorgadji Shear Zone to the west and the MSZ to the east (Figure 6.14) in which it is possible to find:-

(1) North-northeast trending shear zones that are 500-600 meters wide and spaced approximately 10-13 km.

(2) Northwest and east-northeast trending mylonite zones which sometimes conjugate with each other. They are 150-300 meters wide and hosted between the north-northeast trending shear zones.

Mylonite zones within the 1st order shear domain are characterized by a mylonitic foliation (S_1-C_{my}) that is penetrative and tight. S_1-C_{my} is defined by potash feldspar and quartz sigma (σ) and delta (δ) clasts, a stretching lineation (L_{1my}) defined by hornblende, and small scale shear bands. Northwest and east-northeast trending conjugate mylonite zones are restricted to within the 1st order shear domain. In contrast, north-northeast trending mylonite zones are hosted by north-northeast trending broad shear zones, and merge with northwest and east-northeast trending conjugate mylonite zone to form a complex mylonite array, as for example reported by Tshibubudze et al. (2009) where the mylonite zones exist within the MSZ but merges with the east-northeast mylonite (Chapter 5).

Domain analysis of the mylonite zones has shown that,

(1) Northwest trending mylonite zones in the GGGT have a calculated mean principal orientation of S_1-C_{my} of 320°/64° E (Figure 6.9a), and L_{1my} of 60°→039° (Figure 6.9b). The spread of the data around the primitive circle on equal area stereographic projections (Figure 6.9 a,b) could be due to;

(a) Variation in the strike and dip of S_1-C_{my} across the width of the mylonite zone.

(b) Drag folding against the D1 north-northeast trending shears/mylonite.

(c) Folding along northeast trending fold axes (calculated beta axis 63°→036°) in D2 (Section 6.5.3).

Shear bands and potash feldspar and quartz sigma (σ) and delta (δ) clasts in the northwest trending mylonite zones, report that displacement was principally reverse during D1, with a small dextral component that (Figure 6.10) indicates north block up (NBU) and towards the southwest.

(2) East-northeast trending mylonite zones have a calculated mean principal orientation of S_1-C_{my} of 065°/71° N (Figure 6.11a), and L_{1my} of 29°→051° (Figure 6.11b). The spread of the data around the primitive circle on equal area stereographic projections (Figure 6.11a,b) could be due to;

(a) Variation in the strike and dip of S_1-C_{my} across the width of the mylonite.

(b) Down dip variation.

(c) Folding along northeast trending fold axes (calculated beta axis 1°→064°) in D2 (Section 6.5.3).

The sense of displacement as determined from δ and σ quartz and potash feldspar clasts, S_1-C_{my} shear bands, and L_{1my} lineation, indicates sinistral strike-slip with a reverse component at some station points. In general displacement was north block up (NBU) during an interpreted southwest-northeast directed palaeo-principal compressive stress, with tectonic transport to the southwest.

(3) North-northeast trending mylonite zones have a calculated mean principal orientation of S_1-C_{my} of 021°/76° E (Figure 6.12a), and L_{1my} of 50°→053° (Figure 6.12b). The spread of the data around the primitive circle on stereographic projections (Figure 6.12a,b) could be due to;

(a) Variation in the strike and dip of S_1-C_{my} across the width of the mylonite.

(b) Down dip variation.

(c) Folding along northeast trending fold axes (calculated beta axis 41°→033°) during D2 (Section 6.5.3).

Shear bands, potash feldspar and quartz sigma (σ) and delta (δ) clasts, and an L_{1my} stretching lineation indicate that displacement was dextral (reverse) with east block up (EBU) during an interpreted southwest-northeast directed palaeo-principal compressive stress, with tectonic transport to the southwest.

(4) At the intersection of the northwest and north-northeast trending mylonite zones L-tectonites dominate the rock units and have a calculated mean principal direction of 72°→029°.

Away from the northwest, east-northeast and north-northeast trending mylonite zones, D1 is generally characterized by:

(1) A northwest trending foliation, that dips moderately to the northeast (Figure 6.13a) and refracts across rock units.

(2) Mesoscopic quartz-albite veins that are folded and transposed (Figure 6.13b). The veins are isoclinal and asymmetrically folded along northwest trending fold axes.

(3) Dilational jogs that are right-stepping and are composed of breccias of host rocks and quartz-carbonate-sulphides veins (Figure 6.13c). They are aligned along a northwest trend.

(4) Conjugate sets of joints that are north-northwest and northeast trending.

(5) North-northeast trending left-stepping en-echelon tension gashes (Figure 6.13d).

In summary, D1 ductile-brittle deformation in the GGGT is characterized by dextral (reverse) displacement along a 1st order shear corridor within which it is possible to define; (1) reverse (dextral) northwest trending mylonite zones, and north-northeast trending mylonite zones, (2) sinistral strike-slip to oblique displacement on east-northeast trending mylonite zones, (3) a penetrative regular northeast plunging lineation L_{1my}, (4) a penetrative northwest trending S_1-C_{my} to S_{1my} foliation, and (5) quartz-carbonate vein arrays. Kinematic analysis has indicated that the palaeo-principal compressive stress was southwest-northeast directed during D1. The overall tectonic transport direction was towards the southwest.

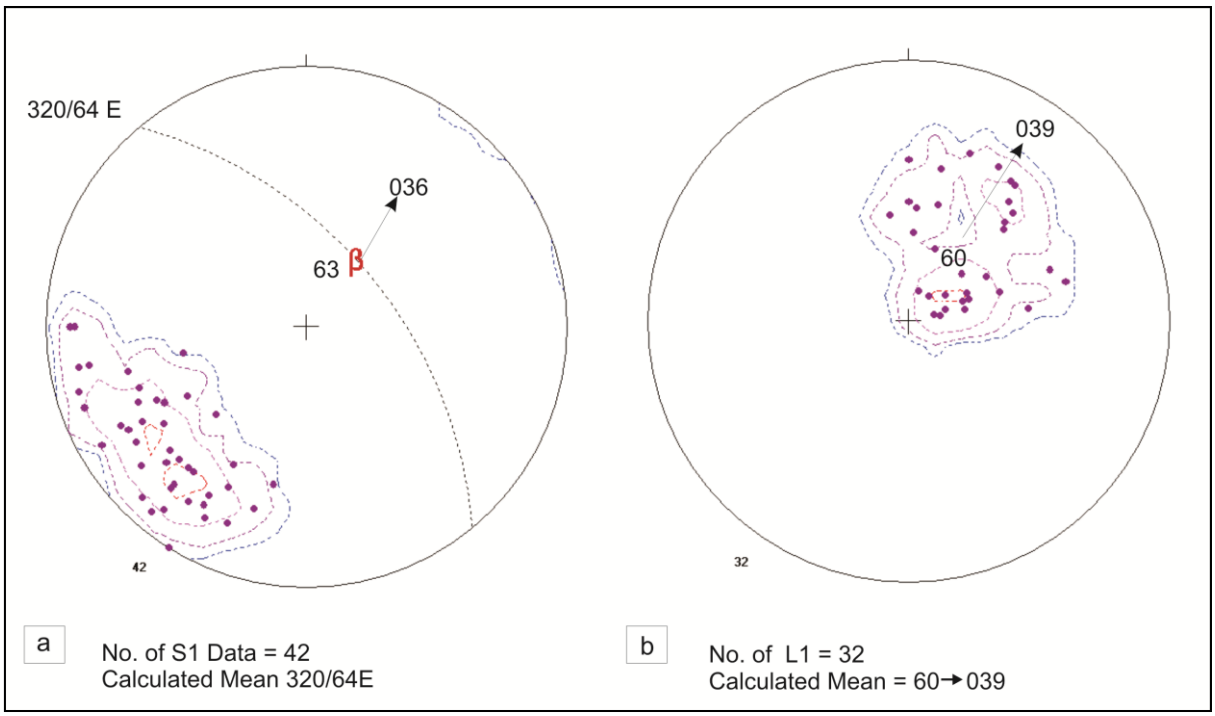

Figure 6.9: Equal area stereographic projection of poles and contour plot of mylonitic foliation and lineation data measured along the D1 mylonite zones. (a) D1 mylonite zones in the GGGT have a

calculated mean principal orientation of 320°/64° E with calculated β axis of 63°→036°. (b) L_{1my} has a mean principal direction of 60°→039°.

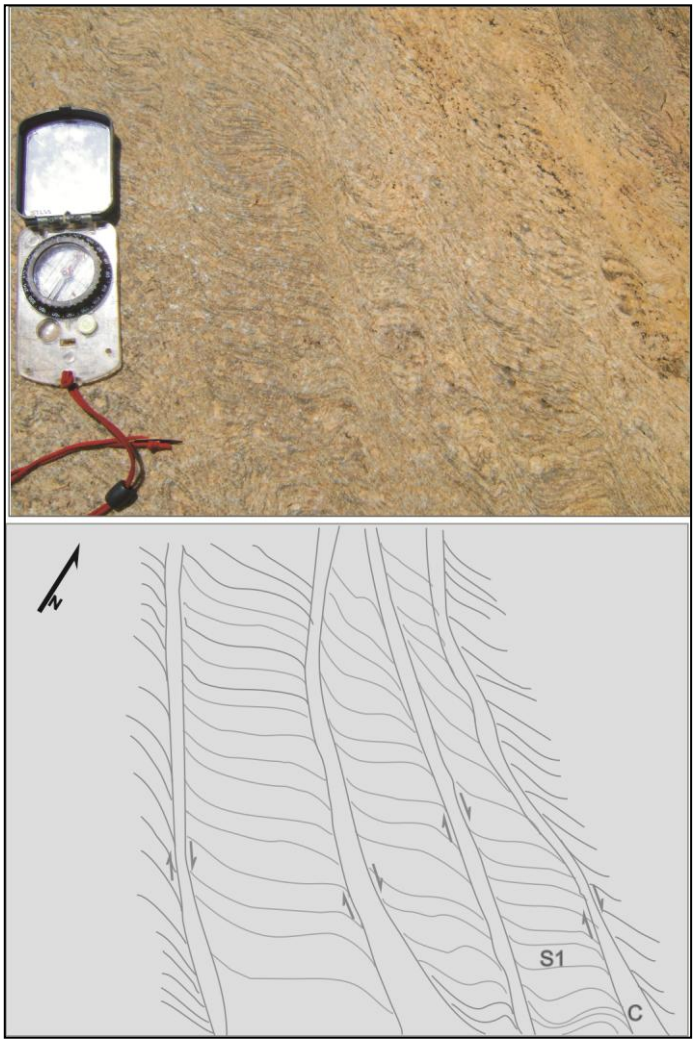

Figure 6.10: A photograph and sketch of the outcrop along the Billiata West mylonite zone, showing a well developed mylonitic S_1-C_{my} fabric that indicates a dextral displacement.

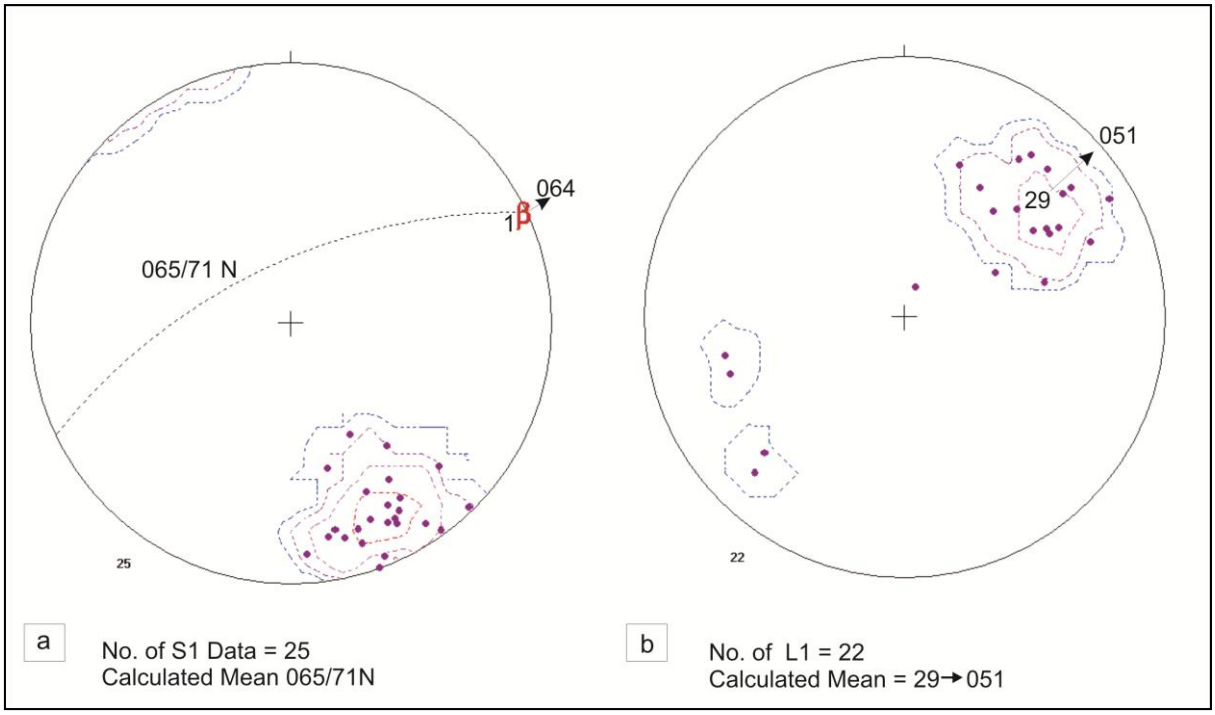

Figure 6.11: Equal area stereographic projection of poles and contour plot of mylonitic foliation and lineation data measured along D1 mylonite zones. (a) East-northeast trending mylonite zones in the GGGT have a calculated mean principal orientation of 065°/71° N. (b) The mineral lineation data has a mean principal direction of L_{1my} of 29°→051°. The calculated beta axis has an orientation of 1°→064°.

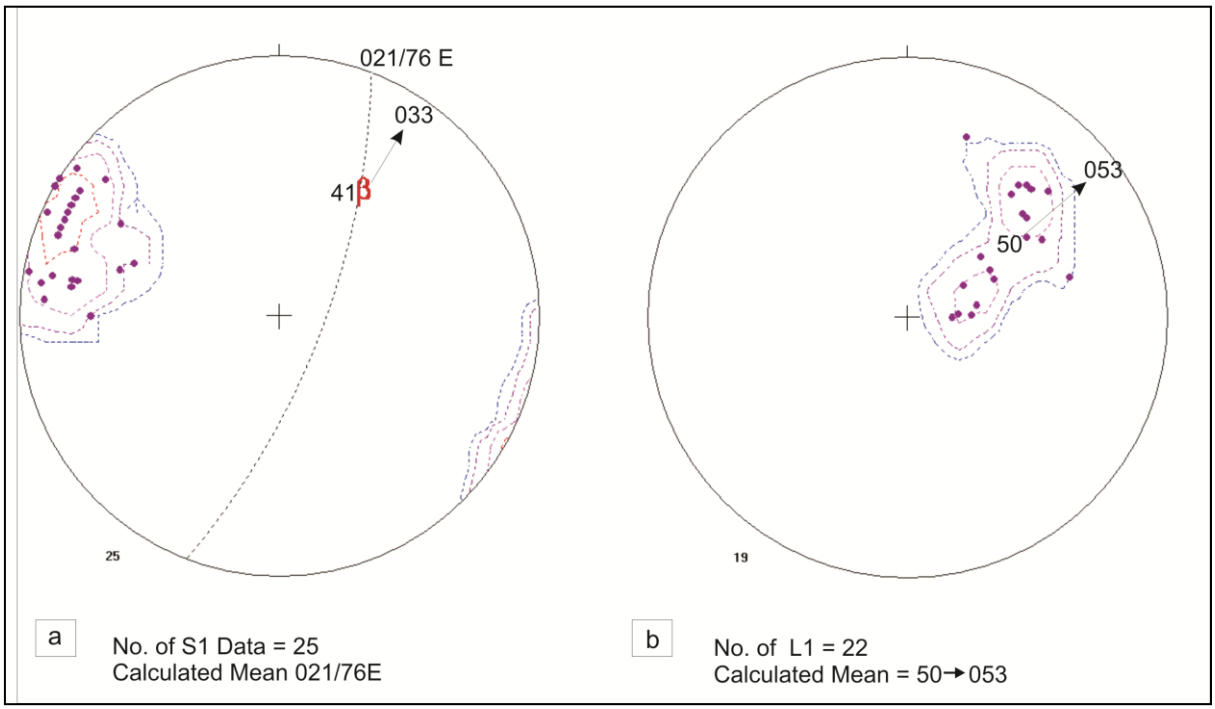

Figure 6.12: Equal area stereographic projection of poles and contour plot of mylonitic foliation and lineation data measured along the mylonite zones. (a) North-northeast trending mylonite zones in the GGGT have a calculated mean principal orientation of 021°/76° E, with a calculated beta axis of 41°→033°. (b) The mineral lineation data has a mean principal direction of L_{1my} of 50°→053°.

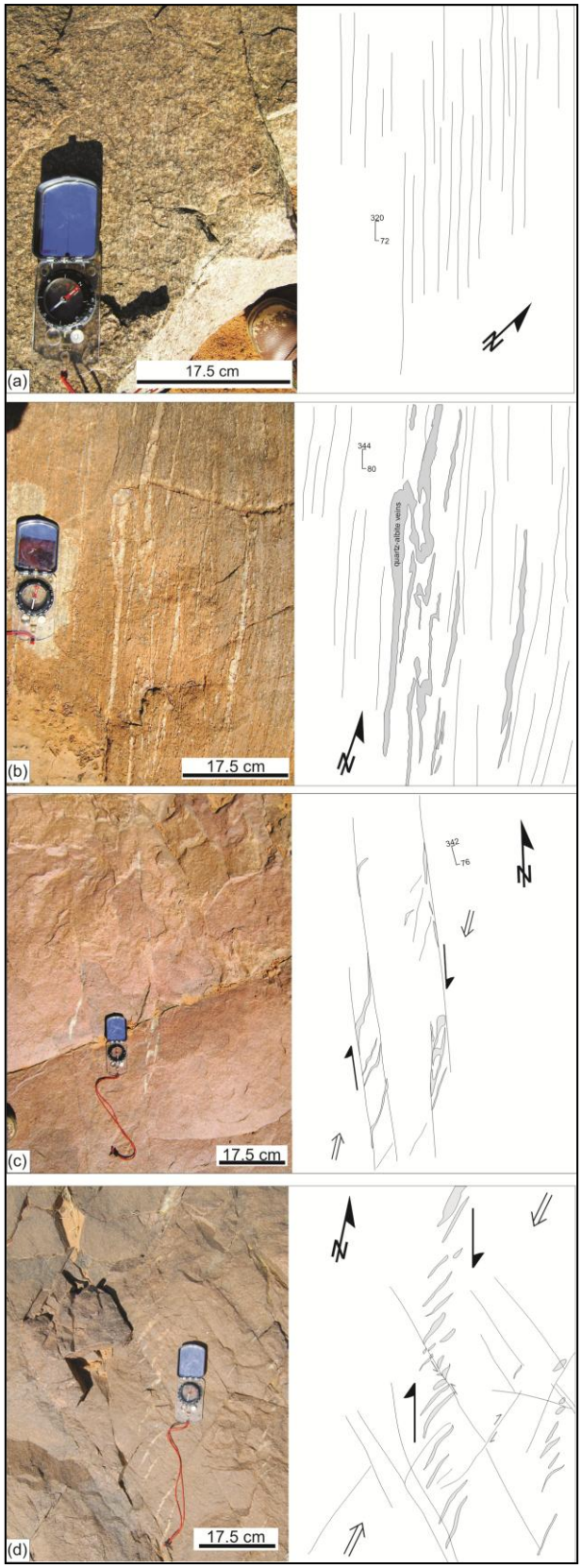

Figure 6.13: Outside the mylonite zones, D1 is associated with, (a) a northwest trending foliation, which dips moderately to the northeast. (b) Mesoscopic quartz-albite veins that are folded and transposed, the veins are isoclinal and asymmetrically folded along northwest trending fold axes. (c) Dilational jogs that are right stepping and are composed of breccia of host rocks and quartz-carbonate-sulphides veins. (d) North-northeast trending left stepping en-echelon tension gashes.

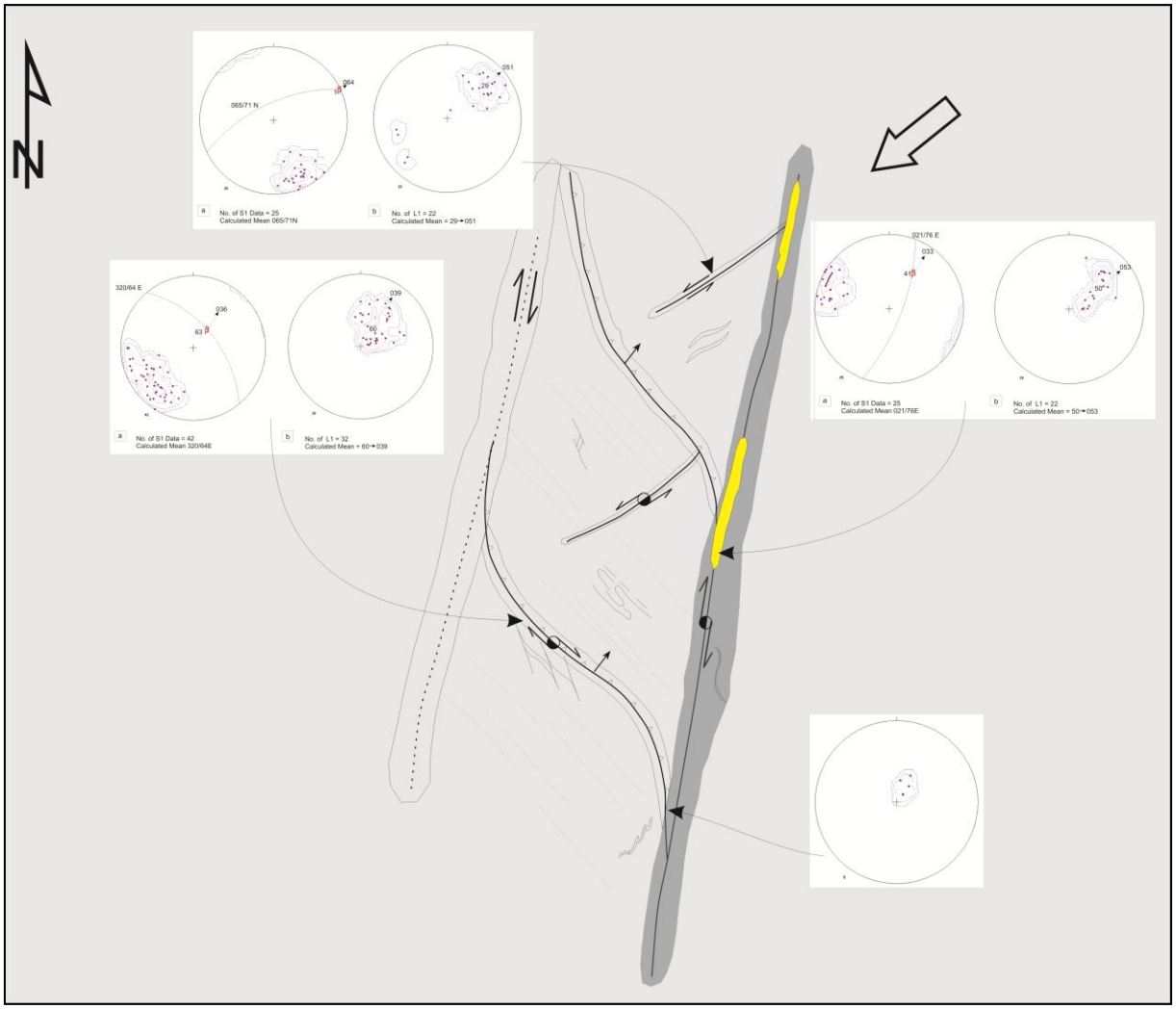

Figure 6.14: The schematic summary of the overall tectonics during D1 deformation, depicting the structures that are associated with D1 deformation along the mylonite zones (yellow) and outside the mylonite zones. The tectonic transport direction in D1 is towards the southwest.

6.5.3. D2 Deformation

The D2 deformation in the GGGT is brittle-(ductile) and characterized by; (1) reactivation of north-northeast trending D1 shear zones (Figure 6.14), (2) reactivation of east-northeast trending D1 mylonite as shears-mylonite zones, (3) formation of north-northeast trending faults within the 1st order scale domain but outside mylonite and shear zones, and (4) formation of S_2-C shear bands within and crosscutting D1 mylonite zones, and (5) formation of conjugate joint sets across the GGGT. A schematic summary of the tectonics elements and overall structural architecture of D2 on D1 is presented in Figure 6.18.

The 1st order north-northeast trending shear zones host arrays of buck quartz-carbonate veins that are right-stepping. They are enclosed by S_2-C to S_2 quartz-chlorite-muscovite ± biotite ± hornblende schist.

The mylonite zones within the 1st order north-northeast trending shears are defined by a mylonitic foliation (S_2-C_{my}) that is penetrative and tight. S_2-C_{my} is defined by glassy quartz ± potash

feldspar ± plagioclase ± cordierite sigma (σ) and delta (δ) porphyroblasts in a glassy quartz ± potash feldspar matrix depending on the rock type. The approximately 80-90% matrix to porphyroblast ratio indicates mylonite to ultramylonite, *sensu stricto* (Sibson, 1977; Killick, 2003; Vernon, 2004). The stretching mineral lineation, L_{2my} is resolved by hornblende ± potash feldspar ± plagioclase ± rodded quartz which are flattened and boudinaged/mullionaged. Domain analysis of the mylonite zones has shown that,

(1) North-northeast trending mylonite zones have a calculated mean principal orientation of S_2-C of 031°/81° E (Figure 6.15a), and L_{2my} of 76°→106° (Figure 6.15b). The spread of the data around the primitive circle on equal area stereographic projections could be due to;

(a) The sigmoidal shape of the plane across the length of the plane and a down dip.

(b) Variation in the strike and dip of S_2-C_{my} across the width of the mylonite zone.

S_2-C_{my} shear bands, and potash feldspar, plagioclase, cordierite and quartz sigma (σ) and delta (δ) clasts suggest that displacement was sinistral during D2, with a reverse component and east block up (EBU).

(2) East-northeast trending mylonite zones are complex. Adjacent to the MSZ the mylonites are strongly affected by sinistral displacement on the MSZ and are purely strike-slip with a calculated average L_{2my} of 9°→056° (Figure 6.16a). Distal to the MSZ (15 kms) the dip of the plane of the mylonite flattens to form a north dipping thrust plane with north block up, and a mean calculated stretching lineation of L_{2my} of 59°→316° (Figure 6.16b). In the distal position S_2-C_{my} has a calculated mean principal orientation of 060°/64° N (Figure 6.16c). The spread of the data around the primitive circle could be due to;

(a) Variation in the strike and dip of S_2-C_{my} across the width of the mylonite.

(b) The sigmoidal shape of the plane across the length of the mylonite zone and down dip variation.

(c) Folding along west-northwest trending fold axes in D3 (Section 6.5.4).

In summary, the sense of displacement on the east-northeast trending mylonites, as determined from δ and σ quartz and potash feldspar clasts, S_2-C_{my} shear bands, and L_{2my} lineation, indicates a reverse displacement with north block up (NBU) distal to the MSZ, and a dextral strike-slip component adjacent to the MSZ, during an interpreted southeast-northwest directed palaeo-compressive stress, with tectonic transport towards the southeast.

Distal to the north-northeast and east-northeast trending mylonite zones in the GGGT, D2 is characterized by the formation of;

(1) A regional northeast to east-northeast trending crenulating and disjunctive S_2-C cleavage (Figure 6.17a).

(2) North-northeast trending faults with fault planes that are chloritized and potassically altered (Figure 6.17b).

(3) Northeast trending boudinaged mafic xenoliths in granodiorite (Figure 6.17c).

(4) Sigmoidal en-echelon (V_2) quartz-carbonate veins which step right and crosscut S_1-C. Displacement along the plane of V_2 was sinistral during vein formation (Figure 6.17d).

(5) Isoclinally folded V_1 quartz-carbonate veins with north-northeast trending fold axes (F_2). F_2 plunges towards the north-northeast (Figure 6.17e).

In summary, D2 brittle-(ductile) deformation in the GGGT is characterized by sinistral (reverse) displacement and reactivation along the 1st order north-northeast trending domain, within which it is possible to define a reverse-oblique and dextral strike-slip displacement/reactivation along east-northeast trending mylonite zones and faults, formation of a crenulating to disjunctive S_2-C to S_2 foliation, and a dominantly northwest plunging L_2 lineation. These suggest that the palaeo-principal compressive stress may have been southeast-northwest directed, with overall tectonic transport towards the southeast during D2.

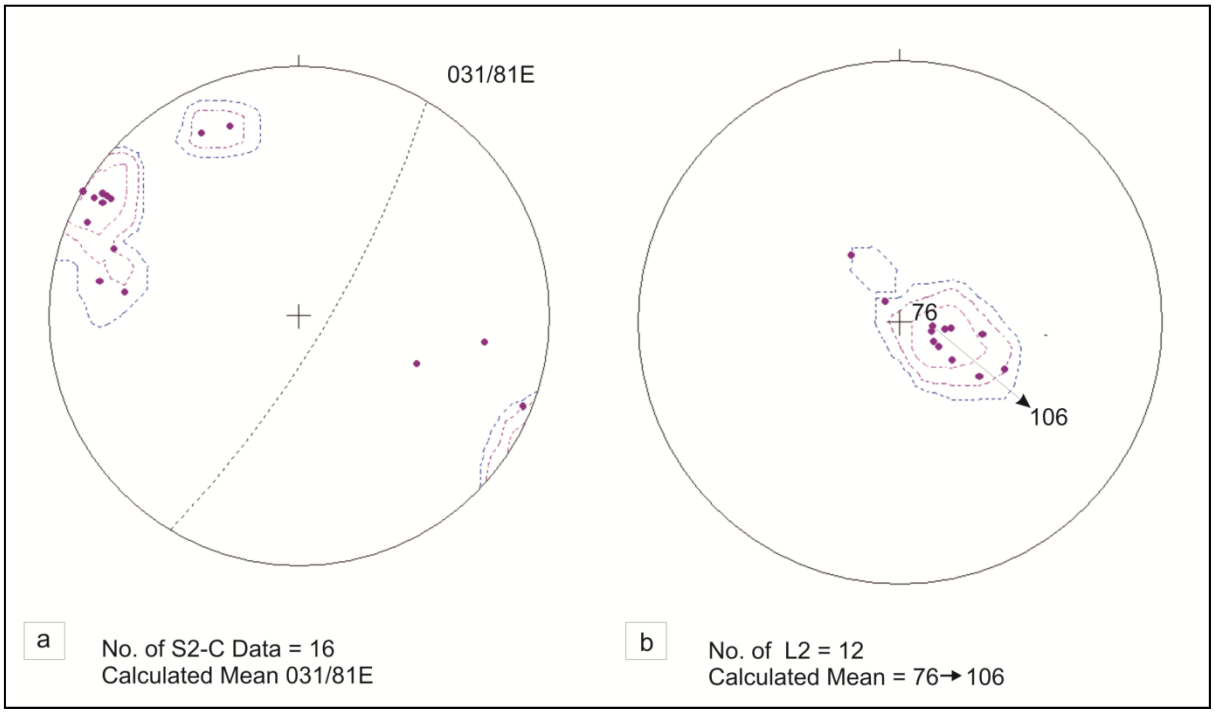

Figure 6.15: Equal area stereographic projection of poles and contour plot of D2 mylonitic foliation and lineation data measured along the mylonite zones. (a) North-northeast trending mylonite zones in the GGGT have a calculated mean principal orientation of 031°/81° E. (b) The mineral lineation data has a mean principal direction of L_{2my} of 76°→106°.

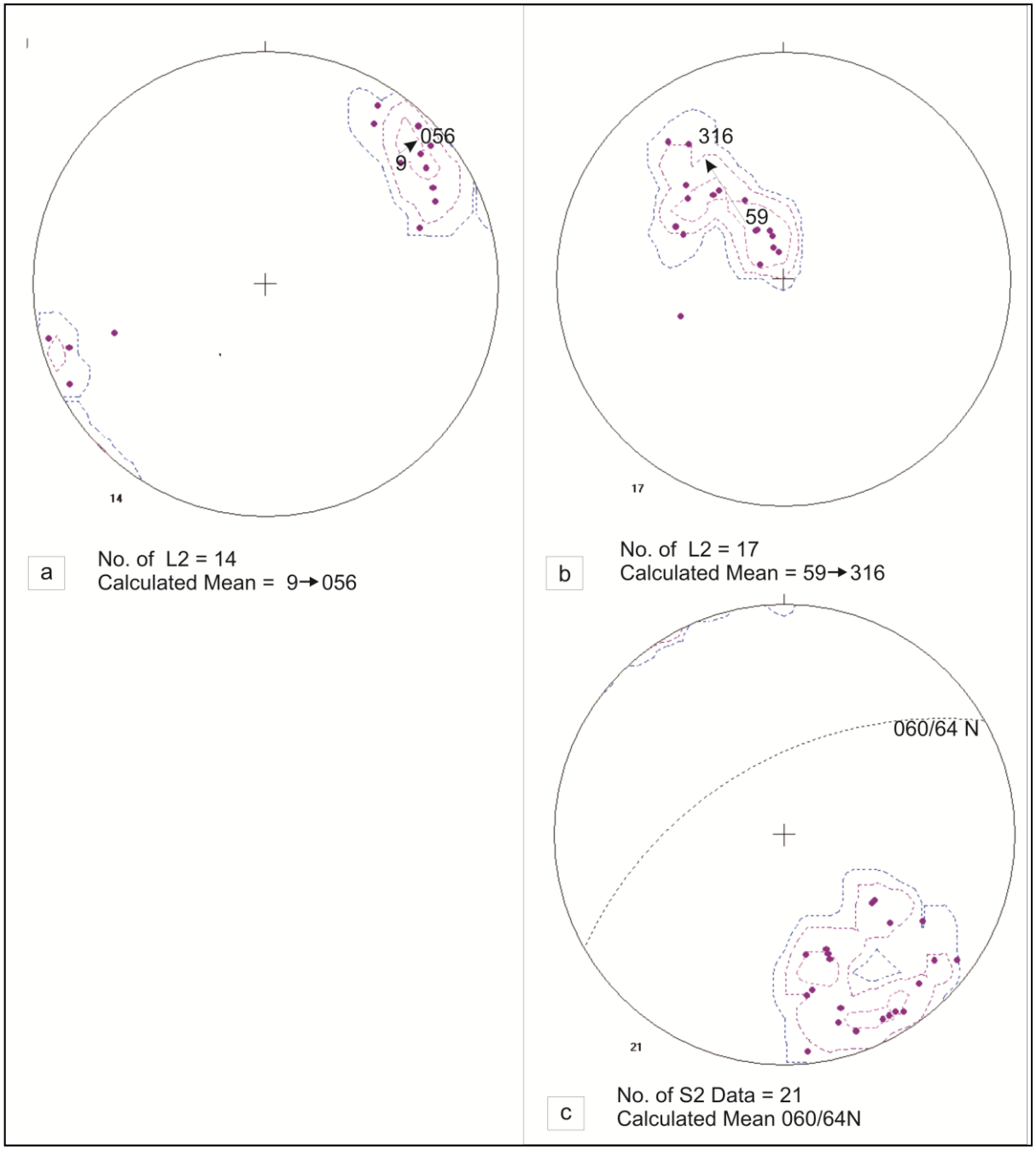

Figure 6.16: Equal area stereographic projection of poles and contour plot of D2 mylonitic foliation and lineation data measured along the mylonite zones. (a) East-northeast L_{2my} adjacent to the MSZ with a calculated average of 9°→056°. (b) Mean calculated stretching lineation L_{2my} with a mean principal direction of 59°→316° distal to the MSZ. (c) S_2-C_{my} of east-northeast trending mylonite zones has a calculated mean principal orientation of 060°/64° N.

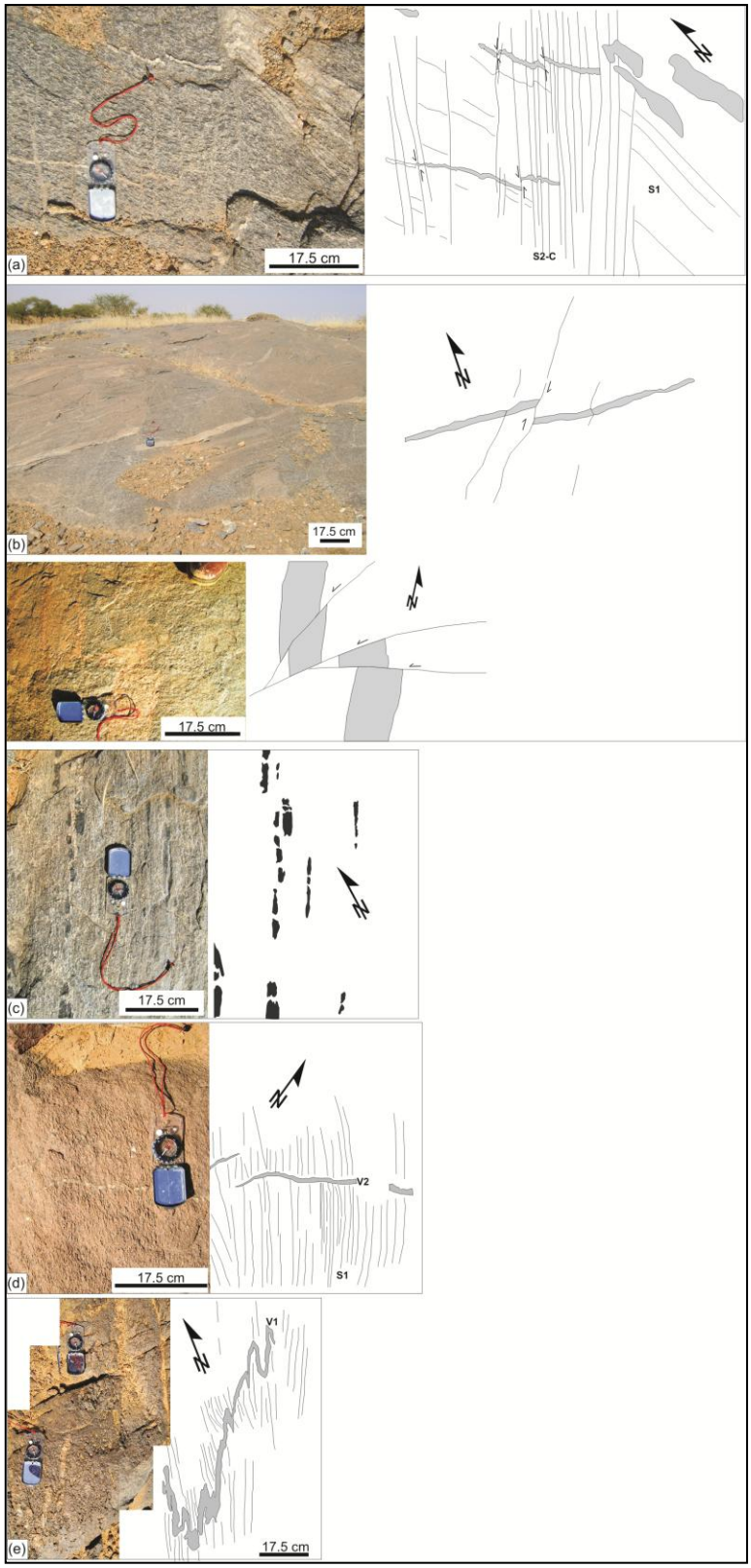

Figure 6.17: Distal to the mylonite zones in the GGGT, D2 is associated with the formation of, (a) Northeast to east-northeast trending crenulating and disjunctive regional S_2-C cleavage. (b) North-northeast trending faults with fault planes that are chloritized. (c) Northeast trending boudinaged mafic xenoliths in granodiorite. (d) Sigmoidal en-echelon (V_2) quartz-carbonate veins which step right and crosscut S_1-C. (e) Isoclinally folded V_1 quartz-carbonate veins with north-northeast trending fold axes (F_2).

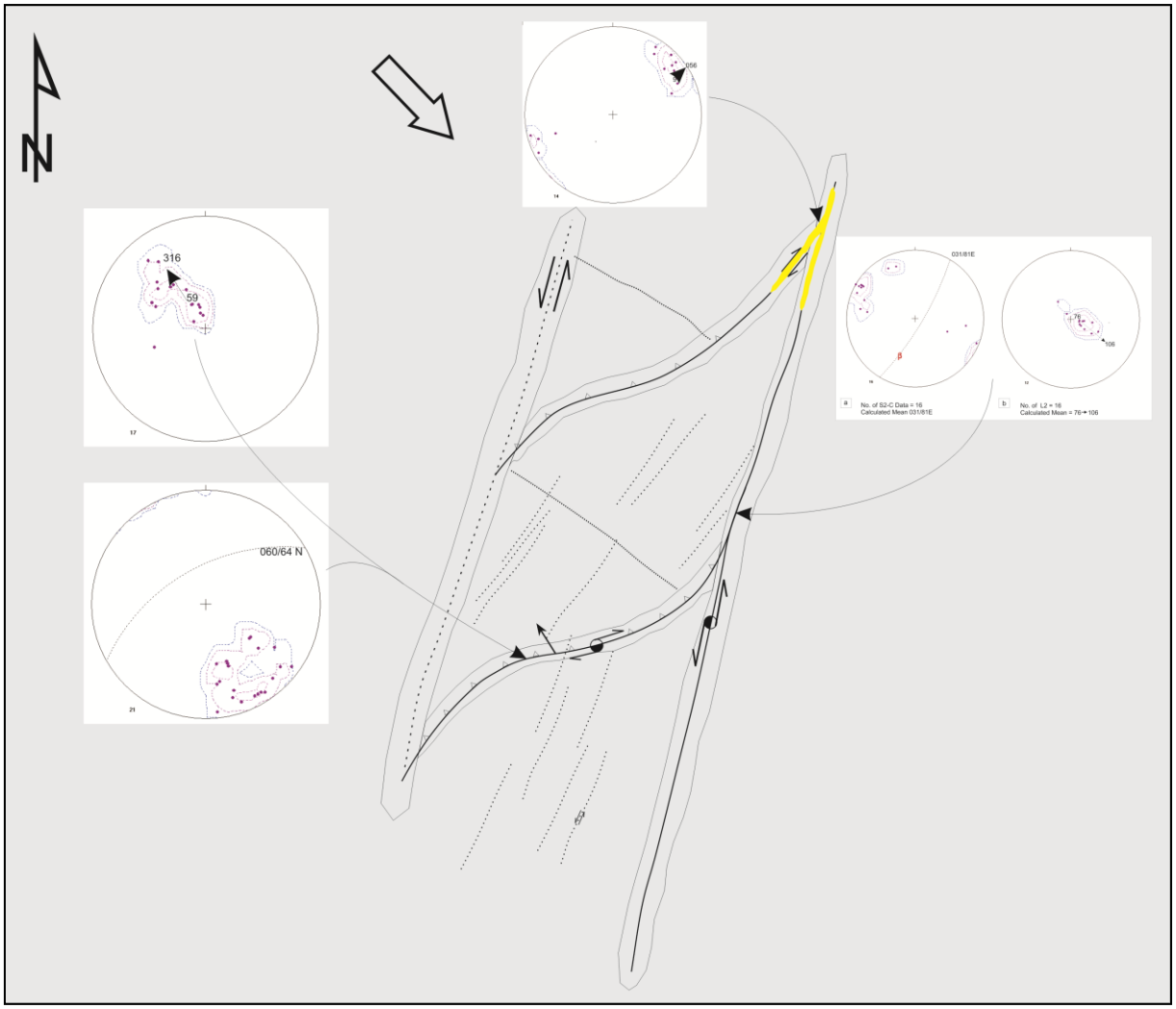

Figure 6.18: The schematic summary of the overall tectonics during D2 deformation, depicting the structures that were reactivated or formed during D2 deformation. The tectonic transport direction in D2 was towards the southwest. Yellow lines are indicating the mylonite zone.

6.5.4. D3 Deformation

The D3 deformation in the GGGT is brittle in character, and characterized by the formation of a west-northwest trending fracture cleavage (S_3) and conjugate fault sets. S_3 is defined by a pervasive and parallel set of close spaced fractures that crosscut the D1 and D2 mylonite-ultramylonite zones (Figure 6.19). The sense of displacement along the conjugate sets of faults is dextral strike-slip on east-northeast trending faults and sinistral strike-slip on west-northwest trending faults. These suggest that the palaeo-principal compressive stress may have been equally directed to the north and south (north-south shortening) during D3.

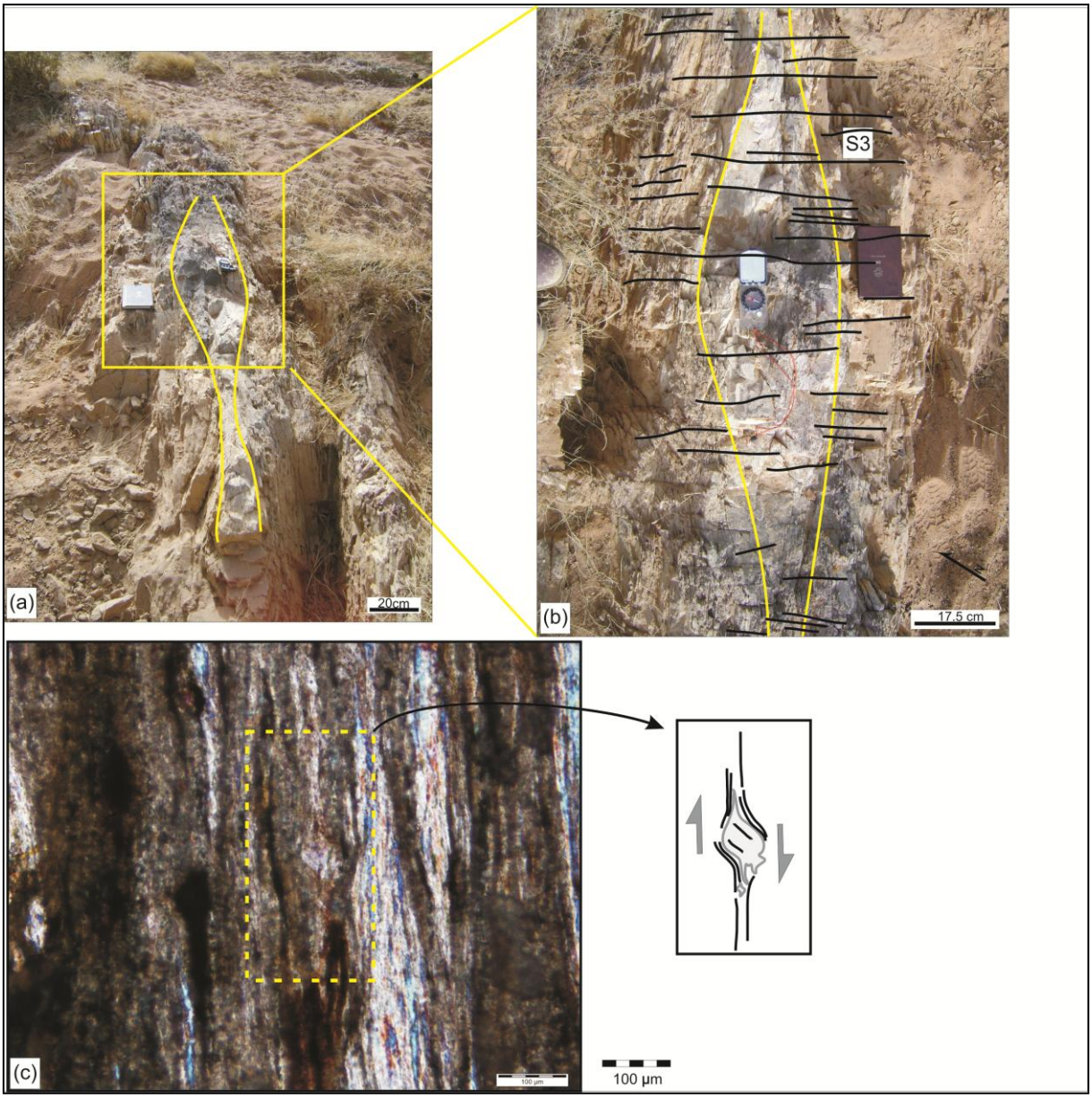

Figure 6.19: Photographs of the well exposed boudinage along the Sabce ultra-mylonite Zone. (a and b) The plan view of a boudin enclosed by S_1 and S_2 along the Sabce ultra-mylonite Zone that is later crosscut by S_3 foliation UTM 30P 0794388, 1593212). (c) A photomicrograph the ultra-mylonite under crossed polarized light. The potash feldspar sigma clast exhibits dextral displacement in polished thin section scale during D2.

6.6. Metamorphism

Regional metamorphic grade across the GGGT varies in a complex way. Metamorphic grade is granulite facies to lower amphibolite facies across the GGGT. The metamorphic assemblages in the Lilengo gneiss complex are dominated by gneissosity of re-crystallized quartz, plagioclase ± potash feldspar (orthoclase) ± hornblende ± biotite ± garnet and ± magnetite.

The metasedimentary rocks at Billiata region host andalusite crystals with sillimanite cores that indicate high P-T conditions where sillimanite and andalusite were stable, that is approximately 3.5 Kbar and 500°C, or upper greenschist to amphibolite (Holdaway, 1971; Pattison, 1992; Blatt et al.,

2006) (Figure 6.20a, b). This mineral assemblage implies high grade metamorphic facies conditions existed in the Billiata region.

Elsewhere in the GGGT the metamorphic grade attained upper greenschist to amphibolite facies especially in the Kel-Enguef metamorphic belt with mineral assemblages of hornblende, biotite, carbonate, quartz, albite, and muscovite, which are overprinted by epidote, sericite, chlorite greenschist mineral assemblages.

Metamorphic grade attained amphibolite-granulite facies in mylonite to ultramylonite zones, and attained granulite facies in the Lilengo gneiss complex.

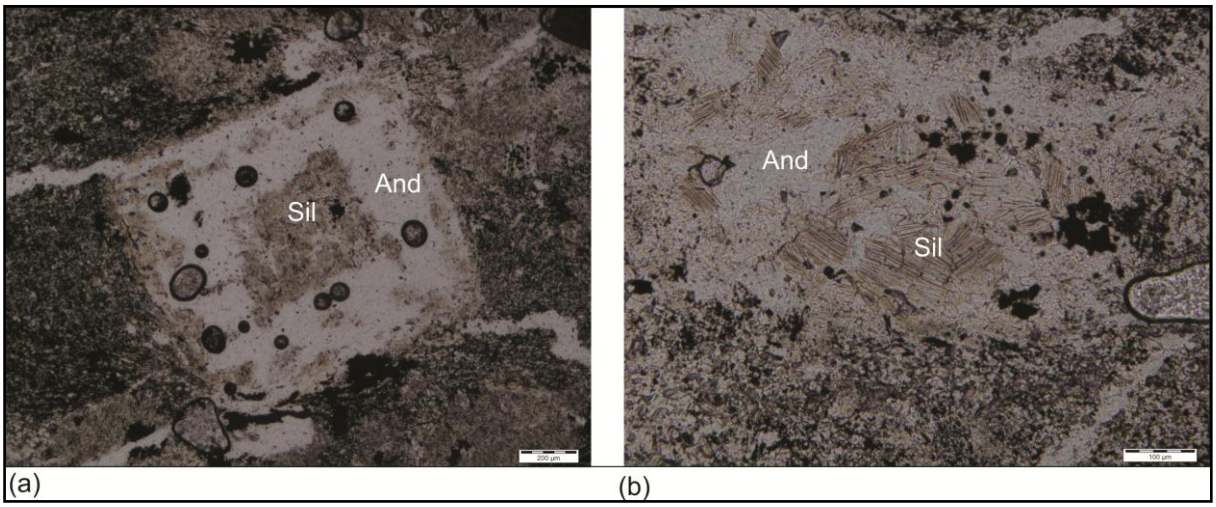

Figure 6.20: A photomicrograph of the andalusite (And) and sillimanite (Sil) porphyroblasts from manganese rich shale at Billiata under crossed polarized light. (a) The core of the andalusite is made up of sillimanite crystals and the marginal rims are andalusite with minor clusters of inclusions of sillimanite. (b) The inclusions of sillimanite crystals occur within the andalusite porphyroblast indicating that the P-T conditions reached sillimanite and andalusite stability field.

6.7. Tectonic history of the Gorom-Gorom granitoid terrane

The tectonic history of the GGGT records an interrelationship between several phases of pluton emplacement, and several structural events in which at least 3 unique regional deformation events were recorded, i.e., D1, D2 and D3. Six phases of plutonic emplacement are recognized. The phases have been described as follows: (1) Mrs Pink granite, (2) granodiorite-tonalite with hornblende phenocrysts and mafic xenoliths, (3), a second phase of granodiorite, (4) Gabbro-pyroxenite dykes, (5) Aplite-granite dykes, (6) Dolerite dykes.

The relative timing of geological events as established from crosscutting relationships in the GGGT is summarised in Figure 6.21 and includes:

(1) The Lilengo gneiss complex with migmatites is expressed by partial melting and recrystallisation. The metamorphic conditions attained granulite facies.

An angular unconformity exists between the Lilengo gneiss complex and the Birimian Supergroup indicating that uplift and erosion took place at some stage prior to deposition of the Birimian Supergroup. The depositions of the metasedimentary units (greywacke, siltstone-shale and chemical sedimentary rock) were deposited on the angular unconformity.

(2) The emplacement of the Mrs Pink granite, hornblende-bearing granodiorite and crosscutting pyroxenite and gabbro dykes.

The Mrs Pink granite is intruded by the hornblende-bearing granodiorite tonalite.

(3) D1 ductile-brittle deformation in the GGGT is characterized by a dextral (reverse) displacement along a 1st order domain, within which it is possible to define, (1) reverse (dextral) displacement along northwest trending mylonite zones and faults, and north-northeast trending mylonite zones, (3) sinistral strike-slip to oblique displacement on east-northeast trending mylonite zones, (4) a penetrative regular northeast plunging lineation, (5) a penetrative northwest trending S_1-C to S_1 foliation, and (6) a quartz-carbonate vein array. These suggest that the palaeo-principal compressive stress may have been southwest directed during D1.

(4) D1 deformation was followed by the emplacement of the equigranular granodiorite pluton and pegmatites.

(5) D2 brittle-(ductile) deformation in the GGGT is characterized by sinistral (reverse) displacement and reactivation along the 1st order north-northeast trending domain, within which it is possible to define a reverse-oblique and dextral strike-slip displacement/reactivation along east-northeast trending mylonite zones and faults, formation of a crenulating to disjunctive S_2-C to S_2 foliation, and a dominantly northwest plunging L_2 lineation. These suggest that the palaeo-principal compressive stress may have been directed to the southeast during D2.

(6) The D2 event was followed by emplacement of granodiorite, pegmatite, and aplite-granite.

(7) The D3 deformation: The D3 deformation in the GGGT is brittle in character, and associated with the formation of west-northwest trending fracture cleavage (S_3) and conjugate fault sets.

(8) The D3 deformation was followed by the intrusion of west-northwest trending dolerite dykes.

The transition from D1 (brittle-ductile) to D2 (brittle-(ductile) to D3 (brittle) suggest a progressive exhumation of the terrane.

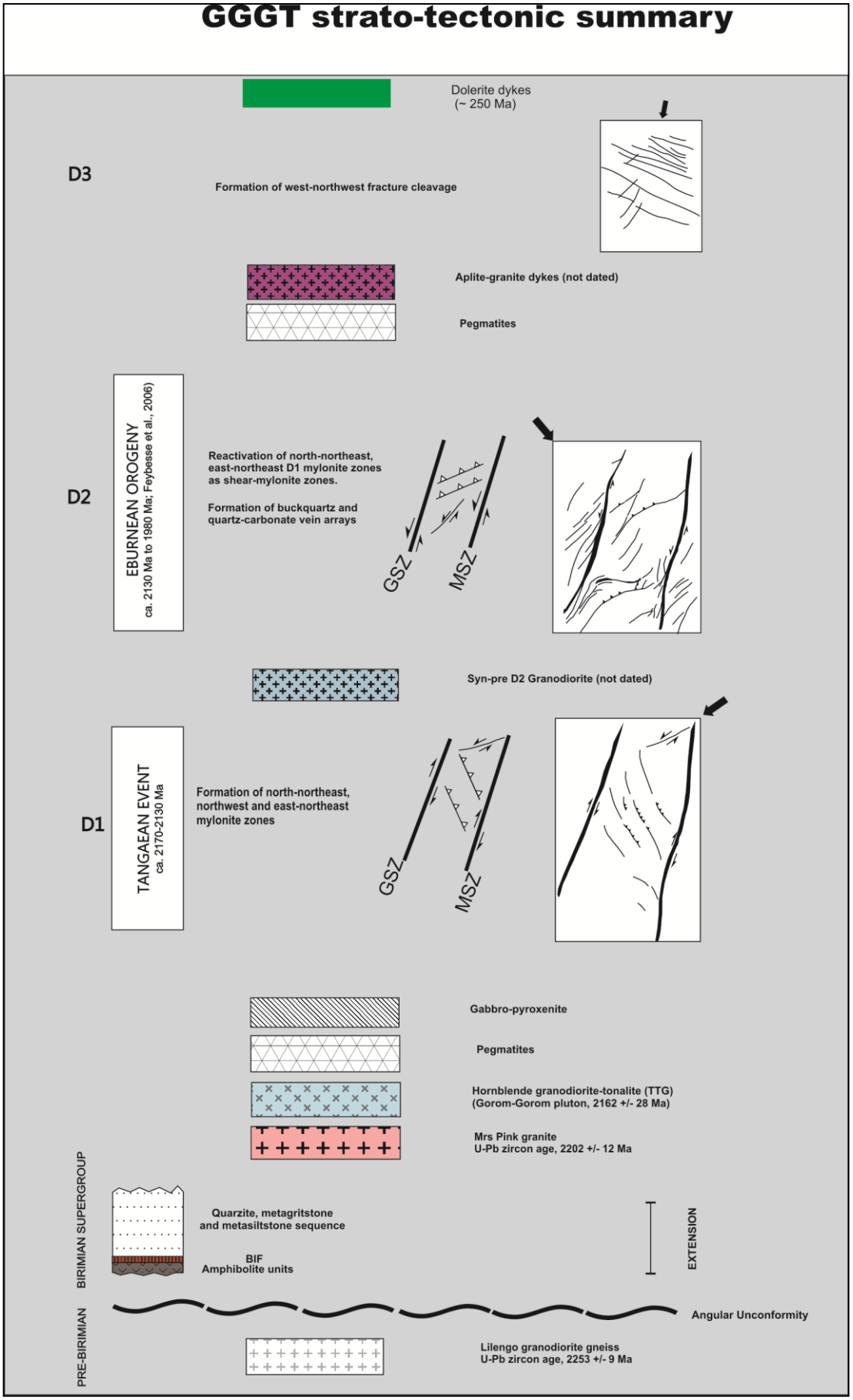

Figure 6.21: Schematic strato-tectonic summary of the GGGT.

CHAPTER 7
GEOCHEMISTRY AND GEOCHRONOLOGY

7.1. Preamble

Parts of Chapter 7 were published under the reference: "*Tshibubudze, A., Hein, K.A.A., Peters, L.F.H., Woolfe, A.J., McCuaig, T.C., 2013 'Oldest U-Pb crystallisation age for the West African Craton from the Oudalan-Gorouol belt of Burkina Faso' South African Journal of Geology 116, 169-181"* which is presented in the Appendix D.

7.2. Introduction

In polyphase metamorphic terranes of any age, relative chronological studies coupled with isotopic dating can be a reliable source of information regarding the absolute age of geological events. The geochemistry and isotopic ages of selected samples of batholiths, plutons, dykes and sills related to crystallisation, metamorphism, mineralisation and deformation periods have been published for the WAC by Hirdes et al. (1987, 1992, 1996), Milési et al. (1989), Leube et al. (1990), Léger et al. (1992), Davis et al. (1994), Pons et al. (1995), Bossière et al. (1996), Hirdes and Davis, (1998, 2002), Oberthür et al. (1998), Egal et al. (2002), Castaing et al. (2003), Dioh et al. (2006), Feybesse et al. (2006), De Kock et al. (2011, 2012) and Tapsoba et al. (2013a, 2013b); in contrast, no ages have been reported for the OGB and GGGT. It is for this reason that a suite of samples were chosen from the field specifically to provide information about crystallisation ages, timing of structural events, metamorphism and mineralisation (Figure 7.1). The principal aim of conducting absolute geochronology was to constrain the relative chronologies established from integrated field studies, as reported in Chapters 5 and 6. U-Pb geochronology was conducted on zircons from samples of Lilengo gneiss complex, Mrs Pink granite, Gorom-Gorom granodiorite pluton, porphyritic monzodiorite, Dori granodiorite pluton, migmatitic gneiss, porphyritic granodiorite, and the Tin-Taradat pluton.

In most geochronological studies undertaken on rocks from the West African Craton (WAC), the oldest U-Pb and Pb-Pb ages are reported as inherited zircon ages. They include reports by: (1) Gasquet et al. (2003) from the Dabakala tonalite (Côte d'lvoire) at 2312 ± 17 Ma, (2) Thomas et al. (2009) from the Gondo granite gneiss in Ghana at 2876 Ma, (3) Siegfried et al. (2009) from the Ifantayire granite gneiss in Ghana at 2386 and 2258 Ma, and (4) De Kock et al. (2009) from the Bomburi granodiorite in Ghana at 2227 Ma. The oldest U-Pb crystallisation ages reported include: (1) in Burkina Faso from a rhyolitic tuff in the Goren greenstone belt at 2238 ± 5 Ma (Castaing et al., 2003) and; (2) in Ghana from a gabbro unit in the Sefwi belt at 2222 ± 32 Ma (K-Ar age) (Feybesse et al., 2006). However, the results from the OGB and GGGT gave some of the oldest crystallisation ages

yet recorded in the WAC (Tshibubudze et al., 2013; Appendix D) and combined with relative chronological studies, constrain the tectonic evolution of the OGB and GGGT.

The OGB and GGGT in the northeast of Burkina Faso (Figure 7.1) hosts metamorphosed volcanic and sedimentary sequences of the Birimian Supergroup that were folded and deformed concomitant to emplacement of a suite of tonalite-trondhjemite-granodiorite (TTG) granitoids (Chapter 5 and 6; Tshibubudze and Hein, 2013). Studies by Tshibubudze et al. (2009), Tshibubudze and Hein (2010; 2013), Peters (2011) and Woolfe (2011) in the OGB and GGGT have constrained the relative chronology of key units. Relative chronologies have established that;

- The Lilengo gneiss complex and the Mrs Pink granite are crosscut by D1 and D2 (Chapter 6).
- The sample of the Lilengo gneiss complex constrains the maximum age of D1 (Chapter 6).
- The sample of migmatitic gneiss in the Lilengo gneiss, constrains the maximum age of metamorphism related to partial melting. It also constrains the maximum age of deposition of the Birimian Supergroup in the Kel Enguef metamorphic belt (Chapter 6).
- The granite clast from the metaconglomerate unit of the Dembam Member (Peters, 2011, Tshibubudze et al., 2013; Appendix D) constrains the age of a possible eroded protolith, and thus provides a provenance age, but limits the age of deposition to the age of the granite clast.
- The Mrs Pink granite is intruded by the Tin-Taradat granodiorite and both are crosscut by the MSZ (Chapter 5). The Mrs Pink granite sample constrains the maximum age of the Tin-Taradat granodiorite and the crystallisation age of Mrs Pink granite. Several samples of the Mrs Pink granite were collected for geochemical analyses.
- The age of Tin-Taradat granodiorite pluton constrains the maximum age of the MSZ. The Tin-Taradat granodiorite is crosscut by structures that host gold mineralization (Chapter 5, Appendix B). The sample of the Tin-Taradat granodiorite constrains the maximum age of gold mineralization.
- The sample of the Gorom-Gorom granodiorite which intrudes the Lilengo gneiss complex and is crosscut by the MSZ, constrains the minimum age of the gneiss and the crystallisation age of the Gorom-Gorom granodiorite.
- The sample of the Dori granodiorite gneiss which intrudes the metavolcanic and metasedimentary units in the OGB, constrains the crystallisation age of the batholith and the minimum age of the metavolcanic sequences.
- The porphyritic granodiorite and the porphyritic monzonite intrudes the metasedimentary units. They are folded along F_2 northeast and F_1 northwest trending axes. The samples of porphyritic granodiorite constrains F_2 and F_1 (thus D2 and D1). Gold mineralization is hosted in quartz veins in porphyritic monzonite ; the age of the monzonite constrains maximum age of gold mineralization.

The whole rock geochemical analyses, results and diagrams are given in Appendix I. The results include the ICP-MS and XRF data. The diagrams include the TAS, R1-R2, and tectono-magmatic discrimination diagrams.

7.3. Methodology

The samples selected for geochronological study were collected where the geology was well understood, and a relative chronology of structural events had been established. Zircon extraction and mounting were undertaken at the EarthLab at the University of the Witwatersrand Johannesburg in South Africa. A representative sample was collected from each crushed sample for ICP-MS and XRF analysis. Cathodoluminescence (CL) and backscattered-electron (BSE) imaging using the scanning electron microscope (JEOL JSM 6400), were conducted at the Centre for Microscopy, Characterisation and Analysis at the University of Western Australia. Ion microprobe analyses were completed using the SHRIMP II (John de Laetre Laboratory) at the Curtin University of Technology in Western Australia. Details of the extraction process, imaging, zircon analysis and data processing are detailed in Section 3.4.

The SHRIMP U-Pb zircon data were reduced using the SQUID 2.50® (Ludwig, 2009) and Isoplot 3.00® softwares (Ludwig, 2003), with Microsoft Excel macro add-ins. U-Pb data were plotted using the normal Wetherill Concordia-Discordia diagram option in Isoplot 3.00®.

The geochemical classification and nomenclature of samples BF_1144, BF_1146, BF_1147, BF_1149, BF_1153, BF_1156, BF_1157, BF_1332, BF_1368 and BF_1369 used the total alkali versus silica (TAS) by Middlemost (1994) after Cox et al. (1979), and Wilson (1989). Sample BF_1299 was excluded from the classification because it is the product of partial melting.

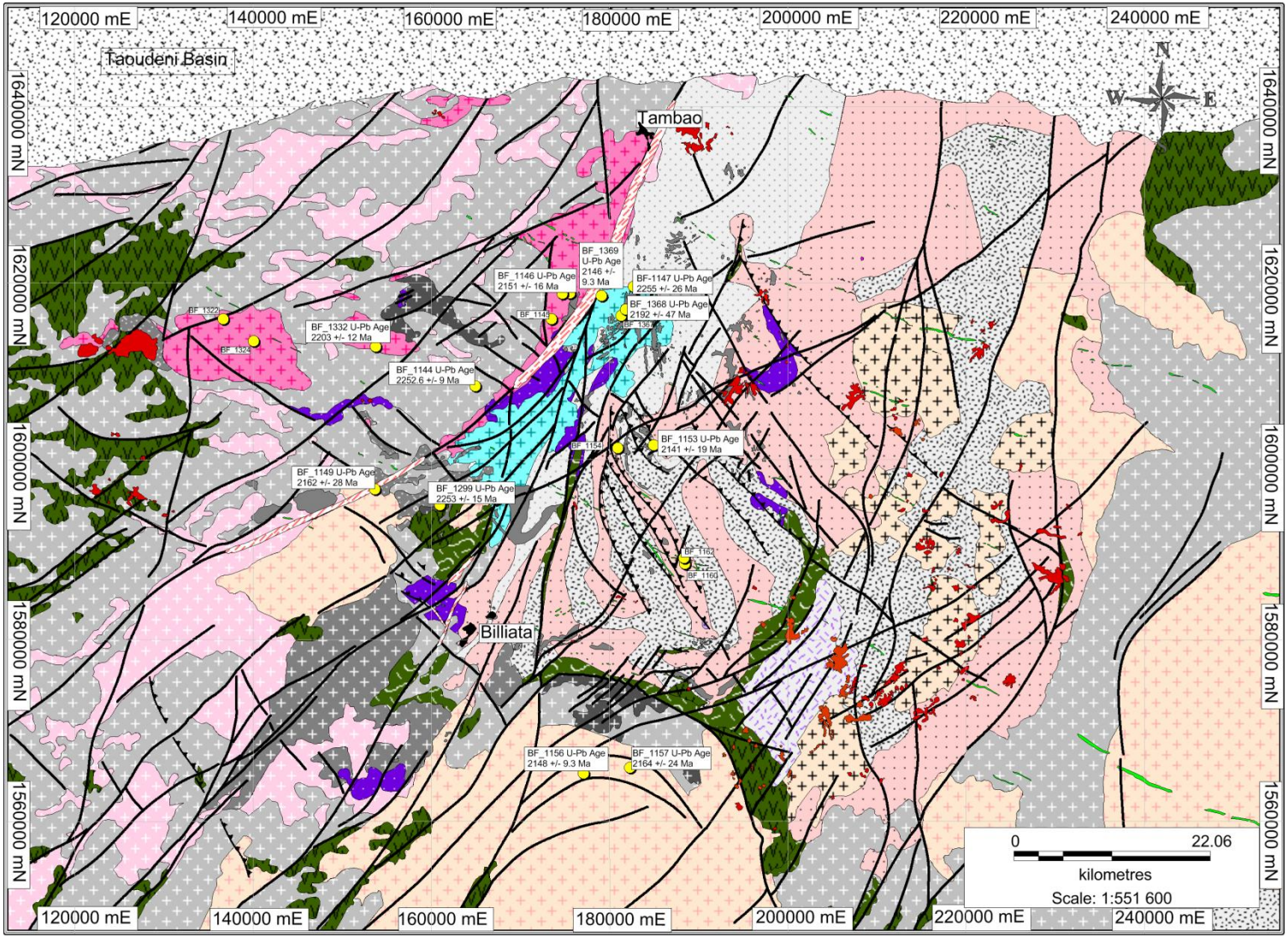

Figure 7.1: Geology map of the study area with sample location for the analysed samples (yellow dots and age boxes). Several other yellow dots are locations points of the several samples collected during the study.

7.4. Characteristics of sample, U-Pb zircon data and age constraints

7.4.1. Sample BF_1144 - Lilengo Gneiss Complex

The Lilengo gneiss (Figures 7.2a, b) crops out northeast of the town of Gorom-Gorom at UTM 30P 1608135 0811742. It has well-defined leucocratic and melanocratic layers. The melanocratic layers are dominated by hornblende, biotite (with a preferred orientation) and magnetite, while the leucocratic layers are dominated by plagioclase, potassium feldspar and quartz (Figure 7.2b). The quartz crystals exhibit undulose extinction. Accessory crystals of apatite and zircon are hosted within, and interstitial to, hornblende and plagioclase. The Lilengo gneiss is migmatitic in part and exhibits flow folding. It is crosscut by gabbro-pyroxenite dykes.

Geochemically, a whole rock sample of the Lilengo gneiss plots as granodiorite (Appendix K, L) in the acidic magma field (c.f., Middlemost, 1994). The tectono-magmatic discrimination diagram indicates correspondence with volcanic-arc type granitoids (Figure 7.3a, b).

The results of 20 analysed grain spots are summarized in (Table 7.1) and plotted in (Figure 7.2d). Most of the zircons are subhedral to euhedral and exhibit oscillatory zoning around euhedral unzoned cores (Figure 7.2c). The cores were specifically targeted to obtain the crystallisation age. Grain spots 10.1, 11.1, 14.1, and 16.1 in Table 7.1 gave $^{207}Pb/^{206}Pb$ ages of 2276 ± 15, 2284 ± 23, 2277 ± 16 and 2272 ± 33 Ma possibly reflecting the age of the source rocks. The majority of the grain spots define a Pb loss line within error, with a calculated upper intercept age of 2252.6 ± 9.0 Ma (i.e., 2253 ± 9 Ma). This age is interpreted as being the crystallisation age of the magma.

7.4.2. Sample BF_1146 and BF_1332 – Mrs Pink granite

The Mrs Pink granite (Figure 7.4a) crops out southwest of the town of Markoye at UTM 30P 1618845 0822069 (Figure 7.1). The Mrs Pink granite is medium to coarse crystalline and composed of millimetre-sized crystals of potassium feldspar, quartz, plagioclase, biotite and hornblende in a quartz-feldspar rich groundmass. Adjacent to the Markoye Shear Zone the granite is foliated and lineated.

The Mrs Pink granite is crosscut by granodiorite dykes indicating that the granite is older than the granodiorite in the area. The granite is crosscut by pseudotachylite and quartz veins. Petrographically, the Mrs Pink granite sample is composed of re-crystallized quartz, microcline, plagioclase, biotite and aggregates of hornblende (Figure 7.4b).

A geochemical analysis of a whole rock sample of the Mrs Pink granite plots as an alkali-granite in the R1-R2 plutonic chemical variation diagram (c.f., De la Roche et al., 1980), and plots as a granite on the TAS diagram (c.f., Middlemost, 1994). The tectono-magmatic discrimination diagram (Figure 7.3a, b) after Pearce et al. (1984) indicates correspondence with within-plate Granitoids (WPG).

The zircons from Sample BF_1146 are typically >50 µm in size and euhedral. They exhibit fine planar zoning. Thirteen zircons were analysed; four zircons were analysed in two spots. The analytical results of 17 analysed grain spots are summarized in Table 7.2 and plotted in Figure 7.4d, e. Most of the zircons exhibited growth rings (Figure 7.4c) and both the cores and the rims were targeted.

Of the four zircons that were analysed in two spots, grain spot 2.1 (core) gave a $^{207}Pb/^{206}Pb$ age of 2172 ± 11 Ma and the rim spot 2.2 gave an age of 2152 ± 12 Ma (Table 7.2). The age of grain spot 2.1 is interpreted as the crystallisation age and 2.2 is interpreted as the new growth age during a metamorphic event. Grain spot 7.1 gave an interpreted crystallisation age of 2141 ± 13 Ma with an interpreted metamorphic age at 2114 ± 9 Ma. Grain spot 12.1 and 12.2 also gave interpreted crystallisation and metamorphic ages at 2127 ± 10 Ma and 2093 ± 14 Ma, respectively. Grain spot 4.1 and 4.2 gave a younger core age of 2126 ± 9 Ma, than a rim age of 2146 ± 11 Ma, possibly indicating recrystallisation of the core (Pidgeon, 1992; Zegers, 1996), or a range of analytical or zircon morphology problems as described by Castiñeiras et al. (2010) and Butera et al. (2001). The analyses were consequently discarded from the age calculation. Grain spot 1.1 gave a concordant $^{207}Pb/^{206}Pb$ age of 2208 ± 28 Ma. The majority of the zircons with single grain spots gave a concordant U-Pb age value with a calculated upper intercept age of 2151 ± 16 Ma on 13 grain spots. The calculated mean age of coherent group of 13 grain spots is 2140.3 ± 9.6 Ma (Figure 7.4e).

Sample BF_1332 of the Mrs Pink granite (Figure 7.5a) was collected at UTM 30P 1612261 0800455 (Figure 7.1) and is foliated. The granite is coarse crystalline and composed of potassium feldspar, quartz, microcline, hornblende, plagioclase and biotite. Petrographically, it is dominated by greater than 1 mm re-crystallized quartz with undulose extinction, microcline, and minor plagioclase, hornblende, opaque minerals, and biotite crystals (Figure 7.5b). Quartz crystals are recrystallized to < 1 mm sub-quartz grains. The groundmass is composed of <1 mm crystals of quartz, microcline, plagioclase, biotite, interstitial chlorite, orthoclase and opaque crystals of magnetite.

Geochemical analysis of Sample BF_1332 of the Mrs Pink granite plots as a diorite in the R1-R2 plutonic chemical variation diagram (c.f., De la Roche et al, 1980), and as a gabbro on the TAS diagram (c.f., Middlemost, 1994). The tectono-magmatic discrimination diagram (Figure 7.3a, b) after Pearce et al. (1984) indicates correspondence with volcanic-arc type granitoids. Samples BF_1145, BF_1146, BF 1322, BF_1324 and BF_1333 plot as granites and have high silica content compared to sample BF_1332.

The results of 23 analysed grain spots are summarized in Table 7.3 and plotted in Figure 7.5d. 21 zircons were analysed and two of this were analysed in two spots. The data suggests that there is lead loss and gain along the regression line. Most of the zircons are euhedral and have irregular growth rings patterns (Figure 7.5c) and are > 70 µm in size. Both the cores and the rims were targeted to obtain the interpreted crystallisation and metamorphic ages.

Grain spot (Table 7.3) 16.1 (core) gave a concordant crystallisation $^{207}Pb/^{206}Pb$ age of 2210 ± 5 Ma, and the rim spot 16.2 gave a metamorphic age of 2153 ± 6 Ma. Grain spot 6.1 gave the oldest

$^{207}Pb/^{206}Pb$ age at 2247 ± 19 Ma. The youngest age from grain spot 1.1 is unreliable due to high concentration of radiogenic Pb. The majority of the grain spots gave a concordant U-Pb age values with a calculated upper intercept age of 2203 ± 12 Ma and lower intercept at 512 ± 54 Ma.

The geochemical analysis of sample BF_1332 does not correspond to the petrographic description of BF_1332. The age constrains for the Mrs Pink granite needs further constrains with another sample to clarify the age of BF_1332. However the age of BF_1332 could also represent the age of early diorite and this could explain the age difference between the two samples analysed (BF_1146 and BF_1332).

7.4.3. Sample BF_1147 – Granite

Sample BF_1147 is of a granite (*sensu stricto*) boulder that was extracted as an entity from a polymictic conglomerate (the Dembam Member) that forms a marker bed within a 4.5 km thick sequence of greywacke beds east of the village of Markoye at UTM 31P 1619591 0182783. The Dembam Member occupies a position at the top of the stratigraphy of the OGB (Tshibubudze et al., 2009; Peters, 2011; Tshibubudze and Hein, 2013). The matrix-supported polymictic pebble-cobble boulder conglomerate (Figure 7.6a) is approximately 10 m thick. Pebbles, cobbles and boulders are sub-angular to sub-rounded and cemented in a cross-bedded matrix of poorly sorted and coarse-grained greywacke. The pebbles, cobbles and boulders making up the conglomerate include fuchsitic chert, black chert, granodiorite (*sensu-stricto*), granite (*sensu-stricto*), gabbro, basalt, andesite, vein-quartz, finely laminated sandstone interbedded with mudstone that host small-scale slump folds, and quartz-rich and volcaniclastic metasediments. The size and sub-rounded form of the pebbles, cobbles and boulders, and the poor sorting of the Dembam Member suggests that the site of deposition sourced rocks from nearby.

The granite boulder extracted from the Dembam Member is composed of coarse crystals of quartz, plagioclase, potash feldspar and chlorite. The potash feldspar is more dominant than the plagioclase, making up more than 45% of the sample.

Petrographically, the granite clast consists of coarse crystals of highly altered plagioclase, re-crystallized quartz that exhibits undulose extinction, albite, chlorite, altered microcline and ~2mm size orthoclase crystals (Figure 7.6b). Hornblende and opaque (magnetite) crystals make up less than 2 % of the groundmass.

Geochemically, Sample BF_1147 plots as granite and in the acidic magma field (c.f., Middlemost, 1994). The tectono-magmatic discrimination diagram after Pearce et al. (1984) indicates correspondence with volcanic-arc type granites.

The data of 20 analysed grain spots of zircons (Figure 7.6c) from sample BF_1147 are summarized in Table 7.4 and the data are plotted in Figure 7.6d. Most of the zircons exhibit oscillatory zoning (but not all), and they are subhedral in shape (Figure 7.6c). The cores of the zircons were targeted. Grain spot 18.1 (Table 7.4) gave a 2% discordant $^{207}Pb/^{206}Pb$ age of 2326 ± 21 Ma reflecting

the age of the source rocks. Grain spot 5.1 gave a 2% discordant $^{207}Pb/^{206}Pb$ age of 2160 ± 12 Ma which is younger than all the other grain spots reflecting an event which might have resulted in Pb loss. The majority of the zircons gave similar $^{207}Pb/^{206}Pb$ ages. The distribution along the regression curve indicated lead loss at 2195-2147 Ma and 2101-1934 Ma with a calculated upper intercept U-Pb age of 2255 ± 26 Ma and lower calculated intercept age of 556 ± 120 Ma.

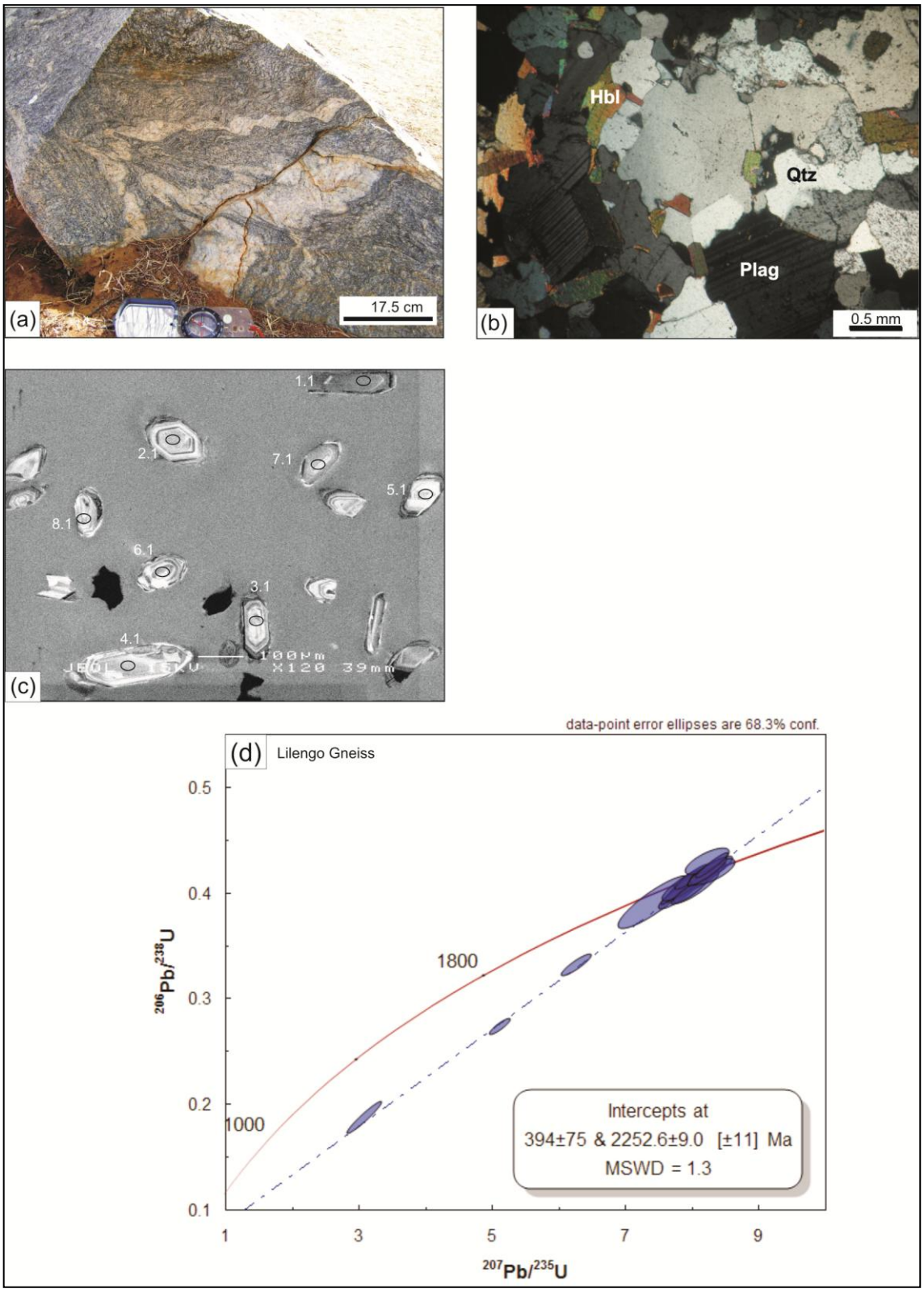

Figure 7.2: (a) Granodiorite gneiss with folded leucocratic layers that are dominated by plagioclase and quartz minerals (UTM, 30P 1608135, 0811742). (b) Photomicrograph of the sample BF-1144, (Hbl = hornblende, Qtz = quartz, Plag = plagioclase crystals). (c) Cathodoluminesence images of zircon crystals that were analysed, they have well defined cores and rims, the cores were targeted. Numbers refers to the grain number in Table 7.1. Ellipses mark the location of the analysed spots. (d) The U-Pb Concordia diagram of the data points of the granodiorite gneiss.

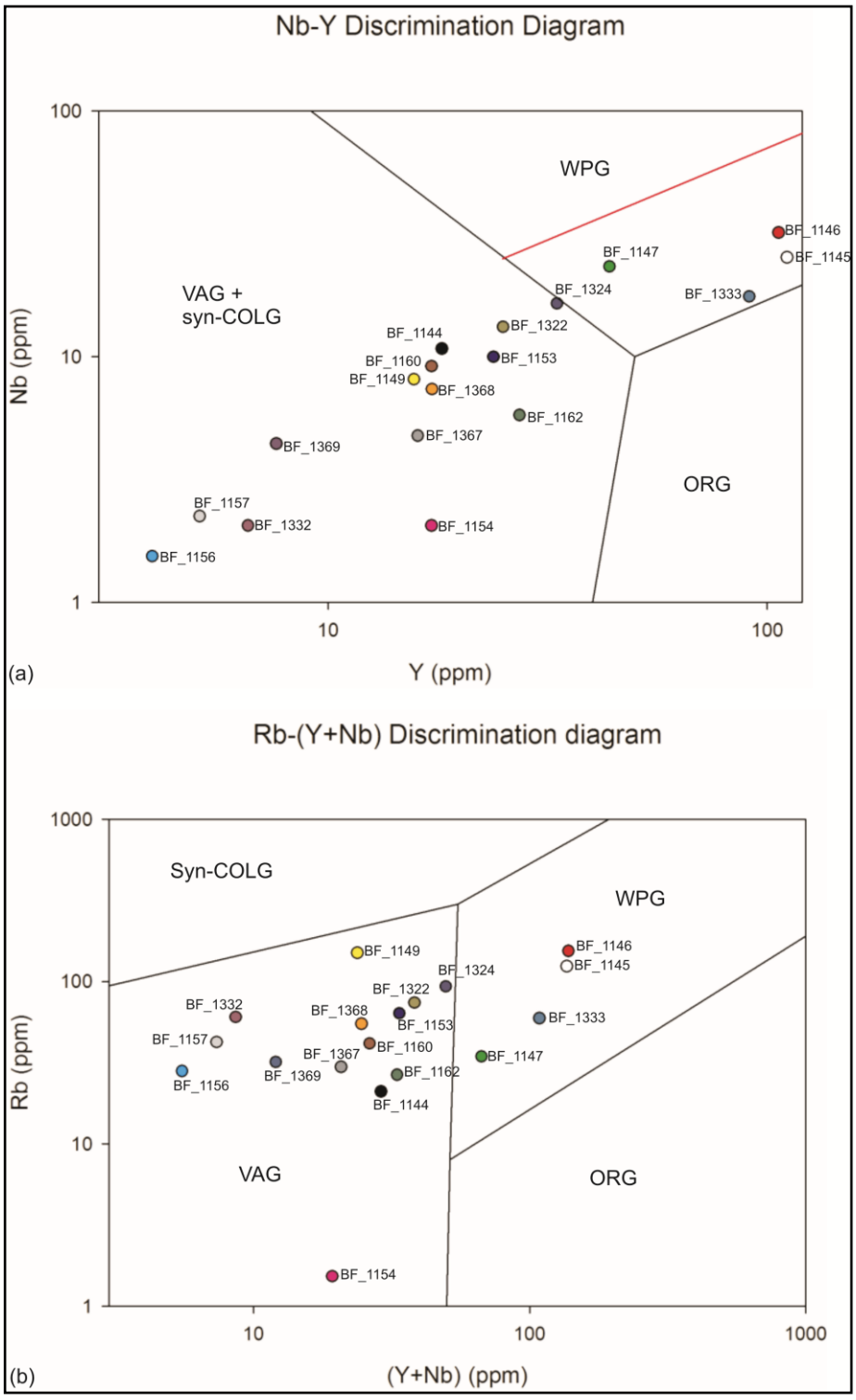

Figure 7.3: Tectono-magmatic discrimination diagrams for granitoids (a) Nb-Y granite discrimination diagram showing the fields of volcanic arc (VAG), syn-collisional (syn-COLG), within plate (WPG), and ocean ridge (ORG) granites, red line is the boundary for ORG from anomalous ridges after Pearce

et al. (1984). The diagram does not discriminate between syn-collisional and volcanic-arc granites and hence diagram (b) was also plotted. (b) Rb-(Y+Nb) tectono-magmatic discrimination diagram for granitoids sampled and aliased for geochemical composition and geochronology. The Rb-(Y+Nb) tectono-magmatic discrimination diagram discriminates between syn-collisional and volcanic-arc granites.

Table 7.1: Summary of SHRIMP U-Pb zircon data, sample BF_1144.

Summary of SHRIMP U-Pb zircon data, sample BF_1144_Lilengo gneiss																			
Grain spot	% $^{206}Pb_c$	U (ppm)	Th (ppm)	$^{232}Th/^{238}U$	$^{206}Pb^*$ (ppm)	(1) $^{206}Pb/^{238}U$ Age		(1) $^{207}Pb/^{206}Pb$ Age		% Discordant	(1) $^{238}U/^{206}Pb^*$	±%	(1) $^{207}Pb^*/^{206}Pb^*$	±%	(1) $^{207}Pb^*/^{235}U$	±%	(1) $^{206}Pb^*/^{238}U$	±%	err corr
1.1	0.06	276	141	0.53	98	2232	±30	2252	±10	+1	2.42	1.6	0.1421	0.6	8.10	1.7	0.414	1.6	0.94
2.1	0.02	61	34	0.57	22	2215	±35	2229	±12	+1	2.44	1.9	0.1402	0.7	7.92	2.0	0.410	1.9	0.94
3.1	0.35	34	9	0.28	12	2130	±75	2202	±40	+4	2.55	4.2	0.1380	2.3	7.45	4.7	0.392	4.2	0.88
4.1	0.05	61	35	0.59	21	2206	±51	2250	±22	+2	2.45	2.7	0.1419	1.3	7.98	3.0	0.408	2.7	0.91
5.1	0.27	38	18	0.48	13	2159	±39	2254	±21	+5	2.51	2.1	0.1422	1.2	7.80	2.4	0.398	2.1	0.87
6.1	--	61	41	0.70	22	2273	±36	2267	±21	-0	2.36	1.9	0.1432	1.2	8.35	2.3	0.423	1.9	0.84
7.1	0.05	66	37	0.59	23	2201	±53	2235	±13	+2	2.46	2.9	0.1407	0.7	7.89	2.9	0.407	2.9	0.97
8.1	0.22	120	43	0.37	28	1559	±25	2179	±16	+32	3.66	1.8	0.1362	0.9	5.14	2.0	0.274	1.8	0.89
9.1	0.25	130	69	0.54	37	1849	±33	2190	±18	+18	3.01	2.1	0.1370	1.0	6.27	2.3	0.332	2.1	0.89
10.1	--	41	20	0.50	15	2241	±39	2276	±15	+2	2.41	2.1	0.1440	0.8	8.25	2.2	0.416	2.1	0.92
11.1	--	78	38	0.51	27	2193	±46	2284	±23	+5	2.47	2.5	0.1447	1.4	8.08	2.8	0.405	2.5	0.88
12.1	0.02	75	42	0.57	26	2203	±46	2236	±25	+2	2.45	2.5	0.1407	1.4	7.90	2.8	0.407	2.5	0.86
13.1	0.11	57	28	0.51	20	2237	±37	2230	±15	-0	2.41	1.9	0.1402	0.9	8.02	2.1	0.415	1.9	0.91
14.1	--	54	28	0.53	19	2175	±37	2277	±16	+5	2.49	2.0	0.1441	0.9	7.97	2.2	0.401	2.0	0.91
15.1	0.04	71	44	0.65	26	2260	±36	2254	±19	-0	2.38	1.9	0.1422	1.1	8.23	2.2	0.420	1.9	0.86
16.1	--	59	43	0.75	21	2262	±37	2272	±33	+1	2.38	2.0	0.1437	1.9	8.33	2.7	0.420	2.0	0.72
17.1	0.11	61	37	0.63	23	2306	±37	2216	±32	-5	2.33	1.9	0.1391	1.9	8.25	2.7	0.430	1.9	0.72
18.1	1.24	133	43	0.33	21	1108	±54	1953	±29	+47	5.33	5.3	0.1198	1.6	3.10	5.5	0.188	5.3	0.96
19.1	--	36	13	0.36	13	2260	±41	2256	±17	-0	2.38	2.1	0.1424	1.0	8.24	2.4	0.420	2.1	0.91
20.1	0.03	84	33	0.40	31	2289	±35	2247	±11	-2	2.35	1.8	0.1416	0.6	8.32	1.9	0.426	1.8	0.95
Errors are 1-sigma; Pb_c and Pb^* indicate the common and radiogenic portions, respectively.																			
Error in Standard calibration was 0.48% (not included in above errors but required when comparing data from different mounts).																			
(1) Common Pb corrected using measured ^{204}Pb.																			

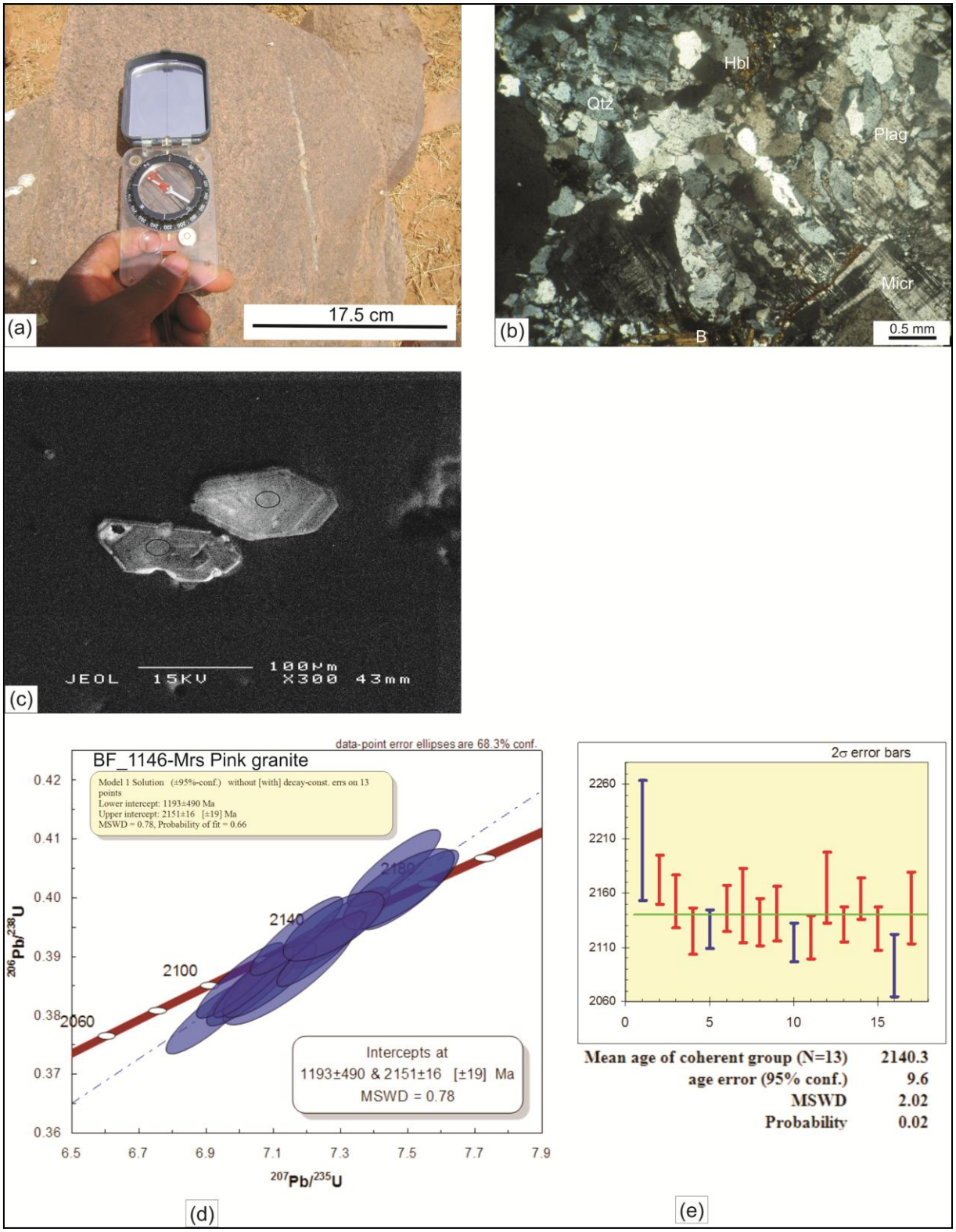

Figure 7.4: Mrs Pink granite sampled proximal to the MSZ (UTM, 30P 1618845, 0822069). (a) Field image of the Mrs Pink granite sample. (b) Photomicrograph of the sample BF_1146, (Hbl = hornblende, Qtz = quartz, Micr = Microcline, B = Biotite, Plag = plagioclase crystals) (c) Cathodoluminesence images of zircon crystals that were analysed, they have well defined cores and oscillatory rims, the cores were targeted. Ellipses mark the location of the analysed spots. (d) The U-Pb Concordia diagram of the strongly concordant data points of the Mrs Pink granite. (e) Age distribution bars of the calculated mean age of coherent group on 13 spots analysis.

Table 7.2: Summary of SHRIMP U-Pb zircon data, sample BF_1146.

Summary of SHRIMP U-Pb zircon data, sample BF_1146_Mrs Pink granite																			
Grain spot	% $^{206}Pb_c$	U (ppm)	Th (ppm)	$^{232}Th/^{238}U$	$^{206}Pb^*$ (ppm)	(1) $^{206}Pb/^{238}U$ Age		(1) $^{207}Pb/^{206}Pb$ Age		% Discordant	(1) $^{238}U/^{206}Pb^*$	±%	(1) $^{207}Pb^*/^{206}Pb^*$	±%	(1) $^{207}Pb^*/^{235}U$	±%	(1) $^{206}Pb^*/^{238}U$	±%	err corr
1.1	1.78	112	50	0.459	38	2145	±20	2208	±28	+3	2.534	1.09	0.1385	1.59	7.54	1.9	0.395	1.09	0.57
2.1	--	111	45	0.414	38	2175	±21	2172	±11	-0	2.492	1.11	0.1357	0.65	7.51	1.3	0.401	1.11	0.86
2.2	0.04	98	34	0.357	33	2146	±21	2152	±12	+0	2.532	1.14	0.1341	0.69	7.30	1.3	0.395	1.14	0.85
3.1	0.11	137	51	0.383	45	2074	±19	2125	±11	+3	2.635	1.06	0.1320	0.61	6.91	1.2	0.380	1.06	0.87
4.1	0.01	151	67	0.463	54	2234	±20	2126	±9	-6	2.414	1.04	0.1321	0.52	7.55	1.2	0.414	1.04	0.89
4.2	--	191	58	0.312	66	2192	±20	2146	±11	-3	2.469	1.07	0.1336	0.60	7.46	1.2	0.405	1.07	0.87
5.1	0.24	42	11	0.260	14	2111	±28	2148	±17	+2	2.581	1.54	0.1338	0.99	7.15	1.8	0.387	1.54	0.84
6.1	0.02	95	44	0.480	31	2099	±21	2133	±11	+2	2.598	1.15	0.1326	0.62	7.04	1.3	0.385	1.15	0.88
7.1	0.25	114	46	0.423	38	2104	±20	2141	±13	+2	2.590	1.09	0.1332	0.72	7.09	1.3	0.386	1.09	0.83
7.2	0.18	177	56	0.330	53	1930	±16	2114	±9	+10	2.864	0.99	0.1312	0.51	6.32	1.1	0.349	0.99	0.89
8.1	0.03	110	35	0.330	36	2104	±20	2119	±10	+1	2.591	1.10	0.1316	0.56	7.00	1.2	0.386	1.10	0.89
9.1	0.77	103	41	0.416	35	2176	±21	2164	±16	-1	2.491	1.13	0.1350	0.94	7.47	1.5	0.401	1.13	0.77
10.1	0.03	145	48	0.338	48	2102	±18	2131	±8	+2	2.593	1.02	0.1325	0.46	7.04	1.1	0.386	1.02	0.91
11.1	0.03	118	38	0.331	40	2129	±19	2155	±9	+1	2.556	1.07	0.1343	0.54	7.24	1.2	0.391	1.07	0.89
12.1	0.04	97	31	0.325	33	2139	±20	2127	±10	-1	2.542	1.12	0.1322	0.58	7.17	1.3	0.393	1.12	0.89
12.2	0.18	206	68	0.339	58	1825	±15	2093	±14	+15	3.056	0.95	0.1296	0.82	5.85	1.3	0.327	0.95	0.76
13.1	0.01	161	54	0.348	55	2147	±18	2146	±17	-0	2.531	0.99	0.1336	0.95	7.28	1.4	0.395	0.99	0.72
Errors are 1-sigma; Pb_c and Pb^* indicate the common and radiogenic portions, respectively.																			
Error in Standard calibration was 0.33% (not included in above errors but required when comparing data from different mounts).																			
(1) Common Pb corrected using measured ^{204}Pb.																			

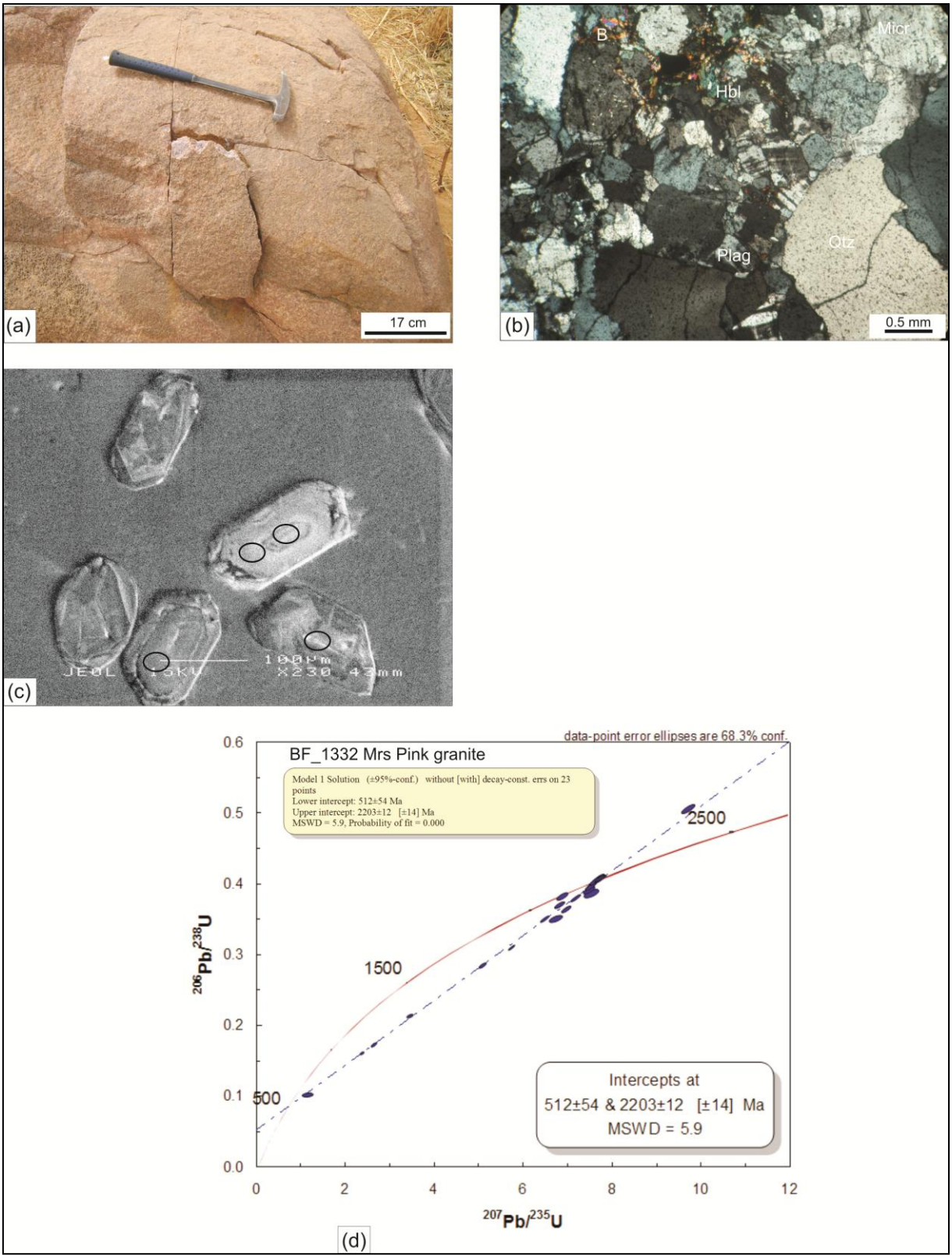

Figure 7.5: (a) Outcrop image of Mrs Pink granite (UTM, 30P 1612261, 0800455), it was given the name due to its outstanding pink colour. (b) Microstructural composition of the Mrs Pink granite, minerals include biotite (B), hornblende (hbl), microcline (Micr), Quartz (Qtz), and Plagioclase (plag). (c) Cathodoluminesence image of the zircon crystals that were analysed. The Ellipses indicate the analysed spot. Where the rims could be analysed, both the core and the rim were targeted with the beam for analysis. (d) The U-Pb Concordia age diagram of the data points from the Mrs Pink granite. The data points are discordant along a single discordia.

Table 7.3: Summary of SHRIMP U-Pb zircon data, sample BF_1332.

Summary of SHRIMP U-Pb zircon data, sample BF_1332_Mrs Pink granite																			
Grain spot	% $^{206}Pb_c$	U (ppm)	Th (ppm)	$^{232}Th/^{238}U$	$^{206}Pb^*$ (ppm)	(1) $^{206}Pb/^{238}U$ Age		(1) $^{207}Pb/^{206}Pb$ Age		% Discordant	(1) $^{238}U/^{206}Pb^*$	±%	(1) $^{207}Pb^*/^{206}Pb^*$	±%	(1) $^{207}Pb^*/^{235}U$	±%	(1) $^{206}Pb^*/^{238}U$	±%	err corr
1.1	9.93	969	425	0.453	87	638	±11	1199	±134	+49	9.612	1.81	0.0801	6.79	1.15	7.0	0.104	1.81	0.26
1.2	1.08	526	178	0.350	97	1256	±10	1903	±21	+37	4.649	0.86	0.1165	1.15	3.45	1.4	0.215	0.86	0.60
2.1	1.58	535	185	0.358	131	1621	±12	2088	±12	+25	3.497	0.85	0.1293	0.69	5.10	1.1	0.286	0.85	0.78
3.1	1.63	420	264	0.649	134	2033	±15	2149	±11	+6	2.697	0.88	0.1338	0.64	6.84	1.1	0.371	0.88	0.81
4.1	0.08	338	125	0.382	117	2188	±17	2186	±6	-0	2.474	0.91	0.1367	0.36	7.62	1.0	0.404	0.91	0.93
5.1	1.26	1036	352	0.351	450	2640	±18	2223	±10	-23	1.976	0.83	0.1396	0.58	9.74	1.0	0.506	0.83	0.82
6.1	2.30	211	93	0.454	70	2109	±18	2247	±19	+7	2.583	1.01	0.1416	1.13	7.56	1.5	0.387	1.01	0.67
7.1	1.24	452	329	0.752	142	2006	±15	2213	±11	+11	2.739	0.88	0.1389	0.61	6.99	1.1	0.365	0.88	0.82
8.1	0.10	269	121	0.463	93	2173	±17	2192	±7	+1	2.494	0.95	0.1372	0.43	7.58	1.0	0.401	0.95	0.91
9.1	1.16	454	168	0.381	153	2132	±16	2213	±13	+4	2.552	0.88	0.1388	0.78	7.50	1.2	0.392	0.88	0.75
10.1	1.18	710	280	0.408	106	1037	±10	1798	±17	+46	5.730	1.06	0.1099	0.91	2.64	1.4	0.175	1.06	0.76
11.1	0.42	501	233	0.481	151	1939	±14	2155	±7	+12	2.849	0.84	0.1343	0.40	6.50	0.9	0.351	0.84	0.90
12.1	0.29	360	160	0.461	126	2209	±16	2193	±11	-1	2.447	0.88	0.1373	0.62	7.73	1.1	0.409	0.88	0.82
13.1	1.11	557	207	0.384	78	970	±8	1729	±18	+47	6.159	0.84	0.1058	0.95	2.37	1.3	0.162	0.84	0.66
14.1	0.49	307	139	0.468	105	2158	±17	2198	±9	+2	2.515	0.90	0.1377	0.52	7.55	1.0	0.398	0.90	0.87
15.1	0.48	570	305	0.552	188	2089	±17	2109	±14	+1	2.613	0.93	0.1308	0.79	6.90	1.2	0.383	0.93	0.76
16.1	0.09	651	280	0.444	228	2206	±15	2210	±5	+0	2.451	0.83	0.1386	0.27	7.80	0.9	0.408	0.83	0.95
16.2	0.02	1221	394	0.334	326	1746	±12	2153	±6	+22	3.216	0.80	0.1341	0.33	5.75	0.9	0.311	0.80	0.92
17.1	--	122	54	0.456	42	2157	±19	2200	±9	+2	2.516	1.06	0.1378	0.51	7.55	1.2	0.397	1.06	0.90
18.1	1.05	227	102	0.462	69	1941	±16	2220	±19	+15	2.845	0.95	0.1394	1.08	6.76	1.4	0.351	0.95	0.66
19.1	--	152	61	0.411	53	2191	±19	2191	±9	+0	2.471	1.02	0.1371	0.50	7.65	1.1	0.405	1.02	0.90
20.1	0.16	346	122	0.365	113	2079	±16	2194	±7	+6	2.627	0.88	0.1373	0.40	7.21	1.0	0.381	0.88	0.91
21.1	0.03	327	185	0.584	115	2208	±17	2196	±6	-1	2.449	0.89	0.1375	0.32	7.74	0.9	0.408	0.89	0.94
Errors are 1-sigma; Pb_c and Pb^* indicate the common and radiogenic portions, respectively.																			
Error in Standard calibration was 0.33% (not included in above errors but required when comparing data from different mounts).																			
(1) Common Pb corrected using measured ^{204}Pb.																			

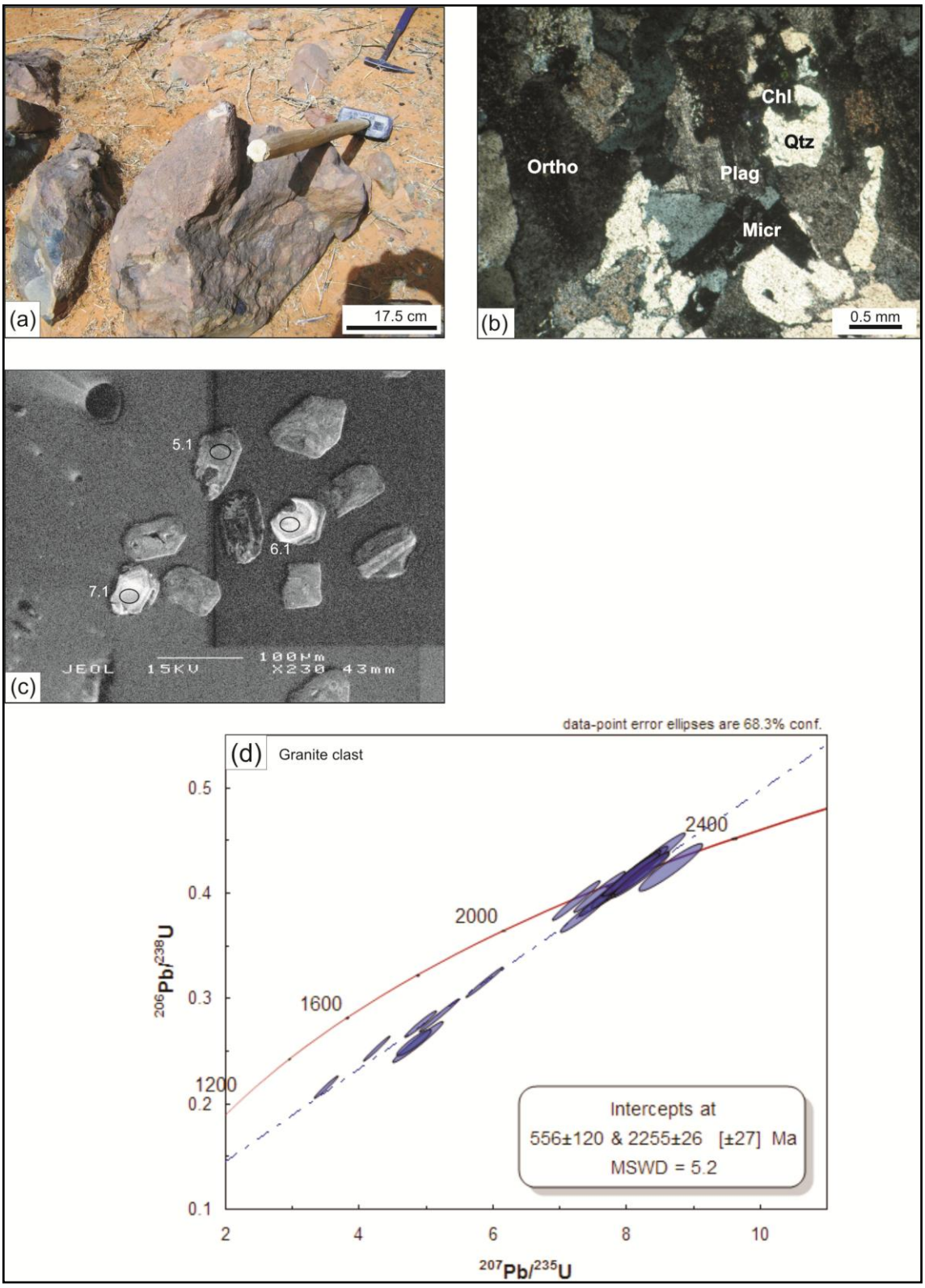

Figure 7.6: (a) The Dembam Member polymictic conglomerate east of the village of Markoye (UTM, 31P 1619591, 0182783). (b) Photomicrograph of the sample BF_1147, the Plag (plagioclase), Ortho (orthoclase) and Micr (microcline) crystals are altered, and the Chl (chlorite) is growing over the re-crystallised Qtz (quartz). (c) Zircon crystals that were analysed, they lack well defined rims, the cores were targeted. Numbers refers to the grain number in Table 7.3. Ellipses mark the location of the analysed spots. (d) U-Pb Concordia diagram for the granite clast.

Table 7.4: Summary of SHRIMP U-Pb zircon data, sample BF_1147.

Summary of SHRIMP U-Pb zircon data, sample BF_1147_Granite clast from the metaconglomerate.																			
Grain spot	% $^{206}Pb_c$	U (ppm)	Th (ppm)	$^{232}Th/^{238}U$	$^{206}Pb^*$ (ppm)	(1) $^{206}Pb/^{238}U$ Age		(1) $^{207}Pb/^{206}Pb$ Age		% Discordant	(1) $^{238}U/^{206}Pb^*$	±%	(1) $^{207}Pb^*/^{206}Pb^*$	±%	(1) $^{207}Pb^*/^{235}U$	±%	(1) $^{206}Pb^*/^{238}U$	±%	err corr
1.1	0.41	94	51	0.57	21	1480	±66	2195	±20	+36	3.87	5.0	0.1374	1.15	4.89	5.1	0.258	5.0	0.97
2.1	0.50	126	110	0.90	41	2075	±56	2245	±15	+9	2.63	3.2	0.1414	0.87	7.40	3.3	0.380	3.2	0.96
3.1	0.35	71	37	0.54	25	2192	±61	2244	±17	+3	2.47	3.3	0.1413	0.97	7.89	3.4	0.405	3.3	0.96
4.1	0.56	524	619	1.22	97	1257	±38	1934	±12	+38	4.64	3.3	0.1185	0.66	3.52	3.4	0.215	3.3	0.98
5.1	--	107	45	0.43	36	2131	±58	2160	±12	+2	2.55	3.2	0.1347	0.70	7.27	3.3	0.392	3.2	0.98
6.1	0.16	72	44	0.64	27	2327	±64	2242	±15	-4	2.30	3.3	0.1412	0.85	8.46	3.4	0.435	3.3	0.97
7.1	0.05	81	58	0.74	27	2155	±59	2234	±13	+4	2.52	3.2	0.1406	0.73	7.69	3.3	0.397	3.2	0.98
8.1	0.33	539	73	0.14	117	1448	±40	2003	±9	+31	3.97	3.1	0.1232	0.52	4.28	3.2	0.252	3.1	0.99
9.1	0.97	196	181	0.95	43	1476	±42	2182	±24	+36	3.89	3.2	0.1364	1.36	4.84	3.4	0.257	3.2	0.92
10.1	1.30	502	583	1.20	119	1565	±43	2101	±13	+29	3.64	3.1	0.1302	0.73	4.93	3.2	0.275	3.1	0.97
11.1	--	249	200	0.83	88	2223	±59	2259	±7	+2	2.43	3.1	0.1426	0.39	8.10	3.2	0.412	3.1	0.99
12.1	--	59	35	0.60	22	2273	±64	2237	±16	-2	2.37	3.3	0.1408	0.94	8.21	3.5	0.423	3.3	0.96
13.1	0.36	371	365	1.02	90	1604	±52	2147	±10	+28	3.54	3.7	0.1337	0.57	5.21	3.7	0.283	3.7	0.99
14.1	0.04	53	38	0.74	19	2243	±64	2268	±17	+1	2.40	3.4	0.1433	0.97	8.22	3.5	0.416	3.4	0.96
15.1	0.24	427	421	1.02	115	1763	±48	2175	±8	+22	3.18	3.1	0.1358	0.46	5.89	3.1	0.315	3.1	0.99
16.1	0.09	94	67	0.73	34	2251	±67	2231	±12	-1	2.39	3.5	0.1403	0.72	8.08	3.6	0.418	3.5	0.98
17.1	0.00	56	34	0.62	20	2246	±63	2238	±14	-0	2.40	3.3	0.1409	0.83	8.09	3.4	0.417	3.3	0.97
18.1	--	42	16	0.39	15	2278	±66	2326	±21	+2	2.36	3.5	0.1483	1.24	8.66	3.7	0.424	3.5	0.94
19.1	--	79	52	0.68	28	2250	±62	2263	±13	+1	2.39	3.3	0.1430	0.75	8.23	3.4	0.418	3.3	0.97
20.1	--	101	39	0.40	35	2170	±59	2200	±12	+2	2.50	3.2	0.1378	0.68	7.60	3.3	0.400	3.2	0.98
Errors are 1-sigma; Pb_c and Pb^* indicate the common and radiogenic portions, respectively.																			
Error in Standard calibration was 0.71% (not included in above errors but required when comparing data from different mounts).																			
(1) Common Pb corrected using measured ^{204}Pb.																			

7.4.4. Sample BF_1149 – Gorom-Gorom granodiorite pluton

The Gorom-Gorom pluton (Figure 7.7a) crops out south of the town of Gorom-Gorom at UTM 30P 1596251 0800771 (Figure 7.1). It is composed of coarse crystals of >1 mm size dominated by quartz, plagioclase, potassium feldspar and muscovite. It has an equigranular texture and it is crosscut by fractures with potassium feldspar alteration in places. Petrographically, the Gorom-Gorom granodiorite is dominated by microcline, quartz with undulose extinction, plagioclase and late muscovite (Figure 7.7b).

The Gorom-Gorom pluton sample whole rock geochemical data plots as granite in the R1-R2 plutonic chemical variation diagram (c.f., De la Roche et al., 1980), and plots as a granite on the TAS diagram (c.f., Middlemost, 1994). The tectono-magmatic discrimination diagram (Figure 7.3a, b) after Pearce et al. (1984) indicates correspondence with volcanic-arc type granitoids.

The analytical results of 20 zircons analysed in 21 grain spots are summarized in Table 7.5 and plotted in Figure 7.7d. Most of the zircons are euhedral and exhibit growth rings (Figure 7.7c). The cores were specifically targeted to obtain the interpreted crystallisation age. Grain spot 2.1, 2.2, 17.1, and 20.1 are considered to be unreliable because they are very discordant and have high radiogenic Pb percentage counts. Grain spots 1.1 and 18.1 gave oldest $^{207}Pb/^{206}Pb$ ages of 2240 ± 14 Ma and 2270 ± 36 Ma, respectively, and these are interpreted as inherited or xenocrystic zircon ages. Grain spot 4.1 gave the youngest $^{207}Pb/^{206}Pb$ age of 2098 ± 52 Ma reflecting a possible Pb loss at this age. The rest of the grain spots define a Pb loss line within error, with a calculated concordant U-Pb age of 2162 ± 28 Ma. This age is interpreted as a crystallisation age of the Gorom-Gorom granodiorite.

7.4.5. Sample BF_1153 – Porphyritic monzodiorite

Sample BF_1153 was collected at UTM 31P 1601807 0185023. It is composed of randomly orientated phenocrysts of potassium feldspar (to 2 cm in size) in a mafic glassy groundmass (Figure 7.8a). It is dominated by plagioclase and potassium feldspar, and chlorite.

Petrographically the porphyritic monzodiorite is composed of phenocrysts of altered orthoclase (> 2mm in size). The fine groundmass is dominated by 0.5 mm crystals of plagioclase, chlorite, microcline and albite (Figure 7.8b).

Sample BF_1153 plots as a monzodiorite in the TAS diagram (c.f., Middlemost, 1994). The tectono-magmatic discrimination diagram (Figure 7.3a, b) after Pearce et al. (1984) indicates correspondence with volcanic-arc type granitoids.

Only five zircon crystals were recovered from this sample and two were lost during polishing. Of the three analysed zircons, two were analysed in two spots, and one in one spot. The zircons are euhedral with oscillatory zoning and the cores are unzoned. The results of 5 analysed grain spots are plotted in Figure 7.8d. The grain spots gave a Pb loss line within error, with a calculated concordant U-Pb age from the upper intercept of 2141 ± 19 Ma.

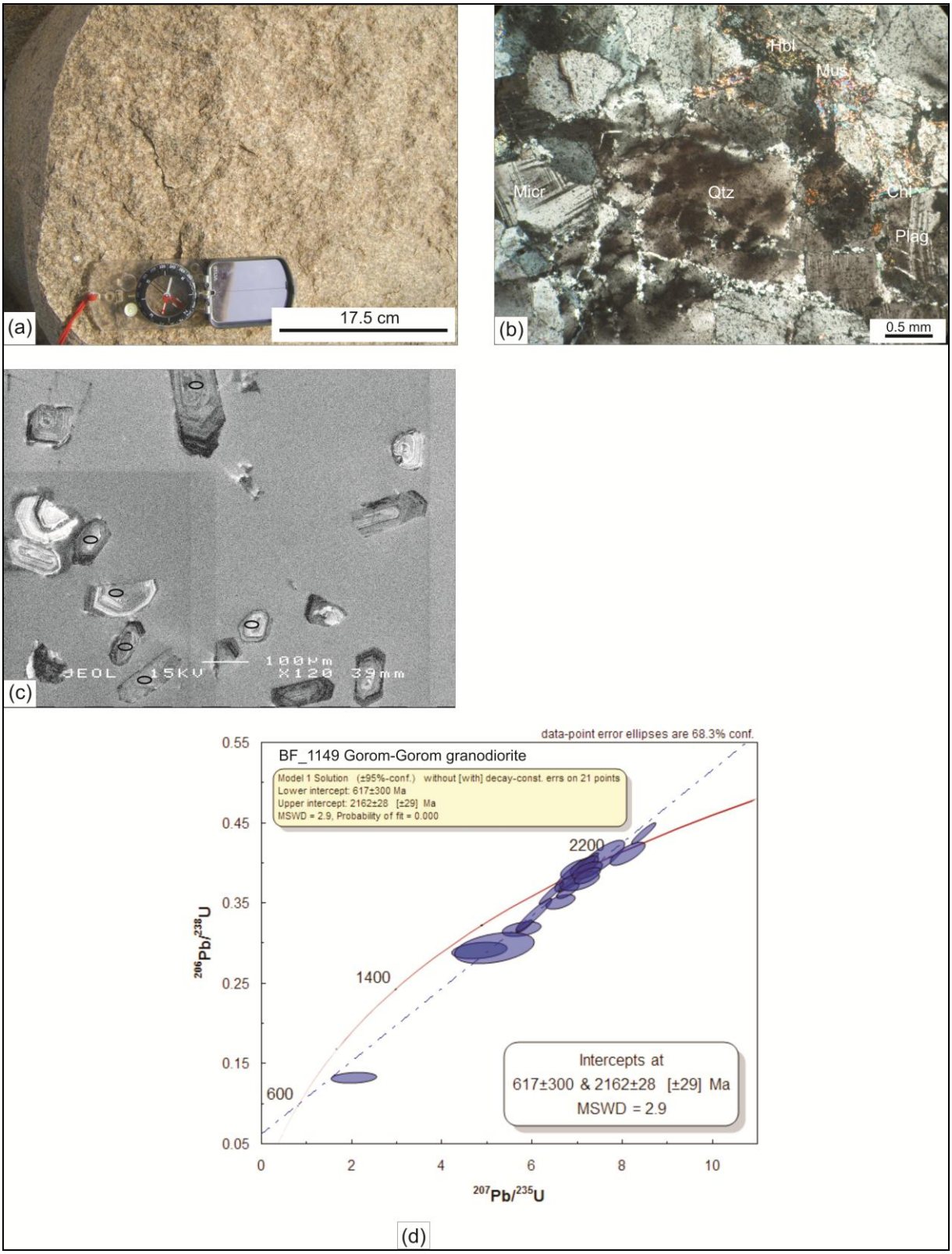

Figure 7.7: (a) The Gorom-Gorom granodiorite (UTM, 30P 1596251, 0800771). (b) Photomicrograph of the sample BF_1149, the Plag (plagioclase), Ortho (orthoclase) and Micr (microcline) crystals are altered, and the Chl (chlorite), Mus (muscovite) and Hbl (hornblende) are growing interstitial to the recrystallised Qtz (quartz). (c) Zircon crystals that were analysed, the cores were targeted. Ellipses mark the location of the analysed spots. (d) U-Pb Concordia diagram for the Gorom-Gorom granodiorite.

Table 7.5: Summary of SHRIMP U-Pb zircon data, sample BF_1149.

Summary of SHRIMP U-Pb zircon data, sample BF_1149_Gorom-Gorom granite																				
Grain spot	% $^{206}Pb_c$	U (ppm)	Th (ppm)	$^{232}Th/^{238}U$	$^{206}Pb^*$ (ppm)	(1) $^{206}Pb/^{238}U$ Age		(1) $^{207}Pb/^{206}Pb$ Age		% Discordant	(1) $^{238}U/^{206}Pb^*$	±%	(1) $^{207}Pb^*/^{206}Pb^*$	±%	(1) $^{207}Pb^*/^{235}U$	±%	(1) $^{206}Pb^*/^{238}U$	± %	err corr
1.1	0.07	66	30	0.47	25	2335	±39	2240	±14	-5	2.29	2.0	0.1410	0.8	8.49	2.1	0.437	2.0	0.93
2.1	18.02	53	37	0.71	13	1647	±35	1966	±145	+18	3.44	2.4	0.1206	8.1	4.84	8.5	0.291	2.4	0.28
2.2	10.48	189	145	0.79	51	1777	±29	2124	±79	+19	3.15	1.9	0.1319	4.5	5.77	4.9	0.317	1.9	0.38
3.1	0.11	214	69	0.34	72	2136	±32	2139	±15	+0	2.55	1.8	0.1331	0.9	7.21	2.0	0.393	1.8	0.90
4.1	0.18	52	21	0.42	17	2134	±39	2098	±52	-2	2.55	2.1	0.1300	2.9	7.03	3.6	0.392	2.1	0.59
5.1	2.18	99	33	0.34	34	2151	±34	2105	±30	-3	2.52	1.9	0.1305	1.7	7.13	2.5	0.396	1.9	0.74
6.1	1.67	459	174	0.39	126	1794	±26	2125	±16	+18	3.12	1.6	0.1320	0.9	5.84	1.9	0.321	1.6	0.87
7.1	0.16	719	58	0.08	207	1862	±67	2112	±28	+14	2.99	4.2	0.1310	1.6	6.05	4.5	0.335	4.2	0.94
8.1	0.31	131	44	0.35	46	2193	±69	2161	±48	-2	2.47	3.7	0.1348	2.8	7.53	4.6	0.405	3.7	0.80
9.1	10.18	240	170	0.73	72	1941	±29	2193	±46	+13	2.85	1.8	0.1372	2.7	6.65	3.2	0.351	1.8	0.55
10.1	0.13	67	21	0.32	23	2170	±37	2112	±15	-3	2.50	2.0	0.1311	0.9	7.23	2.2	0.400	2.0	0.92
11.1	0.12	177	73	0.43	57	2043	±32	2126	±10	+5	2.68	1.8	0.1321	0.6	6.79	1.9	0.373	1.8	0.95
12.1	0.22	180	54	0.31	60	2104	±70	2117	±43	+1	2.59	3.9	0.1314	2.5	6.99	4.6	0.386	3.9	0.84
13.1	2.64	129	38	0.30	41	2006	±32	2166	±28	+9	2.74	1.9	0.1352	1.6	6.80	2.5	0.365	1.9	0.76
14.1	2.77	95	43	0.46	31	2062	±36	2176	±62	+6	2.65	2.1	0.1359	3.6	7.06	4.1	0.377	2.1	0.50
15.1	0.04	2629	243	0.10	817	1991	±43	2084	±17	+5	2.76	2.5	0.1289	1.0	6.43	2.7	0.362	2.5	0.93
16.1	0.39	92	38	0.42	31	2126	±35	2157	±42	+2	2.56	1.9	0.1344	2.4	7.24	3.1	0.391	1.9	0.62
17.1	15.50	280	115	0.43	71	1659	±63	2073	±183	+23	3.41	4.3	0.1282	10.4	5.18	11.3	0.293	4.3	0.38
18.1	0.15	31	11	0.38	11	2218	±44	2270	±36	+3	2.43	2.4	0.1435	2.1	8.13	3.2	0.411	2.4	0.74
19.1	1.55	195	45	0.24	64	2093	±31	2188	±35	+5	2.61	1.8	0.1369	2.0	7.24	2.7	0.383	1.8	0.66
20.1	33.49	258	38	0.15	29	801	±23	1851	±285	+60	7.56	3.1	0.1132	15.7	2.06	16.0	0.132	3.1	0.19
Errors are 1-sigma; Pb_c and Pb^* indicate the common and radiogenic portions, respectively																				
Error in Standard calibration was 0.48% (not included in above errors but required when comparing data from different mounts).																				
(1) Common Pb corrected using measured ^{204}Pb.																				

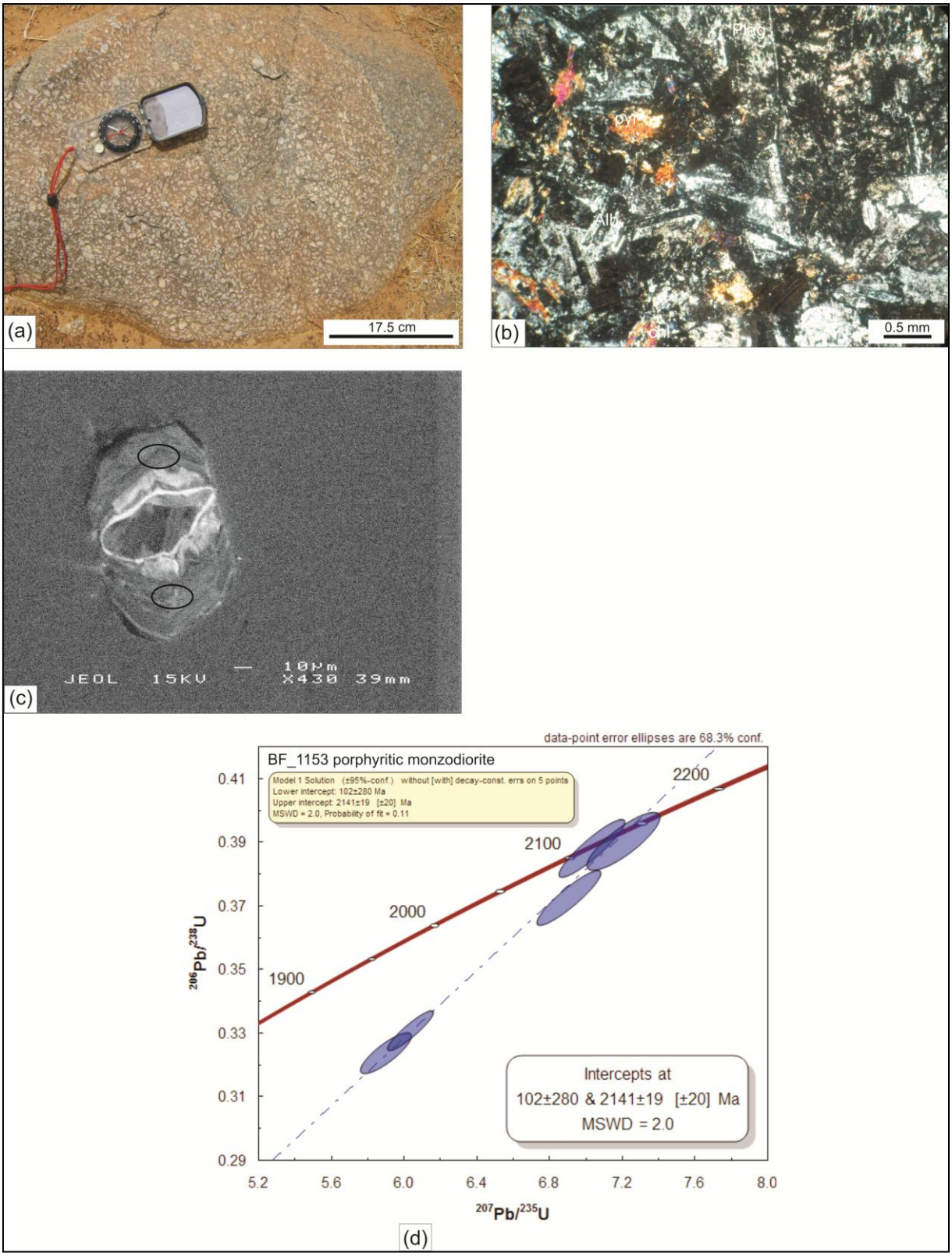

Figure 7.8: (a) The porphyritic monzodiorite (UTM, 31P 1601807, 0185023) from the OGB with euhedral and sub-rounded plagioclase crystals. (b) The microstructure of the porphyritic monzonite is dominated by dusty plagioclase (plag), Albite (alb), Pyroxene (pyr) and interstitial chlorite. (c) Cathodoluminesence image of one of the zircon crystal that was analysed with two spots. (d) The U-Pb Concordia-discordant diagram with the calculated age data plot from the five analysed spots.

7.4.6. Sample BF_1156 and BF_1157- Dori granodiorite gneiss

The Dori granodiorite gneiss (Figure 7.9a) crops out north of the town of Dori at UTM 31P 1564900 0177188 (Figure 7.1) and is deformed (Chapter 5). It is composed of coarse crystals (>1 mm in size) dominated by quartz, plagioclase, potassium feldspar, hornblende and biotite. It has well-defined leucocratic and melanocratic layers in places. The melanocratic layers are dominated by hornblende, biotite (with a preferred orientation) and magnetite crystals, while the leucocratic layers are dominated by plagioclase, potassium feldspar (microcline) and quartz (Figure 7.9b). The quartz crystals exhibit undulose extinction, and intergrowths with alkali feldspar. Accessory apatite and zircon occur within, and interstitial to, hornblende and plagioclase. The Dori granodiorite gneiss is migmatitic in part. The Dori granodiorite gneiss is also crosscut by gabbro-pyroxenite dykes and pegmatites.

The geochemical analysis of Sample BF_1156 of the Dori granodiorite gneiss plots in the granodiorite field and along the granite-alkali granite border line in the R1-R2 plutonic chemical variation diagram (c.f., De la Roche et al, 1980), and as a granites on the TAS diagram (c.f., Middlemost, 1994). The tectono-magmatic discrimination diagram (Figure 7.3a, b) after Pearce et al. (1984) indicates correspondence with volcanic-arc granitoids.

The results of 15 zircons analysed in 16 grain spots for sample BF_1156 are summarized in Table 7.6 and plotted in Figure 7.9 (d, e). Most of the zircons are euhedral and exhibit fine growth rings (Figure 7.9c). The zircons are >75 µm in size and the cores were specifically targeted to obtain the interpreted crystallisation age. Grain spots 2.1 and 2.2 gave a core age of 2105 ± 10 Ma, which is younger than the rim age of 2142 ± 16 Ma respectively. The younger core age in this zircon may indicate core recrystallisation (Pidgeon, 1992; Zegers, 1996), or a range of analytical or zircon morphology problems as described by Castiñeiras et al. (2010) and Butera et al. (2001). The analyses were consequently discarded from the age calculation. Grain spots 3.1 in Table 7.6 gave the oldest $^{207}Pb/^{206}Pb$ ages of 2170 ± 18 Ma. Grain spot 5.1 and 15.1 gave the youngest $^{207}Pb/^{206}Pb$ ages of 1940 ± 44 Ma and 2022 ± 9 Ma respectively. The age of grain spot 5.1 is unreliable due to its high discordant percentage while the age from grain spot 15.1 could reflect the age of the metamorphic event that resulted in Pb loss. The majority of the grain spots gave a concordant U-Pb age defining a Pb loss line with a calculated upper intercept age of 2148 ± 9.3 Ma. The calculated mean age of coherent group of 12 grain spots is 2137 ± 6.6 Ma (Figure 7.9e).

Sample BF_1157 from the Dori batholith collected at UTM 31P 1565561 0182376, exhibits well-defined leucocratic and melanocratic layers (Figure 7.10a). The melanocratic layers are dominated by hornblende, biotite (with a preferred orientation), microcline and magnetite, while the leucocratic layers are dominated by plagioclase, potassium feldspar (microcline) and quartz. The quartz and hornblende crystals replace microcline. Quartz and plagioclase exhibit myrmekite texture. Accessory apatite and zircon occur within, and interstitial to hornblende and plagioclase (Figure 7.10b).

The results of 16 analysed grain spots are summarized in Table 7.7, and plotted in Figure 7.10d. Most of the zircons are euhedral and are > 50 µm in size. They exhibit fine planar growth rings (Figure 7.10c). The cores and rims were targeted for analysis. Grain spots 2.1 and 3.1, gave core ages of $^{207}Pb/^{206}Pb$ age of 2139 ± 10 Ma (spot 1.1) and 2136 ± 12 Ma (spot 3.1) respectively, which are within error. The rims of grain spots 1.2 and 3.2 gave $^{207}Pb/^{206}Pb$ ages of 2104 ± 9 Ma (spot 1.2) and 2111 ± 10 Ma (spot 3.2) which are also within error. There is a significant time difference between the ages obtained from the two rims and the ages from the two cores. The ages from the cores could reflect the interpreted age of crystallisation; the ages from the rims are interpreted as metamorphic event. Grain spot 13.1 gave a zircon core age of 2200 ± 17 Ma that is probably related to inheritance; the core may be xenocrystic from older rock units such as BF_1332, BF_1144 and BF_1299. The youngest $^{207}Pb/^{206}Pb$ age is from the rim, grain spot 1.2 at 2104 ± 9 Ma.

The majority of the grain spots gave a concordant U-Pb age values defining a Pb loss line with a calculated upper intercept age of 2164 ± 24 Ma.

7.4.7 Sample BF_1299 – Migmatitic gneiss

Sample BF_1299 was collected from a group of isolated and small outcrops northeast of the town of Gorom-Gorom and south of the village of Kel Enguef in the Kel Enguef belt at UTM 30P 1594675 0808119. The belt is composed of clastic and chemical sedimentary rocks that are metamorphosed from upper greenschist facies to amphibolite facies (c.f., Woolfe, 2011). The rocks exhibit a well-developed, northerly-dipping, bedding (compositional layering) parallel foliation. The coarse crystalline migmatitic gneiss anomalously crops out at the contact between amphibolite in the south and upper greenschist facies rocks in the north.

In outcrops, the migmatitic gneiss have well-developed leucocratic and melanocratic layers that are folded (Figure 7.11a). They range in thickness from 1.0 mm to 5 cm. The melanocratic layers are dominated by hornblende and quartz with accessory biotite and plagioclase, while the leucocratic layers are dominated by plagioclase and quartz (up to 2 mm in diameter) with accessory potash feldspar, muscovite and biotite (Figure 7.11b). Veins of coarse-grained quartz and plagioclase cross cut the migmatite.

Petrographically, the migmatitic gneiss is composed of coarse crystals of quartz, plagioclase and hornblende, but biotite, zircon, sphene and magnetite, make up approximately 5 % of the groundmass (Figure 7.11b). Leucocratic layers are medium-grained with crystals up to 2 mm in diameter. Interstitial magnetite, associated with zircon and sphene, is common in these layers and also occurs as inclusions.

The results from 20 analysed grain spots of zircons (Figure 7.11c) from sample BF_1299 are summarized in (Table 7.8) and are plotted in (Figure 7.11d). The cores of the zircons were targeted, the zircons did not exhibit well-defined growth rings and are dominantly subhedral in shape (Figure 7.11c). Grain spots 2.1, 3.1, 6.1, 7.1, 8.1, 9.1, 13.1 and 15.1 to 20.1 have high uranium concentration

and the mean age of coherent group of these 13 spots is 1955 ± 257 Ma, while grain spots 1.1, 4.1, 5.1, 10.1, 11.1, 12.1, and 14.1 in (Table 7.8) gave a mean age on 7 spots of 2268 ± 29 Ma. The low uranium phase concentration age probably reflects the age of the source rocks and the high concentration phase age probably reflects the age related to the partial melting phase. The concordant data of all the 20 grain spots define a Pb loss line within error, with a calculated upper intercept age of 2253 ± 15 Ma.

7.4.8. Sample BF_1368 – Porphyritic granodiorite

The porphyritic granodiorite crops out east of the town of Markoye in the fold hinge of a syncline at UTM 31P 1617054 0181894. The porphyritic granodiorite has contact metamorphosed the sedimentary units to hornblende hornfels facies. It is composed of coarse crystals (>2 mm in size) of randomly orientated anhedral to euhedral phenocrysts of potassium feldspar in a mafic glassy groundmass (Figure 7.12a). It is dominated by plagioclase and potassium feldspar, and chlorite.

Petrographically, it is composed of phenocrysts of altered orthoclase, quartz and plagioclase which are > 2 mm in size. The groundmass is dominated by crystals of quartz, orthoclase, plagioclase, and muscovite (Figure 7.12b). Muscovite occurs as a replacement mineral.

The geochemical analysis of Sample BF_1368 of the porphyritic granodiorite plots in the granodiorite field in the TAS diagram (c.f., Middlemost, 1994). The tectono-magmatic discrimination diagram (Figure 7.3a, b) after Pearce et al. (1984) indicates correspondence with volcanic-arc granitoids.

The results of 16 analysed zircons on 16 different grain spots are summarized in Table 7.9 and plotted in Figures 7.12 (d, e). The analysed zircons were euhedral and have fine regular zoning. The grain spots gave a U-Pb age of 2207 ± 38 Ma on 16 grain spots. When grain spot 7.1, 8.1 and 12.1 are filtered due to high percentage of discordance, the remaining grain spots gave a U-Pb concordant age of 2192 ± 47 Ma on 13 spots (Figure 7.12e). The age data of the porphyritic granodiorite constrains the upper age of the metasediments rocks which the porphyritic granodiorite intruded, i.e., they are older than 2192 ± 47 Ma in the OGB.

7.4.9. Sample BF_1369 – Tin-Taradat granodiorite

The Tin-Taradat granodiorite (Figure 7.13a) crops out along the MSZ at Tin-Taradat at UTM 31P 1618574 0179168. The granodiorite is coarse to medium, and composed of crystals of plagioclase, quartz, hornblende and biotite. It is crosscut by pseudotachylite veins west of the MSZ. It hosts elongate mafic xenoliths that trend northwest.

Petrographically, it is composed of coarse crystals of (>1 mm in size) microcline, quartz with undulose extinction, altered orthoclase, altered plagioclase, and aggregates of biotite that are replaced by chlorite (Figure 7.13b). The hornblende is interstitial to quartz microcline crystals.

The geochemical results for the Tin-Taradat granodiorite plots as a granodiorite in the R1-R2 plutonic chemical variation diagram (c.f., De la Roche et al., 1980). The tectono-magmatic discrimination diagram (Figure 7.3a, b) after Pearce et al. (1984) indicates correspondence with volcanic-arc granitoids.

Fourteen euhedral zircons with oscillatory zoning (Figure 7.13c) were analysed in 16 different grain spots. Two of the zircons were analysed in two grain spots. The analytic results of 16 analysed grain spots are summarized in Table 7.10 and plotted in Figure 7.13d. The zircon cores were specifically targeted to obtain the interpreted crystallisation age. Grain spots 1.1 and 1.2 gave $^{207}Pb/^{206}Pb$ ages of 2123 ± 12 Ma for the core and 1921 ± 29 Ma for the rim respectively. Grain spot 2.1 and 2.2 gave a younger core age of 2125 ± 16 Ma and a rim age of 2151 ± 9 Ma, may indicate core recrystallisation (Pidgeon, 1992; Zegers, 1996), or a range of analytical or zircon morphology problems as described by Castiñeiras et al. (2010) and Butera et al. (2001). The analyses were consequently discarded from the age calculation. The grain spots gave a calculated concordant U-Pb age values with a calculated upper intercept age of 2146.2 ± 9.3 Ma and lower intercept at 450 ± 47 Ma. The upper intercept age at 2146 ± 9 Ma is interpreted as the crystallisation age of the Tin-Taradat pluton.

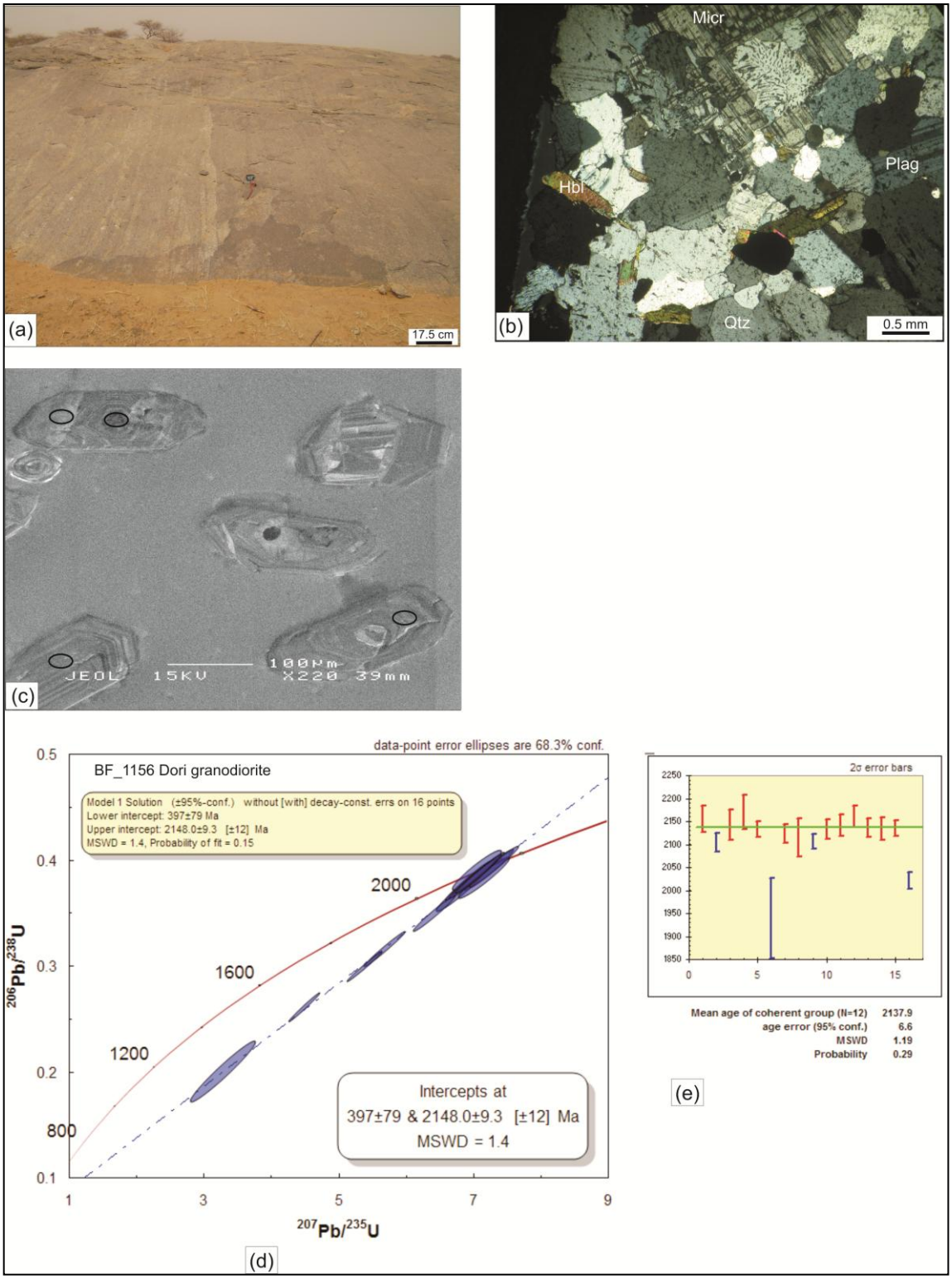

Figure 7.9: Dori granodiorite gneiss (UTM, 31P 1564900, 0177188). (a) Field image of the Dori granodiorite gneiss showing a development of leucocratic and melanocratic layers. (b) Photomicrograph showing alignment of hornblende (Hbl), and the Plag (plagioclase), Qtz (quartz) and Micr (microcline) crystals that dominate the leucocratic bands. (c) Zircon crystals that were analysed, they have well defined oscillatory zoning, the cores and rims of the zircon crystals were targeted. Ellipses mark the location of the analysed spots. (d) The U-Pb Concordia diagram of the Dori granodiorite gneiss. The data plot show a strong concordant age at 2148 Ma. (e) Mean coherent age of 12 spots grains with 2σ error bars. The mean coherent age of 12 grains (2137.9 ± 6.6 Ma) is younger than the Concordia age of 2148 ± 9.3 Ma on 16 grain spots.

Table 7.6: Summary of SHRIMP U-Pb zircon data, sample BF_1156.

Summary of SHRIMP U-Pb zircon data, sample BF_1156_Dori granodiorite gneiss																			
Grain spot	% $^{206}Pb_c$	U (ppm)	Th (ppm)	$^{232}Th/^{238}U$	$^{206}Pb^*$ (ppm)	(1) $^{206}Pb/^{238}U$ Age		(1) $^{207}Pb/^{206}Pb$ Age		% Discordant	(1) $^{238}U/^{206}Pb^*$	±%	(1) $^{207}Pb^*/^{206}Pb^*$	±%	(1) $^{207}Pb^*/^{235}U$	±%	(1) $^{206}Pb^*/^{238}U$	±%	err corr
1.1	0.12	82	40	0.50	28	2125	±59	2155	±14	+2	2.56	3.2	0.1343	0.80	7.23	3.3	0.391	3.2	0.97
2.1	0.29	275	127	0.48	75	1770	±53	2105	±10	+18	3.16	3.4	0.1305	0.58	5.69	3.5	0.316	3.4	0.99
2.2	0.10	153	6	0.04	48	2026	±55	2142	±16	+6	2.71	3.2	0.1333	0.94	6.79	3.3	0.369	3.2	0.96
3.1	--	50	15	0.30	16	2093	±60	2170	±18	+4	2.61	3.4	0.1355	1.05	7.17	3.5	0.384	3.4	0.95
4.1	0.02	197	74	0.39	65	2100	±56	2132	±9	+2	2.60	3.1	0.1326	0.49	7.04	3.2	0.385	3.1	0.99
5.1	0.49	205	31	0.16	35	1179	±102	1940	±44	+43	4.98	9.5	0.1189	2.45	3.29	9.8	0.201	9.5	0.97
6.1	--	155	50	0.33	51	2079	±56	2123	±10	+2	2.63	3.2	0.1319	0.57	6.92	3.2	0.381	3.2	0.98
7.1	0.00	84	44	0.54	28	2124	±59	2114	±21	-1	2.56	3.2	0.1312	1.18	7.06	3.4	0.390	3.2	0.94
8.1	0.13	312	51	0.17	80	1688	±46	2107	±8	+23	3.34	3.1	0.1306	0.46	5.39	3.2	0.299	3.1	0.99
9.1	0.05	137	65	0.49	45	2105	±57	2133	±11	+2	2.59	3.2	0.1327	0.60	7.06	3.2	0.386	3.2	0.98
10.1	--	129	9	0.07	39	1934	±53	2141	±12	+11	2.86	3.2	0.1332	0.66	6.43	3.2	0.350	3.2	0.98
11.1	--	114	53	0.48	39	2139	±58	2161	±12	+1	2.54	3.2	0.1348	0.67	7.31	3.3	0.394	3.2	0.98
12.1	0.03	146	68	0.48	49	2116	±57	2137	±10	+1	2.57	3.2	0.1329	0.58	7.12	3.2	0.389	3.2	0.98
13.1	0.03	227	12	0.05	75	2089	±58	2134	±12	+3	2.61	3.2	0.1327	0.71	7.00	3.3	0.383	3.2	0.98
14.1	0.05	218	79	0.38	72	2108	±56	2135	±8	+2	2.59	3.1	0.1328	0.48	7.08	3.2	0.387	3.1	0.99
15.1	0.40	553	93	0.17	124	1498	±46	2022	±9	+29	3.82	3.5	0.1245	0.52	4.49	3.5	0.262	3.5	0.99
Errors are 1-sigma; Pb_c and Pb^* indicate the common and radiogenic portions, respectively.																			
Error in Standard calibration was 0.71% (not included in above errors but required when comparing data from different mounts).																			
(1) Common Pb corrected using measured ^{204}Pb.																			

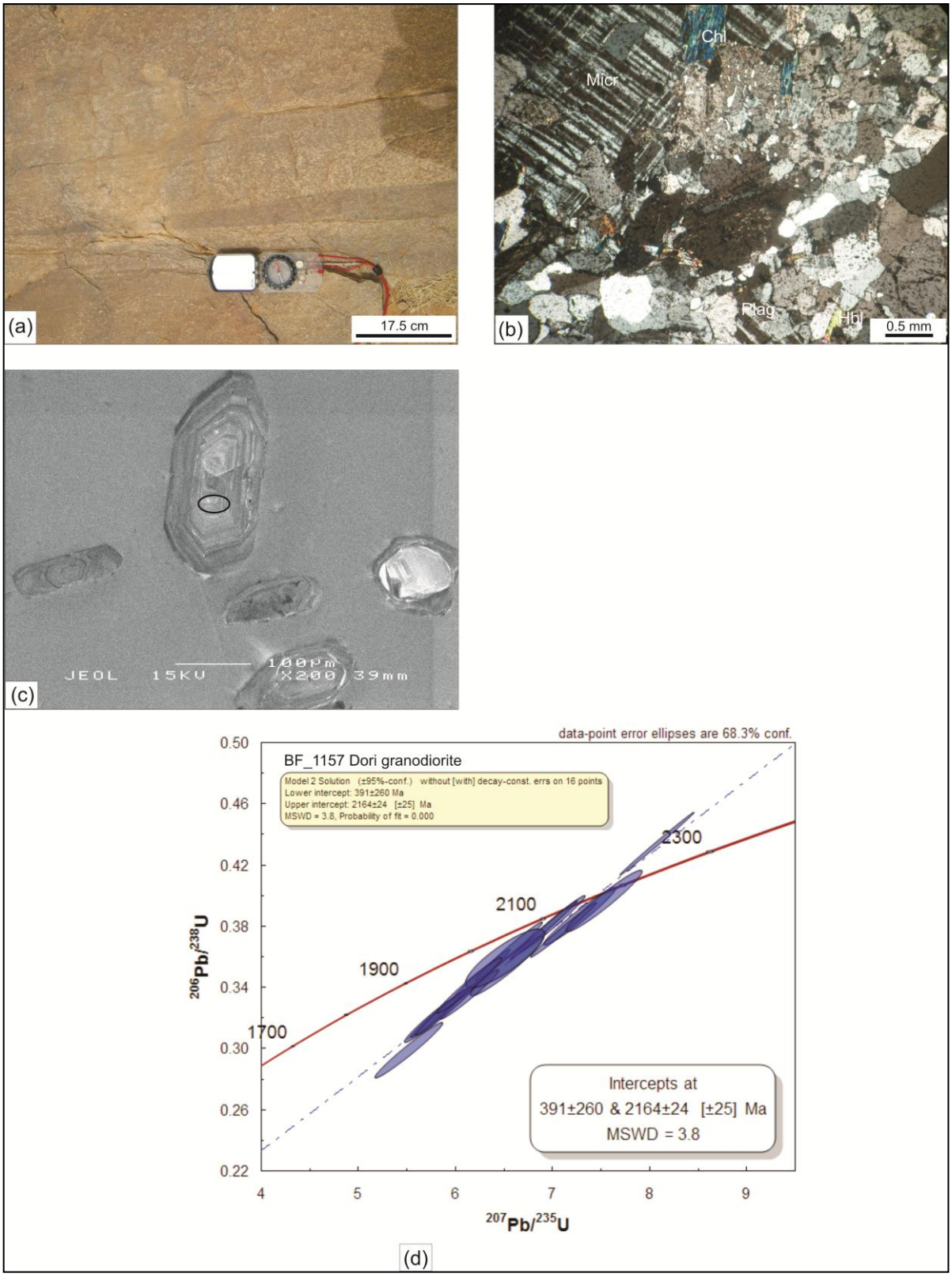

Figure 7.10: Dori granodiorite gneiss (UTM, 31P 1565561, 0182376). (a) Outcrop field image of the Dori granodiorite gneiss showing a development of leucocratic and melanocratic layers. (b) Photomicrograph showing the microstructural composition that consist of chlorite (Chl), hornblende (Hbl), Plag (plagioclase), Qtz (quartz) and Micr (microcline) crystals that dominate the leucocratic bands. (c) Zircon crystals that were analysed, they have well defined oscillatory zoning, the cores and rims of the zircon crystals were targeted. Ellipses mark the location of the analysed spots. (d) The U-Pb Concordia diagram of the data from the Dori granodiorite.

Table 7.7: Summary of SHRIMP U-Pb zircon data, sample BF_1157.

Summary of SHRIMP U-Pb zircon data, sample BF_1157_Dori granodiorite gneiss																			
Grain spot	% $^{206}Pb_c$	U (ppm)	Th (ppm)	$^{232}Th/^{238}U$	$^{206}Pb^*$ (ppm)	(1) $^{206}Pb/^{238}U$ Age		(1) $^{207}Pb/^{206}Pb$ Age		% Discordant	(1) $^{238}U/^{206}Pb^*$	±%	(1) $^{207}Pb^*/^{206}Pb^*$	±%	(1) $^{207}Pb^*/^{235}U$	±%	(1) $^{206}Pb^*/^{238}U$	±%	err corr
1.1	0.02	114	14	0.13	37	2084	±57	2139	±10	+3	2.62	3.2	0.1331	0.58	7.00	3.2	0.382	3.2	0.98
1.2	0.29	298	58	0.20	89	1928	±52	2104	±9	+10	2.87	3.1	0.1305	0.50	6.27	3.2	0.349	3.1	0.99
2.1	0.79	101	45	0.46	31	1954	±61	2150	±20	+11	2.82	3.6	0.1339	1.16	6.54	3.8	0.354	3.6	0.95
3.1	0.25	135	80	0.61	39	1866	±51	2136	±12	+15	2.98	3.2	0.1329	0.71	6.15	3.2	0.336	3.2	0.98
3.2	0.42	310	89	0.30	86	1805	±51	2111	±10	+17	3.10	3.3	0.1309	0.58	5.83	3.3	0.323	3.3	0.98
4.1	0.62	326	126	0.40	89	1786	±50	2113	±14	+18	3.13	3.2	0.1311	0.79	5.77	3.3	0.319	3.2	0.97
5.1	--	531	392	0.76	198	2324	±61	2165	±4	-9	2.30	3.1	0.1351	0.24	8.08	3.1	0.434	3.1	1.00
6.1	0.35	196	87	0.46	61	2000	±59	2107	±11	+6	2.75	3.4	0.1307	0.61	6.55	3.5	0.364	3.4	0.98
7.1	0.13	386	128	0.34	125	2064	±58	2136	±7	+4	2.65	3.3	0.1329	0.38	6.91	3.3	0.377	3.3	0.99
8.1	0.15	77	34	0.46	26	2107	±58	2186	±14	+4	2.59	3.2	0.1367	0.83	7.29	3.3	0.387	3.2	0.97
9.1	0.06	113	41	0.38	31	1817	±54	2118	±12	+16	3.07	3.4	0.1315	0.71	5.90	3.5	0.326	3.4	0.98
10.1	0.86	187	81	0.45	48	1686	±60	2151	±16	+25	3.35	4.1	0.1340	0.90	5.52	4.2	0.299	4.1	0.98
11.1	--	225	18	0.08	73	2064	±55	2189	±8	+7	2.65	3.1	0.1369	0.44	7.12	3.2	0.377	3.1	0.99
12.1	0.94	30	13	0.45	9	1977	±60	2120	±38	+8	2.79	3.5	0.1316	2.19	6.52	4.1	0.359	3.5	0.85
13.1	--	53	15	0.29	18	2153	±61	2200	±17	+2	2.52	3.3	0.1378	0.95	7.54	3.5	0.397	3.3	0.96
14.1	0.44	201	78	0.40	59	1894	±58	2106	±14	+12	2.93	3.5	0.1306	0.77	6.15	3.6	0.342	3.5	0.98
Errors are 1-sigma; Pb_c and Pb^* indicate the common and radiogenic portions, respectively.																			
Error in Standard calibration was 0.71% (not included in above errors but required when comparing data from different mounts).																			
(1) Common Pb corrected using measured ^{204}Pb.																			

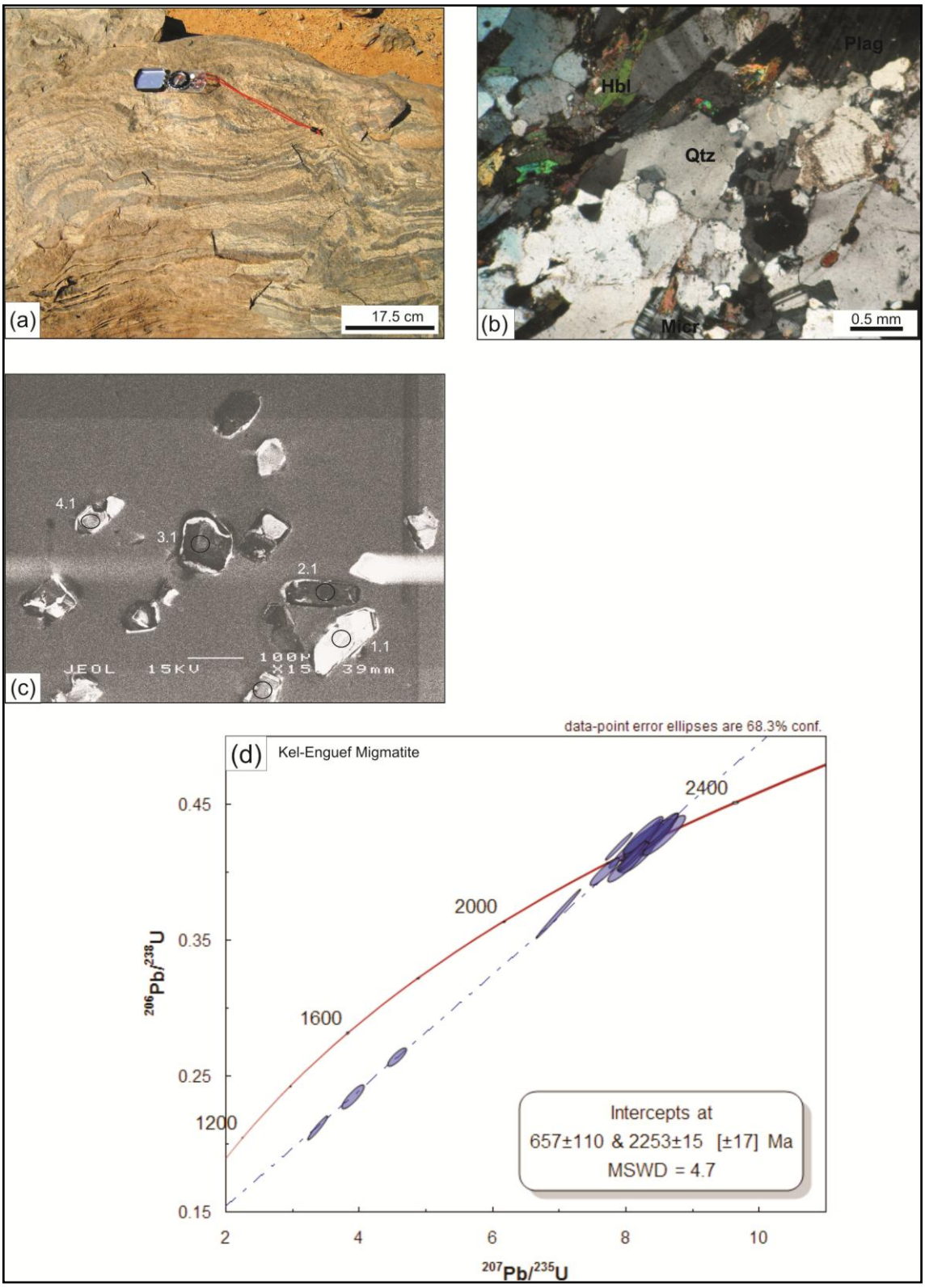

Figure 7.11: (a) The Kel Enguef migmatite unit showing flow texture that developed during re-crystallization (UTM, 30P 1594675, 0808119). (b) Photomicrograph of the sample BF_1299, showing alignment of hornblende (Hbl), and the Plag (plagioclase), Qtz (quartz) and Micr (microcline) crystals that dominate the leucocratic bands. (c) Zircon crystals that were analysed, they lack well defined rims, the cores of the zircon crystals were targeted. Numbers refers to the grain number in Table 7.2. Ellipses mark the location of the analysed spots. (d) The U-Pb Concordia diagram of the migmatite.

Table 7.8: Summary of SHRIMP U-Pb zircon data, sample BF_1299.

Summary of SHRIMP U-Pb zircon data, sample BF_1299_Kel-Enguef migmatite																			
Grain spot	% $^{206}Pb_c$	U (ppm)	Th (ppm)	$^{232}Th/^{238}U$	$^{206}Pb^*$ (ppm)	(1) $^{206}Pb/^{238}U$ Age		(1) $^{207}Pb/^{206}Pb$ Age		% Discordant	(1) $^{238}U/^{206}Pb^*$	±%	(1) $^{207}Pb^*/^{206}Pb^*$	±%	(1) $^{207}Pb^*/^{235}U$	±%	(1) $^{206}Pb^*/^{238}U$	±%	err. corr.
1.1	--	53	19	0.38	19	2279	±38	2247	±13	-2	2.36	2.0	0.1416	0.8	8.28	2.1	0.424	2.0	0.90
2.1	--	375	265	0.73	137	2278	±47	2240	±6	-2	2.36	2.5	0.1410	0.3	8.24	2.5	0.424	2.5	0.97
3.1	0.13	173	69	0.41	62	2245	±40	2226	±9	-1	2.40	2.1	0.1399	0.5	8.03	2.2	0.417	2.1	0.96
4.1	--	92	43	0.49	32	2223	±34	2279	±19	+3	2.43	1.8	0.1443	1.1	8.19	2.1	0.412	1.8	0.81
5.1	--	98	43	0.45	36	2281	±35	2285	±11	+0	2.36	1.8	0.1447	0.7	8.47	1.9	0.425	1.8	0.90
6.1	0.25	672	78	0.12	136	1360	±30	1971	±26	+34	4.26	2.4	0.1210	1.5	3.92	2.9	0.235	2.4	0.85
7.1	--	197	108	0.57	72	2298	±33	2268	±21	-2	2.33	1.7	0.1433	1.2	8.46	2.1	0.428	1.7	0.72
8.1	0.05	402	165	0.42	128	2027	±56	2195	±6	+9	2.71	3.2	0.1374	0.3	7.00	3.2	0.370	3.2	0.98
9.1	0.03	402	214	0.55	145	2257	±31	2188	±6	-4	2.38	1.6	0.1369	0.3	7.91	1.7	0.419	1.6	0.91
10.1	--	33	11	0.34	12	2293	±44	2295	±19	+0	2.34	2.3	0.1456	1.1	8.58	2.5	0.427	2.3	0.85
11.1	0.65	62	24	0.40	23	2276	±38	2250	±22	-1	2.36	2.0	0.1418	1.2	8.28	2.3	0.423	2.0	0.88
12.1	0.04	37	14	0.40	14	2303	±42	2269	±16	-2	2.33	2.2	0.1435	0.9	8.49	2.4	0.429	2.2	0.90
13.1	0.10	311	219	0.73	114	2293	±42	2231	±16	-3	2.34	2.2	0.1403	0.9	8.26	2.3	0.427	2.2	0.88
14.1	0.18	58	23	0.40	20	2192	±37	2270	±16	+4	2.47	2.0	0.1435	0.9	8.01	2.2	0.405	2.0	0.89
15.1	0.02	193	116	0.62	72	2316	±34	2272	±8	-2	2.31	1.7	0.1437	0.5	8.56	1.8	0.432	1.7	0.89
16.1	0.22	419	34	0.08	95	1511	±22	2043	±20	+29	3.79	1.6	0.1260	1.1	4.59	2.0	0.264	1.6	0.84
17.1	--	225	95	0.44	77	2171	±31	2218	±13	+2	2.50	1.7	0.1393	0.8	7.69	1.9	0.400	1.7	0.89
18.1	--	154	83	0.56	54	2220	±33	2267	±9	+2	2.43	1.8	0.1433	0.5	8.12	1.8	0.411	1.8	0.89
19.1	0.06	259	162	0.65	92	2224	±32	2258	±7	+2	2.43	1.7	0.1425	0.4	8.09	1.8	0.412	1.7	0.93
20.1	0.29	419	34	0.08	76	1241	±32	1889	±16	+38	4.71	2.8	0.1156	0.9	3.38	3.0	0.212	2.8	0.96
Errors are 1-sigma; Pb_c and Pb^* indicate the common and radiogenic portions, respectively.																			
Error in Standard calibration was 0.48% (not included in above errors but required when comparing data from different mounts).																			
(1) Common Pb corrected using measured ^{204}Pb.																			

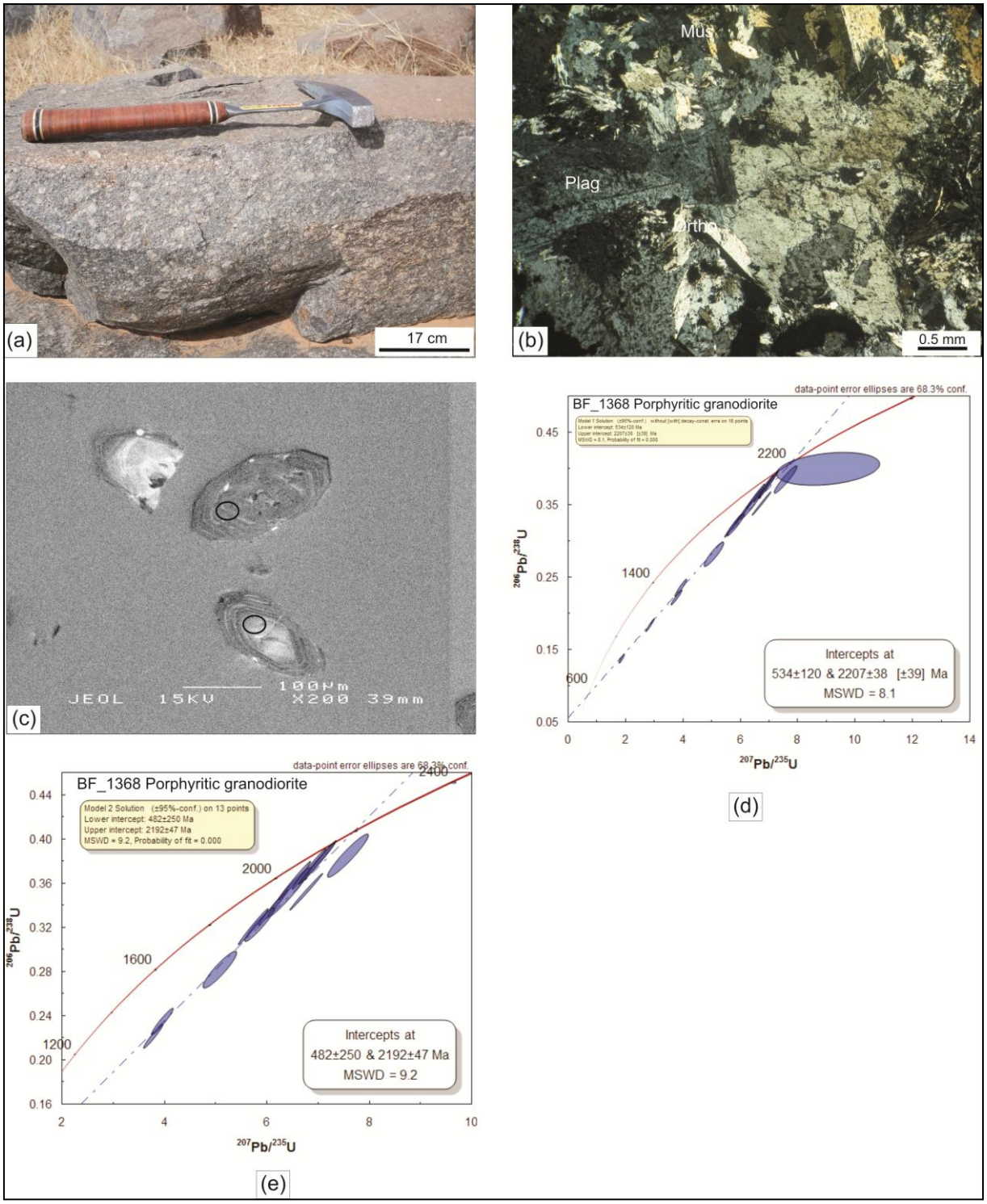

Figure 7.12: (a) The porphyritic granodiorite (UTM, 31P 1617054, 0181894) outcrops at the fold east of Markoye village. (b) The minerals are altered and include muscovite (Mus), plagioclase (plag), orthoclase (Ortho), and quartz. (c) Cathodoluminesence image of the zircon crystals that were analysed. The Ellipses indicate the analysed spot. (d) The U-Pb Concordia age diagram on 16 grain spots. (e) U-Pb Concordia age diagram on 13 grain spots after eliminating the 3 spots with high percentage of discordance.

Table 7.9: Summary of SHRIMP U-Pb zircon data, sample BF_1368.

Summary of SHRIMP U-Pb zircon data, sample BF_1368_Porphyritic granodiorite																			
Grain spot	% $^{206}Pb_c$	U (ppm)	Th (ppm)	$^{232}Th/^{238}U$	$^{206}Pb^*$ (ppm)	(1) $^{206}Pb/^{238}U$ Age		(1) $^{207}Pb/^{206}Pb$ Age		% Discordant	(1) $^{238}U/^{206}Pb^*$	±%	(1) $^{207}Pb^*/^{206}Pb^*$	±%	(1) $^{207}Pb^*/^{235}U$	±%	(1) $^{206}Pb^*/^{238}U$	±%	err corr
1.1	1.04	532	176	0.34	107	1361	±42	1990	±19	+35	4.26	3.4	0.1223	1.04	3.96	3.5	0.235	3.4	0.96
2.1	0.05	114	108	0.98	34	1942	±69	2138	±20	+11	2.84	4.1	0.1330	1.14	6.45	4.3	0.351	4.1	0.96
3.1	0.15	272	93	0.35	79	1875	±51	2120	±8	+13	2.96	3.1	0.1316	0.48	6.13	3.2	0.338	3.1	0.99
4.1	0.01	322	266	0.85	97	1941	±52	2225	±6	+15	2.85	3.1	0.1398	0.33	6.77	3.1	0.351	3.1	0.99
5.1	0.03	353	64	0.19	98	1800	±50	2126	±19	+18	3.11	3.2	0.1321	1.09	5.86	3.3	0.322	3.2	0.95
6.1	--	217	69	0.33	71	2073	±59	2152	±8	+4	2.64	3.3	0.1341	0.45	7.01	3.3	0.379	3.3	0.99
7.1	0.31	148	66	0.46	51	2166	±70	2505	±209	+16	2.50	3.8	0.1648	12	9.07	13.0	0.399	3.8	0.29
8.1	0.76	721	130	0.19	85	831	±25	1619	±24	+52	7.27	3.2	0.0997	1.29	1.89	3.5	0.138	3.2	0.93
9.1	--	242	83	0.36	77	2041	±56	2138	±7	+5	2.68	3.2	0.1330	0.42	6.83	3.3	0.372	3.2	0.99
10.1	0.43	170	74	0.45	56	2099	±59	2263	±20	+8	2.60	3.3	0.1429	1.17	7.58	3.5	0.385	3.3	0.94
11.1	0.28	291	162	0.58	80	1793	±51	2096	±9	+17	3.12	3.3	0.1299	0.50	5.74	3.3	0.321	3.3	0.99
12.1	0.40	578	191	0.34	91	1086	±35	1859	±14	+45	5.45	3.5	0.1137	0.77	2.88	3.5	0.184	3.5	0.98
13.1	0.55	262	103	0.41	50	1290	±38	2017	±15	+40	4.51	3.2	0.1241	0.87	3.79	3.3	0.222	3.2	0.97
14.1	0.09	261	127	0.50	81	1993	±54	2113	±8	+7	2.76	3.1	0.1311	0.46	6.55	3.2	0.362	3.1	0.99
15.1	0.25	441	168	0.39	107	1599	±55	2114	±30	+27	3.55	3.9	0.1312	1.73	5.10	4.3	0.282	3.9	0.91
16.1	--	183	92	0.52	59	2064	±58	2152	±8	+5	2.65	3.3	0.1341	0.47	6.98	3.3	0.377	3.3	0.99
Errors are 1-sigma; Pb_c and Pb^* indicate the common and radiogenic portions, respectively.																			
Error in Standard calibration was 0.71% (not included in above errors but required when comparing data from different mounts).																			
(1) Common Pb corrected using measured ^{204}Pb.																			

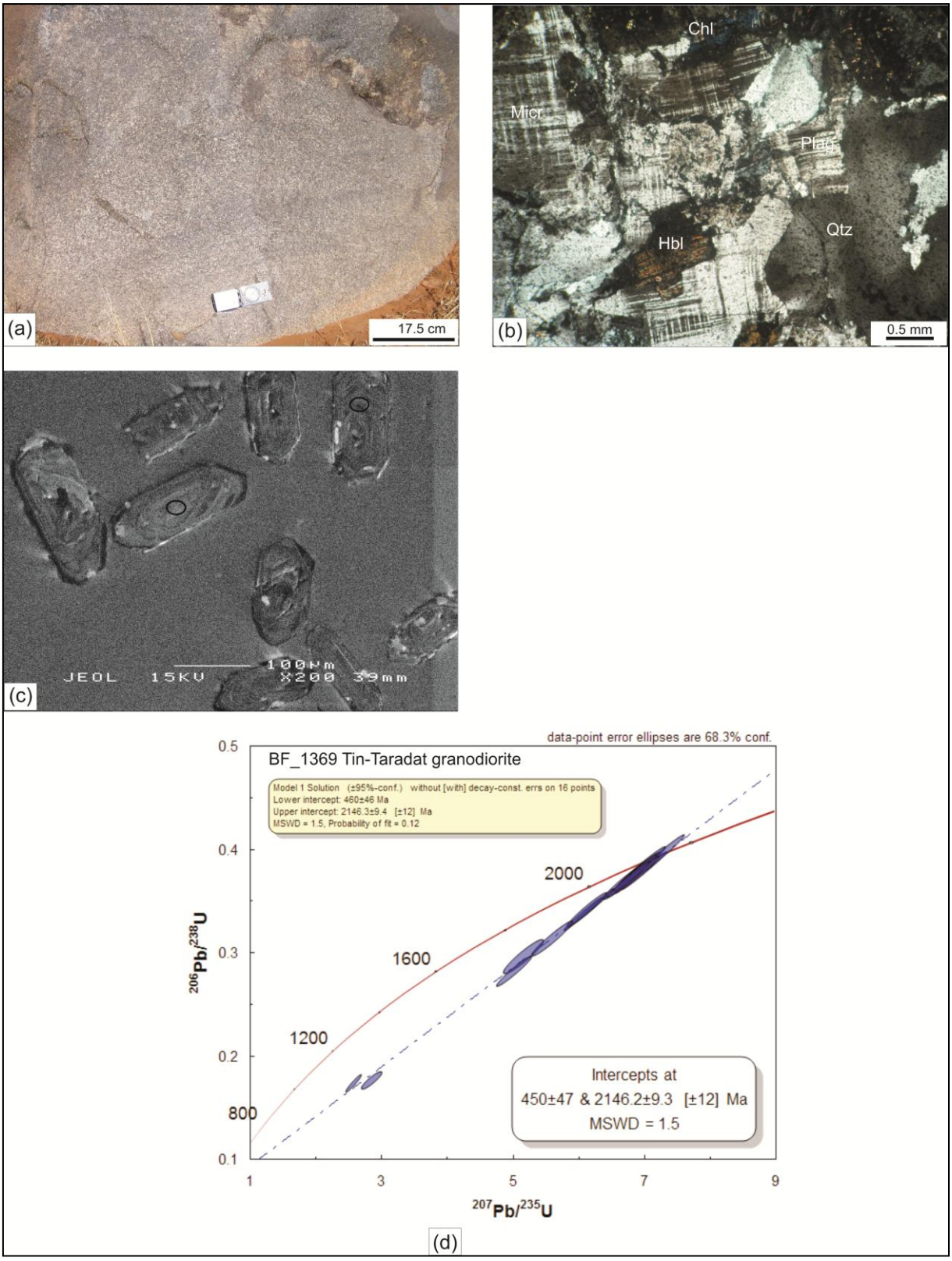

Figure 7.13: (a) Tin-Taradat granodiorite has banding in places (UTM, 31P 1618574, 0179168). (b) The photomicrograph showing the interlocking crystals of microcline (Micr), quartz (qtz), plagioclase (plag) and hornblende (hbl) with overprinting chlorite (Chl). (c) Cathodoluminesence image of the euhedral zircon crystals that were analysed. (d) U-Pb Concordia age diagram calculated on 16 grain spots.

Table 7.10: Summary of SHRIMP U-Pb zircon data, sample BF_1369.

Summary of SHRIMP U-Pb zircon data, sample BF_1369_Tin-Taradat granodiorite																			
Grain spot	% $^{206}Pb_c$	U (ppm)	Th (ppm)	$^{232}Th/^{238}U$	$^{206}Pb^*$ (ppm)	(1) $^{206}Pb/^{238}U$ Age		(1) $^{207}Pb/^{206}Pb$ Age		% Discordant	(1) $^{238}U/^{206}Pb^*$	±%	(1) $^{207}Pb^*/^{206}Pb^*$	±%	(1) $^{207}Pb^*/^{235}U$	±%	(1) $^{206}Pb^*/^{238}U$	±%	err corr
1.1	0.09	121	55	0.47	40	2092	±60	2123	±12	+2	2.61	3.3	0.1319	0.66	6.97	3.4	0.383	3.3	0.98
1.2	2.26	493	134	0.28	75	1046	±31	1921	±29	+49	5.68	3.2	0.1177	1.59	2.86	3.6	0.176	3.2	0.90
2.1	0.03	165	63	0.40	53	2030	±58	2125	±16	+5	2.70	3.4	0.1320	0.91	6.74	3.5	0.370	3.4	0.96
2.2	--	177	74	0.43	57	2072	±56	2151	±9	+4	2.64	3.1	0.1340	0.50	7.00	3.2	0.379	3.1	0.99
3.1	0.01	354	121	0.35	105	1912	±52	2115	±6	+11	2.90	3.1	0.1313	0.37	6.25	3.1	0.345	3.1	0.99
4.1	0.02	95	36	0.40	31	2069	±57	2130	±12	+3	2.64	3.2	0.1324	0.67	6.91	3.3	0.378	3.2	0.98
5.1	0.51	591	247	0.43	88	1031	±30	1762	±17	+45	5.76	3.1	0.1078	0.93	2.58	3.2	0.173	3.1	0.96
6.1	0.03	119	23	0.20	40	2145	±58	2142	±11	-0	2.53	3.2	0.1333	0.62	7.26	3.2	0.395	3.2	0.98
7.1	0.11	237	99	0.43	69	1873	±51	2105	±9	+13	2.97	3.1	0.1305	0.51	6.07	3.2	0.337	3.1	0.99
8.1	0.45	162	52	0.33	48	1895	±52	2100	±14	+11	2.93	3.2	0.1301	0.81	6.13	3.3	0.342	3.2	0.97
9.1	1.24	94	44	0.48	24	1673	±54	2050	±25	+21	3.37	3.7	0.1265	1.44	5.17	4.0	0.296	3.7	0.93
10.1	0.87	193	108	0.58	47	1601	±49	2089	±16	+26	3.55	3.4	0.1293	0.90	5.03	3.6	0.282	3.4	0.97
11.1	0.07	158	54	0.36	51	2062	±56	2124	±10	+3	2.65	3.2	0.1320	0.54	6.86	3.2	0.377	3.2	0.99
12.1	--	144	37	0.27	47	2053	±56	2143	±10	+5	2.67	3.2	0.1333	0.55	6.90	3.2	0.375	3.2	0.99
13.1	0.18	322	125	0.40	87	1758	±55	2095	±18	+18	3.19	3.6	0.1298	1.03	5.61	3.7	0.313	3.6	0.96
14.1	0.06	164	41	0.26	52	2034	±55	2128	±9	+5	2.70	3.2	0.1322	0.52	6.76	3.2	0.371	3.2	0.99
Errors are 1-sigma; Pb_c and Pb^* indicate the common and radiogenic portions, respectively.																			
Error in Standard calibration was 0.71% (not included in above errors but required when comparing data from different mounts).																			
(1) Common Pb corrected using measured ^{204}Pb.																			

7.5. Summarized results of U-Pb SHRIMP ages according to their significance

The U-Pb ages are summarized in Tables 7.11, 7.12 and in Figure 7.14. Where both the core and the rim were analysed the ages are also compared for their significance and implications. Samples BF_1144 and BF_1299 of the Lilengo gneiss complex give an average age of 2253 Ma with inherited ages of 2280-2270 Ma, reflecting the age of the source or pre-existing crust.

Sample BF_1147, the granite boulder from the Dembam Member which gave a U-Pb concordant age of 2255 ± 26 Ma, currently constrains the maximum age of the Birimian Supergroup and an angular unconformity between the Lilengo gneiss and the Birimian Supergroup in the OGB and GGGT, because (reasonably) the granite body from which the boulder eroded must have crystallised prior to erosion. The age corresponds well with samples BF_1144 and BF_1299, and again, could constrain the crystallisation age of the protolith.

The maximum age of the Birimian Supergroup is constrained by the age of the porphyritic granodiorite (sample BF_1368) at 2207 ± 38 Ma or 2192 ± 47 Ma. It can therefore be reasonably argued that the Birimian Supergroup in the Oudalan region was deposited between 2253 and 2207 or 2192 Ma. It is clear that the Birimian Supergroup was present at 2203 Ma because it is intruded by the Mrs Pink granite. Plutonism and deposition may have been coeval at that age.

D1 deformation is constrained by the age of the Dori granodiorite gneiss (Sample BF_1156 and BF_1157), the Mrs Pink granite (Sample BF_1146), and the Tin-Taradat granodiorite (Sample BF 1369) at 2165-2137 Ma.

D2 deformation is not constrained. The new growth/recrystallisation ages/rim ages are within the 2130-1980 Ma ages assigned to the Eburnean orogeny by Feybesse et al. (2006).

D3 is not constrained by any of the analysed samples.

Table 7.11: Summary table of the U-Pb SHRIMP ages from the analysed samples.

Sample Name	Sample Number	Crystallisation age	Inherited/ Xenocrystic zircon ages	New growth/ recrystallisation age	Core and rim ages for two spots zircons	
					Core	Rim
Lilengo gneiss	BF_1144	2253 ± 9 Ma	2276 ± 15 Ma			
			2284 ± 23 Ma			
			2277 ± 16 Ma			
			2272 ± 33 Ma			
Mrs Pink granite	BF_1146			2140 ± 9.6 Ma	2172 ± 11 Ma	2152 ± 12 Ma
					2141 ± 13 Ma	2114 ± 9 Ma
		2151 ± 16 Ma	2208 ± 28 Ma	2126 ± 9 Ma	2127 ± 10 Ma	2093 ± 14 Ma
					2126 ± 9 Ma	2146 ± 11 Ma
Granite clast	BF_1147	2255 ± 26 Ma	2326 ± 21 Ma			
Gorom-Gorom granodiorite	BF_1149	2162 ± 28 Ma	2240 ± 14 Ma			
			2270 ± 36 Ma			
Porphyritic monzodiorite	BF_1153	2141 ± 19 Ma				
Dori granodiorite gneiss	BF_1156	2148 ± 9.3 Ma		2105 ± 10 Ma	2105 ± 10 Ma	2142 ± 16 Ma
Dori granodiorite gneiss	BF_1157	2164 ± 24 Ma	2200 ± 17 Ma	2104 ± 9 Ma	2139 ± 10 Ma	2104 ± 9 Ma
					2136 ± 12 Ma	2111 ± 10 Ma
Lilengo migmatitic gneiss	BF_1299	2253 ± 15 Ma	2268 ± 29 Ma	1955 ± 257 Ma		
Mrs Pink granite	BF_1332	2203 ± 12 Ma	2247 ± 19 Ma			
Porphyritic granodiorite	BF_1368	2207 ± 38 Ma				
Tin-Taradat granodiorite	BF_1369	2146 ± 9 Ma		2125 ± 16 Ma	2123 ± 12 Ma	1921 ± 29 Ma

Table 7.12: Summary table of the U-Pb SHRIMP lower intercept ages from the analysed samples.

Lower Intercepts age range (Ma)						
Range 1	Range 2	Range 3	Range 4	Range 5	Range 6	Range 7
120 ± 28	394 ± 75	450 ± 47	512 ± 54	617 ± 300	1193 ± 490	1955 ± 257
	397 ± 79	482 ± 250	534 ± 120	657 ± 300		
	391 ± 260		556 ± 120			

The lower intercept ages in Table 7.12 indicate a probable metamorphic age. In interpretation the age range 1 can be related to the breakup of Gondwana when Africa separated from South America and the Equatorial-Atlantic plume generation around 138-68 Ma (Riley and Knight, 2001; Segev, 2002). The age range 2 can be ascribed to the emplacement of the Central Atlantic Magmatic Province around 200 Ma (Deckart et al. 2005). The age range 3 to 6 can be ascribed to the Pan-African tectono-thermal activity. The Pan-African tectono-thermal activity has been suggested to have occurred from 1200 Ma to 450 Ma (Caby et al. 1981; Gass, 1981; Villeneuve, 1989). The Pan-African tectono-thermal activity is further subdivided into three major divisions, that is (1) the Lower Pan-African (1200-1000 Ma) (Gass, 1981), (2) Middle Pan-African or Pan African I (1000-600 Ma) (Gass, 1981; Villeneuve, 1989), and the (3) Upper Pan-African or Pan African II (600-450 Ma) (Gass, 1981; Villeneuve, 1989). The lower intercept age ranges 2 to 6, overlap with the Middle/Pan African I and Upper /Pan African II events. These time frames are marked by the rifting of the eastern margin of the WAC around 800 Ma and an E-W collision of the WAC and the Tuareg Shield at around 600 Ma (Caby et al. 1981, Bertrand et al. 1986; Liégeois et al. 2013). The range 7 age overlaps with the Eburnean Orogeny and with the time frame that Liégeois et al. (1991) had suggested that it is related to the tectonic reactivation with the WAC.

7.6. REE geochemistry

The samples analysed for geochronology were also analysed for their trace element geochemistry. The REE elements data is normalised using the chondritic meteorite values after Anders and Grevesse (1989). The chondrite normalising values are attached in Appendix J.

The samples are plotted in Figure 7.15a. Samples BF_1156 (Dori granodiorite), BF_1157 (Dori granodiorite), BF_1369 (Tin-Taradat pluton), and BF_1332 (Mrs Pink granite) show a strong

depletion of HREE, which can indicate either the presence of garnet (Rollinson, 1993), or zircon in the source, or garnet involvement and deep melting or crystallisation under high pressure. These samples have steep REE pattern with insignificant to positive Europium anomalies. These patterns are common in Archaean TTG suites (c.f. Condie 1993; Taylor and McLennan 1995; Rudnick and Gao, 2003) and are characteristic of lower crustal melts (Rudnick and Gao, op cit.).

The Lilengo gneiss (BF_1144), Mrs Pink granite samples, BF_1145, BF_1146, BF_1322, BF_1324, BF_1333, granite clast (BF_1147), Gorom-Gorom granodiorite (BF_1149), porphyritic monzodiorite (BF_1153, BF_1160, BF_1367), gabbro (BF_1154, BF_1162) and the porphyritic granodiorite (BF_1368) exhibit a REE patterns with near flat HREE (Figure 7.15a). These rocks will require involvement of lower crustal melting processes indicating no significant involvement of garnet in the source regions. The flat HREE patterns indicate the absence of garnet and that melting or crystallisation occurred in the lower crust. Flat HREE and LREE enrichment and negative Europium is typical of post Archaean granitoids (Kemp and Hawkesworth, 2003) and resembles crystallisation in the upper continental crust (White, 2012).

All samples analysed and plotted in Figure 7.15a have a slight enrichment in LREE with relation to HREE and the chondrite and this can be accounted for by the presence of hornblende in the melt (Rollinson, 1993). The magma is enriched in potassium feldspar and plagioclase which is reported by the negative Europium anomaly in most of these samples because Europium is compatible with plagioclase and potassium feldspar (Rollinson, 1993; Kemp and Hawkesworth, 2003). The dominant negative Europium anomaly in the REE patterns indicates the removal of feldspar from the melt by crystal fractionation, or partial melting of a rock in which the feldspar is retained in the source. The enrichment in LREE and the negative Europium anomaly present in these rocks can be associated with crystallisation in the upper continental crust (Rudnick and Gao, 2003; White, 2012). The samples with no Europium anomaly would have evolved from the middle crust. The samples with positive Europium anomaly (BF_1156, BF_1157, BF_1332 and BF_1369) would have evolved from the lower crust (Rudnick and Gao, 2003).

A multi-element diagram that compares the samples chemistry with the mantle source is plotted in Figure 7.15b. There is a slight negative anomaly in Nb, for all samples plotted in the multi-element diagram. This negative anomaly can be indicative of crystallisation in the continental crust and may suggest crustal involvement in the magma processes (Rollinson, 1993). Secondly the samples are highly depleted in phosphorus which is compatible in apatite, which occurs in most of the samples. The Sr anomaly reported in all the samples indicate that the magma may be related to the upper crust (negative Sr anomaly), middle crust (no Sr anomaly) and lower crust (positive Sr anomaly) (Rudnick and Gao, 2003).

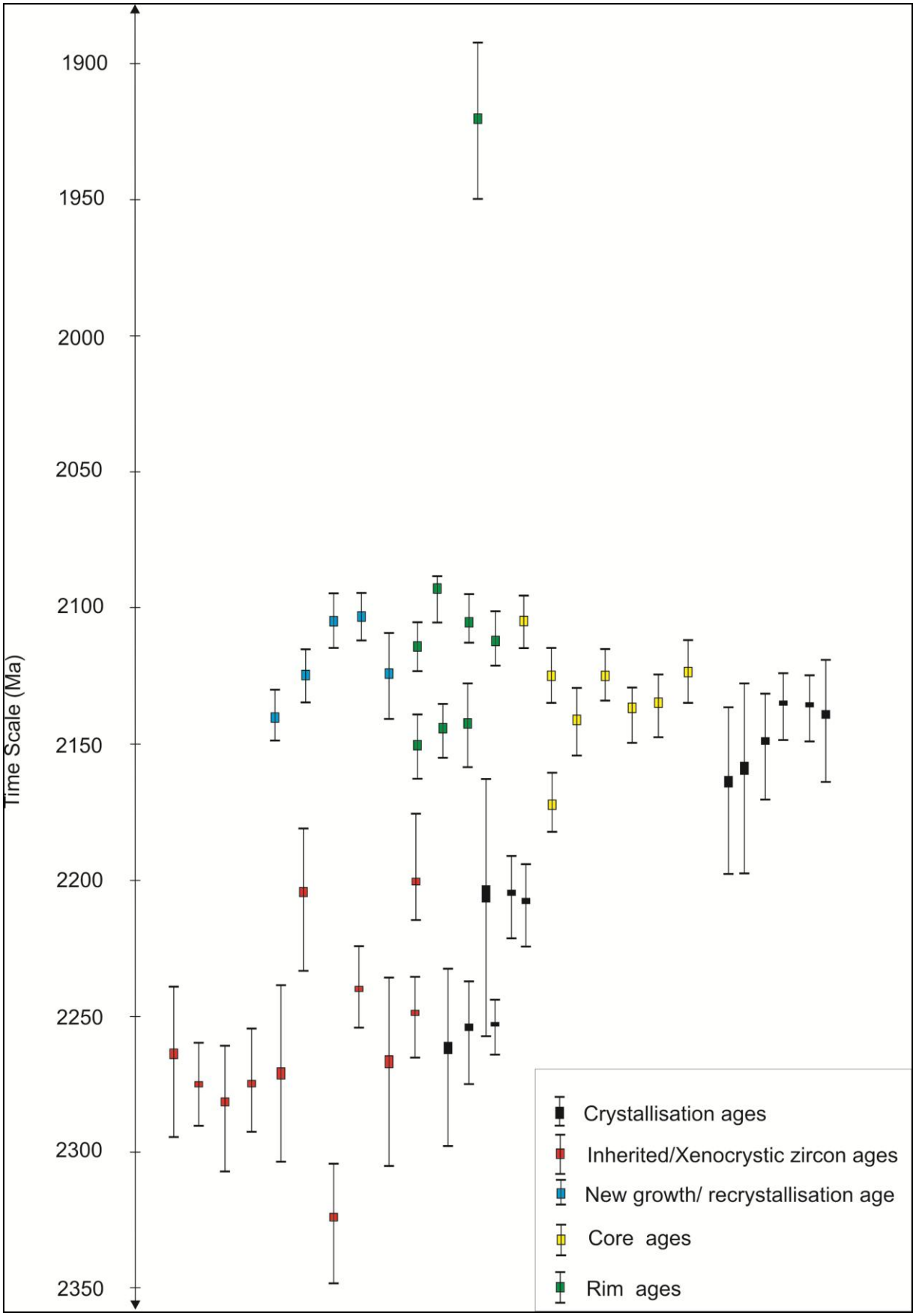

Figure 7.14: The U-Pb ages summary plot, indicating the distribution of crystallisation, inherited, new growth, core and rim ages from the analyzed samples in Table 7.11.

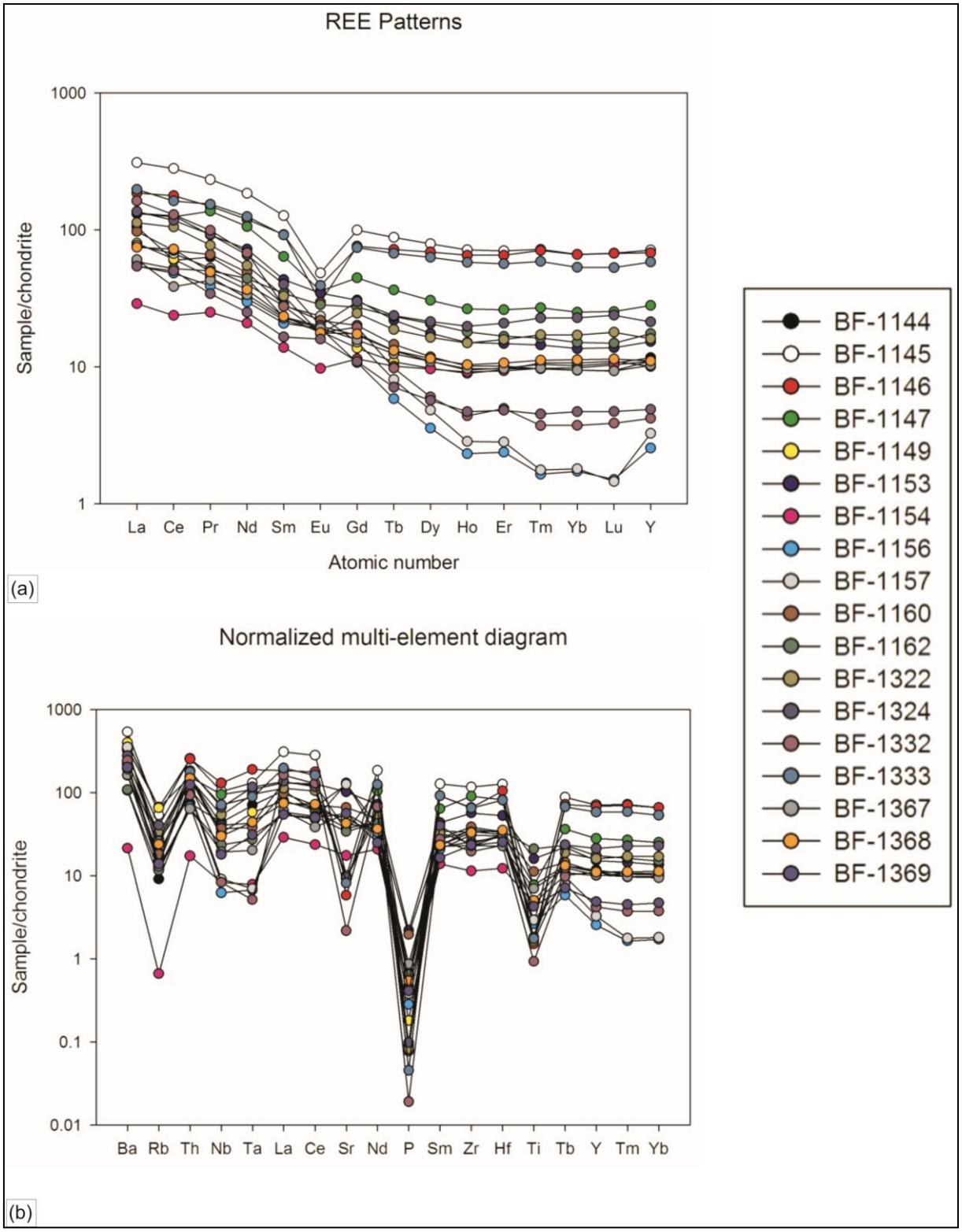

Figure 7.15: (a) Whole rock REE patterns for samples collected for geochronology, normalised to condrite meteorite. The majority of samples (felsic granitoids) exhibit a REE pattern with near flat HREE. (b) Multi-elements diagram for the samples collected for geochronology analysis. All the samples have a significant depletion in phosphorus.

CHAPTER 8
DISCUSSION AND SYNTHESIS

8.1. Introduction

The integration of desktop studies, structural field mapping, petrographic studies and analytical methods including geochemical and isotope SHRIMP dating techniques have provided a wide range of information about the strato-tectono-magmatic evolution of the OGB and GGGT. A number of successive structural, metamorphic, mineralization and magmatic events have been constrained in time through integration of field mapping and U-Pb geochronology.

The tectonic history of the OGB and the GGGT is summarized according to the relative chronologies as established during field studies, and data from the OGB and GGGT are combined into one regional tectonic model. Gold mineralisation is contextualized within this strato-tectonic history. The absolute geochronology, as established in this research, is integrated with relative chronological evidence and compared with published data for the West African Craton. A tectonic model for the northeast of Burkina Faso is thereby established.

8.2. Tectonic overview of the OGB and GGGT

The tectonic overview of the OGB and the GGGT records complex interrelationships between deposition of metavolcanic and metasedimentary sequences, several phases of pluton emplacement, several tectonic events in which at least 3 unique regional deformations were recorded, i.e., D1, D2 and D3, and gold metallogenesis. The relative timing of geological events as established from crosscutting relationships and absolute ages for the OGB and GGGT is summarised in Figure 8.1. The boundary between the two tectonic domains is marked by the MSZ.

8.2.1. Pre-Birimian to Birimian

The basement rocks of the OGB and the GGGT are formed by the Lilengo gneiss complex. The Lilengo gneiss complex is expressed by partial melting and recrystallisation of pre-Birimian supracrust to form a gneiss migmatite complex. The metamorphic conditions attained granulite facies. These rocks are similar in composition to orthogneisses described by Lemoine et al. (1990) in Cote d'Ivoire and Burkina Faso, Pons et al. (1995) in Niger, Hirdes et al. (1996) in Cote d'Ivoire, Gueye et al. (2008) in the KKI, and De Kock et al. (2009) in Ghana, where they are consistently described as basement rocks. However, there is a considerable variation in the ages of these gneissic complexes across the WAC which is discussed in Section 8.3.

The Lilengo gneiss complex was intruded by the Mrs Pink Granite and hornblende granodiorite-tonalite pre to syn-deposition of the Birimian Supergroup. An angular unconformity exists between the

pre-Birimian rocks and the Birimian Supergroup indicating that uplift and erosion took place at some stage prior to deposition in the Birimian Oudalan basin. Deposition of metavolcanic sequences, volcanoclastic greywacke, siltstone-shale and chemical sedimentary rock is interpreted to have taken place on the angular unconformity, in a deltaic continental shelf environment on the margin of a back arc basin (Tshibubudze et al., 2009; Peters, 2011; Woolfe, 2011).

The units include (1) a meta-volcanic sequence (basaltic hyaloclastite) and amphibolites, (2) a gritstone-greywacke-siltstone-shale sequence, (3) a sandy dolomite unit and carbonaceous BIF, (4) a conglomerate-gritstone-greywacke-siltstone-shale sequence including the Dembam Member of Peters (2011), and (5) a volcanoclastic greywacke sequence.

The mafic volcanic and metasedimentary sequences were subsequently intruded by a suite of TTG plutons, and subsequently monzonite dykes and sills, and gabbro pyroxenite dykes. These intrusions include the Dori Batholith, Gorom-Gorom and the Tin-Taradat granodiorite plutons, with contact metamorphism of the country rock.

During the emplacement of the TTG suite plutons the rocks were metamorphosed attaining amphibolite to granulite facies around the pluton margins. Emplacement accompanied formation of marginal shear zones such as the DMSZ ($D_{1\text{-}x}$), and an igneous foliation. Emplacement also accompanied exhumation of granulite facies gneiss and migmatite.

The presence of granulite facies gneiss and migmatites is interpreted as being related to the exhumation process of pre-existing deep metasedimentary basin as described by Vidal et al. (2009), Lompo (2009) and Ganne et al. (2014). Vidal et al. (2009) and Lompo (2009) claimed vertical tectonics and crustal overturning related to magmatic emplacement in a plume with formation of geosynclines at the margins of the plutons. However, in the OGB there is no magmato-structural evidence of coeval geosynclinal formation along the margin of any plutons during emplacement. For example, emplacement of the Dori batholith was vertical along the north marginal shear (DMSZ) but near horizontal along the eastern margin of the batholith.

Granulite facies gneiss and migmatites are restricted to the northern margin of the batholith. Ganne et al. (2014) proposed that migmitites and gneisses are entrained in the pluton emplacement process, effectively resolves a discordance between magmatic facies and entrained facies rocks. This seems to be the case along the northern margin of the Dori batholith where migmatites and gneiss parallel the batholith margin.

Subsequent to pluton emplacement, the TTG plutons and rocks of the Birimian Supergroup were intruded by gabbro-diorite-pyroxenite, and monzonite sills and dykes. In the northeast of Burkina Faso the gabbro-diorite-pyroxenite intrusions are interpreted as co-magmatic with Birimian volcanics (Beziat et al., 2000; Hein et al., 2004). However, in the study area, the gabbro-diorite-pyroxenite crosscut the Dori batholith, Tin-Taradat granodiorite and Gorom-Gorom granodiorite, which intrude the Birimian Supergroup. The plutons are dated at 2164 ± 24 Ma, 2146 ± 9.3 Ma and 2162 ± 28 Ma,

respectively. It follows that the gabbro-diorite-pyroxenite are younger than 2146 ± 9.3 Ma and not co-magmatic with volcanics in the Supergroup.

8.2.2. D1 Deformation – The Tangaean Event

The pre-Birimian to Birimian supracrustal rocks and intrusions were regionally metamorphosed during ductile-brittle deformation in D1 to greenschist to amphibolite facies. However, along shear and mylonite zones, metamorphic facies range from amphibolite to granulite indicating variation in P-T conditions along the trend of the structures. The formation of isolated mylonite zones and pseudotachylites (PS_1) along the trend of D1 shear zones is interpreted as strain localization related to variation in composition of parent rocks, with formation taking place in the middle to lower crust.

Norris and Cooper (2003) reported strain localization in the lower crust along the 1-2 km wide Alpine fault mylonite zone in New Zealand. Sibson (1975) reported that mylonite zone formation is restricted to mid-crustal levels of about 10-20 km and relates to buildup of finite and high shear strain (Berthé et al., 1979; Lister and Snoke, 1984). Magloughlin and Spray (1992), Sibson (1977) and Allen (1979) added that pseudotachylite formation occurs at shallow crustal levels of about 2-10 km and postdates formation of mylonite zones. However, Sibson (1975, 1977) and Barker (2005) assigned the lower limit of pseudotachylite formation to 10-15 km, which is the transition zone from brittle to ductile dominant deformation regimes. Allen (1979) proposed that the subsequent exhumation and reactivation of mylonite to higher crustal level explains the formation of pseudotachylite by frictional melting rather than an increase in frictional temperature to 900-1100° C during seismic failure (Mackenzie and Brune, 1972; Sibson, 1975, 1977, 1986; O'Hara, 2001; Barker, 2005). Sibson (1975, 1977) stated that contemporaneous formation of mylonite and pseudotachylite is possible but occurs at different crustal levels. Allen (1979), Sibson (1980) and Passchier (1982) proposed that it is possible for pseudotachylite to form in a ductile regime at the cessation of an aseismic shear where strain hardening has taken place.

From this information it is argued that there was a localized buildup of finite and high shear strain during D1 ductile-brittle deformation in the study area to produce ultramylonites (Mukosi and Sabce mylonite zones), mylonites (Sabce, Billiata, southern MSZ) and psuedotachylites (north MSZ) along and within first-order scale shear zones. The implication from the studies of Allen (1979), Sibson (1980) and Passchier (1982) is that the ultramylonite, mylonite and psuedotachylite in the study area formed near the ductile-brittle transition zone at crustal depths of 10-15 km. Through seismic cycling, D1 shear zones were subjected to localized variations in pressure and ultimately temperature. There is therefore also a localized variation in metamorphic grade along and within first-order scale shear zones that ranges from upper greenschist to granulite (silliminite stability, Chapter 6). A further implication is that a considerable portion of the crust has been eroded since the Palaeoproterozoic, perhaps in the order of approximately 10 km or more.

Furthermore, D1 is characterized by dextral (reverse) displacement within north-northeast trending structural domains namely, the GGGT domain compartmentalized by the Gorgadji Shear Zone to the west and the Markoye Shear Zone to the east; the OGB domain compartmentalized by the Markoye Shear Zone to the west and the Kargouna Shear Zone to the east. The domains are compartmentalized by complex shear zones in which it is possible to define ultramylonite, mylonite and pseudotachylite (PS_1), while within domains it is possible to define; (1) northwest and north-northeast trending ultramylonite, mylonite and psuedotachylite zones that report reverse (dextral) displacement, (2) northwest-trending thrust-folds (F_1), and (3) a penetrative regular northeast plunging lineation (L_1).

Specifically, in the OGB domain, D1 is characterized by the formation of north-northeast trending mylonite-shear zones, namely, the Saoga Branch of the MSZ, and the Afu Branch of the KSZC. Northwest trending thrusts are associated with formation of quartz-chlorite-muscovite schist (dominantly S_1 to S_1-C foliation) (Chapter 5). Greenschist to amphibolite facies generally characterizes D1 in the OGB, with upper greenschist to granulite facies within shear-mylonite zones.

In contrast, in the GGGT domain D1 is characterized by the formation of sinistral strike-slip to oblique displacement on east-northeast trending mylonite zones (Sabce Mylonite Zone) and north-northeast trending mylonite-shear zones, including, the Saoga Branch of the MSZ. The mylonites have a penetrative northwest trending S_1-C to S_1 mylonitic foliation (Billiata Mylonite Zone). Upper greenschist to amphibolite facies generally characterizes D1 in the GGGT domain, with upper greenschist to granulite facies within shear-mylonite zones.

D1 is recognised across northeast Burkina Faso including in the Goren Belt (Hein, 2010), Bouroum-Yalago belts (Vanin et al., 2004), and Belahouro region (McCuaig, 2006; McCuaig et al., 2009). It is also recognized in the Pissila Batholith as crosscutting the Saaba Gneiss Complex (Simoko, 2012). Baratoux et al. (2011) and Metelka et al. (2011) also reported in their studies of south-western Burkina Faso in the Boromo, Houndé and Banfora belts.

Hein (2010) defined D1 from the Goren Belt as characterized by the formation of northwest trending dextral-reverse shear zones, northwest trending thrust-folds (F_1), and a penetrative S_1-C schistosity. Hein (2010) and Simoko (2012) reported northwest trending mylonite zones in crosscut to the Pissila Batholith, although recent studies suggest that these form part of the Saaba gneiss complex which is older than granodiorite plutons in the Pissila Batholith (pers comm.; Hein 2014). From the southern Bouroum Belt, Vanin et al. (2004) reported northwest trending shear and mylonite zones in the Tarpako region, and in the northern Bouroum Belt, McCuaig (2006) and McCuaig et al. (2009) defined D1 in the Belahouro region as characterized by the formation of a northwest trending layer parallel foliation (S_1) and north-verging thrust faults, folds (F_1). In the southwest of Burkina Faso, Baratoux et al. (2011) and Metelka et al. (2011) reported D1 as being defined by a uniform north-northwest to north-northeast trending foliation (S_1). They recognized that D1 may also correspond

with development of north and north-northeast trending shear zones, high strain zones, magmatic foliation (S_1), and folds (F_1).

In the study area, the palaeo-principal compressive stress direction in D1 is interpreted to be southwest-directed based on fold-thrust vergence; lineations, orientation of extensional vein (V_1) and psuedotachylite (PS_1). This compares well with southwest directed palaeo-principal compressive stress of Hein (2010) for the Goren Belt; and symmetric northeast to southwest palaeo-principal compressive stress of McCuaig (2006) and McCuaig et al. (2009) for the northern Bouroum Belt. D1 has been termed the Tangaean Event by Tshibubudze et al. (2009), Tshibubudze and Hein (2010), Hein (2010), Baratoux et al. (2011), Metelka et al. (2011), and Tshibubudze and Hein (2013), and corresponds with Eburnean I and Eoeburnean of Ghana.

D1 was succeeded by the emplacement of the Dolbel Batholith in the OGB and granodiorite in the GGGT. These intrusions crosscut D1 structures (Chapter 5 and 6); they are therefore older than D1. The age of the Dobel batholith is poorly constrained by an imprecise Rb-Sr isochron of 2137 ± 126 Ma (Léger et al., 1992), but it is important to note that Pons et al. (1995) reported the existence of discontinuous zones of orthogneiss marginal to the batholiths. Their descriptions are remarkably similar to those of Tshibubudze and Hein (2013) of gneiss around the margin of the Dori Batholith. Pons et al. (1995) attributed the emplacement of gneiss as being related to diapiric processes which is similar to that concluded by Ganne et al. (2014).

8.2.3. D2 Deformation – The Eburnean Orogeny

Subsequent to deformation in D1, the supracrustal rocks and intrusions in the study area were regionally metamorphosed during brittle-(ductile) deformation in D2 to greenschist facies. D2 is characterized by sinistral (reverse) displacement and reactivation along the 1st order north-northeast trending structural domains. Within the domains, it is possible to define reverse-oblique displacement/reactivation along east-northeast trending shears-mylonite zones, and refolding of F_1 by northeast-trending F_2 (Figure 8.1).

D2 is reported by Milési et al. (1991, 1992), Feybesse et al. (2006), Hein (2010), De Kock et al. (2011, 2012); Baratoux et al. (2011), Perrouty et al. (2012), and others, as the dominate phase of deformation affecting the WAC. According to these authors, D2 in its early phase, is marked by northwest-southeast crustal shortening with local development of crenulation cleavages, isoclinal folds, shear zones, and thrust faults. In its later phase D2 is marked by north-northwest to south-southeast shortening with development of north-northeast strike-slip to oblique faults and shears. The shift from early D2 to later D2 is progressive (Feybesse et al., 2006).

In the OGB, D2 is represented by north-northeast shear zones such as the Koreziéna Branch of the MSZ, and the Waho Branch of the KSZC. East-northeast trending shears generally dip to the southeast. A pervasive, crenulating to disjunctive S_2-C to S_2 foliation is ubiquitous across the study area. A southeast plunging L_2 stretching lineation (Chapter 5) and macroscopic buck-quartz-carbonate

veins present throughout the OGB and GGGT domains. In the GGGT, D2 is represented by reactivated east-northeast trending mylonite zones as shear-mylonite zones, and a northwest plunging L_2 stretching lineation (Chapter 6). D2 shears are generally quartz-chlorite ± muscovite shears.

In D2, northwest-trending D1 thrust-folds where dilated to form gold-bearing quartz-sulphide veins which predominate in the OGB. These include quartz-sulphide and quartz-sulphide-carbonate sheeted and stockwork veins, iron-rich cataclasites, and gold-bearing buck quartz (in north-northeast trending D2 shear zones). Artisanal mine workings are located in areas where these gold-bearing quartz-sulphide veins proliferate (Chapter 4, 5) and particularly where NW trending D1 structures are disjunctively crosscut by NE trending D2 shears. A deep saprolite profile is also important (Milési et al., 1992; Nikiéma, 1992; Tshibubudze et al., 2009). In contrast to the OGB, there is a notable absence of gold-bearing quartz-sulphide veins in the GGGT, and a thin saprolite profile is developed; artisanal activity is thereby limited to small isolated pits.

The D2 deformation is reasonably correlated with the deformation during the polycyclic Eburnean Orogeny of Feybesse et al. (2006) that is constrained at 2130-1980 Ma, were northwest-southeast crustal shortening was followed by north-northwest to south-southeast shortening with development of strike-slip faults and shears.

The D2 deformation was succeeded by intrusion of pegmatite veins/dykes and aplite-granite dykes. The intrusion of pegmatite veins/dykes and aplite-granite dykes were succeeded by D3.

Based on the kinematic data available, the palaeo-principal compressive stress ($\sigma 1$) in D2 is interpreted to be northwest-directed in the OGB, and southeast-directed in the GGGT. This difference in transport direction across the MSZ suggests that the MSZ possibly acted as an oblique-slip shear during D2. As described by Wilson (1965), Kearey and Vine (1996) transport direction across major strike-slip faults or shears can be opposed in direction where there is shortening along the fault/shear. Thus the MSZ may have been a zone of considerable shortening during D2. The interpreted palaeo-principal compressive stress in D2 in the study area is similar to that interpreted by Milési et al. (1991, 1992), Feybesse et al. (2006), Hein (2010), De Kock et al. (2011, 2012); Baratoux et al. (2011), and Perrouty et al. (2012) as being southeast-northwest directed.

8.2.4. D3 Deformation – Wabo Tampelse Event

In the study area, D3 deformation is brittle in character but weakly expressed across the study area. In the GGGT, it is characterized by the formation of a west-northwest trending fracture cleavage (S_3) and conjugate faults sets. The fault sets dip moderately north and south. In the OGB, D3 is associated with the formation of kink or chevron folds. S_3 in the OGB and GGGT is interpreted to have developed during a north-south compression.

D3 was first recognised from the Goren belt where it was termed the Wabo-Tampelse Event by Hein et al. (2004) who reported the presence of west-northwest trending shears and folds (F_3), and a crenulation cleavage (S_3), in crosscutting relationship to D2 structures. D3 was subsequently

recognised in western Burkina Faso by Baratoux et al. (2011) who noted the presence of kink or chevron folds in the Houndé greenstone belt. Baratoux et al. (2011) and Metelka et al. (2011) attributed D3 with the development of north or south dipping thrust faults, an east to west trending crenulation cleavage, and kink or chevron folds.

The D3 deformation in the OGB and GGGT was succeeded by the intrusion of west-northwest trending dolerite-gabbro dykes that are dated at 250 Ma (Hottin and Ouedraogo, 1992).

8.2.5 Comparison of the GGGT and OGB

There is a stunning similarity in strato-tectonic histories between the OGB and the GGGT, as depicted in the schematic strato-tectonic charts in Figures 8.1 and 8.2. The Lilengo gneiss complex does not outcrop in the OGB but is interpreted as basement to the OGB. The angular unconformity mapped in the GGGT is interpreted as the base of the Birimian Supergroup in the study area.

The Birimian stratigraphic sequence in the study area is made up of mafic volcanic units that present as amphibolite in the GGGT. A carbonaceous BIF sequence in the GGGT is correlated with the sandy dolomite in the OGB. Quartzite-metagritstone and metasiltstone sequence in the GGGT is correlated with the conglomerate-greywacke-siltstone-shale sequence in the OGB. The upper greywacke sequence in the OGB including the Dembam Member is absent in the GGGT.

The emplacement of plutons and dykes can also be easily correlated across the study area. Mrs Pink granite and the TTG suite plutons that are syn to post Birimian in age occur in the OGB and GGGT. Gabbro-diorite-pyroxenite, post-D1 to syn-D2 TTG suite plutons, and post-D3 dolerite dykes crop out across the study area. Monzonite dykes and sills are found only in the OGB, while aplite-granite dykes and pegmatites are recognised only in the GGGT. The Dori batholith and contact aureole is restricted to the OGB.

Similarly, the structural architecture of the OGB and GGGT domains is near identical as discussed in Sections 8.2.2 and 8.2.3. The domains were subjected to similar tectonic regimes.

8.3. Geochronology overview

The relative geochronological overview of the OGB and the GGGT, as establish in Chapters 5 and 6, is constrained by U-Pb zircon geochronology of magmatic rocks as presented in Chapter 7. The relative and absolute chronological data support a robust strato-tectonic model for crustal development in the study area.

Zircons usually form during initial magmatic crystallisation and during partial melting (Andersson et al., 2002; Hoskin and Schaltegger, 2003) and have high closure temperatures, and thus the U-Pb zircon ages, depending on the morphology and source, will represent the magmatic crystallisation age (Hoskin and Schaltegger, op cit). Later events can produce magmatic rims that can give the age of the later events (Andersson et al., 2002; Hoskin and Schaltegger, 2003). Zircon

crystallisation ages when used together with relative chronologies can constrain the maximum or minimum ages of either, deposition, structural and metamorphic events, and or mineralisation. Thus the U-Pb zircon ages of the OGB and GGGT constrains the maximum and minimum ages of volcanic and sedimentary deposition, tectonic events, emplacement of igneous rocks and mineralisation in the region. The geochronological data, together with the relative strato-tectonic regime for the study area, is summarized in Figures 8.1, 8.3 and 8.4.

In general, the geochronological ages obtained from samples of intrusive from the OGB and GGGT correspond with ages obtained in the northeast of Burkina Faso, and the WAC. In northeast Burkina Faso, two broad emplacement events are recognised (Castaing et al., 2003; Naba et al., 2004); (1) a TTG suite that intruded supracrustal rocks at 2210-2110 Ma and (2) A granite suite localized along shear zones at 2150 and 2130 Ma (Castaing et al., 2003).

However, the age of TTG and granite emplacement across the WAC was constrained to three discrete magmatic cycles at 2200 Ma, 2160-2130 Ma and 2100-2070 Ma by Pawlig et al. (2006) and Gueye et al. (2007; 2008). Magmatic Cycle 1 at 2200 Ma corresponds well with crystallisation ages in the study area obtained for Mrs Pink granite at 2203 ± 12 Ma and porphyritic granodiorite at 2207 ± 38 Ma in the study area. Magmatic cycle 2 at 2160-2130 Ma corresponds well with crystallisation ages obtained for the Gorom-Gorom pluton (2162 ± 28 Ma), Dori Batholith (2164 ± 24 Ma and 2148 ± 9.3 Ma), Tin-Taradat pluton (2146 ± 9.3 Ma), and monzonite porphyry dykes and sills (2141 ± 19 Ma).

Additionally, U-Pb zircon ages of 2158-2151 Ma of Tapsoba et al. (2013b) from the Goren, southern Bouroum and Yalago belts corresponds with regional Magmatic Cycle 2 of Pawlig et al. (2006) and Gueye et al. (2007; 2008), as well as Magmatic Cycle 2 in the study area. A U-Pb zircon age of 2132 ± 4 Ma for the Belahoura Granite in the northern Bouroum belt (McCuaig, 2006), corresponds with Magmatic Cycle 2 of Pawlig et al. (2006) and Gueye et al. (2007; 2008), for which there is no equivalent U-Pb zircon age in the study area. U-Pb zircon ages of 2170 ± 9 Ma for granodiorite in the Liptako region (Niger) (Ama Salah et al., 1996) and 2181 ± 7 Ma for granodiorite from the Yalago belt (Burkina Faso) (Tapsoba et al., 2013a, b) do not correspond with magmatic cycles in the study area, however when the errors are considered these ages likely correspond to magmatic cycle 2 in the study area.

In contrast, geochronological data from 2 samples of the Lilengo gneiss complex present the oldest outcropping Palaeoproterozoic supracrustal rocks yet found in the WAC. Samples gave convincing U-Pb concordant crystallisation ages of 2253 ± 9 Ma and 2253 ± 15 Ma and likely represent the age of crystallisation of a parent gneiss of granodioritic composition. It is also likely that this age can be the crystallisation age of a pre-metamorphic protolith, since the low uranium phase zircons from migmatitic gneiss gave a mean age of 2268 ± 29 Ma, which is within error of the age from the Lilengo gneiss (Figure 8.4).

A sample of a granite boulder from the Dembam Member gave a concordant age of 2255 ± 26 Ma, and this age is interpreted as the age of crystallisation of a granite pluton that was eroded from a site nearby before deposition in the upper stratigraphy of the Birimian Oudalan basin.

The three ages from the Lilengo gneiss complex and the granite boulder give U-Pb concordant crystallisation ages of 2253 ± 9 Ma, 2253 ± 15 Ma, and 2255 ± 26 Ma. These ages may constrain the crystallisation age of a gneissic protolith/basement on which the Birimian Supergroup was deposited, or an early group of granitoids that was emplaced in the hinterland during formation of the Birimian basin around 2200 Ma (Figure 8.3).

The granite boulder from the Dembam Member which gave a U-Pb concordant age of 2255 ± 26 Ma, currently constrains the maximum age of the Birimian Supergroup in the OGB, because (reasonably) the granite body from which the boulder eroded must have crystallised prior to erosion. It follows that if the Lilengo gneiss complex and the granite boulder constrains the age of a protolith on which the Birimian Supergroup was deposited, they indirectly provide a minimum age for the rocks in the hinterland. Based on the pebble-cobble-boulder fraction of the Dembam Member, the rocks in the hinterland were composed of granite and granodiorites, volcaniclastic and mafic volcanic rocks, gabbro, metasedimentary rocks and quartz veins.

The crystallisation age of Mrs Pink granite is 2203 ± 12 Ma with total recrystallisation of the zircon cores concomitant to deformation and metamorphism at 2167-2135 Ma (2151 ± 16 Ma), and further deformation and metamorphism at 2114-2093 Ma (zircon rim ages). Samples collected from outcrops that are crosscut or deformed constrain the age of D1 and D2 and the absolute ages of crystallisation of magmatic rocks. The Mrs Pink granite age constrains the minimum age of Lilengo gneiss complex, and constrains the maximum age of the Tin-Taradat pluton (TTG). The porphyritic granodiorite (2207 ± 38 Ma; U-Pb zircon) that intruded the Dembam Member was folded and metamorphosed during D1 and D2 (Tshibubudze and Hein, 2013). The age of 2207 ± 38 Ma indicates that the metasedimentary units in the OGB are at least older than 2207 Ma (Peters, 2011; Tshibubudze and Hein, 2013; Tshibubudze et al., 2013). Importantly, an approximately 40 Ma hiatus can be interpreted between the Lilengo gneiss complex and the Mrs Pink granite. It can reasonably be argued that deposition in the Birimian Oudalan basin began during this 40 Ma hiatus.

From this, it is interpreted that exhumation and erosion took place concomitant to deposition in the Birimian Oudalan basin; deposition likely began at approximately 2240-2200 Ma which concurs with estimation for the onset of basin formation by Castaing et al. (2003). Moreover, it is interpreted that crustal extension began at that time to form the Oudalan basin and lasted until 2169 Ma, which is the maximum age of post-Birimian TTG suite plutons (e.g., Dori Batholith, Tin Taradat).

The Gorom-Gorom pluton was emplaced at 2162 ± 28 Ma. The crystallisation age of the Dori Batholith is constrained at 2164 ± 24 Ma and 2148 ± 9.3 Ma. The Tin-Taradat pluton was emplaced at around 2146 ± 9.3 Ma. The monzonite porphyry dykes and sills gave a crystallisation age of 2141 ± 19 Ma. These intrusions can be summarized as (1) a suite that was emplaced at 2164-2162 Ma and (2) a

suite which emplaced at 2148-2141 Ma. Taking error into account, the TTG suites span the time interval 2188-2139 Ma, which accords well with magmatic cycle 2 of Gueye et al. (2007, 2008) for the KKI, and 2190-2150 Ma of Tapsoba et al (2013a) for northeast Burkina Faso. However, it is possible that Magmatic Cycle 2 is made up of discrete magmatic pulses.

Importantly, the 2164-2162 Ma age gives the maximum age of D1 in the OGB (Tshibubudze and Hein, 2013), and logically gives a maximum age to the formation of the D1 MSZ (with error this could extend to 2188 Ma). However, the 2148-2141 Ma does not constrain D1 (or MSZ), but D1 probably continued until 2141 ± 19 Ma because monzodiorite porphyry dykes and sills are folded about F_1 fold axes.

Additionally, the crystallisation ages for the Dori Batholith gave 2164 ± 24 Ma and 2148 ± 9.3 Ma; the 2164 Ma was obtained for a sample collected ~8 km from the batholith margin, while the 2148 Ma age was derived for a sample collected ~11 km from the margin (Figure 7.1). This indicates that the Dori batholith is composed of different TTG pulses.

The monzonite porphyry dykes and sills, which gave a crystallisation age of 2141 ± 19 Ma, and the Tin-Taradat pluton at 2146 ± 9.3 Ma, are crosscut by auriferous quartz-carbonate veins at the Essakane and Tin Taradat artisanal mines. Thereby the monzonite porphyry dykes and sills and the Tin-Taradat pluton constrain the maximum age of gold mineralization in the OGB.

8.4. Gold metallogenesis in the OGB and GGGT

Gold mineralisation in the study area has a spatial and temporal relationship with both D1 and D2 structures (Chapter 5). Gold mineralization in the OGB is located in Essakane North, Essakane Main Zone (Mine area), Essakane South, Gossey, Korizena, Bom Kodjele, Bom Kodjele East, Kossa and Kossa South, KBF, Fantio, Fatatako, Tin Zoubratan, Tin Taradat, Takabougou, Tassiri, Falagountou, Gaigou, and Sokadie artisanal mine sites (Appendix F). Gold mineralisation is sited along 5 northwest trending metallogenic corridors, and specifically, where northeast-trending faults and shears crosscut northwest trending thrust-folds (Chapter 5). D1 structures where dilated in D2 (during the Eburnean Orogeny) with development of sheeted and stockwork vein systems (Section 8.2.3).

As stated in Section 8.2.3, northwest-trending D1 thrust-folds where dilated in D2 to form gold-bearing quartz-sulphide veins. These include quartz-sulphide and quartz-sulphide-carbonate sheeted and stockwork veins, iron-rich cataclasites, and gold-bearing buck quartz (in north-northeast trending D2 shears. Artisanal mine workings are located in areas where these gold-bearing quartz-sulphide veins proliferate (Chapter 4, 5) and particularly where northwest trending D1 structures are disjunctively crosscut by northeast trending D2 shears. Monzonite porphyry dykes and sills and the Tin-Taradat pluton constrain the maximum age of gold mineralization in the study area to 2141 ± 19 Ma and 2146 ± 9.3 Ma (U-Pb zircon). Thus the metallogenic model for the OGB and GGGT accords

with Foster and Piper (1993), Groves et al. (1998), Feybesse et al. (2006) and Béziat et al. (2008) in that gold mineralisation is syn-deformational in the study area and formed during the Eburnean Orogeny (D2), i.e., orogenic gold style, but with the proviso that structural preparation was necessary in D1 to facilitate metallogenesis in D2. The source of the metals may have been the supracrustal rocks of the Oudalan belt, but the source of the fluids is currently not known and should be investigated.

In general, during thermal events associated with new crustal growth there is often large-scale fluid migration along deep seated structures. An increased thermal gradient is needed to initiate crustal migration of fluids during an orogenic event (Goldfarb et al., 2001). Ore-forming fluids may be generated or set in motion by syn-tectonic thermal processes at depth relative to syn-orogenic magmatism (Cameron, 1988; Groves et al., 1998). If sulphur bearing fluid migrates through a complex pattern of fracture networks, it is capable of leaching and transporting a significant amount of gold along its flow path. This gold is eventually deposited in secondary and tertiary structures adjacent to a major fault structure at shallow crustal level (Goldfarb et al., 2001).

In this context, the MSZ and Kargouna Shear Zone as first order scale structures, may have acted as sites of fluid migration, with deposition in second and third order splay shears. This is evidenced by the present of gold-bearing buck quartz veins in the MSZ and Kargouna Shear Zone, with the main mineralisation being deposited in secondary structures such as the Essakane and Falagountou trends.

Additionally, gold mineralisation in sheeted and stockwork veins second and third order splay shears is preferentially hosted in massive competent rocks units including conglomerate, greywacke, quartzite, monzonite dykes, pyroxenite-gabbro sills and D1 buck quartz veins. Gold in fine veinlets is hosted in massive shale units. Gold is also hosted in veins in the Tin Taradat granodiorite, monzodiorite porphyry dykes and sills, and in gold-molybdenite-copper veins in the Dolbel Batholith.

Several styles of gold deposit are now recognised in the West African craton (WAXI, 2013) including gold hosted by disseminated pyrite in tourmalinized stratabound mineralization (e.g., Loulo, Dommanget et al., 1993; Fouillac et al., 1993), in northwest-trending structural jogs in sodically altered shear zones (e.g. Gounkoto, Quick, 2011; Taparko and Bouroum, Vanin et al., 2004), shear-hosted gold/turbidite-hosted gold (Obuasi, Allibone et al., 2002; Berge, 2011; Inata, McCauig et al., 2009), high-grade lode gold (e.g., Bagassi, Hein et al., submitted (b)), gold-molybdenum (e.g., Bonikro; Allibone, 2010; Hein et al., submitted), sheeted vein type gold (Diabatou, Béziat et al., 2008; Siguiri, Steyn, 2012), intrusion-related gold (e.g., Morila, Hammond et al., 2011; FE3, Hein and Matabane, submitted), Eocene-Miocene placer gold above a fault (Matsheka and Hein, 2011; Yatela, Hein et al., submitted), and placer deposits (Tarkwa gold; Davis et al., 1994).

For shear-hosted and vein style gold deposits, there is a very strong consistent association of gold mineralization with low-medium grade greenschist facies in these deposits (Allibone et al., 2002;

Bourges et al., 1994; Gueye et al., 2013), and this is also true for shear-hosted and vein style gold in the study area.

Foster and Piper (1993), Groves et al. (1998), Feybesse et al. (2006) and Béziat et al. (2008) have restricted gold mineralization of the WAC to the Eburnean tectono-thermal event, due to many common characteristics the individual deposits share with similar metamorphic terrane hosted gold deposits in other parts of the world (Milési et al., 1991; Feybesse et al., 2006). Exceptions to this is early gold at Kiaka (southwest Burkina Faso) and Wassa (Ghana) (Figure 2.1) which predate the Eburnean orogeny (WAXI, 2013).

There is a strong structural control to gold mineralization at all levels (first- and second- or third-order structures) within the craton. Much of the gold mineralization was probably generated by hydrothermal activity accompanying the late stages of the Eburnean tectono-thermal event at 2100-1950 Ma (Allibone et al., 2002; Goldfarb et al., 2001; Foster and Piper, 1993). The bulk of gold production from the West Africa craton has come from sulphudized ductile-brittle shear zones and structurally controlled vein arrays hosted by the volcano-sedimentary sequences of the Birimian sequences (Allibone et al., 2002; Goldfarb et al., 2001; Foster and Piper, 1993; Bourges et al., 1994; Milési et al., 1991).

8.5 Strato-tectonic-metallogenic model and the WAC

The strato-tectonic-metallogenic model developed for the study area from the relative and absolute data presented in the preceding chapters is characterised by unconformable deposition of volcanic and sedimentary rocks of the Birimian Supergroup in the Oudalan basin at 2240-2169 Ma (71 Ma in total) on a gneissic complex (the Lilengo gneiss complex, 2255-2253 Ma) in an arc to back-arc setting (Figure 8.5a). These supracrustal rocks were deformed during the Tangaean Event (D1, 2164-2141 Ma) (Figure 8.5b), Eburnean orogeny (D2, 2130-1980 Ma; Feybesse et al., 2006) (Figure 8.5c), and the Wabo-Tampelse Event (D3, undated). The MSZ was formed in D1 at ca. 2164 Ma as a dextral (reverse) shear and was reactivated during D2 as a sinistral oblique-slip shear. High strain shear zones and mylonites formed in D1 relative to moderate strain shear zones in D2. Regional metamorphism in D1 attained greenschist to amphibolite facies, with amphibolite to granulite facies in high strain D1 shear zones and mylonites. Regional metamorphism in D2 attained greenschist to lower amphibolite facies. Two distinctive magmatic events at 2200 Ma and 2164-2141 Ma in the study area correspond with regional magmatic Cycle 1 and 2 of Pawlig et al. (2006) and Gueye et al. (2007, 2008). Magmatic Cycle 1 was probably syn-depositional to the Birimian Supergroup in the study area (Figure 8.5a). Magmatic Cycle 2 took place pre to syn-D1 and included emplacement of TTG suite plutons across the study area (Figure 8.5b). The gold deposits of the Essakane goldfield were formed at ca. 2.1 Ga during deformation in D2 and corresponds to a significant gold metallogenic phase associated with the regional Eburnean orogeny (2130-1980 Ma, Feybesse et al, 2006) (Figure 8.5c). Dilation of D1

structures in D2 was critical for developing favourable sites of gold mineralisation in the Essakane goldfield.

A competency contrast in lithological units played a role in gold mineralisation, with a high level of fracturing/veining being favourable for gold deposition in competent rocks (e.g., massive greywacke, massive siltstones, and buck quartz veins). Gold mineralisation is controlled and hosted along northwest trending and northeast trending structures. Continuous concentrations of reservable gold grade are hosted in northwest trending fold-thrusts (e.g., Essakane, Kossa, Tassiri), as opposed to northeast trending shears. D1 structures where dilated in D2 to host gold-bearing quartz-carbonate-sulphide veins, in association with sericite-chlorite-carbonate alteration. The intersection of D1 and D2 structures are favourable sites for economic gold. These structural criteria must be included in any exploration strategy in the Oudalan region in order to delineate Essakane style gold metal occurrences.

Integrated stratigraphic, structural, geochronological and metallogenic studies have also lead to a fuller understanding of the tectonic evolution of northeast Burkina Faso, and thus the WAC as a whole. These studies have defined the presence of a gneiss basement termed the Lilengo gneiss complex, with recognition of an angular unconformity that defines the basal contact of the Birimian Supergroup

The geochronological data from the Lilengo gneiss complex at 2255-2253 Ma presents the oldest outcropping Palaeoproterozoic supracrustal rocks yet identified in the WAC (and its proximal erosional product in the Dembam Member) when compared with published oldest U-Pb and Pb-Pb ages reported as inherited zircon ages by Gasquet et al. (2003), Thomas et al. (2009), Siegfried et al. (2009) and De Kock et al. (2009), and oldest U-Pb crystallisation ages reported by Castaing et al. (2003) from Burkina Faso, and K-Ar ages by Feybesse et al. (2006) from the Sefwi belt in Ghana. The Lilengo gneiss complex is interpreted as a gneissic protolith on which the OGB basin was deposited, or an early group of granitoids that were emplaced in the hinterland during formation of the OGB basin. In any event the crystallisation ages are markedly older than those of 2200 Ma for first magmatic cycle of Birimian granitoids in the WAC, as proposed by Dia et al. (1997), Feybesse et al. (2006), Gueye et al. (2008) and De Kock et al. (2011).

The tectonic environment of deposition of the overlying Birimian Supergroup (in the Oudalan Basin) can be interpreted as an arc to backarc. This supports conclusions made by the many researchers who have studied the volcano-sedimentary sequences in several greenstone belt including the Djibo belt (Roddaz et al., 2007), Bouroum belt (Lompo, 2009); Goren belt (Hein et al., 2004; Peters, 2014), Tiebélé belt (Ilboudo, 2010), Houndé-Boromo belts (Baratoux et al., 2011). It supports an argument for regional classification of the lower Birimian as an arc to back-arc sequence of rocks in revision to Abouchami and Boher (1990), Feybesse et al. (1990), Leube et al. (1990), Milési et al. (1991, 1992), Davis et al. (1994), and Hirdes et al. (1996), who classified the lower Birimian as a sedimentary sequence.

The manganese-bearing chemical metasedimentary units of the Birimian Supergroup, as represented by the manganese deposits of Tambão and Billiata, were formed by heat driven sea water convection system that provided hydrothermal solutions from submarine volcanic centres (Melcher, 1995). They are thus volcanogenic exhalite deposits as concluded by Peters (2014).

The supracrustal rocks of the WAC were deformed and metamorphosed in D1 (Tangaean/ Eoeburnean/ Eburnean I), D2 (Eburnean Orogeny) and D3 (Wabo Tampelse Event). The emplacement of TTG granitoids occurred at deep crustal level as suggested by Vidal et al. (2009), Lompo (2009; 2010), and metamorphism attained granulite facies (Ganne et al., 2014). D1 at 2164-2141 Ma is an equivalent of the 2.20-2.15 Ma deformation event described by Tshibubudze et al. (2009, Appendix E), Hein (2010), Baratoux et al. (2011), De Kock et al. (2011, 2012), Perrouty et al. (2012), Tshibubudze and Hein (2013, Chapter 5, Appendix B), and Tapsoba et al. (2013b), which pre-dates the Eburnean Orogeny.

D2 in the study area is similar in character to studies completed by Feybesse et al. (2006) in which northwest-southeast shortening in EO_A was followed by north-northwest to south-southeast shortening in EO_B with development of sinistral strike-slip faults and shears. The Eburnean Orogeny (D2) led to crustal maturation which enabled the formation of economic gold concentration in quartz vein system.

D3 is correlated with the Wabo-Tampelse Event of Hein et al. (2004), which is characterized by west-northwest trending shears and folds that developed during a period of north-south compression.

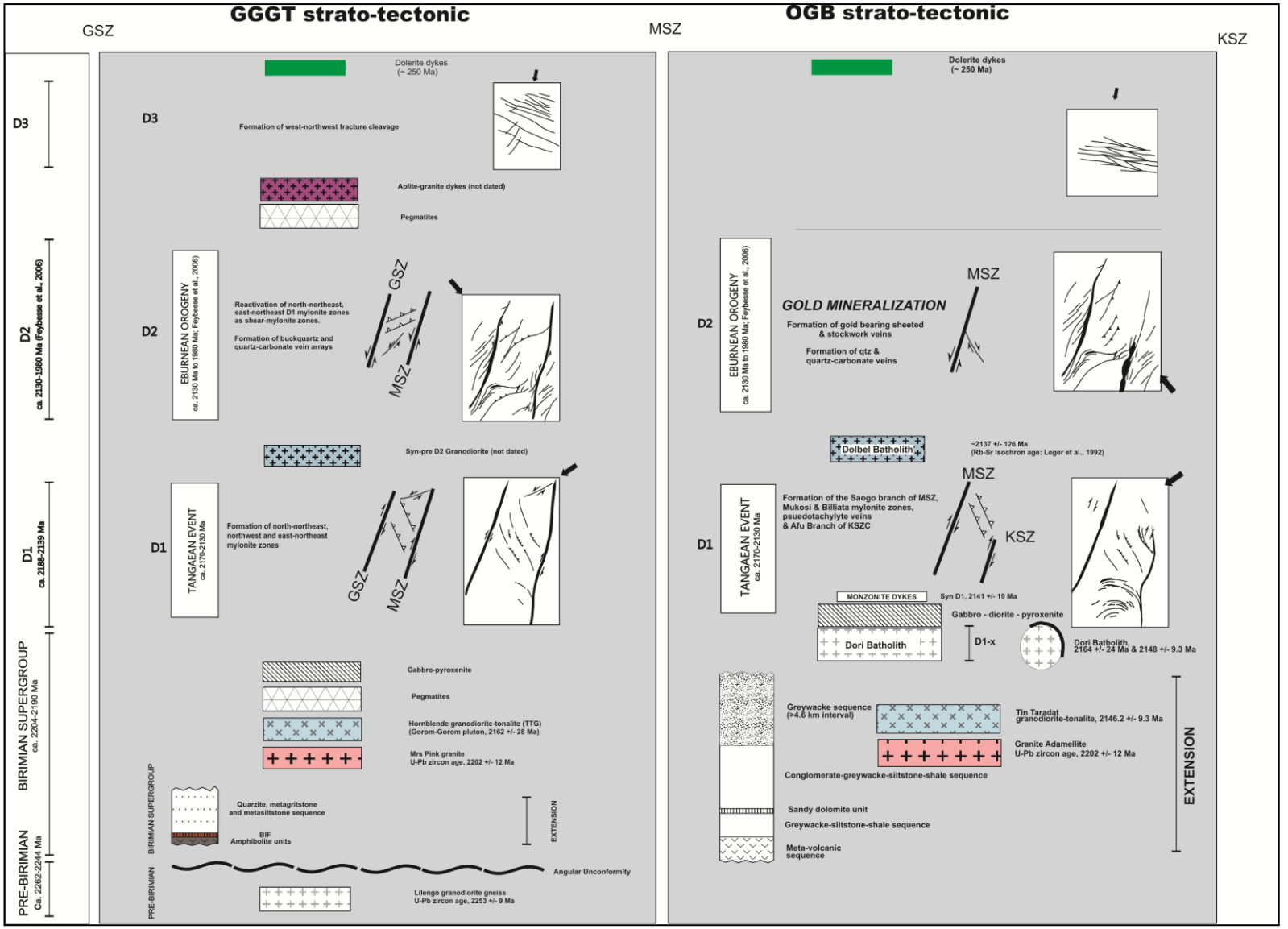

Figure 8.1: The schematic strato-tectonic summary for the OGB and GGGT established from crosscutting relationships and U-Pb ages.

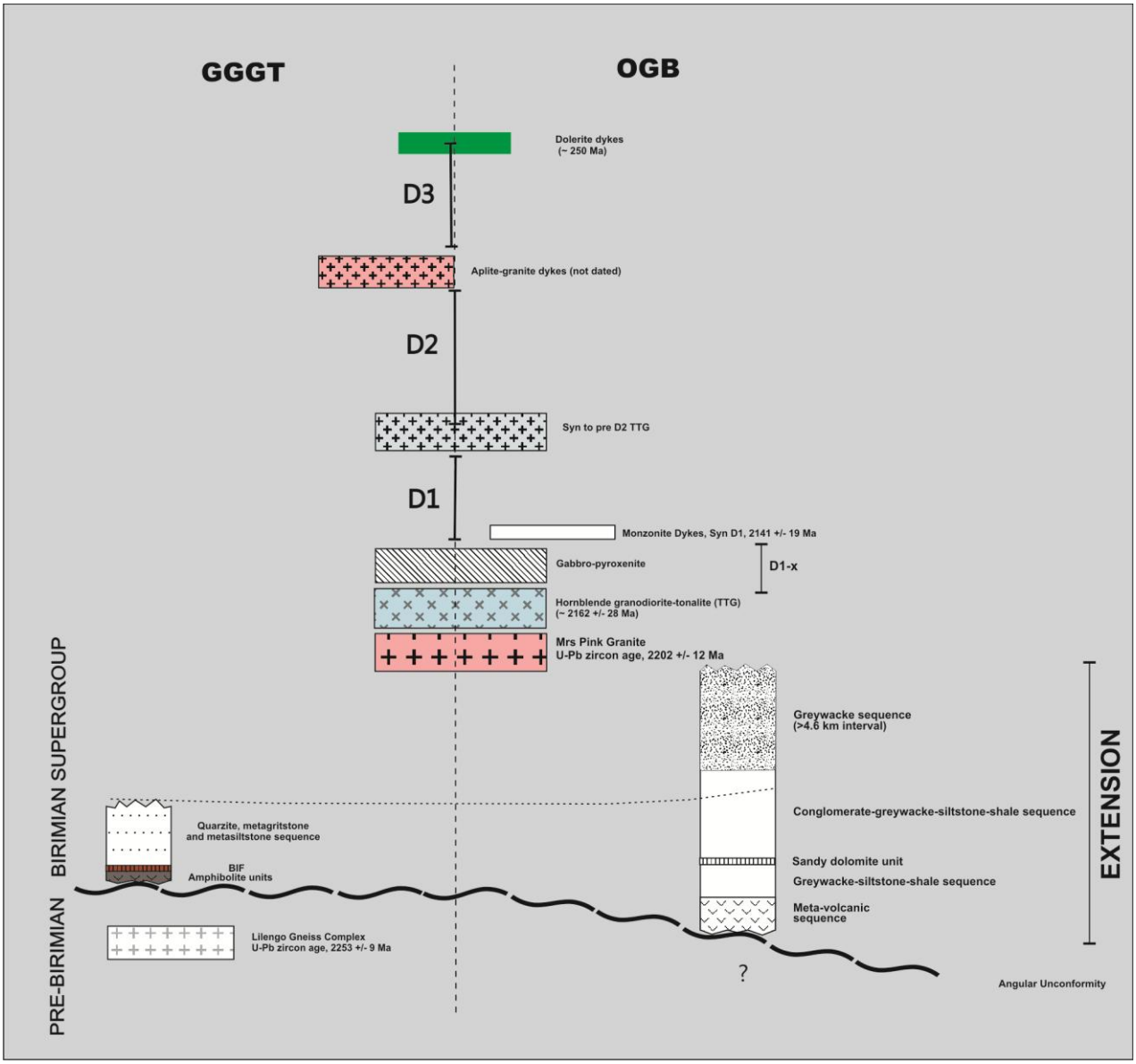

Figure 8.2: Combined strato-tectono-magmatic summary of the OGB and GGGT, showing similarity and differences across the MSZ between the two terranes.

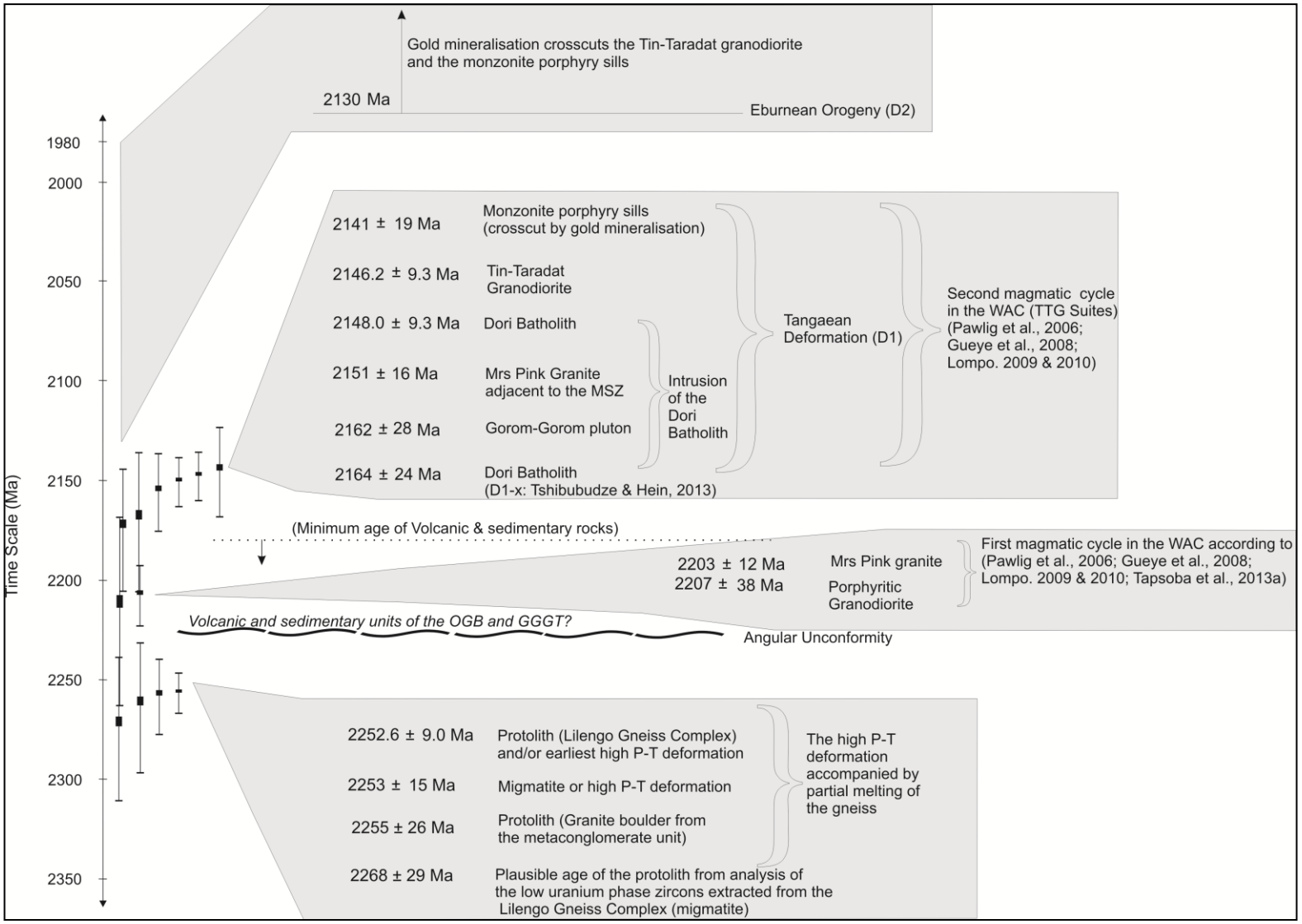

Figure 8.3: Summary of geochronology results in a flow chat format, from oldest to youngest, and their possible implications for the region and the WAC.

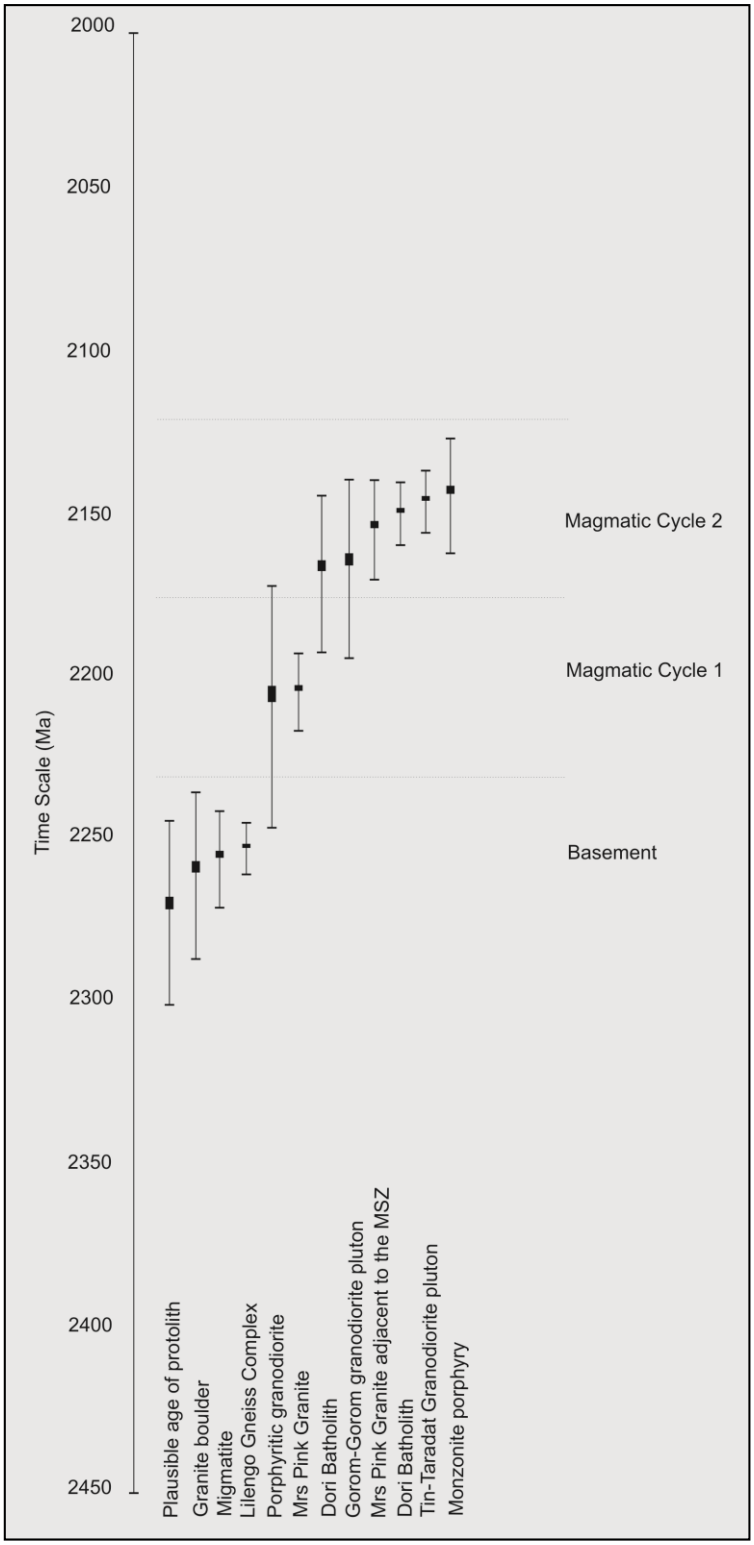

Figure 8.4: Summary plot for the crystallisation U-Pb ages established from the OGB and GGGT, as reported and plotted in Figure 8.3. The ages obtained from intrusive rocks of the OGB and GGGT correspond with the magmatic cycles reported in the WAC.

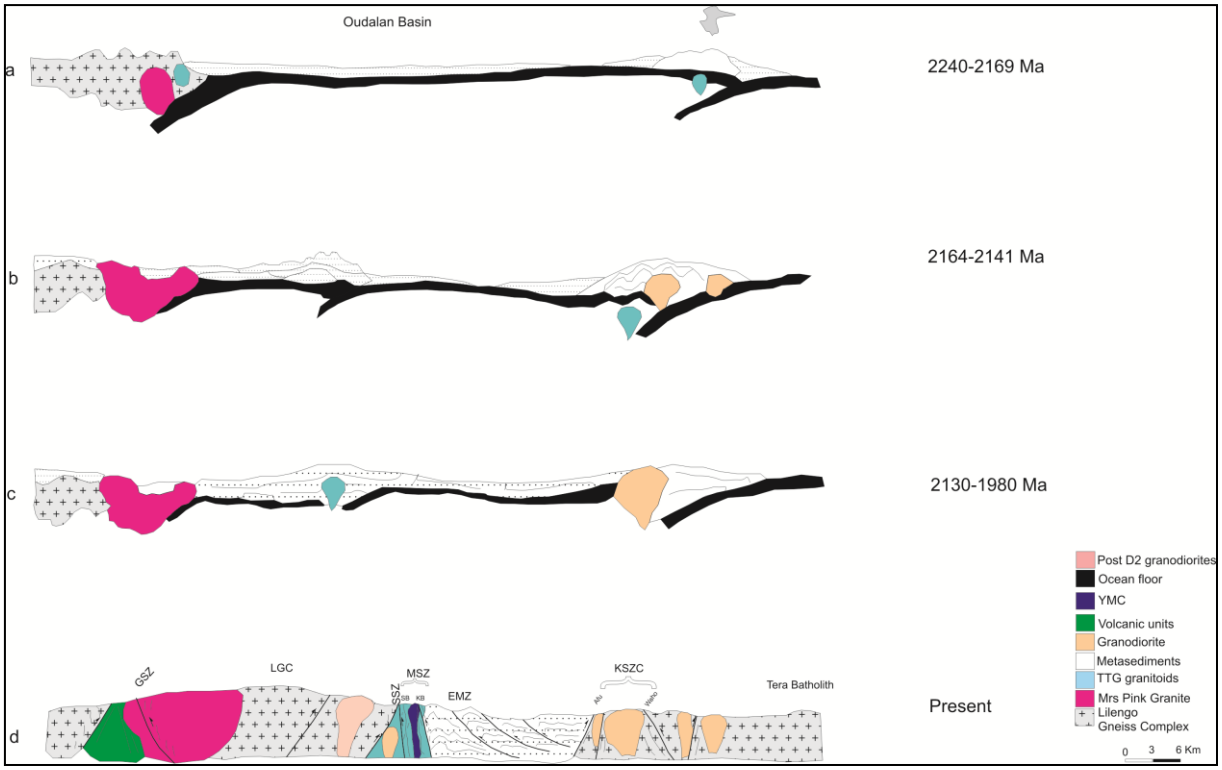

Figure 8.5: Tectonic evolution of the OGB and GGGT. (a) Formation of the Oudalan basin and the deposition of the Birimian type sequence within the back arc basin. (b) Deformation in D1 associated with plutonic emplacement and basin inversion. (c) Deformation in D2 during the Eburnean Orogeny with syn-tectonic emplacement of TTG. (d) The present day west to east cross-section from the GGGT to the OGB across the MSZ.

CHAPTER 9
CONCLUSIONS

The integrated strato-tectonic, geophysical, geochemical, geochronological and metallogenic studies of the OGB and the GGGT have established the regional stratigraphic framework of the OGB and GGGT making correlations with other provinces across the WAC possible.

(1) Integrated stratigraphic, structural, geochronological and metallogenic studies have lead to a fuller understanding of the tectonic evolution of northeast Burkina Faso, and thus the WAC as a whole. These studies have defined the presence of a gneiss basement termed the Lilengo Gneiss Complex, with recognition of an angular unconformity that defines the basal contact of the Birimian Supergroup. The geochronological data from Lilengo Gneiss Complex at 2255-2253 Ma presents the oldest outcropping Palaeoproterozoic supracrustal rocks yet identified in the WAC.

(2) The Lilengo gneiss complex is interpreted as a gneissic protolith on which the OGB basin was deposited.

(3) The basal sequence of the Birimian Supergroup of the OGB and GGGT consists of metamorphosed basic pillow lavas and basalt/amphibolite (metavolcanics sequences). These rocks are overlain by intercalations of metamorphosed volcaniclastic, greywacke, siltstone-shale, BIF-sandy dolomite, quartzite, gritstone-siltstone, conglomerate-greywacke sequence. They were contact metamorphosed to hornblende-hornfels facies adjacent to granitoids, dykes and sills which intrude them. The rocks of the Birimian Supergroup are metamorphosed to upper greenschist-amphibolite facies and schistosed (in part), folded and crosscut by shear zones and faults. These sequences of the Birimian Supergroup are interpreted to have been deposited in an arc to back arc setting. Exhumation and erosion took place concomitant to deposition in the Birimian Oudalan basin. Deposition likely began at approximately 2240-2200 Ma.

(4) U-Pb zircon geochronology has provided a conclusion to a long lasting argument of whether the conglomerates units in the OGB are Tarkwa Group in age. The metamorphosed conglomerate and the sediments are intruded by the porphyritic granodiorite and folded along with the sediment. The geochronological indicated that the minimum age of the sediments is 2207 Ma; this cannot be Tarkwa which is 2150 - 2130 Ma or 2107 – 2097 Ma. Clearly for rocks to be defined or classified as Tarkwaian rocks outside the type locality, the rocks must have similar lithological character to the type locality in Ghana, and the stratigraphic position of those rocks should be established. In summary the Tarkwa Group does not crop out in the OGB and GGGT.

(5) The plutonic rocks mapped in the region include the tonalite-trondhjemite-granodiorite (TTG), Mrs Pink granite, pyroxenite-gabbro, monzonite porphyritic dykes sills and dolerite dykes. The TTG, pyroxenite-gabbro, monzonite porphyritic dykes and sills, and dolerite-gabbro have a geochemical signature that indicates they are related to volcanic arc magma sources, while Mrs Pink

granite has a within-plate geochemical signature. The ultra-mafic units are aligned along a northeast and northwest trend.

(6) The geochemical trend of analysed magmatic rocks sampled in this study suggests evolution from within-plate to a volcanic arc environment, suggesting that an early basement continental mass rifted apart and developed into a volcanic arc.

(7) The U-Pb SHRIMP zircon ages of the intrusive rocks in the study area are grouped into two distinctive magmatic cycles, cycle 1 at 2200 Ma, and cycle 2 at 2160 – 2130 Ma. The ages from the OGB and GGGT correlates to the first or early magmatic cycle at 2200 Ma, is associated with the emplacement of the Mrs Pink granite and the porphyritic granodiorite plutons (TTG). The second magmatic cycle in the OGB and GGGT is associated with the emplacement of Dori Batholith, Tin-Taradat, and the Gorom-Gorom Plutons around 2164 - 2141 Ma. A third magmatic cycle might be represented by the Dolbel Granodiorite (2137 ± 126 Ma: Rb-Sr isochron; Léger et al., 1992) and the late granodiorite (not dated) that crosscut the OGB and the GGGT syn to post D2 deformation. U-Pb zircon ages of the syn to post D2 deformation will probably constrain the third magmatic cycle.

(8) The interpretation of geophysical data indicates that the area is dominated by northeast to north-northeast and northwest trending structural lineaments, and minor west-northwest trending lineaments. The drainage pattern represents a modified parallel-dendritic pattern, indicating a possible structural control to the drainage in the area. The lineaments are structural lineaments which represent shears, faults. This highlights the importance of geophysical, and remotely sensed data, such as LANDSAT and ASTER to extract geographical and geological data in field mapping to create a base strato-structural-metallogenic hypothesis map.

(9) The Birimian Supergroup in the OGB and GGGT were deformed and metamorphosed during 3 regional deformation events and concomitant to pluton emplacement. The magmatic-tectonic event, as manifested by the emplacement of the Dori Batholith ($D_{1\text{-}x}$), was succeeded by deformation during Tangaean/ Eoeburnean/ Eburnean I (D1: 2164-2141 Ma) and the Eburnean Orogeny (D2: 2130-1980 Ma) and the Wabo Tampelse event (D3: undated).

(10) The emplacement of the Dori Batholith in $D_{1\text{-}x}$ was accompanied by aureole deformation and the development of proto-mylonite, migmatite, gneiss and schist. Emplacement occurred at a deep crustal level and contact metamorphism attained granulite facies.

(11) Pre-Birimian to Birimian supracrustal rocks and intrusions were regionally metamorphosed during ductile-brittle deformation in D1 to lower greenschist to lower amphibolite facies. However, along shear and mylonite zones, metamorphic facies range from amphibolite to granulite indicating variation in P-T conditions and strain localization along the trend of the structures.

(12) Subsequent to deformation in D1, the supracrustal rocks and intrusions in the study area were regionally metamorphosed during brittle-(ductile) deformation in D2 to greenschist facies. In D2, northwest-trending D1 thrust-folds were dilated to form gold-bearing quartz-sulphide veins which predominate in the OGB. These include quartz-sulphide and quartz-sulphide-carbonate sheeted and

stockwork veins, iron-rich cataclasites, and gold-bearing buck quartz (in north-northeast trending D2 shear zones). Artisanal mine workings are located in areas where these gold-bearing quartz-sulphide veins proliferate and particularly where northwest trending D1 structures are disjunctively crosscut by northeast trending D2 shears.

(13) The D1 thrust-folds are significant because they host gold mineralization in V_2 sheeted veins in the folded hangingwall of thrusts. They include gold mineralisation in the Essakane Mine, the Tassiri prospect, and the Kossa deposit. Gold mineralisation at the Bom Kodjelé artisanal is hosted in the Bom Kodjelé Shear Zone (thrust), and at the Falagountou deposit. Continuous concentrations of reservable gold grade are hosted in northwest-trending fold-thrusts, as opposed to northeast trending shears.

(14) Gold mineralisation is sited along 5 northwest-trending metallogenic corridors, specifically, where northeast-trending faults and shears crosscut or coalesce with northwest-trending thrust-folds (or geophysical lineaments), or where north-west trending faults coalesce with north-northeast trending shear zones. D1 structures where dilated in D2 (during the Eburnean Orogeny) with development of sheeted and stockwork vein systems. Gold mineralisation occur as (1) vein hosted gold associated with pyrite in sheeted and stockwork quartz-carbonate veins, (2) as disseminated gold in the host rocks/shear zones; associated with pyrite, arsenopyrite, sphalerite and other sulphides.

(15) An intimate relationship exists between the tectonic development of the OGB and deposition of gold metallogenesis. Second and third-order northwest-trending splay faults and shears of the Tangaean deformation (D1) matured as sites of gold deposition during the Eburnean Orogeny (D2). The deposits are thereby structurally hosted. The gold deposits of the Essakane goldfield correspond to a significant gold metallogenic phase associated with the regional Eburnean orogeny (2130-1980 Ma).

CHAPTER 10
SUGGESTIONS FOR FUTURE WORK

1. The U-Pb zircon geochronology of the Dolbel pluton, and post D2 granodiorite in the GGGT. This would help to better constrain the age of D2.
2. Detailed study of the geochemistry of the Layered Mafic intrusions with particular reference to the mineralization potential.
3. A detailed study of the metamorphic conditions along the Mukosi Mylonite Zone and the pseudotachylite vein arrays. This will require a detailed PT study along the length of the MSZ, so the P-T conditions can be documented for D1 and D2.
4. Detailed study focused on understanding the tectonics of Tin-Takanet–Bellekcire Fault/shear zone and Gorgadji Shear Zone. This would help to fully understand the basin development in the area.
5. A study focus on understanding Fe-Ti-V mineralization in Tin Edia deposit.
6. A detailed ore genesis study should be undertaken in the OGB so to understand the source of fluid during the mineralisation phase. This can be coupled with a detailed study of the molybdenite-copper bearing granodiorite pluton crosscut by the KSZC (Waho Branch).
7. A detailed analysis of the zircon rims from the Lilengo Gneiss Complex to better constrain the pre-Tangaean metamorphic event which resulted in partial melting to form migmatites. Hf isotopes analysis of zircons could be useful in determining the age of the protolith. The partial melting age and the proposed crystallisation ages could be further constrained by analysing the zircon overgrowth zones of the cores in Lilengo Gneiss Complex.

REFERENCES

Abouchami, W., Boher, M., 1990. A major 2.1 Ga event of mafic magmatism in West Africa: and early stage of crustal accretion. Journal of Geophysical Research 95 (B11), 17605-17629.

Allen, A.R., 1979. Mechanism of frictional fusion in fault rock. Journal of Structural Geology 1, 231-243.

Allibone, A.H., 2010. Geology of the Bonikro Mine, Cote d'Ivoire. Unpublished Report by Rodinian Pty Ltd, 47p.

Allibone, A.H., McCuaig, T.C., Harris, D., Etheridge, M., Munroe, S., Byrne, D., Amanor, J., Grapong, W., 2002. Structural controls on gold mineralization at the Ashanti deposit, Obuasi, Ghana. In: Goldfarb, R.J., and Nielsen, R.L. (Editors), Integrated methods for discovery: Global exploration in the twenty-first century. Society of Economic Geologists Special Publication 9, 65-93.

Altermann, W., 2002. The evolution of life and its impact on sedimentation. In: Altermann, W., Corcoran, P.L. (Eds.), Precambrian sedimentary environments: A modern approach to ancient depositional systems. Special Publication, The International Association of Sedimentologists 33, 15-32.

Allum, J.A.E., 1966. Photogeology and Regional Mapping (1st edition). Pergamon Press, Oxford, 111p.

Alkire, S, Aguilar. G.R., 2012. Least developed countries and the multidimensional poverty index (MPI). Oxford Poverty and Human Development Initiative, 2p. (www.ophi.org.uk)

Ama Salah, I., Liegeois, J-P., Pouclet, A., 1996. Evolution d'un arc insulaire océanique birimien précoce au Liptako nigérien (Sirba): géologie, géochronologie et géochimie. Journal of African Earth Sciences 22, 235-254.

Anders, E., Grevesse, N., 1989. Abundances of the elements: meteoric and solar. Geochimica et Cosmochimica Acta 53, 197-214.

Anders, E., Ebihara, M., 1982. Solar-System Abundances of the Elements. Geochimica et Cosmochimica Acta 46 (11), 2,363-2,380. doi: 10.1016/0016-7037(82)90208-3.

Andersson, J., Möller, C., Johansson, L., 2002. Zircon geochronology of migmatite gneisses along the mylonite zone (S Sweden): a major Sveconorwegian terrane boundary in the Baltic Shield. Precambrian Research 114, 121-147.

Anon., 2008. Essakane Project, Geologycal Context of EMZ deposit. Powerpoint Presentation to OreZone, 25-27 October 2008.

Baratoux, L., Metelka, V., Naba, S., Jessell, M, W., Gregoire, M., Ganne, J., 2011. Juvenile Palaeoproterozoic crust evolution during the Eburnean Orogeny (~2.2-2.0 Ga), western Burkina Faso. Precambrian Research 191, 18-45.

Barker, S.L.L., 2005. Pseudotachylyte-generating faults in Central Otago, New Zealand. Tectonophysics 397, 211-223.

Beauvais, A., Ruffet, G., Hénocque, O., Colin, F., 2008. Chemical and physical erosion rhythms of the West African Cenozoic morphogenesis: The 39Ar-40Ar dating of supergene K-Mn oxides. Journal of Geophysical Research 113; F04007 doi:10.1029/2008JF000996.

Berge, J., 2011. Paleoproterozoic, turbidite, gold deposits of the Ashanti gold belt (Ghana, West Africa): Comparative analysis of turbidite-hosted gold deposits and an updated genetic model. Ore Geology Reviews 39, 91-100.

Berthé, D., Choukroune, P., Jegouzo, P., 1979. Orthogeniss, mylonite and non coaxial deformation of granites: the example of the South Armorican Shear Zone. Journal of Structural Geology 1, 31-42.

Bertrand, J.M., Michard, A., Boullier, A.M., Dautel, D., 1986. Structure and U/Pb geochronology of central Hoggar (Algeria): A reappraisal of its Pan-African evolution. Tectonics 5, 955-972.

Béziat, D., Bourges, F., Debat, P., Lompo, M., Martin, F., Tollon, F., 2000. A Palaeoproterozoic ultramafic-mafic assemblage and associated volcanic rocks of the Boromo greenstone belt: fractionates originating from island-arc volcanic activity in the West African craton. Precambrian Research 101, 25-47.

Béziat, D., Dubois, M., Debat, P., Nikiéma, S., Salvi, S., Tollon, F., 2008. Gold metallogeny in the Birimian craton of Burkina Faso (West Africa). Journal of African Earth Sciences 50, 215-233.

Boher, M., Abouchami, W., Michard, A., Albarede, F., Arndt, N.T., 1992. Crustal growth in West Africa at 2.1 Ga. Journal of Geophysical Research 97 (B1), 345-369.

Bossière, G., Bonkoungou, I., Peucat, J.J., Pupin, J.P., 1996. Origin and age of Palaeoproterozoic conglomerates and sandstones of the Tarkwaian Group in Burkina Faso, West Africa. Precambrian Research 80, 153-172.

Bourges, F., Debat, P., Grandin, G., Parizot, J.C., Tollon, F., Baras, E., Ouedraogo, M.F., 1994. Relations entre cristallisations de quartz et concentrations aurifères (exemple des filous aurifères du Birimien du Burkina Faso, Afrique de l'Ouest). Comptes Rendus de L'Académie des Sciences 319, II, 543-550.

Blatt, H., Tracy, J., Owens, B.E., 2006. Petrology, Igneous, Sedimentary, and metamorphic -3rd edition. W.H. Freeman and Company, 41 Madison Avenue, New York, NY 10010. 530p.

Brown, E.T., Bourlés, D.L., Colin, F., Sanfo, Z., Raisbeck, G.M., Yiou, F., 1994. The development of iron crust lateritic systems in Burkina Faso, West Africa examined with in-situ-produced cosmogenic nuclides. Earth and Planetary Science Letters 124, 19-33.

Brown, M., 2001. Crustal melting and granite magmatism: key issues. Physics and Chemistry of the Earth 26, 201-212.

Burke, K., Gunnell, Y., 2008. The African erosion surface: a continental-scale synthesis of geomorphology, tectonics, and environmental change over the past 180 million years. Published by Geological Society of America. ISBN 0813712017, 9780813712017, 34-40.

Butera, K.M., Williams, I.S., Blevin, P.L., Simpson, C.J., 2001. Zircon U-Pb dating of early Paleozoic monzonitic intrusive from the Goonumba area, New South Gales. Australian Journal of Earth Sciences 48, 457-464.

Caby, R., Bertrand, J. M. L., Black, R., 1981. Pan-African ocean closure and continental collision in the Hoggar-Iforas segment, central Sahara. In: Kröner, A. (Editor), Developments in Precambrian Geology 4, Precambrian Plate Tectonics. Elsevier Scientific Publishing Company, Oxford, 407-434.

Cameron, E.M., 1988. Archean gold: Relation to granulite formation and redox zoning in the crust. Geology 16, 109-112.

Capus, G., Bourrelier, P., Souley, M., 2004. Uranium mining in Niger; status and perspectives of a top five producing country. World Nuclear Association Annual Symposium, 8-10 September 2004, London.

Castaing, C., Billa, M., Milési, J.P., Thiéblemont, D., Le Mentour, J., Egal, E., Donzeau, M. (BRGM) (coordonnateurs) et Guerrot, C., Cocherie, A., Chevremont, P., Tegyey, M., Itard, Y. (BRGM), Zida, B., Ouedraogo, I., Kote, S., Kabore, B.E., Ouedraogo, C. (BUMIGEB), Ki, J.C., Zunino (ANTEA), 2003. Notice explicative de la Carte géologique et minière du Burkina Faso à 1/1 000 000.

Castiñeiras, P., Garcia, F. D., Barreiro, J.G., 2010. REE-assisted U-Pb zircon age (SHRIMP) of an anatectic granodiorite: constraints on the evolution of the A Silva granodiorite, Iberian allochthonous complexes. Lithos 116, 153-166.

Cheilletz, A., Barbey, P., Lama, C. Pons, J., Zimmermann, J-L., Dautel, D., 1994. Age de refroidissement de la croûte juvénile birimienne d'Afrique de l'Ouest; Données U-Pb, Rb-Sr et K-Ar sur les formations à 2,1 Ga du SW-Niger. Comptes Rendus de l'Académie des Sciences de Paris, Série II, Sciences de la Terre et des Planetes 319, 435-442.

Davis, J., Miller, J., Thebaud, N., McCuaig, C., Begg, G., Jessell, M., Hein, K.A.A., Baratoux, L., (Submitted). Stratigraphic Correlation West Africa/Leo Man Craton. Precambrian Research Special Publication.

Davis, G.H., Reynolds, S.J., 1996. Structural geology of rocks and regions. John Wiley and Sons, Inc, Canada, 775p.

Condie, K.C., 1993. Chemical composition and evolution of the upper continental crust: contrasting results from surface samples and shales. Chemical Geology 104, 1-37.

Cox, K.G., Bell, J.D., Pankhurst, R.J., 1979. The interpretation of igneous rocks. Allen and Unwin, London, 450p.

Davis, D.W., Hirdes, W., Schaltegger, U., Nunoo, E.A., 1994. U-Pb age constraints on deposition and provenance of Birimian and gold-bearing Tarkwaian sediments in Ghana, West Africa. Precambrian Research 67, 89-107.

Debat, P., Nikiéma, S., Mercier, A., Lompo, M., Béziat, D., Bourges, F., Roddaz, M., Salvi, S., Tollon, F., Wenmenga, U., 2003. A new metamorphic constraint for the Eburnean orogeny from Paleoproterozoic formation of the Man shield (Aribinda and Tampelga countries, Burkina Faso. Precambrian Research 123, 47-65.

Deckart, K., Bertrand, H., Liégeois, J.P., 2005. Geochemistry and Sr, Nd, Pb isotopic composition of the Central Atlantic Magmatic Province (CAMP) in Guyana and Guinea. Lithos 82, 289-314.

De Jongh, W.K., 1973. X-Ray fluorescence analysis applying theoretical matrix corrections. Stainless steel X-Ray Spectrom 2, 151-158.

De Kock, G.S., Theveniaut, H., Botha, P.M.W., Gyapong. W., 2012. Timing the structural events in the Palaeoproterozoic Bole-Nangodi belt terrane and adjacent Maluwe basin, West African craton, in central-west Ghana. Journal of African EarthSciences 65, 1-24.

De Kock G.S., Armstrong, R.A., Siegfried, H.P., Thomas, E., 2011. Geochronology of the Birim Supergroup of the West African craton in the Wa-Bolé region of west-central Ghana: Implications for the stratigraphic framework. Journal of African Earth Sciences 59, 1-40.

De Kock, G.S., Theveniaut, H., Botha, P.W., Gyapong, W., 2009. Geological Map Explanation, Map Sheet 0803B (1:100 000). CGS/BRGM/Geoman. Geological Survey Department of Ghana, 354p.

De la Roche, H., Leterrier, J., Grandclaude, P., Marchal, M., 1980. A classification of volcanic and plutonic rocks using R1 R2 diagram and major element analyses - Its relationships with current nomenclature. Chemical Geology 29, 183-210.

Delisle, P.C., 2003. Structural analysis of the Essakane deposit, Burkina Faso, West Africa. Unpublished Report, 3p.

Dia, A., Van Schmus, W. R., Kröner,, A., 1997. Isotopic constraints on the age and formation of a Palaeoproterozoic volcanic arc complex in the Kedougou Inlier; eastern Senegal, West Africa. Journal of African Earth Sciences 24, 197-213.

Dioh, E., Béziat, D., Debat, P., Grégoire, M., Ngom, P.M., 2006. Diversity of the Palaeoproterozoic granitoids of the Kédougou Inlier (eastern Sénégal): petrographical and geochemical constraints. Journal of African Earth Sciences 44, 351-371.

Dommanget, A., Milési, J.P., Diallo, M., 1993. The Loulo gold and tourmaline-bearing deposit. Mineralium Deposita 28, 253-263.

Drury, S.A., 2001. Image interpretation in geology, 3rd Edition. Nelson Thornes Ltd, Delta place, United Kingdom, 290p.

Egal, E., Thiéblemont, D., Lahondère, D., Guerrot, C., Costea, C.A., Iliescu, D., Delor, C., Goujou, J.C., Lafon, J.M., Tegyey, M., Diaby, S., Kolié, P., 2002. Late Eburnean granitization and

tectonics along the western and northwestern margin of the Archean Kénéma-Man domain (Guinea, West African Craton). Precambrian Research 117, 57-84.

Eriksson, P.G., Catuneanu, O., Sarkar, S., Tirsgaard, H., 2005. Patterns of sedimentation in the Precambrian. Sedimentary Geology 176, 17-42.

Eriksson, P.G., Condie, K.C., Tirsgaard, H., Mueller, W.U., Altermann, W., Miall, A.D., Aspler, L.B., Catuneanu, O., Chiarenzelli, J.R., 1998. Precambrian clastic sedimentation systems. Sedimentary Geology 120, 5-53.

Feybesse, J.L., Billa, M., Guerrot, C., Duguey, E., Lescuyer, J.L., Milési, J.P., Bouchot, V., 2006. The Palaeoproterozoic Ghanaian province: Geodynamic model and ore controls, including regional stress modelling. Precambrian Research 149, 149-196.

Feybesse, J.L., Milési, J.P., 1994. The Archaean/Proterozoic contact zone in West Africa: a mountain belt of decollement thrusting and folding on a continental margin related to 2.1 Ga convergence of Archaean cratons? Precambrian Research 69, 199-227.

Feybesse, J.L., Milési, J.P., Ouedraogo, M.F., Prost, A., 1990. La "ceinture" protérozoïque inférieur de Boromo-Goren (Burkina Faso): un exemple d'interférence entre deux phases transcurrentes éburnéennes. Comptes Rendus de L'Académie des Sciences 310, II, 1353-1360.

Fossen, H., 2010. Strutural Geology. Cambridge University Press, Cambridge CB28 RU, United Kingdom, 463p.

Foster, R.P., Piper, D.P., 1993. Archean lode gold deposits in Africa: crustal setting, metallogenesis and cratonization. Ore Geology Reviews 8, 303-347.

Fouillac, A.M., Dommanget, A., Milési, J.P., 1993. A carbon, oxygen, hydrogen and sulfur isotopic study of the gold mineralization at Loulo, Mali. Chemical Geology 106, 47-62.

Ganne, J., Gerbault, M., Block., 2014. Thermo-mechanical modelling of lower crust exhumation-contraints from the metamorphic record of the Palaeoproterozoic Eburnean orogeny, West African Craton. Precambrian Research 243, 88-109.

Ganne, J., De Andrade, V., Weinberg, R., Dubacq, B., Vidal, O., Kagambega, N., Naba, S., Baratoux, L., Jessel, M., Allibon, J., 2012. Modern-style plate subduction preserved in the Palaeoproterozoic West African Craton. Nature Geosciences 5, 60-65.

Gass, I. G., 1981. Pan-African (Upper Proterozoic) plate tectonics of the Arabian-Nubian Shield. In : A, Kröner (Editor), Developments in Precambrian Geology 4, Precambrian Plate Tectonics. Elsevier Scientific Publishing Company, Oxford, 387-405.

Gasquet, D., Barbey, P., Adou, M., Paquette, J.L., 2003. Structure, Sr-Nd isotope geochemistry and zircon U-Pb geochronology of the granitoids of the Dabakala area (Côte d'lvoire): evidence for a crustal growth event in the Palaeoproterozoic of West Africa? Precambrian Research 127, 329-354.

Geller, E., Weil, J., Blumel, D., Rappaport, A., Wagner, C., Taylor, R., 2003. Dictionary of geology and mineralogy 2nd Edition. McGraw-Hill, New York, 420p.

Gerrard, A.J., 1990. Mountain Environments: An examination of physical geography of mountains. Belhaven Press, London, 310p.

Gibbs, M.T., Bluth, G.J.S., Fawcett, P.J., Kump, L.R., 1999. Global chemical erosion over the last 250MY: variations due to changes in Paleogeography, Paleoclimate, and Paleogeology. American Journal of Science 299, 611-651.

Gignac, L., Glacken, I.M., Hawxby, J., Gignac, L.P., Bedell, P., 2009. IAMGOLD Corporation: updated feasibility study-Essakane gold project, Burkina Faso. Unpublished technical report to IAMGOLD Corporation, March 3rd_Essakane_43-101_Final, 193p.

Gleeson, C.F., Poulin, R. 1989. Gold exploration in Niger using soils and termitaria. Journal of Geochemical Exploration 31, 253-283.

Goldfarb, R.J., Groves, D.I., Gardoll, S., 2001. Orogenic gold and geologic time: a global synthesis. Ore Geology Reviews 18, 1-75.

Gregg, T.K.P., Smith, D.K., 2003. Volcanic investigations of the Puna Ridge, Hawai'i: relations of lava flow morphologies and underlying slopes. Journal of Volcanology and Geothermal Research 126, 63-77.

Groves, D.I., Goldfarb, R.J., Gebre-Mariam, M., Hagemann, S.G., Rorbert, F., 1998. Orogenic gold deposits: A proposed classification in the context of their crustal distribution and relationship to other gold deposit types. Ore Geology Reviews 13, 7-27.

Gueye, M., Van Den Kerkhof, A.M., Hein, U.F., Diene, M., Mücke, M., Siegesmund, S., 2011. Structural control, fluid inclusions and cathodoluminescence studies of Birimian gold-bearing quratz vein systems in the paleoproterozoic Mako belt, southeastern Senegal. South African Journal of Geology 116, 199-218.

Gueye, M., Ngom, P.M., Diène, M., Thiam, Y., Siegesmund, S., Wemmer, K., Pawlig, S., 2008. Intrusive rocks and tectono-metamorphic evolution of the Mako Palaeoproterozoic belt (Eastern Senegal, West Africa). Journal of African Earth Sciences 50, 88-110.

Gueye, M., Siegesmund, S., Wemmer, K., Pawlig, S., Drobe, M., Nolte, N., 2007. New evidence of an early Birimian evolution in the West African Craton: An example from the Kedougou-Kenieba Inlier, southeast Senegal. South African Journal of Geology 110, 511-534.

Hammond, N.Q., Robb, L., Foya, S., Ishiyama, D., 2011. Mineralogical, fluid inclusion and stable isotope characteristics of Birimian orogenic gold mineralization at the Morila mine, Mali, West Africa. Ore Geology Reviews 39, 218-229.

Hastings, D., 1982. On the tectonics and metallogenesis of West Africa: A model incorporating new geophysical data. Geoexploration 20, 295-327.

Harcouët, V., Guillou-Frottier, L., Bonneville, A., Bouchot, V., Milési, J.P., 2007. Geological and thermal conditions before the major Palaeoproterozoic gold-mineralization event at Ashanti, Ghana, as inferred from improved thermal modeling. Precambrian Research 154, 71–87.

Hein, K.A.A., Matabane, R.M., Diarra. M., (In preparation). Geology of the FE3 open casts, Sadiola goldfield, Kedougou-Kéniéba Inlier, western Mali.

Hein, K.A.A., Bruguier, O., Matsheka, I.R., Borsch, D., Caby, R., Monié, P., submitted (a) Styles of gold mineralisation in the Yatela deposit in the northern Kédougou-Kénieba Inlier, Mali. In (Markwitz, V., Hein, K.A.A., Robb, L. (Editors), Minerals Atlas Monograph of West Africa. Published by the Geological Society of South Africa.

Hein, K.A.A., Kinane, N.J.A., Sibthorpe, R., submitted (b). The Bagassi gold deposits on the eastern margin of the Houndé greenstone belt, Burkina Faso. In (Markwitz, V., Hein, K.A.A., Robb, L. (Editors), Minerals Atlas Monograph of West Africa. Published by the Geological Society of South Africa.

Hein, K.A.A., 2010. Succession of structural events in the Goren Greenstone belt (Burkina Faso); Implications for West African tectonics. Journal of African Earth Sciences 56, 83-94.

Hein, K.A.A, Tshibubudze, A., 2007. Relative chronology of tectonic events in the region east of Gorom-Gorom, Burkina Faso. Unpublished Report, Report 1 and 2 to Orezone Resources Inc, 15p.

Hein, K.A.A., Morel, V., Kagoné, O., Kiemde, F., Mayes, K., 2004. Birimian lithological succession and structural evolution in the Goren segment of the Boromo-Goren greenstone belt, Burkina Faso. Journal of African Earth Sciences 39, 1-23.

Herrmann, S.M., Anyamba, A., Tucker, C., 2005. Recent trends in vegetation dynamics in the African Sahel and their relationship to climate. Global Environmental Change 15, 394-404.

Hirdes, W., Davis, D.W., 2002. U-Pd geochronology of Palaeoproterozoic rocks in the southern part of the Kedougou-Kéniéba Inlier, Senegal, West Africa: Evidence for diachronous accretionary development of the Eburnean province. Precambrian Research 118, 83-99.

Hirdes, W., Davis, D.W., 1998. First U-Pb zircon age of extrusive volcanism in the Birimian Supergroup of Ghana/West Africa. Journal of African Earth Sciences 27, 291-294.

Hirdes, W., Davis, D.W., Lüdtke, G., Konan, G., 1996. Two generations of Birimian (Palaeoproterozoic) volcanic belts in north-eastern Côte d'Ivoire (West Africa): consequences for the 'Birimian Controversy'. Precambrian Research 80, 173-191.

Hirdes, W., Davis, D.W., Eisenlohr, B.N., 1992. Reassessment of Proterozoic granitoid ages in Ghana on basis of U/Pb zircon and monazite dating. Precambrian Research 56, 89-96.

Hirdes, W., Saager, R., Leube, A., 1987. The Tarkwaian group of Ghana: new aspects to its tectonic setting, structural evolution, gold mineralization and provenance area.

Holland, T.J.B., Norris R.J., 1979. Deformed pillow lavas from the central Hohe Tauern, Austria, and their bearing on the origin of epidote-banded greenstones. Earth and Planetary Science Letters 43, 397-405.

Holcombe, R., 2008. GEOrient, Version 9. Holcombe Caughlin Associates, Australia.

Holdaway, M. J., 1971. Stability of andalusite and the aluminium silicate phase diagram. American Journal of Science 271, 97-131.

Hoskin, P.W.O., Schaltegger, U., 2003. The composition of zircon and igneous and metamorphic petrogenesis. Reviews in Mineralogy and Geochemistry 53, 27-62.

Hottin, G., Ouedraogo, O.F., 1992. Carte Géologique du Burkina Faso (2nd edition). Bureau de Recherches Géologique et Minières, Burkina Faso.

Humphris, S.E., Thompson, G., 1978. Hydrothermal alteration of oceanic basalts by seawater. Geochimica et Cosmochimica Acta 42, 107-125.

IAMGOLD Corporation., 2012. Essakane Gold Mine, Burkina Faso. [WWW]. http://www.iamgold.com/English/Operations/Operating-Mines/Essakane/default.aspx. (07 March 2013).

Ilboudo, H., 2010. Le gite d'amas sulfure de Tiébélé (Burkina Faso-Afrique de l'Ouest). Facies lithologiques, structures et mineralisation. PhD These, Universite de Ouagadougou, 184p.

Isles, D.J., Cooke, A.C., Hallberg, J.A., 1990. Aeromagnetic evaluation in gold deposits of the Yilgarn Block, Western Australia. In: Nature, Genesis and Exploration Guides (Editors: S.E. Ho, D.I. Groves, J.M. Bennet). Published by the key centre, University of Western Australia, 20.

Jaques, E., Zida, B., Billa, M., Greffié, C., Thomassin, J.F., 2006. Artisanal and Small-Scale Gold Mines in Burkina Faso: Today and Tomorrow, in G. M. Hilson (Editor.), *Small-Scale Mining, Rural Subsistence and Poverty in West Africa*, Rugby, UK: Practical Action Publishing, 115-134.

Jeambrun, M., Delfour, J., Gravost, M., 1970. Carte géologique de L'Oudalan. Bureau De Recherches Geologiques et Minières, Burkina Faso.

Junner, N.R., 1935. Gold in the Gold Coast, Ghana Geological Survey Memoir 4, 67p.

Junner, N.R., 1940. Geology of the gold coast and Western Togoland (with revised geological map). Gold Coast Geological Survey Bulletin 11, 40p.

Kandji, S.T., Verchot, L., Mackensen, J., 2006. Climate change and variability in the Sahel Region, impacts and adaptation strategies in the agricultural sector. United Nations Environment Programme and World Agroforestry Centre, 58p.

Keary, P., Vine, F.J., 1996. Global tectonics, 2nd ed. Blackwell Publishing. 350 Main Street, Malden, USA, 333p.

Kemp, A.I.S., Hawkesworth, C.J., 2003. Granitic perspectives on the generation and secular evolution of the continental crust. Treatise on Geochemistry 3, 349-410.

Kerr, D.J., 2004a. Geology and Exploration potential of the Falagountou Gold Deposit, Essakan Joint Venture project, North-eastern Burkina Faso. Unpublished Report to Orezone Resources Inc and Goldfields International Ltd, Report 007-ES-01, 17p.

Kerr, D.J., 2004b. Technical Note: Preliminary vein study of the Essakan Main Deposit, Essakan Joint Venture project, North-eastern Burkina Faso. Unpublished Report to Orezone Resources Inc and Goldfields International Ltd, Report 007-ES-02, 11p.

Kerr, D.J., 2004c. Technical Note: Sokadie Prospect, Essakan Joint Venture project, North-eastern Burkina Faso. Unpublished Report to Orezone Resources Inc and Goldfields International Ltd, Report 007-ES-03, 16p.

Kerr, D.J., 2004d. Technical Note: Tassiri Prospect, Essakan Joint Venture project, North-eastern Burkina Faso. Unpublished Report to Orezone Resources Inc and Goldfields International Ltd, Report 007-ES-04, 20p.

Kerr, D.J., 2004e. Technical Note: Preliminary vein study of the Essakan Main Deposit, Essakan Joint Venture project, North-eastern Burkina Faso. Unpublished Report to Orezone Resources Incorporated and Gold Fields International Limited, Report 007-ES-02, 11p.

Killick, A.M., 2003. Fault rock classification: an aid to structural interpretation in mine and exploration geology. South African Journal of Geology 106, 395-402.

Kröner, A., 1981. Precambrian Plate Tectonics. In: Kröner, A., (Editor), Developments in Precambrian Geology 4, Precambrian Plate Tectonics. Elsevier Scientific Publishing Company, Oxford, 57-83.

Ledru, P., Pons, J., Milési, J.P., Feybesse, J.L., Johan. V., 1991. Transcurrent tectonics and polycyclic evolution in the lower Proterozoic of Senegal-Mali. Precambrian Research 50, 337-354.

Léger, J.M., Liègeois, J.P., Pouclet, A., Vicat, J.P., 1992. Occurrence of syntectonic alkali-pyroxene granites of Eburnean age (2.1 Ga) in Western Niger. In: Abstracts, 14^{éme} Réunion Annuelle des Sciences de la Terre, Toulouse, France. Société Géologique de France, 96p.

Lemoine, S., Tempier, P., Bassot, J.P., Caen-Vachette, M., Vialette, Y., Taure, S., Wenmenga, U., 1990. The Burkinian orogenic cycle, precursor of the Eburnian Orogeny in West Africa. Geological Journal 25, 171-188.

Leube, A., Hirdes, W., Mauer, R., Kesse, G.O., 1990. The early Proterozoic Birimian Supergroup of Ghana and some aspects of its associated gold mineralization. Precambrian Research 46, 139-165.

Liégeois, J.P., Abdelsalam, M.G., Ennih, N., Ouabadi, A., 2013. Metacratons: Nature, genesis and behaviour. Gondwana Research 23, 220-237.

Liégeois, J.P., Claessens, W., Camara, D., Klerkx, J., 1991. Short-lived Eburnian Orogeny in southern Mali. Geology, tectonics, U-Pb and Rb-Sr geochronology. Precambrian Research 50, 111-136.

Lister, G.S., Snoke, A.W., 1984. S-C Mylonites. Journal of Structural Geology 6, 617-638.

Lompo, M., 2009. Geodynamic evolution of the 2.25-2.0 Ga Palaeoproterozoic magmatic rocks in the Man-Leo Shield of the West African Craton. A model of subsidence of an oceanic plateau. In: Reddy, S.M., Mazumder, R., Evans, D.A.D, Collins, A.S. (Eds.), Palaeoproterozoic

Supercontinents and global evolution. Geological Society, London, Special Publication 323, 231-254.

Lompo, M., 2010. Palaeoproterozoic structural evolution of the Man-Leo Shield (West Africa). Key structures for vertical to transcurrent tectonics. Journal of African Earth Sciences 58, 19-36.

Lompo, M., 2001. Le Paléoprotérozoïque (Birimien) du Burkina Faso Afrique de l′ Ouest Évolution crustale et concentrations aurifères. UFR/ SVT Département de Géologie, Équipes de Pétrophysique et Tectonique, Universite de Ouagadougou, 135p.

Ludwig, K.R., 2003. Isoplot 3.00, A geochronological toolkit for Microsoft Excel, Berkeley Geochronology Centre, Berkeley, Special Publication 4, 70p.

Ludwig, K.R., 2009. Squid 2.50, A user's manual, Berkeley Geochronology Centre, Berkeley, California, USA, 95p.

Luning, S., 2008. Liberalisation of the gold mining sector in Burkina Faso. Review of African Political Economy 117, 387-401.

Mabidi, T., Thiart, C., de Wit, M.J., 2007. Secular changes recorded in mineralization of African crust. Journal of African Earth Sciences 47, 88-94.

Mackenzie, D., Brune, J.N., 1972. Melting on fault planes during large earthquakes. Geophysical Journal of the Royal Astronomical Society 29, 65-78.

Magloughlin, J.F., Spray, J.G., 1992. Frictional melting processes and products in geological materials: introduction and discussion. Tectonophysics 204, 197-206.

Matabane, M., R., 2008. The geology of the FE3 open-cast, Sadiola, Mali: stratigraphy, structure and intrusive. Unpublished Honours Thesis, University of the Witwatersrand Johannesburg, 65p.

Matsheka, I.R., Hein, K.A.A., 2011. Character morphology and origin of gold from selected mines in the Yatela and Sadiola goldfields, Mali, West Africa. Poster presentation to the WAXI Sponsors meeting, 28th March to 1 April 2011, Ouagadougou, Burkina Faso.

Mayes, K., 1997. 1:600 000 scale airborne magnetic, TMI reduced to the pole of Eastern Burkina Faso with sun angle illumination, A315 E45, Adindan datum, NUTM30 Projection, traverse spacing 1 km, line direction N-S. North Ltd.

Mazor, E., Heymann, D., Anders, E., 1970. Noble gases in carbonaceous chondrites. Geochimica et Cosmochimica Acta 34, 781–824.

McCaffrey, R., Zwick, P.C., Bock, Y., Prawirodirdjo, L., Genrich, J.F., Stevens, C.W., Puntodewo, S.S.O., Subarya, C., 2000. Strain partitioning during oblique plate convergence in northern Sumatra: Geodetic and seismologic constraints and numerical modelling. Journal of Geophysical Research 105, 363-376.

McClay, K.R., 1991. The mapping of geological structures. John Wiley and Sons Ltd, The Atrium, Southern Gate, Chichester, West Sussex PO 19 8SQ, England, 161p.

McCuaig, T.C., Kerrich, R., 1998. P-T-t-deformation-fluid characteristics of lode gold deposits: evidence from alteration systematics. Ore Geology Reviews 12, 381-453.

McCuaig, T.C., 2006. Review of Belahouro exploration strategy. Unpublished report prepared for Goldbelt Resources Ltd, 54p.

McCuaig, T.C., Williams, P.R., Ouedraogo, M.F., Turner, P., 2009. Seeing through deformation to early basin architecture in the Birimian: the Northern Burkina Faso example. PowerPoint presentation to University of Western Australia, 09/11/2012 (Unpublished).

Melcher, F., 1995. Genesis of chemical sediments in Birimian greenstone belts: evidence from gondites and related manganese-bearing rocks from northern Ghana. Mineralogical Magazine 59, 229-251.

Mickus, K., 2008. Regional gravity analysis of Burkina Faso: Implications for the location of metallic ore deposits. Journal of African Earth Sciences 50, 55-66.

Metelka, V., Baratoux, L., Naba, S., Jessell, M.W., 2011. A geophysically constrained litho-structural analysis of the Eburnean greenstone belts and associated Granitoid domains, Burkina Faso, West Africa. Precambrian Research 190, 48-69.

Middlemost, A.K., 1994. Naming materials in the magma/igneous rock system. Earth-Science Reviews 37, 215-224.

Milési, J.P., Feybesse, J.L., Ledru, P., Dommanget, A., Ouedraogo, M.F., Marcoux, E., Prost, A., Vinchon, Ch., Sylvain, J.P., Johan, V., Tegyey, M., Calvez, J.Y., Lagny, P. 1989. West African gold deposits, in their lower Proterozoic lithostructural setting. Chronique de la Recherché Minière 497, 3-98.

Milési, J.P., Ledru, P., Ankrah, P., Johan, V., Marcoux, E., Vinchon, Ch., 1991. The metallogenic relationship between Birimian and Tarkwaian gold deposits in Ghana. Mineralium Deposita 26, 228-238.

Milési, J.P., Ledru, P., Feybesse, J.L., Dommanget, A., Marcoux, E., 1992. Early Proterozoic ore deposits and tectonics of the Birimian orogenic belt, West Africa. Precambrian Research 58, 305-344.

Miller, R.B., Paterson, S.R., 1999. In defence of magmatic diapirs. Journal of Structural Geology 21, 1161-1173.

Mobbs, P.M., 1997. The mineral industry of Niger-1997. 3p. Website www.minerals.usgs.gov/minerals/pubs/country/**1997**/9247097.pdf

Montanari, D., Corti, G., Sani, F., Del Ventisette, C., Bonini, M., Moratti, G., 2010. Experimental investigation on granite emplacement during shortening. Tectonophysics 484, 147-155.

Naba, S., Lompo, M., Debat, P., Bouchez, J.L., Béziat, D., 2004. Structure and emplacement model for late-orogenic Palaeoproterozoic granitoids: the Tenkodogo-Yamba elongate pluton (Eastern Burkina Faso). Journal of African Earth Sciences 38, 41-57.

Navas, A.S., Reddy, B.J., Nieto, F., 2004. Spectroscopic study of chromium, iron, OH, fluid and mineral inclusions in uvarovite and fuchsite. Spectrochimica Acta Part A 60, 2261-2268.

Neyberg, H., Ladaron, D., Martin, H., Verkaeren, J., 1980. The vanadiferous -magnetite deposits of the Oursi region, Upper Volta. Economic Geology 7, 1042-1052.

Nikiéma, S.J., 1992. Contexte structural et implications métallogénies au sein du permis "Essakan", dans le sillon de Dori: Géométrie des corps aurifères. Unpublished PhD Thesis, Université of Dakar, 38p.

Nkuna, B., 2009. Ore genesis of the Essakane, Falagountou and Sokadie Au deposits: Oudalan-Gorouol Greenstone Belt (OGGB), Burkina Faso, West African Craton (WAC). Unpublished Honours thesis, University of the Witwatersrand Johannesburg, 60p.

Norrish. K., Hutton. J.T., 1969. An accurate X-Ray spectrographic method for the analysis of a wide range of geological samples. Geochimica et Cosmochimica Acta 33, 431- 453.

Norris, R.J., Cooper, A.F., 2003. Very high strains recorded in mylonites along the Alpine Fault, New Zealand: implications for the deep structure of plate boundary faults. Journal of Structural Geology 25, 2141-2157.

Oberthür, T., Vetter, U., Davis, D.W., Amonor, J.A., 1998. Age constraints on gold mineralization and Palaeoproterozoic crustal evolution in the Ashanti belt of southern Ghana. Precambrian Research 89, 129-143.

O'Hara, K.D., 2001. A pseudotachylite geothermometer. Journal of Structural Geology 23, 1345-1357.

Ouedraogo, M.F., Prost, A.E., 1986. Mise en evidence des relations entre schistosites et plissements dans la ceinture volcanique birrimienne de Yako-Batié (Burkina Faso). Comptes Rendus de l'Académie des Sciences de Paris, Série II 303, 1713-1718.

Passchier, C.W., 1982. Pseudotachylite and the development of ultramylonite bands in the Saint-Barthélémy Massif, French Pyrenees. Journal of Structural Geology 4, 69-79.

Paterson, S.R., Fowler Jr, T. K., 1993. Re-examining pluton emplacement processes. Journal of Structural Geology 15, 191-206.

Paterson, S.R., Vernon, R.H., Fowler Jr., T.K., 1991. Aureole tectonics. In: Kerrick, D.M. (Ed.), Contact Metamorphism. Mineralogical Society of America Reviews in Mineralogy 26, 673–722.

Pattison, D. R. M., 1992. Stability of andalusite and sillimanite and Al_2SiO_5 triple point: constraints from the Ballachulish Aureole, Scotland. Journal of Geology 100, 423-446.

Pawlig, S., Gueye, M., Klischies, R., Schwarz, S., Wemmer, K., Siegesmund, S., 2006. Geochemical and Sr-Nd isotopic data on the Birimian of the Kedougou-Kenieba Inlier (Eastern Senegal): Implications on the Palaeoproterozoic evolution of the West African Craton. South African Journal of Geology 109, 411-427.

Pearce, J.A., Harris, N. B.W., Tindle, A.G., 1984. Trace element discrimination diagrams for the tectonic interpretation of granitic rocks. Journal of Petrology 25, 956–983.

Perrouty, S., Ailleres, L., Jessell, M, W., Baratoux, L., Bourassa, Y., 2012. Revised Eburnean geodynamic evolution of the gold-rich southern Ashanti belt, Ghana, with new field and geophysical evidence of pre-Tarkwaian deformations. Precambrian Research 204, 12-39.

Peters, L.F.H., 2011. Geology of the eastern Markoye region, Oudalan-Gorouol greenstone belt, NE Burkina Faso. Unpublished Honours Thesis. University of the Witwatersrand, Johannesburg, 61p.

Peters, L.F.H., 2014. The volcanology, geochemistry and metallogenic potential of the Goren volcano-sedimentary belt, Northeast Burkina Faso, West Africa. MSc Thesis. University of the Witwatersrand, Johannesburg, 138p.

Pidgeon, R.T., 1992. Recrystallisation of oscillatory zoned zircon: some geochronological and petrological implications. Contributions to Mineralogy and Petrology 110, 463-472.

Pigois, J.P., Groves, D.I., Fletcher, I.R., McNaughton, N.J., Snee, L.W., 2003. Age constraints on Tarkwaian paleoplacer and lode-gold formation in the Tarkwa–Damang district, SW Ghana. Mineralium Deposita 38, 695–714.

Pons, J., Barley, P., Dupuis, D., Léger, J.M., 1995. Mechanisms of pluton emplacement and structural evolution of a 2.1 G.a juvenile continental crust: the Birimian of south western Niger. Precambrian Research 70, 281-301.

Quick, R., 2011. Gounkoto – a new multi-million ounce gold discovery in the Loulo district of Mali West Africa. Presentation and Abstract to the Geological Society of South Africa Gold Day, 13 April 2011.

Ramsay, J.G., 1979. Shear zone geometry: a review. Journal of Structural Geology 2, 83-99.

Riley, R., Knight, K.B., 2001. Age of pre-break-up Gondwana magmatism. Antarctic Science 13, 99-110.

Roddaz, M., Debat, P., Nikiéma, S., 2007. Geochemistry of upper Birimian sediments (major and trace elements and Nd-Sr isotopes) and implications for weathering and tectonic setting of the late Palaeoproterozoic crust. Precambrian Research 159, 197-211.

Rogers, J., 2001. Technical Report, Essakan Project Regional Mapping. Unpublished Report to Ranger Minerals NL, 24p.

Rogers, J. and Dong, F., 2000. Technical Report-Essakane Prospect, Burkina Faso, Company report (unpublished). ABOSSO Goldfields Limited, Accra, Ghana, 14p.

Rollinson, H. R., 1993. Using Geochemical Data: Evaluation, Presentation, Interpretation. Longman Geochemistry Series, Routledge Publishers, 711 Third Avenue, New York, NY 10017, USA, 384p.

Rudnick, R. L., Gao, S., 2003. Composition of the Continental Crust. Treatise on Geochemistry 3, 1-64.

Segev, A., 2002. Flood basalts, continental breakup and the dispersal of Gondwana: evidence for periodic migration of upwelling mantle flows (plumes). European Geosciences Union Stephan Mueller Special Publication Series 2, 171-191.

Seymour, L., T. Peters, J. Adlam, W. Phillips., 2012. Burkina Faso. Mining Journal Special publication, 1-28, ISSN 0026-5225.

Shackleton, R. M., 1995. Tectonic evolution of greenstone belts. *In* Coward, M.P., Ries, A.C., (Editors), Early Precambrian Processes, Geological Society Special Publications 95, 53-65.

Shanmugan, G., 1997. The Bouma sequences and turbidite mind set. Earth-Science Reviews 42, 201-229.

Shido, F., Miyashiro, A., Ewing, M., 1974. Compositional variation in pillow lavas from the mid-Atlantic ridge. Marine Geology 16, 177-190.

Sibson, R.H., 1975. Generation of pseudotachylite by ancient seismic faulting. Geophysical Journal of the Royal Astronomical Society 43, 775-794.

Sibson, R.H., 1977. Fault rocks and fault mechanisms. Journal of Geological Society London 133, 191-213.

Sibson, R.H., 1980. Transient discontinuities in ductile shear zones. Journal of Structural Geology 2, 165-171.

Sibson, R.H., Robert, F., Poulsen, H., 1988. High-angle reverse faults, fluid-pressure cycling, and mesothermal gold-quartz deposits. Geology 16, 551-555.

Sibson, R.H., 1986. Brecciation processes in fault zones: inferences from earthquake rupturing. Pure and Applied Geophysics 124, 159-175.

Sibson, R.H., 2000. Fluid involvement in normal faulting. Journal of Geodynamics 29, 469-499.

Siegfried, P., Aggenbach, A., Clarke, B., Delor, C., Yves Roig, J., 2009. Geological Map Explanation, Map Sheet 0903D (1:100 000). CGS/BRGM/Geoman. Geological Survey Department of Ghana.

Simoko, H., 2012. Petrology, geochemistry and structure of the Pissila batholith and the Saaba Zone gneiss. Unpublished Honours Thesis, University of the Witwatersrand Johannesburg, 43p.

Sylvester, P.J., Attoh, K., 1992. Lithostratigraphy and composition of 2.1 Ga greenstone belts of the West African Craton and their bearing on crustal evolution and the Archean-Proterozoic boundary. Journal of Geology 100, 377–393.

Soto-Viruet, Y., 2010. The mineral industries of Mali and Niger. U.S Geological Survey Minerals Year Book 28.1.

Steyn, J. G., 2012. Structural geology and controls of gold mineralization in the Siguiri Mine, Guinea, West Africa. Unpublished MSc Thesis, University of Stellenbosch, 147p.

Stern, R.A., 2001. A new isotopic and trace-element standard for the ion microprobe: preliminary thermal ionization mass spectrometry (TIMS) U-Pb and electron-microprobe data; Radiogenic

age and isotopic studies: Report 14, Geological Survey of Canada, Current Research 2001-F1, 11p.

Sultan, L., Björklund, P.P., 2006. Depositional environments at a Palaeoproterozoic continental margin, Västervik basin, SE Sweden. Precambrian Research 145, 243-271.

Taner, M. F., 2004. Report on the petrographic and mineralogical study of one mineralized sample from the Essakan gold deposit area, Burkina Faso, of the Orezone Resources Inc. Unpublished Report, 21p.

Tapsoba, B., Lo, C.H., Jahn, B.M., Chung, S.L., 2013a. Chemical and Sr-Nd isotopic composition and zircon U-Pb ages of the Birimian granitoids from NE Burkina Faso, West African Craton: Implications for regional tectonics. Precambrian Research 235, 208-229.

Tapsoba, B., Lo, C.H., Wenmenga, U., Jahn, B.M., Chung, S.L., 2013b. 40 Ar/39Ar thermochronology of Paleoproterozoic granitoids of northeast Burkina Faso, West African Craton: Implications on the geodynamic setting and crustal evolution. Precambrian Research 224, 364-396.

Taylor. P.N., Moorbath. S., Leube, A., Hirdes, W., 1992. Early Proterozoic crustal evolution in the Birimian of Ghana: constraints from geochronology and isotope geochemistry. Precambrian Research 56, 97-111.

Taylor, S.R., McLennan, S.M., 1995. The geochemical evolution of the continental crust. Reviews in Geophysics 33, 241-265.

Thiéblemont, D., Goujou, J.C., Egal, E., Cocherie, A., Delor, C., Lafon, J.M., Fanning, C.M., 2004. Archaean evolution of the Leo Rise and its Eburnean reworking. Journal of African Earth Sciences 39, 97-104.

Thiéblemont, D., Delor, C., Cocherie, A., Lafon, J.M., Goujou, J.C., Baldé, A., Bah, M., Sané, H., Fanning, C.M., 2001. A 3.5 Ga granite-gneiss basement in Guinea: further evidence for early Archean accretion within the West African Craton. Precambrian Research 108, 179-194.

Thiessen, R.L., Means, W.D., 1980. Classification of fold interference patterns: a re-examination. Journal of Structural Geology 2 (3), 311–316.

Thomas, E., Baglow, N., Viljoen, J., Siaka, Z., 2009. Geological Map Explanation, Map Sheet 0903D (1:100 000). CGS/BRGM/Geoman. Geological Survey Department of Ghana.

Tshibubudze, A., Hein, K.A.A., Pratas, M., Rogers, J., submitted. Gold mineralization in the Essakane goldfield, Burkina Faso. In (Markwitz, V, Hein, K.A.A., Robb, L. (Editors), Minerals Atlas Monograph of West Africa. Published by the Geological Society of South Africa.

Tshibubudze, A., Hein, K.A.A., 2013. Structural setting of gold deposits in the Oudalan-Gorouol volcano-sedimentary belt east of the Markoye Shear Zone, West African craton. Journal of African Earth Sciences 80, 31-47.

Tshibubudze, A., Hein, K.A.A., Peters, L.F.H., Woolfe, A.J., McCuaig, T.C., 2013. Oldest U-Pb crystallization age for the West African Craton from the Oudalan-Gorouol belt of Burkina Faso. South African Journal of Geology 116, 169-181.

Tshibubudze, A., Hein, K.A.A., 2010. Tectonic evolution of the Oudalan-Gorouol greenstone belt in northeast Burkina Faso and Niger, West African craton. Geophysical Research Abstracts. Volume 12, EGU2010-708, 2010 EGU General Assembly 2010, ISSN of eISSN: 1607-7962.

Tshibubudze, A., Hein, K.A.A., Marquis, P. 2009. The Markoye Shear Zone in northeast Burkina Faso. Journal of African Earth Sciences 55, 245-256.

Tshibubudze, A., 2007. Relative timing of structural events: The Markoye Fault and its association to gold mineralization. Unpublished Honours Thesis, University of the Witwatersrand Johannesburg, 78p.

Tunks, A.J., Selley, D., Rogers, J.R., Brabham, G., 2004. Vein mineralization at the Damang gold mine, Ghana: controls on mineralization. Journal of Structural Geology 26, 1257-1273.

Turner, P., Hall, R.P., Hughes, D.J., Whalley, J.S., 1993. The sediment-dominated Boundiali-Bagoé supracrustal belt and neighbouring granitic rocks, northern Côte d'Ivoire, West Africa: a Tarkwaian connection ?. Journal of African Earth Sciences 17 (1), 1-11.

Twidale, C.R., 1982. Granite Landforms. Elsevier Scientific Publishing Company, Amsterdam, The Netherlands, 359p.

Vanin, D., Michaud, M., Thalenhorst, H., Reipas, K., 2004. Taparko-Bouroum project, Burkina Faso. Unpublished Technical report 43-101 F1 to High River Gold Mines Ltd, 186p.

Vernon, R.H., 2004. A practical guide to rock microstructure. Cambridge University Press, Cambridge CB2 2RU, UK, 594p.

Vidal, M., Alric, G., 1994. The Palaeoproterozoic (Birimian) of Haute-Comoe in the West African craton Ivory Coast: a transtensional back-arc basin. Precambrian Research 65, 207–229.

Vidal, M., Gumiaux, C., Cagnard, F., Pouchet, A., Ouattara, G., Pichon, M., 2009. Evolution of a Paleoproterozoic 'weak type' orogeny in the West African Craton. Tectonophysics 477, 145-159.

Villeneuve, M., 1989. The geology of the Madina-Kouta Basin (Guinea-Senegal) and its significance for the geodynamic evolution of the western part of the West African craton during the Upper Proterozoic period. Precambrian Research 44, 305-322.

WAXI, 2013. Confidential Final Report, P934A West African Exploration Initiative Stage 2, 924 pages with 917 pages of appendices.

Wegener, A., 1964. The origin of Continents and Oceans. Dover Publications, New York, 272p.

Werthmann, K., 2009. Working in a boom-town: Female perspective on gold mining in Burkina Faso. Resource Policy 34, 18-23.

White, W.M., 2012. Geochemistry. Wiley-Blackwell, 111 River Street, Hoboken, NJ 07030-5774, USA, 637p.

Wilson, M., 1989. Igneous petrogenesis. Published by Unwin Hyman, London, 466p.

Wison, J.T., 1965. A new class of faults and their bearing on continental drift. Nature 207, 343-347.

Wimmenauer, W., Bryhni, I., 2007. Migmatites and related rocks. A proposal on behalf of IUGS subcommission on the systematic of metamorphic rocks. Web version 01.02.07, paper 6, 1-5.

Wingate, M.T.D., Kirkland, C.L., 2011, Introduction to geochronology information released in 2011. Geological Survey of Western Australia, 5p.

Woolfe, A., 2011. Stratigraphy and metamorphic facies in the Kel Enguef metamorphic belt near Gorom-Gorom, NE Burkina Faso. Unpublished Honours thesis, University of the Witwatersrand Johannesburg, 62p.

Zegers, T.E., 1996. Structural, kinematic and metalogenic evolution of selected domains of the Pilbara granitoid-greenstone terrane, implications for mid Archean tectonic regimes. Geologica Ultraiectina, Mededelingen van de Faculteit Aardwetenschappen Universiteit Utrecht No. 146.

Zhao, G., Cawood, P.A., Wilde, S.A., Sun, M., 2002. Review of global 2.1–1.8 Ga orogens: implications for a pre-Rodinia supercontinent. Earth-Science Reviews 59, 125–162.

Zonou, S., Karche, J.P., Lapierre, H., Lemoine, S., Rossy, M., 1985. Tholeiitic and calc-alkaline volcanisms in the upper Birimian formations of Bouroum (NE of Burkina Faso). Comptes Rendus de l'Académie des Sciences 301, 309-314.

APPENDIX A

Tshibubudze, A., Hein, K.A.A., 2010. Tectonic evolution of the Oudalan-Gorouol greenstone belt in NE Burkina Faso and Niger, West African craton. Geophysical Research Abstracts. Volume 12, EGU2010-708, 2010 EGU General Assembly 2010, ISSN of eISSN: 1607-7962.

Geophysical Research Abstracts
Vol. 12, EGU2010-708, 2010
EGU General Assembly 2010

Tectonic evolution of the Oudalan-Gorouol greenstone belt in NE Burkina Faso and Niger, West African craton.

Asinne TSHIBUBUDZE (1,,) and Kim A.A. HEIN (,,)

(1) Corresponding Author; School of Geosciences; University of the Witwatersrand Johannesburg; Email: Asinne.Tshibubudze@students.wits.ac.za, () School of Geosciences; University of the Witwatersrand Johannesburg; T: +27-11-717 6623; F: +27-11-717 6579; Email: kim.ncube-hein@wits.ac.za

The Oudalan-Gorouol Greenstone Belt (OGGB) forms part of the Palaeoproterozoic as the Baoulé-Mossi domain of the West African Craton (WAC) and hosts gold deposits at Essakane, Gossey, Korizena, and Falagountou in NE Burkina Faso, and Kossa goldfield in Niger.

The Birimian supracrustal sequences in the OGGB are dominated by meta-volcanoclastic greywacke intercalated meta-conglomerate, siltstone and shale, carbonate (dolomite) and volcanic units pillow basalts). The belt is surrounded by plutonic rocks including granite, TTG suite granitoids and granite gneiss. The sequences where subjected to two phases of deformation, and several phases of contact metamorphosed to hornblende-hornfels facies during emplacement of pyroxenite-gabbro-norite, granodiorite-tonalite and gabbro dykes and porphyritic sills.

The OGGB is bounded and/or crosscut by several major NNE to NE-trending shear zones including the steeply east-dipping Markoye Shear Zone (western margin of the OGGB), Tin Takanet-Bellekcire Shear Zone, Dori Shear Zone, Kargouna Shear Zone, Takabougou Shear Zone, and Bom Kodjelé Shear Zone (transects the centre of the OGGB). The structures were readily identified using LANDSAT, Aster, aeromagnetic and RTP magnetic data, with follow-up strategic mapping, highlighting the value of interpreting geophysical and remotely sensed data in regional mapping in Burkina Faso and Niger.

Structural studies completed in 2007 adjacent to the Essakane gold mine indicated that the NE-trending, first-order crustal-scale Markoye Shear Zone (MSZ) has undergone at least two phases of reactivation concomitant to two phases of regional deformation (Tshibubudze et al., 2009). The first phase of deformation, D1, resulted in the formation of NNW-NW trending folds and thrusts during dextral-reverse displacement on the MSZ. The deformation predates the Eburnean Orogeny is termed the Tangaean Event (meaning low hills in the Moré language of Burkina Faso) and is tentatively dated at ca. 2170-2130 Ma (Hein, 2009). D2 involved a period of SE-NW crustal shortening and sinistral-reverse displacement on the MSZ, and is correlated to the Eburnean Orogeny $\sim$2.1 Ga of Feybesse et al. (2006). Deformation in D2 is characterised by NE-trending regional folds (F2) and a pervasive NE-trending foliation (S2-C to S2).

Since 2007 an identical tectonic history has been established for a number of shear zones in the OGGB including the north-trending Kargouna Shear Zone, which is subtended by NW- and NE-trending shears. However the metamorphic grade and mineral assemblages vary from one shear zone to the next. Structural studies completed adjacent to the Dori batholith have indicated that the MSZ forms a shear complex that was active during pluton emplacement. However, the MSZ has two main branches that join at the location of a mylonite zone located north west of Essakane. Southwest of Essakane, a NW-trending mylonite zone crosscuts the Dori batholith and near the village of Kargouna, which is situated southeast of Essakane, the Kargouna shear crosscuts and deforms the Dori batholith. It is thus likely that the Dori batholith was emplacement prior to D1 in the OGGB.

Gold mineralization in the OGGB is generally hosted in the hanging-wall of NE-trending faults and or NW-trending folds in metasiltstone-sandstone-shale sequences. Nkuna (2009) concluded that the deposits can be classified as orogenic gold deposits under the sub-class of “intrusion related” due to their proximity to plutonic masses, which concurs with geophysical studies for the OGGB.

References:

Feybesse, J.L., Billa, M., Guerrot, C., Duguey, E., Lescuyer, J.L., Milési, J.P., Bouchot, V., 2006. The Palaeo-

proterozoic Ghanaian province: Geodynamic model and ore controls, including regional stress modelling. Precambrian Research 149, 149-196.
Hein, K.A.A., 2009 (In press). Structural chronologies in the Goren Greenstone belt (Burkina Faso); Implications for West African tectonics. Journal of African Earth Sciences.
Tshibubudze, A., Hein, K.A.A., Marquis, P. 2009. The Markoye Shear Zone in NE Burkina Faso. Journal of African Earth Sciences 55, 245-256.
Nkuna, B., 2009 Ore genesis of the Essakane, Falagountou and Sokadie Au deposits: Oudalan-Gorouol Greenstone Belt (OGGB), Burkina Faso, West African Craton (WAC). Unpublished Honours thesis, University of the Witwatersrand Johannesburg, 60p.

APPENDIX B

Tshibubudze, A., Hein, K.A.A., 2013. Structural setting of gold deposits in the Oudalan-Gorouol volcano-sedimentary belt east of the Markoye Shear Zone, West African craton. Journal of African Earth Sciences 80, 31-47. doi: 10.1016/j.jafrearsci.2012.11.010.

Journal of African Earth Sciences 80 (2013) 31–47

Contents lists available at SciVerse ScienceDirect

Journal of African Earth Sciences

journal homepage: www.elsevier.com/locate/jafrearsci

Structural setting of gold deposits in the Oudalan-Gorouol volcano-sedimentary belt east of the Markoye Shear Zone, West African Craton

Asinne Tshibubudze, Kim A.A. Hein *

School of Geosciences, University of the Witwatersrand, Johannesburg, South Africa

ARTICLE INFO

Article history:
Received 19 December 2011
Received in revised form 5 November 2012
Accepted 18 November 2012
Available online 11 December 2012

Keywords:
West African Craton
Burkina Faso
Niger
Birimian
Structure
Tectonics

ABSTRACT

The Oudalan-Gorouol volcano-sedimentary belt (OGB) of Burkina Faso and Niger hosts meta-volcanic and metasedimentary sequences of the Birimian Supergroup that were folded and deformed during emplacement of the Dori Batholith (D_{1-x}), the Tangaean Event (D1) and the Eburnean Orogeny (D2).

The emplacement of the Dori Batholith accompanied aureole deformation (D_{1-x}) and the development of proto-mylonite, migmatite, gneiss and schist on the northern margin of the batholith. Contact metamorphic grade reached granulite facies with partial melting of the supracrustal sequences. Emplacement of the Dori Batholith was succeeded by emplacement of monzonite dykes and sills through the OGB.

The Tangaean Event (D1) accompanied formation of (a) the Saoga Branch of the Markoye Shear Zone (MSZ), (b) the Mukosi and Billiata mylonite zones that are hosted in the MSZ, (c) the Afu Branch of the Kargouna Shear Zone Complex (KSZC), and (d) northwest-trending thrust-folds (F1) that crosscut the OGB and coalesce with the MSZ. Metamorphic grade attained amphibolite facies in mylonite or proto-mylonite zones in the Saoga and Afu branches. D1 was succeeded by emplacement of alkali-granite plutons of the Dolbel Batholith.

The Eburnean Orogeny, D2, accompanied formation of (a) the Korizéna Branch of the MSZ, (b) the Waho Branch of the KSZC, and (c) northeast–trending shear-faults that crosscut the OGB. D2 is manifested by refolding of F1 by northeast-trending F2, and development of a pervasive northeast-trending S2 to S2-C. Metamorphic grade attained greenschist facies during D2 with development of the mineral assemblage quartz–chlorite–muscovite ± actinolite. D2 was succeeded by emplacement of northwest-trending gabbro and dolerite dykes.

The OGB hosts structurally-controlled gold deposits that are sited along five metallogenic corridors and include the Essakane, Tin–Fal, Bom Kodjelé, Kossa and Tassiri Trends. Gold mineralisation is preferentially located where northeast-trending faults and shears crosscut northwest-trending thrust-folds, or where northwest-trending thrust-folds coalesce with north–northeast trending shears. An intimate relationship thus exists between D1 and D2 structures and gold mineralisation in the OGB. Gold in sheeted-stockwork veins is hosted in competent rocks units including conglomerate beds, greywacke, quartzite, monzonite dykes, pyroxenite–gabbro sills and D1 buck quartz veins. Gold in fine veinlets may also be hosted in massive shale units.

1. Introduction

The Oudalan-Gorouol volcano-sedimentary belt (OGB) in northeast Burkina Faso and Niger (Fig. 1) is known for its structurally-hosted gold deposits (Tshibubudze and Hein, 2010) including Essakane, Gosséy, Falagountou, Sokadie, Tin Zoubratan and Takabangou (Fig. 2). The Essakane gold deposit reached production in late 2010 and will become one of the largest gold producers in West Africa and the African continent.

Structural and tectonic studies by Tshibubudze et al. (2009) argued that two deformation events could be recognised without ambiguity in the OGB. Those studies linked tectonic activity on the steeply east-dipping Markoye Shear Zone (MSZ) to regional deformation in the belt. Formation of a northwest-trending fold-thrust belt during D1 was linked to dextral-reverse displacement on the MSZ during the Tangaean Event, (ca. 2170–2130 Ma, Hein, 2010). Progressive development of north–northeast to northeast-trending mylonite and shears, L-tectonites, and vein arrays of pseudotachylite, quartz–carbonate, buck quartz, and quartz cataclasite was linked to sinistral-reverse reactivation of the MSZ during the Eburnean Orogeny (ca. 2130–1980 Ma, Feybesse et al., 2006).

* Corresponding author. Tel.: +27 11 717 6623; fax: +27 11 717 6579.
E-mail addresses: asinne.tshibubudze@students.wits.ac.za (A. Tshibubudze), kim.ncube-hein@wits.ac.za (K.A.A. Hein).

1464-343X/$ - see front matter © 2012 Elsevier Ltd. All rights reserved.
http://dx.doi.org/10.1016/j.jafrearsci.2012.11.010

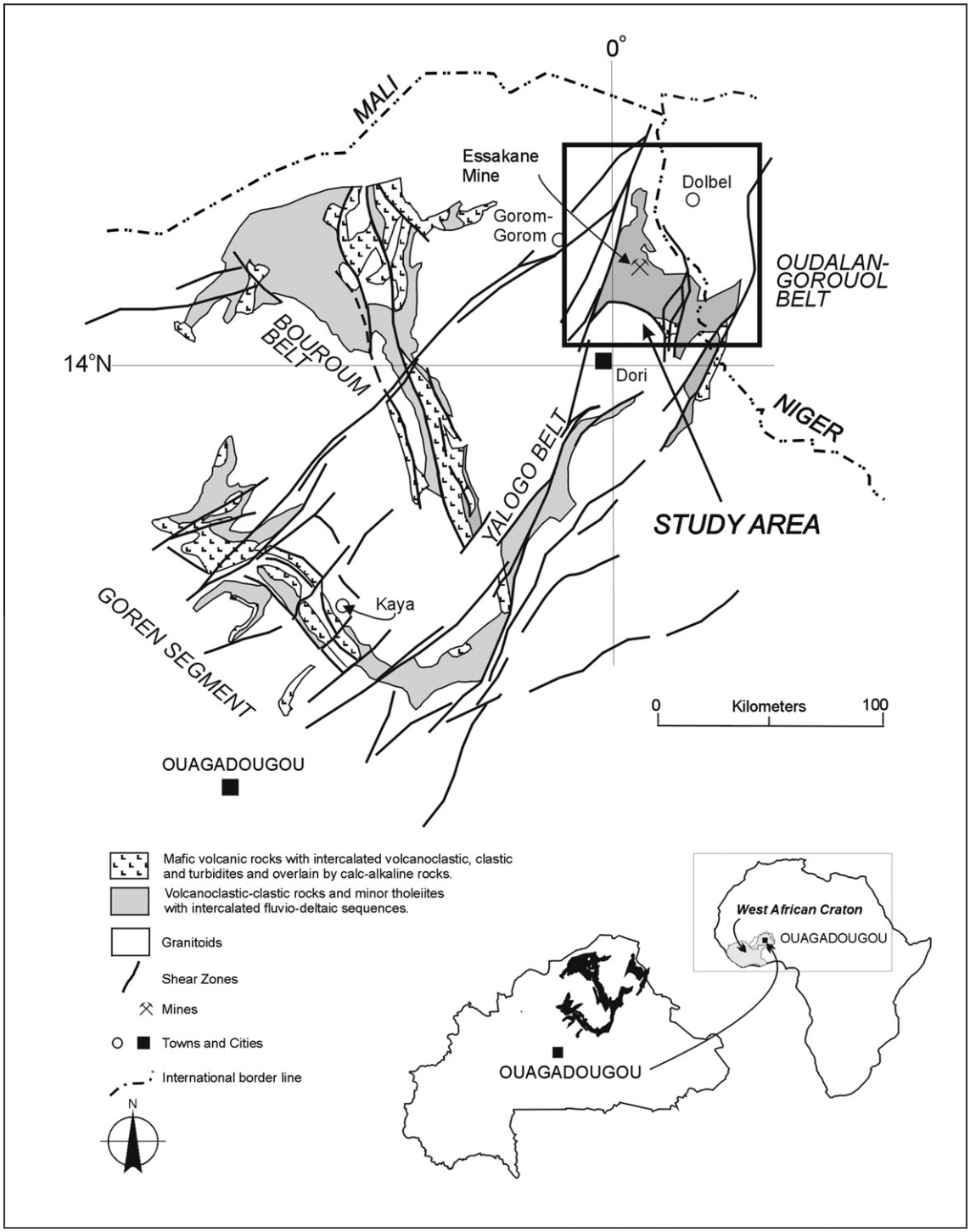

Fig. 1. Location map of the Oudalan Gorouol belt of Burkina Faso and Niger, together with the Bouroum, Yalogo and Goren greenstone belts. Modified after Feybesse et al. (1990) and Hein et al. (2004).

Although Tshibubudze et al. (2009) did not establish a detailed tectonic framework for gold metallogenesis throughout the OGB, vein-stockwork gold mineralization at the Essakane artisanal gold site was interpreted to have formed late in D2. However, our research indicates that an intimate relationship exists between the tectonic development of the OGB in D1 and D2, and formation of gold deposits. Second and third-order splay faults and shears of the Tangaean Event matured as sites of gold deposition during the Eburnean Orogeny. The deposits are thus structurally hosted.

In this paper, we present research on the structural geology of Oudalan-Gorouol belt in Burkina Faso and Niger and for the first time characterise the setting of the Essakane gold mine and gold camp. As new data, we report on the lithologies that ultimately define a volcano-sedimentary belt rather than a greenstone belt (*sensu stricto*), and which host gold mineralisation in the region. We summarise and describe the character of intrusive rocks of the greater Oudalan region and establish a relative chronology of crosscutting relationships that broadly constrains the structural

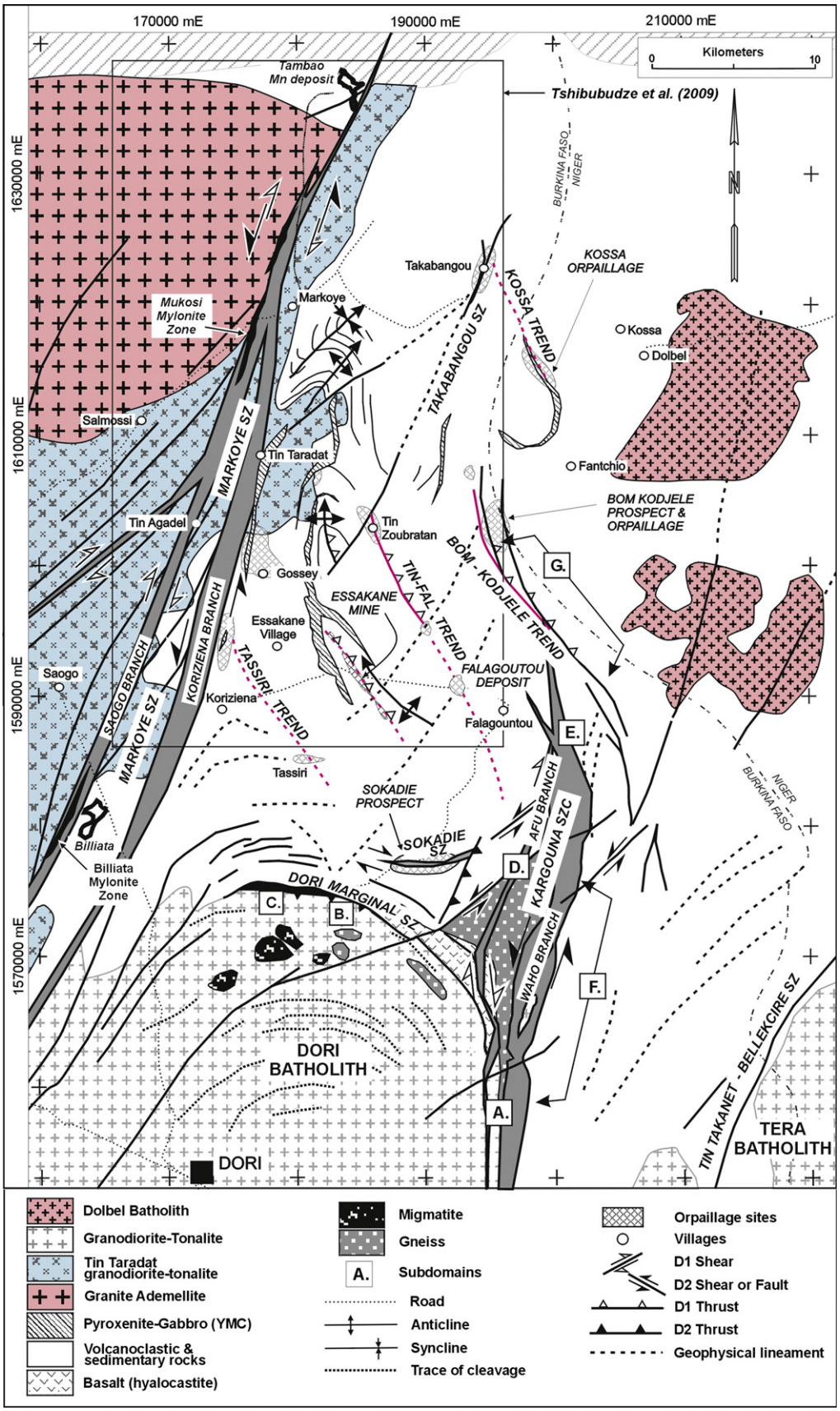

Fig. 2. Schematic geology map of the Oudalan Gorouol belt indicating the location of the Essakane Mine and Gosséy, Falagountou, Sokadie, Tin Zoubratan and Takabangou deposits. The margins of the OGB are defined by (1) the Markoye Shear Zone (MSZ), (2) the Tin Takanet-Bellekcire Shear Zone, and (3) the Dori Marginal Shear Zone (DMSZ) on the southern margin. Research studies by Tshibubudze et al. (2009) of the Markoye Shear Zone are indicated by the box.

evolution of the OGB a tectonic model for the formation of the OGB is proposed.

2. Geological setting

The West African Craton (WAC) is composed of an Archaean–Palaeoproterozoic basement that is divided into the Archaean Kénéma-Man domain (ca. 3.5 Ga) and the Palaeoproterozoic (2.3–1.8 Ga) Baoulé-Mossi domain (Feybesse et al., 2006). The Kénéma-Man domain consists of a granite–gneiss complex and granulitic meta-gabbro (Thiéblemont et al., 2001), while the Baoulé-Mossi domain consists of Birimian meta-sedimentary and meta-volcanic sequences that were deposited at ca. 2.3 Ga (Feybesse et al., 2006; Pawlig et al., 2006). Emplacement of TTG suite granitoids occurred at 2200, 2160–2130 and 2100–2070 Ma, concomitant to greenstone belt deformation (c.f., Hirdes and Davis, 2002; Pawlig et al., 2006; Gueye et al., 2008; Lompo, 2009, 2010) during the Tangaean Event (2170–2130 Ma, c.f. Tshibubudze et al., 2009; Hein, 2010), the polycyclic Eburnean Orogeny (2130–1980 Ma, Feybesse et al., 2006) and the Wabo-Tampelse Event (c.f., Hein et al., 2004; Hein, 2010). The Tarkwa Group unconformably overlies the Birimian sequences (Hastings, 1982; Leube et al., 1990; Milési et al., 1992), but does not crop out in the Oudalan-Gorouol belt (Tshibubudze et al., 2009). It is dated at 2194–2132 Ma (single detrital U–Pb zircon, Davis et al., 1994) or 2133 ± 4 Ma (maximum date from detrital zircon, Pigois et al., 2003) in its type locality in Ghana.

During the Eburnean Orogeny numerous calc-alkaline plutons intruded the Palaeoproterozoic sequences (Pawlig et al., 2006) including tonalite–trondjhemite–granodiorite (TTG), diorite, meta-diorite and leucogranite, and these are collectively termed the Eburnean granitoids (c.f., Pons et al., 1995; Naba et al., 2004; Pawlig et al., 2006; Lompo, 2009; Vidal et al., 2009). Two emplacement events are currently recognised in Burkina Faso (Castaing et al., 2003; Naba et al., 2004), (1) TTG Suite (amphibole-bearing) which is composed of granodiorite, tonalite and quartz–diorite that intruded Birimian supracrustal sequences between 2210 and 2160 Ma (c.f., Castaing et al., 2003; Lompo, 2009, 2010). (2) A granite suite (biotite ± muscovite) that is localised along shear zones and which intruded Birimian supracrustal sequences and TTG suite granitoids between 2150 and 1950 Ma (Castaing et al., 2003; Lompo, 2009, 2010). In the Oudalan Gorouol belt potassic-rich granite (*sensu stricto*) and pyroxenite–gabbro dykes/sills are intruded by granitoids and thus pre-date their emplacement (c.f., Tshibubudze et al., 2009). Northwest and northeast-trending dolerite dykes crosscut the WAC and were probably emplaced during the final breakup of supercontinents at 1.4–1.2 Ga (Zhao et al., 2002).

Several deposits and deposit styles occur in the OGB including; (1) Manganese deposits at Tambão (Beauvais et al., 2008), Billiata and south of the Kel Enguef metamorphic belt (Woolfe, 2011), (2) gold mineralization at Essakane, Gossey, Koreziéna, Falagountou, Takabangou, Tassiri, Bom Kodjelé, Sokadie, and Kossa artisanal mine sites (Milési et al., 1992; Nikiéma, 1992; Castaing et al., 2003; Nkuna, 2009; Tshibubudze et al., 2009), (3) pegmatite veins that host tourmaline, plagioclase and topaz crystals near the village of Tambão, and (4) Pb–Zn–Mo mineralisation in the Kuorki area of Niger (Milési et al., 1989). Several deposits are associated with the sulphidised brittle–ductile shear zones including gold in sheeted and stockwork quartz veins, copper as malachite in buck quartz veins, and tourmaline and topaz in pegmatite and buck quartz veins (Foster and Piper, 1993; Castaing et al., 2003; Feybesse et al., 2006; Tshibubudze, 2007).

There is a strong structural control to gold mineralization at all levels within the WAC (Milési et al., 1989; Castaing et al., 2003). Gold deposits are commonly situated in second or third-order structures adjacent to first-order crustal-scale structures (Groves et al., 1998) and are thus interpreted as epigenic in origin (c.f., Groves et al., 1998; Béziat et al., 2008). Gold mineralization in the OGB is distributed along shear zones as structurally-hosted lode-gold (Nikiéma, 1992; Tshibubudze et al., 2009).

3. Methods and procedures

Field studies were undertaken during 2009–2010 and focussed on mapping of lithologies, igneous rocks and major structures in the hangingwall of the Markoye Shear Zone (MSZ), which trends north–northeast and dips steeply east, i.e., map work took place in the region east of the MSZ and included the Essakane and Falagountou goldfields. This database is reported herein for the first time. Samples for petrographic studies were collected from outcrops across the region and from diamond drill core at the Essakane, Falagountou and Sokadie deposits (Fig. 2). Limited petrographic study of the Essakane and Falagountou gold deposits was reported by Nkuna (2009) and are not repeated herein.

Prior to field mapping, ASTER (1:250 000) and LANDSAT (1:250 000) imagery was interpreted to extract major lineaments and the location of outcrop. The land surface of the northeast of Burkina Faso and Niger is denudated and desertified, but supports fields of maize and cotton. It was important to use remotely sensed data in regional mapping because of the sparse outcrop, but interpretation demanded considerable ground-truthing. The interpretation of geophysical datasets included aeromagnetic (RTP 1st and 2nd vertical derivative aeromagnetic, and TMI RTP) and kilometre-scale gravity, and these supplemented field and remotely sensed datasets. Geographic and geologic reconnaissance studies were conducted before field work commenced. Even though outcrop was limited in the area, several east–west and north–south traverses were completed across the region, from Burkina Faso into the western portion of the Republic of Niger (Fig. 2). Sub-crop mapping proved useful and effective in areas of limited outcrop, or thin sand cover.

GPS co-ordinates were reported in UTM zones 30P and 31P zones using Discovery 3.2® MapInfo Professional V8.5®. The field area is bisected by the Prime Meridian (0° longitude). Structural analysis, calculated means and contour plots used GEOrient 9.2® (Holcombe, 2008).

4. Lithologies of the OGB

The lithologies of the rocks in the area around Essakane have been described by Tshibubudze et al. (2009), but this description has been elaborated to include the entire OGB. The sequences consist of folded, sheared and/or mylonitized volcanic, volcano-sedimentary and sedimentary sequences that were metamorphosed to upper greenschist facies and locally, to amphibolite facies. They underwent contact metamorphism to hornblende–hornfels facies adjacent to intruding granitoids, dykes and sills. Five volcano-sedimentary sequences are defined for the OGB:

(1) A meta-volcanic sequence (~150 m thick) that consists of pyroclastic and tuff beds, hyaloclastic and pillow basalt, and agglomerate (Fig. 3a–c) crops out between the Sokadie artisanal mine and the Dori Batholith (Fig. 2). The pyroclastic facies hosts angular and sub-rounded basalt clasts in a lithified volcanic dust or ash matrix.
(2) A greywacke–siltstone–shale sequence interbedded with rare chert beds and banded iron formation. This sequence disconformably overlies the meta-volcanic sequences.
(3) A sandy dolomite (~5 m thick) crops out south of the Essakane gold mine and hosts stromatoforms (Fig. 3f). It is variably ferriginized, chloritized and epidotized.

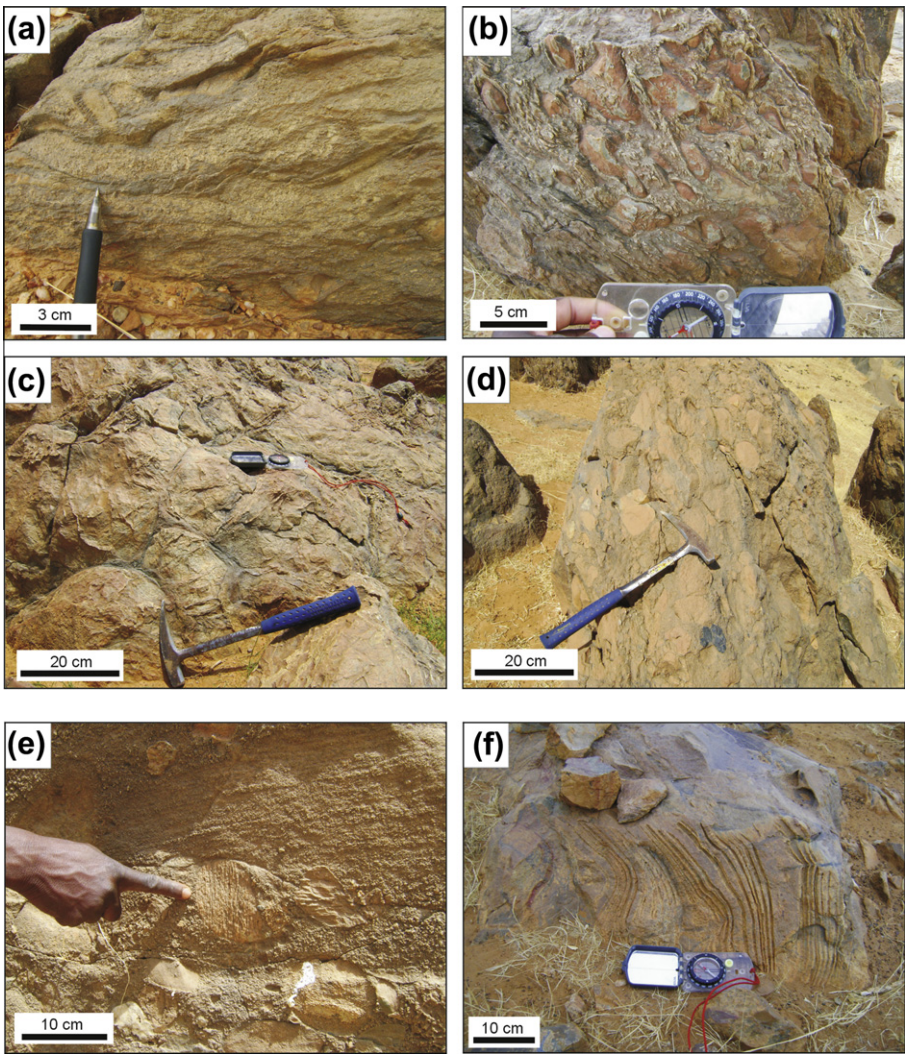

Fig. 3. Lithologies of the OGB. (A) Tuffaceous beds of the meta-volcanic sequence (UTM 31P, 0188468, 1573703). (B) Silicified agglomerate unit of the meta-volcanic sequence near the contact with the Dori Batholith (UTM 31P, 0187383, 1574283). (C) Pillowed basalt of the meta-volcanic sequence near the contact with the Dori Batholith (UTM 31P, 0187383, 1574283). (D) Matrix to clast-supported polymictic conglomerate beds near the Tin Zoubratan artisanal mine (UTM 31P 0183827 1602472). Clasts are composed of angular clasts, pebbles and boulders of granite, granodiorite, gabbro, fuchsitic chert, and chert. (E) Matrix-supported polymictic conglomerate in coarse greywacke; clasts are composed of angular clasts of quartz and quartz–carbonate vein clasts, andesite, basalt, volcaniclastic sedimentary rocks and schist (UTM 31P 0177800 1596649). (F) Stromatoforms in sandy dolomite (~5 m) south of the Essakane gold mine (UTM: 31P 0187303 1588249).

(4) A sequence of interbedded conglomerate–greywacke–siltstone–shale units that conformably overlays the greywacke–siltstone–shale sequence. Conglomerate beds are polymictic and matrix-supported or rarely, clast-supported (Fig. 3d and e). They are composed of sub-rounded to angular clasts, pebbles and boulders (up to 30 cm in diameter) of granite, granodiorite, gabbro, fuchsitic chert, chert, quartz and quartz–carbonate vein clasts, andesite, basalt, volcaniclastic sedimentary rocks and schist. The matrix is generally composed of fine to coarse-grained, poorly-sorted greywacke or gritstone that is sometimes volcaniclastic. The size and variable composition of clasts, pebbles and boulders suggests a provenance that is metamorphic–volcanic–plutonic in character.

(5) A greywacke sequence conformably overlies the conglomerate–greywacke–siltstone–shale sequence. It is composed of bedded, cross-bedded, slump-folded and scoured, medium-grained, quartz and feldspar-rich sandstone. Cross-bedded greywacke beds predominate. Fuchsite layers, thin chert beds, shale with mud-cracks and fine laminations, siltstone, pebble beds and mud balls are intercalated with greywacke units. An interbedded conglomerate member up to 10 m thick is similar in composition to the polymictic, matrix-supported conglomerates in the underlying conglomerate–greywacke–siltstone–shale sequence. Based on stratigraphic studies east of the township of Markoye by Peters (2011), the greywacke sequence exceeds 4.2 km in true stratigraphic thickness.

Laterite is randomly distributed throughout the OGB. In situ laterite was deposited during the Cretaceous–Tertiary (c.f., Brown et al., 1994; Burke and Gunnell, 2008) and was deeply eroded during the Eocene to Miocene epochs (Brown et al., 1994; Beauvais et al., 2008) to form several discrete transported laterite profiles.

5. Intrusive rocks of the Oudalan-Gorouol area

A significant proportion of the Oudalan-Gorouol area is composed of magmatic rocks (Fig. 2). They include the Dori, Tin Taradat, Dolbel and Terra batholiths, the Yacouba Mafic Complex (labelled pyroxenite–gabbro in Fig. 2) (Tshibubudze et al., 2009),

porphyry dykes and sills, a series of north-trending gabbro sills, and northwest-tending gabbro and dolerite dykes that are dated at 250 ± 13 Ma (K–Ar whole rock dating) (Hottin and Ouedraogo, 1992).

The Dori Batholith crops out at the southern margin of the study area (Fig. 2) as a medium-grained hornblende–plagioclase–quartz ± biotite ± K-feldspar granodiorite. It crosscuts and intrudes the metavolcanic and greywacke–siltstone–shale sequences on its northern margin. The granodiorite contains plagioclase phenocrysts (1–2 cm) and hosts mafic xenoliths (Fig. 4a). The batholith has an internal foliation that parallels the intrusive contact on the northern margin of the batholith. The foliation is transitional with, and grades into migmatite and then gneiss at the contact margin; the contact margin is deformed with development of proto-mylonite, LS-tectonite and schist that is herein termed the Dori Marginal Shear Zone (DMSZ). The internal foliation, migmatite, gneiss and DMSZ are interpreted as syn-genetic and syn-emplacement in age. A northwest-trending cleavage (S1), faults and folds crosscut the batholith and the DMSZ indicating a late formation. They are, in turn, crosscut by a northeast-trending cleavage (S2), faults and buck quartz veins (V2), and by west-northwest trending gabbro dykes.

The Tera Batholith is composed of plagioclase feldspar, quartz, hornblende and biotite and is foliated and sheared (Fig. 4b) along the Tin Takanet-Bellekcire Shear Zone, which coalesces with the Kargouna Shear Zone south of the study area (Fig. 2).

The Tin Taradat granodiorite–tonalite crops out south of the town of Markoye and intrudes volcano-sedimentary and sedimentary sequences east of the Markoye Shear Zone (MSZ). The granodiorite–tonalite is coarse to medium-grained and composed of plagioclase, quartz, hornblende and biotite. It hosts elongate-ovoid mafic xenoliths that trend northwest and plunge to the west. Between the Gosséy artisanal mine and Tambão manganese deposit the pluton is foliated and/or sheared in the MSZ (Tshibubudze et al., 2009).

The Dolbel batholith crops out along the eastern margin of the OGB in Niger and consists of several small alkali-granite plutons (Pons et al., 1995) that are imprecisely dated at 2137 ± 126 Ma (Léger et al., 1992; Rb–Sr isochron). The plutons host mafic xenoliths and lithic xenoliths of greywacke–sandstone (Fig. 4c). The

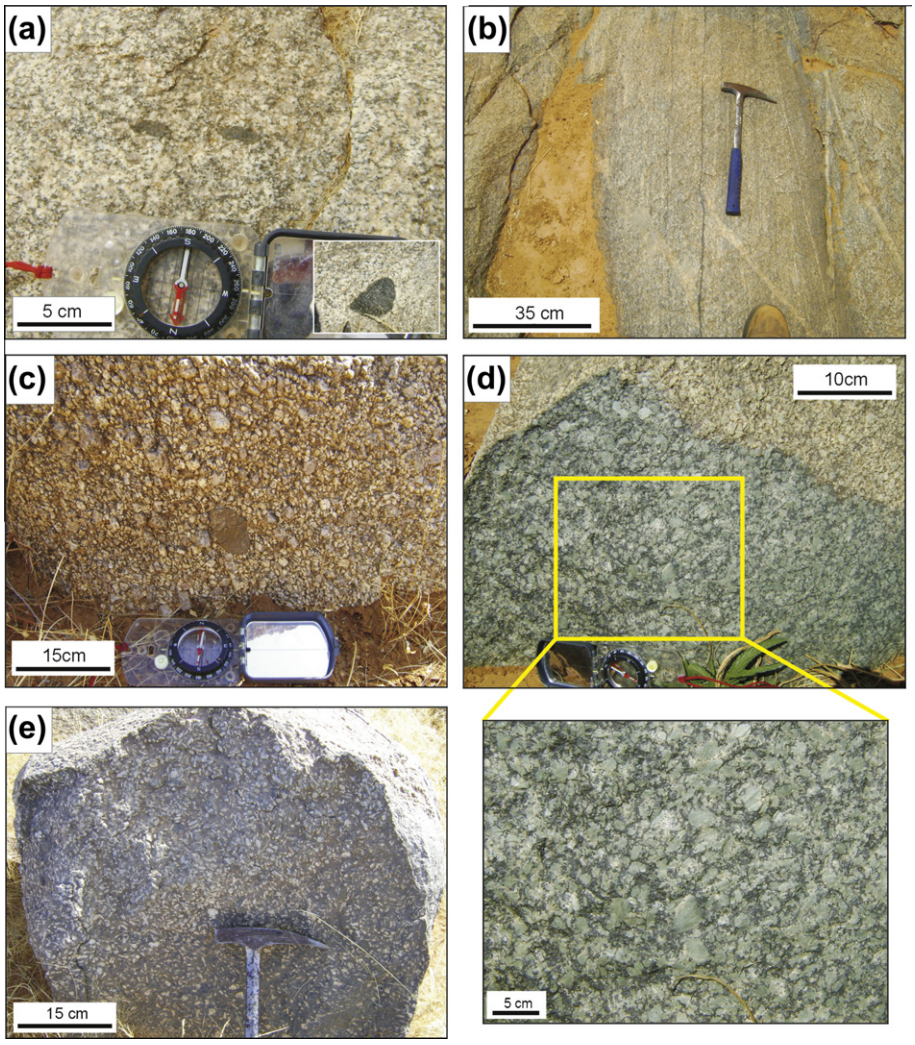

Fig. 4. Intrusion rocks of the Oudalan-Gorouol area. (A) The Dori Batholith is a medium-grained hornblende–plagioclase–quartz ± biotite ± K-feldspar granodiorite. It is phenocrystic in plagioclase (1–2 cm) and hosts mafic xenoliths (UTM 30P 0821592 1559159). (B) The Tera Batholith is situated in the southeast of the study area. It is composed of plagioclase feldspar, quartz, hornblende and biotite and is foliated and sheared along the Tin Takanet-Bellekcire Shear Zone (UTM 31P 0235492 1586086). (C) The Dolbel batholith. The batholith is composed of 5 mm phenocrysts of plagioclase (30% of the total volume) in a medium-grained (0.5–1.0 mm in size) groundmass of quartz and K-feldspar, with accessory biotite and chlorite (UTM 31P 0213792 1614382). (D) Porphyritic monzonite dykes of the OGB. They are composed of phenocrysts of zoned plagioclase in a fine to medium groundmass of quartz, plagioclase, muscovite, biotite, chlorite and sulphides (UTM 31P 0188829 1588399). (E) Porphyritic monzonite dykes of the OGB exhibiting randomly orientated plagioclase phenocrysts that are euhedral to anhedral (UTM 31P 0184195 1602936).

plutons are composed of 5 mm phenocrysts of plagioclase (30% of the total volume) in a medium-grained (0.5–1.0 mm in size) groundmass of quartz and K-feldspar, with accessory biotite and chlorite. They are crosscut by northeast-trending buck quartz–carbonate veins.

The Yacouba Mafic Complex (YMC) as defined by Tshibubudze et al. (2009) crops out northeast of Tin Taradat and near the village of Gosséy adjacent to the MSZ (Fig. 2). It is readily identified from geophysical data in which it presents as a 12 km long, 3 km wide linear north-trending magnetic high. The YMC is a layered pyroxenite–gabbro that hosts lithic xenoliths of meta-greywacke and quartzite. Pyroxenite layers consist of >1 cm pyroxene and olivine phenocrysts in a pyroxene–olivine–nepheline groundmass. The YMC crosscuts the Tin Taradat granodiorite–tonalite. An equal intensity magnetic high that is situated near the Kossa artisanal mine in Niger may be similar in composition to the YMC however, it does not crop out. The magnetic trace forms a crescent-shaped magnetic high.

Furthermore, dolerite–gabbro sills (and dykes) occur throughout the OGB and are bedding parallel in the metasedimentary units, which they contact metamorphosed to hornblende–hornfels facies. The sills (and dykes) are typically composed of medium to coarse crystals of pyroxene, amphibole, plagioclase and magnetite. They are crosscut by a northeast-trending regional cleavage. Several exploration diamond drill holes at the Essakane Mine deposit have intersected the sills; they exhibit sharp contacts with the metasedimentary rocks but have locally folded and veined the rocks in the inner contact aureole. Thin quartz–carbonate veins (less than 2 cm thick) are orientated approximately perpendicular to the contact and are auriferous in disseminated gold.

A series of porphyritic monzonite dykes also occur throughout the OGB and parallel bedding in metasedimentary units. They are porphyritic with phenocrysts of zoned plagioclase in a fine to medium groundmass of quartz, plagioclase, muscovite, biotite, chlorite and sulphides (including chalcopyrite, pyrite and arsenopyrite). Plagioclase phenocrysts are randomly orientated and euhedral to anhedral (Fig. 4d and e). They are folded along northwest-trending fold axes and crosscut by a northeast-trending regional cleavage. Immediately north of the Essakane Mine the dykes host gold mineralisation. They are crosscut by west-northwest trending dolerite–gabbro dykes south of the Falagountou artisanal mine.

A series of northwest-trending dolerite–gabbro dykes crosscut the OGB and intrusive complexes in the northeast of Burkina Faso, and are dated at 250 ± 13 Ma (K–Ar whole rock dating) (Hottin and Ouedraogo, 1992).

6. Shear zones

The margins of the OGB are defined by (1) the Markoye Shear Zone (MSZ) on the western margin which hosts the Koreziéna, Gosséy and Tin Taradat gold prospects, (2) the Tin Takanet-Bellekcire Shear Zone on the eastern margin in Niger, and (3) the Dori Marginal Shear Zone (DMSZ) on the southern margin. The northern margin of the OGB is bounded by sediments of the Meso to NeoProterozoic Taoudeni Basin (Fig. 2). The Tin Takanet-Bellekcire Shear Zone, which hosts gold artisanal mines along its length was not extensively studied due to limited access and is not discussed further. The Kargouna Shear Zone Complex (KSZC) lies central to the OGB and crosscuts the Dori Batholith and the DMSZ on the eastern margin of the batholith; it therefore formed during or after emplacement of the batholith and the DMSZ. The KSZC hosts gold deposits approximately 6 km east of the town of Falagountou.

Between the MSZ and the KSZC, the OGB is crosscut by several northwest and northeast-trending splay shears including the Takabangou Shear Zone, which hosts the Takabangou prospect and artisanal mine. The belt is also crosscut by northwest-trending, southwest-verging thrust-folds. Northwest-trending shears and thrust folds are crosscut by northeast-trending shears.

The thrust-folds are significant because they host gold mineralization in sheeted veins in the folded hangingwall of thrusts. They include gold mineralisation in the Essakane Mine, the Tassiri prospect, and the Kossa deposit (Fig. 2). Gold mineralisation at the Bom Kodjelé artisanal mine is hosted in the Bom Kodjelé Shear Zone (thrust), while gold mineralisation at the Falagountou deposit is hosted in an anticline, but the fold is not well exposed.

6.1. Markoye Shear Zone (MSZ)

The Markoye Shear Zone trends north–northeast between the towns of Markoye and Saoga where it hosts gold deposits and artisanal mines at Gosséy and Tin Taradat, and a gold prospect at Koreziéna (Fig. 2). The MSZ is defined by a wide zone of quartz–muscovite schist that is transitional with, and encloses mylonite zones, including the Mukosi Mylonite Zone (Tshibubudze et al., 2009). The Mukosi Mylonite Zone is situated in the northeast of the study area in a flexure in the MSZ where the Tin Taradat granodiorite adjoins a granite–adamellite in the western block. Macroscopic boudins of the Tin Taradat granodiorite and granite–adamellite are enclosed by siliceous ultramylonite and mylonite. Numerous metre to centimetre-scale pseudotachylite veins splay southwest into the western block of the MSZ, and northeast into the eastern block of the MSZ away from the mylonite zone. Buck quartz–carbonate and quartz cataclasite veins are hosted in quartz–muscovite schist throughout the MSZ. This schist is crosscut by narrow, discontinuous quartz–chlorite (±muscovite) shears.

The studies between the Tambão and Billiata manganese deposits (Fig. 2) showed that the MSZ has two main branches. These coalesce near the town of Markoye. The western branch (herein termed the Saogo branch) trends north–northeast. It is characterised by dextral-reverse displacement (with east block up) as indicated by shear bands and sigma clasts in mylonite in the Billiata and Mukosi Mylonite zones. Southwest and northwest-trending anastomosing mylonite zones splay-off the Saogo branch into the western block of the MSZ.

The eastern branch of the MSZ (herein termed the Koreziéna branch) trends northerly and is characterised by sinistral-reverse displacement (east block up) as evidenced by S2-C foliation in quartz–muscovite schist and massive macroscopic sigmoidal buck–quartz–carbonate veins (V2) and iron-rich cataclasites that are right-stepping. The buck quartz–carbonate veins are crosscut by narrow (mm-scale), discontinuous quartz–chlorite (±muscovite) shears. Mylonite does not occur in the Koreziéna branch in the study area.

The region between the Saogo and Koreziéna branches of the MSZ is poorly exposed and covered by sand dunes, but subcrop and outcrop mapping on the limited exposures indicated that the region consists of Fe–manganese rich metasedimentary rocks (at Billiata), polymictic meta-conglomerate, siltstone, meta-volcaniclastic greywacke and quartzite. The meta-sedimentary rocks are isoclinally folded (F2) at all scales and boudinaged. The folds plunge steeply to the northeast. The folded rocks are crosscut by narrow shear zones (~1 m wide) that trend north–northeasterly.

The region north of the town of Markoye where the Saogo and Koreziéna branches coalesce is poorly exposed because of sand dune cover. However, mylonite crops out on the western margin of the MSZ, and schistosed granodiorite crops out on the eastern margin of the MSZ. Immediately east of the Tambão manganese deposit, an anastomosing foliation in granodiorite marks the north–northeast strike extent of the Koreziéna branch. Thereby it is interpreted that the Saogo branch terminates between Markoye and Tambão, and that the Koreziéna branch weakens.

Furthermore, structural and kinematic studies in the region between the towns of Markoye and Koreziéna by Tshibubudze (2007), Tshibubudze et al. (2009), and Tshibubudze and Hein (2010) have demonstrated that the OGB underwent at least two phases of deformation, with dextral-reverse displacement (east block up) in D1 on the MSZ being followed by sinistral-reverse displacement (east block up) in D2. It is now evident from the extended studies that we undertook in 2008–2010 that the Saogo branch formed during dextral reverse displacement in D1 with development of mylonite, ultramylonite and pseudotachylite veins, while the Koreziéna branch formed during sinistral reverse displacement in D2 with development of buck quartz and quartz cataclasite veins in a quartz–chlorite–muscovite schist. It is important to note that the Koreziéna branch and not the Saogo branch, is an important host to auriferous buck quartz veins and artisanal mines.

6.2. Dori Marginal Shear Zone (DMSZ)

The Dori Marginal Shear Zone (DMSZ) bounds the southern margin of the OGB (Figs. 2 and 5). The DMSZ is not known to host gold deposits but small artisanal pits suggest that gold may have been found historically. The DMSZ is crosscut by the KSZC, D1 and D2 structures (including faults, folds, foliations and veins) and west-northwest trending dolerite–gabbro dykes.

The DMSZ parallels the outcrop margin of the Dori Batholith; it is thus arcuate in outcrop form (Fig. 5a). It consists of proto-mylonite, LS tectonite (LS_{1-x}) and schist at the contact with the Dori Batholith and these are crosscut by a northwest-trending disjunctive cleavage (S1) which in turn, is crosscut by a weak, non-penetrative northeast-trending foliation (S2). The proto-mylonite is glassy and intensely lineated or rodded (L_{1-x}). It hosts numerous intrafolial and isoclinal folds (F_{1-x}) that plunge steeply to the south. Horizontal quartz–ankerite veins (V_{1-x}) are developed perpendicular to L_{1-x} and are interpreted to have formed during vertical stretch on the DMSZ (Fig. 5b).

Three subdomains (A, B and C) have been defined along the DMSZ (Fig. 2); equal area stereographic projections of poles to foliation are presented in Fig. 6a–f. Sub-domain A is north–northwest trending and steeply west-dipping with a calculated mean strike and dip for S_{1-x} of 333°/70°W. Subdomains B and C trend west-northwesterly with calculated mean strikes and dips for S_{1-x} of 291°/77°N and 275°/81°S, respectively. The mean calculated dip and dip direction for L_{1-x} in Subdomain C is 70° towards 214° (Fig. 6d) with southwest block up (as indicated from accretion steps), which is consistent with reverse-(sinistral) displacement in that location, i.e., block transport was towards the northeast (Fig. 5c).

S_{1-x} and V_{1-x} are crosscut by S2 and folded by F2. The calculated mean strike and dip for S2 in Subdomains A and B are 048°/75°N and 011°/81°E (Fig. 6e and f), respectively; S2 in Subdomain C trends northeast (based on limited data). S2 is disjunctive to crenulating and refracts across the Dori Batholith, or where rock units are competent.

In summary, proto-mylonite, LS tectonite (LS_{1-x} and L_{1-x}), horizontal extension veins (V_{1-x}), and schist (S_{1-x}) of the DMSZ, together with the (1) marginal gneiss in the chilled margin of the Dori Batholith, (2) the migmatite, and (3) the foliation in the batholith, comprise a broad zone of deformation that formed synchronous to pluton emplacement. These were subsequently deformed and overprinted in D1 by S1 (northwest-trending discontinuous disjunctive cleavage), drag folded against F2 faults and overprinted by S2 (northeast-trending penetrative continuous disjunctive cleavage).

6.3. The Kargouna Shear Zone Complex (KSZC)

The Kargouna Shear Zone Complex consists of the Afu and Waho branches (Figs. 2 and 7). The Afu Branch is moderately west-dipping, while the Waho Branch is moderately to steeply east-dipping. They are characterised by quartz–chlorite–muscovite schist that hosts brecciated, sigmoidal buck quartz–carbonate veins, and iron-rich cataclasite veins. The buck quartz–carbonate veins are tourmaline-rich near the contact margin of the Dori Batholith. The region between the branches is composed of biotite–amphibole–potassium feldspar gneiss that is sericitised.

The Afu Branch crosscuts the Dori Batholith, DMSZ, Sokadie Shear Zone, gneissic rocks northeast of the Dori Batholith, and metasedimentary and metavolcanic rocks in the contact aureole of the Dori Batholith. The Afu branch thus formed after D_{1-x}. In Subdomains D and E (Fig. 2) the Afu Branch dips moderately west with a mean calculated dip and strike of S1 of 024°/60°W and 024°/53°W, respectively. Displacement in the Afu Branch is dextral strike-slip as indicated from the asymmetry of boudins, mesoscopic mica fish, limited S1-C schistosity, and a near horizontal L1 (stretching lineation). S1 and S1-C schistosity are crosscut by a northeast-trending, steeply south-dipping foliation (S2) and northeast-trending sigmoidal buck quartz veins (V2) that measure approximately 40–50 m in length.

The Waho Branch (Subdomain F in Fig. 2) crosscuts the Dori Batholith, gneissic rocks northeast of the Dori Batholith, metasedimentary and metavolcanic rocks in the contact aureole of the Dori Batholith, and S1 and F1. The Waho Branch therefore formed after D_{1-x} and D1. The Waho Branch dips moderately to steeply east with a mean calculated strike and dip of S2 of 021°/69°E. Displacement in the Waho branch is sinistral strike-slip as indicated from the asymmetry of boudins, numerous sigma clasts (of dominantly quartz), shear bands, limited S2-C foliation, and a near horizontal stretching lineation (L2) (Fig. 7). In this branch, north-trending asymmetric buck quartz vein (10–20 m in length) step-right indicating sinistral displacement along the length of the branch. The Waho Branch is crosscut by porphyritic granodiorite and a west-northwest trending foliation (S3) that is non-penetrative and non-pervasive.

6.4. Takabangou Shear Zone

The Takabangou Shear Zone crosscuts F1 thrust-folds, folded monzonite dykes, gabbro–pyroxenite dykes and sills, and S1 and V1 north of Essakane and at the Tin Zoubratan prospect (Fig. 2). The shear therefore formed after D1. It trends north–northeast and dips moderately southeast with a mean calculated strike and dip of S2 of 042°/55°E. It consists of quartz–chlorite–muscovite schist that grades into mylonite; it exhibits numerous delta and sigma clasts that indicate that sinistral-reverse displacement (southeast block up) was dominant during formation of the shear zone. A stretching lineation generally plunges southeast with a mean calculated dip–dip direction of 43° towards 171°.

The northwestern block of the Takabangou Shear Zone is composed of re-crystallised volcaniclastic greywacke (of the greywacke sequence), while the southeastern block is composed of conglomerate–greywacke–siltstone–shale units that are crosscut by quartz–carbonate veins.

6.5. Sokadie Shear Zone

The triangular region between the DMSZ and the KSZC is structurally complex (Fig. 2). The region hosts deformed pillow and hyaloclastite basalt, and meta-sedimentary rocks of the overlying (unconformably) greywacke–siltstone–shale sequence. The Sokadie Shear Zone bounds the northern margin of the region, while

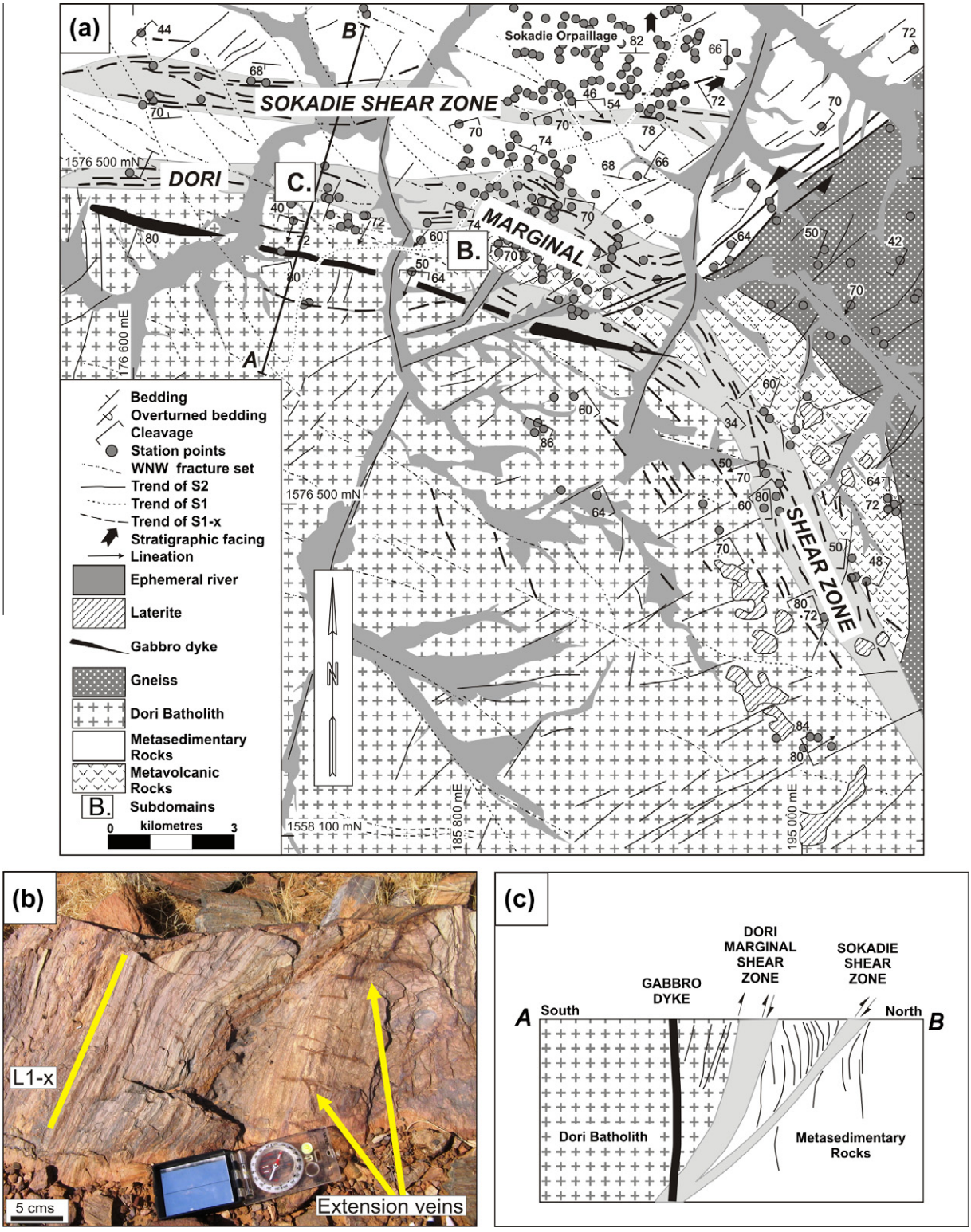

Fig. 5. (A) Schematic map of the Dori Marginal Shear Zone (DMSZ) and Sokadie Shear Zone. (B) The DMSZ hosts numerous quartz–ankerite extension veins (V_{1-x}) and is intensely lineated and rodded as manifested by L_{1-x}. (C) Cross section through the DMSZ along section line A–B. The DMSZ and Sokadie Shear Zone dip steeply to moderately south and exhibited reverse displacement with south block up.

the Waho Branch (of the KSZC) and the DMSZ bound the eastern and south-western margins, respectively. A northeast-trending sinistral shear-fault crosscuts and displaces the metavolcanic and metasedimentary units in the Sokadie region, and the Dori Batholith.

The Sokadie Shear Zone hosts the Sokadie artisanal mine and prospect and is the site of several discontinuous buck quartz veins (20–30 m long), and numerous mesoscopic folded and boudinaged quartz–carbonate veins (Nkuna, 2009). It is crosscut by the northerly-trending thrust, a non-pervasive, northwest-trending foliation

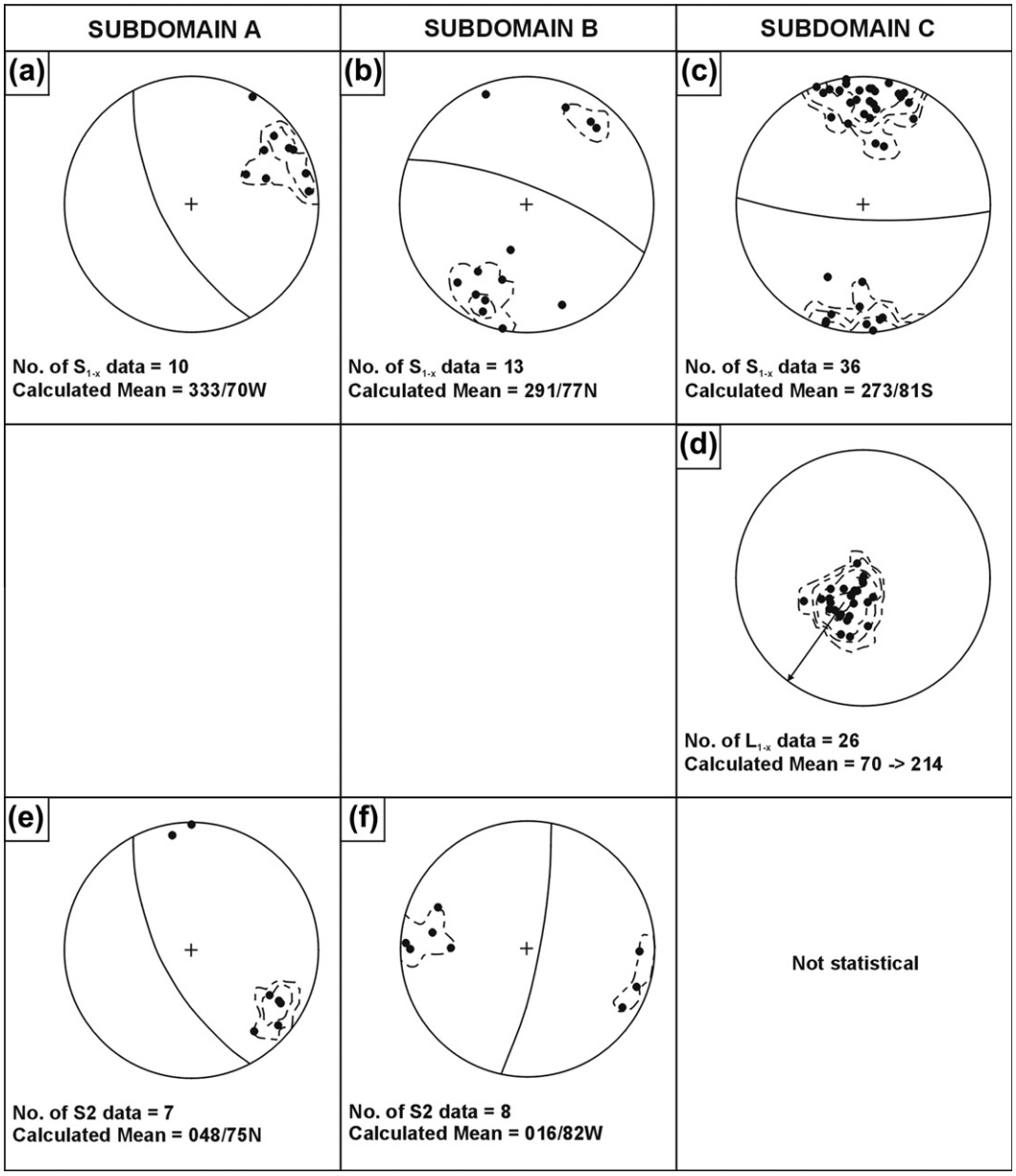

Fig. 6. Equal area stereographic projections of poles to S_{1-x}, L_{1-x} and S2 in Subdomains A–C. S2 is disjunctive and crosscut the DMSZ and Dori Batholith.

(interpreted as S1), a northeast-trending penetrative disjunctive cleavage (interpreted to be S2) and west-northwest trending gabbro dykes. The Sokadie Shear Zone thus predates those structures; it is consequently interpreted as being a co-shear to the DMSZ, which it sub-parallels.

At the Sokadie artisanal mine, S_{1-x}–C schistosity in the Sokadie Shear Zone indicates that displacement was dextral strike-slip. At the Sokadie artisanal mine the shear zone is steeply south-dipping and composed of quartz–chlorite–ankerite ± sulphide ± cordierite schist (interpreted as S_{1-x} to S_{1-x}–C) with a mean calculated strike and dip of 070°/68°S. The shear hosts a complex array of tight to isoclinally-folded quartz–carbonate veins, massive buck quartz veins, and a moderately to steeply plunging lineation (L_{1-x}) with a calculated mean of 68° towards 159°. At the Sokadie artisanal mine it exhibits evidence of progressive deformation (in outcrop and diamond core) with several stages of quartz–carbonate vein development in which older veins are sequentially deformed, folded and boudinaged before being overprinted by a second, third or even a fourth set of veins. The Sokadie deposit and artisanal mine has been interpreted by Kerr (2004) as a mineralised system in an east–west trending synform that plunges toward the southeast.

7. Gold trends

Sites of gold mineralisation in the OGB occur where northeast-trending geophysical lineaments that are interpreted to be D2 faults or shear zones, crosscut northwest-trending geophysical lineaments or D1 thrust-folds. They may also occur where northwest-trending geophysical lineaments or D1 thrust-folds coalesce with north–northeast trending D2 shear zones such as the Koreziéna branch of the MSZ. These sites of gold mineralization are distributed along trends including the Essakane Mine Trend, Tin Zoubratan–Falagountou Trend (herein termed the Tin–Fal Trend), Bom Kodjelé Trend, Tassiri Trend and Kossa Trend.

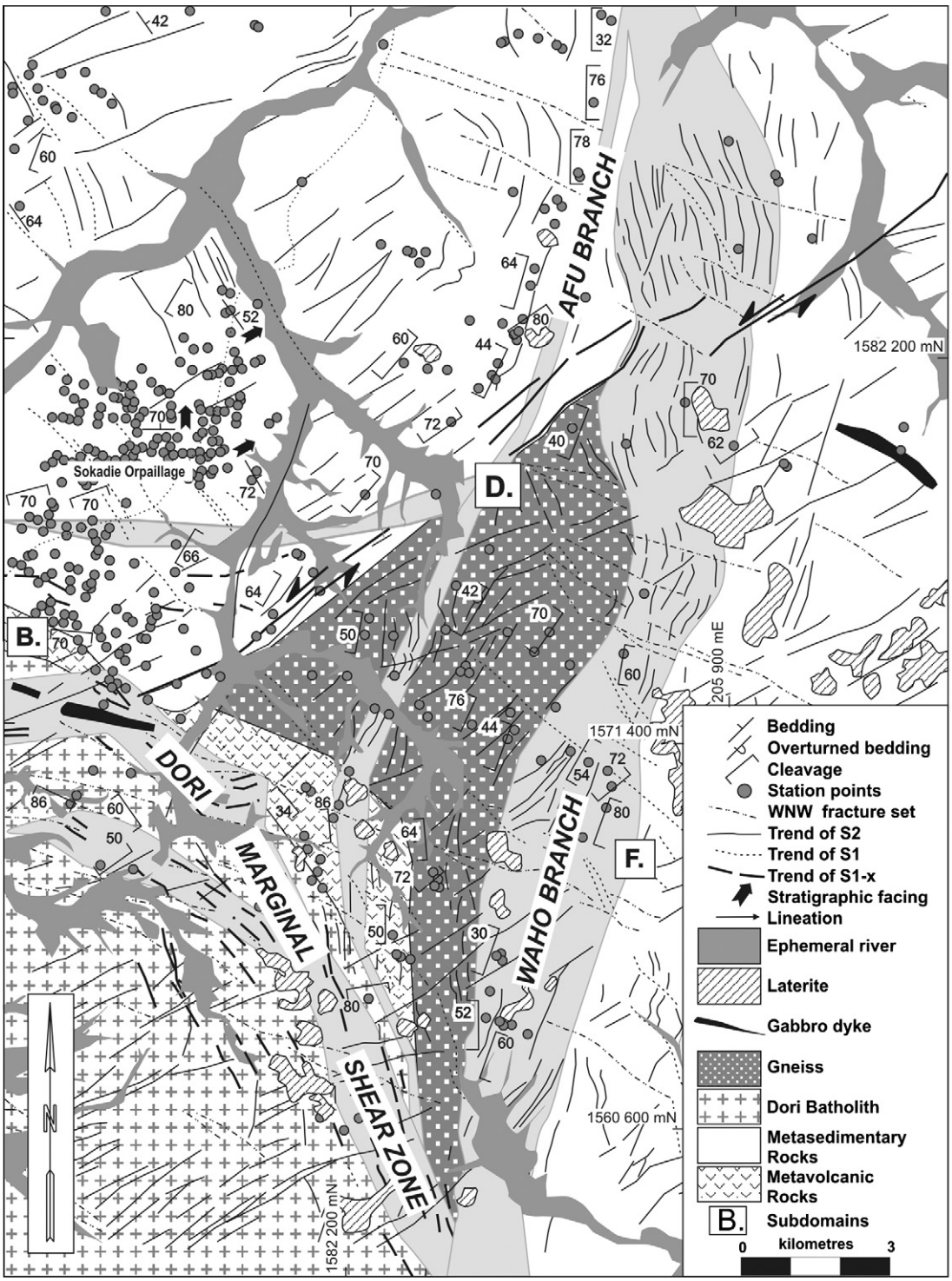

Fig. 7. Schematic map of the Kargouna Shear Zone Complex. The Afu Branch is moderately west-dipping. The Waho Branch dips moderately to steeply east. The Afu Branch crosscuts the Dori Batholith, DMSZ, Sokadie Shear Zone, gneissic rocks northeast of the Dori Batholith, and metasedimentary and metavolcanic rocks in the contact aureole of the Dori Batholith.

7.1. Essakane Mine Trend

The Essakane Mine Trend is characterised by an open asymmetric anticline (F1) whose fold hinge dips moderately northeast. The fold closes and plunges gently to the northwest. Fold vergence is southwest indicating that tectonic transport was towards the southwest during fold formation.

The dominant rock types of the Essakane artisanal mine are a deeply weathered sequence of interbedded conglomerate–greywacke–siltstone–shale; a dolomite unit subcrops southeast of the Essakane Mine. Several generations of auriferous veins are recognised in trenches that crosscut the Essakane Main Zone including arsenopyrite–pyrite–gold mineralisation in quartz veins that are crosscut by vein-stockwork gold mineralization (Tshibubudze et al., 2009) and these formed during D2 because the veins crosscut F1 and S1.

The Essakane Mine Trend is crosscut by the northeast-trending Takabangou Shear Zone (Fig. 2). Northeast-trending geophysical

lineaments that are parallel to the Takabangou Shear Zone, and are interpreted to be faults or shear zones, crosscut the Essakane Trend at Essakane South, and between Essakane South and the Sokadie artisanal mine (Fig. 2).

7.2. Tin Zoubratan–Falagountou Trend (Tin–Fal Trend)

The northwest-trending (Tin–Fal Trend is defined by an upright, shallowly southeast to northwest-plunging anticline–syncline pair that is tight to isoclinal in form. The calculated mean of the fold plunge is 7° towards 151°, but the fold axis is refolded along northeast-trending F2 fold axes. The syncline near the Tin Zoubratan artisanal mine is tight to isoclinal and closes to the northwest with a calculated fold plunge of 32° towards 173°.

The Tin–Fal Trend hosts several artisanal mine sites including the Tin Zoubratan and Falagountou sites. They are hosted in the conglomerate–greywacke–siltstone–shale sequence. The artisanal mine sites are located where the Tin–Fal Trend is crosscut by northeast-trending shears and/or northeast-trending geophysical lineaments that are interpreted to be faults or shear zones. In these sites of intersection, the metasedimentary rocks are hosted by auriferous buck and stockwork quartz veins. Malachite staining indicates the presence of copper sulphides (Nkuna, 2009).

7.3. Bom Kodjelé Trend

The Bom Kodjelé Trend is an approximately 3 km wide thrust zone that trends north–northwest and dips moderately northeast (Figs. 2 and 8a–d). It is dominated by quartz–chlorite–muscovite schist that hosts brecciated and boudinaged buck–quartz–carbonate ± tourmaline veins and iron-rich cataclasites (V1). The dominantly S1 to S1-C foliation has a mean calculated strike and dip of 354°/53°E (Fig. 8b), but the northerly trend of calculated data expresses refolding of S1 and S1-C by F2 folds, and drag folding of S1 and S1-C near the margin of northeast-trending faults. Symmetrical boudins of quartz (vein) generally plunges 48° towards 053°; they are scarred by a strong stretching lineation and slickensides (L1). Displacement on the Bom Kodjelé Trend is thereby dominantly reverse with northeast block up.

The Bom Kodjelé Trend is crosscut by a disjunctive to crenulating S2 foliation that trends northeast, with a mean calculated strike and dip of 061°/79°N (Fig. 8c). It parallels northeast-trending faults that host rare northeast-trending buck quartz veins. The mean calculated dip and dip direction of F2 folds is 20° towards 053° (Fig. 8d).

The Bom Kodjelé Trend hosts gold mineralisation at the Bom Kodjelé artisanal mine, and 6 km east of the town of Falagountou where the Bom Kodjelé Shear Zone coalesces with the KSZC. The artisanal mines are located where northeast-trending geophysical lineaments (that are interpreted to be D2 faults or shear zones) intersect the Bom Kodjelé Trend. In these sites of intersection, the metasedimentary rocks host auriferous buck and stockwork quartz veins that are interpreted to have formed during D2 based on these crosscutting relationships.

7.4. Tassiri Trend

The Tassiri Trend hosts gold mineralisation at the Tassiri artisanal mine and north of the town of Koreziéna where the Tassiri Trend coalesces with the Koreziéna branch of the MSZ. The Tassiri artisanal mine is the site of a 100 × 60 m artisan opencast that is peppered with shafts. These may exceed 10 m in depth. The artisanal mine is hosted in folded, but deeply weathered (kaolinized) metasedimentary rocks of the conglomerate–greywacke–siltstone–shale sequence that are folded about a northwest-trending F1 fold (anticline) axis. The host rocks are also crosscut by sheeted northwest-trending stockwork quartz–carbonate veins with a mean calculated strike and dip of 348°/44°E. The sheeted veins form an open antiform within F1.

The Tassiri artisanal mine is crosscut by a weathered mafic dyke. The dyke is crosscut by S1 that is predominately defined by chlorite; the mean calculated strike and dip of S1 is 342°/46°E.

7.5. Kossa Trend

The northwest-trending Kossa Trend hosts the Kossa, Kossa South and KBF prospects and the Kossa artisanal mine, and is coincident with a northwest-trending geophysical lineament. The prospects are hosted in a corridor of tightly folded metasedimentary rocks in which northwest-trending fold axes (F1) are refolded about northeast-trending fold axis (F2). The Kossa artisanal mine is situated adjacent to a crescent-shaped magnetic high that is interpreted to be a layered pyroxenite–gabbro because of its equal magnetic signature to the Yacouba Mafic Complex.

8. Discussion

8.1. Tectonic history

In this study we have demonstrated that the tectonic history of the OGB records a complex interrelationship between pluton emplacement, structure and gold metallogenesis in which at least two unique regional deformation events took place, i.e., D1 and D2. The meta-volcanic sequence, greywacke–siltstone–shale sequence, sandy dolomite unit, interbedded conglomerate–greywacke–siltstone–shale sequence and greywacke sequence were folded, sheared and/or mylonitized during these events. D1 and D2 were preceded by emplacement of the Dori Batholith, with development of proto-mylonite to schist in the country rock, and migmatite and gneiss at the pluton margin.

Regional metamorphic grade across the OGB is thereby complex. Background metamorphic grade is greenschist facies. Low grade greenschist facies assemblages in the north of the OGB (east of the town of Markoye) grade into greenschist (Tshibubudze et al., 2009; Peters, 2011) or lower amphibolite facies in the south of the OGB (at Sokadie artisanal mine). Metamorphic grade attained amphibolite facies in mylonite or proto-mylonite zones in the Saoga and Afu branches, and attained granulite facies in migmatites in the Dori Batholith (i.e., banded coarse grained assemblage of plagioclase, hornblende and quartz). D1 shear zones generally attained upper greenschist to amphibolite facies with development of a mineral assemblage of quartz–chlorite–muscovite ± chloritoid to biotite–potash feldspar ± hornblende. D2 shear zones generally attained greenschist facies with development of a mineral assemblage of quartz–chlorite–muscovite ± actinolite. In the contact aureole of dykes and sills, metamorphic grade attained hornblende–hornfels facies with development of a mineral assemblage of hornblende–biotite ± cordierite ± sulphides in the proximal contact aureole and epidote–chlorite ± albite ± sulphides in the medial contact aureole. Granulite facies metamorphism accompanied partial melting of metavolcanic and metasedimentary rocks and development of migmatite in the chilled margin of the Dori Batholith.

The relative tectonic history of the OGB is summarized in Fig. 9, as established from crosscutting relationships and published geochronology for the northeast of Burkina Faso:

1. The inferred basement rocks of the OGB include the granite–adamellite and the Tin-Taradat granodiorite–tonalite (the age of the intrusions is the focus of current geochronology studies). The Tin-Taradat granodiorite–tonalite intruded the granite–adamellite and hosts its enclaves (Tshibubudze et al., 2009),

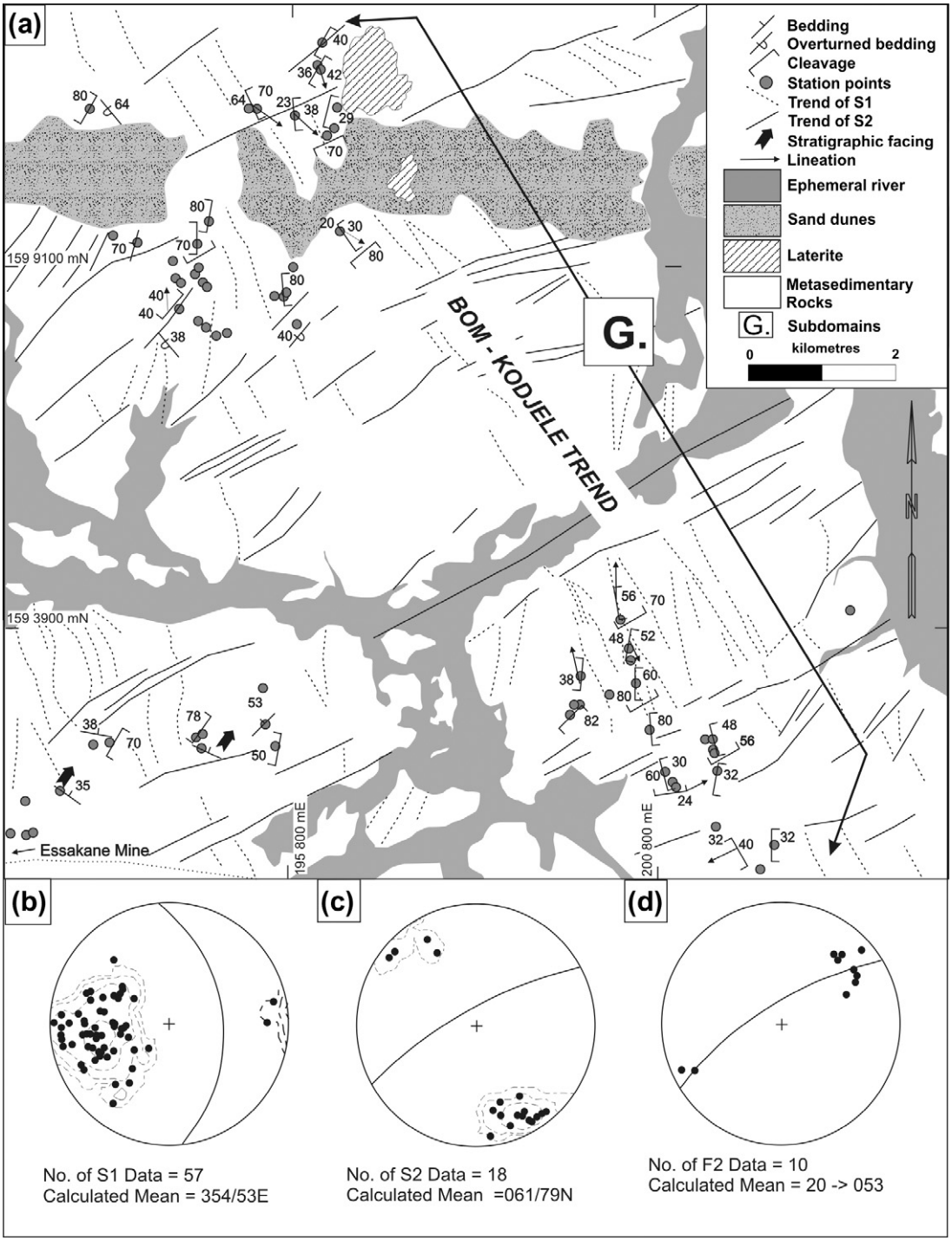

Fig. 8. Schematic map of the Bom Kodjele Trend. It is an approximately 3 km wide thrust zone that trends north–northwest and dips moderately northeast. It is dominated by quartz–chlorite–muscovite schist that hosts brecciated and boudinaged buck–quartz–carbonate ± tourmaline veins and iron-rich cataclasites.

which indicates that the granite–adamellite is the oldest rock unit in the OGB.

2. Mafic volcanic and metasedimentary sequences were deposited above the basement units during basin formation. The units include (1) the meta-volcanic sequence (basaltic hyaloclastite), (2) a greywacke–siltstone–shale sequence, (3) a sandy dolomite unit, (4) a conglomerate–greywacke–siltstone–shale sequence and (5) a greywacke sequence. The supracrustal sequences are herein assigned to the Birimian Supergroup based on correlation with studies by Feybesse et al. (1990), Leube et al. (1990), Hirdes et al. (1996), Milési et al. (1991, 1992), Hein et al. (2004) and Lompo (2009). The environment of deposition has been interpreted as a shallow marine continental shelf or delta-front setting (c.f., Tshibubudze et al., 2009; Peters, 2011).
3. The mafic volcanic and metasedimentary sequences were subsequently intruded by gabbro–diorite–pyroxenite sills/dykes, or gabbro–diorite–pyroxenite sills/dykes were emplaced synchronous to deposition. Béziat et al. (2000) interpreted that

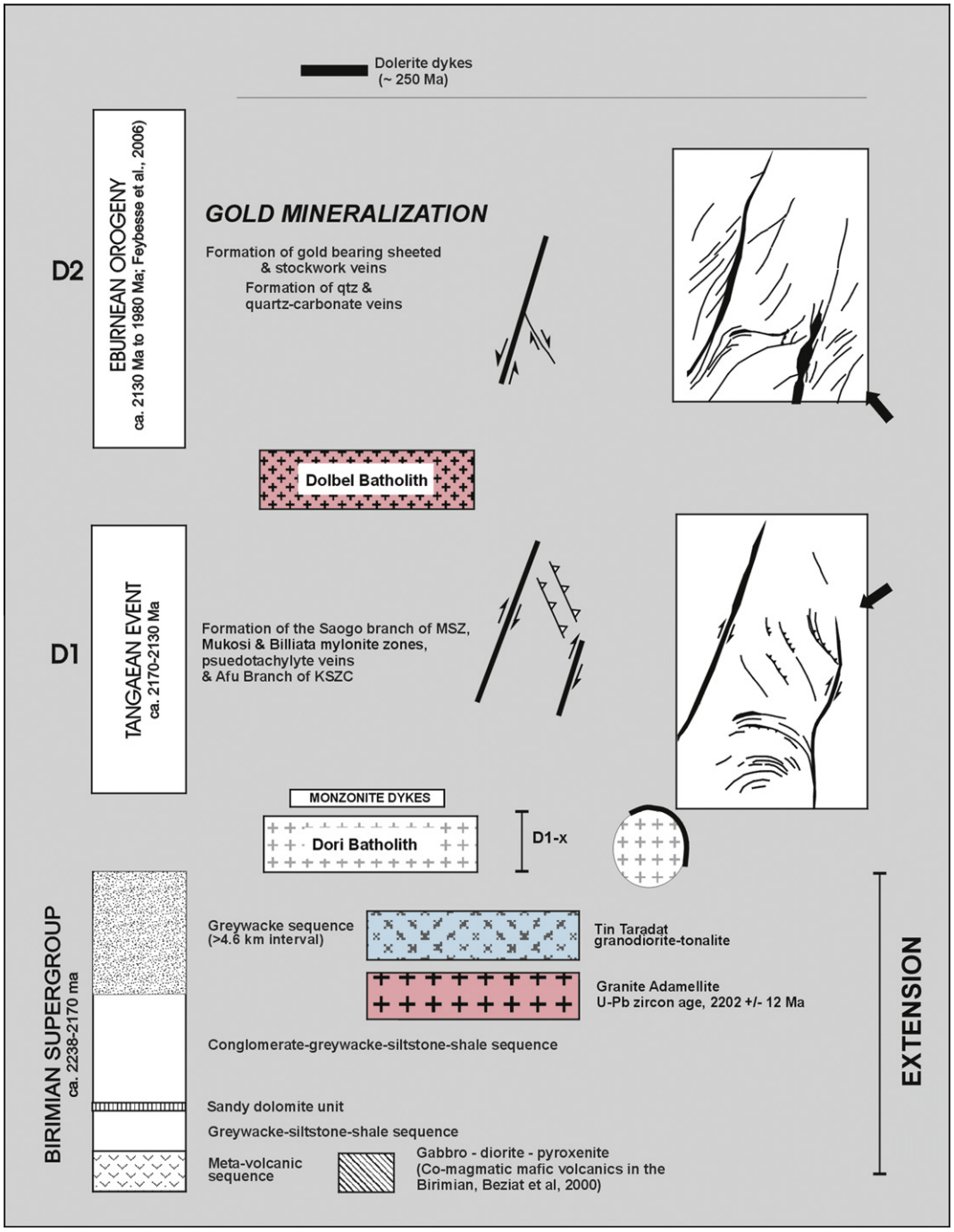

Fig. 9. Schematic evolution of the strato-tectonic relationships in the OGB.

gabbro, diorite and trondhjemite intrusions were syn-tectonic with emplacement of meta-volcanic sequences in the West African Craton and co-magmatic. In concurrence, the gabbro–diorite–pyroxenite sills/dykes in the OGB (including the YMC) are tentatively assigned as co-magmatic with the metavolcanic sequences of the OGB.

4. The supracrustal sequences were subsequently intruded by the Dori Batholith with contact metamorphism of the country rock. Metamorphism to granulite facies accompanied formation of the DMSZ, marginal gneiss, an internal foliation and migmatite in D_{1-x}. The emplacement direction was towards the northeast along the northern margin of the Dori Batholith, as indicated by the stretching lineation (L_{1-x}) that plunges steeply southwest.
5. The supracrustal sequences were intruded by monzonite sills/dykes. They sills/dykes crosscut the granite–adamellite and Tin-Taradat granodiorite–tonalite. They are folded by F1 and crosscut by S1. They were therefore emplacement pre-D1. The relative timing with respect to the Dori Batholith is not known.
6. The supracrustal sequences, gabbro–diorite–pyroxenite sills/dykes, Dori Batholith and monzonite sills/dykes were deformed in D1. D1 is associated with the formation of (a) the Saoga Branch of the MSZ, (b) the Mukosi and Billiata mylonite zones, (c) the Afu Branch of the KSZC, and (d) northwest-trending thrust-folds (F1) that crosscut the OGB and coalesce with the MSZ. The sense of displacement on the Saoga Branch of the MSZ and the Afu Branch of the KSZC in D1 was dextral (reverse)

as manifested by development of S1 to S1-C foliations, macroscopic to mesoscopic asymmetric boudins, *en echelon* pseudotachylite veins, shear bands, sigma clasts, mesoscopic mica fish and a strong stretching lineation (L1) The palaeo-compressive stress direction in D1 is interpreted to be southwest-directed. This event has been defined as the Tangaean Event by Tshibubudze et al. (2009), Tshibubudze and Hein (2010) and Hein (2010) and is tentatively dated at 2170–2130 Ma.

7. The Dolbel Batholith was emplaced post-D1 and crosscuts D1 structures including F1 folds. It is crosscut by D2 buck quartz veins and S2.
8. The second deformation, D2, is associated with the formation of the Korizéna Branch of the MSZ, the Waho Branch of the KSZC, and northeast–trending faults that transect the OGB. D2 is manifested by refolding of F1 by northeast-trending F2, and development of a pervasive northeast-trending cleavage (S2 to S2-C). The sense of displacement along the Korizéna Branch of the MSZ and Waho Branch of the KSZC was sinistral (reverse). D2 was accompanied by dilation of northwest-trending D1 thrust-folds to form (a) auriferous quartz and quartz–carbonate sheeted and stockwork veins, (b) quartz–chlorite ± muscovite shears (sinistral brittle–ductile shear zones), (c) quartz–chlorite–ankerite ± sulphide ± cordierite schist, (d) massive macroscopic sigmoidal buck–quartz–carbonate veins, (e) iron-rich cataclasites, and (f) auriferous buck quartz veins. S1 was folded and/or crenulated. Discontinuous quartz–chlorite (±muscovite) shears, boudins, sigma clasts, shear bands, and a stretching lineation (L2) also formed during D2. The palaeo-compressive stress in D2 is interpreted to be northwest-directed. The event is herein correlated with the deformation during the Eburnean Orogeny of Feybesse et al. (2006) that is dated at 2130–1980 Ma.
9. D2 was succeeded by the intrusion of west-northwest trending dolerite–gabbro dykes that crosscut the granite–adamellite, Tin-Taradat granodiorite–tonalite, supracrustal sequences, the Dori Batholith, and D1 and D2 structures. They are dated at 250 Ma (Hottin and Ouedraogo, 1992).

8.2. Emplacement of the Dori Batholith

The emplacement of the Dori Batholith was accompanied by aureole deformation and the development of proto-mylonite, migmatite, gneiss and schist. The deformation is assigned to D_{1-x} because it is restricted to the margin of the batholith. D_{1-x} is crosscut by D1 and D2 (gold-bearing) structures.

Vidal et al. (2009) and Lompo (2009, 2010) contended that the tectonic evolution of the Eburnean Orogeny was initiated by a "weak-type" vertical tectonic event involving the diapiric ascent of magma and deformation of the country rock synchronous to cooling and crystallisation (Vidal et al., 2009; Lompo, 2010). They proposed a vertical tectonic (diapiric) model for the emplacement of early Eburnean granitoids of the West African Craton that intruded at 2200–2198 Ma during a regional scale northwest–southeast orientated horizontal shortening event (Gueye et al., 2008; Lompo, 2009; de Kock et al., 2011) in the Eburnean Orogeny. Vidal et al. (2009) and Lompo (2009) added that during the ascent of granitoids, the country rocks were transported downwards along the margins of the intrusions, and folded to produce upright narrow synclines (Miller and Paterson, 1999; Vidal et al., 2009; Lompo, 2009). Marginal shear zones formed during horizontal flow of magma at a high angle to the regional-scale horizontal shortening.

The suggestion that an early "weak-type" deformation may have affected the WAC is consistent with crosscutting relationships in the OGB that indicate the Dori Batholith was emplaced early in the tectonic evolution of the belt. However, the manner of emplacement is not *sensu stricto* diapiric in character and the relative timing of emplacement does not correspond with emplacement during the Eburnean Orogeny.

In comparison with diapirism as proposed by Paterson et al. (1991), Paterson and Fowler (1993) and Miller and Paterson (1999), the proto-mylonite and schist along the northern margin of the Dori Batholith dips towards the batholith (not outward) and records a reverse sense of displacement (not normal), with pluton block up (i.e., southwest block up). Displacement on the DMSZ on the northern margin is towards the northeast with development of an east–west trending synform in the Sokadie region (Kerr, 2004), but displacement on the eastern margin of the batholith along KSZC is characteristically strike-slip (whether in the Afu or Waho branches). Thus apparent diapirism may be restricted to a small section of the northern margin.

Alternatively, the structural relationships observed for the DMSZ and the Dori Batholith accords with experimental models for pluton/batholith emplacement that takes place at the onset of compressive regimes (c.f., Montanari et al., 2010). In these models pluton/batholith emplacement is facilitated by development of inward-dipping reverse faults (such as the DMSZ and Sokadie Shear Zone) and fault-related drag folds at the margins of the pluton/batholith (such as the synform in the Sokadie region), and a macroscopic anticline (dome) above the pluton/batholith.

Given this, we interpret that the Dori Batholith was emplaced during onset of a compressive regime that is described by the Tangaean Event of Tshibubudze et al. (2009), Tshibubudze and Hein (2010) and Hein (2010) based on the crosscutting features that indicate that the Dori Batholith was emplaced pre-D1, D1 being the Tangaean Event. Furthermore emplacement of the Dori Batholith probably included wall rock stoping, roof uplift as evidenced from angular wall rock enclaves along the margins between Subdomains A and B, formation of marginal shear zones, and migmatite (c.f., Paterson and Fowler, 1993; Brown, 2001; Montanari et al., 2010).

8.3. Gold metallogenesis

Several styles of gold deposit are now recognised in the West African Craton including gold hosted by disseminated pyrite in tourmalinized stratabound mineralization (Dommanget et al., 1993; Fouillac et al., 1993), in northwest-trending structural jogs in sodically altered shear zones (Quick, 2011), sheeted vein type gold (Béziat et al., 2008), intrusion-related gold (Hein and Matabane, in press), Eocene–Miocene placer gold above a fault (Matsheka and Hein, 2011), and numerous placer deposits.

From the data presented we concur with Foster and Piper (1993), Groves et al. (1998), Feybesse et al. (2006) and Béziat et al. (2008) that gold mineralisation in the OGB formed during deformation associated with the Eburnean Orogeny. Gold mineralisation has a spatial and temporal relationship with both D1 and D2 structures. Gold mineralisation is sited along five northwest-trending metallogenic corridors, and specifically, where northeast-trending faults and shears crosscut northwest-trending thrust-folds. D1 structures where dilated in D2 (during the Eburnean Orogeny) with development of sheeted and stockwork vein systems. The sites of intersection effectively became fluid conduits. The source of gold is interpreted to be the metasedimentary rock sequences. However, the source of fluid is not known and is the subject of on-going ore genesis studies in the OGB. Gold mineralisation in sheeted and stockwork veins preferentially occurs in massive competent rocks units including conglomerate beds, greywacke, quartzite, monzonite dykes, pyroxenite–gabbro sills and D1 buck quartz veins. Gold in fine veinlets may also be hosted in massive shale units. Gold is also hosted in veins in the Tin Taradat granodiorite–diorite and in gold–molybdenite–copper veins in the Dolbel Batholith.

9. Conclusions

An intimate relationship exists between the tectonic development of the OGB and deposition of gold metallogenesis. Mafic volcanic and metasedimentary sequences of the (1) the meta-volcanic sequence (basaltic hyaloclastite), (2) a greywacke–siltstone–shale sequence, (3) a sandy dolomite unit, (4) a conglomerate–greywacke–siltstone–shale sequence, and (5) a greywacke sequence were deformed and metamorphosed during two regional deformation events and emplacement of plutons.

The emplacement of the Dori Batholith in D_{1-x} was accompanied by aureole deformation and the development of proto-mylonite, migmatite, gneiss and schist, with contact metamorphism to granulite facies. The inward-dipping DMSZ and Sokadie Shear Zone (reverse sense of displacement with pluton up), and fault-related drag folds at the margins of the pluton/batholith suggest that the batholith may have been emplaced at the onset of the Tangaean Event.

The magmatic-tectonic event, as manifested by the emplacement of the Dori Batholith (D_{1-x}), was succeeded by deformation during the Tangaean Event (D1) and the Eburnean Orogeny (D2). Metamorphic grade during regional deformation attained lower greenschist to lower amphibolite facies. Second and third-order northwest-trending splay faults and shears of the Tangaean Event matured as sites of gold deposition during the Eburnean Orogeny. The deposits are structurally thereby hosted.

Gold mineralisation is sited along five northwest-trending metallogenic corridors, specifically, where northeast-trending faults and shears crosscut or coalesce with northwest-trending thrust-folds (or geophysical lineaments), or where northwest-trending faults coalesce with north–northeast trending shear zones. D1 structures where dilated in D2 (during the Eburnean Orogeny) with development of sheeted and stockwork vein systems.

Acknowledgements

This research was sponsored by a BHP Billiton scholarship through the University of the Witwatersrand, Johannesburg, the AMIRA WAXI P934 Phase II sponsors, Orezone Resources (Burkina Faso), IAMGOLD Essakane S.A. and Anglogold Ashanti. We acknowledge M. Lompo and S. Naba of the University of Ouagadougou for assisting with transport logistics. We wish to gratefully acknowledge AMIRA International and the industry sponsors, including AusAid and the ARC Linkage Project LP110100667, for their support of the WAXI Project (P934A). We are also appreciative of the contribution of the various Geological Surveys/Department of Mines in West Africa as sponsors in-kind of WAXI. Finally, we wish to recognize our WAXI research colleagues from the various Institutions from around the world.

This manuscript was significantly improved by the careful reviews of K. Saalmann, and two anonymous reviewers.

References

Beauvais, A., Ruffett, G., Hénocque, O., Colin, F., 2008. Chemical and physical erosion rhythms of the West African Cenozoic morphogenesis: the ^{39}Ar–^{40}Ar dating of supergene K–Mn oxides. Journal of Geophysical Research 113, F04007. http://dx.doi.org/10.1029/2008JF000996.

Béziat, D., Bourges, F., Debat, P., Lompo, M., Martin, F., Tollon, F., 2000. A Paleoproterozoic ultramafic–mafic assemblage and associated volcanic rocks of the Boromo greenstone belt: fractionates originating from island-arc volcanic activity in the West African craton. Precambrian Research 101, 25–47.

Béziat, D., Dubois, M., Debat, P., Nikiéma, S., Salvi, S., Tollon, F., 2008. Gold metallogeny in the Birimian craton of Burkina Faso (West Africa). Journal of African Earth Sciences 50, 215–233.

Brown, E.T., Bourlés, D.L., Colin, F., Sanfo, Z., Raisbeck, G.M., Yiou, F., 1994. The development of iron crust lateritic systems in Burkina Faso, West Africa examined with in-situ-produced cosmogenic nuclides. Earth and Planetary Science Letters 124, 19–33.

Brown, M., 2001. Crustal melting and granite magmatism: key issues. Physics and Chemistry of the Earth 26, 201–212.

Burke, K., Gunnell, Y., 2008. The African Erosion Surface: A Continental-Scale Synthesis of Geomorphology, Tectonics, and Environmental Change over the Past 180 million years. Geological Society of America, pp. 34–40. ISBN: 0813712017, 9780813712017.

Castaing, C., Billa, M., Milési, J.P., Thiéblemont, D., Le Mentour, J., Egal, E., Donzeau, M. (BRGM) (coordonnateurs) et Guerrot, C., Cocherie, A., Chevremont, P., Tegyey, M., Itard, Y. (BRGM), Zida, B., Ouedraogo, I., Kote, S., Kabore, B.E., Ouedraogo, C. (BUMIGEB), Ki, J.C., Zunino (ANTEA), 2003. Notice explicative de la Carte géologique et minière du Burkina Faso à 1/1 000 000.

Davis, D.W., Hirdes, W., Schaltegger, U., Nunoo, E.A., 1994. U–Pb age constraints on deposition and provenance of Birimian and gold-bearing Tarkwaian sediments in Ghana, West Africa. Precambrian Research 67, 89–107.

De Kock, G.S., Armstrong, R.A., Siegfried, H.P., Thomas, E., 2011. Geochronology of the Birim Supergroup of the West African craton in the Wa-Bolé region of west-central Ghana: implications for the stratigraphic framework. Journal of African Earth Sciences 59, 1–40.

Dommanget, A., Milési, J.P., Diallo, M., 1993. The Loulo gold and tourmaline-bearing deposit. Mineralium Deposita 28, 253–263.

Feybesse, J.L., Billa, M., Guerrot, C., Duguey, E., Lescuyer, J.L., Milési, J.P., Bouchot, V., 2006. The Palaeoproterozoic Ghanaian province: geodynamic model and ore controls, including regional stress modelling. Precambrian Research 149, 149–196.

Feybesse, J.L., Milési, J.P., Ouedraogo, M.F., Prost, A., 1990. La "ceinture" protérozoïque inférieur de Boromo-Goren (Burkina Faso): un exemple d'interférence entre deux phases transcurrentes éburnéennes. Comptes Rendus de L'Académie des Sciences 310(II), 1353–1360.

Foster, R.P., Piper, D.P., 1993. Archaean lode gold deposits in Africa: crustal setting, metallogenesis and cratonization. Ore Geology Reviews 8, 303–347.

Fouillac, A.M., Dommanget, A., Milési, J.P., 1993. A carbon, oxygen, hydrogen and sulfur isotopic study of the gold mineralization at Loulo, Mali. Chemical Geology 106, 47–62.

Groves, D.I., Goldfarb, R.J., Gebre-Mariam, M., Hagemann, S.G., Rorbert, F., 1998. Orogenic gold deposits: a proposed classification in the context of their crustal distribution and relationship to other gold deposit types. Ore Geology Reviews 13, 7–27.

Gueye, M., Ngom, P.M., Diène, M., Thiam, Y., Siegesmund, S., Wemmer, K., Pawlig, S., 2008. Intrusive rocks and tectono-metamorphic evolution of the Mako Paleoproterozoic belt (Eastern Senegal, West Africa). Journal of African Earth Sciences 50, 88–110.

Hastings, D., 1982. On the tectonics and metallogenesis of West Africa: a model incorporating new geophysical data. Geoexploration 20, 295–327.

Hein, K.A.A., 2010. Succession of structural events in the Goren Greenstone belt (Burkina Faso); implications for West African tectonics. Journal of African Earth Sciences 56, 83–94.

Hein, K.A.A., Matabane, M.R., in press. The gold-bearing intrusion-related deposits of theFE3 opencast gold mines, Sadiola goldfield, Kedougou-Kéniéba Inlier, western Mali. Ore Geology Reviews..

Hein, K.A.A., Morel, V., Kagoné, O., Kiemde, F., Mayes, K., 2004. Birimian lithological succession and structural evolution in the Goren segment of the Boromo-Goren greenstone belt, Burkina Faso. Journal of African Earth Sciences 39, 1–23.

Hirdes, W., Davis, D.W., 2002. U–Pd geochronology of Palaeoproterozoic rocks in the southern part of the Kedougou-Kéniéba Inlier, Senegal, West Africa: evidence for diachronous accretionary development of the Eburnean province. Precambrian Research 118, 83–99.

Hirdes, W., Davis, D.W., Lüdtke, G., Konan, G., 1996. Two generations of Birimian (Paleoproterozoic) volcanic belts in north-eastern Côte d'Ivoire (West Africa): consequences for the 'Birimian Controversy'. Precambrian Research 80, 173–191.

Holcombe, R., 2008. Georient, Version 9. Holcombe Caughlin_Associates, Australia.

Hottin, G., Ouedraogo, O.F., 1992. Carte Géologique du Burkina Faso, second ed.. Bureau de Recherches Géologique et Miniéres, Burkina Faso.

Kerr, D.J., 2004. Technical Note: Sokadie Prospect, Essakan Joint Venture Project, North-eastern Burkina Faso. Unpublished Report to Orezone Resources Incorporated and Goldfields International Limited, Report 007-ES-03, 16p.

Léger, J.M., Liègeois, J.P., Pouclet, A., Vicat, J.P., 1992. Occurrence of syntectonic alkali-pyroxene granites of Eburnean age (2.1 Ga) in Western Niger. In: Abstracts, 14éme Réunion Annuelle des Sciences de la Terre, Toulouse, France. Société Géologique de France, p. 96.

Leube, A., Hirdes, W., Mauer, R., Kesse, G.O., 1990. The early Proterozoic Birimian Supergroup of Ghana and some aspects of its associated gold mineralization. Precambrian Research 46, 139–165.

Lompo, M., 2009. Geodynamic evolution of the 2.25-2.0Ga Palaeoproterozoic magmatic rocks in the Man-Leo Shield of the West African Craton: a model of subsidence of an oceanic plateau. In: Reddy, S.M., Mazumder, R., Evans, D.A.D., Collins, A.S. (Eds.), Palaeoproterozoic Supercontinents and global evolution. Geological Society, Special Publication 323, London, pp. 231–254.

Lompo, M., 2010. Paleoproterozoic structural evolution of the Man-Leo Shield (West Africa). Key structures for vertical to transcurrent tectonics. Journal of African Earth Sciences 58, 19–36.

Matsheka, I.R., Hein, K.A.A., 2011. Character morphology and origin of gold from selected mines in the Yatela and Sadiola goldfields, Mali, West Africa. Poster Presentation to the WAXI Sponsors Meeting, 28th March to 1 April 2011, Ouagadougou, Burkina Faso.

Milési, J.P., Feybesse, J.L., Ledru, P., Dommanget, A., Ouedraogo, M.F., Marcoux, E., Prost, A., Vinchon, Ch., Sylvain, J.P., Johan, V., Tegyey, M., Calvez, J.Y., Lagny, P., 1989. West African gold deposits, in their lower Proterozoic lithostructural setting. Chronique de la Recherché Minière 497, 3–98.

Milési, J.P., Ledru, P., Ankrah, P., Johan, V., Marcoux, E., Vinchon, Ch., 1991. The metallogenic relationship between Birimian and Tarkwaian gold deposits in Ghana. Mineralium Deposita 26, 228–238.

Milési, J.P., Ledru, P., Feybesse, J.L., Dommanget, A., Marcoux, E., 1992. Early Proterozoic ore deposits and tectonics of the Birimian orogenic belt, West Africa. Precambrian Research 58, 305–344.

Miller, R.B., Paterson, S.R., 1999. In defense of magmatic diapirs. Journal of Structural Geology 21, 1161–1173.

Montanari, D., Corti, G., Sani, F., Del Ventisette, C., Bonini, M., Moratti, G., 2010. Experimental investigation on granite emplacement during shortening. Tectonophysics 484, 147–155.

Naba, S., Lompo, M., Debat, P., Bouchez, J.L., Béziat, D., 2004. Structure and emplacement model for late-orogenic Palaeoproterozoic granitoids: the Tenkodogo-Yamba elongate pluton (Eastern Burkina Faso). Journal of African Earth Sciences 38, 41–57.

Nikiéma, S.J., 1992. Contexte structural et implications métallogénies au sein du permis ''Essakan'', dans le sillon de Dori: Géométrie des corps aurifères. Unpublished PhD Thèses. Université of Dakar, 38p.

Nkuna, B., 2009. Ore genesis of the Essakane, Falagountou and Sokadie Au Deposits: Oudalan-Gorouol Greenstone Belt (OGGB), Burkina Faso, West African Craton (WAC). Unpublished Honours Thesis, University of the Witwatersrand, Johannesburg, 60p.

Paterson, S.R., Fowler Jr, T.K., 1993. Re-examining pluton emplacement processes. Journal of Structural Geology 15, 191–206.

Paterson, S.R., Vernon, R.H., Fowler Jr., T.K., 1991. Aureole tectonics. In: Kerrick, D.M. (Ed.), Contact Metamorphism. Mineralogical Society of America Reviews in Mineralogy 26, pp. 673–722.

Pawlig, S., Gueye, M., Klischies, R., Schwarz, S., Wemmer, K., Siegesmund, S., 2006. Geochemical and Sr–Nd isotopic data on the Birimian of the Kedougou-Kenieba Inlier (Eastern Senegal): implications on the Palaeoproterozoic evolution of the West African Craton. South African Journal of Geology 109, 411–427.

Peters, L., 2011. The Geology of East Markoye, Northeast Burkina Faso. Unpublished Honours Thesis, University of the Witwatersrand, Johannesburg, 62p.

Pigois, J.P., Groves, D.I., Fletcher, I.R., McNaughton, N.J., Snee, L.W., 2003. Age constraints on Tarkwaian paleoplacer and lode-gold formation in the Tarkwa–Damang district, SW Ghana. Mineralium Deposita 38, 695–714.

Pons, J., Barley, P., Dupuis, D., Léger, J.M., 1995. Mechanisms of pluton emplacement and structural evolution of a 2.1 Ga juvenile continental crust: the Birimian of south western Niger. Precambrian Research 70, 281–301.

Quick, R., 2011. Gounkoto – a new multi-million ounce gold discovery in the Loulo district of Mali West Africa. Presentation and Abstract to the Geological Society of South Africa Gold Day, 13 April 2011.

Thiéblemont, D., Delor, C., Cocherie, A., Lafon, J.M., Goujou, J.C., Baldé, A., Bah, M., Sané, H., Fanning, C.M., 2001. A 3.5 Ga granite–gneiss basement in Guinea: further evidence for early Archaean accretion within the West African Craton. Precambrian Research 108, 179–194.

Tshibubudze, A., 2007. Relative Timing of Structural Events: The Markoye Fault and its Association to Gold Mineralization. Unpublished Honours Thesis, University of the Witwatersrand, Johannesburg, 78p.

Tshibubudze, A., Hein, K.A.A., 2010. Tectonic evolution of the Oudalan-Gorouol greenstone belt in northeast Burkina Faso and Niger, West African craton. Geophysical Research Abstracts 12, EGU2010-708 (2010 EGU General Assembly 2010, ISSN of eISSN: 1607–7962).

Tshibubudze, A., Hein, K.A.A., Marquis, P., 2009. The Markoye Shear Zone in northeast Burkina Faso. Journal of African Earth Sciences 55, 245–256.

Vidal, M., Gumiaux, C., Cagnard, F., Pouchet, A., Ouattara, G., Pichon, M., 2009. Evolution of a Paleoproterozoic 'weak type' orogeny in the West African Craton. Tectonophysics 477, 145–159.

Woolfe, A., 2011. Stratigraphy and Metamorphic Facies in the Kel Engief Metamorphic Belt Near Gorom Gorom, NE Burkina Faso. Unpublished Honours Thesis, University of the Witwatersrand, Johannesburg.

Zhao, G., Cawood, P.A., Wilde, S.A., Sun, M., 2002. Review of global 2.1–1.8 Ga orogens: implications for a pre-Rodinia supercontinent. Earth-Science Reviews 59, 125–162.

APPENDIX C

Tshibubudze, A., Hein, K.A.A., Pratas, M., Rogers, J., submitted. Gold mineralization in the Essakane goldfield, Burkina Faso. In (Markwitz, V, Hein, K.A.A., Robb, L. (Editors), Minerals Atlas Monograph of West Africa. Published by the Geological Society of South Africa.

*Tshibubudze, A., Hein, K.A.A., Pratas, M., Rogers, J., in prep. Gold mineralization in the Essakane goldfield, Burkina Faso. In (Markwitz, V, Hein, K.A.A., Robb, L. (Editors), Minerals Atlas Monograph of West Africa. Published by the Geological Society of South Africa, pp ***.*

Gold mineralisation in the Essakane goldfield, Burkina Faso

Asinne TSHIBUBUDZE, Kim A.A. HEIN
School of Geosciences; University of the Witwatersrand, Johannesburg, South Africa
Mario PRATAS
IAMGold Essakane
Jamie ROGERS
IAMGOLD

Deposit name	Essakane
Commodity of exploitation	Au
Location	Small overview figure in black/white: craton and country scale map, including other deposits in the vicinity (task for Vanessa)
Longitude Latitude	0.0753 14.384
Geographic location	NE-Burkina Faso; Dori region; Boundary of Oudalan and Seno provinces; approx. 330 km NE of Ouagadougou
Geological location	West African craton; Leo-Man Shield; Baoulé-Mossi domain; Oudalan-Gorouol greenstone belt
Deposit status	Mine since 2010
Deposit type	Orogenic; quartz-carbonate stockwork veins
Current owner	90% IAMGOLD Corporation (since 2009); 10% Government of Burkina Faso
Average grade Tonnage	Essakane gold mine (2012): proven and probable reserves 102.9 Mt @ 1.0 g/t for 3.29 million contained ounces, measured and indicated resources of 139.7 Mt @ 0.9 g/t for 4.15 million ounces attributable contained ounces.
Past production	Artisanal mining only; Essakane began production in 2010.

1. Exploration history

The Essakane goldfield is situated in the Oudalan-Gorouol volcano-sedimentary belt (OGB) in the northeast of Burkina Faso, 320km northeast of the City of Ouagadougou (Fig. 1). It hosts numerous gold deposits and workings including those at Essakane, Gosséy, Falagountou, Sokadie, Tin Zoubratan and Takabangou (Fig. 2).

Mining activities in the Essakane goldfield in Burkina Faso have been traced to the early 1960s, where mining was carried out by artisanal miners who, according to Gleeson and Poulin (1989) used quartz vein debris as indicators of gold prospectivity. Formalised small scale mining at Essakane was conducted by Compagnie d'Exploitation des Mines d'Or du Burkina (CEMOB), which was owned by the government of Burkina Faso. However modern artisanal gold mining began around 1980 (Jaques et al., 2006; Luning, 2008; Werthmann, 2009). The principal operations conducted by CEMOB were the treatment of the mine tailings that were collected from artisans working for gold.

In 1996, CIMC (Coronation International Mining Corporation) secured title and acquired 6 more exploration licences. In 2000 Ranger Minerals conducted. Gold Fields joined the JV in 2002 with Orezone Resources and completed pre-feasibility study in 2006

BHP, Coronation International Mining Corporation and Ranger Minerals NL undertook further exploration; several phases of drilling by Ranger Minerlas NL led to a JV of Orezone Resources and CIMC, but in 2003 the permits were transferred to the Joint Venture partners of Gold Fields Mining International (Pty) Ltd and Orezone Resources Inc.

Orezone Resources Inc acquired the full rights over the Essakane permits, and after intensive mapping, trenching, diamond, and reverse circulation drilling programs reported approximately 4 million ounces of Measured and Indicated Resources and 1.3 million ounces of Inferred Resource using a 0.5 g/tonne cut-off grade (Gignac et al., 2009).

During 2008 the Essakane deposit and permits were sold to IAMGOLD Corporation who is now the operator and owner. IAMGOLD has development the Essakane mine site with construction of treatment plant and crushers, and an opencast mine on the site of the Essakane deposit (Fig. 3), with an approximately 5 million ounces of Measured and Indicated Resource calculated at 1.1 g/t gold reported on the 31 December 2011 (IAMGOLD Corporation, 2012).

2. Regional geological overview

The Essakane goldfield includes all gold deposits and workings in the OGB (Fig. 2). The geology, structure and metallogenesis of the OGB has been studied by Jeambrun et al. (1970), Nikiéma (1992), Pons et al. (1995), Rogers and Dong (2000), Rogers (2001), Delisle (2003), Kerr (2004a-e) and Tshibubudze et al. (2009; 2013) and Tshibubudze and Hein (2013). Studies by Rogers (2001), Rogers and Dong (2000), Delisle (2003) and Kerr (2004a-e) are limited to the gold deposits and their immediate host rocks, or selective petrographic work of samples collected from these deposits (cf. Taner, 2004).

The OGB comprises an intercalated sequence of mafic-intermediate hyaloclastite basalt, greywacke, siltstone, shale and minor carbonate, and these are overlain conformably by a 4.6km thick succession of chert-greywacke-gritstone unit. The lithologies were sheared, folded and mylonitized in at least two unique deformation events (D1 and D2), defined as the Tangaean Event (2170–2130 Ma, c.f. Tshibubudze et al., 2009; Hein, 2010) and the Eburnean Orogeny (ca. 2130-1980 Ma ca. Feybesse et al., 2006). The OGB was intruded by a number of granodiorite-tonalite batholiths. The Dori batholith crops out in the south of the OGB and intrudes volcano-sedimentary rocks on its northern margin, while the Tin Taradat granodiorite intrudes the northern portion of the OGB. The Dolbel Batholith of Pons et al. (1995) crops out in the northeast of the goldfield. Gabbro-dolerite dykes cross-cut the stratigraphy throughout the OGB and are characterised by a medium to coarse-grained mineral assemblage that consists of plagioclase, clinopyroxene and hornblende. They are cross-cut by northeast trending regional cleavage. Monzonite dykes crosscut the supracrustal rocks in the Essakane gold mine and across the central north of the OGB.

3. Host rocks

The host rocks to the gold deposits in the Essakane goldfield consist of folded, sheared and/or mylonitized volcanic, volcano-sedimentary and sedimentary sequences that were metamorphosed to upper greenschist facies and locally, to amphibolite facies. They were contact metamorphosed to hornblende-hornfels facies adjacent to TTG suite granitoids, gabbro-pyroxenite and monzonite dykes and sills which intrude them.

The stratigraphy of the OGB includes (1) a basal meta-volcanic sequence, (2) a greywacke-siltstone-shale sequence interbedded with rare chert beds and banded iron formation, (3) a thin sandy dolomite unit, (4) a sequence of interbedded conglomerate-greywacke-siltstone-shale units, and (5) a greywacke sequence intercalated with a polymictic conglomerate marker bed locally termed the Dembam Member (Peters, 2011; Tshibubudze and Hein, 2013; Tshibubudze et al., 2013). Based on stratigraphic studies east of the township of Markoye by Peters (2011), the greywacke sequence exceeds 4.2 kilometres in true stratigraphic thickness.

Laterite is randomly distributed throughout the OGB. In-situ laterite was deposited during the Cretaceous-Tertiary (c.f., Brown et al., 1994; Burke and Gunnell, 2008) and was deeply eroded during the Eocene to Miocene epochs (Brown et al., 1994; Beauvais et al., 2008) to form several discrete transported laterite profiles.

4. Timing of mineralization

The Dori Batholith, Tin Taradat granodiorite (U-Pb zircon) and monazite porphyry dykes and sills have been dated at 2164 ± 24 Ma, 2146 ± 9.3 Ma, 2141 ± 19 Ma by U-Pb zircon geochronology (Tshibubudze, 2014). The monzonite porphyry dykes and sills, and the Tin-Taradat pluton, constrain the maximum age of gold mineralization in the study area, because they are crosscut by auriferous quartz-carbonate veins at the Essakane and Tin Taradat artisanal mines. Thus the metallogenic model for the OGB and GGGT accords with Foster and Piper (1993), Groves et al. (1998), Feybesse et al. (2006) and Béziat et al. (2008) in that gold mineralisation is syn-deformational in the Essakane goldfield and formed during the Eburnean Orogeny (D2) at. 2130-1980 Ma, i.e., the Essakane goldfield hosts deposits that orogenic gold in style, but with the proviso that structural preparation was necessary in D1 to facilitate metallogenesis in D2.

5. Metamorphic grade

The regional metamorphic grade attained greenschist facies as defined by a chlorite-epidote-actinolite mineral assemblage. At Essakane, the metamorphic grades vary; D1 shear zones generally attained upper greenschist to amphibolite facies with development of a mineral assemblage of quartz–chlorite–muscovite, biotite–potassium feldspar and subordinate hornblende. D2 shear zones attained greenschist facies with the mineral assemblage of quartz–chlorite–muscovite ± actinolite. In the contact aureole of dykes and sills, metamorphism attained hornblende–hornfels facies with development of hornblende–biotite with lesser amounts of cordierite and sulphides in the proximal contact aureole, and epidote–chlorite and subordinate albite and sulphides in the medial contact aureole.

6. Alteration features

The alteration assemblage includes sericite-carbonate-silica ± albite ± arsenopyrite ± pyrite, where arsenopyrite and pyrite occur adjacent to and within quartz veins. A 1-3m lateritic alteration zone is developed at surface, underlain by a 30 to 50 m thick upper saprolite zone and a 10 to 30 m thick lower saprolite zone. Competent rock occurs beneath the lower saprolite zone.

7. Mineralization

Ore mineralogy / Accessory minerals

Gold associated with quartz-carbonate stockwork veins is confined to the lower stratigraphic succession of meta-sedimentary rocks and occurs with pyrite, arsenopyrite and traces of pyrrhotite, galena and hematite (i.e., Au-Fe-As-Pb). Gangue minerals present are quartz-carbonate-chlorite-(muscovite). Free gold occurs within veins (Figs. 4, 5) and as intergrowths in arsenopyrite.

Ore body characteristics

The ore body has a strike length of 2500m and is characterised by narrow quartz-veins ranging in thickness from 1 to 30cm. Stockwork veinlets cross-cut planar vein sets and are discordant with respect to strata. The deposit is characterised by an upright asymmetric anticline that opens to the north. Gold mineralization follows the fold plunge and has been confirmed at depth to 270m.

8. Geometric and kinematic controls

Gold mineralisation in the study area has a spatial and temporal relationship with both D1 and D2 structures. Gold mineralization in the OGB is located in Essakane North, Essakane Main Zone (Mine area), Essakane South, Gossey, Korizena, Bom Kodjele, Bom Kodjele East, Kossa and Kossa South, KBF, Fantio, Fatatako, Tin Zoubratan, Tin Taradat, Takabougou, Tassiri, Falagountou, Gaigou, and Sokadie artisanal mine sites (Fig. 2). Gold mineralisation is sited along 5 northwest trending metallogenic corridors, and specifically, where northeast-trending faults and shears crosscut northwest trending thrust-folds. Northwest-trending D1 thrust-folds where dilated in D2 to form gold-bearing quartz-sulphide veins. These include quartz-sulphide and quartz-sulphide-carbonate sheeted and stockwork veins, iron-rich cataclasites, and gold-bearing buck quartz (in north-northeast trending D2 shears. Artisanal mine workings are located in areas where these gold-bearing quartz-sulphide veins proliferate and particularly where NW trending D1 structures are disjunctively crosscut by NE trending D2 shears.

Additionally, gold mineralisation is hosted in massive competent rocks units including conglomerate, greywacke, quartzite, monzonite dykes, pyroxenite-gabbro sills and D1 buck quartz veins. Gold in fine veinlets is hosted in massive shale units. Gold is also hosted in veins in the Tin Taradat granodiorite, monzodiorite porphyry dykes and sills, and in gold-molybdenite-copper veins in the Dolbel Batholith.

Acknowledgements

This research was sponsored by a BHP Billiton scholarship through the University of the Witwatersrand, Johannesburg, the AMIRA WAXI P934 Phase II sponsors, Orezone Resources (Burkina Faso), IAMGOLD Essakane S.A. and Anglogold Ashanti. We acknowledge M. Lompo and S. Naba of the University of Ouagadougou for assisting with transport logistics. We wish to gratefully acknowledge AMIRA International and the industry sponsors, including AusAid and the ARC Linkage Project LP110100667, for their support of the WAXI Project (P934A). We are also appreciative of the contribution of the various Geological Surveys/Department of Mines in West Africa as sponsors in-kind of WAXI. Finally, we wish to recognize our WAXI research colleagues from the various Institutions from around the world.

References

Anon., 2008. Essakane Project, Geologycal Context of EMZ deposit. Powerpoint Presentation to OreZone, 25-27 Octobre 2008.

Béziat, D., Dubois, M., Debat, P., Nikiéma, S., Salvi, S., Tollon, F., 2008. Gold metallogeny in the Birimian craton of Burkina Faso (West Africa). Journal of African Earth Sciences 50, 215-233.

Delisle, P.C., 2003. Structural analysis of the Essakane deposit, Burkina Faso, West Africa. Unpublished Report, 3p.

Feybesse, J.L., Milési, J.P., Ouedraogo, M.F., Prost, A., 1990. La “ceinture” protérozoïque inférieur de Boromo-Goren (Burkina Faso): un exemple d’interférence entre deux phases transcurrentes éburnéennes. Comptes Rendus de L’Académie des Sciences 310, II, 1353-1360.

Foster, R.P., Piper, D.P., 1993. Archaean lode gold deposits in Africa: crustal setting, metallogenesis and cratonization. Ore Geology Reviews 8, 303-347.

Gignac, L., Glacken, I.M., Hawxby, J., Gignac, L.P., Bedell, P., 2009. IAMGOLD Corporation: updated feasibility study-Essakane gold project, Burkina Faso. Unpublished technical report to IAMGOLD Corporation, March 3rd_Essakane_43-101_Final, 193p.

Gleeson, C.F., Poulin, R. 1989. Gold exploration in Niger using soils and termitaria. Journal of Geochemical Exploration 31, 253-283.

Groves, D.I., Goldfarb, R.J., Gebre-Mariam, M., Hagemann, S.G., Rorbert, F., 1998. Orogenic gold deposits: A proposed classification in the context of their crustal distribution and relationship to other gold deposit types. Ore Geology Reviews 13, 7-27.

IAMGOLD Corporation, 2012. Essakane Gold Mine, Burkina Faso. (WWW), http://www.iamgold.com/English/Operations/Operating-Mines/Essakane/default.aspx. (07 March 2013).

Jaques E., Zida, B., Billa, M., Greffié, C., Thomassin, J.F., 2006. Artisanal and Small-Scale Gold Mines in Burkina Faso: Today and Tomorrow, *in* G.M. Hilson (Editor), *Small-Scale Mining,*

Rural Subsistence and Poverty in West Africa, Rugby, UK: Practical Action Publishing, pp. 115-134.

Jeambrun, M., Delfour, J., Gravost, M., 1970. Carte géologique de L'Oudalan. Bureau De Recherches Geologiques et Minières, Burkina Faso.

Kerr, D.J., 2004a. Geology and Exploration potential of the Falagountou Gold Deposit, Essakan Joint Venture project, North-eastern Burkina Faso. Unpublished Report to Orezone Resources Inc and Goldfields International Ltd, Report 007-ES-01, 17p.

Kerr, D.J., 2004b. Technical Note: Preliminary vein study of the Essakan Main Deposit, Essakan Joint Venture project, North-eastern Burkina Faso. Unpublished Report to Orezone Resources Inc and Goldfields International Ltd, Report 007-ES-02, 11p.

Kerr, D.J., 2004c. Technical Note: Sokadie Prospect, Essakan Joint Venture project, North-eastern Burkina Faso. Unpublished Report to Orezone Resources Inc and Goldfields International Ltd, Report 007-ES-03, 16p.

Kerr, D.J., 2004d. Technical Note: Tassiri Prospect, Essakan Joint Venture project, North-eastern Burkina Faso. Unpublished Report to Orezone Resources Inc and Goldfields International Ltd, Report 007-ES-04, 20p.

Kerr, D.J., 2004e. Technical Note: Preliminary vein study of the Essakan Main Deposit, Essakan Joint Venture project, North-eastern Burkina Faso. Unpublished Report to Orezone Resources Incorporated and Gold Fields International Limited, Report 007-ES-02, 11p.

Luning, S., 2008. Liberalisation of the gold mining sector in Burkina Faso. Review of African Political Economy 117, 387-401.

Nikiéma, S.J., 1992. Contexte structural et implications métallogénies au sein du permis "Essakan", dans le sillon de Dori: Géométrie des corps aurifères. Unpublished PhD Thesis, Université of Dakar, 38p.

Peters, L., 2011. Geology of the eastern Markoye region, Oudalan-Gorouol greenstone belt, NE Burkina Faso. University of the Witwatersrand, Johannesburg, p 61.

Pons, J., Barley, P., Dupuis, D., Léger, J.M., 1995. Mechanisms of pluton emplacement and structural evolution of a 2.1 G.a juvenile continental crust: the Birimian of south western Niger. Precambrian Research 70, 281-301.

Rogers, J., 2001. Technical Report, Essakan Project Regional Mapping. Unpublished Report to Ranger Minerals NL, 24p.

Rogers, J., Dong, F., 2000. Technical Report-Essakane Prospect, Burkina Faso, Company report (unpublished). ABOSSO Goldfields Limited, Accra, Ghana, 14p.

Taner, M. F., 2004. Report on the petrographic and mineralogical study of one mineralized sample from the Essakan gold deposit area, Burkina Faso, of the Orezone Resources Inc. Unpublished Report, 21p.

Tshibubudze, A., Hein, K.A.A., 2013. Structural setting of gold deposits in the Oudalan-Gorouol volcano-sedimentary belt east of the Markoye Shear Zone, West African craton. Journal of African Earth Sciences 80, 31–47.

Tshibubudze, A., Hein, K.A.A., Marquis, P. 2009. The Markoye Shear Zone in northeast Burkina Faso. Journal of African Earth Sciences 55, 245-256.

Tshibubudze, A., Hein, K.A.A., Peters, L.F.H., Woolfe, A.J., McCauig, T.C., 2013. Oldest U-Pb crystallization age for the West African craton from the Oudalan-Gorouol belt of Burkina Faso. South African Journal of Geology 116, 169-181.

Tshibubudze, A., submitted. The regional geology and structural setting of gold deposits in the Oudalan-Gorouol volcano-sedimentary Belt (OGB), Burkina Faso and Niger, West Africa. PhD thesis, University of the Witwatersrand Johannesburg, 270 p.

Werthmann, K., 2009. Working in a boom-town: Female perspective on gold mining in Burkina Faso. Resource Policy 34, 18-23.

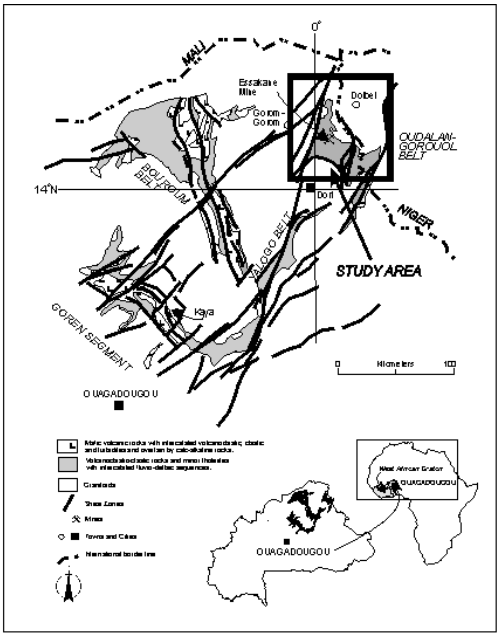

Fig. 1: *Location of the Essakane goldfield in the northeast of Burkina Faso in the Oudalan-Gorouol greenstone belt.*

Fig. 4: *1.217 Kg nugget of gold-quartz from 18m depth in the Essakane ore deposit (Anon, 2008).*

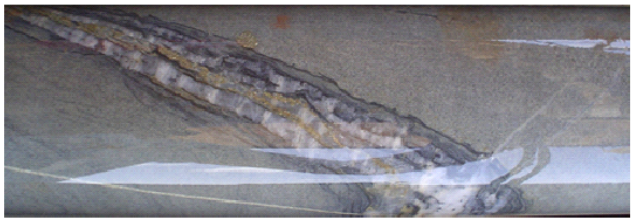

Fig. 5: *Gold in sheeted veins as intersected in the Essakane mine in borehole EDD0051 at 85 m depth (Anon, 2008).*

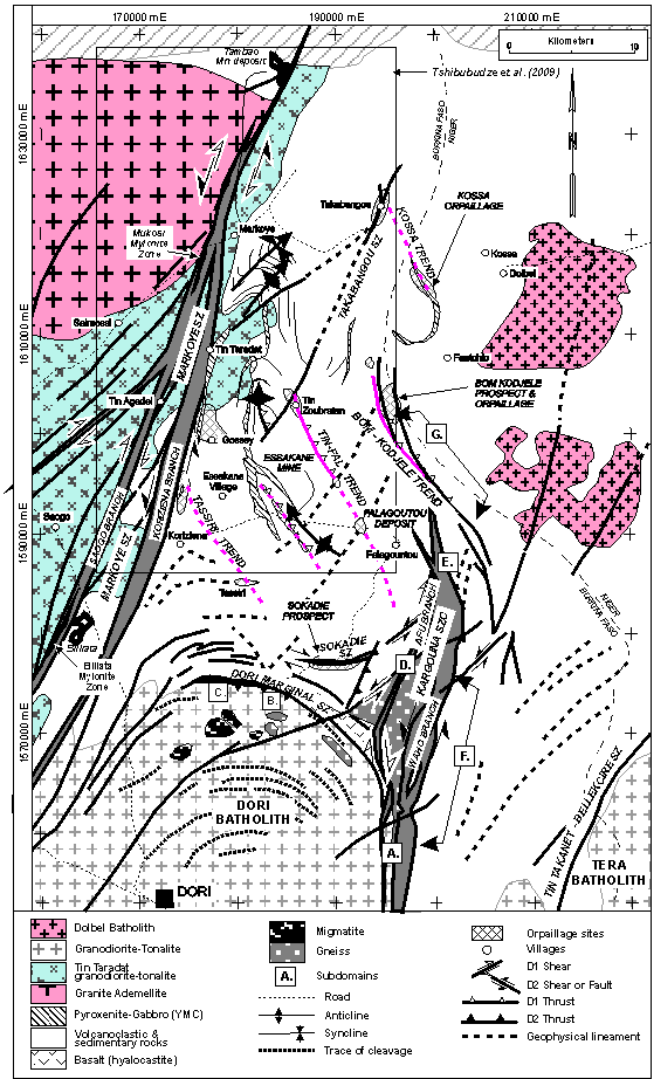

Fig. 2: *Location of gold deposits in the Essakane goldfield (after Tshibubudze and Hein, 2013). Gold mineralisation is sited along 5 northwest trending metallogenic corridors, and specifically, where northeast-trending faults and shears crosscut northwest trending thrust-folds.*

Fig. 3: *The Essakane mine site as seen from GoogleEarth with treatment plant and crushers, and an opencast mine on the site of the Essakane deposit.*

APPENDIX D

Tshibubudze, A., Hein, K.A.A., Peters L. F.H., Woolfe, A., McCuaig, T.C, 2013. Oldest U-Pb crystallisation ages from the Oudalan-Gorouol belt of Burkina Faso. South African Journal of Geology 116, 69-80. doi:10.2113/gssajg.116.1.169.

OLDEST U-PB CRYSTALLISATION AGE FOR THE WEST AFRICAN CRATON FROM THE OUDALAN-GOROUOL BELT OF BURKINA FASO

A. TSHIBUBUDZE
School of Geosciences; University of the Witwatersrand Johannesburg, South Africa
e-mail: asinne.tshibubudze@wits.ac.za

K.A.A. HEIN
Corresponding Author, School of Geosciences; University of the Witwatersrand Johannesburg, South Africa
e-mail: kim.ncube-hein@wits.ac.za

L.F.H. PETERS
School of Geosciences; University of the Witwatersrand Johannesburg, South Africa
e-mail: luke.peters@students.wits.ac.za

A.J. WOOLFE
P O Box 883, Bromhof, 2154, South Africa
e-mail: alex.woolfe@live.co.za

T.C. McCUAIG
Centre for Exploration Targeting (M006), School of Earth and Environment, The University of Western Australia, 35 Stirling Highway, Crawley, 6009, Western Australia
e-mail: campbell.mccuaig@uwa.edu.au

ABSTRACT

U-Pb geochronological data from the northern and western extensions of the Oudalan-Gorouol volcano-sedimentary belt (OGB) on 3 samples of granodiorite gneiss (sample BF_1144), migmatitic gneiss (sample BF_1299), and granite clast from a metaconglomerate (sample BF_1147) gave the oldest U-Pb crystallisation ages for outcropping Palaeoproterozoic rocks yet identified in the West African Craton (WAC).

The U-Pb concordant crystallisation ages of 2253 ± 9 Ma and 2253 ± 15 Ma for samples BF_1144 and BF_1299, respectively, likely represent the age of crystallisation of parent granodiorite gneiss and may constrain the age of a gneissic protolith on which the OGB basin was deposited, or an early group of granitoids that was emplaced in the hinterland during formation of the OGB basin.

A concordant age of 2255 ± 26 Ma for sample BF_1147 is interpreted as the age of crystallisation of a granite pluton that was eroded from a site nearby before becoming part of the Dembam Member, and constrains the maximum age of the Birimian Supergroup in the OGB.

The older Pb-Pb ages on zircons from the granodiorite gneiss, migmatitic gneiss and granite clast are in the range ~2.34 to ~2.27 Ga, and are interpreted as inherited from pre-existing zircon cores. They are similar to Pb-Pb ages reported as inherited zircon ages from the Dabakala tonalitic gneiss (in Cote d'Ivoire).

Introduction

In most geochronological studies undertaken on rocks from the West African Craton (WAC), the oldest U-Pb and Pb-Pb ages are reported as inherited zircon ages. They include reports by: (1) Gasquet et al. (2003) from the Dabakala tonalite (Côte d'lvoire) at 2312 ± 17 Ma, (2) Thomas et al. (2009) from the Gondo granite gneiss in Ghana at 2876 Ma, (3) Siegfried et al. (2009) from the Ifantayire granite gneiss in Ghana at between ~2.39 and ~2.26 Ga, and (4) De Kock et al. (2009) from the Bomburi granodiorite in Ghana at ~2.23 Ga. The oldest U-Pb crystallisation ages reported include: (1) in Burkina Faso from a rhyolitic tuff in the Goren greenstone belt at 2238 ± 5 Ma (Castaing et al., 2003) and; (2) in Ghana from a gabbro unit in the Sefwi belt at 2222 ± 32 Ma (K-Ar age) (Feybesse et al., 2006).

The Oudalan-Gorouol volcano-sedimentary belt (OGB) in the northeast of Burkina Faso in the West African Craton (WAC) (Figure 1) hosts metamorphosed volcanic and sedimentary sequences of the Birimian Supergroup that were folded and deformed concomitant to emplacement of tonalite-trondhjemite-granodiorite (TTG) suite granitoids (Tshibubudze and Hein, 2013). Studies by Tshibubudze et al. (2009), Tshibubudze and

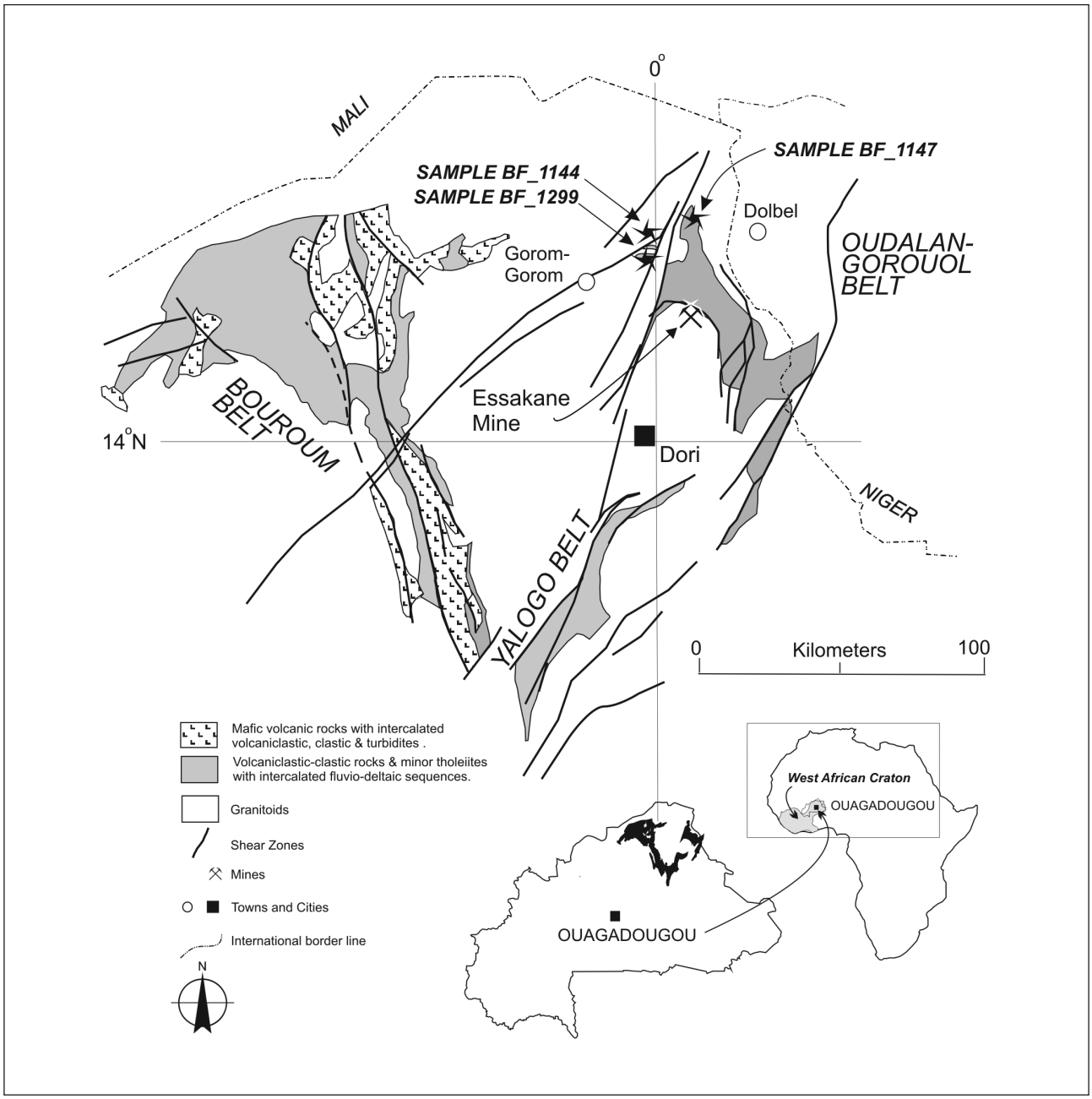

Figure 1. *Location map of the Oudalan-Gorouol volcano-sedimentary belt with sample location for the analysed samples BF_1114, BF_1299 and BF_1147.*

Hein (2010; 2013), Peters (2011) and Woolfe (2011) in the OGB have constrained the relative chronology of key units in the region, and along the Markoye Shear Zone and western footwall to the shear zone but because the OGB is significantly covered by sand dunes of the southern Sahara Desert, the spatial relationships between key units is sometimes obscure, requiring that field studies be supported by absolute geochronological data.

In this study, we report the oldest zircon U-Pb crystallisation ages yet measured in the WAC on three unique samples of rock from the Oudalan province of Burkina Faso (Figure 1). The geochronology and the geology suggests that basement to the Birimian Supergroup may possibly be found in the northeast of Burkina Faso, or alternatively, that a >2200 Ma syn-Birimian granite-granodiorite suite can be found in that region, the 2200 Ma age being regarded as the 1st magmatic event in the WAC as published by Pawlig et al. (2006), Gueye et al. (2007; 2008), Lompo (2009, 2010) and Vidal et al. (2009).

Geological setting

The meta-sedimentary and metavolcanic sequences of the Birimian Supergroup of the WAC were deposited sometime between ~2.24 and ~2.17 Ga. These sequences are dated (using Pb-Pb and U-Pb zircon) at between 2238 ± 5 Ma (Sample MD1264) from a rhyolitic

tuff in the Goren greenstone belt in central Burkina Faso, and 2171 ± 7 Ma for rhyolite (Sample MD0207) from the Hounde greenstone belt in southwest Burkina Faso (Castaing et al., 2003). The sequences were intruded by TTG suite granitoids during three discrete magmatic events at ~2.2, ~2.16 to ~2.13 and ~2.1 to ~2.07 Ga (Pawlig et al., 2006; Gueye et al., 2008; Vidal et al., 2009; Lompo, 2009; 2010). Emplacement was concomitant to greenstone belt deformation (c.f., Hirdes and Davis, 2002; Pawlig et al., 2006; Gueye et al., 2007; 2008; Lompo, 2009; 2010) during; (1) the Tangaean Event sometime between ~2.17 and ~2.13 Ga (Tshibubudze et al., 2009; Hein, 2010), or ~2.16 and 2.12 Ga (Baratoux et al., 2011; Metelka et al., 2011); (2) the polycyclic Eburnean Orogeny between ~2.13 and ~1.98 Ga, (Milési et al., 1991; 1992; Boher et al., 1992, Feybesse et al., 2006; Perrouty et al., 2012) and; (3) the Wabo-Tampelse Event (Hein et al., 2004; Hein, 2010).

Gabbro, meta-gabbro, diorite and trondhjemite intrusions are interpreted as syn-tectonic with extrusion of meta-volcanic sequences of the Birimian Supergroup (Béziat et al., 2000; Hein et al., 2004) and co-magmatic (Béziat et al., 2000).

In the OGB, the Birimian Supergroup consists of folded, sheared and/or mylonitized volcanic, volcano-sedimentary and sedimentary sequences that were metamorphosed to upper greenschist facies and locally, to amphibolite facies (Tshibubudze and Hein, 2013). They were contact metamorphosed to hornblende-hornfels facies adjacent to granitoids, dykes and sills.

The stratigraphy of the OGB includes; (1) a basal meta-volcanic sequence; (2) a greywacke-siltstone-shale sequence interbedded with rare chert beds and banded iron formation; (3) a sandy dolomite unit; (4) a sequence of interbedded conglomerate-greywacke-siltstone-shale units and; (5) a greywacke sequence intercalated with a polymictic conglomerate marker bed locally termed the Dembam Member (Peters, 2011; Tshibubudze and Hein, 2013).

Methodology

The three samples selected for geochronological study were collected where the geology was well understood, and a relative chronology of structural events had been established.

Zircon extraction and mounting were undertaken at the EarthLab at the University of the Witwatersrand Johannesburg in South Africa. A representative sample was collected from each crushed sample for ICP-MS and XRF analyses. Cathodoluminescence (CL) imaging and backscattered-electron (BSE) imaging using the scanning electron microscope (JEOL JSM 6400) were conducted at the Centre for Microscopy, Characterisation and Analysis at the University of Western Australia. Ion microprobe analyses were completed using the SHRIMP II (John de Laetre Laboratory) at the Curtin University of Technology in Western Australia. Details of the extraction process, imaging, zircon analysis and data processing are detailed in Appendix A.

The SHRIMP U-Pb zircon data were reduced using the SQUID 2.50 (Ludwig, 2009) and Isoplot 3.00 (Ludwig, 2003), with Microsoft Excel macro add-ins. U-Pb data were plotted using the normal Wetherill Concordia-discordia diagram option in Isoplot 3.0.

The geochemical classification and nomenclature of samples BF_1144 and BF_1147 used the total alkali versus silica (TAS) by Middlemost (1994) after Cox et al. (1979), and Wilson (1989). Sample BF_1299 was excluded from the classification because it is the product of partial melting.

Sample geology and age constraints

Sample BF_1144 - granodiorite gneiss

The granodiorite gneiss (Figures 2a, b) crops out northeast of the town of Gorom-Gorom at UTM 30P 1608135 0811742. It has well-defined leucocratic and melanocratic layers. The melanocratic layers are dominated by hornblende, biotite (with a preferred orientation) and magnetite, while the leucocratic layers are dominated by plagioclase, potassium feldspar and quartz (Figure 2b). The quartz crystals exhibit undulose extinction. Accessory crystals of apatite and zircon are hosted within, and interstitial to, hornblende and plagioclase. The gneiss is migmatitic in part and exhibits flow folding. It is crosscut by gabbro-pyroxenite dykes.

Geochemically, a whole rock sample of the gneiss plots as granodiorite in the acidic magma field (c.f., Middlemost, 1994), and is classified as calc-alkaline in the AFM (alkali-iron-magnesium) diagram. The tectono-magmatic discrimination diagram after Pearce et al. (1984) indicates correspondence with volcanic-arc type granitoids.

The results of 20 analysed grain spots are summarized in Table 1 and plotted in Figure 2d. Most of the zircons are subhedral to euhedral and they exhibit oscillatory zoning around euhedral unzoned cores (Figure 2c) and the cores were specifically targeted to obtain the crystallisation age. Grain spots 10.1, 11.1, 14.1, and 16.1 in Table 1 gave Pb-Pb ages of 2276 ± 15, 2284 ± 23, 2277 ± 16 and 2272 ± 33 Ma reflecting the age of the source rocks. The majority of the grain spots define a Pb loss line within error with a calculated upper intercept age of 2252.6 ± 9.0 Ma (i.e., 2253 ± 9 Ma).

Sample BF_1299 – migmatitic gneiss

Sample BF_1299 was collected from a group of isolated and small outcrops northeast of the town of Gorom-Gorom and south of the village of Kel Enguef in the Kel Enguef belt at UTM 30P 1594675 0808119. The belt is composed of clastic and chemical sedimentary rocks that are metamorphosed from upper greenschist facies to amphibolite facies (c.f., Woolfe, 2011). The rocks exhibit a well-developed, northerly-dipping, bedding (compositional layering) parallel foliation. The coarse crystalline migmatitic gneiss anomalously crops out at the contact between amphibolite in the south and upper greenschist facies rocks in the north.

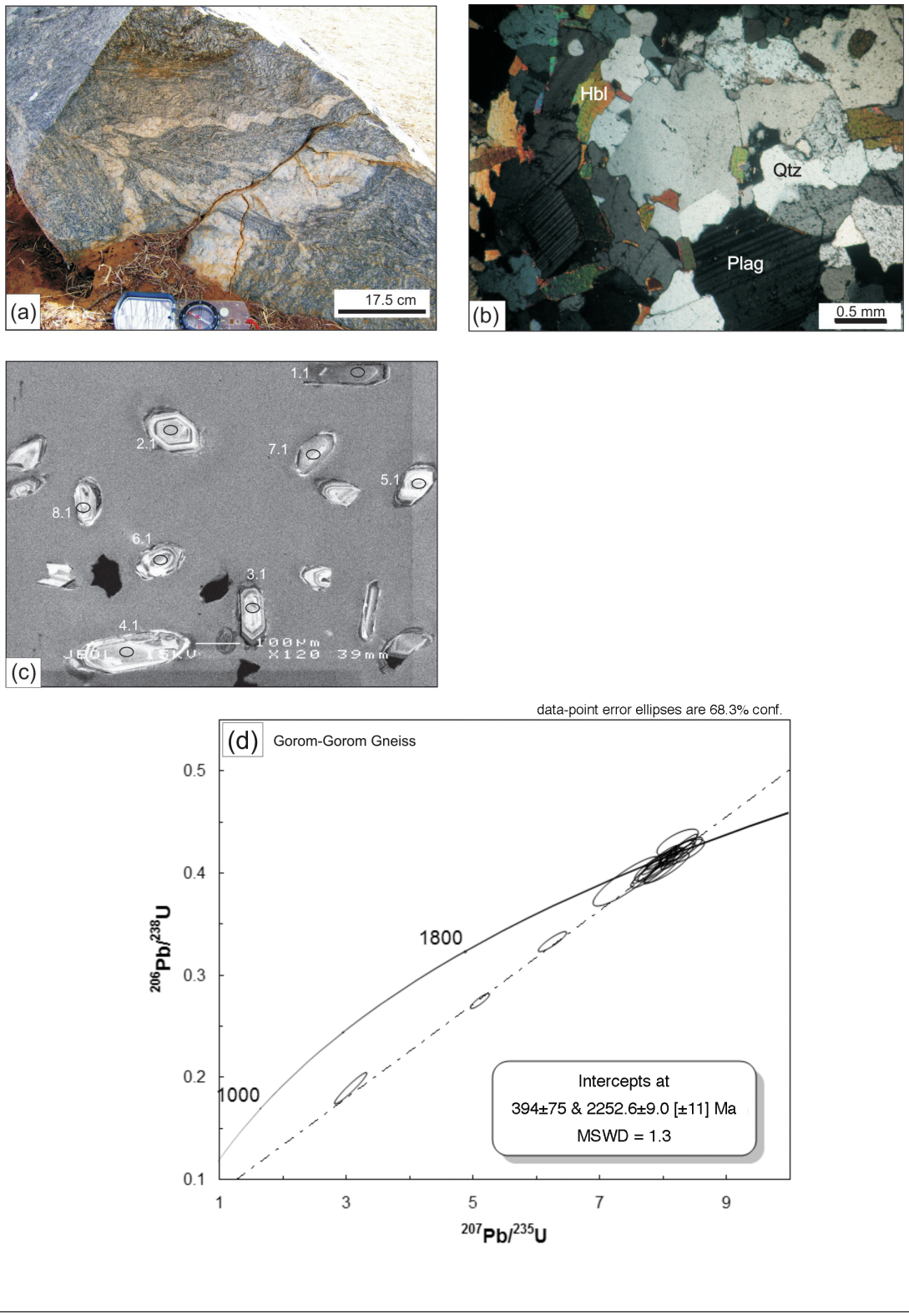

Figure 2. *(**a**) Granodiorite gneiss with folded leucocratic layers that are dominated by plagioclase and quartz minerals (UTM, 30P 0811742: 1608135), (**b**) Photomicrograph of the sample BF_1144, (Hbl = hornblende, Qtz = quartz, Plag = plagioclase crystals). (**c**) Cathodoluminesence images of zircon crystals that were analysed, they have well defined cores and rims, the cores were targeted. Numbers refers to the grain number in Table 1. Ellipses mark the location of the analysed spots. (**d**) The U-Pb Concordia diagram of the granodiorite gneiss.*

Table 1. Summary of SHRIMP U-Pb zircon data, sample BF_1144_Gorom-Gorom Gneiss.

Grain spot	% $^{206}Pb_c$	U (ppm)	Th (ppm)	$^{206}Pb/^{238}U^1$ Age		$^{207}Pb/^{206}Pb^1$ Age		% Discordant	$^{238}U/^{206}Pb^{*1}$	±%	$^{207}Pb^*/^{206}Pb^{*1}$	±%	$^{207}Pb^*/^{235}U^1$	±%	$^{206}Pb^*/^{238}U^1$	±%	err. corr.
1.1	0.06	276	141	2232	±30	2252	±10	+1	2.42	1.6	0.1421	0.6	8.10	1.7	0.414	1.6	0.94
2.1	0.02	61	34	2215	±35	2229	±12	+1	2.44	1.9	0.1402	0.7	7.92	2.0	0.410	1.9	0.94
3.1	0.35	34	9	2130	±75	2202	±40	+4	2.55	4.2	0.1380	2.3	7.45	4.7	0.392	4.2	0.88
4.1	0.05	61	35	2206	±51	2250	±22	+2	2.45	2.7	0.1419	1.3	7.98	3.0	0.408	2.7	0.91
5.1	0.27	38	18	2159	±39	2254	±21	+5	2.51	2.1	0.1422	1.2	7.80	2.4	0.398	2.1	0.87
6.1	–	61	41	2273	±36	2267	±21	-0	2.36	1.9	0.1432	1.2	8.35	2.3	0.423	1.9	0.84
7.1	0.05	66	37	2201	±53	2235	±13	+2	2.46	2.9	0.1407	0.7	7.89	2.9	0.407	2.9	0.97
8.1	0.22	120	43	1559	±25	2179	±16	+32	3.66	1.8	0.1362	0.9	5.14	2.0	0.274	1.8	0.89
9.1	0.25	130	69	1849	±33	2190	±18	+18	3.01	2.1	0.1370	1.0	6.27	2.3	0.332	2.1	0.89
10.1	–	41	20	2241	±39	2276	±15	+2	2.41	2.1	0.1440	0.8	8.25	2.2	0.416	2.1	0.92
11.1	–	78	38	2193	±46	2284	±23	+5	2.47	2.5	0.1447	1.4	8.08	2.8	0.405	2.5	0.88
12.1	0.02	75	42	2203	±46	2236	±25	+2	2.45	2.5	0.1407	1.4	7.90	2.8	0.407	2.5	0.86
13.1	0.11	57	28	2237	±37	2230	±15	-0	2.41	1.9	0.1402	0.9	8.02	2.1	0.415	1.9	0.91
14.1	–	54	28	2175	±37	2277	±16	+5	2.49	2.0	0.1441	0.9	7.97	2.2	0.401	2.0	0.91
15.1	0.04	71	44	2260	±36	2254	±19	-0	2.38	1.9	0.1422	1.1	8.23	2.2	0.420	1.9	0.86
16.1	–	59	43	2262	±37	2272	±33	+1	2.38	2.0	0.1437	1.9	8.33	2.7	0.420	2.0	0.72
17.1	0.11	61	37	2306	±37	2216	±32	-5	2.33	1.9	0.1391	1.9	8.25	2.7	0.430	1.9	0.72
18.1	1.24	133	43	1108	±54	1953	±29	+47	5.33	5.3	0.1198	1.6	3.10	5.5	0.188	5.3	0.96
19.1	–	36	13	2260	±41	2256	±17	-0	2.38	2.1	0.1424	1.0	8.24	2.4	0.420	2.1	0.91
20.1	0.03	84	33	2289	±35	2247	±11	-2	2.35	1.8	0.1416	0.6	8.32	1.9	0.426	1.8	0.95

Errors are 1-sigma; Pb_c and Pb^* indicate the common and radiogenic portions, respectively.

Error in Standard calibration was 0.48% (not included in above errors but required when comparing data from different mounts).

[1] Common Pb corrected using measured ^{204}Pb.

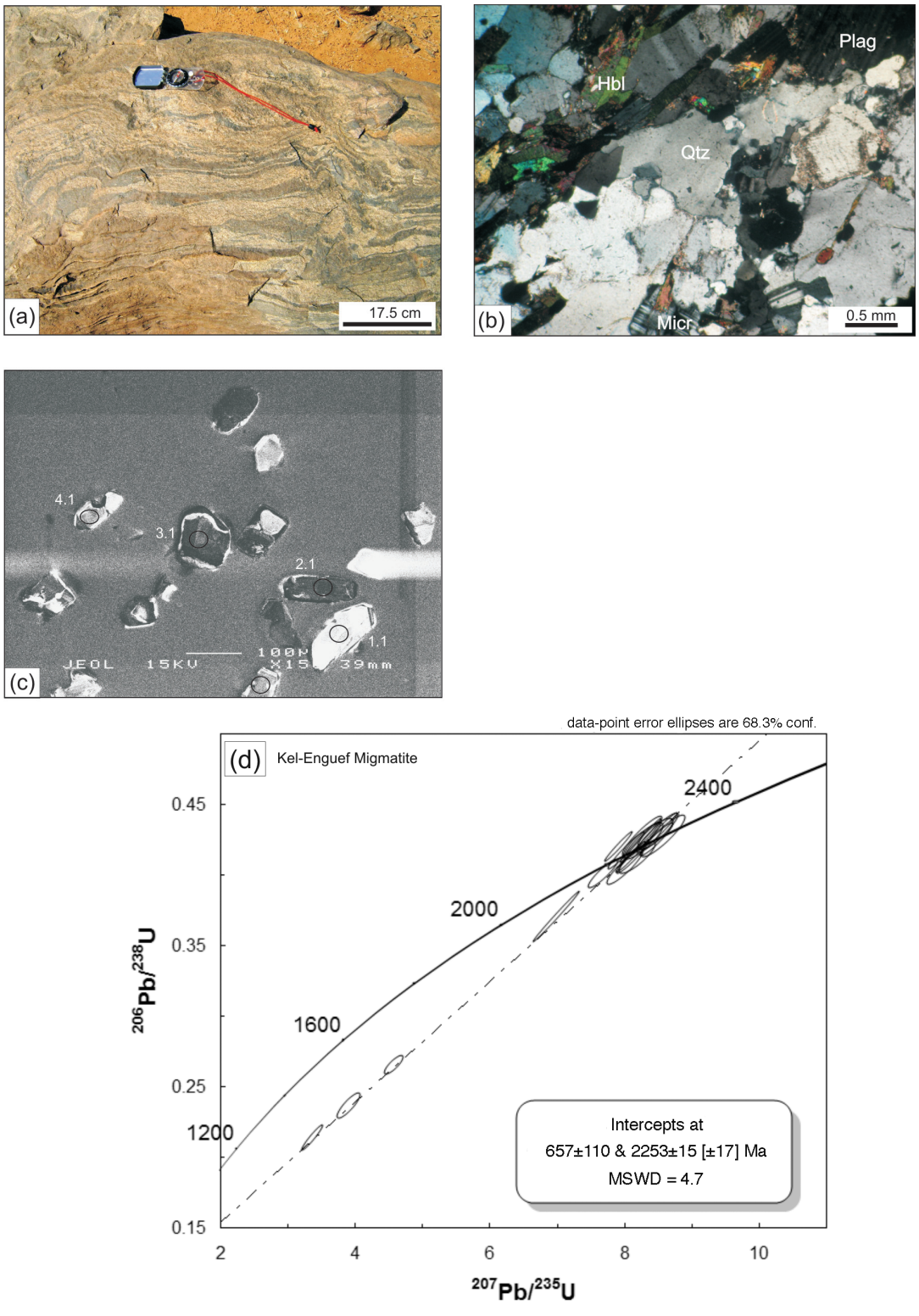

Figure 3. *(**a**) The Kel Enguef migmatite unit showing flow texture that developed during re-crystallisation (UTM, 30P 0808119: 1594675). (**b**) Photomicrograph of the sample BF_1299, showing alignment of hornblende (Hbl), and the Plag (plagioclase), Qtz (quartz) and Micr (microcline) crystals that dominate the leucocratic bands. (**c**) Zircon crystals that were analysed, they lack well defined rims, the cores of the zircon crystals were targeted. Numbers refers to the grain number in Table 2. Ellipses mark the location of the analysed spots. (**d**) The U-Pb Concordia diagram of the migmatite.*

Table 2. Summary of SHRIMP U-Pb zircon data, sample BF_1299_Kel-Enguef migmatite.

Grain spot	% $^{206}Pb_c$	U (ppm)	Th (ppm)	$^{232}Th/^{238}U$	$^{206}Pb^*$ (ppm)	$^{206}Pb/^{238}U^1$ Age		$^{207}Pb/^{206}Pb^1$ Age		% Discordant	$^{238}U/^{206}Pb^{*1}$	±%	$^{207}Pb^*/^{206}Pb^{*1}$	±%	$^{207}Pb^*/^{235}U^1$	±%	$^{206}Pb^*/^{238}U^1$	±%	err. corr.
1.1	–	53	19	0.38	19	2279	±38	2247	±13	-2	2.36	2.0	0.1416	0.8	8.28	2.1	0.424	2.0	0.90
2.1	–	375	265	0.73	137	2278	±47	2240	±6	-2	2.36	2.5	0.1410	0.3	8.24	2.5	0.424	2.5	0.97
3.1	0.13	173	69	0.41	62	2245	±40	2226	±9	-1	2.40	2.1	0.1399	0.5	8.03	2.2	0.417	2.1	0.96
4.1	–	92	43	0.49	32	2223	±34	2279	±19	+3	2.43	1.8	0.1443	1.1	8.19	2.1	0.412	1.8	0.81
5.1	–	98	43	0.45	36	2281	±35	2285	±11	+0	2.36	1.8	0.1447	0.7	8.47	1.9	0.425	1.8	0.90
6.1	0.25	672	78	0.12	136	1360	±30	1971	±26	+34	4.26	2.4	0.1210	1.5	3.92	2.9	0.235	2.4	0.85
7.1	–	197	108	0.57	72	2298	±33	2268	±21	-2	2.33	1.7	0.1433	1.2	8.46	2.1	0.428	1.7	0.72
8.1	0.05	402	165	0.42	128	2027	±56	2195	±6	+9	2.71	3.2	0.1374	0.3	7.00	3.2	0.370	3.2	0.98
9.1	0.03	402	214	0.55	145	2257	±31	2188	±6	-4	2.38	1.6	0.1369	0.3	7.91	1.7	0.419	1.6	0.91
10.1	–	33	11	0.34	12	2293	±44	2295	±19	+0	2.34	2.3	0.1456	1.1	8.58	2.5	0.427	2.3	0.85
11.1	0.65	62	24	0.40	23	2276	±38	2250	±22	-1	2.36	2.0	0.1418	1.2	8.28	2.3	0.423	2.0	0.88
12.1	0.04	37	14	0.40	14	2303	±42	2269	±16	-2	2.33	2.2	0.1435	0.9	8.49	2.4	0.429	2.2	0.90
13.1	0.10	311	219	0.73	114	2293	±42	2231	±16	-3	2.34	2.2	0.1403	0.9	8.26	2.3	0.427	2.2	0.88
14.1	0.18	58	23	0.40	20	2192	±37	2270	±16	+4	2.47	2.0	0.1435	0.9	8.01	2.2	0.405	2.0	0.89
15.1	0.02	193	116	0.62	72	2316	±34	2272	±8	-2	2.31	1.7	0.1437	0.5	8.56	1.8	0.432	1.7	0.89
16.1	0.22	419	34	0.08	95	1511	±22	2043	±20	+29	3.79	1.6	0.1260	1.1	4.59	2.0	0.264	1.6	0.84
17.1	–	225	95	0.44	77	2171	±31	2218	±13	+2	2.50	1.7	0.1393	0.8	7.69	1.9	0.400	1.7	0.89
18.1	–	154	83	0.56	54	2220	±33	2267	±9	+2	2.43	1.8	0.1433	0.5	8.12	1.8	0.411	1.8	0.89
19.1	0.06	259	162	0.65	92	2224	±32	2258	±7	+2	2.43	1.7	0.1425	0.4	8.09	1.8	0.412	1.7	0.93
20.1	0.29	419	34	0.08	76	1241	±32	1889	±16	+38	4.71	2.8	0.1156	0.9	3.38	3.0	0.212	2.8	0.96

Errors are 1-sigma; Pb_c and Pb^* indicate the common and radiogenic portions, respectively.

Error in Standard calibration was 0.48% (not included in above errors but required when comparing data from different mounts).

[1] Common Pb corrected using measured ^{204}Pb.

Table 3. Summary of SHRIMP U-Pb zircon data, sample BF_1147_Granite clasts from the metaconglomerate.

Grain spot	% $^{206}Pb_c$	U (ppm)	Th (ppm)	$^{232}Th/^{238}U$	$^{206}Pb^*$ (ppm)	$^{206}Pb/^{238}U^1$ Age		$^{207}Pb/^{206}Pb^1$ Age		% Discordant	$^{238}U/^{206}Pb^{*1}$	±%	$^{207}Pb^*/^{206}Pb^{*1}$	±%	$^{207}Pb^*/^{235}U^1$	±%	$^{206}Pb^*/^{238}U^1$	±%	err. corr.
1.1	0.41	94	51	0.57	21	1480	±66	2195	±20	+36	3.87	5.0	0.1374	1.15	4.89	5.1	0.258	5.0	0.97
2.1	0.50	126	110	0.90	41	2075	±56	2245	±15	+9	2.63	3.2	0.1414	0.87	7.40	3.3	0.380	3.2	0.96
3.1	0.35	71	37	0.54	25	2192	±61	2244	±17	+3	2.47	3.3	0.1413	0.97	7.89	3.4	0.405	3.3	0.96
4.1	0.56	524	619	1.22	97	1257	±38	1934	±12	+38	4.64	3.3	0.1185	0.66	3.52	3.4	0.215	3.3	0.98
5.1	–	107	45	0.43	36	2131	±58	2160	±12	+2	2.55	3.2	0.1347	0.70	7.27	3.3	0.392	3.2	0.98
6.1	0.16	72	44	0.64	27	2327	±64	2242	±15	-4	2.30	3.3	0.1412	0.85	8.46	3.4	0.435	3.3	0.97
7.1	0.05	81	58	0.74	27	2155	±59	2234	±13	+4	2.52	3.2	0.1406	0.73	7.69	3.3	0.397	3.2	0.98
8.1	0.33	539	73	0.14	117	1448	±40	2003	±9	+31	3.97	3.1	0.1232	0.52	4.28	3.2	0.252	3.1	0.99
9.1	0.97	196	181	0.95	43	1476	±42	2182	±24	+36	3.89	3.2	0.1364	1.36	4.84	3.4	0.257	3.2	0.92
10.1	1.30	502	583	1.20	119	1565	±43	2101	±13	+29	3.64	3.1	0.1302	0.73	4.93	3.2	0.275	3.1	0.97
11.1	–	249	200	0.83	88	2223	±59	2259	±7	+2	2.43	3.1	0.1426	0.39	8.10	3.2	0.412	3.1	0.99
12.1	–	59	35	0.60	22	2273	±64	2237	±16	-2	2.37	3.3	0.1408	0.94	8.21	3.5	0.423	3.3	0.96
13.1	0.36	371	365	1.02	90	1604	±52	2147	±10	+28	3.54	3.7	0.1337	0.57	5.21	3.7	0.283	3.7	0.99
14.1	0.04	53	38	0.74	19	2243	±64	2268	±17	+1	2.40	3.4	0.1433	0.97	8.22	3.5	0.416	3.4	0.96
15.1	0.24	427	421	1.02	115	1763	±48	2175	±8	+22	3.18	3.1	0.1358	0.46	5.89	3.1	0.315	3.1	0.99
16.1	0.09	94	67	0.73	34	2251	±67	2231	±12	-1	2.39	3.5	0.1403	0.72	8.08	3.6	0.418	3.5	0.98
17.1	0.00	56	34	0.62	20	2246	±63	2238	±14	-0	2.40	3.3	0.1409	0.83	8.09	3.4	0.417	3.3	0.97
18.1	–	42	16	0.39	15	2278	±66	2326	±21	+2	2.36	3.5	0.1483	1.24	8.66	3.7	0.424	3.5	0.94
19.1	–	79	52	0.68	28	2250	±62	2263	±13	+1	2.39	3.3	0.1430	0.75	8.23	3.4	0.418	3.3	0.97
20.1	–	101	39	0.40	35	2170	±59	2200	±12	+2	2.50	3.2	0.1378	0.68	7.60	3.3	0.400	3.2	0.98

Errors are 1-sigma; Pb_c and Pb^* indicate the common and radiogenic portions, respectively.

Error in Standard calibration was 0.71% (not included in above errors but required when comparing data from different mounts).

[1] Common Pb corrected using measured ^{204}Pb.

In outcrops, the migmatitic gneiss have well-developed leucocratic and melanocratic layers that are folded (Figure 3a). They range in thickness from 1.0 mm to 5 cm. The melanocratic layers are dominated by hornblende and quartz with accessory biotite and plagioclase, while the leucocratic layers are dominated by plagioclase and quartz (up to 2 mm in diameter) with accessory potash feldspar, muscovite and biotite (Figure 3b). Veins of coarse-grained quartz and plagioclase cross cut the migmatite.

Petrographically, the migmatitic gneiss is composed of coarse crystals of quartz, plagioclase and hornblende, but biotite, zircon, sphene and magnetite, make up approximately 5% of the groundmass (Figure 3b). Leucocratic layers are medium-grained with crystals up to 2 mm in diameter. Interstitial magnetite, associated with zircon and sphene, is common in these layers and also occurs as inclusions.

The results from 20 analysed grain spots of zircons (Figure 3c) from sample BF_1299 are summarized in Table 2 and are plotted in Figure 3d. The cores of the zircons were targeted, the zircons did not exhibit well-defined growth rings and are dominantly subhedral in shape (Figure 3c). Grain spots 2.1, 3.1, 6.1, 7.1, 8.1, 9.1, 13.1 and 15.1 to 20.1 have high uranium concentration and the mean age of coherent group of these 13 spots is 1955 ± 257 Ma, while grain spots 1.1, 4.1, 5.1, 10.1, 11.1, 12.1, and 14.1 in Table 2 gave a mean age on 7 spots of 2268 ± 29 Ma. The low uranium phase concentration age probably reflects the age of the source rocks and the high concentration phase age probably reflects the age related to the partial melting phase. The concordant data of all the 20 grain spots define a Pb loss line within error with a calculated upper intercept age of 2253 ± 15 Ma.

Sample BF_1147 – granite

Sample BF_1147 is of a granite (*sensu stricto*) boulder that was extracted as an entity from a polymictic conglomerate (the Dembam Member) that forms a marker bed within a 4.5 km thick sequence of greywacke beds east of the village of Markoye at UTM 31P 1619591 0182783. The Dembam Member occupies a position at the top of the stratigraphy of the OGB (Tshibubudze et al., 2009; Peters, 2011; Tshibubudze and Hein, 2013). The matrix-supported polymictic pebble-cobble boulder conglomerate (Figure 4a) is approximately 10 m thick. Pebbles, cobbles and boulders are sub-angular to sub-rounded and cemented in a cross-bedded matrix of poorly sorted and coarse-grained greywacke. The pebbles, cobbles and boulders making up the conglomerate include fuchsitic chert, black chert, granodiorite (sensu-stricto), granite (sensu-stricto), gabbro, basalt, andesite, vein-quartz, finely laminated sandstone interbedded with mudstone that host small-scale slump folds, and quartz-rich and volcaniclastic metasediments. The size and sub-rounded form of the pebbles, cobbles and boulders, and the poor sorting of the Dembam Member suggests that the site of deposition sourced rocks from nearby.

The granite boulder extracted from the Dembam Member is composed of coarse crystals of quartz, plagioclase, potash feldspar and chlorite. The potash feldspar is more dominant than the plagioclase, making up more than 45% of the sample.

Petrographically, the granite clast consists of coarse crystals of highly altered plagioclase, re-crystallized quartz that exhibits undulose extinction, albite, chlorite, altered microcline and ~2mm size orthoclase crystals (Figure 4b). Hornblende and opaque (magnetite) crystals make up less than 2% of the groundmass.

Geochemically, sample BF_1147 plots as granite and in the acidic magma field (c.f., Middlemost, 1994), and is classified as calc-alkaline in the AFM (alkali-iron-magnesium) diagram. The tectono-magmatic discrimination diagram after Pearce et al. (1984) indicates correspondence with volcanic-arc type granites.

The data of 20 analysed grain spots of zircons (Figure 4c) from sample BF_1147 are summarized in Table 3 and the data are plotted in Figure 4d. Most of the zircons exhibit oscillatory zoning (but not all), and they are subhedral in shape (Figure 4c). The cores of the zircons were targeted. Grain spot 18.1 in Table 3 gave a 2% discordant Pb-Pb age of 2326 ± 21 Ma reflecting the age of the source rocks. Grain spot 5.1 gave a 2% discordant Pb-Pb age of 2160 ± 12 Ma which is younger than all the other grain spots reflecting an event which might have resulted in Pb loss. The majority of the zircons gave similar Pb-Pb ages. The distribution along the regression curve indicated lead loss at ~2.2 to ~2.15 Ga and ~2.1 to ~1.92 Ga with a calculated upper intercept U-Pb age of 2255 ± 26 Ma and lower calculated intercept age of 556 ± 120 Ma.

Discussion and conclusions

The geochronological data from 3 samples from the OGB present the oldest outcropping Palaeoproterozoic supracrustal rocks yet found in the WAC (and its proximal erosional product in the Dembam Member) when compared with published oldest U-Pb and Pb-Pb ages reported as inherited zircon ages by Gasquet et al. (2003), De Kock et al. (2009), Siegfried et al. (2009) and Thomas et al. (2009) and oldest U-Pb crystallisation ages reported by Castaing et al. (2003) from Burkina Faso, and K-Ar ages by Feybesse et al. (2006) from the Sefwi belt in Ghana. Samples BF_1144 (granodiorite gneiss) and BF_1299 (migmatitic gneiss) gave convincing U-Pb concordant crystallisation ages of 2253 ± 9 Ma and 2253 ± 15 Ma and likely represent the age of crystallisation of a parent gneiss with granodioritic composition. It is also likely that this age can be the crystallisation age of a pre-metamorphic protolith, since the low uranium phase zircons from migmatitic gneiss (BF_1299) gave a mean age of 2268 ± 29 Ma which is within error of the age from the granodiorite gneiss (BF_1144). This pre-metamorphic protolith was later partially melted around 1955 ± 257 Ma indicated by the

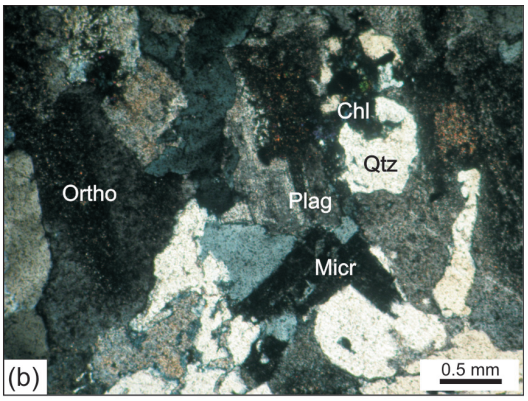

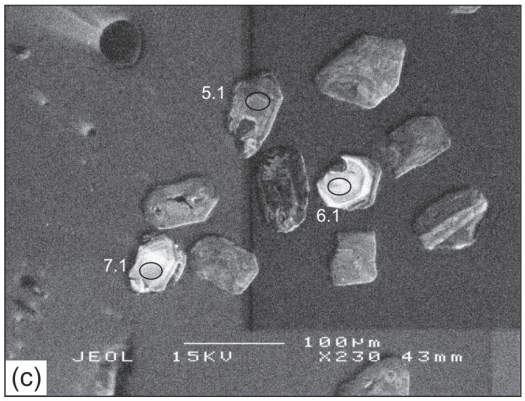

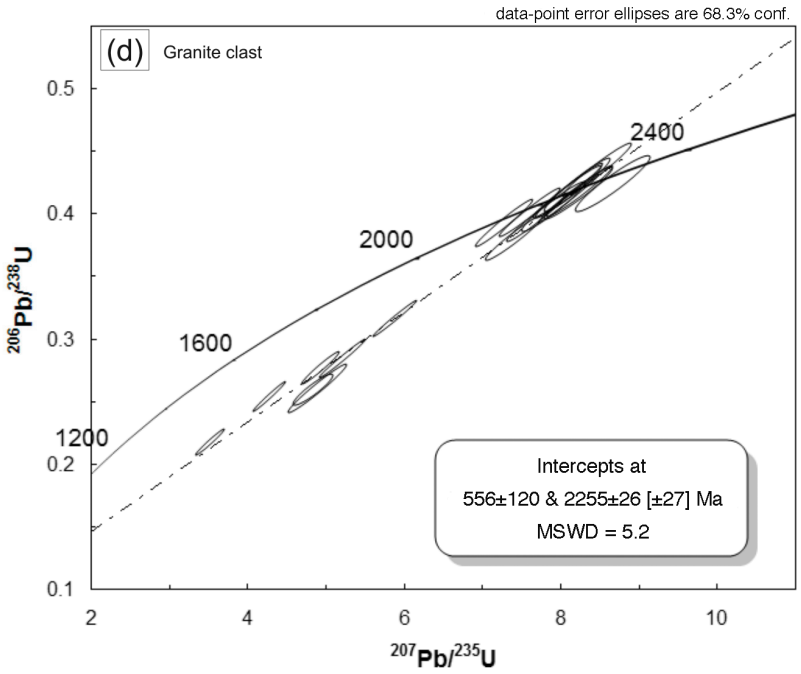

Figure 4. *(**a**) The Dembam Member polymictic conglomerate east of the village of Markoye (UTM, 31P 0182783: 1619591). (**b**) Photomicrograph of the sample BF_1147, the Plag (plagioclase), Ortho (orthoclase) and Micr (microcline) crystals are altered, and the Chl (chlorite) is growing over the re-crystallised Qtz (quartz). (**c**) Zircon crystals that were analysed, they lack well defined rims, the cores were targeted. Numbers refers to the grain number in Table 3. Ellipses mark the location of the analysed spots. (**d**) U-Pb Concordia diagram for the granite clast.*

high uranium phase zircons form the migmatitic gneiss. The partial melting age and the proposed crystallisation ages could be further constrained by analysing the overgrowth zones of the cores in sample BF_1144 (granodiorite gneiss). Sample BF_1147 gave a concordant age of 2255 ± 26 Ma and is interpreted as the age of crystallisation of a granite pluton that was eroded from a site nearby before becoming part of the Dembam Member (Birimian Supergroup).

Samples BF_1144 (granodiorite gneiss) and BF_1299 (migmatitic gneiss) with U-Pb concordant crystallisation ages of 2253 ± 9 Ma and 2253 ± 15 Ma, respectively, may constrain the crystallisation age of a gneissic protolith on which the OGB basin was deposited, or an early group of granitoids that was emplaced in the hinterland during formation of the OGB basin. In any event the crystallisation ages are markedly older than those of ~2.2 Ga for first magmatic cycle of Birimian granitoids in the WAC, as proposed by Dia et al. (1997), Feybesse et al. (2006), Gueye et al. (2007; 2008) and De Kock et al. (2011). Perhaps the first magmatic cycle can be extended to include the ages liberated from samples BF_1144 and BF_1299 to ~2.26 to ~2.2 Ga, or alternatively, that an older magmatic cycle can now be defined relative to that proposed by Pawlig et al. (2006), Gueye et al. (2007; 2008), Lompo (2009; 2010) and Vidal et al. (2009).

Sample BF_1147, the granite boulder from the Dembam Member which gave a U-Pb concordant age of 2255 ± 26 Ma, currently constrains the maximum age of the Birimian Supergroup in the OGB, because (reasonably) the granite body from which the boulder eroded must have crystallised prior to erosion. The age corresponds well with samples BF_1144 and BF_1299, and again, could constrain the crystallisation age of a protolith on which the OGB basin was deposited, or an early group of granitoids that were emplaced in the hinterland during formation of the OGB basin.

It follows that if samples BF_1144, BF_1299 and BF_1147 constrain the age of a protolith on which the OGB basin was deposited, they indirectly provide a minimum age for the rocks in the hinterland, which based on the pebble-cobble-boulder fraction of the Dembam Member, were composed of granite and granodiorites, volcaniclastic and mafic volcanic rocks, gabbro, metasedimentary rocks and quartz veins.

Alternatively, if samples BF_1144, BF_1299 and BF_1147 constrain the age of an early group of granitoids that were emplaced in the hinterland during formation of the OGB basin, the age is (again) markedly older than those of ~2.2 Ga for first magmatic cycle of Birimian granitoids in the WAC, supporting the proposal to extend the first magmatic cycle of Birimian granitoids to ~2.26 to ~2.2 Ga, or alternatively, to define an older magmatic cycle.

Unfortunately, it has not been possible to establish whether the granite-granodiorite plutons, as represented by the analysed samples, were unconformably overlain by the Birimian Supergroup of the OGB (thus forming the basement to the OGB basin), because an unconformity has not been found anywhere in the field area due to extensive sand dune cover. Similarly, it has also not been possible to establish an intrusive relationship between the ~2.26 to ~2.25 Ga granite-granodiorites with any Birimian supracrustal rocks in the region. Certainly, the crystallisation ages are older than the ~2.24 Ga geochron established from a rhyolite in the Goren greenstone belt by Castaing et al. (2003), and indicate that the Birimian Supergroup is at least as old as ~2.26 to ~2.25 Ga in the northeast of Burkina Faso.

The analysed cores to zircons from the granodiorite gneiss, migmatitic gneiss and granite clast gave Pb-Pb ages in the range ~2.34 to ~2.27 Ga. They are interpreted as inherited from pre-exiting zircon cores and are similar to Pb-Pb ages reported as inherited zircon ages by Gasquet et al. (2003) from the Dabakala tonalitic gneiss in northeast Cote d'Ivoire.

Acknowledgements

This research was made possible with the assistance of the staff of EarthLab at the University of Witwatersrand Johannesburg, Curtin University of Technology John de Laetre Centre, University of Western Australia Centre for Exploration and Targeting (CET), IAMGOLD's Ouagadougou and Essakane Mine offices, the University of Ouagadougou, and especially J. Aphane, A. Kennedy, R. Taylor, H. Gao, C. Isaac, B. Li, C. Schindler, L. Parra Avila, and M. Sadiwidi.

Funding for sampling and analysis were provided by IAMGOLD Essakane SA and BHP Billiton.

We wish to gratefully acknowledge AMIRA International and the industry sponsors, including AusAid and the ARC Linkage Project LP110100667, for their support of the WAXI project (P934A). We are also appreciative of the contribution of the various Geological Surveys/Department of Mines in West Africa as sponsors in-kind of WAXI. We wish to recognize our WAXI research colleagues from the various Institutions from around the world. Finally, we would like to thank D.W. Davis and the anonymous reviewer for their constructive reviews that have helped us improve the manuscript.

References

Baratoux, L., Metelka, V., Naba, S., Jessell, M, W., Gregoire, M. and Ganne, J., 2011. Juvenile Paleoproterozoic crust evolution during the Eburnean orogeny (~2.2-2.0 Ga), western Burkina Faso. Precambrian Research, 191, 18-45.

Béziat, D., Bourges, F., Debat, P., Lompo, M., Martin, F. and Tollon, F., 2000. A Paleoproterozoic ultramafic-mafic assemblage and associated volcanic rocks of the Boromo greenstone belt: fractionates originating from island-arc volcanic activity in the West African craton. Precambrian Research, 101, 25-47.

Boher, M., Abouchami, W., Michard, A., Albarede, F. and Arndt, N.T., 1992. Crustal growth in West Africa at 2.1 Ga. Journal of Geophysical Research, 97 (B1), 345-369.

Castaing, C., Billa, M., Milési, J.P., Thiéblemont, D., Le Mentour, J., Egal, E., Donzeau, M. (BRGM) (coordonnateurs) et Guerrot, C., Cocherie, A., Chevremont, P., Tegyey, M., Itard, Y. (BRGM), Zida, B., Ouedraogo, I., Kote, S., Kabore, B.E., Ouedraogo, C. (BUMIGEB), and Ki, J.C., Zunino

(ANTEA), 2003. Notice explicative de la Carte géologique et miniére du Burkina Faso à 1/1 000 000.

Cox, K.G., Bell, J.D. and Pankhurst, R.J., 1979. The interpretation of igneous rocks. Allen and Unwin, London, 450pp.

De Kock, G.S., Armstrong, R.A., Siegfried, H.P. and Thomas, E., 2011. Geochronology of the Birim Supergroup of the West African craton in the Wa-Bolé region of west-central Ghana: Implications for the stratigraphic framework. Journal of African Earth Sciences, 59, 1-40.

De Kock, G.S., Theveniaut, H., Botha, P.W. and Gyapong, W., 2009. Geological Map Explanation, Map Sheet 0803B (1:100 000). CGS/BRGM/Geoman. Geological Survey Department of Ghana, 354pp.

Dia, A., Van Schmus, W. R. and Kröner, A., 1997. Isotopic constraints on the age and formation of a Palaeoproterozoic volcanic arc complex in the Kedougou Inlier; eastern Senegal, West Africa. Journal of African Earth Sciences, 24, 197-213.

Feybesse, J.L., Billa, M., Guerrot, C., Duguey, E., Lescuyer, J.L., Milési, J.P. and Bouchot, V., 2006. The Palaeoproterozoic Ghanaian province: Geodynamic model and ore controls, including regional stress modelling. Precambrian Research, 149, 149-196.

Gasquet, D., Barbey, P., Adou, M. and Paquette, J.L., 2003. Structure, Sr-Nd isotope geochemistry and zircon U-Pb geochronology of the granitoids of the Dabakala area (Côte d'lvoire): evidence for a crustal growth event in the Palaeoproterozoic of West Africa? Precambrian Research, 127, 329-354.

Gueye, M., Ngom, P.M., Diène, M., Thiam, Y., Siegesmund, S., Wemmer, K. and Pawlig, S., 2008. Intrusive rocks and tectono-metamorphic evolution of the Mako Paleoproterozoic belt (Eastern Senegal, West Africa). Journal of African Earth Sciences, 50, 88-110.

Gueye, M., Siegesmund, S., Wemmer, K., Pawlig, S., Drobe, M. and Nolte, N., 2007. New evidence of an early Birimian evolution in the West African Craton: An example from the Kedougou-Kenieba Inlier, southeast Senegal. South African Journal of Geology, 110, 511-534.

Hein, K.A.A., 2010. Succession of structural events in the Goren Greenstone Belt (Burkina Faso); implications for West African tectonics. Journal of African Earth Sciences, 56, 83-94.

Hein, K.A.A., Morel, V., Kagoné, O., Kiemde, F. and Mayes, K., 2004. Birimian lithological succession and structural evolution in the Goren segment of the Boromo-Goren greenstone belt, Burkina Faso. Journal of African Earth Sciences, 39, 1-23.

Hirdes, W. and Davis, D.W., 2002. U-Pd geochronology of Palaeoproterozoic rocks in the southern part of the Kedougou-Kéniéba Inlier, Senegal, West Africa: Evidence for diachronous accretionary development of the Eburnean province. Precambrian Research, 118, 83-99.

Lompo, M., 2009. Geodynamic evolution of the 2.25-2.0Ga Palaeoproterozoic magmatic rocks in the Man-Leo Shield of the West African Craton. A model of subsidence of an oceanic plateau. In: S.M. Reddy, R. Mazumder, D.A.D. Evans and A.S. Collins, (Editors), Palaeoproterozoic Supercontinents and global evolution. Geological Society, London, Special Publication, 323, 231-254.

Lompo, M., 2010. Paleoproterozoic structural evolution of the Man-Leo Shield (West Africa). Key structures for vertical to transcurrent tectonics. Journal of African Earth Sciences, 58, 19-36.

Ludwig, K.R., 2003. Isoplot 3.00, A geochronological toolkit for Microsoft Excel, Berkeley Geochronology Centre, Berkeley, Special Publication 4, 70pp.

Ludwig, K.R., 2009. Squid 2.50, A user's manual, Berkeley Geochronology Centre, Berkeley, California, USA, 95pp.

Metelka, V., Baratoux, L., Naba, S. and Jessell, M.W., 2011. A geophysically constrained litho-structural analysis of the Eburnean greenstone belts and associated Granitoid domains, Burkina Faso, West Africa. Precambrian Research, 190, 48-69.

Middlemost, A.K., 1994. Naming materials in the magma/igneous rock system. Earth-Science Reviews, 37, 215-224.

Milési, J.P., Ledru, P., Ankrah, P., Johan, V., Marcoux, E. and Vinchon, Ch., 1991. The metallogenic relationship between Birimian and Tarkwaian gold deposits in Ghana. Mineralium Deposita, 26, 228-238.

Milési, J.P., Ledru, P., Feybesse, J.L., Dommanget, A. and Marcoux, E., 1992. Early Proterozoic ore deposits and tectonics of the Birimian orogenic belt, West Africa. Precambrian Research, 58, 305-344.

Pawlig, S., Gueye, M., Klischies, R., Schwarz, S., Wemmer, K. and Siegesmund, S., 2006. Geochemical and Sr-Nd isotopic data on the Birimian of the Kedougou-Kenieba Inlier (Eastern Senegal): Implications on the Palaeoproterozoic evolution of the West African Craton. South African Journal of Geology, 109, 411-427.

Pearce, J.A., Harris, N. B.W. and Tindle, A.G., 1984. Trace element discrimination diagrams for the tectonic interpretation of granitic rocks. Journal of Petrology, 25, 956–983.

Perrouty, S., Ailleres, L., Jessell, M, W., Baratoux, L. and Bourassa, Y., 2012. Revised Eburnean geodynamic evolution of the gold-rich southern Ashanti belt, Ghana, with new field and geophysical evidence of pre-Tarkwaian deformations. Precambrian Research 204, 12-39.

Peters, L., 2011. Geology of the eastern Markoye region, Oudalan-Gorouol greenstone belt, NE Burkina Faso. Unpublished Honours thesis, University of the Witwatersrand, South Africa, 61pp.

Siegfried, P., Aggenbach, A., Clarke, B., Delor, C. and Yves Roig, J., 2009. Geological Map Explanation, Map Sheet 0903D (1:100 000). CGS/BRGM/Geoman. Geological Survey Department of Ghana.

Stern, R.A., 2001. A new isotopic and trace-element standard for the ion microprobe: preliminary thermal ionization mass spectrometry (TIMS) U-Pb and electron-microprobe data; Radiogenic age and isotopic studies: Report 14, Geological Survey of Canada, Current Research 2001-F1, 11pp.

Thomas, E., Baglow, N., Viljoen, J. and Siaka, Z., 2009. Geological Map Explanation, Map Sheet 0903D (1:100 000). CGS/BRGM/Geoman. Geological Survey Department of Ghana.

Tshibubudze, A. and Hein, K.A.A., 2013. Structural setting of gold deposits in the Oudalan-Gorouol volcano-sedimentary belt east of the Markoye Shear Zone, West African craton. Journal of African Earth Sciences, 80, 31-47.

Tshibubudze, A. and Hein, K.A.A., 2010. Tectonic evolution of the Oudalan-Gorouol greenstone belt in northeast Burkina Faso and Niger, West African craton. Geophysical Research Abstracts. Volume 12, EGU2010-708, 2010 EGU General Assembly 2010, ISSN of eISSN: 1607-7962.

Tshibubudze, A., Hein, K.A.A. and Marquis, P. 2009. The Markoye Shear Zone in northeast Burkina Faso. Journal of African Earth Sciences, 55, 245-256.

Vidal, M., Gumiaux, C., Cagnard, F., Pouchet, A., Ouattara, G. and Pichon, M., 2009. Evolution of a Paleoproterozoic 'weak type' orogeny in the West African Craton. Tectonophysics, 477, 145-159.

Wilson, M., 1989. Igneous petrogenesis. Published by Unwin Hyman, London, 466pp.

Woolfe, A., 2011. Stratigraphy and metamorphic facies in the Kel Enguef metamorphic belt near Gorom Gorom, NE Burkina Faso. Unpublished Honours thesis, University of the Witwatersrand, South Africa, 62pp.

Editorial handling: J.M. Barton Jnr.

Appendix A – Sample preparation

The samples selected for geochronological study were collected where the stratigraphic position and relative chronology was well understood and established.

The samples were trimmed of any weathered surface, washed, and then crushed to centimetre-size fragments in a jaw crusher at EarthLab at the University of the Witwatersrand Johannesburg. A representative sample of ~50g was collected from each crushed sample for ICP-MS and XRF analyses.

The remaining fraction was milled to 500 μm for mineral separation. The 500 μm and 250 μm sieve separates were collected, and gravity separated on a Wifley percussion table. The heavy separates were dried overnight in an oven at 80°C. A hand magnet was used to remove magnetite and iron fillings. The remaining separates were treated in a glass separating funnel using heavy liquid separation with Bromoform ($CHBr_3$: 2.89 g/cm^3). The funnel was constantly stirred to facilitate density separation. The heavy mineral separates were then drained on a filter paper and washed with distilled water and acetone and dried in the oven at 80°C. These heavy mineral concentrates were processed on the basis of magnetic susceptibility using the Frantz magnetic separator. The longitudinal tilt of 5° and a magnetic current from 0.15 to 1.5 A was used. The remaining non-magnetic separates were purified using methylene iodine (CH_2I_2: 3.3 g/cm^3) to obtain a concentrate of minerals with density greater than 3.3 g/cm^3. Finally, the zircons population was handpicked and sorted on the basis of colour, size, and shape of individual crystals, or the other minerals were handpicked-out to leave only zircons. All other fractions were retained for storage and future reference.

For each sample a population of about 80 to 100 zircon crystals were selected and placed on a 25 mm diameter mount with 3 standards. The standards used included; (1) NBS610 (Glass) calibration for common (^{204}Pb); (2) BR266 with a standardized age of 559 Ma and has 903 ppm U (calibration standard for zircon after Stern, 2001); (3) OGC 1 (Owens Gully Diorite: 3465 Ma), which is a standard used to monitor the ^{207}Pb/^{206}Pb ratio. Each mount had a maximum of three different samples. A map was created for the mounts to mark were each sample and standard was located.

The mount face was ground with wet sandpaper P2000 (14 to 15 μm) grit and polished using fine (3 to 1/4 μm) diamond powder. The mount was then cleaned and dried before coating with gold (to 40 nm thickness). The gold was melted at 5 to 6 A in a gold coating machine with a slow increase in current to evaporate any impurities. The edge-to-edge resistance was checked if it was higher than 15 ohms.

Each mount was photographed in reflected light. Cathodoluminescence (CL) imaging revealed the internal structure of zircons, and backscattered-electron (BSE) imaging resolved imperfections in the zircons using the scanning electron microscope (JEOL JSM 6400) at the Centre for Microscopy, Characterisation and Analysis at the University of Western Australia. Crystals of good quality analysed in this study (not with fractures and/or uranium spots) were selected on the basis of their reflected-light, CL, and BSE characteristics.

The ion microprobe analyses of the samples were completed using the SHRIMP II (John de Laetre Laboratory) at the Curtin University of Technology in Western Australia. The analysis of ~15 to 20 grains per sample was completed with a primary beam at 10 keV, with a spot diameter of ~20 μm. The net primary ion current ranged between 2.0 to 3.0 nA during 6 cycle/scans through the required isotopic mass ranges for each spot. The BR266 standard was analysed 10 to 20 times as a minimum for all SHRIMP sessions to monitor and compensate for instrumental drift. OGC1 was analysed ~3 to 4 times for each session.

The SHRIMP U-Pb zircon data were reduced using the SQUID 2.50 (Ludwig, 2009) and Isoplot 3.00 (Ludwig, 2003), with Microsoft Excel macro add-ins. Data was corrected for common Pb using measured ^{204}Pb. The uncertainties for all individual isotopic ratios and dates analysed for each session were taken at a 1σ level. The weighted mean dates are reported with 95% confidence level. The U-Pb data were plotted using the normal Wetherill Concordia-discordia diagram option in Isoplot 3.0. The geochemical classification and nomenclature of samples BF_1144 and BF_1147 used the total alkali versus silica (TAS) by Middlemost (1994) after Cox et al. (1979) and Wilson (1989). Sample BF_1299 was excluded from the classification because it is the product of partial melting.

APPENDIX E

Tshibubudze, A., Hein, K.A.A., Marquis, P., 2009. The Markoye Shear Zone in NE Burkina Faso. Journal of African Earth Sciences 55, 245-256. doi: 10.1016/j.jafrearsci.2009.04.009.

Journal of African Earth Sciences 55 (2009) 245–256

Contents lists available at ScienceDirect

Journal of African Earth Sciences

journal homepage: www.elsevier.com/locate/jafrearsci

The Markoye Shear Zone in NE Burkina Faso

Asinne Tshibubudze [a], Kim A.A. Hein [a,*], Pascal Marquis [b]

[a] School of Geosciences, University of the Witwatersrand, Private Bag 3, P.O. WITS, Johannesburg 2050, South Africa
[b] Orezone Resources Inc., 290 Picton Ave, Suite 201, Ottawa, ON, Canada K1Z 8P8

ARTICLE INFO

Article history:
Received 24 September 2008
Received in revised form 14 April 2009
Accepted 28 April 2009
Available online 13 May 2009

Keywords:
Birimian
Structure
Tectonics
Burkina Faso
West African Craton
Gold

ABSTRACT

Birimian supracrustal sequences in NE Burkina Faso are dominated by meta-volcaniclastic greywacke, intercalated meta-conglomerate, siltstone and shale. The sequences where subjected to two phases of deformation and contact metamorphosed to hornblende–hornfels facies during emplacement of pyroxenite–gabbro–norite (Yacouba Mafic complex), granodiorite–tonalite (Tin Taradat granodiorite–tonalite) and dolerite dykes.

Structural studies indicated that the NE-trending, first-order crustal-scale Markoye Shear Zone (MSZ; Markoye Fault of [Jeambrun, M., Delfour, J., Gravost, M., 1970. Carte géologique de L'Oudalan. Bureau De Recherches Geologiques et Miniéres, Burkina Faso.]) has undergone at least two phases of reactivation concomitant to two phases of regional deformation. The first phase of deformation, D1, resulted in the formation of NNW-NW trending folds and thrusts during dextral-reverse displacement on the MSZ. The deformation is termed the Tangaean Event and predates the Eburnean Orogeny. D2 phase involved a period of SE–NW crustal shortening and sinistral-reverse displacement on the MSZ, and is correlated to the Eburnean Orogeny ~2.1 Ga. Deformation in D2 is characterised by NE-trending regional folds (F2) and a pervasive NE-trending foliation (S2-C to S2). Within the MSZ, deformation is characterised by NNE-trending zones of mylonite that are bordered in the hangingwall and footwall by pseudotachylite veins. Buck quartz-carbonate veins and quartz cataclasite veins crosscut the mylonite zones and are, in turn, crosscut by quartz–chlorite–(muscovite) shears that formed during reactivation of the MSZ late in D2. Several generations of veins are recognised at the Essakane main deposit (EMZ): Arsenopyrite–pyrite–gold mineralization in quartz veins formed in D1 during metasomatic alteration of the host rocks; Vein-stockwork gold mineralization is interpreted to have formed late in D2.

1. Introduction

The NE-trending Markoye Shear Zone (MSZ) is a first-order crustal-scale structure that transects the Palaeoproterozoic Birimian Domain of the West African Craton in the east of Burkina Faso (Fig. 1). Between the towns of Dori and Tambão, which are situated west of the international border of Burkina Faso with Niger and south of the border with Mali, the position of the MSZ has been clearly established from combined regional magnetic data (RTP and RTP first vertical derivative) and Landsat imagery. The shear zone marks the western boundary of the Oudalan-Gorouol greenstone belt which extends into Niger. The greenstone belt hosts gold mineralization at Essakane goldfield, and numerous gold artisan sites throughout the study area.

According to Milési et al. (1989, 1992), Castaing et al. (2003) the MSZ is the boundary that separates Eburnean granitoids to the west from the Tarkwa Group meta-sedimentary units to the east. In Milési et al. (1989, 1991, 1992) and Hottin and Ouedraogo (1992), the MSZ is classified as a westerly-dipping thrust. However, unpublished structural studies completed for Ranger Minerals concluded that the MSZ is an east-verging thrust (Rogers and Dong, 2000) and part of a regional dextral strike-slip system.

In early 2007, the MSZ became the focus of structural studies by Orezone Resources Inc. to investigate the spatial and temporal relationships between gold deposits at the Essakane goldfield and to clarify the tectonic activity on the MSZ. During those studies, the lithologies and structure of a region between the Essakane goldfield and Tambão manganese deposit were documented. Numerous traverses where conducted across the MSZ and a GPS-referenced litho-structural database was established for the region. The results of those investigations indicate that stratigraphic and tectonic maps for the Oudalan-Gorouol greenstone belt, and regional geological maps for NE Burkina Faso need revision.

2. Geological setting

The overall lithostratigraphy of the eastern part of Burkina Faso is defined by NE-trending Birimian meta-sedimentary and

* Corresponding author. Tel.: +27 11 717 6623; fax: +27 11 717 6579.
E-mail addresses: Asinne.Tshibubudze@students.wits.ac.za (A. Tshibubudze), kim.hein@wits.ac.za (K.A.A. Hein), pmarquis@orezone.com (P. Marquis).

1464-343X/$ - see front matter © 2009 Elsevier Ltd. All rights reserved.
doi:10.1016/j.jafrearsci.2009.04.009

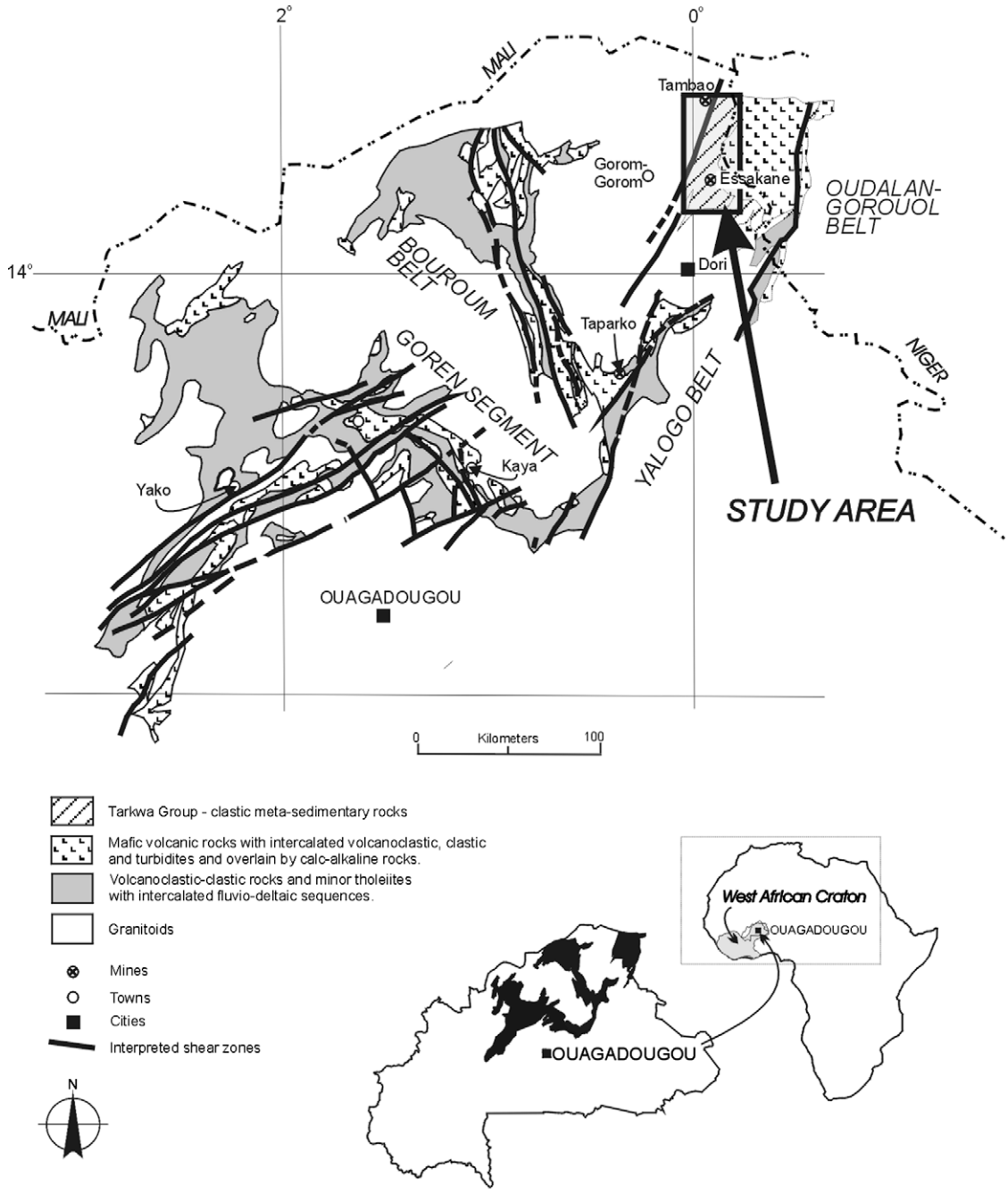

Fig. 1. The Oudalan-Gorouol greenstone belt of Burkina Faso and Niger, together with the Bouroum, Yalogo and Goren greenstone belts. The study area lies on the western margin of the Oudalan-Gorouol greenstone belt, approximately, 310 km NE of Ouagadougou. Modified after Feybesse et al. (1990) and Hein et al. (2004).

meta-volcanic sequences. The meta-volcanic sequences are dated (using Pb–Pb zircon) at between 2238 ± 5 Ma for a rhyolitic tuff from the Goren greenstone belt and 2171 ± 7 Ma for rhyolite from the Boromo greenstone belt (Castaing et al., 2003). The Tarkwa Group (2149–2132 Ma; U–Pb zircon, Davis et al., 1994) unconformably overlies the Birimian sequences. The Birimian sequences and Tarkwa Group are intruded by Eburnean granitoids at 2210–2095 Ma (combined Pb–Pb zircon, U–Th zircon, U–Th–Pb monazite and K–Ar; Castaing et al., 2003). Both sequences were deformed during the Eburnean Orogeny at 2100–2000 Ma (Milési et al., 1991, 1992; Ledru et al., 1991).

Junner (1935; 1940) in Leube et al. (1990) divided the Birimian stratigraphy into two parts. The lower Birimian series (B1) is predominantly sedimentary in origin and includes dacitic/rhyodacitic meta-volcaniclastic sediments, meta-greywacke with intercalated black meta-siltstone and manganiferous chert, argillite, shale and chemical meta-sedimentary rocks (Feybesse et al., 1990; Leube et al., 1990; Hirdes et al., 1996; Milési et al., 1991, 1992). The upper Birimian series (B2) consists of metamorphosed basic (tholeiitic pillow lavas of basaltic composition) and intermediate lavas and pyroclastic rocks (Leube et al., 1990; Milési et al., 1991, 1992; Hirdes et al., 1996). The layout of the Birimian stratigraphy is the subject of controversy: Hirdes et al. (1996) considered B2 to be younger than B1, however, Milési et al. (1991, 1992), Feybesse and Milési (1994) considered B1 to be younger than B2. In contrast, Hein et al. (2004) concluded that meta-volcanic and meta-pyroclastic units are interbedded with meta-sedimentary rocks throughout the type locality in the Goren greenstone belt.

During the polycyclic Eburnean Orogeny, numerous calc-alkaline plutons intruded the Palaeoproterozoic sequences (Pawlig et al., 2006) including tonalite (TTG), granodiorite, diorite and meta-diorite, and these are collectively termed Eburnean granitoids (Pons et al., 1995; Naba et al., 2004; Pawlig et al., 2006). The tectono-magmatic event related to the intrusion of the granitoids is dated at 2200–2070 Ma (U–Pb dating; Liégois et al., 1991). The granitoids comprise 50–70% of the Palaeoproterozoic basement of West Africa (Milési et al., 1989; Naba et al., 2004). Two emplacement events have been established (Castaing et al., 2003; Naba et al., 2004). A TTG Suite which is composed of granodiorite, tonalite and quartz-diorite was emplaced between 2210 and 2100 Ma (c.f. Castaing et al., 2003). The tonalite suite intruded and contact metamorphosed the Birimian sequences, and is banded (layered) and foliated in places (Hein et al., 2004; Naba et al., 2004). A granite suite intruded both the Birimian and the TTG suite and was emplaced between 2150 and 2095 Ma (c.f. Castaing et al., 2003). Gabbro, meta-gabbro, diorite and trondhjemite intrusions are syn-tectonic with emplacement of Birimian metavolcanic sequences and co-magmatic (Béziat et al., 2000). WNW-trending dolerite dykes crosscut all Birimian sequences, the Tarkwa Group and intrusive complexes in the NE of Burkina Faso, and are dated at 250 ± 13 Ma (K–Ar whole rock dating) (Hottin and Ouedraogo, 1992).

The Birimian sequences were metamorphosed during the Eburnean Orogeny with further metamorphism related to intrusion of granitoids. Metamorphic grade is greenschist facies (Milési et al., 1989, 1991; Bossière et al., 1996; Hirdes et al., 1996) with formation of chlorite–muscovite dominant mineral assemblages, and low to medium grade amphibolite facies with hornblende and andalusite dominant mineral assemblages (Bossière et al., 1996; Béziat et al., 2000; Naba et al., 2004) particularly in the contact aureole of granitoids (Pawlig et al., 2006).

The Tarkwa Group is defined from Ghana as comprising clastic meta-sedimentary rocks derived from erosion of the Birimian sequences (Leube et al., 1990; Milési et al., 1991). The Tarkwa Group unconformably overlies the Birimian sequence (Leube et al., 1990; Milési et al., 1992; Castaing et al., 2003). Milési et al. (1989, 1991) assigned deformation and greenschist facies metamorphism of the Tarkwa Group to the Eburnean Orogeny.

The Tarkwa Group has been divided into three units: the Banket series, phyllite unit and the meta-sandstone unit. The Banket series is further divided into the Banket quartz lithic meta-sandstone unit and the Banket meta-conglomerate unit (Tunks et al., 2004). Kwesie (1984 in Milési et al., 1991) and Kesse (1985 in Milési et al., 1991) characterised the meta-conglomerate unit in the Tarkwa region in Ghana as monomictic, consisting of over 90% rounded vein-quartz pebbles and approximately, 10% schist and quartzite pebbles. The matrix is mainly composed of 'silica' and black sands that are rich in heavy minerals including magnetite, ilmenite, rutile and tourmaline (Milési et al., 1989, 1991; Bossière et al., 1996). The Tarkwa Group meta-conglomerate hosts, and has been the source for, economic gold at the Tarkwa Mine, Ghana (Milési et al., 1991).

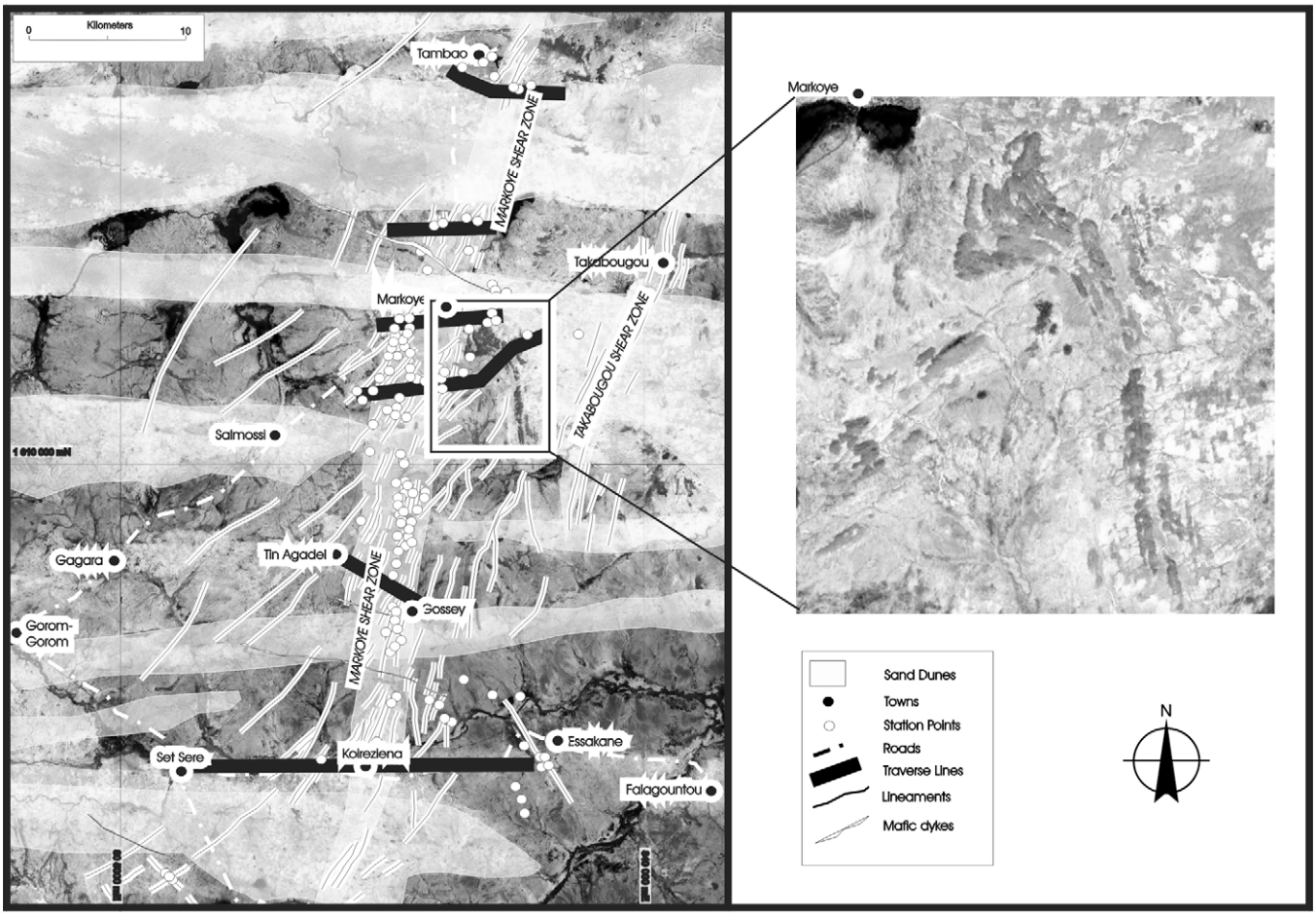

Fig. 2. Interpretative geology map of the Markoye Shear Zone based on combined regional magnetic data (RTP and RTP 1st vertical derivative), Landsat imagery, with Landsat image p194r050_741 as underlay. An interference fold pattern east of the town of Markoye is evident in the Aster image p194r050_741. East-west traverses across the MSZ are shown as black lines and station point data as white dots.

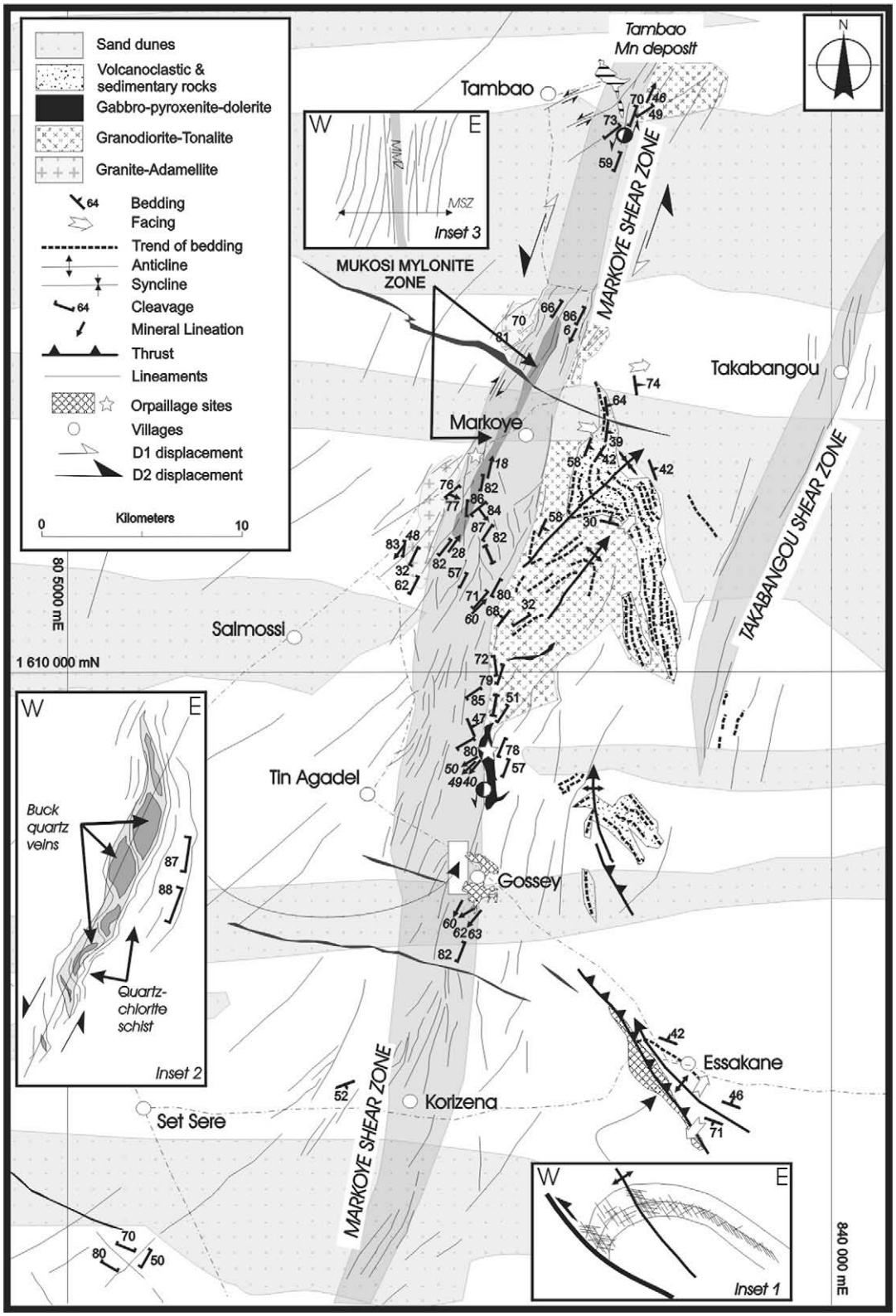

Fig. 3. Summary geology map of the geology of the MSZ, showing the position of selected towns, villages and sites of orpaillage activity. The MSZ is approximately, 5 km wide and subtended to the west and east by NE-trending shear zones. The Mukosi Mylonite Zone west of the town of Markoye is approximately, 20 km long and 0.25 km wide. The manganese deposit at Tambão is situated close to border with Niger. The Essakane gold orpaillage is characterised by an inclined, open and asymmetric anticline which is subtended in the footwall by a thrust (inset 1). Buck quartz-carbonate (±tourmaline) veins crop out along the Markoye Shear Zone, particularly at the Gosséy orpaillage (inset 2).

Bossière et al. (1996) established that the metamorphosed sequences of the Tarkwa Group of Burkina Faso (in the study area) were different from those defined in Ghana in that they contain euhedral zircons. North of the Essakane goldfield in Burkina Faso,

the Tarkwa Group meta-sedimentary rocks are deformed. Structural studies in the far NE of Burkina Faso are limited however, investigations by Nikiema et al. (1993), Cheilletz et al. (1994), Pons et al. (1995), Ama Salah et al. (1996), Bourges et al. (1998), Debat et al. (2003), Hein et al. (2004) in western Niger and the Goren, Bouroum and Yalago greenstone belts of Burkina Faso defined regional-scale NW-trending shear or mylonite zones in association with a NW-trending a regional foliation. Westerly-trending folds and thrusts have been mapped in the Goren, Bouroum and Yalgo greenstone belts in crosscutting relationship to NW-trending folds and foliation. Milési et al. (1991, 1992), Hirdes and Davis (1998), Hirdes et al. (1996) interpreted that the MSZ formed during the Eburnean Orogeny at 2150–2095 Ma.

The West African Craton hosts many mineral deposits, for example, gold, diamond, iron, manganese, silver, lead and zinc (Hastings, 1982; Milési et al., 1992). Several deposits and deposit styles occur in the Oudalan-Gorouol greenstone belt including; (1) Manganese mineralization at Tambăo close to border with Niger, (2) gold mineralization at Essakane, Gossey, Korizéna and Falagountou orpaillage (artisan) sites (Milési et al., 1992; Castaing et al., 2003), and (3) pegmatites veins bearing tourmaline, plagioclase and topaz crystals south of Tambăo (Figs. 2 and 3). Several deposits are associated with sulphidised brittle–ductile shear zones, including gold in sheeted and stockwork quartz veins, copper as malachite in buck quartz veins, and tourmaline and topaz in pegmatite and buck quartz veins (Foster and Piper, 1993; Lompo, 2001; Castaing et al., 2003). Foster and Piper (1993), Béziat et al. (2008) have restricted gold mineralization in the West African Craton to the Eburnean tectono-thermal event, but this does not include gold hosted by Tarkwa Group meta-sedimentary units in Ghana (Milési et al., 1991; Feybesse et al., 2006). Bossière et al. (1996) concluded that the Tarkwa Group meta-sedimentary units in the study area have no economic value.

3. Methodology

Prior to detailed litho-structural mapping in January and March 2007, magnetic data (RTP and RTP first vertical derivative) and Landsat imagery were used to delineate the position, width and overall trend of the MSZ. From this study, the MSZ is approximately, 5 km wide and associated with several NE-trending shear zones that crop out to the west and east (Fig. 3). An interference fold pattern east of the MSZ is evident from Landsat imagery. Westerly-trending longitudinal sand-dunes transect the study area.

Geographic and geologic reconnaissance studies of the area were conducted before completion of several east–west traverses across the MSZ to confirm accessibility (Fig. 2). Lithological and structural data were recorded for station points on traverse lines. GPS position was established using UTM grid co-ordinates (WGS 84, 30P, 31P). Due to the high degree of disturbance, sites of orpaillage activity provided limited, but important lithological data. Stratigraphic facing was readily established from primary sedimentary features (e.g., bed gradation, scour and fill, slumps, cross-bedding, ripple marks). In areas of limited outcrop, with a thin cover of ferricrete or alluvium, sub-crop mapping was used to provide qualitative stratigraphic data. This combined data has been summarised in Figs. 2 and 3 and is detailed below.

4. Rock types

The rocks of the study area consist of metamorphosed, folded, sheared and/or mylonitized volcano-sedimentary and sedimentary sequences. They crop out on prominent hills east and southeast of the village of Markoye and in rare outcrops throughout the Essakane goldfield, but outcrop in the study is limited (less than 25%). The lithostratigraphy defines open to tight folds that trend NNW and NE creating a macroscopic fold inference pattern. Two sequences are defined:

1. A volcaniclastic greywacke sequence that is composed of bedded to cross-bedded, slump-folded, medium-grained, quartz and feldspar-rich sand. Greywacke beds predominate (Fig. 4a). Fuchsite layers (Cr–muscovite, c.f., Navas et al., 2004), thin chert beds, shale with mud-cracks and fine laminations, siltstone and rare pebble beds and mud balls are intercalated with greywacke units.
2. A sequence of interbedded conglomerate–greywacke–siltstone–shale units that conformably overlays the volcaniclastic greywacke sequence. Conglomerate beds are polymictic and matrix-supported (Fig. 4b and c). They are composed of subrounded to angular boulders (up to 30 cm in diameter) of granite, granodiorite, gabbro, chert, quartz vein clasts, andesite, basalt and volcaniclastic sedimentary rocks (Fig. 4c). The matrix is generally composed of fine to coarse-grained, poorly-sorted volcaniclastic greywacke or gritstone.

The volcano-sedimentary and sedimentary sequences were intruded by granite–adamellite and granodiorite–tonalite plutons, and pyroxenite–gabbro–norite and dolerite dykes. The plutons and dykes have contact metamorphosed the rocks of the region to hornblende–hornfels facies. In most places, lithologies are capped by laterite and alluvium and/or dune sand profile.

The dominant rock types of the Essakane goldfield are deeply weathered greywacke–siltstone–shale interbeds that host quartz-carbonate veins. Gold–arsenopyrite–pyrite mineralization occurs within the alteration halo surrounding veins, particularly in competent greywacke units. The greywacke–siltstone–shale units are mesoscopically folded. Siltstone units are spotted with ovoid porphyroblasts of cordierite suggesting thermal metamorphism. The sequence has been contact metamorphosed to hornblende–hornfels facies in the contact aureole of dolerite dykes. Rare stromatoforms occur in siltstone sequences south of the Gossey orpaillage (artisan mine).

Laterite is randomly distributed throughout the northern part of the study area. In an isotopic study conducted across the West African Craton, using ^{10}Be and ^{26}Al isotopic depletion ratios of laterite, Brown et al. (1994) concluded that in-situ laterite in Burkina Faso formed during the upper Cretaceous to Eocene.

5. Intrusions

5.1. Granite–adamellite

A granite–adamellite pluton crops out in prominent hills west of the MSZ and near the village of Markoye (Figs. 3 and 4d and e). It is medium to coarse grained, and composed of millimetre-sized crystals of potassium feldspar, quartz, plagioclase, biotite and hornblende in a quartz–feldspar groundmass. The granite–adamellite is foliated and lineated.

5.2. Yacouba Mafic complex (YMC)

The YMC crops out 5 km north of the Gossey orpaillage (Figs. 3 and 4f) and has contact metamorphosed supracrustal rocks to hornblende–hornfels facies. The YMC comprises a layered pyroxenite and gabbro complex and hosts discontinuous gabbro–norite layers that contain rare lithic xenoliths. Pyroxenite layers consist of >1 cm pyroxene and olivine phenocrysts in a pyroxene–olivine–nepheline groundmass. Several NW-trending gabbro–dolerite and pyroxenite dykes radiate away from the main intrusion.

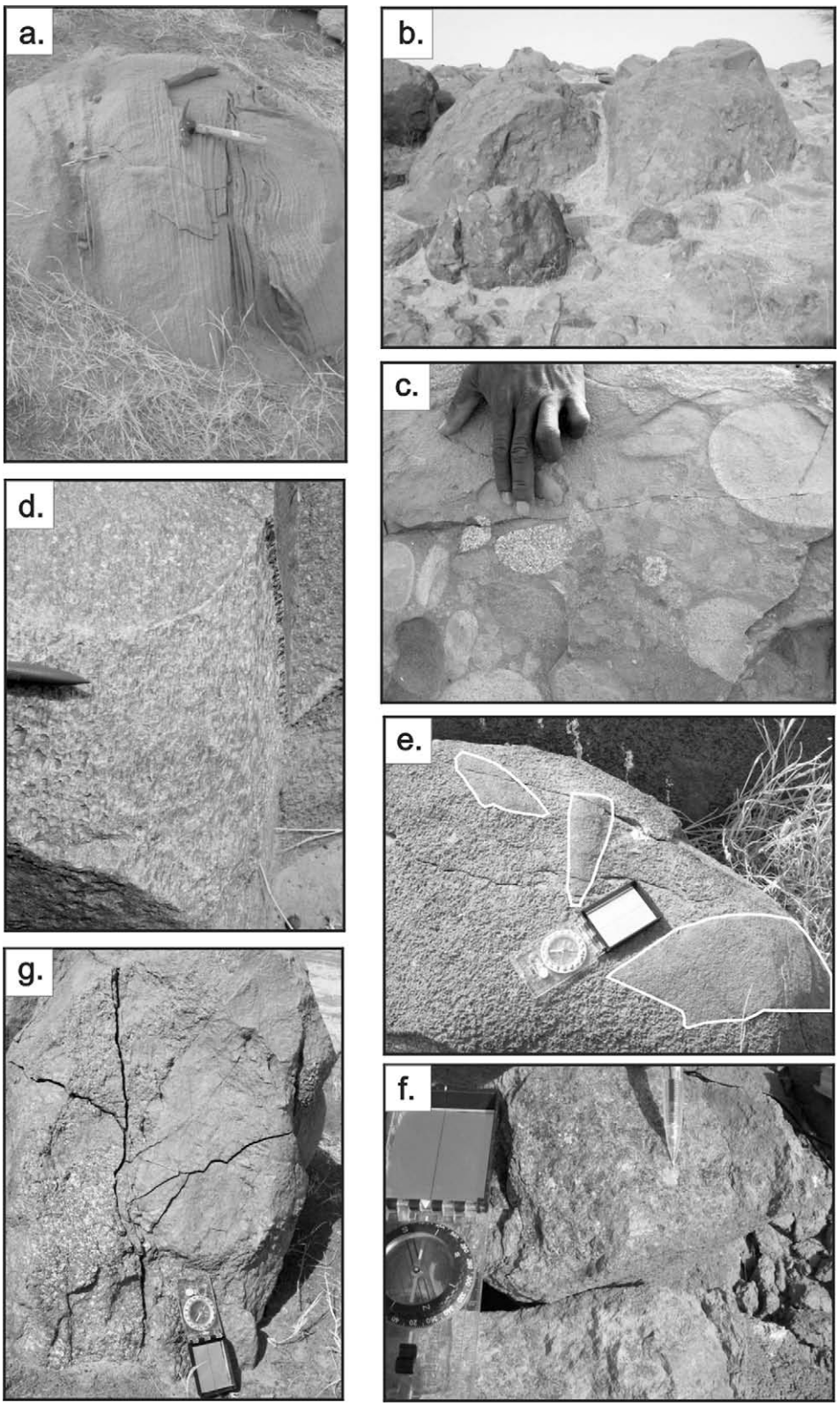

Fig. 4. (a) Typical greywacke beds of the volcanoclastic greywacke sequence (31P 0183624, 1621482, station 006) crop out sporadically, but readily exhibit cross-bedding and slump-folding. (b) and (c) Conglomerate beds of the interbedded conglomerate–greywacke–siltstone–shale sequence. Conglomerate beds are polymictic and matrix-supported. They are composed of sub-rounded to angular boulders (up to 30 cm in diameter) of granite–adamellite, granodiorite, gabbro, chert, vein quartz, andesite, basalt and volcanoclastic sedimentary rocks in a greywacke–gritstone matrix (31P 0182691, 1619700; station 161). (d) Granite–adamellite pluton is composed of millimetre-sized crystals of potassium feldspar, quartz, plagioclase, biotite and hornblende in a quartz–feldspar groundmass. The granite–adamellite is foliated and lineated (30P 0819980, 1615449; station 128). (e) The Tin Taradat granodiorite–tonalite intrudes the granite–adamellite (31P 0176940, 1614340, station 100). Angular xenoliths of these rock types are scattered throughout the carapace. (f) and (g) Pyroxenite of the Yacouba Mafic complex (31P 0177094, 1605509; station 25) is intruded by the Tin Taradat granodiorite–tonalite (31P 0178809, 1612867, station 089). The granodiorite–tonalite is coarse to medium, and composed of plagioclase, quartz, hornblende and biotite.

The inner contact aureole of the YMC and radiating dykes is characterised by numerous contraction fractures and veins. The YMC and associated aureole are crosscut by buck quartz and quartz-carbonate veins, some of which are prospective for gold mineralization.

5.3. Tin Taradat granodiorite–tonalite

The Tin Taradat granodiorite–tonalite crops out over less than 20% of the study area and intrudes volcano-sedimentary and sedimentary sequences east of the MSZ. It also intrudes the granite–adamellite and Yacouba Mafic complex, and angular xenoliths of these rock types are hosted by the carapace of the granodiorite–tonalite (Fig. 4e and g).

The granodiorite–tonalite is coarse to medium, and composed of plagioclase, quartz, hornblende and biotite. It hosts elongate-ovoid mafic xenoliths that trend NW and plunge westerly. Between Gossey orpaillage and Tambão manganese deposit (Fig. 3), the pluton is foliated or sheared in the MSZ (Fig. 5a), but is also crosscut by discrete quartz–chlorite–(muscovite) shears, numerous mesocopic pseudotachylite veins (Fig. 5b) and rare plagioclase–tourmaline–topaz pegmatite veins.

5.4. Dolerite dykes

A swarm of NW-trending dolerite dykes crosscuts the study area. They are composed of plagioclase, clinopyroxene and magnetite, and are granophyric in texture. The dykes crosscut greywacke–siltstone sequences at the Essakane goldfield, which they contact metamorphose to hornblende–hornfels facies.

6. Structure

The study region has been divided into discrete structural domains:

1. Domain 1 – Broad NNE-trending shear zones that include the Markoye and Takabangou shear zones (Fig. 3). The MSZ is ~5 km wide and is steeply dipping. It is a composite structure of discontinuous faults, shears, L-tectonites, zones of

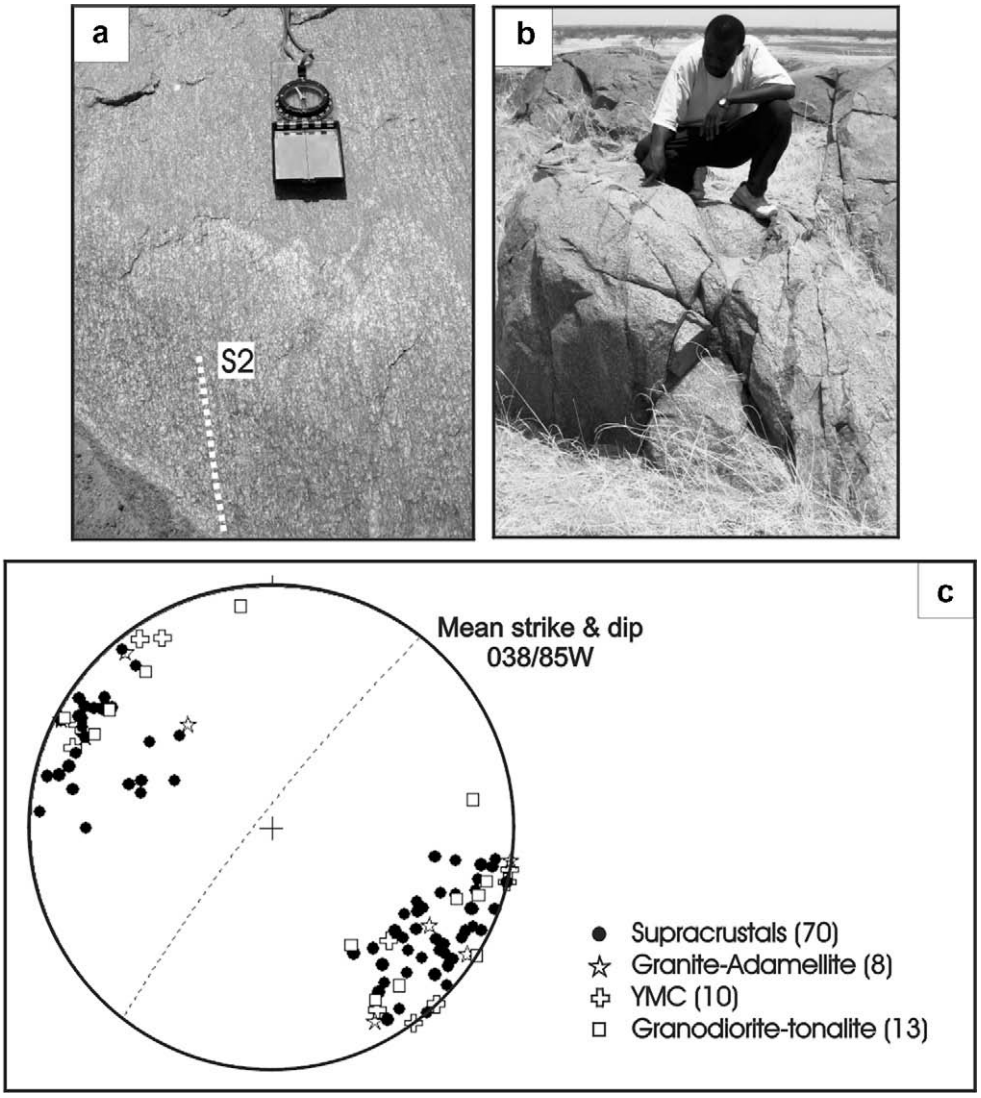

Fig. 5. (a) The granodiorite–tonalite between Gossey orpaillage and Tambão manganese deposit is foliated or sheared in the MSZ (31P 0184509, 1634808, station 164). (b) The granodiorite–tonalite is crosscut by numerous mesocopic psuedotachylyte veins south and SW of the village of Markoye (31P 0177835, 1616478, station 150). (c) Equal area stereographic projection of poles of S2-C and S2 from the study area. The foliation crosscuts supracrustal rocks, granite–adamellite, the YMC and Tin Taradat granodiorite–tonalite indicating it formed after those rocks where emplaced.

mylonitisation and pseudotachylite vein complexes. It hosts en-échelon buck quartz and quartz-carbonate vein arrays, and late discontinuous quartz–chlorite–(muscovite) shears. The MSZ has undergone at least two phases of brittle–ductile deformation (dextral-reverse followed by sinistral-reverse). The Takabangou shear zone is currently the focus of further investigation by the authors.

2. Domain 2 – The domain between NNE-trending shears is characterised by NW-NNW or NE-trending shear zones, asymmetric folds, and foliations. NW–NNW trending shear zones and folds (F1) are crosscut by NE-trending shear zones and folds (F2). NE-trending shear zones and F2 curve into and join the MSZ (Fig. 3), and occasionally host buck quartz, cataclastite, quartz-carbonate and pseudotachylite vein arrays. The superposition of F2 on F1 has resulted in a type 2 interference pattern which is characterised by symmetric to non-symmetric, crescent shaped domes and basins (Thiessen and Means, 1980).

Consequenlty, two deformations, D1 and D2, are currently defined in the study area. D1 resulted in the development of the NW–NNW trending shears and west-verging asymmetric folds (F1), and the sense of displacement on the MSZ was dextral (reverse). D2 marked a period of sinistral (reverse) displacement on the MSZ with refolding of F1 to form NE-trending folds (F2).

6.1. Deformation event D1

D1 is associated with the formation of meso- to macroscopic NW–NNW trending folds (F1) that are evident at the Essakane orpaillage (in exploration trenches) and NE of Gossey orpaillage (Fig. 3). The folds are associated with NNW-trending thrusts that dip eastward. South of the township of Set Sere and within the MSZ, NNW-trending shears are crosscut by NE-trending shears.

At Essakane, gold mineralization in crosscutting stockwork and breccia quartz-carbonate veins is hosted by a shallowly north plunging F1 anticline (facing determined from scour and fill, and graded beds). The fold is asymmetric and open to overturned (Fig. 3, inset 1). A pervasive cleavage was not apparent, but the rocks in the Essakane orpaillage are deeply weathered. The fold profile indicates that the axial plane is moderately east-dipping. The data suggests that the tectonic transport during formation of F1 and thrusts at Essakane was approximately, SW.

6.2. Deformation event D2

D2 is marked by the period of progressive SE-NW crustal shortening in which NE-trending folds (F2), L-S tectonite, pseudotachylite veins, buck quartz-carbonate (±tourmaline) veins, cataclasite

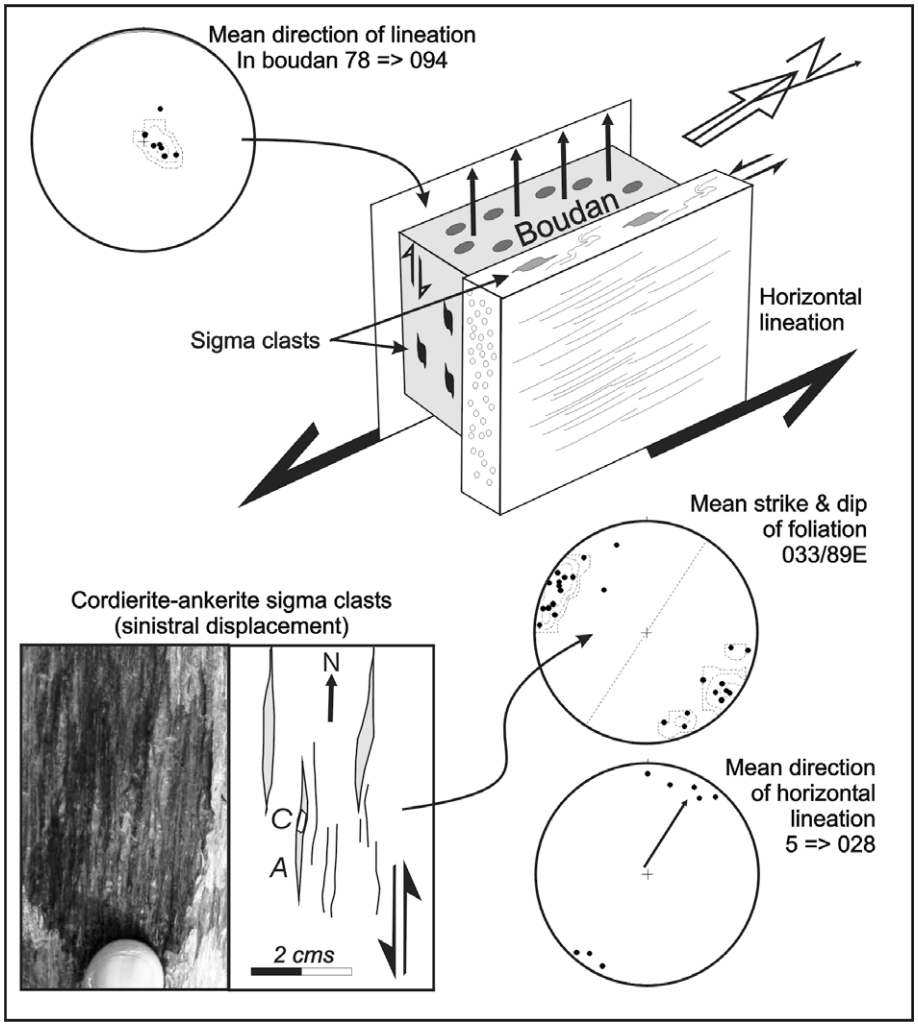

Fig. 6. Schematic of the Mukosi Mylonite Zone west of the town of Markoye. NNE-trending macro-boudins, with a mean direction of stretching lineation of 78° towards 094°, are bounded by discrete zones of quartz–mylonite or shear, with a mean strike and dip of 033°/98° E and near horizontal stretching lineation of 5° towards 028°. Sigma clasts of cordierite (C) with ankerite tails (A) describe sinistral displacement in the plane of the shears.

and quartz–chlorite–(muscovite) shears where formed. A pervasive NE-NNE trending S2-C to S2 disjunctive foliation, with a calculated mean strike and dip of 038° 85°W (Fig. 5c), crosscuts supracrustal rocks, granite–adamellite, the YMC and Tin Taradat granodiorite–tonalite, and also formed during D2. The foliation is weakly refracted northward in the YMC and Tin Taradat granodiorite–tonalite.

D2 also marks a period of sinistral (reverse) displacement on the MSZ. A zone of mylonite to ultra-mylonite in the MSZ is inferred to have formed during D2; the zone is herein termed the Mukosi Mylonite Zone or MMZ.

The MMZ crops out southwest of the town of Markoye and is NNE-trending. It crosscuts meta-sedimentary rocks and granite–adamellite indicating it formed after deposition of sedimentary units and emplacement of local plutons. A well-developed stretching lineation occurs in outcrops of granite–adamellite west of the MMZ (Fig. 4d).

The MMZ is characterised by NNE-trending macro-boudins that are bounded by discrete zones of mylonite or shear (Fig. 6). Macro-boudins are defined by a vertical to steeply east-plunging stretching lineation (calculated mean of 78° towards 098°), and σ and δ porphyroblasts. Displacement within the boudins is thus interpreted as vertical to steep (east). The steeply-dipping zones of mylonite or shear that bound macro-boudins are characterised by a steeply east-dipping, NNE-trending foliation (calculated mean strike and dip of 033°/89°E) and a near horizontal stretching lineation that trends NE. They host shear bands, extension fractures, meso-isoclinal and asymmetric intrafolial folds and, together with numerous σ and δ clasts including sigmoidal porphyroblasts of cordierite and ankerite, define a sinistral sense of displacement. Interestingly, these NNE-trending zones of mylonite or shear are continuous in the field into NE-trending pseudotachylite vein arrays that crosscut granite–adamellite and the Tin Taradat granodiorite–tonalite to the east and west of the MSZ, respectively.

With respect to pseudotachylite vein arrays, they crop out in the region between Tin Agadel and NW of the town of Markoye, and Salmossi village eastward for a distance of 10–15 km. They present as centimetre-scale veinlets to en echelon lode-type veins (up to 100 m long and 5 m wide), multiple, stockwork or breccia vein types. In the Tin Taradat granodiorite–tonalite, they occur as conjugate vein sets, and rarely as shear veins. The veins and lodes are interpreted to have formed during high strain conditions and sinistral displacement on the MMZ, the resulting frictional heat melting the host rocks (Davis and Reynolds, 1996).

Buck quartz-carbonate (±tourmaline) veins crop out at several locations along the MSZ, particularly north and south of Gossey orpaillage. They attain a maximum size of 150 m long and 10 m wide, or are developed as small lenticular bodies. They are commonly sinusoidal and form a left-stepping en echelon array that is suggestive of sinistral displacement during their formation (Fig. 3, inset 2). The lodes rarely host centimetre-sized arsenopyrite ($AsFeS_2$) crystals and copper oxide as malachite ($Cu_2CO_3(OH)_2$). A number of buck quartz-carbonate veins are fractured, boudinaged and lineated, producing an egg box type outcrop.

North of the Gossey Orpaillage buck quartz-carbonate veins are juxtaposed with a gold-bearing quartz Fe-rich cataclasite lode that is bounded by a quartz–chlorite–(muscovite) shear. The lode and shear crosscuts the Yacouba Mafic complex and is the site of an artisan gold mine. An historic artisan mine in quartz–chlorite–(muscovite) shear is also situated 3 km west of the town of Markoye where it crosscuts the MMZ, and discontinuous quartz–chlorite–(muscovite) shears crosscut the MSZ throughout the study area. The shears are interpreted as late reactivation of the MSZ. The calculated mean strike and dip of the schistosity in quartz–chlorite–(muscovite) shears is 025°/86°W.

7. Discussion

7.1. Supracrustal rocks and environment of deposition

Although limited by the availability of outcrop in the study area, two stratigraphic sequences are recognised in the Oudalan-Gorouol greenstone belt; a volcanoclastic greywacke sequence and an interbedded conglomerate–greywacke–siltstone–shale sequence. Our observations indicate that these supracrustal rocks were contact metamorphosed to hornblende–hornfels facies during emplacement of the YMC, Tin Taradat granodiorite–tonalite and dolerite dykes, but primary sedimentary features are preserved as compositional layers including graded bedding, cross-bedding, ripple marks, slumps, and scour and fill. These primary structures indicate a single environment of deposition: shallow marine continental shelf or a delta-front setting. The fining-up sequence (graded bedding), slumps (gravity flow), mud balls, ripples, scour and fill, mud-cracks and laminations in the meta-volcaniclastic greywacke sequence suggests that the setting was subjected to tidal and or turbidity currents (Eriksson et al., 1998, 2005; Sultan and Björklund, 2006). The upward-fining, laminations, slumps, and graded beds with scour and fill bases, are characteristic of turbidity currents that operate at a delta front (Shanmugan, 1997; Sultan and Björklund, 2006), and the ripples are characteristic of tidal currents (Sultan and Björklund, 2006). The presence of stromatolites in greywacke–siltstone beds also suggests shallow marine environment of deposition with high sea salinity (Altermann, 2002; Eriksson et al., 2005).The conglomerate units were probably deposited in a proximal-medial setting in a deltaic environment (Eriksson et al., 1998) or could indicate fluvial deposition.

These sequences are currently assigned to the Tarkwa Group (Milési et al., 1989, 1992; Castaing et al., 2003), but this is perhaps not the best classification. Conglomerate units that characterise the Tarkwa Group in Ghana (c.f. Milési et al., 1989, 1991; Bossière et al., 1996) generally consist of greater than 90% rounded vein-quartz pebbles and 10% schist and quartzite pebbles in a black sand matrix, which does not accord with the character and composition of the numerous conglomerate units of the study area: they consist of sub-angular to sub-rounded clasts and boulders of basalt, andesite, granodiorite (*sensu-stricto*), granite (*sensu-stricto*), volcaniclastic meta-sediments, chert, and lithic fragments in a greywacke–lithic matrix, and are in no way similar to Tarkwa Group conglomerates in Ghana. Moreover, the poverty or absence of clasts or boulders that are composed of meta-sedimentary rocks, dacite/rhyodacite, manganiferous chert, chemical sediments and/or pyroclastic rocks, which together with basic (tholeiitic pillow lavas and basalt) and intermediate lavas characterise the Birimian sequences, is problematic and contradictory. The conglomerate units do not reflect erosion of the Birimian sequences as described by Leube et al., 1990, Milési et al., 1991. Further to this, an unconformity that separates Birimian and Tarkwaian sequences (Leube et al., 1990; Milési et al., 1992; Castaing et al., 2003) has not been found in the study area, or established for the Oudalan-Gorouol greenstone belt; therefore it cannot be concluded that the supracrustal rocks of the region belong to the Tarkwa Group. They are tentatively reclassified as Birimian flysch-type sediments.

7.2. Structural and metamorphic history

The Palaeoproterozoic supracrustal rocks of the Oudalan-Gorouol greenstone belt in the study area have been folded, mylonitised, sheared and regional metamorphosed during at least two deformation events, and contact metamorphosed by syn- to post-orogenic plutons and late dolerite dykes. The structural and metamorphic history of the study area is summarised in Fig. 7.

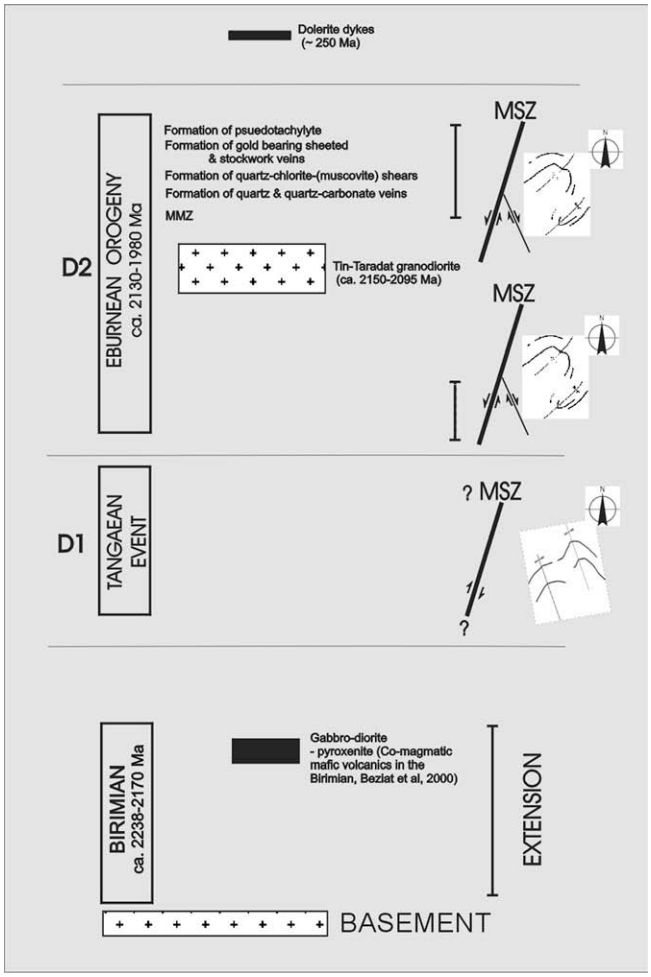

Fig. 7. Event chart for the Markoye Shear Zone and western Oudalan-Gorouol greenstone belt, incorporating stratigraphic and structural events from this study.

The supracrustal rocks where intruded and contact metamorphosed by the Yacouba Mafic complex (YMC) which comprises a pyroxenite–gabbro–norite body with radiating dykes. These are crosscut by D2 quartz–chlorite–(muscovite) shears. The YMC is intruded by the Tin Taradat pluton. It follows that the YMC was emplaced during or after deposition of the supracrustal rocks, and before D2 and emplacement of the granodiorite–tonalite. As stated by Ama Salah et al. (1996), Béziat et al. (2000), mafic intrusions in eastern Burkina Faso are syn-tectonic with Birimian meta-volcanic sequences and co-magmatic. The YMC is thereby tentatively assigned to that tectonic event.

Although the relationship of the granite–adamellite west of Markoye is poorly constrained with respect to the YMC and D1, relative chronologies demonstrate that it was emplaced before the Tin Taradat granodiorite–tonalite and before D2. Xenoliths of granite–adamellite occur in the granodiorite–tonalite, and the granite–adamellite is crosscut by D2 mylonite and shears. The granitoid is lineated and foliated (by S2-C and S2) and crosscut by pseudotachylite veins. It was therefore emplaced pre-D2 and perhaps pre- to syn-D1. Certainly, its relative age does not allow to be assigned to an Eburnean magmatic event at 2210–2100 Ma for emplacement of TTG suite plutons, and 2150–2095 Ma for emplacement of granitoid suite plutons, because it is intruded by the TTG granitoid–tonalite and is therefore older than those rocks. It is suggested that the granite–adamellite forms part of an undefined basement rock series in the study.

Subsequent to deposition of supracrustal rocks and emplacement of the YMC, the rocks of the region were folded to form a NNW-NW trending fold–thrust belt (during D1). NNW-NW trending folds at Essakane and Gossey orpaillages were formed at this time, and displacement on the MSZ was dextral (reverse). Tectonic transport was to the SW, as indicated by fold asymmetry and fold–thrust vergence. This concurs with Rogers and Dong (2000) who concluded that the MSZ was part of a dextral strike-slip system.

Following deformation event D1, the supracrustal rocks where folded and regional metamorphosed to greenschist facies (D2). D2 deformation accompanied emplacement of the Tin Taradat granodiorite–tonalite and concomitant contact metamorphism to hornblende–hornfels facies during the Eburnean Orogeny (Boher et al., 1992; Pons et al., 1995; Béziat et al., 2000; Hein et al., 2004; Naba et al., 2004). Displacement on the MSZ was sinistral (reverse). The Mukosi Mylonite Zone (MMZ) and ancillary pseudotachylite vein arrays formed during high strain frictional melting after emplacement and cooling of the granodiorite–tonalite. Quartz–carbonate veins, cataclasite veins and quartz–chlorite–(muscovite) shears (some hosting gold mineralization) formed late during progressive deformation and continued sinistral-reverse displacement on the MSZ. Discrete and discontinuous high strain zones in the MSZ were expressed locally by the formation of L-tectonites (e.g., as egg box textured quartz-carbonate veins).

A series of WNW-trending dolerite dykes were emplaced during the Phanerozoic and crosscut all rock units in the study area.

The relative chronologies and crosscutting relationships indicate that the MSZ has been active over a considerable period of time and tectonic activity was intimately linked to regional deformation. The MSZ is a complex structure which is steeply east-dipping, i.e., the MMZ is interpreted as the axis of the MSZ and is steeply east-dipping and the trend of enclosing foliations (irrespective of host rock type) is steeply west-dipping.

Importantly, the two deformation events recorded in the study area can not reflect a single progressive deformation because NNW-NW trending D1 shears and folds are crosscut by NE-trending D2 shears and folds, and displacement on the MSZ shifted from dextral-reverse to sinistral-reverse, i.e., one tectonic regime crosscuts another. This can only be attributed to a fundamental shift in the palaeo-stress field from SW-directed to NW-directed, and/or, the existence of two discrete and unrelated compressional events separated by time. This notion is supported by observations of Ouedraogo and Prost (1986), Feybesse et al. (1990), Hein et al. (2004) from the Boromo and Goren greenstone belts in Burkina Faso, where NW-trending folds and foliations that formed prior to the Eburnean tectono-thermal event, are recorded. Ledru et al. (1991) also noted the presence of foliations and refolded foliations in the Kedougou Inlier of West Africa that formed prior to the Eburnean tectono-thermal event. They suggested that the foliations and refolded foliations indicated an older tectonic phase that trended NW-SE to N-S.

Moreover, the character of deformation from D1 to D2 is quite different. Deformation event D1 was characterised by formation of open asymmetric folds and thrusts, while deformation event D2 was characterised by folds, shears, mylonite and formation of vein arrays of pseudotachylite and quartz carbonate. Deformation event 1 can be classified as a discrete tectonic event and is therefore introduced as the Tangaean Event (Tanga meaning low hills in the Mossi language). The Tangaean Event is the focus of ongoing research by the authors through the AMIRA P934 WAXI project (phase II).

8. Tectonic evolution and conclusions

The tectonic evolution of the MSZ in the Oudalan-Gorouol greenstone belt may be described by following events:

1. The lithologies of the greenstone belt adjacent to MSZ record the deposition of volcaniclastic greywacke and interbedded conglomerate–greywacke–siltstone–shale sequences on an inferred granite–adamellite basement, in a marine–deltaic environment. The emplacement of pyroxenite–gabbro–norite (Yacouba Mafic complex) is interpreted as syn-tectonic with Birimian sequences and co-magmatic.
2. The formation of a NW-trending fold-thrust belt in D1 (during the Tangaean Event), preceded the Eburnean Orogeny. The Essakane orpaillage straddles the hinge and eastern limb of an F1 anticline and is characterised by crosscutting vein arrays, stockwork veins and breccia lodes.
3. The second deformation, D2, was expressed through the development of NNE to NE-trending mylonite (the MMZ) and quartz–chlorite–(muscovite) shears, NE-trending folds (F2) and a penetrative S2-C to S2 foliation, L-tectonites, and vein arrays of pseudotachylite, quartz-carbonate, buck quartz, and quartz cataclasite. Regional metamorphism was to greenschist facies. Emplacement of granodiorite–tonalite and concomitant contact metamorphism to hornblende–hornfels facies preceded formation of pseudotachylite vein arrays.
4. The steeply east-dipping MSZ has been active over a considerable period of time and tectonic activity was intimately linked to regional deformation. Field data indicates that displacement on the MSZ was dextral-reverse during D1 and sinistral reverse during D2. Steeply west-dipping foliations are observed in the hangingwall and footwall of the MMZ. The MSZ is thus steeply east-dipping.

Acknowledgements

This project was supported by AngloGold Ashanti, Goldfields Mining, Orezone Resources Inc., AMIRA P934 sponsors and University of Ouagadougou. The staff at Orezone Resources offices in Ouagadougou and Essakane, and Prof. M. Lompo and Mr. Y. Traoré assisted with field logistics, transport and accommodation. This manuscript was significantly improved by the careful reviews of T.C. McCuaig and all other reviewers. M. Jessell provided the Aster image and completed an initial review of the manuscript.

References

Altermann, W., 2002. The evolution of life and its impact on sedimentation. In: Altermann, W., Corcoran, P.L. (Eds.), Precambrian Sedimentary Environments: A Modern Approach to Ancient Depositional Systems. The International Association of Sedimentologists, pp. 15–32 (Special Publication No. 33).

Ama Salah, I., Liegeois, J-P., Pouclet, A., 1996. Evolution d'un arc insulaire océanique birimien précoce au Liptako nigérien (Sirba): géologie, géochronologie et géochimie. Journal of African Earth Sciences 22, 235–254.

Béziat, D., Bourges, F., Debat, P., Lompo, M., Martin, F., Tollon, F., 2000. A Paleoproterozoic ultramafic-mafic assemblage and associated volcanic rocks of the Boromo greenstone belt: fractionates originating from island-arc volcanic activity in the West African craton. Precambrian Research 101, 25–47.

Béziat, D., Dubois, M., Debat, P., Nikiéma, S., Salvi, S., Tollon, F., 2008. Gold metallogeny in the Birimian craton of Burkina Faso (West Africa). Journal of African Earth Sciences 50, 215–233.

Boher, M., Abouchami, W., Michard, A., Albarede, F., Arndt, N.T., 1992. Crustal growth in West Africa at 2.1 Ga. Journal of Geophysical Research 97 (B1), 345–369.

Bossière, G., Bonkoungou, I., Peucat, J.J., Pupin, J.P., 1996. Origin and age of Palaeoproterozoic conglomerates and sandstones of the Tarkwaian Group in Burkina Faso, West Africa. Precambrian Research 80, 153–172.

Bourges, F., Debat, P., Tollon, F., Munoz, M., Ingles, J., 1998. The geology of the Taparko gold deposit, Birimian greenstone belt, Burkina Faso, West Africa. Mineralium Deposita 33, 591–605.

Brown, E.T., Bourlès, D.L., Colin, F., Safno, Z., Raisbeck, G.M., Yiou, F., 1994. The development of iron crust lateritic systems in Burkina Faso, West Africa examined with in-situ-produced cosmogenic nuclides. Earth and Planetary Science Letters 124, 19–33.

Castaing, C., Billa, M., Milési, J.P., Thiéblemont, D., Le Mentour, J., Egal, E., Donzeau, M. (BRGM) (coordonnateurs) et Guerrot, C., Cocherie, A., Chevremont, P., Tegyey, M., Itard, Y. (BRGM), Zida, B., Ouedraogo, I., Kote, S., Kabore, B.E., Ouedraogo, C. (BUMIGEB), Ki, J.C., Zunino (ANTEA), 2003. Notice explicative de la Carte géologique et miniére du Burkina Faso à 1/1 000 000.

Cheilletz, A., Barbey, P., Lama, C., Pons, J., Zimmermann, J-L., Dautel, D., 1994. Age de refroidissement de la croûte juvénile birimienne d'Afrique de l'Ouest; Données U–Pb, Rb–Sr et K–Ar sur les formations à 2, 1 Ga du SW-Niger. Comptes Rendus de l'Académie des Sciences de Paris, Série II, Sciences de la Terre et des Planetes 319, 435–442.

Davis, D.W., Hirdes, W., Schaltegger, Nunoo, A., 1994. U–Pb age constraints on deposition and provenance of Birimian and gold-bearing Tarkwaian sediments in Ghana, West Africa. Precambrian Research 67, 89–107.

Davis, G.H., Reynolds, S.J., 1996. Structural Geology of Rocks and Regions. John Wiley and Sons Inc., Canada. 775 p..

Debat, P., Nikiéma, S., Mercier, A., Lompo, M., Béziat, D., Bourges, F., Roddaz, M., Salvi, S., Tollon, F., Wenmenga, U., 2003. A new metamorphic constraint for the Eburnean orogeny from Paleoproterozoic formations of the Man shield (Aribinda and Tampelga countries, Burkina Faso). Precambrian Research 123, 47–65.

Eriksson, P.G., Catuneanu, O., Sarkar, S., Tirsgaard, H., 2005. Patterns of sedimentation in the Precambrian. Sedimentary Geology 176, 17–42.

Eriksson, P.G., Condie, K.C., Tirsgaard, H., Mueller, W.U., Altermann, W., Miall, A.D., Aspler, L.B., Catuneanu, O., Chiarenzelli, J.R., 1998. Precambrian clastic sedimentation systems. Sedimentary Geology 120, 5–53.

Feybesse, J.L., Billa, M., Guerrot, C., Duguey, E., Lescuyer, J.L., Milési, J.P., Bouchot, V., 2006. The Palaeoproterozoic Ghanaian province. Geodynamic model and ore controls, including regional stress modelling. Precambrian Research 149, 149–196.

Feybesse, J.L., Milési, J.P., 1994. The Archaean/Proterozoic contact zone in West Africa: a mountain belt of decollement thrusting and folding on a continental margin related to 2.1 Ga convergence of Archaean cratons? Precambrian Research 69, 199–227.

Feybesse, J.L., Milési, J.P., Ouedraogo, M.F., Prost, A., 1990. La ''ceinture'' protérozoïque inférieur de Boromo–Goren (Burkina Faso): un exemple d'interférence entre deux phases transcurrentes éburnéennes. Comptes Rendus de L'Académie des Sciences 310 (II), 1353–1360.

Foster, R.P., Piper, D.P., 1993. Archaean lode gold deposits in Africa: crustal setting, metallogenesis and cratonization. Ore Geology Reviews 8, 303–347.

Hein, K.A.A., Morel, V., Kagoné, O., Kiemde, F., Mayes, K., 2004. Birimian lithological succession and structural evolution in the Goren segment of the Boromo–Goren greenstone belt, Burkina Faso. Journal of African Earth Sciences 39, 1–23.

Hastings, D.A., 1982. On the tectonics and metallogenesis of West Africa: a model incorporating new geophysical data. Geoexploration 20, 295–327.

Hirdes, W., Davis, D.W., 1998. First U–Pb zircon age of extrusive volcanism in the Birimian Supergroup of Ghana/West Africa. Journal of African Earth Sciences 27, 291–294.

Hirdes, W., Davis, D.W., Lüdtke, G., Konan, G., 1996. Two generations of Birimian (Paleoproterozoic) volcanic belts in north-eastern Côte d'Ivoire (West Africa): consequences for the 'Birimian controversy'. Precambrian Research 80, 173–191.

Hottin, G., Ouedraogo, O.F., 1992. Carte Géologique du Burkina Faso, second ed. Bureau de Recherches Géologique et Miniéres, Burkina Faso.

Jeambrun, M., Delfour, J., Gravost, M., 1970. Carte géologique de L'Oudalan. Bureau De Recherches Geologiques et Miniéres, Burkina Faso.

Junner, N.R., 1935. Gold in the gold coast, Ghana Geological Survey Memoir, No. 4, 67pp.

Junner, N.R., 1940. Geology of the gold coast and Western Togoland (with revised geological map). Gold Coast Geological Survey Bulletin, No. 11, 40pp.

Ledru, P., Pons, J., Milési, J.P., Feybesse, J.L., Johan, V., 1991. Transcurrent tectonics and polycyclic evolution in lower Proterozoic of Senegal-Mali. Precambrian Research 50, 337–354.

Leube, A., Hirdes, W., Mauer, R., Kesse, G.O., 1990. The early Proterozoic Birimian Supergroup of Ghana and some aspects of its associated gold mineralization. Precambrian Research 46, 139–165.

Liégois, J.-P., Claessens, W., Camara, D., Klerkx, J., 1991. Shortlived Eburnian orogeny in southern Mali. Geology, tectonics, U–Pb and Rb–Sr geochronology. Precambrian Research 50, 111–136.

Lompo, M., 2001. Le Paléoprotérozoique (Birimien) du Burkina Faso Afrique de l'Ouest Évolution crustale et concentrations aurifères. UFR/ SVT Département de Géologie, Équipes de Pétrophysique et Tectonique, Universite de Ouagadougou, 135 p.

Milési, J.P., Feybesse, J.L., Ledru, P., Dommanget, A., Ouedraogo, M.F., Marcoux, E., Prost, A., Vinchon, Ch., Sylvain, J.P., Johan, V., Tegyey, M., Calvez, J.Y., Lagny, P., 1989. West African gold deposits, in their lower Proterozoic lithostructural setting. Chronique de la Recherché Minière 497, 3–98.

Milési, J.P., Ledru, P., Ankrah, P., Johan, V., Marcoux, E., Vinchon, Ch., 1991. The metallogenic relationship between Birimian and Tarkwaian gold deposits in Ghana. Mineralium Deposita 26, 228–238.

Milési, J.P., Ledru, P., Feybesse, J.L., Dommanget, A., Marcoux, E., 1992. Early Proterozoic ore deposits and tectonics of the Birimian orogenic belt, West Africa. Precambrian Research 58, 305–344.

Naba, S., Lompo, M., Debat, P., Bouchez, J.L., Béziat, D., 2004. Structure and emplacement model for late-orogenic Palaeoproterozoic granitoids: the Tenkodogo-Yamba elongate pluton (Eastern Burkina Faso). Journal of African Earth Sciences 38, 41–57.

Navas, A.S., Reddy, B.J., Nieto, F., 2004. Spectroscopic study of chromium, iron, OH, fluid and mineral inclusions in uvarovite and fuchsite. Spectrochimica Acta Part A 60, 2261–2268.

Nikiema, S., Benkhelil, J., Corsini, M., Bourges, F., Dia, A., Maurin, J-C., 1993. Tectonique transcurrente éburnéenne au sein du craton ouest-africain: exemple du sillon de Djibo (Burkina Faso). Comptes Rendus de l'Académie des Sciences de Paris, Série II 316, 661–668.

Ouedraogo, M.F., Prost, A.E., 1986. Mise en evidence des relations entre schistosites et plissements dans la ceinture volcanique birrimienne de Yako-Batié (Burkina Faso). Comptes Rendus de l'Académie des Sciences de Paris, Série II 303, 1713–1718.

Pawlig, S., Gueye, M., Klischies, R., Schwarz, S., Wemmer, K., Siegesmund, S., 2006. Geochemical and Sr-Nd isotopic data on the Birimian of the Kedougou–Kenieba Inlier (Eastern Senegal): implications on the Palaeoproterozoic evolution of the West African Craton. South African Journal of Geology 109, 411–427.

Pons, J., Barley, P., Dupuis, D., Léger, J.M., 1995. Mechanisms of pluton emplacement and structural evolution of a 2.1 G.a juvenile continental crust: the Birimian of south western Niger. Precambrian Research 70, 281–301.

Rogers, J., Dong, F., 2000. Technical Report-Essakane Prospect, Burkina Faso, Company Report. ABOSSO Goldfields Limited, Accra, Ghana, 14 p. (unpublished).

Shanmugan, G., 1997. The Bouma sequences and turbidite mind set. Earth-Science Reviews 42, 201–229.

Sultan, L., Björklund, P.P., 2006. Depositional environments at a Palaeoproterozoic continental margin, Västervik basin, SE Sweden. Precambrian Research 145, 243–271.

Thiessen, R.L., Means, W.D., 1980. Classification of fold interference patterns: a reexamination. Journal of Structural Geology 2 (3), 311–316.

Tunks, A.J., Selley, D., Rogers, J.R., Brabham, G., 2004. Vein mineralization at the Damang gold mine, Ghana: controls on mineralization. Journal of Structural Geology 26, 1257–1273.

APPENDIX F

Regional map and cross-section (west - east across the map)

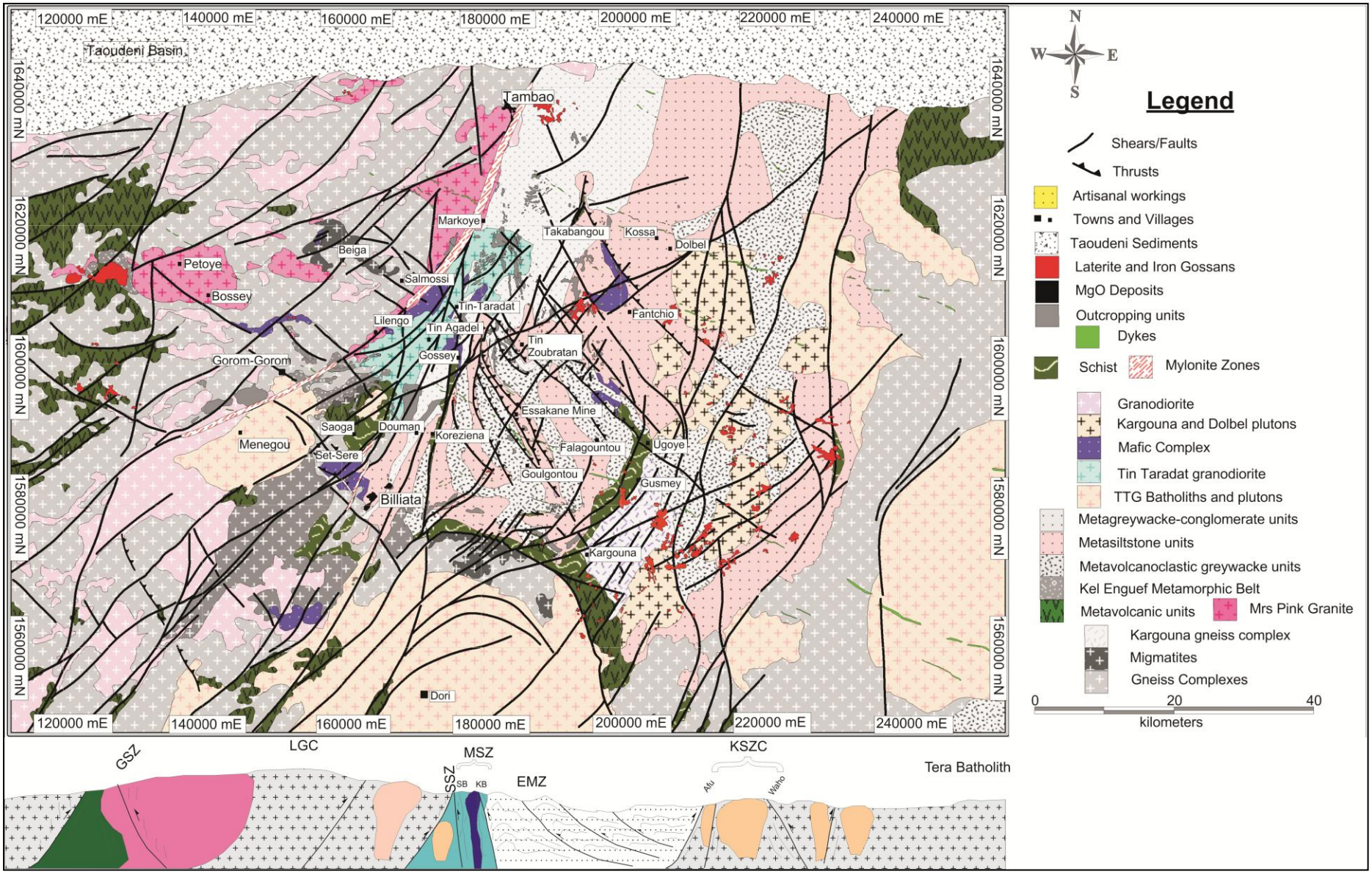
120000 mE
140000 mE
160000 mE
180000 mE
200000 mE
220000 mE
240000 mE
1640000 mN
1620000 mN
1600000 mN
1580000 mN
1560000 mN
Taoudeni Basin
Tambao
Markoye
Takabangou
Kossa
Dolbel
Beiga
Petoye
Salmossi
Bossey
Tin-Taradat
Fantchio
Lilengo
Tin Agadel
Tin Zoubratan
Gossey
Gorom-Gorom
Essakane Mine
Saoga
Douman
Koreziena
Falagountou
Ugoye
Menegou
Set-Sere
Goulgontou
Gusmey
Billiata
Kargouna
Dori
N
W
E
S
Legend
Shears/Faults
Thrusts
Artisanal workings
Towns and Villages
Taoudeni Sediments
Laterite and Iron Gossans
MgO Deposits
Outcropping units
Dykes
Schist
Mylonite Zones
Granodiorite
Kargouna and Dolbel plutons
Mafic Complex
Tin Taradat granodiorite
TTG Batholiths and plutons
Metagreywacke-conglomerate units
Metasiltstone units
Metavolcanoclastic greywacke units
Kel Enguef Metamorphic Belt
Metavolcanic units
Mrs Pink Granite
Kargouna gneiss complex
Migmatites
Gneiss Complexes
0
20
40
kilometers
GSZ
LGC
MSZ
SSZ
SB
KB
EMZ
KSZC
Afu
Waho
Tera Batholith

APPENDIX G

Data base spreadsheet file of structural measurements, lithological description, geochemical analysis results and geochronology data (CD).

APPENDIX H

The standard methods and calibration standards used at the EarthLab for ICP-MS and XRF analysis.

XRF analysis:

H.1. Major elements whole rock analysis preparation and data collection:

All major elements were analyzed for on an infinitely thick fused disk. During the preparation of the fused disks all samples were ignited at 1000 ˚C for 40 minutes and the LOI was calculated. The ignited sample was mixed with a commercially available pre-ignited flux (with composition $Li_2B_4O_7$= 47%, Li_2CO_3 = 36.7%, La_2O_3 = 16%) with a ratio of 1:5 and fired for 40 minutes at 1000 ˚C. This was then poured and pressed by a mechanical press into a fused disk.

H.1.1. Data collection:

All data collection was performed on a PANalytical PW2404 WD XRF with a Rhodium tube set at 50kV and current of 50 mA, and analysis time of 40 sec per an element and 20 sec per background. Backgrounds were measured for Si, Al, Mg, Na and P only. The Table below give specific elemental data:

Table H1: Table of specific elemental data.

Element	Analysis Line	Crystal	Collimator	Detector
Ti	Ka	LiF 200	150 µm	Flow
Ca	Ka	LiF 200	150 µm	Flow
K	Ka	PE 002-C	550 µm	Flow
Si	Ka	PE 002-C	550 µm	Flow
Al	Ka	PE 002-C	550 µm	Flow
Mg	Ka	PX 1	550 µm	Flow
Na	Ka	PX 1	550 µm	Flow
P	Ka	Ge 111-C	550 µm	Flow
Ni	Ka	LiF 220	150 µm	Duplex
Fe	Kb	LiF 220	150 µm	Flow
Mn	Ka	LiF 220	150 µm	Duplex
Cr	Ka	LiF 220	150 µm	Duplex

The elemental concentrations were obtained by comparison to 13 known standards. The standards used are: W2, GSP1, BHVO2, AGV2, G2, DTS1, PCC1, BCR2, NIM N, NIM P, NIM S, NIM D, NIM G. A synthetic internal standard was run after every 5 analyses to monitor and compensate for instrumental drift.

H.2. Trace element analysis and data collection:

All trace elements were analyzed for on an infinitely thick pressed pellet. The preparation of the pressed pellet involved an approximately 6g of sample. This was mixed with three drops of 4% commercially purchased Mowiol (polyvinyl alcohol). This mixture was then pressed under 10 ton pressure into an aluminium cup using a 40 ton press. The pressed pellet was allowed to dry for 24 hours prior to analysis.

H.2.1. Data collection:

All data collection was performed on a PANalytical PW2404 WD XRF with a Rhodium tube set at 50kV and a current of 50 mA. The instrument parameters for each element were as per Protrace recommendation.

The raw data was processed by the PANalytical software Protrace. The standards used for the calibration are the Protrace standards supplied by PANalytical. Protrace drift standards were run after every 5 analyses to compensate for instrumental drift. Internal checks were performed by analyzing known standards as unknowns and comparing to reported concentrations. The known standards used were AGV2, BHVO2, GSP2, NIM D and NIM S.

H.3. Standards used for calibration of PW2404 XRFS for silicate analysis

The X-Ray tube used is a Rhodium tube and was run at 50KV and 50 mA. The method used is by Norrish and Hutton (1969).

Table H2: Standards used for calibration of PW2404 XRFS for silicate analysis.

Standard	%Fe2O3	%MnO	%TiO2	%CaO	%K2O	%P2O5	%SiO2	%Al2O3	%MgO	%Na2O	%LOI	%Total
NIM-G	2.02	0.02	0.00	0.79	5.03	0.01	76.31	12.18	0.06	3.39	0.45	100.42
NIM-S	1.41	0.01	0.00	0.68	15.40	0.12	63.85	17.40	0.46	0.43	0.28	99.70
NIM-N	8.96	0.18	0.20	11.49	0.25	0.03	52.57	16.48	7.49	2.46	-0.40	99.83
NIM-D	16.87	0.22	0.02	0.28	0.01	0.01	38.66	0.30	43.18	0.04	-0.93	99.42
NIM-P	12.77	0.22	0.20	2.67	0.09	0.02	51.39	4.20	25.47	0.37	-0.84	96.03
AN-G	3.39	0.04	0.22	16.03	0.13	0.01	46.67	30.04	1.81	1.64	0.65	99.84
AC-E	2.54	0.06	0.11	0.34	4.51	0.01	70.63	14.76	0.03	6.57	0.37	99.53
MA-N	0.47	0.04	0.01	0.59	3.19	1.40	66.86	17.69	0.04	5.86	1.82	97.60
AGV-2	6.69	0.10	1.05	5.20	2.88	0.48	59.30	16.91	1.79	4.19	1.59	100.18
FK-N	0.09	0.01	0.02	0.11	12.88	0.02	65.37	18.71	0.01	2.59	0.54	99.82
BHVO-2	12.30	0.17	2.73	11.40	0.52	0.27	49.90	13.50	7.23	2.22	-0.71	99.53
MICA-FE	25.65	0.35	2.50	0.43	8.75	0.45	34.40	19.50	4.55	0.30	2.00	98.88

H.4. Analytical precision for major element analysis

The analysis is based on duplicate samples representing 5 calibrations.

Table H3: Analytical precision for major element analysis.

Element	Standard deviation	Absolute % error	Relative Error - %	Standard Range %
Fe2O3	0.09	-0.03	-3.7	0.09 - 26.65
MnO	0.01	-0.009	4.8	0.01 – 0.35
TiO2	0.07	-0.04	13.7	0.00 – 2.69
CaO	0.04	0.003	0.2	0.11 – 16.03
K2O	0.07	0.005	-5.6	0.01 – 15.40
P2O5	0.02	-0.02	14.2	0.01 – 1.40
SiO2	0.36	0.06	-0.09	34.40 – 76.31
Al2O3	0.07	0.07	1.3	0.30 – 30.04
MgO	0.18	-0.05	-6.1	0.03 – 43.18
Na2O	0.13	-0.05	-6.8	0.04 – 6.57
LOI	0.26	-0.21	7.1	
Total	0.58	-0.18	0.2	

H.5. Standards used for calibration of PW2404 XRFS for trace element analysis

Regression lines were calculated using SuperQ software with the De Jongh model (De Jongh, 1973) for matrix correction (α-coefficients), and a rhodium x-ray tube (4KW) was used.

Table H4: Standards used for calibration of PW2404 XRFS for trace element analysis.

Standard	ppm Rb	ppm Sr	ppm Y	ppm Zr	ppm Nb	ppm Co	ppm Ni	ppm Cu	ppm Zn	% TIO2	ppm V	ppm Cr	ppm Ba
AGV-1	67	662	21	225	15	15	17	60	88	1.06	123	12	1221
GA	175	310	21	150	12	5	7	16	80	0.38	38	12	840
GH	390	10	75	150	85	1	3	14	85	0.08	5	6	20
G-2	170	478	11	300	13	5	5	11	85	0.49	36	9	1880
NIM-G	325	10	143	300	53	0	8	12	50	0	2	12	120
NIM-S	530	62	1	20	0	3	7	19	10	0	10	12	2420
NIM-P	4	32	5	15	0	110	555	18	100	0.2	230	23950	46
NIM-N	5	260	7	14	0	58	120	14	68	0.2	220	30	102
NIM-D	0	3	0	8	0	208	2040	10	90	0.02	40	2870	10
PCC-1	0	0	0	0	1	110	2400	10	42	0.01	30	2730	1
BR	47	1320	30	250	98	52	260	72	160	2.6	235	380	1050
BHVO-1	11	403	28	179	19	45	121	136	105	2.71	317	289	139
MAG-1	149	146	28	126	12	20	53	30	130	0.75	140	97	479
SGR-1	83	420	13	53	5	12	29	66	74	0.26	128	30	290
SCO-1	112	174	26	160	11	11	27	29	103	0.63	131	68	570
QLO-1	74	336	24	185	10	7	6	29	61	0.62	54	3	1370

STM-1	118	700	46	1210	268	1	3	5	235	0.14	9	4	560
RGM-1	149	108	25	219	9	2	4	12	32	0.27	13	4	807
SDC-1	127	183	40	290	18	18	38	30	103	1.01	102	64	630
DR-N	73	400	28	125	8	35	15	50	145	1.09	220	42	385
GS-N	185	570	19	235	21	65	34	20	48	0.68	65	55	1400
MICA-FE	2200	5	50	800	270	23	35	5	1300	2.5	135	90	150
MICA-MG	1300	27	0	20	120	24	110	4	290	1.63	90	100	4000
FK-N	860	39	0	13	0	16	3	2	10	0.02	3	5	200
BX-N	10	110	114	520	58	35	190	18	75	2.37	310	290	34
DT-N	5	27	10	370	0	12	16	9	28	1.4	150	240	130
UB-N	6	10	3	8	0	100	2000	28	85	0.11	75	2300	30
GXR-1	14	259	0	38	1	8	41	1110	760	0.06	76	13	680
GXR-2	78	160	17	269	11	9	21	76	530	0.5	52	36	2240
GXR-3	92	950	15	63	2	43	60	15	207	0.17	42	19	5000
GXR-4	160	221	14	186	10	15	42	6520	73	0.48	87	64	1640
GXR-6	90	35	14	110	8	14	27	66	118	0.83	186	96	1300
GSP-1	254	234	29	530	26	7	10	34	103	0.66	53	13	1310
MA-N	3600	84	1	27	173	1	3	140	220	0.01	5	3	42
AN-G	0	76	8	15	2	25	35	19	20	0.22	70	50	34

H.6. Analytical precision for trace element analysis

The analysis represents 5 calibrations.

Table H5: Analytical precision values for trace element analysis.

Element	LLD-ppm	Standard deviation	Absolute error-ppm	Relative Error - %
Rb	3	2	1.0	-1.9
Sr	3	2	1.3	0.4
Y	3	2	-0.7	-3.7
Zr	8	3	4.3	1.2
Nb	3	1	-2.4	-8.5
V	12	9	-3.8	-12.7
Cr	12	7	0.7	5.2
Co	6	2	0.7	-10.7
Ni	6	2	0.6	-9.3
Cu	6	5	1.9	-0.3
Zn	6	2	2.8	-6.2
Ba	20	7	12.0	3.1
Pb	10	2	3.1	
As	15	2	4.7	

APPENDIX I

Geochemical analysis results (XRF and ICP-MS)

Table I1: Table of results for XRF analysis for samples collected for U-Pb geochronological study.

	SiO2	Al2O3	Fe2O3	FeO	MnO	MgO	CaO	Na2O	K2O	TiO2	P2O5	Cr2O3	NiO	TOTAL
BF_1144	71.33	14.28	0.37	3.01	0.06	1.35	3.99	3.9	1.17	0.5	0.14	0	0	100.1
BF_1145	71.17	16.1	0.17	1.39	0.03	0.77	2.21	5.66	2.24	0.26	0.11	0	0	100.1
BF_1146	79.09	11.36	0.15	1.25	0.04	0.14	0.54	3.75	4.14	0.1	0.02	0	0	100.56
BF_1147	73.84	12.78	0.34	2.74	0.08	0.84	2.49	3.39	3.17	0.53	0.1	0	0	100.3
BF_1149	75.44	14.25	0.1	0.78	0.05	0.25	1.23	4.41	3.97	0.1	0.04	0	0	100.62
BF_1153	55.36	18.9	0.84	6.77	0.13	3.01	7.44	3.86	2.58	0.97	0.45	0.01	0	100.32
BF_1154	53.14	9.1	1.16	9.38	0.22	16.19	8.14	2.46	0.15	0.4	0.12	0.14	0.04	100.65
BF_1156	71.93	15.82	0.16	1.3	0.02	0.62	2.5	5.67	1.86	0.24	0.09	0.01	0	100.19
BF_1157	77.66	11.77	0.22	1.75	0.05	0.14	0.63	3.83	3.93	0.16	0.02	0.01	0	100.15
BF_1160	78.43	12.11	0.09	0.76	0.02	0.11	0.31	3.77	4.85	0.09	0.01	0	0	100.56
BF_1162	54.99	19.46	0.77	6.26	0.11	2.78	7.26	4.28	2.48	1.02	0.56	0.01	0	100
BF_1322	76.48	12.99	0.15	1.19	0.05	0.28	1.1	4.37	3.45	0.17	0.03	0	0	100.25
BF_1324	76.95	12.8	0.15	1.22	0.04	0.26	0.96	4.41	3.54	0.18	0.04	0	0	100.55
BF_1332	53.72	13.59	1.57	12.73	0.21	4.66	8.32	2.88	1.04	1.66	0.19	0.01	0.01	100.59
BF_1333	63.57	15.89	0.51	4.17	0.08	2.86	4.95	4.17	2.56	0.49	0.22	0.01	0	99.49
BF_1367	56.78	15.57	0.86	6.96	0.14	6.28	7.72	2.96	2	0.69	0.23	0.05	0.01	100.27
BF_1368	68.82	14.95	0.41	3.35	0.08	1.45	3.25	3.92	3.4	0.48	0.16	0	0	100.29
BF_1369	75.93	11.84	0.23	1.89	0.05	0.13	0.92	3.73	4.28	0.17	0.02	0	0	99.18

Table I2: Table of whole rock trace element analysis in ppm for all samples collected for U-Pb geochronology.

	Sc	V	Cr	Co	Ni	Cu	Zn	Ga	Rb	Sr	Y	Zr	Nb	Mo	Ba	Pb	Th	U
BF_1144	7.5	51.6	9.9	9.0	11.6	28.9	43.4	15.7	27.6	308.3	12.1	120.5	7.8	0.5	309.2	2.0	4.8	0.7
BF_1145	1.6	2.6	1.1	2.4	3.9	4.4	80.4	20.7	96.8	57.8	73.6	300.5	17.2	1.5	950.6	11.3	4.4	3.1
BF_1146	0.1	5.1	5.5	3.0	1.9	5.8	66.5	20.5	123.1	38.7	77.1	188.7	21.6	0.8	731.7	13.6	6.1	2.2
BF_1147	4.4	41.1	1.4	8.7	6.1	16.4	27.7	14.7	54.5	281.5	33.1	274.4	18.6	1.2	625.4	0.9	1.6	1.7
BF_1149	2.0	3.8	0.7	2.7	2.8	5.0	25.6	18.0	122.6	289.0	11.6	76.1	5.4	0.6	675.5	13.1	3.9	3.9
BF_1153	18.8	159.4	85.3	30.9	33.8	119.6	76.9	19.8	77.1	620.7	16.9	171.3	7.1	2.2	647.3	6.9	3.7	1.7
BF_1154	30.6	140.0	933.9	69.2	282.0	6.5	82.7	9.0	2.7	128.5	14.4	45.8	3.0	0.9	49.9	0.6	0.2	1.0
BF_1156	0.9	18.8	0.6	5.3	2.0	11.0	41.6	19.8	34.2	1059.0	3.1	120.2	0.5	0.5	773.7	6.8	1.6	4.0
BF_1157	1.6	18.7	8.9	8.4	5.4	7.4	48.2	22.0	55.0	1107.4	4.8	143.0	1.6	0.3	949.6	10.2	3.1	4.8
BF_1160	15.7	110.2	67.4	26.2	22.2	116.0	77.3	22.5	77.2	630.2	20.3	198.9	8.9	3.0	539.9	7.4	6.7	5.0
BF_1162	27.8	326.5	20.6	55.0	41.4	86.6	109.0	23.6	34.1	281.0	22.2	130.5	7.0	1.4	265.6	4.0	8.0	1.3
BF_1322	1.1	4.3	4.6	2.7	3.5	5.4	23.4	11.7	101.4	89.2	24.9	116.3	11.5	0.2	624.3	7.2	4.1	2.6
BF_1324	2.1	5.2	0.3	3.4	3.7	4.0	23.2	12.8	106.0	80.9	32.9	125.1	14.8	1.1	621.3	13.0	5.9	2.7
BF_1332	1.3	0.9	5.6	1.7	2.1	3.0	16.3	11.9	67.4	18.7	5.3	69.1	2.4	1.0	551.6	7.2	3.4	0.5
BF_1333	0.2	1.1	0.9	1.2	3.3	6.0	83.4	22.2	66.9	70.5	81.8	295.8	17.1	1.4	955.9	8.2	6.4	0.9
BF_1367	21.0	136.2	305.0	38.0	99.5	56.0	70.8	15.7	54.4	519.9	16.6	113.6	6.7	1.3	537.3	8.1	9.3	0.3
BF_1368	12.2	57.7	18.0	13.6	7.5	16.0	52.3	16.9	108.2	384.5	18.7	139.4	6.2	0.2	630.6	11.0	5.0	3.7
BF_1369	5.3	45.3	33.4	8.8	10.5	9.6	48.0	18.1	74.7	538.6	8.0	96.8	4.2	0.0	772.6	11.6	7.6	1.5

Table I3: Table of ICP-MS analytical data from the samples collected for U-Pb geochronology.

	BF 1144	BF 1145	BF 1146	BF 1147	BF 1149	BF 1153	BF 1154	BF 1156	BF 1157	BF 1160	BF 1162	BF 1322	BF 1324	BF 1332	BF 1333	BF 1367	BF 1368	BF 1369
Li	12.46	13.855	23.995	3.716	76.732	17.815	6.953	20.830	30.166	14.698	15.858	26.799	12.189	3.413	2.583	13.918	15.499	37.889
P	847.91	110.358	94.157	576.58	220.962	2695.321	508.907	345.881	463.037	2400.164	786.305	100.199	120.221	23.254	55.473	1060.568	662.851	500.946
Sc	6.802	3.99	2.741	6.781	3.303	16.581	36.248	2.172	2.967	11.210	31.787	2.466	3.690	0.752	3.199	20.025	6.566	4.508
Ti	3391.555	1154.158	658.737	3343.786	711.346	6988.68	2041.157	1150.528	1279.905	4903.129	9187.307	755.843	792.838	406.273	763.347	3047.172	2198.168	1869.419
V	73.128	1.533	0.714	43.818	5.949	156.345	144.636	16.800	16.726	104.913	328.197	5.497	5.026	0.508	0.987	132.929	49.976	40.199
Cr	49.181	3.273	2.87	37.838	4.64	87.722	1014.170	5.030	7.843	54.939	24.882	2.025	1.654	1.273	1.961	248.435	14.982	28.189
Co	12.299	1.206	1.173	8.785	1.812	31.194	71.612	3.367	4.017	17.023	49.103	1.798	1.675	0.732	1.027	23.845	8.731	7.891
Ni	90.603	4.318	5.526	52.552	12.842	32.347	278.320	8.783	11.069	54.459	49.231	6.166	6.496	7.480	5.989	94.577	12.551	15.982
Cu	33.155	3.12	6.489	23.42	14.066	153.288	11.104	9.239	6.892	91.380	90.301	3.038	3.785	2.568	2.314	46.203	12.345	9.626
Zn	42.62	86.462	75.707	42.699	52.369	87.971	75.984	42.326	48.649	54.373	104.425	26.241	29.476	27.586	69.104	46.453	47.485	46.379
Ga	12.235	26.733	24.941	13.599	23.23	25.097	10.403	19.738	20.345	13.898	20.203	11.893	12.244	10.646	18.612	10.200	14.988	16.005
As	0.177	0.247	0.35	0.276	0.092	1.431	0.770	0.058	0.069	1.136	0.615	0.058	0.071	0.068	0.140	1.051	0.244	1.314
Rb	21.04	124.195	154.108	34.6	150.521	63.687	1.527	28.093	42.426	41.459	26.587	74.053	93.173	60.400	59.576	29.746	54.872	31.907
Sr	291.972	77.89	45.475	270.904	385.57	796.367	136.746	1017.729	983.015	517.699	264.883	72.793	74.827	17.033	63.622	439.387	332.947	437.545
Y	18.173	111.025	106.201	43.795	15.7	23.815	17.222	3.977	5.105	17.223	27.312	25.049	33.216	6.573	91.105	16.001	17.254	7.626
Zr	142.006	459.357	261.103	357.616	100.97	223.78	45.078	122.718	134.597	152.292	132.364	95.899	89.932	77.489	256.507	90.831	130.451	92.268
Nb	10.789	25.368	31.994	23.303	8.086	9.996	2.056	1.542	2.245	9.139	5.784	13.215	16.466	2.055	17.584	4.765	7.378	4.425
Ba	248.396	1256.951	786.204	507.838	935.736	752.623	50.297	>8000	827.194	378.339	254.677	537.419	654.695	567.318	>8000	381.969	451.107	472.696
Sn	1.222	4.971	3.726	4.768	4.942	3.512	0.656	1.161	1.893	1.710	1.586	2.257	2.122	0.519	2.511	1.156	1.733	1.554
Cs	0.36	2.489	5.197	0.963	6.161	0.972	0.167	1.352	1.654	0.949	1.238	1.341	1.834	0.160	0.243	1.632	2.644	2.691
La	24.77	72.712	43.602	30.913	18.781	31.133	6.792	12.757	18.107	22.890	13.788	26.495	31.980	38.258	46.407	14.244	17.498	12.740
Ce	36.164	169.488	107.111	75.086	36.996	76.469	14.324	29.152	40.539	42.732	31.446	63.434	70.901	78.005	98.063	23.229	43.777	30.313
Pr	5.636	20.803	13.262	12.234	4.027	8.168	2.229	3.486	4.685	5.886	4.486	6.889	8.276	8.865	13.720	3.823	4.400	3.044
Nd	19.995	83.577	53.992	47.945	14.337	32.76	9.445	13.489	18.129	22.133	20.024	24.876	29.702	30.786	56.724	15.220	16.619	11.315
Sm	3.4	18.735	13.587	9.428	3.232	6.382	2.042	3.055	4.095	4.179	5.071	4.844	5.900	4.062	13.479	3.340	3.434	2.432

Eu	1.111	2.715	1.661	2.003	1.022	1.935	0.546	1.070	1.318	1.222	1.594	0.982	1.121	0.996	2.200	1.076	0.995	0.894
Gd	3.349	19.586	14.947	8.78	2.697	6.043	2.253	2.115	2.983	3.955	5.352	4.842	5.901	3.838	14.598	3.094	3.421	2.146
Tb	0.476	3.199	2.613	1.322	0.396	0.797	0.367	0.213	0.293	0.530	0.848	0.682	0.859	0.355	2.448	0.452	0.479	0.258
Dy	2.668	19.227	16.745	7.429	2.37	4.265	2.342	0.868	1.173	2.877	5.027	3.982	5.199	1.464	15.335	2.655	2.793	1.383
Ho	0.528	3.975	3.631	1.471	0.499	0.84	0.510	0.129	0.159	0.563	1.001	0.831	1.099	0.245	3.227	0.538	0.576	0.262
Er	1.558	11.165	10.377	4.154	1.514	2.354	1.489	0.378	0.449	1.609	2.660	2.516	3.312	0.789	9.002	1.542	1.698	0.765
Tm	0.252	1.746	1.715	0.653	0.258	0.35	0.236	0.040	0.043	0.234	0.394	0.415	0.551	0.090	1.423	0.236	0.271	0.109
Yb	1.658	10.773	10.75	4.079	1.736	2.211	1.596	0.280	0.293	1.535	2.450	2.771	3.716	0.608	8.674	1.538	1.831	0.766
Lu	0.259	1.643	1.637	0.615	0.267	0.336	0.251	0.037	0.035	0.228	0.362	0.435	0.579	0.094	1.290	0.227	0.278	0.115
Hf	3.438	13.214	10.899	8.558	3.054	5.499	1.279	3.103	3.258	3.523	3.597	3.226	3.173	2.431	8.466	2.364	3.670	2.644
Ta	1.006	1.86	2.697	1.554	0.823	0.613	0.112	0.095	0.099	0.542	0.388	1.362	1.656	0.073	1.262	0.289	0.630	0.442
W	0.02	0.735	2.089	0.188	0.103	0.719	0.233	0.019	0.027	0.741	0.383	0.216	0.431	0.029	0.281	0.406	0.249	0.353
Pb	2.792	13.441	16.752	3.606	23.071	15.015	1.159	11.004	13.505	7.672	4.316	8.695	13.318	9.508	9.853	4.679	10.199	15.608
Th	2.197	7.553	7.471	4.596	4.585	4.526	0.509	2.021	2.877	3.297	1.868	4.320	5.408	2.750	5.226	1.876	4.367	3.668
U	0.166	2.535	2.98	1.487	1.217	2.147	0.189	0.825	0.857	1.198	0.632	1.559	1.879	0.284	1.529	0.649	2.051	1.670

APPENDIX J

The chondrite meteorite normalising values after Anders and Grevesse (1989).

Solar-System Abundances of the Elements, Based on Meteorites (Atoms/1E6 Si)										
Element		This Work [*]	Anders and Ebihara (1982) [*]	s (%)	N [1]	Mean Cl Chondr. [2]		Orgueil [3]		N
1	H	2.79E+10	2.72E+10					2.02	%	2
2	He	2.72E+09	2.18E+09					56	nL/g	
3	Li	57.1	59.7	9.2	4	1.5	ppm	1.49	ppm	3
4	Be	0.73	0.78	9.5	8	24.9	ppb	24.9	ppb	0
5	B	21.2	24	10	1	870	ppb	870	ppb	1
6	C	1.01E+07	1.21E+07					3.45	%	7
7	N	3.13E+06	2.48E+06					3180	ppm	4
8	O	2.38E+07	2.01E+07	10				46.4	%	4
9	F	843	843	15	7	60.7	ppm	58.2	ppm	5
10	Ne	3.44E+06	3.76E+06	14				203	pL/g	
11	Na	5.74E+04	5.70E+04	7.1	20	5000	ppm	4900	ppm	14
12	Mg	1.074E+06	1.075E+06	3.8	15	9.89	%	9.53	%	11
13	Al	8.49E+04	8.49E+04	3.6	19	8680	ppm	8690	ppm	13
14	Si	1.00E+06	1.00E+06	4.4	9	10.64	%	10.67	%	4
15	P	1.04E+04	1.04E+04	10	4	1220	ppm	1180	ppm	3
16	S	5.15E+05	5.15E+05	13	5	6.25	%	5.25	%	2
17	Cl	5240	5240	15	10	704	ppm	698	ppm	8
18	Ar	1.01E+05	1.04E+05	6				751	pL/g	7
19	K	3770	3770	7.7	29	558	ppm	566	ppm	20
20	Ca	61100	61100	7.1	15	9280	ppm	9020	ppm	12
21	Sc	34.2	33.8	8.6	18	5.82	ppm	5.83	ppm	12
22	Ti	2400	2400	5	7	436	ppm	436	ppm	7

23	V	293	295	5.1	9	56.5	ppm	56.2	ppm	7
24	Cr	13500	13400	7.6	13	2660	ppm	2660	ppm	9
25	Mn	9550	9510	9.6	20	1990	ppm	1980	ppm	12
26	Fe	9.00E+05	9.00E+05	2.7	19	19.04	%	18.51	%	14
27	Co	2250	2250	6.6	18	502	ppm	507	ppm	12
28	Ni	4.93E+04	4.93E+04	5.1	27	1.1	%	1.1	%	21
29	Cu	522	514	11	8	126	ppm	119	ppm	5
30	Zn	1260	1260	4.4	27	312	ppm	311	ppm	17
31	Ga	37.8	37.8	6.9	14	10	ppm	10.1	ppm	10
32	Ge	119	118	9.6	31	32.7	ppm	32.6	ppm	23
33	As	6.56	6.79	12	18	1.86	ppm	1.85	ppm	13
34	Se	62.1	62.1	6.4	18	18.6	ppm	18.2	ppm	11
35	Br	11.8	11.8	19	18	3.57	ppm	3.56	ppm	10
36	Kr	45	45.3	18				8.7	pL/g	7
37	Rb	7.09	7.09	6.6	19	2.3	ppm	2.3	ppm	13
38	Sr	23.5	23.8	8.1	18	7.8	ppm	7.8	ppm	15
39	Y	4.64	4.64	6	5	1.56	ppm	1.53	ppm	4
40	Zr	11.4	10.7	6.4	5	3.94	ppm	3.95	ppm	5
41	Nb	0.698	0.71	1.4	2	246	ppb	246	ppb	2
42	Mo	2.55	2.52	5.5	2	928	ppb	928	ppb	2
44	Ru	1.86	1.86	5.4	9	712	ppb	714	ppb	5
45	Rh	0.344	0.344	8	7	134	ppb	134	ppb	0
46	Pd	1.39	1.39	6.6	25	560	ppb	556	ppb	17
47	Ag	0.486	0.529	2.9	6	199	ppb	197	ppb	5
48	Cd	1.61	1.69	6.5	30	686	ppb	680	ppb	21
49	In	0.184	0.184	6.4	24	80	ppb	77.8	ppb	16
50	Sn	3.82	3.82	9.4	11	1720	ppb	1680	ppb	9
51	Sb	0.309	0.352	18	22	142	ppb	133	ppb	15
52	Te	4.81	4.91	10	17	2320	ppb	2270	ppb	12
53	I	0.9	0.9	21	11	433	ppb	433	ppb	0

54	Xe	4.7	4.35	20				8.6	pL/g	6
55	Cs	0.372	0.372	5.6	20	187	ppb	186	ppb	11
56	Ba	4.49	4.36	6.3	8	2340	ppb	2340	ppb	8
57	La	0.446	0.448	2	4	234.7	ppb	236	ppb	9
58	Ce	1.136	1.16	1.7	4	603.2	ppb	619	ppb	8
59	Pr	0.1669	0.174	2.4	20	89.1	ppb	90	ppb	2
60	Nd	0.8279	0.836	1.3	4	452.4	ppb	463	ppb	11
62	Sm	0.2582	0.261	1.3	4	147.1	ppb	144	ppb	10
63	Eu	0.0973	0.0972	1.6	4	56	ppb	54.7	ppb	17
64	Gd	0.33	0.331	1.4	4	196.6	ppb	199	ppb	7
65	Tb	0.0603	0.0589	2.2	21	36.3	ppb	35.3	ppb	4
66	Dy	0.3942	0.398	1.4	4	242.7	ppb	246	ppb	6
67	Ho	0.0889	0.0875	2.4	23	55.6	ppb	55.2	ppb	3
68	Er	0.2508	0.253	1.3	4	158.9	ppb	162	ppb	6
69	Tm	0.0378	0.0386	2.3	20	24.2	ppb	22	ppb	1
70	Yb	0.2479	0.243	1.6	4	162.5	ppb	166	ppb	12
71	Lu	0.0367	0.0369	1.3	4	24.3	ppb	24.5	ppb	12
72	Hf	0.154	0.176	1.9	3	104	ppb	108	ppb	3
73	Ta	0.0207	0.0226	1.8	2	14.2	ppb	14	ppb	1
74	W	0.133	0.137	5.1	3	92.6	ppb	92.3	ppb	3
75	Re	0.0517	0.0507	9.4	21	36.5	ppb	37.1	ppb	15
76	Os	0.675	0.717	6.3	16	486	ppb	483	ppb	12
77	Ir	0.661	0.66	6.1	36	481	ppb	474	ppb	27
78	Pt	1.34	1.37	7.4	10	990	ppb	973	ppb	9
79	Au	0.187	0.186	15	41	140	ppb	145	ppb	27
80	Hg	0.34	0.52	12		258	ppb	258	ppb	0
81	Ti	0.184	0.184	9.4	18	142	ppb	143	ppb	12
82	Pb	3.15	3.15	7.8	3	2470	ppb	2430	ppb	1
83	Bi	0.144	0.144	8.2	13	114	ppb	111	ppb	7
90	Th	0.0335	0.0335	5.7	9	29.4	ppb	28.6	ppb	1

92	U	0.009	0.009	8.4	16	8.1	ppb	8.1	ppb	7

[*] Abundances of Mg, S, and Fe are based on average of mean values for individual meteorites. For the remaining elements, a straight average of all acceptable analyses was used.
[1] Dashes indicate solar or interpolated abundances; parentheses mean that the abundance is based at least in part on meteorites of other classes.
[2] Cl chondrite mean (for Si = 10.64%) is calculated from the atomic abundances in column 2, using the relation C = 3.788 x 1E-3 HA, where C = weight concentration (ppm), H = atomic abundance, and A = atomic weight. However, these values have not been renormalized to 100%.
[3] Abundances of HCNO in Orgueil are from sources given in Anders and Ebihara (1982). Abundances of noble gases (in nL/g or pL/g at STP) are not for the elements but for the principal isotopes He4, Ne20, Ar36, Kr84, Xe132 (J2; Mazor et al., 1970). As He and Ne in bulk Orgueil are derived mainly from the solar wind, the indigenous values for these two are based on ratios for NaOH-etched Orgueil silicates: Ne20/Ar36 = 0.27 and He4/Ne20 = 277(J2).

APPENDIX K

R1-R2 plutonic chemical variation diagram

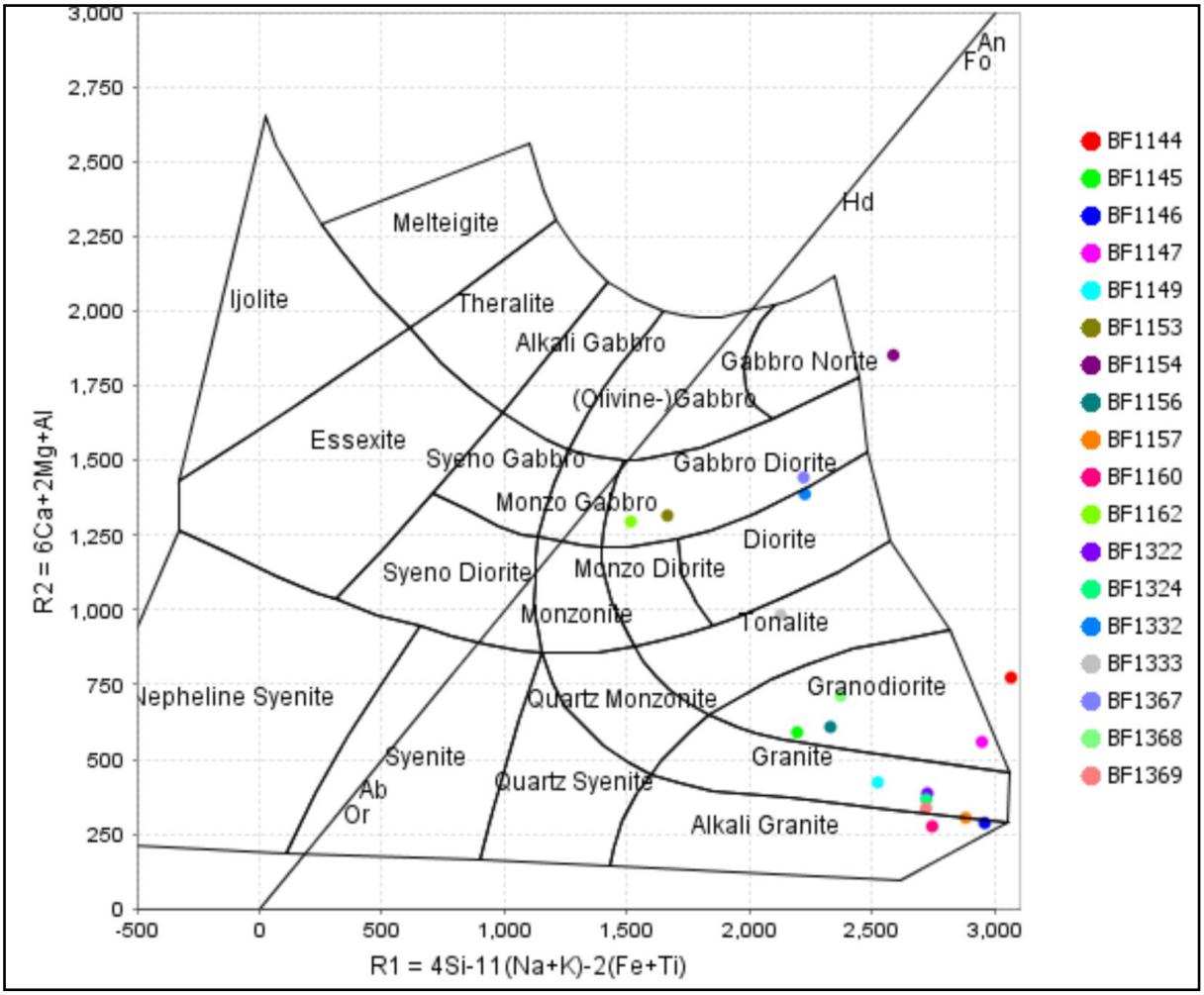

APPENDIX L

TAS Diagram

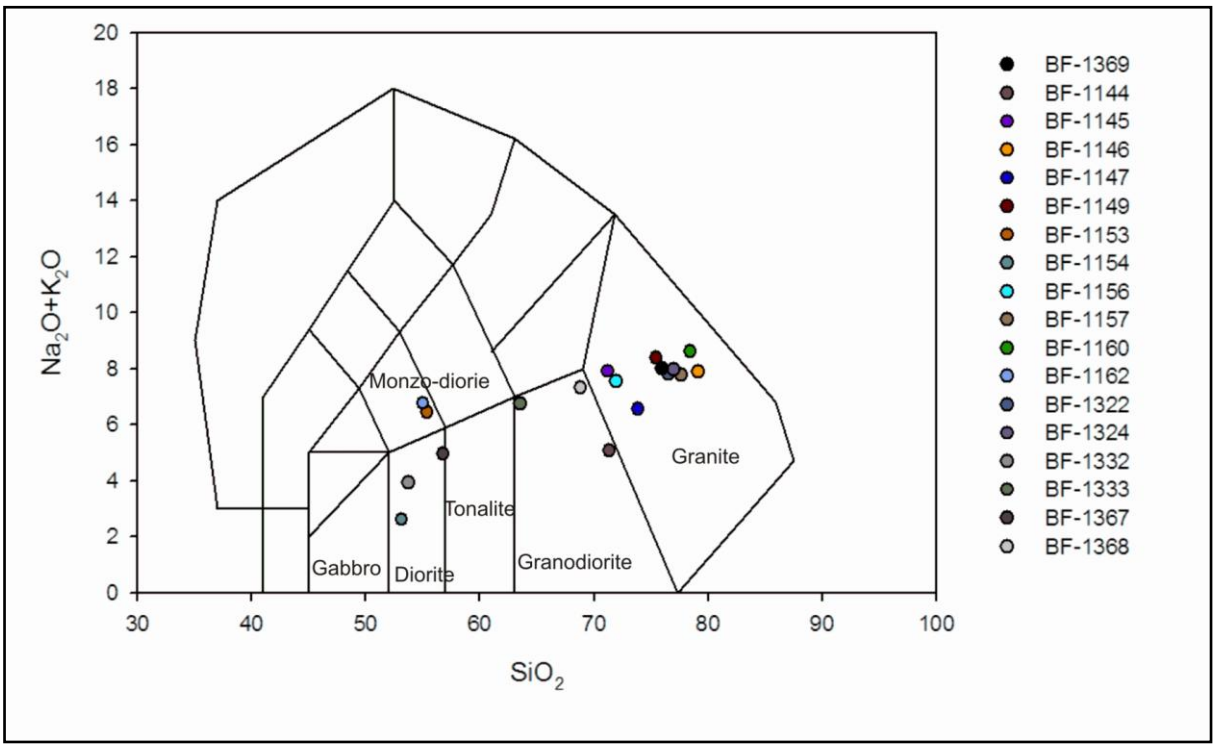

Alkaline/Sub alkaline classification diagram